4D laboratory experiments of oblique extension and scissor tectonics, structural inheritance and sedimentation: implications for rift evolution, rift propagation and rift segment interaction

Inauguraldissertation
Der Philosophisch-naturwissenschaftlichen Fakultät
der Universität Bern

vorgelegt von

Frank Zwaan

von den Niederlanden

Leiter der Arbeit:
Prof. Dr. Guido Schreurs
Institut für Geologie

4D laboratory experiments of oblique extension and scissor tectonics, structural inheritance and sedimentation: implications for rift evolution, rift propagation and rift segment interaction

Inauguraldissertation
Der Philosophisch-naturwissenschaftlichen Fakultät
der Universität Bern

vorgelegt von

Frank Zwaan

von den Niederlanden

Leiter der Arbeit:
Prof. Dr. Guido Schreurs
Institut für Geologie

Von der Philosophisch-naturwissenschaftlichen Fakultät angenommen

Bern, 03 November 2017   Der Dekan:
                                   Prof. Dr. G. Colangelo

The correct citation is:

Zwaan, F. 2017. 4D laboratory experiments of oblique extension and scissor tectonics, structural inheritance and sedimentation: implications for rift evolution, rift propagation and rift segment interaction. PhD Thesis, University of Bern, Switzerland.

Bern, October 2017

The author
Frank Zwaan

The promotor
Prof. Dr. Guido Schreurs

An appropriate quote to start with

"Nada se edifica sobre la piedra, todo sobre la arena,
pero nuestro deber es edificar como si fuera piedra la arena…"*
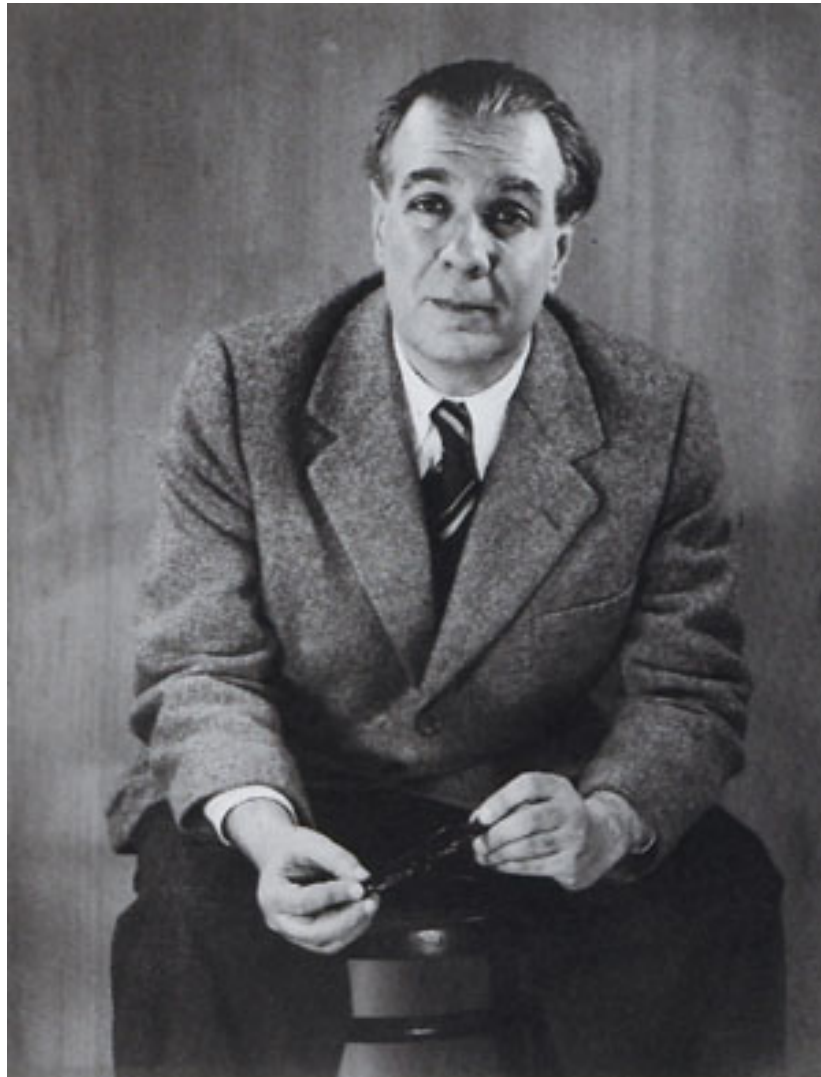

Photo: Grete Stern (1951)

Jorge Luis Borges

From the poem: "Fragmentos de un evangelio apócrifo" in: "Elogio de la sombra" (1969)

* "Nothing is built on stone; all is built on sand,
but we must build as if the sand were stone…"

Acknowledgements

Dear reader,

The work you have now before you might take you some hours to read. Yet it represents 4 years of my work and life in Bern. It has been a long and eventful road, along which I learned many new things, got to know many kind and interesting people, visited many an exciting city and/or geological site had in general a lot of fun.

First of all, I should thank my PhD supervisor Guido Schreurs for setting up this project and getting it funded by the Swiss National Science Foundation (SNF). Guido has always kindly provided me with the necessary support and advice to get the job done. But he also gave me the freedom me pursue my own ideas and designs, creating a very pleasant working environment, which I highly appreciated.

Next I owe much to my good friend Olivier Prevost-Bouré, a fellow and student at the *Université Rennes 1* in France, where we both followed the first year of the Master *Sciences de la Terre* (as part of my joint degree at the *Vrije Universiteit Amster-dam*). It was he who notified me of this position in Bern, as he was looking for a PhD position but knew analogue modelling was not exactly his cup of tea. Yet he knew me well enough to realize this would be the perfect place for me.

At the time I was working on my MSc Thesis at Shell Oil Company back in the Netherlands and although the project itself was higly interesting and even worth a publication, I was missing the university environment. So when Olivier's email came in, I immediately sent a message to Guido whether the position was still open. Luckily it was, so I submitred an application. The next thing I knew I flew to Basel with a cheap Easyjet flight and took a horribly expensive SBB/CFF/FFS train to Bern. After a visit of the institute, Guido and I had a good lunch at the *Kornhauskelle*r, where he explained the project and offered me the position. Thus the adventure began.

Getting the project "analogue modelling of oblique extension" of the ground took me some time as the beautiful "Namazu" sandbox machine, designed and built during the PhD project of my predecessor Matthias Klinkmüller, harboured some tenacious defects that needed solving. With generous financial support from Marco Herwegh and the technical expertise from IPEK Rapperswil (Reto Gwerder, Rudolf Kamber, Michael Ziltener, Christoph Zolliker and Prof. Theodor Wüst) the machine, now baptized "Namazu" after the earthquake-causing catfish from Japanese mythology, was much improved and ready for some tectonic action. Simultaneously, Claude Grau started a BSc Thesis at IPEK, involving the design of a new and unique machine, the "Xissor", to model scissor tectonics and rift propagation. This machine was also assembled by the engineers from IPEK, with SNF funding and additional financial support from Marco Herwegh and The Berne University Research Foundation.

Meanwhile, Susanne Buiter and John Naliboff, two numerical modellers from the Geological Survey of Norway, invited Guido and me to the land of the Norse. Between the fieldtrips, exploring the amazing landscapes and geology, we planned a combined effort to model rift segment interaction under oblique extension conditions. The result is my first article and I cannot thank Guido, John and Susanne enough for their help writing and correcting the manuscript to get it ready for publication. Also my second paper is a spin-off of this initial undertaking, and we are currently planning further analogue-numerical comparisons of extensional tectonics. It is safe to say that this international collaboration has been a crucial factor for my first cautious steps into the business of science.

Furthermore, this project involved a lot of traveling. For various interesting CUSO-courses I visited many beautiful Swiss cities and regions. Further trips with the university also improved my rudimentary understanding

of Alpine geology, but the institute excursions to Iceland and Albania* were truly amazing experiences that I shall never forget. I should also thank Guido for sending me on many conferences in Switzerland, around Europe and the world. Presenting my results and discussing with other scientists was unbelievably valuable to improve the quality of my work and to develop new concepts and ideas. The trip to San Francisco was something special, which also led to a fruitful collaboration with fellow PhD candidate Jakub Fedorik and his chef Giovanni Toscani from the University of Pavia. A 2014 conference in London allowed me to meet Jürgen Adam, who helped us to analyse and quantify our CT data in high detail for my third paper.

Talking about CT-scanning, let me express my gratitude to Nicole Schwendener from the forensic department, without whom X-Ray CT-scanning of the analogue models would not have been possible. Nicole was always kind and willing to squeeze in a model run in her schedule. Although I was sometimes afraid she might be sick and tired of watching our sandbox, she was always cheerful, reading some exciting *Krimi* (possibly to compensate for the lack of crime in Bern?) during the long hours in the scanning facility.

I must also mention the people from GFZ Potsdam (Malte Ritter, Tasca Santimano, Mattias Rosenau and Robert Gentzmann) who helped us to test our various viscous silicone-sand mixtures with their advanced rheometers, which greatly improved the model quality. Also Kirsten Busse, who let me experiment with her 3D surface scanning equipment, should not be forgotten.

Of course, I should also thank everybody who I shamelessly exploited to move the Namazu machine from the first floor of our institute to the CT-scanning room at the other side of the Baltzerstrasse. These include not only the occupants of Awesome Office 011 (my office mates Emilie Axellson, Mariia Naumenko-Dèzes, Lena Thöle, Alessandro Maltese, Jisuk Kang) or the Fancy Fellows (the numerous PhD students who I dare not list here, lest I forget someone). Many others, students and professors alike, bore the combined burden of

at least 120 kg of steel, machine, sand and silicone on the slippery Bernese stairs.

These people were also instrumental in having the necessary fun in Bern. We spent many an evening in the Parterre and the notorious Goal Bar, watching the Champions League, the 2014 World Cup and the 2016 European Cup. But also various tasty diners, housewarmings, movie evenings, (Fancy) Friday Beers, hikes in the Alps and swimming in the Aare made life in Bern worth living. I should also thank the 3rd years BSc students for organizing the *Chlouse Fest* every year, a worthy tradition.

Life in the small, slightly odd but amusingly diverse *Confoederatio Helvetica* allowed me to improve my German and French as well, languages being another interest of mine. Now I am working on my Italian for the (Christmas) visits to Tiziana's *famiglia Ticinese* in the Swiss *Sonnestube*. Tiziana's moral and gastronomical support pulled me through the last hot summer months of frantic writing, and we are hoping to spend some years in *la bella Italia* after I finish this PhD project.

Yet in spite of all the foreign adventures, I highly appreciated returning to the North Sea coast once in a while, as the fresh mountain air sometimes becomes a bit too much and one needs a bit of a proper sea breeze and a meal of healthy saltwater fish. Visiting friends and family back home, who always warmly welcomed me with generous amounts of good food, interest in my endeavours, enjoyable chats and merry drinks, made me realize once more that whatever exciting attractions the wide world might offer, the place I grew up in will always have something special.

At the moment however, life is good and the future seems bright, thanks to all the people who helped me on the path towards the completion of this project these past four years. I could not have done it alone, so a big thank you to you all: *hartelijk dank; vielen Dank; merci vielmals; grazie mille; merci beaucoup; muchas gracias; дуже дякую; tusen tack; d'akujem pekne; falemenderit þakka þér fyrir!*

<div align="right">

Frank Zwaan
Bern, October 2017

</div>

* www.geo-albania.jimdo.com

Table of contents

CHAPTER 3

HOW OBLIQUE EXTENSION AND STRUCTURAL INHERITANCE INFLUENCE RIFT SEGMENT LINKAGE: INSIGHTS FROM 4D ANALOG MODELS 81

CHAPTER 4

EFFECTS OF SEDIMENTATION ON RIFT SEGMENT AND TRANSFER ZONE EVOLUTION IN ORTHOGONAL AND OBLIQUE EXTENSION SETTINGS: INSIGHTS FROM ANALOGUE MODELS ANALYSED WITH 4D X-RAY CT AND DIGITAL VOLUME CORRELATION TECHNIQUES 107

CHAPTER 8

Abstract

Extension of the continental lithosphere leads to the formation of continental rift basins. When extension persists, continental break-up and oceanic spreading ensue, creating conjugate passive margins on both sides of a new oceanic basin. Rifts and passive margins have been intensely studied by geologists because of their vast hydrocarbon potential, representing the bulk of the global proven oil and gas resources and are of great importance for human society, housing a considerable share of the world's population. Passive margins, as their name suggest represent the remainders of a successful rifting event leading to continental break-up and have since ceased to experience active extension. In contrast, many continental rifts are still actively deforming. These rift basins are prone to various types of natural hazards but also provide economic opportunities for geothermal energy production.

However, despite the numerous geological studies, the complex tectonic evolution and structural frameworks of rifts and passive margins remain poorly understood; most rifts and passive margins have experienced oblique extension and/or scissor extension as well as the reactivation of pre-existing structures and significant syn-tectonic sedimentation during their history.

The aim of this Thesis, funded by the Swiss National Science Foundation and carried out at the University of Bern, is to improve our understanding of rifting processes using state-of-the-art analogue model experiments. These analogue models simulate the development and propagation of young continental rifts and the interaction between individual rift segments in the context of oblique extension and scissor extension settings, and aslo investigates the role of structural inheritance and sedimentation on the system. In addition, this thesis includes a comparison of various experimental methods involving foam, rubber and base plate set-ups, commonly used for simulations of extensional tectonics. The models are among others analysed with cutting-edge X-Ray computed tomography (XRCT or CT) and digital volume correlation (DVC) techniques for unparalleled 4D visualisation and quantification of internal model evolution.

The experimental method comparison illustrates that structural inheritance is key to focus deformation leading to rift development. In the rubber and foam base set-ups, a viscous basal layer facilitates localization as it buffers distributed deformation, and reduces coupling, allowing the brittle cover to behave as rigid blocks, whereas it prevents the strong and probably exaggerated concentration of faulting along the edge of the base plates that develops in the rigid plate models. The experiments illustrate furthermore that the standard brittle-ductile foam set-up with a seed focussing deformation produces the least amount of boundary effects and is thus respresents best of the set-ups tested for studies of rift basin development. A rubber base setting could in theory be similarly efficient, yet a rubber or foam sidewall will be necessary to reduce boundary effects. The brittle-ductile base plate models for instance develop too much friction along the sidewalls, a problem that may be solved with the use of a lubricant.

Various factors are shown to be of influence on the evolution of a rift basin. Firstly, the application of a linear viscous seed, simulating a linear weak zone in the upper crust, produces a narrow rift basin, where previous authors have often applied wider patches of viscous material or rubber sheets to create a wider rift zone. Furthermore, the rate of extension is shown to control the degree of brittle-ductile coupling, either producing a localized rift along the seed or multiple rift basins throughout the model. Also the amount of extension determines the type of structures present in a rift: a small amount of extension only results in minor deformation along the boundary faults whereas a large amount of extension produces additional faulting within the rift wedge, accompanied by a rising viscous layer. The amount of extension itself

is depends on the degree of extension obliquity, as increasing oblique extension resutls in progressively narrower basins, with steeper boundary faults and oblique internal structures.

Moreover, along-strike variations in extension rate in both time and space may lead to a complex structural configuration, as illustrated by scissor extension models. It appears that such gradients in the rate (and thus amount) of extension are a crucial factor controlling rift propagation.

A final influence on rift basin development is syn-rift sedimentation. The presence of sediments in the rift basin does not affect the initial rift configuration set by large-scale tectonic forces, but its additional weight does influence the structural style within the rift basin, concentrating deformation along a set of major faults instead of a myriad of minor faults and causing increased total subsidence, preventing the viscous layer from rising. High syn-rift sediment influx might even delay continental break-up, but larger-scale plate tectonic processes determine whether a continent is actually broken up in the end.

Most of the factors that influence the evolution of individual rift segments, affect the interaction and linkage between them as well. For instance, a weak seed may localize deformation, but a high extension rate and associated brittle-ductile coupling results in the development of multiple rift basins with little amounts of extension in each, limiting their capacity to interact. Instead, low extension rates focus deformation in a single rift, allowing it to propagate and interact with other segments.

Furthermore, the models illustrate that large rift offsets hinder rift linkage, especially when the extension direction is such that the segments propagate parallel to each other or even apart, although in some cases a strike-slip transfer zone may develop. The interplay between initial seed geometry and extension direction proves to be a crucial factor for rift linkage establishment.

Within this context, secondary structural weaknesses, connecting the main rifts, are of minor importance and are only activated when oriented favourably to the regional extension direction. Syn-rift sedimentation, although of importance for internal rift structures, does not significantly affect the large-scale rift linkage zone formation, especially since these zones experience relatively little subsidence, thus less accommodation space is available for sediment deposition. In contrast to the situation with large-scale rift structures, along-strike extension gradients associated with scissor extension have no strong impact on rift interaction zones, since the extension gradient between the two rift segments is generally minor.

Although top view photographs and CT data allow a thorough insight into the 3D external and internal model evolution, 4D DVC analysis has provided an unprecedented understanding of 3D internal displacement and deformation within the brittle and viscous parts of the models. These results illustrate the strong difference between brittle and viscous behaviour, the sand acting as rigid blocks interrupted by discrete zones of faulting, floating on the viscous layer that shows a distributed flow pattern. Not only does the DVC analysis capture the rising viscous material beneath the rift basins, it also reveals out-of-plane motion of both brittle and viscous material due to interacting rift segments. This last observation is crucial for 2D structural reconstructions of orthogonal extension settings, as both viscous and brittle material can move out of section.

The models are compared with natural examples of continental rifts and rift interaction structures, resembling various structures observed in e.g. the East African Rift System, the North Sea Viking Graben and the Cenozoic European Rift System. However, a comparison with previous models and natural examples also shows a reasonable fit with the geometries of oceanic spreading centres, suggesting that these brittle-viscous set-ups can also be used for the modelling of mid-oceanic ridge settings.

13

Outline of this Thesis

The work presented in this Thesis is organized in a series of individual chapters. Two of these (Chapters 2-3) are already published in international peer review journals whereas; Chapter 4 is currently accepted with minor revisions. Chapters 5-7 describe recent projects and are intended to serve as a basis for three further publications. Chapter 1 introduces the general topics covered by this Thesis, whereas Chapter 8 provides a general summary and conclusions. The topics of the various chapters and the contributions of the individual co-authors are specified below.

<div align="center">

\- Chapter 1 -

General introduction

</div>

This first chapter defines the objectives and research questions to be addressed by this Thesis. It provides information on oblique extension and scissor tectonics with respect to the development and propagation of individual rift basins and their interaction, as well as the importance of structural inheritance and syn-rift sedimentation within a tectonic system. Subsequently an outline of the general methodological approach, including a background of analogue modelling and the motivation for the additional theme (comparing set-ups for experiments of extension tectonics) is given. Also the different experimental machines and set-ups used for this study are described, as well as the various methods applied to analyse the experiments.

<div align="center">

\- Chapter 2 -

Insights into the effects of oblique extension on continental rift interaction from 3D analogue and numerical models

by

Frank Zwaan, Guido Schreurs, John Naliboff and Susanne J.H. Buiter

Published in Tectonophysics (2016)

</div>

This chapter presents a study describing the results of analogue and numerical models of interacting and connecting rift segments under various degrees of oblique extension. This is an important topic, since oblique extension conditions are common in nature and the interaction of rift segments defines the evolution of a rift system towards potential continental break-up. On a smaller scale, rift interaction structures influence the migration of melts and hydrocarbons, and provide structural traps for potential reservoirs as well. X-ray computed tomography (XRCT or CT) techniques allow a unique assessment of the 3D internal evolution of analogue models and a qualitative comparison with the numerical experiments. The first author carried out the analogue experiments and their analysis, and composed the first version of the manuscript. Third author John Naliboff provided the numerical models and their analysis. Together with the second and fourth authors Guido Schreurs and Susanne Buiter, who supervised the analogue and numerical project components of the collaboration, John played a crucial role in planning the experimental set-ups, discussing the data and preparing the final version of the manuscript.

<div align="center">14</div>

- Chapter 3 -

How oblique extension and structural inheritance influence rift segment linkage: Insights from 4D analog models

by

Frank Zwaan and Guido Schreurs

Published in Interpretation (2017)

This third chapter is devoted to a series of analogue experiments focussing on the influences oblique extension and structural inheritance can have on the evolution of rift interaction structures and is in a sense a continuation of the model series presented in Chapter 2. The incorporation of structural inheritances in the models reflects the important control pre-existing weaknesses can have on structures developing during subsequent tectonic phases, whereas the greater range of extension directions (now with both dextral and sinistral extension) are features observed in various regions around the world. Using CT-scanning techniques enables a thorough 4D analysis of the internal model structures. The first author performed the analogue experiments and prepared the first version of the manuscript. The second author and project supervisor (Guido Schreurs) assisted in planning the models, discussing the results and writing the final version of the manuscript.

- Chapter 4 -

Effects of sedimentation on rift segment and transfer zone evolution in orthogonal and oblique extension settings: insights from analogue models analysed with 4D X-ray computed tomography and digital volume correlation techniques

by

Frank Zwaan, Guido Schreurs and Jürgen Adam

Accepted with minor revisions by Global and Planetary Change

This chapter focuses on syn-rift sedimentation and how it might influence rift evolution and rift interaction structures by means of analogue experiments. The topic is of importance since it is recognized that loading and unloading due to surface processes such as erosion and sedimentation may strongly influence the evolution of tectonic systems. The use of CT techniques not only allows a 4D model analysis, but also the application of digital volume correlation (DVC) analysis, revealing displacements within the model and allowing a unparalleled quantification of internal deformation. The first author performed the laboratory experiments, processed the CT data for the subsequent DVC analysis, carried out by third author Jürgen Adam, and drafted the first version of the manuscript. Both the second author and project supervisor Guido Schreurs, who had postulated the topic of this study, and the third author helped in discussing the experimental data and preparing the manuscript for submission.

- Chapter 5 -

Rift propagation under orthogonal and scissor extension conditions: insights from analogue models analysed with 4D X-ray computed tomography

by

Frank Zwaan and Guido Schreurs

In preparation

This chapter compares analogue models of rift propagation processes in either standard orthogonal extension settings or scissor extension settings, involving block rotation and along-strike extension gradients. Although scissor extension deformation is common in nature, most numerical and analogue modellers do not incorporate this feature in their experiments. Thus a systematic comparison study was initiated in order to determine the differences between rift propagation in both tectonic systems. The project comprises the design and construction of a new, custom-designed analogue modelling apparatus and state-of-the-art CT- and surface scanning techniques are used to trace the 3D external and internal model evolution. The first author, who drafted the first version of this manuscript, carried out the models and their analysis. The second author, project supervisor Guido Schreurs, provided aid to interpret the model results and to finalize the current version of the manuscript.

- Chapter 6 -

Evolution of rift linkage zones in orthogonal and scissor extension settings: insights from analogue models analysed with 4D X-ray computed tomography

by

Frank Zwaan and Guido Schreurs

In preparation

This sixth chapter provides a comparison between the evolution of rift interaction processes in either orthogonal extension settings or scissor extension settings. The importance of this effort lies in the observation that scissor extension is a common feature in nature, while analogue and numerical modellers often ignore this factor in their studies. Therefore, a systematic study is necessary to distinguish the differences these tectonic boundary conditions might have on interacting rift segments that define the development of a rift system. The new apparatus used for the experiments in Chapter 5 is also applied in this project and CT analysis enable a full 3D structural evolution analysis. The first author, who wrote the first version of the manuscript, carried out the models and their analysis. The second author Guido Schreurs, in his role as project supervisor supported the project by helping with the interpretation of the experimental data and the completion of this manuscript.

- Chapter 7 -

Comparing different crustal-scale analogue extension model set-ups using X-ray computed tomography (XRCT) techniques

by

Frank Zwaan, Guido Schreurs, John Naliboff, Susanne J. H. Buiter and Jürgen Adam

In preparation

This chapter presents a comparison study between a variety of different experimental set-ups commonly used for modelling crustal-scale extensional tectonics, in order to have a systematic overview of the different deformation mechanisms and the structures they produce. Selected models are CT-scanned, which allows not only a 3D internal analysis of the model evolution, but also a detailed quantification of internal deformation by means of cutting-edge DVC analysis so that these models can ultimately serve as benchmarks for a detailed analogue-numerical modelling comparison study. The first author performed the analogue models and composed the first version of the manuscript. Second author and project supervisor Guido Schreurs assisted the model interpretation and the finalizing of the current manuscript. This study was inspired by the previous collaboration with third and fourth authors John Naliboff and Susanne Buiter (Chapter 2), who were indispensible for planning the model series. Fifth author Jürgen Adam contributed a preliminary DVC analysis of one of the models.

- Chapter 8 -

Conclusion and Outlook

This last chapter provides a summary of the results of this Thesis and describes potential opportunities for future research projects in the field of analogue modelling of (extensional) tectonics in general and at the University of Bern Tectonic Laboratory specifically.

Chapter 1

General Introduction

1.1. Objectives and motivation

Extension of the continental lithosphere leads to the formation of continental rift basins. When extension persists, continental break-up and oceanic spreading ensue, creating conjugate passive margins on both sides of a new oceanic basin. Rifts and passive margins have been intensely studied by geologists beacause of their vast hydrocarbon potential, representing the bulk of the global oil and gas resources (Mann *et al*. 2003), and are of great importance for human society, housing a considerable share of the world's population.

Passive margins, as their name suggest represent the remainders of a successful rifting event leading to continental break-up and have since ceased to experience active extension. In contrast, many continental rifts are still actively deforming. Striking examples are found in the East African Rift System (EARS, e.g. Ebinger 2005; Corti 2009).

Active rift basins are prone to various types of natural hazards (earthquakes, volcanism etc., e.g. Keir *et al*. 2006; Ebinger *et al*. 2010), but also provide economic opportunities for geothermal energy production, already a major energy source in Iceland (Lund & Boyd 2016), due to an enhanced geothermal gradient. Further geothermal potential can be found in the Ethiopian Rift (e.g. Minissale *et al*. 2017 and references therein) and closer to home in the Rhine Graben (Bruel 2002).

However, despite the numerous geological studies, the complex tectonic evolution and structural frameworks of rifts and passive margins remain poorly understood. Not only the vast scales of these systems complicates detailed investigation, but also the fact that most rifts and passive margins have experienced oblique extension and/or scissor extension (Dewey 1975; Dewey *et al*. 1998; Brune *et al*. 2012, Philippon & Corti 2016, Fig. 1.1), the reactivation of pre-existing structures (Morley *et al*. 1990; Nelson *et al*. 1992; Bonini *et al*. 1997; Autin et al. 2013) and significant syn-tectonic sedimentation (e.g. Martín-Barajas *et al*. 2013) during their history.

This project, funded by the Swiss National Science Foundation (SNF Grant nr. 200012_ 147046) and carried out at the University of Bern, aims to improve our understanding of rifting processes using state-of-the-art laboratory experiments. These analogue models, of which a complete overview is provided in Appendix VIII, simulate the development and propagation of young continental rifts and the interaction between individual rift segments in the context of oblique extension and scissor extension settings, as well as the role of structural inheritance and sedimentation on the system. An additional theme involves the systematic testing of a wide range of analogue set-ups commonly used for extensional tectonic models, but of which no standardized comparison has been published to date. The models are among others analysed with cutting-edge X-Ray computed tomography (XRCT or CT) and digital volume correlation (DVC) techniques for unparalleled 4D visualisation and quantification of internal model evolution.

In the following paragraphs of this General Introduction, an overview of the simulated tectonic settings and associated structures is provided, describing the detailed motivation for every theme treated in this Thesis, as well as a description of the analogue modelling methodology, including the back-ground of tectonic modelling and its purpose in geosciences, the different experimental machines and set-ups used in the course of this study as well and the various model techniques applied for the analysis of the various laboratory experiments.
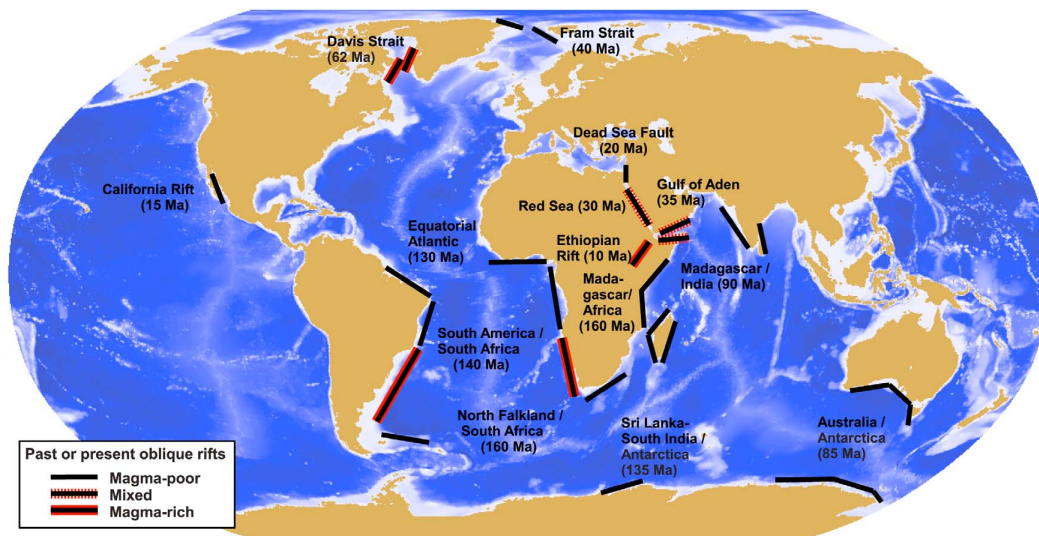
Fig. 1.1. *Overview of obliquely rifted conjugate margins and presently active oblique rifts. Numbers indicate approximate times of rift initiation. Magma-rich margins and rifts are indicated in red, magma-poor margins and rifts in black. If some segments of the same rift are magma-rich and other magma-poor the rift type is designates as mixed. Modified after Brune et al. (2012).*

1.2. Oblique extension

In contrast to orthogonal extension, which implies stretching perpendicular to a developing structure (e.g. a rift basin), oblique extension involves stretching at an angle α with the normal to the strike of the structure, which itself is often aligned to pre-existing structural weaknesses inherited from a preceding tectonic phase (e.g. Withjack & Jamison 1986; Morley *et al*. 1990; Bonini *et al*. 1997; Fig. 1.2). Since extension is rarely orthogonal to the structural trend, and can change over time due to plate tectonic rearrangements or due to the irregular geometries of the world's tectonic plates, most if not all rifts and passive margins have experienced some degree of oblique extension during their development, as pointed out by Dewey (1975) and Dewey *et al*. (1998).

Oblique extension has a distinct influence on fault patterns on the crustal scale, of which examples are found in for instance the North Sea (Erratt *et al*. 1999), Lake Baikal (Delvaux *et al*. 1997) and the Ethiopian Rift in the EARS (e.g. Corti 2008, Corti 2009, Fig. 1.1). These oblique extension structures are amongst others characterized by en echelon rift boundary fault systems oriented at an angle to the extension direction, with intra-rifts faults developing perpendicular to the extension direction (e.g. McClay *et al*. 2002; Erbello *et al*. 2016; Philippon & Corti 2016).

Various authors have modelled oblique extension tectonics, providing crucial insights into the evolution of the complex fault structures as well as the relationships between the main boundary faults and their intra-rift counterparts (e.g. Dauteuil & Brun 1993; McClay & White 1995; Amilibia *et al*. 2005; Agostini *et al*. 2009; Autin *et al*. 2010). Further models have for instance focused on oblique extension and rift asymmetry (Van Wijk 2005), multiphase oblique rifting (Bonini *et al*. 1997). Recent lithospheric-scale simulations have shown how oblique stretching may promote continental break-up, since oblique deformation requires less force to reach the plastic yield limit than orthogonal extension (Brune *et al*. 2012; Bennet & Oskin 2014) and the associated rapid thinning of the lithopshere likely promotes magmatism (Keir *et al*. 2015). However, an important feature of oblique extension systems that has been neglected in most studies is represented by rift interaction structures (Paragraph 1.3).
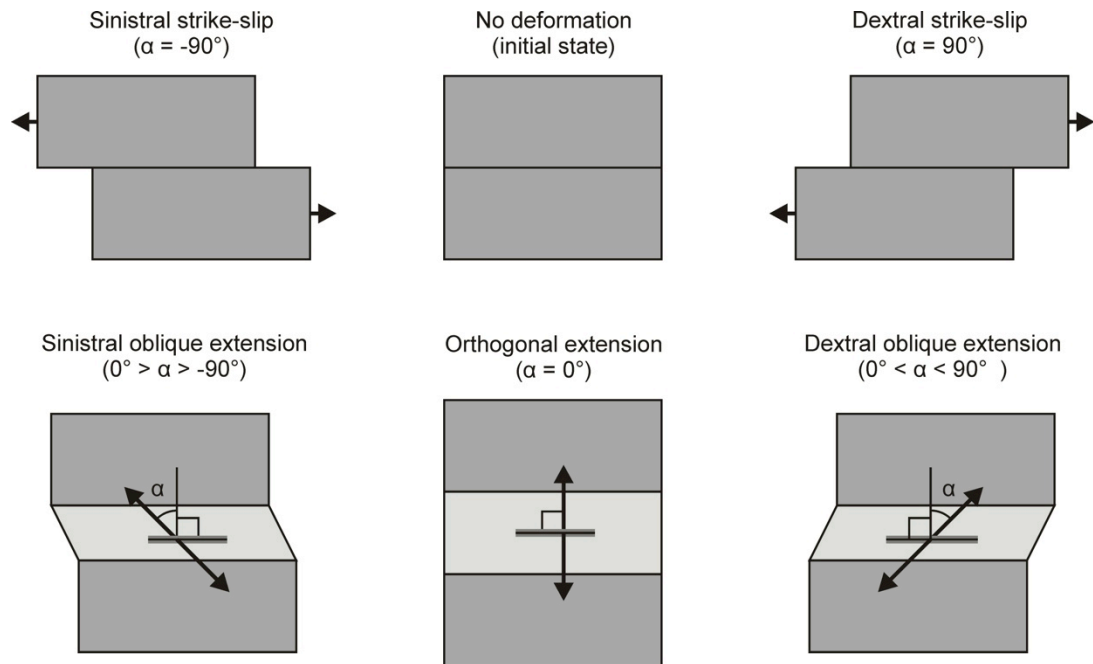
Fig. 1.2. *Definition of oblique extension and strike-slip deformation. Extension direction is defined by angle α, which is 0° during orthogonal extension and -90° and 90° for sinistral and dextral strike-slip motion, respectively. Oblique extension plots between these end members: 0° > α > -90° and 0° < α < 90° for sinistral and dextral oblique extension, respectively.*

1.3. Rift interaction structures

During the initial phases of continental extension, early faulting often nucleates along inherited structural weaknesses. Since these structural inheritances are not always properly aligned, the resulting rift basins, sometimes with very different structural styles, interact and link up with each other as part of a coherent dynamic rift system, for instance in the East African Rift System, the North Sea rift province and the Utah Canyonlands (Fossen *et al*. 2010; Corti 2012, Fig. 1.3a, b).

A wide range of such rift interaction structures occurs in nature and previous authors have proposed various classifications schemes (e.g. Rosendahl 1987; Larsen, 1988; Childs *et al*. 1995; Faulds & Varga 1998). In this work however, a simplified distinction is adopted, between accommodation zones, involving a gradual distribution of deformation between overlapping fault segments or transfer zones, which contain continuous faults connecting both rift basins (Fig. 1.3c, d).

Previous studies have shown that the evolution of rift linkage structures is strongly controlled by the presence and geometries of structural inheritances that may be reactivated during rifting (Mauduit & Dauteuil, 1996; Acocella *et al*. 1999a) or melts (Minor *et al*. 2013). Furthermore, factors such as extension rates and crustal rheology have a strong control on what type of structure may develop (Allken *et al*. 2011, 2012).

Developing rift interaction structures are known to influence fault patterns and fault evolution and thus seismic activity (Faulds & Varga 1998; Gupta & Scholz 2000). The intricate structures that form due to rift segment interaction affect hydrocarbon migration and provide trapping opportunities (Morley *et al*. 1990; Nelson *et al*. 1992; Coskun 1997; Fossen *et al*. 2010). Evolving rift interaction zones also modify drainage patterns and subsequent sedimentation and potential hydrocarbon reservoir distributions

21

in rift basins (Roberts *et al*. 1990). Furthermore, volcanic activity in active rifts is often concentrated at rift interaction zones (Lambiase & Bosworth, 1995; Acocella *et al*. 1999b; Corti *et al*. 2004, Fig. 1.4b).

An important part of the above insights are derived from analogue and numerical simulations. However, these models often only consider orthogonal extension during rift interaction, whereas the effects of both oblique extension and scissor extension on the development of rift interaction structures have been generally neglected to date. Here lies an interesting opportunity for further experimental studies since these types of extension are common in the geological record as described in the previous paragraphs. This topic is pursued in Chapters 2-4, which include various degrees of dextral and sinistral oblique extension, and in Chapter 6, which involves rift interaction in scissor extension conditions. Chapters 3 and 4 also incorporate the effects of secondary structural inheritances, whereas Chapter 4 investigates the influence of syn-rift sedimentation on rift linkage as well.
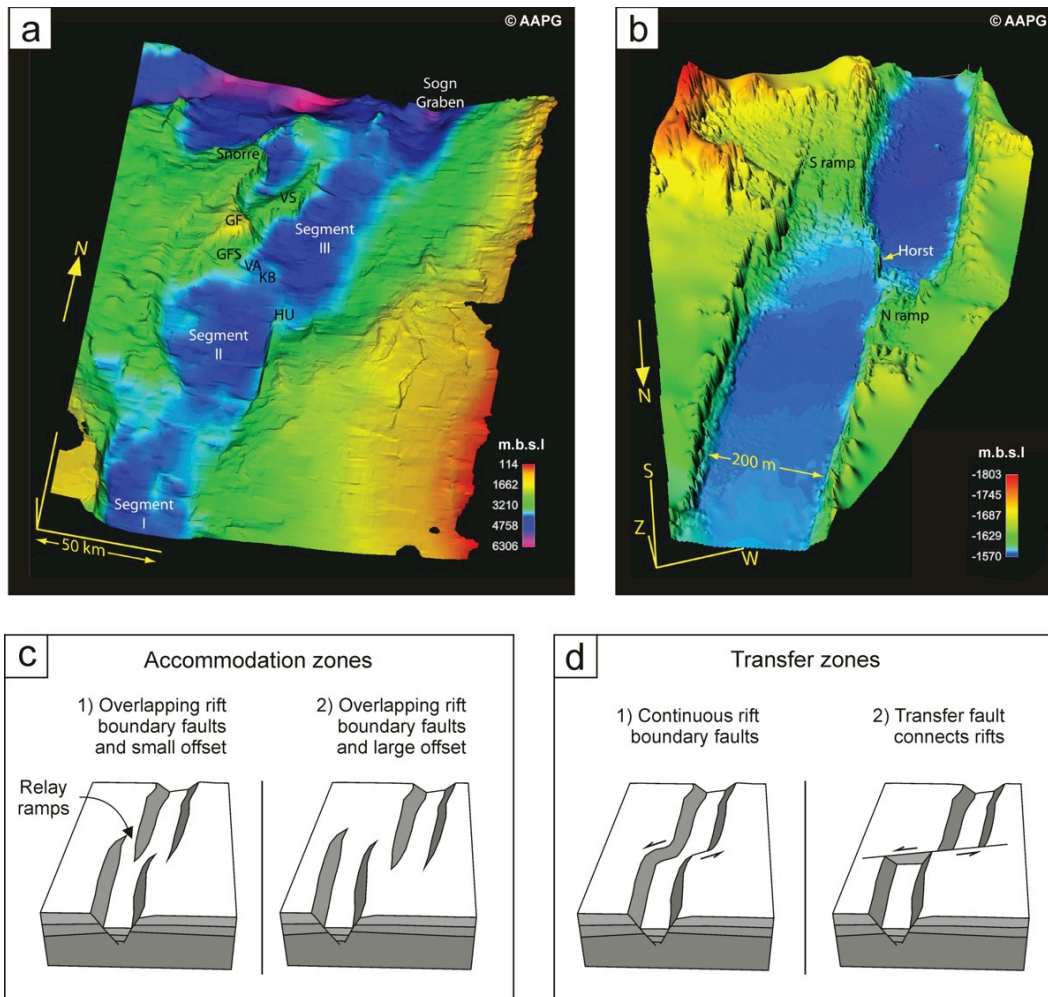
Fig. 1.3. *Natural examples of rift interaction structures. (a-b) Northern part of the right-stepping Viking Graben system (a) and the Devils Lane stepover, Canyonlands, Utah (b). Note the high areas and relay ramps at graben stepovers, associated with oil and/or gas fields in the case of the Viking Graben (GF, GFS, HU, KB, VS and VA). m.b.s.l. = meters below sea level. Modified after Fossen et al. (2010), AAPG© 2010 and reprinted with permission of the AAPG whose permission is required for further use. (c, d) Definition of rift interaction structures as applied in this work. (c) Accomodation zones, in which soft linkage occurs through overlapping fault segments. (d) Transfer zones, in which hard linkage through continues fault structures develops.*

1.4. Structural inheritance: character and geometries

As observed in the previous sections, structural inheritance can play a crucial role in the tectonic development since early deformation tends to localize along the weakest part of the system (Dunbar & Sawyer 1988; Versfelt & Rosendahl 1988; Morley *et al*. 1990; Nelson *et al*. 1992; Corti 2012). These initial structures have a strong influence on the subsequent tectonic evolution (e.g. Bonini *et al*. 1997; Keep & McClay 1997).

Many types of structural inheritance occur in nature, which can be divided in either pervasive or discrete structures (Morley 1999). Pervasive structures exist throughout a geological body, commonly cleavage, schistosity or gneissic foliation, causing strength anisotropies within the specific rock volume. Discrete structures on the other hand, represent a localized plane or zone, i.e. faults or shear zones, of which the strength is lower than that of the surrounding rock.

Such structural weaknesses are formed during a preceding tectonic phase and are often reactivated when tectonic activity continues or resumes. During reactivation, they can locally modify the regional state of stress, thus reorienting or deflecting developing structures (Bell 1996).

Examples in compressional systems include (partial) reactivation of passive margin normal faults in the Alps and Apennines (e.g. Butler *et al*. 2006; Turrini *et al*. 2016). Within extensional domains, structural inheritance is known to have influenced the North Sea rifts, where the Caledonian structural grain was reactivated during a Triassic rift episode, as well as during a Jurassic-Early Cretaceous rift phase (Bartholomew *et al*. 1993; Rattey & Hayward 1993). The structural inheritance caused the oblique opening of various en echelon rift basins in with rift interaction zones in between (Erratt *et al*. 1999, Fig. 1.3a). Similar structures are observed for instance in the Gulf of Suez (McClay & Khalil 1998), the East African Rift System (Corti 2012), the Rio Grande Rift and the Rhine-Bresse Transfer Zone (Fig. 1.4).
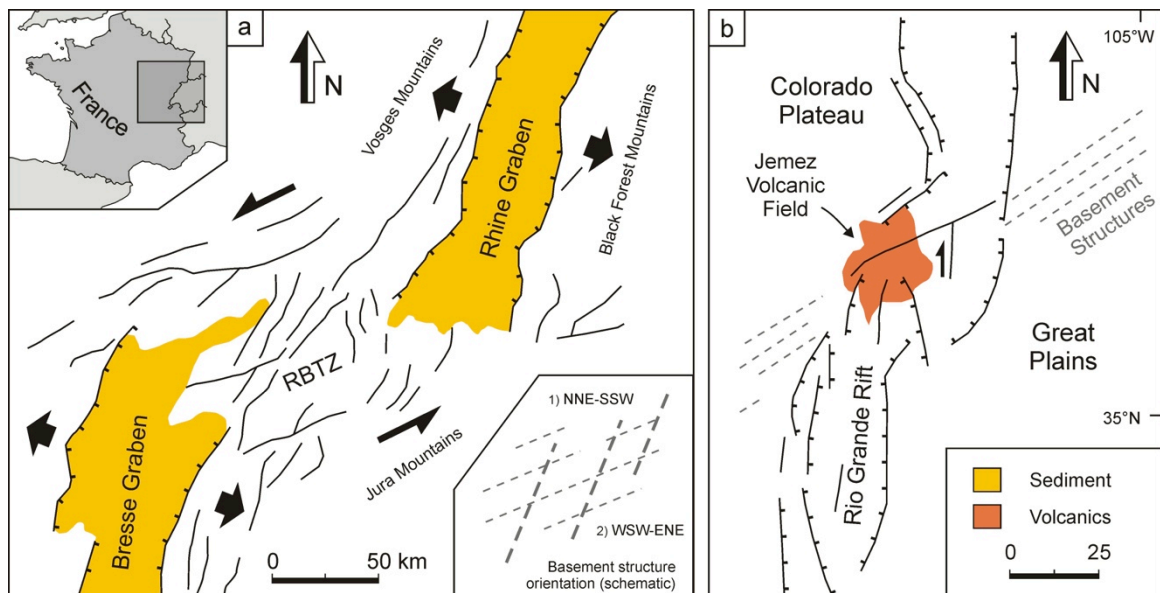
Fig. 1.4. *Natural examples of rift interaction zones influenced by a secondary structural grain (a) Rhine-Bresse Transfer Zone (RBTZ) between the Rhine Graben and Bresse Graben in eastern France. Image modified after Illies (1977) and Ustaszewski et al. (2005). (b) Santo Domingo Relay (SDR) within the Rio Grande Rift (USA). Image modified after Aldrich (1986) and Minor et al. (2013). Hatched lines represent normal faults; the character of faults without motion indications are not specified in the original publications.*

23

In the latter cases, a secondary structural inheritance is observed as well, along which the rift interaction zone is formed. On the other hand, previous studies have also shown that inherited structures are not always reactivated: during post-rift compression of inversion of rift basins, new thrust faults may form while the existing rift boundary faults remain largely inert (Nalpas *et al*. 1995; Brun & Nalpas 1996; Panien *et al*. 2005).

The geometries of pre-existing discrete crustal structures influencing rift evolution, with which this Thesis is concerned, may be classified as follows (Fig. 1.5): They may be continuous, forming a straight and un-interrupted linear weakness, or discontinuous with a length L. Discontinuous structures can either end completely (Fig. 1.5b) or continue with an offset (Fig. 1.5c-g). This offset

geometry can involve underlap or underlap (Fig. 1.5c or 1.5e), described by the angle ϕ (Acocella *et al*. 1999a). When no over- or underlap is involved (ϕ = 90°), a "staircase" offset occurs (Fig. 1.5 d). Another factor is the offset distance, which can be expressed as H (equal to the thickness of the brittle crust, which together with fault angle β controls the rift geometry, Allemand & Brun 1991, Fig. 1.5f, inset). With the value H, natural and modelled settings with different brittle layer thickness can be compared. Finally, a secondary structural grain may occur, connecting the main segments and resulting in a continuous-offset structural weakness trail (Fig 1.5g).

Various (combined) structural inheritance geometries are applied throughout this Thesis (see also overview Table 1.2).
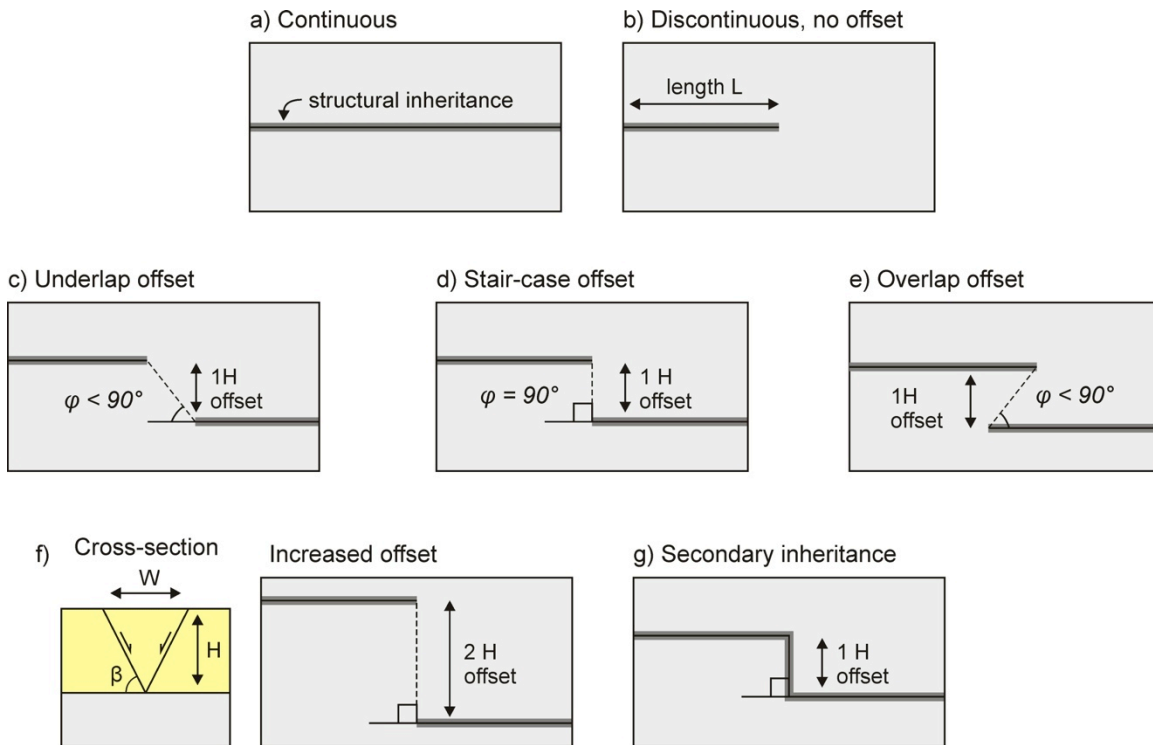
Fig. 1.5. *Top view examples illustrating the structural inheritance geometries as applied in this Thesis. (a) Continuous seed. (b) Discontinuous seed without offset (c) Underlap offset (ϕ < 90°). (d) Staircase offset (ϕ = 90°). (e) Overlap offset (ϕ > 90°). (f) Increased offset, 1 H is the equivalent of the brittle crust thickness, β is the rift boundary fault angle, and W is the initial rift width (Cross-section to the left). After Allemand & Brun (1991). (g) Secondary inheritance, creating a continuous offset crustal weak zone.*

1.5. Syn-tectonic sedimentation

Syn-rift sedimentation is included in this Thesis since various authors have noted the significant influence surface processes may exert on orogenic and rift systems. Erosion and sedimentation may amongst others affect the dynamic topography, crustal fault style, exhumation rates and even slab retreat in active orogens (e.g. Simpson 2006; Stolar *et al*. 2007; Gray & Pysklywec 2012).

In extensional settings, sedimentation is known to influence amongst others fault activity and subsidence rates (Burov & Cloetingh 1997; Burov & Poliakov 2001; Olive *et al*. 2014, Fig. 1.6). It may also suppress salt diapirism (Thomas 1994; Brun & Fort 2008), yet also cause halokinesis due to the uneven loading exerted by prograding sedimentary sequences, "squeezing out" the underlying salt layers (Brun & Fort 2011, and references therein). Strong syn-rift sedimentation can furthermore cause the tectonic system to shift to a narrow rifting mode (Bialas & Buck 2009) or even delay continental break-up (Martín-Barajas *et al*. 2013).

Syn-rift sedimentation processes and their effects on rift and rift interaction structure evolution are addressed in Chapter 4.
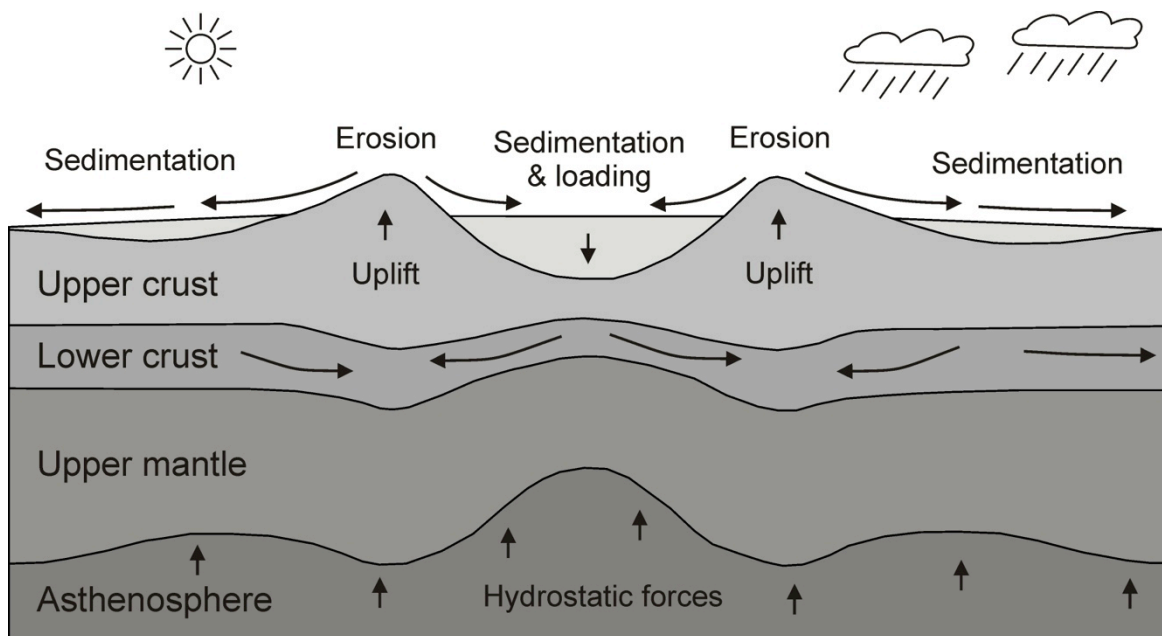

Fig. 1.6. *Depiction of various forces and material fluxes active in a developing rift system. Modified after Burov & Cloetingh (1997).*

25

1.6. Scissor tectonics

The second non-orthogonal extension configuration addressed in this thesis involves the rotation of tectonic plates about a vertical axis, producing along-strike extension gradients (Figs. 1.7, 1.8). Examples of such settings can be found in the Red Sea and the Gulf of Aden (Bellahsen *et al*. 2003; ArRajehi *et al*. 2010), the EARS (Saria *et al*. 2014) and the Arctic (Dick *et al*. 2003, Fig. 1.7). Rotational extension on a small scale can be the result of local tectonic conditions (Fig. 1.8b). On a larger scale however, such along-strike extension gradients are a logical consequence of extension on the terrestrial sphere, with an

Euler pole acting as the rotation axis (Fig. 1.8c). Since a sphere has a constant surface, an extensional system must be compensated by compressional processes elsewhere, for instance on the other side of the Euler pole (Fig. 1.8c), completing a full scissor tectonic system. Such a setting may be observed in the Arctic, where the extending Gakkel Ridge terminates on the Laptev Margin, after which the plate boundary between The North American plate and the Eurasian Plate shifts towards a compressional regime along the Siberian Chersky Range (Imaeva *et al*. 2016 and Fujita *et al*. 2009, Fig. 1.7c).
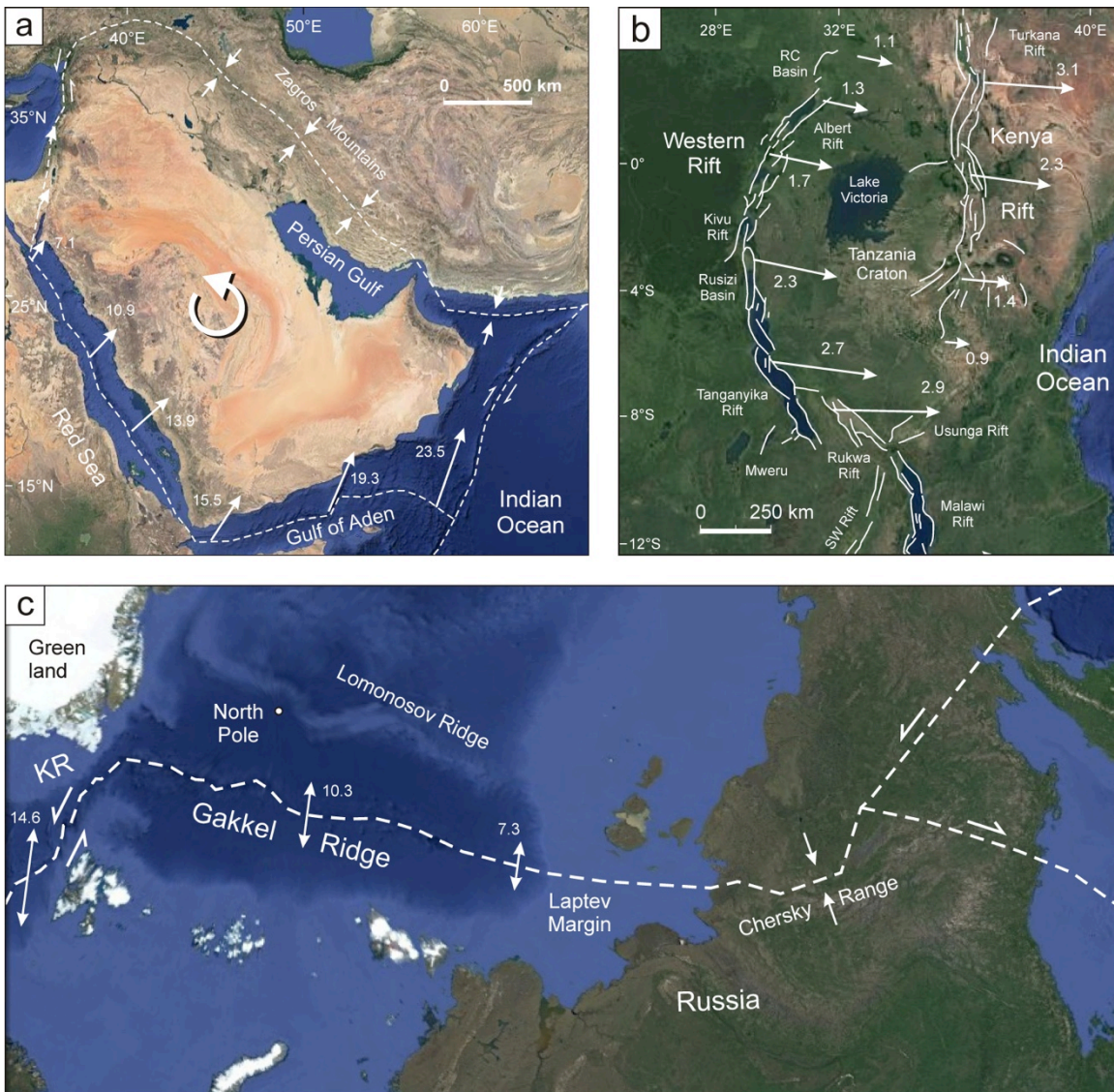
Fig. 1.7. (previous page) *Natural examples of extension gradients along plate boundaries. (a) Red Sea and the Gulf of Aden in association with the counterclockwise block rotation of Arabia. Dotted lines indicate plate boundaries, extension velocities are inferred from GPS measurements. Image modified after Bellahsen et al. (2003) and ArRajehi et al. (2010). (b) Distribution of rift basins and extension gradients in the East African Rift system. RC Basin: Rhino-Camp Basin. Extension velocities are inferred from GPS measurements. Image modified after Ebinger (1989), Acocella et al. (1999a) and Saria et al. (2014). (c) Arctic region, illustrating the increasing extension velocity along the Gakkel ridge, and the compressive domain at the Siberian Chersky Range. KR: Knipovitch Ridge. Image modified after Dick et al. (2003), Imaeva et al. (2016) and Fujita et al. (2009). Background images added from Google Earth, velocities in mm/h.*

_____

Scissor extension systems and their evolution have received limited attention from modellers who traditionally apply constant along-strike deformation rates in their simulations (e.g. Withjack & Jamison, 1986; Michon & Merle 2000; Philippon *et al*. 2015, Fig. 1.8a). An early study by Souriot & Brun (1992) involving analogue models explored the block rotation of the Danakil Block in the Afar section of the East African Rift system. Other publications address the scissor-like opening of the Havre Trough, New Zealand (Benes & Scott, 1996), rotating subduction rollback of the Kuril Basin in the North-western Pacific (Schellart *et al*. 2002; 2003) and the scissor-extensional opening of the South China Sea (Sun *et al*. 2009) by means of laboratory experiments. A recent analogue modelling study focuses on the opening of the Red Sea and the rotation of the Arabian plate (Molnar *et al*. 2017, Fig. 1.7a). Yet additional efforts (e.g. Chapters 5 and 6) are necessary to improve our knowledge of structures developing in scissor tectonic settings.
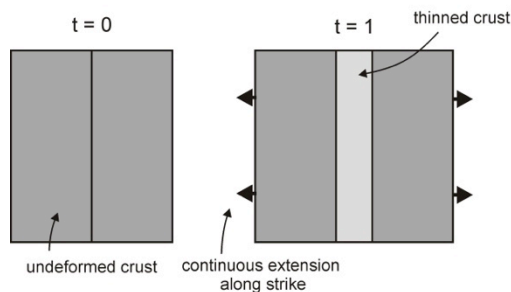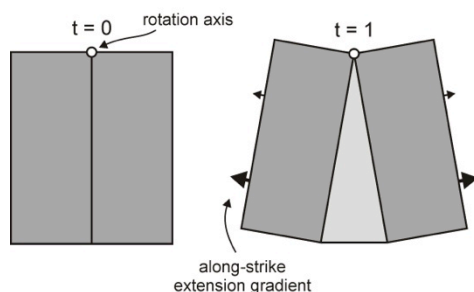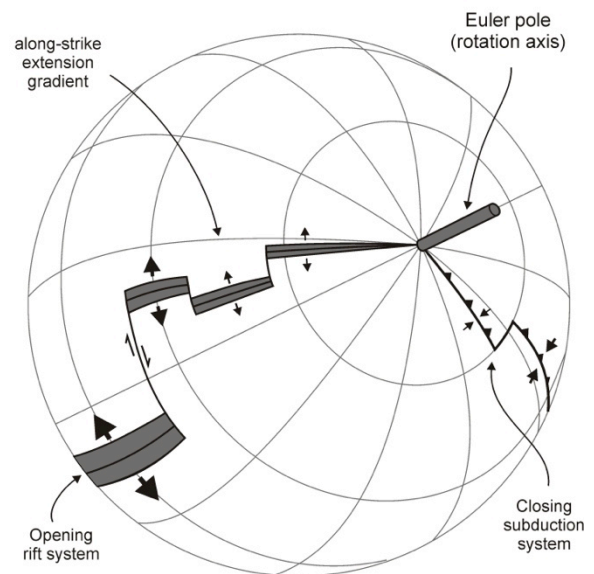

Fig. 1.8. *Differences between (a) the standard extension model set-up with a continuous extension rate along-strike and (b) a scissor extension model set-up involving along an strike-gradients and a rotation axis, which is a logical result of (c) the opening of a rift system on a sphere. Image modified after Vink (1982), Martin, (1984) and Van der Pluijm & Marshak 2004.*

1.7. Rift development and propagation

During its evolution, a rift system not only grows in width, but also in length by propagating along-strike, as observed in the North Sea Rifts, where Jurassic rifting intiated in the Northern North Sea before advancing into the Central North Sea (Rattey & Hayward 1993). Rift propagation occurred on a larger scale during the break-up of Pangea, when rifting initiated in the Central Atlantic, propagating north into the North Atlantic and the Labrador Sea before redirecting extension to the Norwegian Sea and linking up with the Gakkel Ridge in the Arctic Ocean (Coward *et al*. 2003, Fig. 1.7c). Other examples, although in oceanic settings, involve the Mid Atlantic Ridge that is currently propagating away from the Iceland hotspot (Hey *et al*. 2010) and the Taupo Trough continuing into mainland New Zealand (Benes & Scott 1996).

Authors have proposed models for rift propagation in orthogonal extension settings (e.g. Vink 1982, Fig. 1.9a) and modelling studies have applied such boundary conditions to simulate rift propagation (e.g. Van Wijk &

Blackman 2005). However, rift propagation in nature may be closely related to scissor tectonics. The Red Sea and Gulf of Aden have propagated into the Afar region from the north and east, respectively (Beyene & Abdelsalam 2005), both with decreasing extension rates towards the rift tip, as a logical result of the counter-clockwise rotation of the Arabian microplate (Martin 1984; ArRajehi *et al*. 2010, Figs. 1.7a and 1.8c). Similar relationships between propagating rifts and extension gradients could also exist in the East African Rift System (Fig. 1.7b), although recent studies have suggested to a more diachronous rift history there (Torres Acosta *et al*. 2015; Balestrieri *et al*. 2016).

Rift propagation in scissor tectonic settings has been modelled with respect to the Afar region (Souriot & Brun 1992) the New Zealand Havre Trough (Benes & Scott 1996) and the Red Sea (Molnar *et al*. 2017), but further efforts with new modelling methods as those described in Chapter 5 are required to improve our understanding of rift propagation.
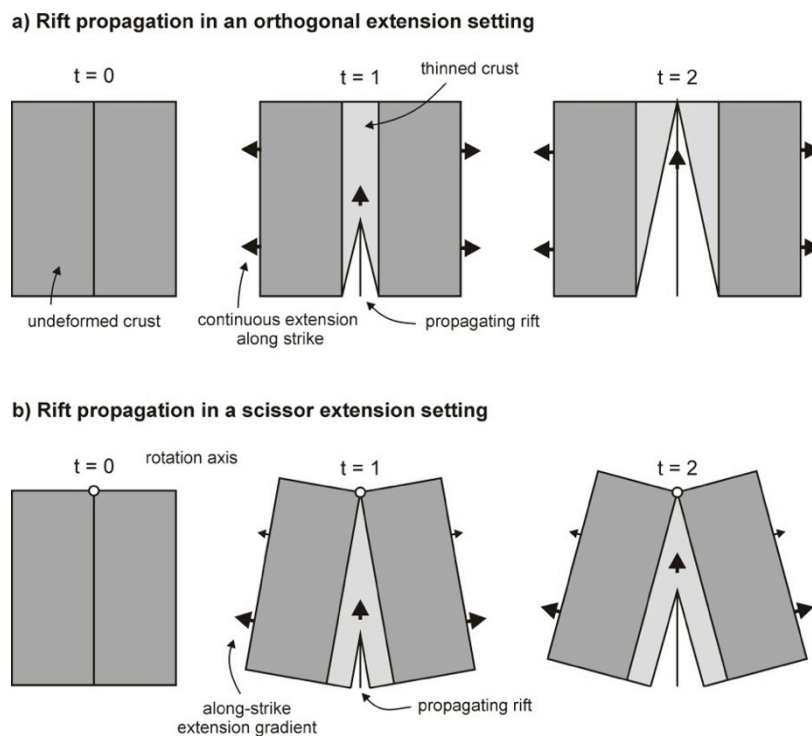

Fig. 1.9. *Comparison between (a) rift propagation in an orthogonal extension setting as proposed by Vink (1982) and (b) a scissor extension setting as proposed by Martin (1984).*

1.8. Background and objectives of analogue modelling

The study of the earth's structure poses a significant challenge, as the rocky globe we call home is huge with a wide range of topographical and geological features that are hard to chart. Earth is furthermore a dynamic planet, constantly changing its appearance through tectonic processes, erosion and sedimentation so that on many places, huge parts of the geological record are either missing or covered by thick sedimentary sequences. Good quality outcrops are rare so often geologists drill boreholes, shoot seismic sections or use seismic tomography to reveal the structures in the subsurface to an impressive degree.

Still our understanding of the large-scale dynamics of plate tectonics and the evolution of associated structures remains a complex matter. Both the size and timescale of the system are many magnitudes larger than the human mind can instinctively comprehend; tectonic processes take millions of years and act over thousands of kilometres. As a consequence, our geological observations provide merely a static snapshot of the current state of affairs on planet Earth. The deformation and kinematics involved in global tectonics remain elusive and the history of many structures is poorly understood. In order to catch a glimpse of the actual dynamic nature of the planet, we can however resort to analogue experiments. These models allow a simulation of plate tectonic processes on a cm to meter scale, in a matter of hours and with the use of simple materials in the laboratory.

The history of analogue modelling goes back to the 19th century, when Sir James Hall performed the first recorded experiment involving the compression of several layers of cloths to simulate folding of sedimentary strata (Hall 1815). Other early experiments were preformed by e.g. Lyell (1871), Daubrée (1879) and Cadell (1988, Fig. 1.10). Additional examples can be found in the extensive overviews provide by Koyi (1997) and Graveleau *et al.* (2012). From these humble beginnings, the science of analogue modelling has significantly evolved. New materials were selected to better represent the different components of the lithosphere (e.g. clay, sand, silicone, Hubbert 1937, 1951 Elmohandes 1981; Basile & Brun 1999; Serra and Nelson 1988; Schellart *et al.* 2002, 2003). Meanwhile scaling theory to ensure geometric, dynamic and kinematic similarity between models and nature has become part of the analogue toolbox (Le Calvez 2002, and references therein). Furthermore, a wide range of machines and set-ups, including centrifuge devices to enhance the gravitational field (e.g. Corti & Manetti 2006), have been developed to reproduce a variation of tectonic settings.

Also the data collection methods improved significantly, so that a modern-day tectonic laboratory may possess not only a camera for time lapse photography of the model surface, but amongst others a state-of-the-art surface scanner or access to a CT-scanner (Colletta *et al.* 1991) and software to subsequently analyse and quantify the surface and internal structures in three dimensions (e.g. Adam *et al.* 2013; Molnar *et al.* 2017).

However, despite their many advantages and the valuable insights laboratory models have provided over the years, the technique has some limitations. Various factors cannot, or only with great difficulty, be incorporated into the experiments. For instance, heating and melting of material, as well as phase changes and the emplacement of oceanic crust after continental break-up pose serious difficulties (Koyi 1997). The laboratory scale of the models (not more than several meters) also means that the models must be relatively simple, i.e. the lithospheric heterogeneities, especially pervasive structures are challenging to implement (Morley 1999). Other limitations may involve logistics: time constraints and availability of expensive model materials, as well as material behaviour and scaling (Koyi 1997; Brun 1999).

The more recent development of numerical modelling may provide a partial solution. Computer simulations allow geologists to apply a wide array of boundary conditions that are difficult or impossible to realize in the lab, including temperature variations, phase

transitions and melting (e.g. Naliboff & Buiter 2015) as well as the use of natural material properties and geological (time)scales instead of downscaled analogue materials (e.g. Beniest *et al.* 2017). However, also numerical models have their drawbacks as they may require vast amounts of costly computer power and seem to have difficulties simulating detailed 3D systems (Zwaan *et al.* 2016; Chapter 2). Furthermore, the results are often heavily dependent on the specific numerical code used for the model (Buiter *et al.* 2006) and in general, the exact properties of the

natural materials are poorly constrained (e.g. Buck 1991; Koyi 1997).

Both analogue and numerical modelling have their advantages and disadvantages. But future attempts to integrate the strengths of both modelling methods will help to get the best out of both worlds. An example of such and collaborative effort is presented in Chapter 2 (Zwaan *et al.* 2016; Chapter 2) and the analogue models described in Chapter 7 are planned to serve as a basis for a future integrated study.
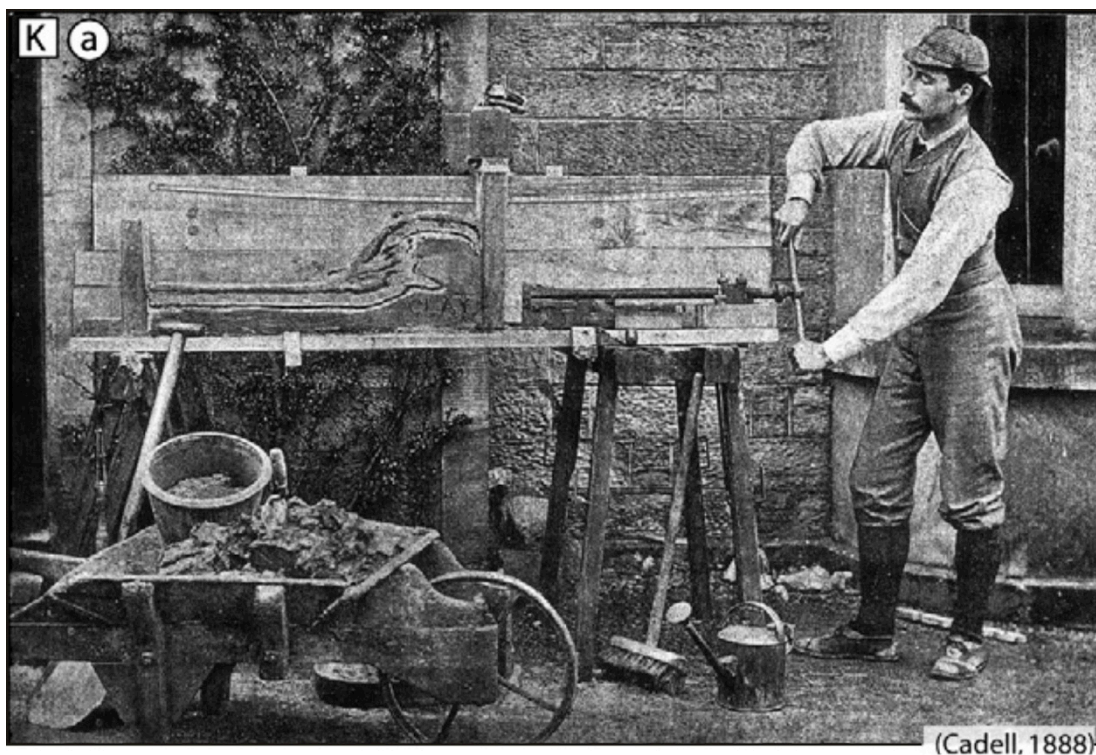

Fig. 1.10. *Classical shortening device operated by Henry Cadell (Cadell 1888).*

1.9. Comparing various set-ups for extensional experiments

As stated in the previous Paragraph, numerous methods have been developed for analogue experiments of tectonic processes. However, the wide variety of model set-ups, involving either a foam base, rubber base, rigid base plates, moving sidewalls or gravity induced deformation and multiple layers of materials, ranging from sand and clay to honey, syrup and water, make it hard to directly compare the results of various studies. Therefore, a

series of models with a range of set-ups for extensional tectonics was run in order to allow a systematic comparison. These models were analysed with the use of CT scans to obtain a detailed insight in the internal model evolution. These models are presented in Chapter 7 and as stated in the previous Paragraph, may serve as a benchmark for future analogue-numerical comparison efforts. More details are listed in Table 1.2.

1.10. Model materials

The experiments performed in the course of this PhD project involve either a brittle-ductile layering to simulate the upper and lower crust, respectively, or a brittle-only layering for upper crustal modelling. Sand is a standard material for the modelling of brittle materials, generally a sedimentary cover, the upper crust or upper lithospheric mantle, producing fault structures with similar angles when deformed.

Two types of sand are available for modelling at the University of Bern Tectonic Laboratory (UniBern TecLab): quartz sand and corundum sand, both supplied by Carlo Bernasconi AG, Switzerland (Carlo AG 2017). Klinkmüller (2011) has previously determined the characteristics of the UniBern TecLab quartz sand, but as the new batches used for this project had a slightly different grain size, a sample was sent to our colleagues at the Helmholtz-Centre Potsdam — GFZ German Research Centre for Geosciences (GFZ Potsdam, Germany). Robert Gentzmann and Matthias Rosenau used their ring shear tester (Ritter et al. 2016, Fig. 1.11) to examine the properties of the new sand for us, which show only minor differences with respect to the old sand (see Table 1.1). The corundum sand is the same as that characterized by Panien et al. (2006) and Klinkmüller (2011).

Furthermore, for all models described in Chapters 4-7, small amounts (2 weight %) of ceramic Zirshot beads were added to the quartz sand. Zirshot has a significantly higher density than quartz and corundum sand (Table 1.1) and creates a pattern on CT images, which is traceable in 3D using novel digital volume correlation (DVC) techniques (Adam et al. 2005; 2013; Zwaan et al. submitted; Chapter 4). These small amounts of additional Zirshot do not significantly influence the rheology of the surrounding quartz sand (Lohrmann et al. 2003).

Silicon oil, Polydimethylsiloxane (PDMS), is a viscous material widely applied to model ductile materials in the Earth's crust or lithosphere (Weijermars 1986; Schellart & Strak 2016). The PDMS applied in the

UniBern TecLab is the commonly used Dow Corning SGM 36 with a Newtonian rheology, that is, its viscosity remains constant with increasing strain along a linear relationship (e.g. Weijermars 1986; Rudolf et al. 2016). Under low strain conditions, it flows, but under higher strain rates $(\dot{\varepsilon})$, it gains in strength. This allows control on the strength of a ductile layer in the model, which determines the degree of brittle-ductile coupling in the system (Fig. 1.12).

The use of pure PDMS has however its disadvantages. As seen in Fig 1.12, the natural strength profiles can only be approximated in models. This is difficult to improve with the current analogue model techniques, although Boutelier et al. (2003) have made an interesting attempt. Furthermore, the density of the PDMS is significantly lower than that of the sand. For modelling of salt tectonic systems this is in fact a pro, as salt layers are lighter than the sedimentary cover at depths higher than ca. 1 km (Jackson & Talbot 1986) and the positive buoyancy induces salt motion and diapirism as observed in nature (e.g. Brun & Fort 2008). However, on a crustal scale, density increases with depth (e.g. Dziewonski & Anderson 1981).
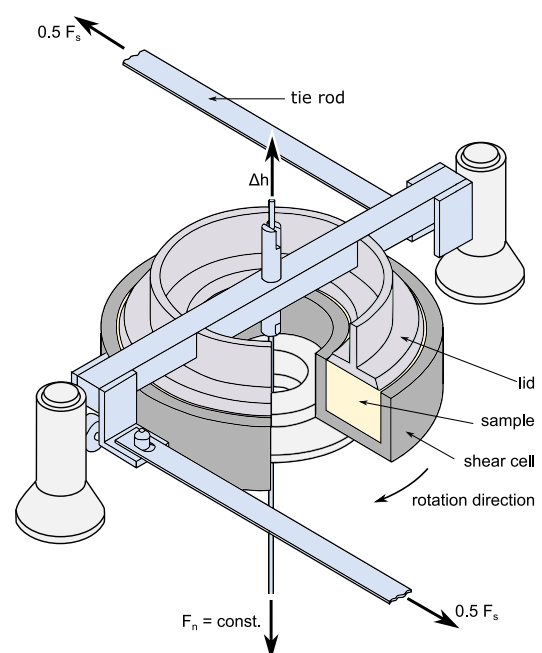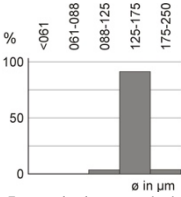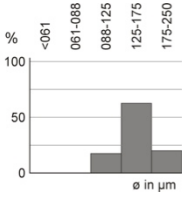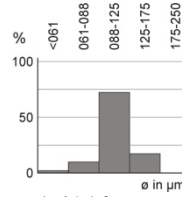
Fig. 1.11. (previous page) *Sketch of the ring-shear tester used to measure the quartz sand properties. The material is sifted into the shear cell, then the lid is placed on top of it, and a constant normal load F_n is applied through a weight. The cell is then rotated, while the lid is kept in place by tie rods. Due to this differential movement between shear cell and lid, a shear zone forms within a sample. Force sensors register the shearing force F_s, which can be transformed into shear stress within the sample using the known geometry of the device. Dilation of the sample is measured as the vertical movement Δh of the lid. Image modified after Panien et al. (2006).*

_____

Table 1.1. *Material characteristics.*

Granular materials		Quartz sand (old)[a]	Quartz sand (new)[b]	Corundum sand[a]	Zirshot[c]
Grain size range		80-200 μm	60-250 μm	88-175 μm	150-210 μm
Grain size distribution (weigth %)					N/A
Grain Shape[d]	- surface texture	Irregularly rounded	-	conchoidal fractures	-
	- roundness	Angular	angular	angular	-
	- form (elongation)[e]	1.63	-	2.00	-
	- sphericity	Low	low	low	-
Density (specific)[c]		2650 kg/m³	2650 kg/m³	1380 kg/m³	3950 kg/m³
Density (sieved)		1560 kg/m³	1560 kg/m³	1890 kg/m³	ca. 2300 kg/m³
Coefficient of internal peak friction		0.71	0.73	0.65	-
Coefficient of dynamic-stable friction		0.61	0.61	0.63	-
Angle of internal peak friction		35.5°	36.1°	37°	-
Angle of dynamic-stable friction		31°	31.4°	32°	-
Strain softening[f]		14%	16%	16%	-
Cohesion		9 ± 18 Pa	9 ± 98 Pa	39 ± 10 Pa	-

Viscous material	PDMS/corundum sand mixture
Weight ratio PDMS : cor. sand	0.965 kg : 1.00 kg
Mixture density	ca. 1600 kg/m³
Viscosity[g]	ca. 1.5·10⁵ Pa·s
Type	near-Newtonian (n = 1.05)[h]

(a) Properties after Panien *et al*. (2016) and Klinkmüller (2011)
(b) Properties measured at GFZ Potsdam
(c) Properties after Carlo AG (2017)
(d) Quartz grain shape determined after Powers (1953)
(e) Elongation: ratio between longest and shortest diameter
(f) Strain softening is the difference between peak strength and dynamic-stable-strength, divided by peak strength
(g) The viscosity value holds for model strain rates < 10^{-4} s^{-1}
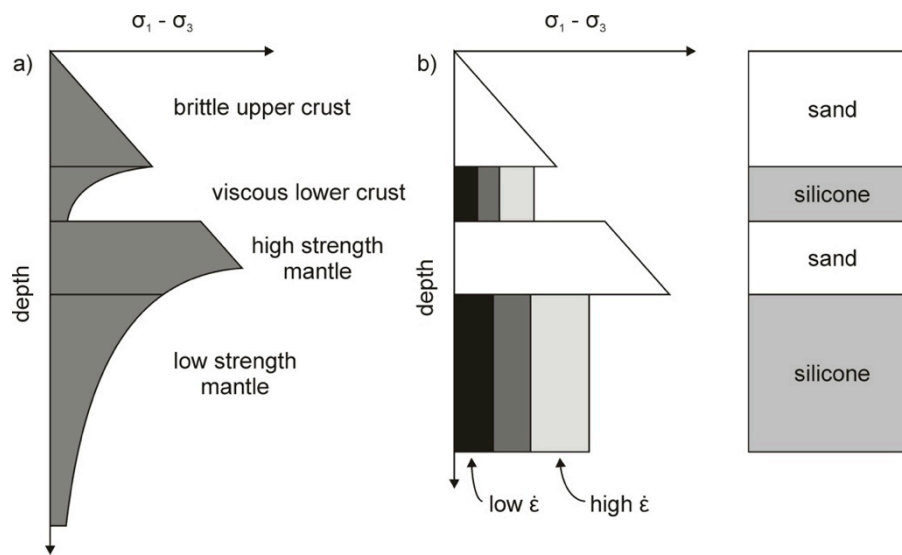(h) Dimensionless stress exponent n indicates sensitivity to strain rate

Fig. 1.12. *Comparison between strength profiles (a) calculated for a four-layer-type continental lithosphere and (b) obtained in sand-silicone models. Image modified after Brun (1999).*

Therefore, the PDMS has to be modified by mixing it with some high-density material. As the models must allow for X-ray computed tomography (XRCT or CT, see Paragraph 1.12) as well, no standard mixes with heavy metal powders (e.g. iron powder, lead powder or FeO, Strak & Schellart 2016; Autin *et al.* 2010) can be applied. Instead, corundum sand was used to increase the PDMS density to ca. 1600 kg/m^3, in order to cancel undesirable buoyancy effects (the quartz sand cover used in most models has a density of 1560 kg/m^3 when sieved into the machine). Similar to the sand for the models described in Chapters 4-7, a small amount of Zirshot is added to the viscous mixture for DVC analysis, with negligible effects on the material behaviour.

Since the density of the viscous material was modified, it was necessary to measure the viscous characteristics of the new mixture. A preliminary test in Bern, using Stokes Law ($F_d = 6\pi\mu Vd$, where F_d is the drag force of the fluid on a sphere, μ is the fluid viscosity, V is the velocity of the sphere relative to the fluid, and d is the diameter of the sphere, Shearer & Hudson) and a tube filled with pure PDMS through which a metal ball, taken from a computer mouse, sinks (Fig. 1.13), yielded a viscosity of ca. 6.5·10^4 Pa·s, which is close to the 1-5·10^4 Pa·s often reported in literature (e.g. Bahroudi *et al.* 2003; Fort *et al.* 2004). The new PDMS/corundum sand mixture with ϱ = ca. 1600 kg/m^3, registered a viscosity of ca. 2.5·10^5 Pa·s using the same technique. Such empirical methods are very useful to determine material properties under laboratory conditions (Montanari *et al.* 2017) and these results were promising, as the characteristics of the mixture did not seem to deviate too much from those of the pure PDMS. Yet more precise analysis to pinpoint the new material's behaviour was desirable.

Matthias Rosenau from GFZ Potsdam generously put the lab's Anton GmbH Physica MCR301 rheometer at my disposal (Di Giuseppe *et al.* 2015; Rudolf *et al.* 2016, Fig. 1.14). With the help of Tasca Santinamo and Malte Ritter, I tested various mixtures of PDMS and corundum sand of which the results are plotted in Fig 1.15. The pure SGM-36 PDMS indeed has a linear (Newtonian) viscosity of ca. 3·10^4 Pa·s, which is in accordance with recent tests by Rudolf *et al.* (2016). As the density of the mixtures increases, the material behaviour changes slightly, but with a stress exponent (n) or 1.05 for ϱ = ca. 1600 kg/m^3 (Fig. 1.15c), the material can be considered near-Newtonian for scaling purposes (Mezger 2006, Paragraph 1.12). The viscosity of 1.5·10^5 Pa·s for this mixture is taken from the lowest shear rate measured, which is closest to the actual shear rates in the analogue experiments (Fig. 1.15a). This viscous mixture is subsequently used as an analogue for the lower crust in all models described in this Thesis.
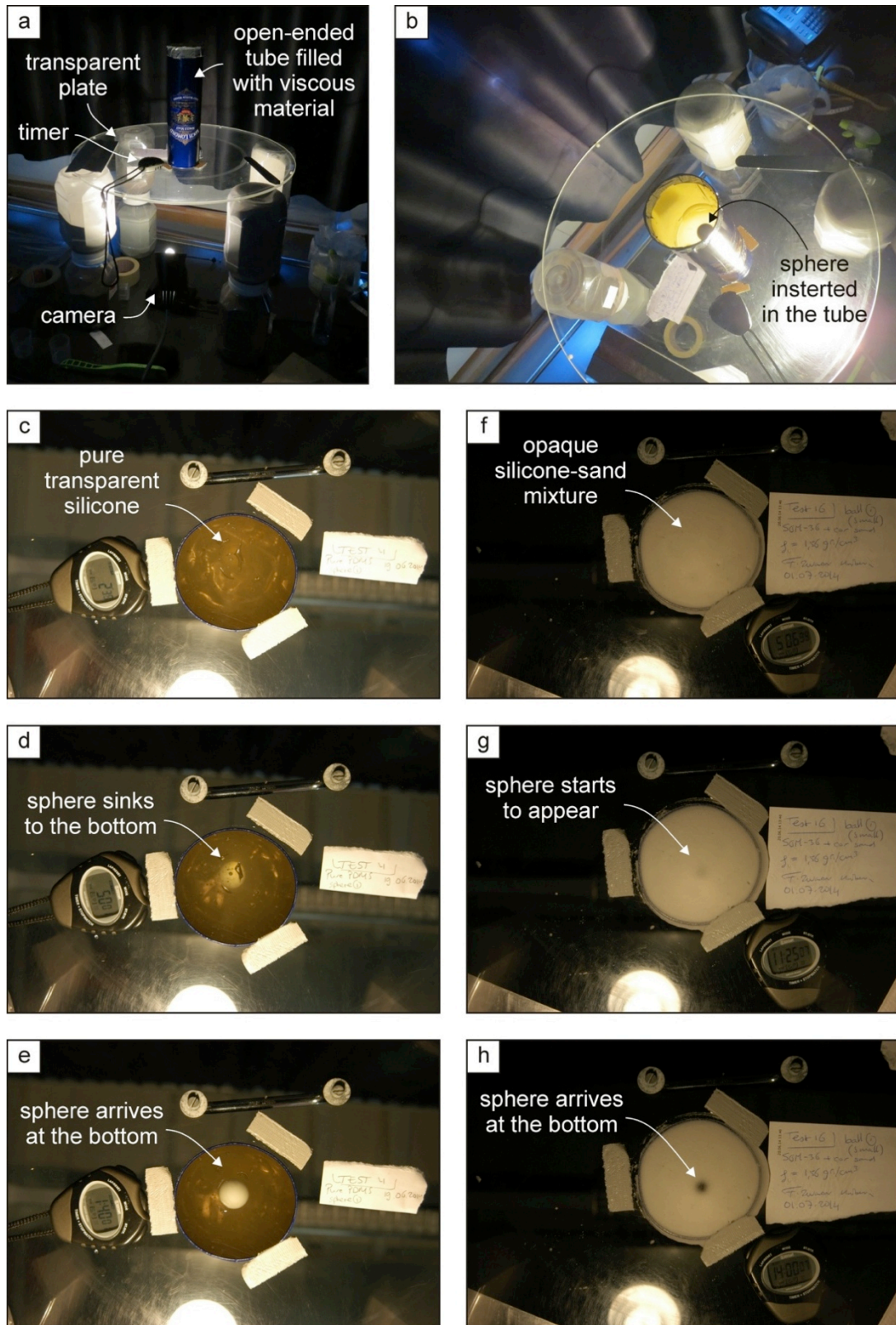
33

Fig. 1.13. *The empirical method, based on Stoke's Law (Shearer & Hudson) to determine the viscosity of viscous materials. (a) Set-up, including a open-ended tube filled with viscous material to be tested, on top of a transparent base. When a sphere of a known size and weight is inserted in the vicious material (b), it sinks and by measuring the time it takes to travel the height of the viscous column (c-d), one can derive the viscosity of the viscous material. However, the PDMS-corundum sand mixtures are opaque, so that timing becomes somewhat of a challenge (f-g).*
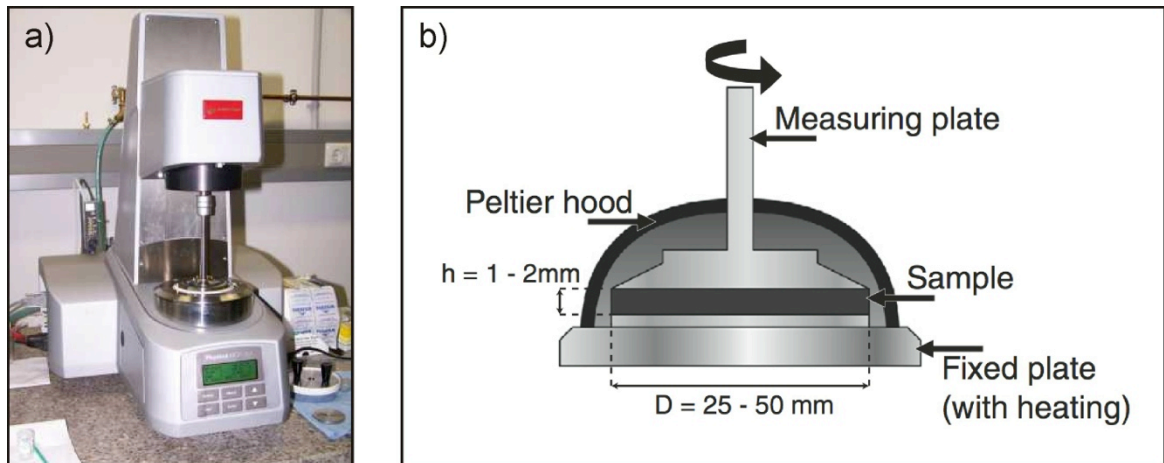
Fig. 1.14. *(a) Physica MCR301 rheometer (Anton GmbH) used for testing the viscous PDMS-corundum sand mixtures at GFZ Potsdam. (b) Schematic drawing of the rheometer setup. The sample material is squeezed between the two plane-parallel plates. The temperature is controlled by a water and air cooled Peltier element located inside the hood and within the lower plate. Image modified after Ritter et al. 2016.*
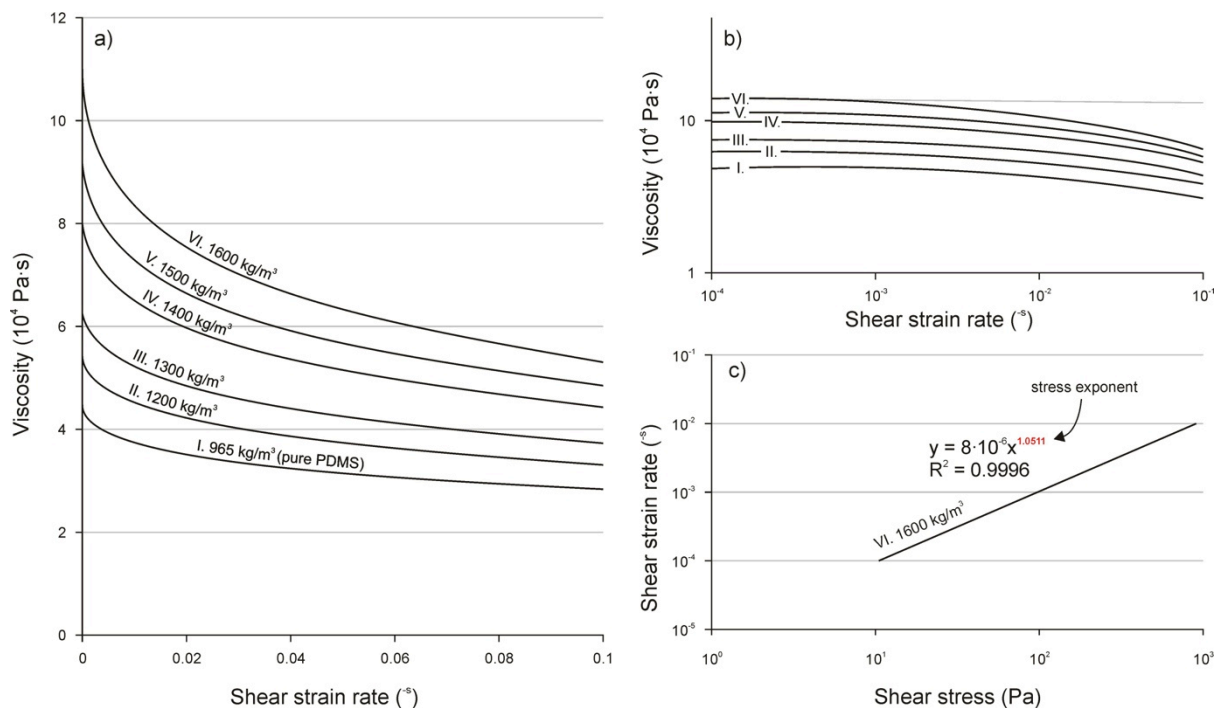
Fig. 1.15. *Results of the oscillary tests of the various sand-corundum sand mixtures (I-VI, 965-1600 kg/cm³, I being the pure SGM-36 PDMS) performed with the Physica MCR301 rheometer (Anton GmbH) at GFZ Potsdam. (a) Viscosity over shear strain. (b) Viscosity over shear strain (log-log plot). (c) Shear strain over shear stress (log-log plot), to determine the stress exponent n (exponent in red) for the ϱ = ca. 1600 kg/m³ mixture, which is used as the standard in this PhD Thesis.*

1.11. Analogue modelling machines

For this work, two analogue modelling devices were applied: the already existing and highly versatile Namazu apparatus (named after the giant catfish that causes earthquakes from Japanese mythology) in which a range of model set-ups can be run, and the newly-built Xissor, which is applied for the modelling of scissor tectonics specifically.

1.11.1. The Namazu apparatus

Designed by my predecessor Matthias Klink-müller, together with students and engineers from the IPEK/HSR Technische Hochschüle Rapperswil and on the basis of an older machine used at the Parisian Institut Français de Pétrol (now IFP Energies nouvelles), the Namazu is a highly adaptable experimental apparatus (Klinkmüller 2011). It contains 5 axes that can all move independently within a wide range of velocities (0.1 to 10,000 mm/h, Fig. 1.16). By combining the motion of these different components, a wide range of (a)symmetrical (oblique) extension or compression conditions can be simulated, as well as (oblique) uplift and subsidence. Precise computer-guided motors control the movement of the axes. The parts of the machine containing the model materials are made of X-ray-transparent materials to allow X-ray computed tomography (XRCT or CT) analysis and the device is specially designed to fit into a medical CT scanner (Fig. 1.17b).

At the start of this project, the Namazu software was not reliable; it would often erase the reference coordinates of the various axes, which could only be recovered through a thorough recalibration and the unavoidable destruction of the experiment. Furthermore, new parts needed to be designed for the models in this Thesis (Appendix IV). With funding from Marco Herwegh and the help of Reto Gwerder, Rudolf Kamber, Michael Ziltener and Theodor Wüst from IPEK Rapperswil, the machine was improved and has been fully functional in the last 3.5 years.

The various axes of the machine allow a wide range of model set-ups. The basic set-up used for most models described in this work consists of a foam (or foam-plexiglass) base, compressed between two sidewalls (Y1 and Y2, Figs. 1.16b, c), on which the model materials are applied (Fig. 1.17c, g). When the sidewalls are driven apart, the foam decompresses and distributed extension is transferred to the overlying model materials (Fig. 1.17g). Moving the X1-axis together with the sidewalls, various degrees of oblique extension can be applied (Figs. 1.16a-c, 17d-f). This foam base method can also be inverted for compressional tectonics (Schreurs & Colletta 1998) and is used in the Xissor machine as well (Paragraph 1.11; Chapter 5). Rods of viscous material on top of the basal silicone layer represent discrete crustal weak zones that localize deformation (Le Calvez & Vendeville 2002), while allowing the developing structures a significant degree of freedom to evolve.

Other set-ups used in this project involve a rubber base and a base plate configuration for orthogonal extension (Chapter 7). The rubber base is attached to the sidewalls and extends uniformly, inducing a similar distributed deformation in the overlying materials as the foam set-up, although serious boundary effects may occur due to contraction effects. Also the more traditional base plate set-up involves fixing parts to the mobile sidewalls, in this case rigid base plates. By moving these plates apart however, all of the material on top of it is translated and deformation is concentrated along the whole length of the edge of the plate, where a velocity discontinuity (VD) occurs. This VD is thus a dominant control on deformation in these models.

The versatility of the Namazu apparatus is underlined by the models carried out by Jakub Fedorik (University of Pavia) during his 2016 stay in Bern (Fedorik *et al*. in prep.). For his models of transcurrent structures interacting with a trust front, the sidewalls were removed and a triple-base plate system controlled by the X1 and Y3 axes was installed. The adaptability to model a wide range of tectonic settings and the access to a medical CT scanner make this machine a highly valuable asset for the UniBern TecLab.
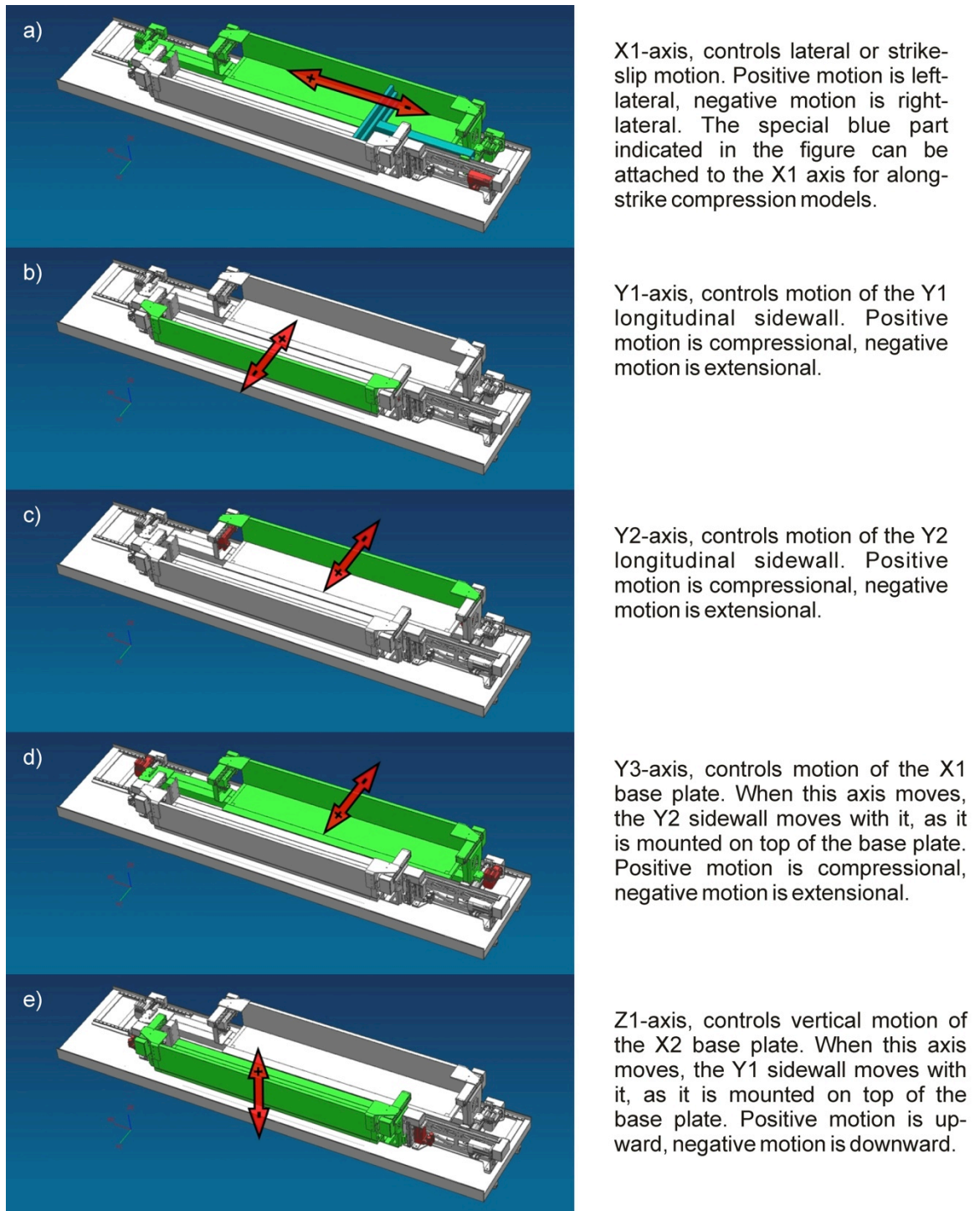
a) X1-axis, controls lateral or strike-slip motion. Positive motion is left-lateral, negative motion is right-lateral. The special blue part indicated in the figure can be attached to the X1 axis for along-strike compression models.

b) Y1-axis, controls motion of the Y1 longitudinal sidewall. Positive motion is compressional, negative motion is extensional.

c) Y2-axis, controls motion of the Y2 longitudinal sidewall. Positive motion is compressional, negative motion is extensional.

d) Y3-axis, controls motion of the X1 base plate. When this axis moves, the Y2 sidewall moves with it, as it is mounted on top of the base plate. Positive motion is compressional, negative motion is extensional.

e) Z1-axis, controls vertical motion of the X2 base plate. When this axis moves, the Y1 sidewall moves with it, as it is mounted on top of the base plate. Positive motion is upward, negative motion is downward.

Fig. 1.16. *Overview of the various components of the Namazu experimental apparatus and their respective motion directions controlled by axes (Y1-3, X1 and Z1).*
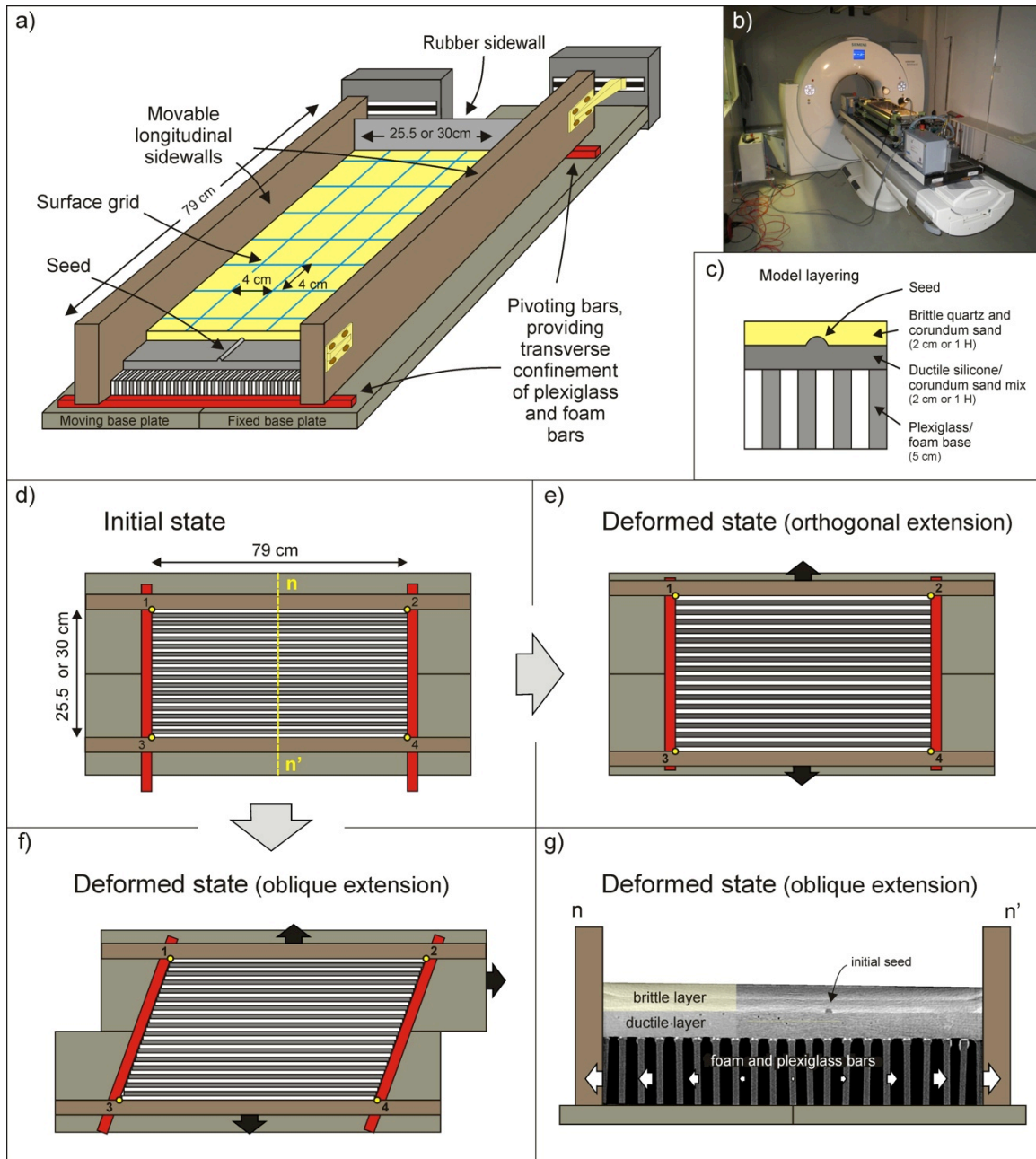
Fig. 1.17. *Set-up for the analogue foam base experiments in the Namazu experimental apparatus. (a) Cut-out view of the experimental apparatus. (b) The Namazu apparatus in the CT scanner of the University of Bern Institute of Forensic Medicine. (c) Compositional layering and associated strength profile, including the seed, where the brittle layer is thinner and deformation is localized. (d) Schematic surface view showing the initial set-up and (e-f) subsequent deformation of the empty apparatus in orthogonal extension and oblique extension, respectively. (e) Example of a CT-derived cross-section (n-n', see (d)), showing the initial model layering and seed geometry. White arrows indicate the velocity gradient at the model base.*

1.11.2. The Xissor apparatus

Next to the Namazu experimental apparatus described above, a novel analogue modelling machine for the simulation of scissor tectonics was developed during this project. Inspired by the observation that in addition to orthogonal and oblique extensional tectonics, extension along-strike gradients due to rotational motion occur in nature (Paragraphs 1.3, 1.5), a collaboration with Prof. Theodor Wüst (IPEK/HSR Technische Hochschüle Rapperswil) was initiated and Claude Grau started designing the Xissor apparatus as part of his BSc Thesis in early 2014. Based on his conceptual design and funded by Marco Herwegh, the Swiss National Science Foundation and the Berne University Research Foundation, Michael Ziltener and Rudolf Kamber developed a final design and assembled the apparatus in late 2015 (Figs 1.18, 1.19, Appendix V).

The machine consists of two longitudinal sidewalls, which rotate about an axis, dividing the machine in a 65 cm long external domain and a 25 cm long compressional domain (Fig. 1.18a, b). The short ends of the Xissor apparatus are curved to account for the rotational motion of the sidewalls, so that no gaps open for the model materials to flow out. Two main set-ups are possible: a foam base set-up and a base plate set-up. The foam option is based on the same method as used in the Namazu: a foam element is compressed between the sidewalls and decompresses as the walls move apart or compresses when the walls close, causing distributed deformation in the overlying materials. Subsequently, seeds can be applied to localize deformation (Chapters 5 and 6).

The second set-up involves the application of rigid base plates and is designed for the scissor extension part of the apparatus only. The machine is compartmentalized, so that the foam set-up parts can be easily replaced with the base plate components. The latter consist of two base plates, curved sidewalls at the short end of the machine and another wall at the scissor axis, to separate the extensional domain from the compressional domain. This division is made because any base plates in the compressional domain will not produce the intended structures. In the extensional part, the plates do not cover the whole base of the model, so that various plate geometries can be installed and tested. A lower platform, on which these plates rest, prevents any materials from moving out of the machine. However, this second set-up has not been tested yet.

Also the Xissor is specially designed for CT-scanning. Therefore all parts of the model near the model materials are X-ray transparent. However, the sidewalls have a buttress framework structure (Fig. 1.19). These sidewall thickness variations cause modest X-ray shadowing effects on the CT images (Paragraph 1.13; Chapters 5 and 6). Furthermore, the machine is ca. 160 cm long, designed to fit in the small elevator of the institute to allow transport from the lab on the first floor of the Institute of Geological Sciences to the CT room of the forensic institute just across the road. The hardware controlling the motors is mounted on a trolley for maximum mobility, which is greatly appreciated after the experiences with the somewhat unwieldy Namazu (ca. 250 cm long, weighing ca. 120 kg), which does not fit in the Institute's elevator and needs to be carried out of the lab, down the stairs by 4 to 5 persons at a time.
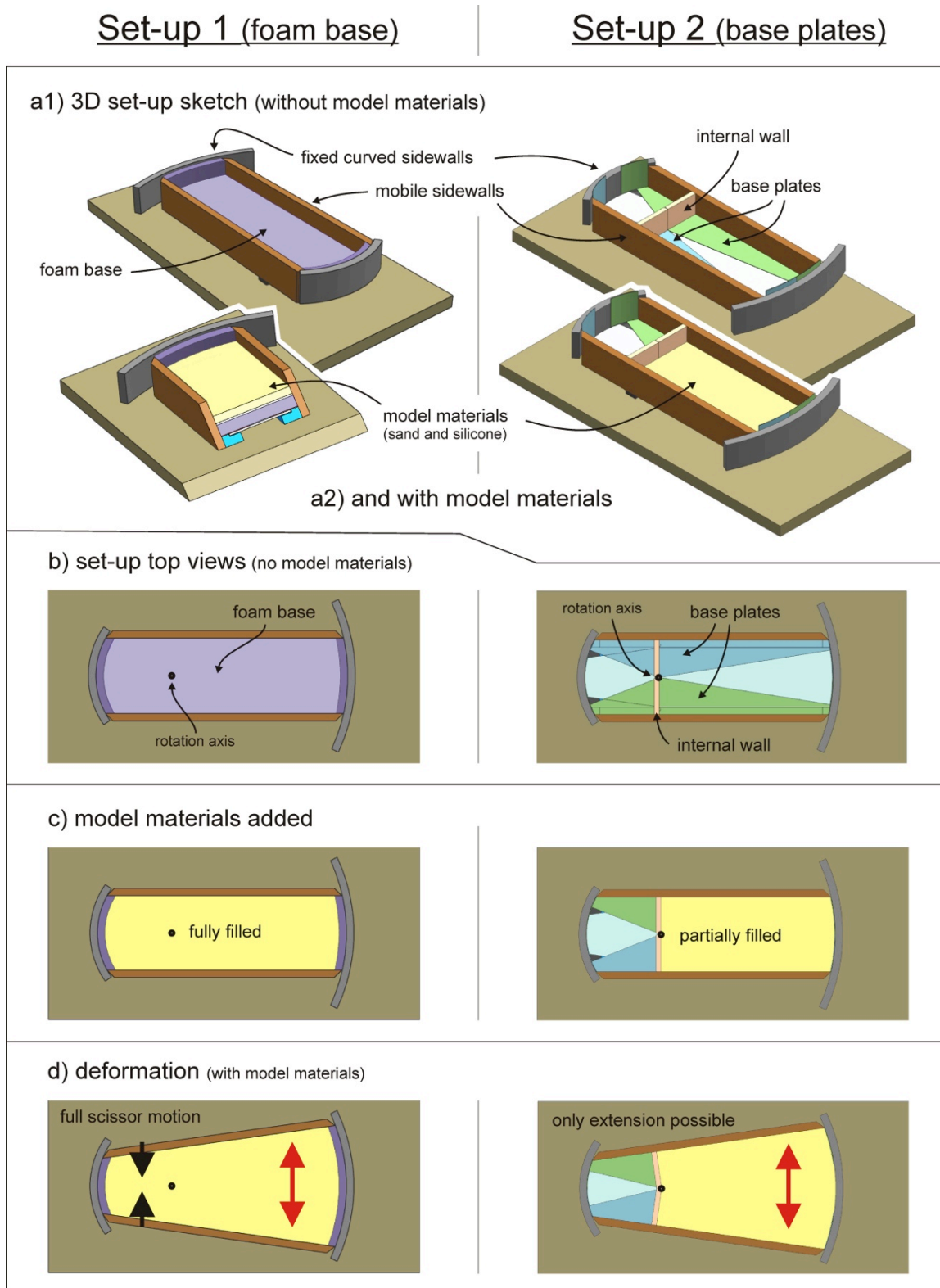
Fig. 1.18. *Overview of potential set-ups allowed by the Xissor experimental apparatus with left the foam base option and right the base plate option. (a) 3D sketch of the machine without (a1) and with model materials (a2). (b-c) Top views of the machine (b) with model materials and (c) without model materials (c). (d) Top view indication the rotational motion about the rotation axis and the resulting scissor deformation of the model materials.*
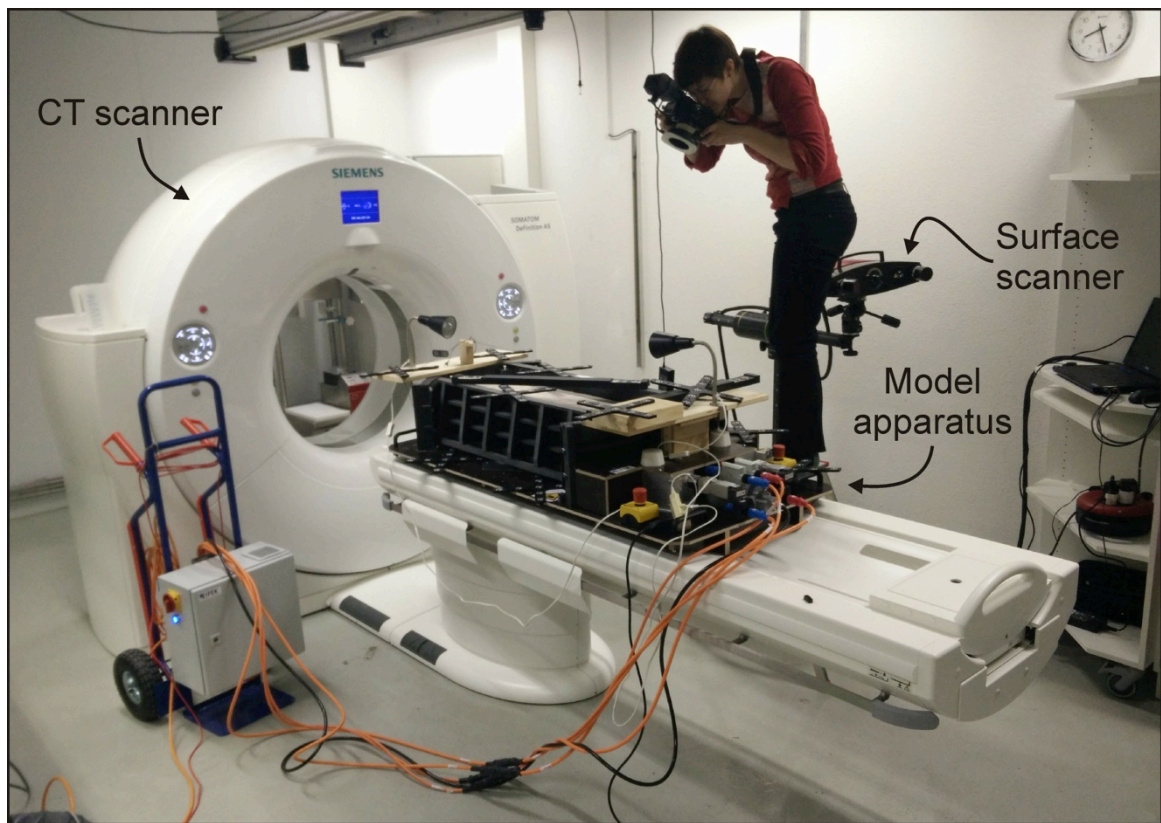
Fig. 1.19. *The Xissor machine in the medical CT scanner at the University of Bern Institute of Forensic Medicine, being prepared for surface scanning by Kirsten Busse (photo by Jakub Fedorik).*

1.12. Model scaling

1.12.1. Concepts of geometrical, kinematic and dynamic similarity

Analogue modelling scaling is necessary to guarantee 1) the geometrical, 2) the kinematic and 3) the dynamic similarity between a model and its natural equivalent (Hubbert 1937, Ramberg 1981; see also the synopsis by Le Calvez 2002, Fig. 1.20). Geometrical similarity implies that all dimensions (length, width, depth, layer thickness) in the analogue model must have the same proportions as the natural example, a requirement met by model 1 in Fig. 1.20a, but which does not apply in the case of model 2.

Kinematic similarity signifies that the model and the natural example maintain geometric similarity during their deformation without developing any temporal distortions along the way. In Fig. 1.20b, model 1 keeps in pace with the deformation in the natural example. The structures in the model 2 example however, show a deviating evolution, as the geometries obtained at t = 3 Ma or t = 3 hour by the natural prototype and model 1, respectively, develop only at t = 4. Therefore the model 2 example fails to meet the criteria for kinematic similarity.

Finally dynamic similarity is established when all forces, stresses and material strengths are properly translated from the natural example to the model scale (Fig. 1.20c). Although it is practically impossible to incorporate all detailed complexities that characterize natural geological settings into a small laboratory experiment, a correct scaling of the dominant factors controlling deformation will allow the scaling criteria to be fulfilled.

A fundamental scaling formula considers the relation between stress (σ), density (ϱ), gravitational acceleration (g) and length or height of an object (h) in models and nature (convention $\sigma^* = \sigma_{model}/\sigma_{nature}$, Hubbert 1937, Ramberg 1981):

$$\sigma^* = \varrho^* \cdot g^* \cdot h^* \qquad (1.1)$$

yielding the ratio of stresses between a model and nature, which will be applied for subsequent scaling of the viscous material (Paragraph 1.12.4).

1.12.2. Layering of the Lithosphere

Although the lithosphere comprises many different lithologies, it is dominated by two rock rheologies allowing large strains: frictional-plastic (brittle) and viscous (ductile) behaviour. Depending on the type of lithosphere (continental or oceanic), the age (old stable, young stable, thickened or stretched), it might contain up to 4 alternating brittle and ductile layers above the asthenosphere: e.g. a brittle upper crust, ductile lower crust, brittle upper mantle and ductile lower mantle (e.g. Brun 1999, Corti *et al.* 2003, Fig. 1.12a). For scaling the crustal-scale models described in this Thesis, the rheology of both the upper and lower crust are to be considered.

1.12.3. Scaling of brittle materials

In the brittle crust, the rheology is generally regarded as time-independent, obeying a Mohr-Coulomb criterion of failure (Byerlee 1978), describing the relation between the shear stress (τ) parallel to a (potential) fault plane required for fault activation, the stress normal to the fault plane (σ_n) as well as the cohesion (C_0) and the angle of internal friction (ϕ) of the material as follows:

$$\tau = C_0 + \sigma_n \tan \phi \qquad (1.2)$$

The brittle behaviour of the upper crust is roughly characterized by angles of internal friction between 31°-40° and cohesion values between 0 and 50 MPa (Byerlee 1978). In order to be properly scaled, model materials must have the same coefficient of internal friction as the upper crust as well as a low cohesion (e.g. Abdelmalak *et al.* 2016). These criteria are met by many granular materials, such as the quartz sand and corundum sand used in the UniBern TecLab, which have a ϕ between 31° and 37° and negligible cohesion (Panien *et al.* 2006; Klinkmüller 2011, Paragraph 1.6, Table 1.1).
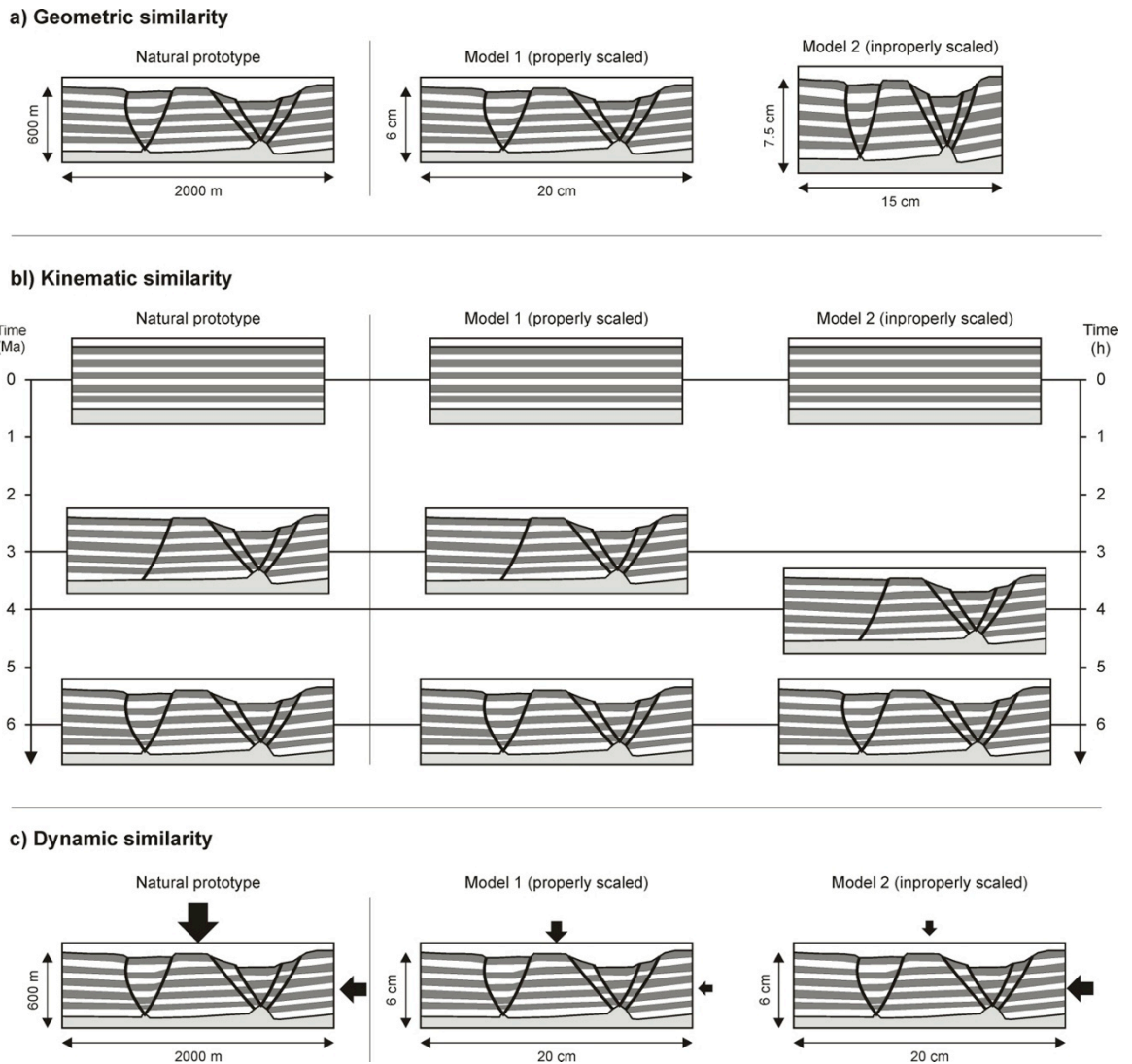
Fig. 1.20. *The concept of geometric, kinematic and dynamic (dis)similarity between a natural prototype of a developing rift and corresponding models. Modified after Le Calvez (2002).*

Sand therefore produces the same fault geometries as crustal rocks (Schellart & Strak 2016, and references therein), ensuring proper geometrical and dynamic similarity between models and nature (Hubbert 1937, Fig. 1.20). Brittle dynamic similarity can furthermore be secured by comparing the dimensionless ratio (R_s) between gravitational stresses and cohesive stress of the model and the natural prototype:

$$R_s = \frac{\text{gravitational stress}}{\text{cohesive strength}} = \frac{\rho \cdot g \cdot h}{C_0} \qquad (1.3)$$

1.12.4. Scaling of viscous materials

In contrast to their brittle counterparts, viscous materials show time-dependent behaviour, defined as the relationship between strain rate ($\dot{\varepsilon}$) and differential stress (σ_{diff}), involving the material viscosity (η) and the stress exponent (n) (Le Calvez, 2002):

$$\sigma_{\text{diff}} = \eta \cdot \dot{\varepsilon}^{\,n} \qquad (1.4)$$

When no strain hardening or softening occurs and n equals 1, the viscosity remains constant

43

and the material is characterized by Newtonian flow, similar to the assumed quartzite-dominated rheology of the lower crust (e.g. Wang *et al*. 1994) and the SGM36 PDMS mixed with corundum sand, used for all models described in this thesis (Paragraph 1.10). Equation 1.4 can subsequently be rewritten and combined with equation 1.1 (Weijermars & Schmeling 1986; Le Calvez 2002) yielding:

$$\sigma* = \eta* \cdot \dot{\varepsilon}* = \varrho*\cdot g*\cdot h* \quad \text{(1.5 and 1.6)}$$

Using the calculated stress ratio and the viscosity ratios (given that the lower crustal viscosity may range between $1\cdot10^{19}$ and $1\cdot10^{23}$ Pa·s, Buck 1991), the strain rate ratio can be derived. Subsequently, the velocity ratio (v*) and the time ratio (t*) is obtained:

$$\dot{\varepsilon}* = v*/h* = \dot{\varepsilon}* \cdot 1/t* \quad \text{(1.6 and 1.7)}$$

so that one can translate a deformation rate or a timespan in the laboratory to their respective values in nature and vice versa.

In order to secure proper dynamic similarity, the dimensionless Ramberg number (R_m), involving the ratio between gravitational stress and viscous stress of the model and its natural equivalent can be compared (Weijermars & Schmeling 1986):

$$R_m = \frac{\text{gravitational stress}}{\text{viscous stress}} = \frac{\rho\cdot g\cdot h}{\dot{\varepsilon}\cdot v} = \frac{\rho\cdot g\cdot h^2}{\eta\cdot v} \quad \text{(1.8)}$$

A final check may be conducted with the dimensionless Reynolds number (R_e) to determine the flow regime of the viscous material (Weijermars & Schmeling 1986), where (L) represents a distance covered at a certain velocity (v):

$$R_e = \frac{\rho\cdot v\cdot L}{\eta} \quad \text{(1.9)}$$

The required flow regime for analogue models is laminar rather than turbulent. The Reynold number is <<1 for any reasonable velocity in analogue models involving Newtonian silicone, indicating laminar flow, which confirms its suitability for tectonic simulations.

1.12.5. Scaling the models in this Thesis

The numerous models described in the following chapters have various differences (layer thickness, extension velocities and model size). However, as described in every individual chapter, the models are always properly scaled with respect to nature and each other. The latter is reflected in the fact that all models with the basic foam set-up described in Paragraph 1.11, produce very similar structures in the context of the different seed geometries and extension directions applied.

1.13. Model analysis

Next to the standard top view time lapse photography to monitor deformation of the model surface, several other techniques for model analysis are available at the UniBern TecLab (Fig 1.21). The surfaces of all models carried out during this project are sprinkled with coffee grains, to create a distinct pattern. This pattern can be traced on images from different time steps by particle image velocitmetry (PIV) techniques so that directions and magnitudes of horizontal displacements are revealed and strain can be calculated (Graveleau *et al*. 2012 and references therein). This method has not yet been applied for the models in this Thesis, but is planned to be included for the experiments described in Chapters 5-7 and has already yielded good results for other model series carried out at the UniBern TecLab (Fedorik *et al*. in prep.).

Through collaboration with the University of Bern Institute of Forensic Medicine, the UniBern TecLab has access to a TRITOP ATOS III surface scanner, used for a scissor tectonic model described in Chapter 5. This device allows the assembly of digital elevation models (DEM, Figs. 1.19. 1.21b) of various time steps during the model run, which can subsequently be used to compute horizontal displacement (uplift and subsidence, Fig. 1.21c). The collaboration also includes the use of a 64 slice Siemens Somaton Definition AS medical CT scanner (Figs. 1.19b, 1.21), with the following raw data acquisition parameters: 140 kV, 300 or 220 mAS and 0.6 mm collimation, and the following image reconstruction parameters: thickness 0.6 mm, increment 0.3 mm, FoV 370 mm, reconstruction kernel I 70s and a matrix resolution of 512 pixels. CT-scanning represents a unique non-destructive method for detailed (sub-mm scale) 3D analysis of the model surface and internal structural evolution (Fig. 1.21d, e). The technique relies on

attenuation contrasts, basically density variations in the model, which show up as different intensities on the CT images (Colletta *et al*. 1991). Faults, or rather discrete shear zones (Panien 2004 and references therein), become visible because the sand experiences a strong local density reduction along fault planes when the grains start moving along each other. In contrast, faults in wet clay for instance, in which no dilatation occurs, are not seen on CT scans. Professional medical software (OsiriX MD for iOS) allows one to move and observe the 3D CT data from every angle, in a similar fashion as is possible with a seismic dataset in for example Petrel. CT analysis is applied for selected models throughout this Thesis. Furthermore, high-quality DEMs for additional vertical surface displacement analysis can be derived from the CT data as well (Fedorik *et al*. in prep.).

The access to CT data provides further possibilities for model analysis. Similar to the top view photographs, the CT data allow in-plane tracing of horizontal and vertical displacements through PIV techniques (Adam *et al*. 2005). The next step is to include the third spatial dimension by correlating volumes at different time steps using digital volume correlation (DVC) methods, so that the full 3D deformation field can be derived (Adam *et al*. 2013, Fig. 1.21f). In order to create a 3D pattern that the software can correlate, small quantities of high-density Zirshot beads are mixed with the model materials. This technique is implemented in Chapters 4 and 6. Other authors have also successfully applied 3D PIV techniques on photographs of models taken from different angles (Strak & Schellart 2014). However, this requires fully transparent model materials, whereas the use of a CT scanner has the great advantage that also the deformation within normally opaque materials is revealed.
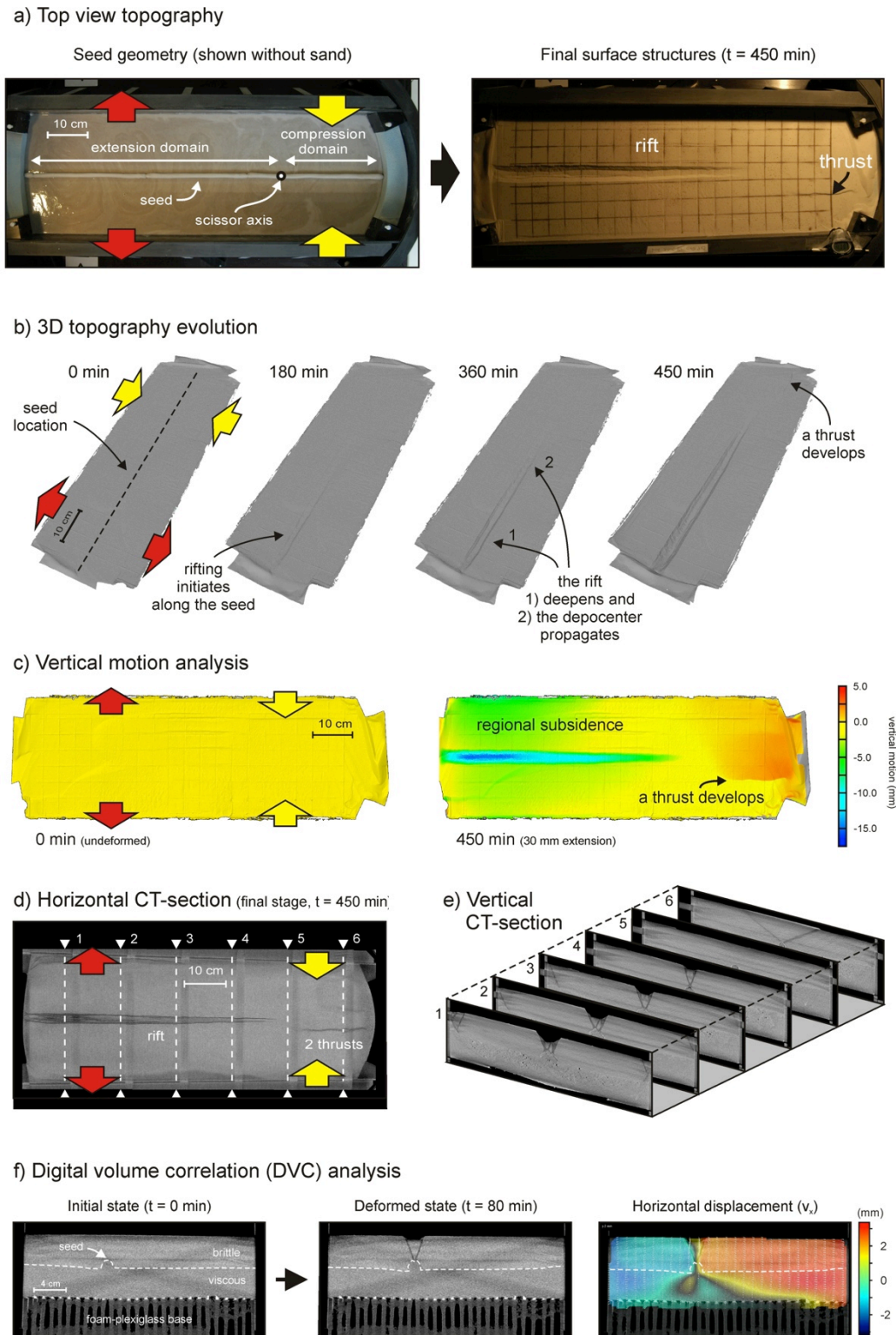
Fig. 1.21. *Techniques available at the UniBern TecLab, showing the analysis of a scissor tectonic model (Model M13 in Chapter 7). (a) Top view time-lapse photography. (b) Digital elevation models (DEM) of different time steps obtained with a surface scanner. (c) Vertical displacement derived from the DEMs. (e) CT analysis: horizontal section (left) and vertical sections (right) revealing the model's internal structures in 3D. (f) Digital volume correlation (DVC) analysis example of Model B from Chapter 4. CT images of initial state (left) and deformed state (middle), used to determine the horizontal displacement field (right). Cold colours indicate leftward motion, warm colours show motion to the right.*

1.14. Summary of themes addresses in this Thesis

Table 1.2 below provides an overview of the various themes and parameters applied in the chapter of this Thesis, as well as the various analysis methods used to examine the model structures and their evolution. The first three chapters focus on oblique extension and its influence on rift interaction structures, including various offset inherited structure geometries and sedimentation. The subsequent two chapters involve scissor tectonics: Chapter 5 focuses on rift development in such a setting, whereas Chapter 6 zooms in on rift interaction zone formation in the same setting. The final chapter investigates the differences between a wide range of experimental set-ups used for the modelling of extension tectonics.

Table 1.2. *Model parameters and analysis techniques applied for this Thesis.*

		Chapter					
		2	**3**	**4**	**5**	**6**	**7**
Extension mechanism	Foam base	X	X	X	X	X	X
	Rubber base						X
	Base plate						X
Materials	Brittle-only (upper crust model)						X
	Brittle-ductile (whole crust model)	X	X	X	X	X	X
Extension direction	Orthogonal	X	X	X	X	X	X
	Dextral oblique	X	X	X			
	Sinistral oblique	X	X	X			
	Scissor				X	X	
Extension velocity	Constant	X	X	X	X	X	X
	Various constant velocities	X	~				X
Structural inheritances	None						X
	Continuous seed				X		X
	Basal velocity discontinuity (VD)						X
	Discontinuous seed, no offset				X		
	Overlap offset (seed)						X
	Stair-case offset (seed)	X	X	X		X	
	Underlap offset (seed)		X			X	
	Offset distance variations (seed)	X					
Surface processes	Sedimentation				X		
Analysis techniques	Top view time-lapse photography	X	X	X	X	X	X
	Particle image velocimety (PIV)				p	p	p
	Topography analysis				p	p	P
	XRCT-scanning	X	X	X	X	X	X
	Digital volume correlation (DVC)			X	p	p	p

(p) Technique planned for further analysis

Chapter 2

Insights into the effects of oblique extension on continental rift interaction from 3D analogue and numerical models

Frank Zwaan[a] *, Guido Schreurs[a], John Naliboff[b], Susanne J. H. Buiter[b,c]

a) Institute of Geological Sciences, University of Bern, Baltzerstrasse 1+3, CH-3012 Bern, Switzerland
b) The Geodynamics Team, Geological Survey of Norway (NGU), Leiv Eirikssons vei 39, 7040 Trondheim, Norway
c) The Centre for Earth Evolution and Dynamics, University of Oslo, Sem Sælands vei 2A, 0371 Oslo, Norway

_____

Abstract

Continental rifts often develop from linkage of distinct rift segments under varying degrees of extension obliquity. These rift segments arise from rift initiation at non-aligned crustal heterogeneities and need to interact to develop a full-scale rift system. Here, we test the effects of 1) oblique extension and 2) initial heterogeneity (seed) offset on continental rift interaction with the use of an improved analogue model set-up. X-ray computer tomography (CT) techniques are used to analyse the 3D models through time and the results are compared with additional numerical models and natural examples. The experimental results reveal that increasing extension obliquity strongly changes rift segment structures from wide rifts in orthogonal settings to narrower rifts with oblique internal structures under oblique extension conditions to narrow strike-slip dominated systems towards the strike-slip domain. We also find that both decreasing seed offset and increasing extension obliquity promote hard linkage of rift segments through the formation of continuous rift boundary faults at the surface. (Initial) soft linkage through the formation of relay ramps is more likely when seed offset increases or extension is more orthogonal. Rather than linking at depth, the rift boundary faults curve around each other at depth and merge towards the surface to form a continuous trough. Orthogonal extension promotes the formation of intra-rift horsts, which may provide hydrocarbon traps in nature.

_____

2.1. Introduction

In the early stages of continental extension, inherited crustal heterogeneities often determine the location of initial rift segments (e.g., Morley *et al.* 1990; Nelson *et al.* 1992; Bonini *et al.* 1997; Corti 2012). This inheritance is commonly formed by lithological contrasts or shear zones resulting from previous deformation stages (e.g. plate convergence and collision, Buiter & Torsvik 2014) that can occur over zones hundreds of kilometres wide. As these inherited heterogeneities are often not properly aligned, early rift segments form separately and need to interact in order to develop a continuous rift system. Evolving rift segments may interact through a transfer zone in which rift boundary faults connect (e.g. by a discrete fault system), or through a distributed accommodation zone in which rift boundary faults do not link (e.g. Rosendahl 1987; Larsen 1988; Childs *et al.* 1995; Faulds & Varga 1998; Fig. 2.1c, d). Examples of rift segment interaction can be found in Iceland (Gudmundsson 1995), the North Sea Viking Graben (Fossen *et al.* 2010), Utah Canyonlands (Trudgill & Cartwright 1994; Fossen *et al.* 2010), offshore Brazil (Milani & Davison 1988), the Gulf of Suez (McClay & Khalil 1998), the Cenozoic European Rift System (Illies 1977; Ustaszewski *et al.* 2005) and the East African Rift System (Morley *et al.* 1990; Corti 2012; Fig. 2.1a, b). Understanding rift interaction processes is of importance since they influence the migration and trapping of hydrocarbons (Fossen *et al.* 2010; Paul & Mitra 2013) and magma (Acocella *et al.* 1999a; Corti *et al.* 2004).

Previous analogue studies of continental rift interaction indicate that the structural evolution is sensitive to various parameters such as the presence and geometry of inherited structural fabrics, melts and detachment layers (Elmohandes 1981; Naylor *et al.* 1994; Acocella *et al.* 1999, 2005; Basile & Brun 1999; Le Calvez & Vendeville 2002; McClay *et al.* 2002; Paul & Mitra 2013). The offset between initial seeds that represent inherited heterogeneities in nature has a first- order influence on rift interaction. Larger seed offsets produce narrower transfer zones (Mauduit & Dauteuil 1996; Acocella *et al.*

1999a) or even no linkage at all (Le Calvez & Vendeville 2002). When rift interaction occurs in analogue models, areas of curved normal and oblique-slip normal faults develop that connect the main rift segments. In the early stages of such experiments, accommodation zones and associated relay structures may develop (e.g. Acocella *et al.* 1999a, 2000). As extension progresses, however, deformation typically localizes to form discrete transfer zones (Acocella *et al.* 2005). In certain models, strain partitioning generates strike-slip faults accompanying the curved (oblique-slip) normal faults. However, the presence of such strike-slip faults is largely limited to cases where the angle be- tween the transfer zone and extension direction is greater than 45° (Acocella *et al.* 1999a). An important constraint on most of these models is the use of rigid base plate set-ups, which force deformation along the base plate edges and which may have a significant impact on the final model results (Morley 1999; Le Calvez & Vendeville 2002; Acocella *et al.* 2005).

Recent 3D numerical modelling of orthogonal continental extension also indicates that a range of structures may form between interacting rifts, with the style of rift interaction influenced by lower crustal viscosity and the interplay between the initial offset between seeds and mag- nitude of strain weakening in shear zones (Allken *et al.* 2011 2012). The degree of brittle-ductile coupling controls the mode of rifting and is a function of crustal viscosity and strain rate. High viscosity and strain rate promote coupling, resulting in widespread rifting, whereas low viscosity and low strain rate reduce coupling, which leads to localized or narrow rifting (Brun 1999; Buiter *et al.* 2008). This subsequently influences the rift interaction structures, as rift segment linkage is more likely when rifting is localized (Allken *et al.* 2012). Additionally, increasing seed offset prevents rift linkage, whereas increasing the rate of strain weakening has the opposite effect. The interplay of these factors determines what type of rift interaction structures forms during orthogonal extension (Allken *et al.* 2011 2012).
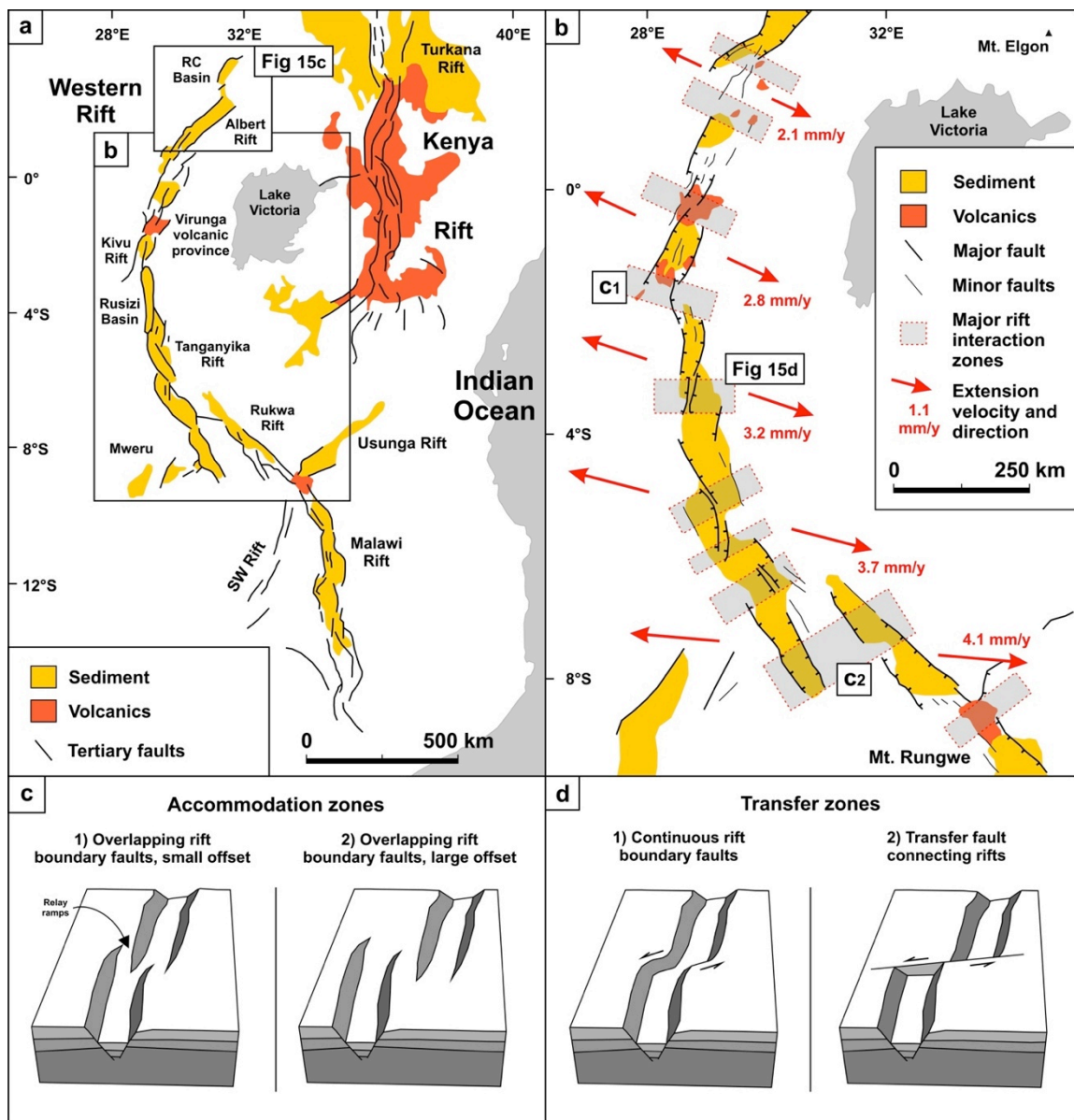
Fig. 2.1. *Examples of rift interaction zones. (a) East African Rift System. Modified after Ebinger (1989) and Dou et al. (2004). RC Basin = Rhino-Camp Basin; (b) Western Branch of the East African Rift System. Location is shown in (a). Modified after Stamps et al. (2008) and Corti (2012). Hatched faults represent normal faults, the character of faults without motion indications are not specified in the original publications. (c-d) Block diagrams depicting the differences between accommodation and transfer zones. (c) Accommodation zones (soft linkage) in which rift boundary faults do not connect, but die out laterally and overlap. Examples are present in the East African Rift System; their locations are shown in (b). (d) Transfer zones (hard linkage) in which the rift boundary faults are continuous from rift to rift (e.g. the Selenga Accommodation Zone in Lake Baikal, Scholz & Hutchinson 2000) or in which a single transfer fault connects both basins (e.g. the Gulf of Suez or Thailand (Acocella et al. 1999a; Morley et al. 2004)).*

This type of model has the advantage that structures have more freedom to develop because the lower crust distributes deformation in contrast to the rigid base plate edges in most analogue set-ups.

The aforementioned analogue and numerical experiments provide important insights in the structure and evolution associated with rift linkage. However, to date no studies exist that systematically examine rift interaction

processes during oblique extension, a parameter which may strongly control the evolution of rift interaction structures (Trudgill & Cartwright 1994) and which promotes eventual continental break-up (Brune *et al.* 2012; Bennett & Oskin 2014).

Here, we present a series of models designed to examine crustal-scale continental rift interaction as a function of oblique extension and rift offset. In contrast to most previous analogue studies that apply a rigid base plate set-up to study rift interaction, our models undergo distributed basal deformation that permits rifts more freedom to evolve (Le Calvez & Vendeville 2002). We also apply X-ray computer tomography (CT) techniques that allow a detailed analysis of internal model geometry with time (e.g. Colletta *et al.* 1991; Schreurs & Colletta 1998; Schreurs *et al.* 2002). The analogue model results are then compared with additional numerical models and natural examples.

2.2. Materials and methods

2.2.1 Material properties

We use a standard brittle-viscous layering of materials generally applied to crustal-scale modelling of continental rifting. Alternating 0.5 cm thick layers of fine quartz sand (ø: 60-250 μm, ϱ: 1560 kg/m^3) and corundum sand (ø: 88-175 μm, ϱ: 1890 kg/m^3) are sieved from ca. 30 cm height into the modelling apparatus to form a 2 cm thick layer that represents the brittle upper crust. We apply this sand alternation to create density contrasts within the brittle layer that are visible on CT images. Granular materials typically show elastic-plastic behaviour where increasing stress first results in strain-hardening, followed by failure at peak strength and a subsequent decrease in strength until the system reaches a state of dynamic stable sliding (Lohrmann *et al.* 2003). The mechanical properties of our granular materials were determined with a ring-shear tester that was filled using the same physical handling technique as the one used to construct our analogue models, i.e. sieving from ca. 30 cm height. Angles of peak- and stable friction are 36.1° and 31.4° for our quartz sand and 37° and 32° for our corundum sand, respectively, with cohesion values in the order of several tens of Pa (Panien *et al.* 2006; Klinkmüller 2011, Table 2.1). As both types of sand have nearly similar mechanical properties, the alternation of these granular materials in our models does not change its characteristics significantly, and we consider that they represent a quite homogeneous upper crust. Note that we are aware of the fact that the sand in our models produces shear zones rather than discrete faults, but here we choose to use the terms "faults" and "shear zones" as equivalent. Further details of our model materials are given in Table 2.1.

A 2 cm thick mixture of silicone (polydimethylsiloxane, PDMS) and the same corundum sand as mentioned above represents the ductile lower crust. This mixture (weight ratio: 0.965 kg of PDMS mixed with 1.0 kg corundum sand) has a density of 1600 kg/m^3, which is close to that of the overlying brittle sand layers (average density of ca. 1700 kg/m^3). We use this viscous mixture to create a more realistic density profile than the use of pure PDMS would provide and so prevent PDMS diapirism. Rheology tests reveal shear-thinning behaviour, but the mixture can be regarded as a near-Newtonian material since its n-value is 1.05. The viscosity of the PDMS/corundum sand mixture is ca. $1.5 \cdot 10^5$ Pa s for our strain rates of ca. $7 \cdot 10^{-6}$/s. The corundum sand remains in suspension for the duration of the model runs and only sinks to the base of the PDMS medium after several weeks.

2.2.2. Experimental set-up

The experimental machine (Fig. 2.2) consists of two longitudinal walls, between which a series of 21 plexiglass and 20 foam bars (0.5 cm and 1 cm wide respectively, all 79 cm long) are tightly stacked, overlying two base plates. Before applying the model layers, the initially 30.5 cm wide plexiglass and foam base is 16% compressed to a 25.5 cm width by driving the rigid sidewalls towards each other with computer-controlled motors. During a

model run, the rigid sidewalls move apart so that the compressed foam expands, creating distributed extensional deformation with a constant velocity gradient at the base of the overlying model material (Fig. 2.2e, f). This contrasts with deformation localizing along the edges of base plates in traditional set-ups (Fig. 2.2f).

One base plate can move laterally, producing a distributed strike-slip component in the overlying model. The combination of strike-slip and orthogonal extension produces oblique extension. Two pivoting bars along the short ends of the model control the lateral motion of the plexiglass and foam bars during oblique extension (Fig. 2.2a, d). Rubber sidewalls confine the overlying model materials at their short ends in order to ensure the same uniform extension as at the model base thus minimizing potential boundary effects due to relative motions between model materials and sidewalls.

Following Le Calvez & Vendeville (2002), semi-cylindrical seeds of the viscous PDMS/corundum sand mixture (ca. 0.3 cm high and ca. 0.5 cm wide) were applied on top of the basal viscous layer to define the geometry of inherited heterogeneities. These are segmented by a "staircase" type seed offset (offset angle $\phi = 90°$ in Fig. 2.2b, after e.g. Corti (2004)), which leaves no space for seeds to under- or overlap each other. Deformation localizes above these discontinuous seeds due to their strength contrast with the relatively strong overlying and adjacent sand layers (Fig. 2.2b, c, e). Note that the seeds we apply will not represent all natural settings involving inherited structure reactivation, in the sense that structural inheritance may have a pervasive or discrete character (Morley 1999). In our models, the seeds clearly represent discrete inherited structures. Similar to Allken *et al.* (2011, 2012) seed offset (H) is described relative to the scale of the crust: a 1 H offset is equal to the thickness of the brittle crust (2 cm in this study), which together with the rift boundary fault angle controls rift geometry (Allemand & Brun 1991). This way, we can easily compare our models with natural and experimental examples that have different brittle layer thicknesses. The seed offset is also varied to

test the influence of rift proximity (Table 2.2). Instead of one seed offset configuration at a time, we apply three different seed offsets representing three simultaneous experiments per model run to increase our modelling efficiency (Fig. 2.2g).

According to the usual convention (e.g. Brune *et al.* 2012; Corti 2012), extension obliquity is defined as the angle α between the extension direction and the normal to the rift or seed trend (Fig. 2.2b, g). In our model series, angle α ranges from 0° (orthogonal extension, perpendicular to seed strike) to 90° (dextral strike-slip movement parallel to seed strike) in steps of 15° (Table 2.2). When applying oblique extension (0° > α > 90°), the long sidewall and base plate motions are adjusted to produce a constant total extension velocity at the desired extension obliquity (Fig. 2.2g).

Selected models are analysed using a 64 slice Siemens Somatom Definition AS X-ray CT-scanner. Because of time constraints and the limited amount of extension that the rubber sidewall and foam-plexiglass base can accommodate, the model run duration is set to 240 min. Several model set-ups are run multiple times and exhibit very similar results, indicating that the model outcomes are well reproducible (Appendix 2C, Fig. 2.C1).
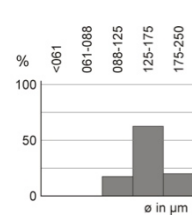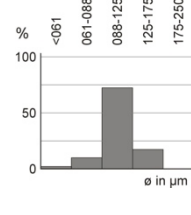
2.2.3. Analogue velocity calibration

he analogue model series consists of 13 model runs, representing a total of 39 different experiments. Out of this set, 18 experiments from 6 model runs provide associated X-ray CT-derived imagery (Table 2.2). An initial set of model runs (EXP472-474, Appendix 2C, Fig. 2.C2) was aimed at finding a practical extension velocity that does not lead to high brittle-ductile coupling (Brun 1999) and associated patterns of distributed faulting that prevent rift linkage (Allken *et al.* 2012). We tested a range of extension velocities between 6 and 30 mm/h. The higher extension velocities result in high brittle-ductile coupling and associated distributed faulting throughout the model. At a velocity of 6 mm/h, however, deformation sufficiently focuses along the pre- defined weak zones to develop the single rift segments that allow us to investigate rift interaction processes under

controlled conditions. An extension velocity of 6 mm/h, which is representative of natural extension velocities (see Paragraph 2.2.5), is subsequently used in all additional models.

After 240 min each model has undergone 2.4 cm (or 1.2 H) of extension (ca. 10% total strain) in the selected extension direction.

Table 2.1. *Material properties. Quartz sand and viscous material characteristics measured at GFZ Potsdam. Corundum sand characteristics from Panien et al. (2006) and Klinkmüller (2011).*

Granular materials		Quartz sand	Corundum sand
Grain size distribution (weigth %)			
Grain shape[a]	- surface texture	-	conchoidal fractures
	- roundness	angular	angular
	- form (elongation)[b]	-	2.00
	- sphericity	low	low
Density (sieved)		1560 kg/m^3	1890 kg/m^3
Coefficient of internal peak friction		0.73	0.65
Coefficient of dynamic-stable friction		0.61	0.63
Angle of internal peak friction		36.1°	37°
Angle of dynamic-stable friction		31.4°	32°
Strain softening[c]		16%	16%
Cohesion		9 ± 98 Pa	39 ± 10 Pa

Viscous material	PDMS/corundum sand mixture
Weight ratio PDMS : corundum sand	0.965 kg : 1.00 kg
Mixture density	ca. 1600 kg/m^3
Viscosity[d]	ca. 1.5·10^5 Pa·s
Type	near-Newtonian (n = 1.05)[e]

(a) Quartz grain shape determined after Powers (1953); (b) Elongation: ratio between longest and shortest diameter; (c) Strain softening is the difference between peak strength and dynamic-stable-strength, divided by peak strength; (d) The viscosity value holds for model strain rates < 10^{-4} s^{-1}; (e) Dimensionless stress exponent n indicates sensitivity to strain rate.
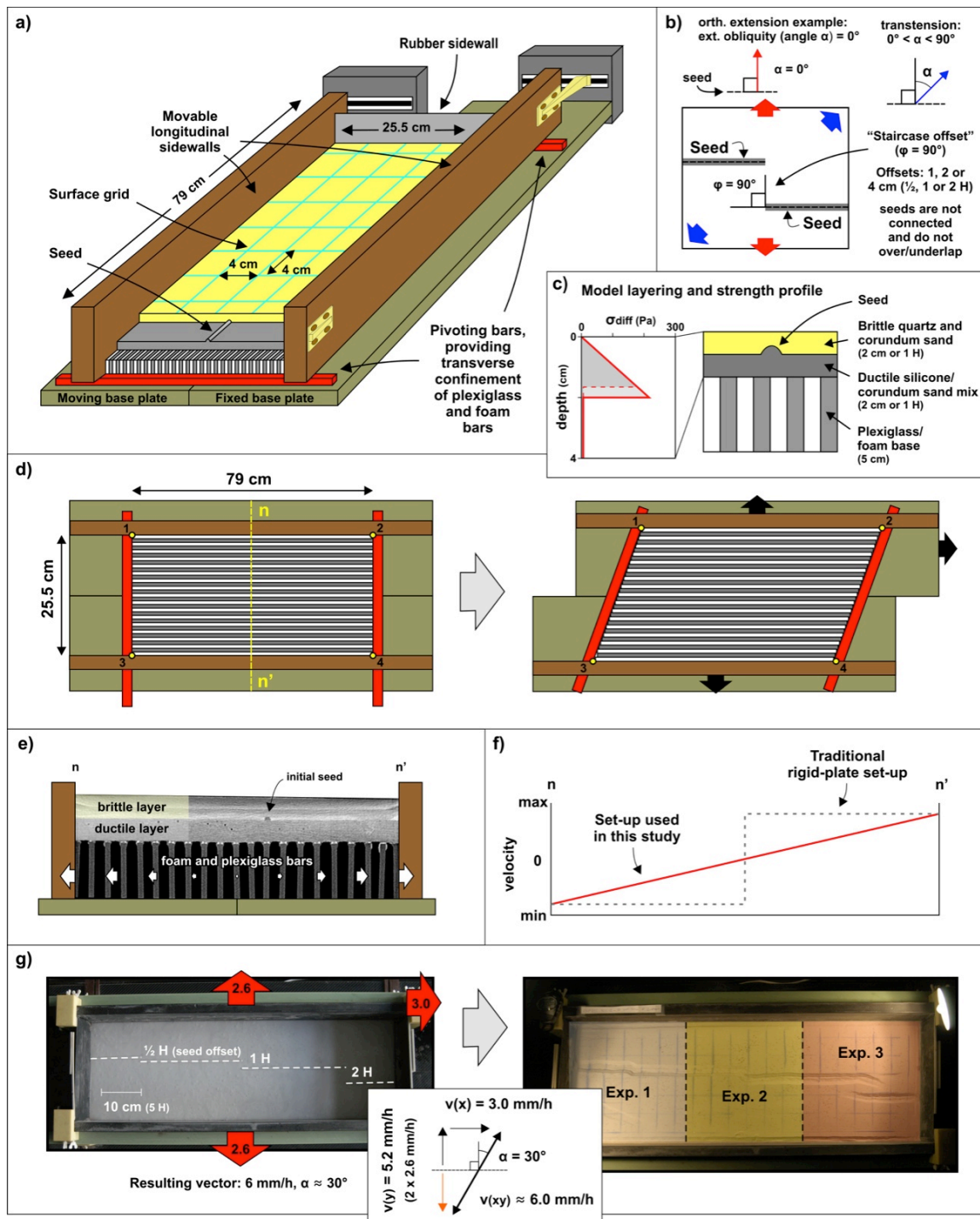
Fig. 2.2. *Set-up of the analogue experiments. a) Cut-out view of the experimental apparatus; b) Surface view showing the definition of extension obliquity (angle α) and seed geometry; c) Compositional layering and associated strength profile. The dotted line indicates the strength profile at the seed, where the brittle layer is thinner. Calculated after Brun (2002); d) Schematic surface view showing the initial set-up and subsequent deformation of the empty apparatus; e) Example of a CT-derived cross-section (n–n', see (d)), showing the initial model layering and seed geometry. White arrows indicate the velocity gradient at the model base; f) Velocity profile (perpendicular to extension direction, see (e)) in current and traditional set-ups; g) Left: Surface view of the PDMS/corundum sand mixture with seed geometry before adding the sand cover. Note that the seeds are not connected. Middle: applied extension obliquity. Right: Top view of the example model showing final surface deformation of three simultaneous experiments.*

Table 2.2. *Summary of analogue model parameters*.

Model run	Ext. obliquity (angle α)	Ext. velocity (mm/h)	Seed offset (H = 2 cm)			CT-scanned	(Parts of) models presented in
			I	II	III		
EXP472	0°	30	1 H	2 H	3 H		Fig. 2.C2
EXP473	0°	20	1 H	2 H	3 H	X	Fig. 2.C2
EXP474	0°	6	1 H	2 H	3 H	X	Fig. 2.C2
EXP483	0°	6	½ H	1 H	2 H		-
EXP498	0°	6	½ H	1 H	2 H	X	Figs. 2.3, 2.5, 2.6, 9 11-15
EXP479	15°	6	½ H	1 H	2 H		Fig. 2.3
EXP478	30°	6	½ H	1 H	2 H		Fig. 2.C1
EXP482	30°	6	½ H	1 H	2 H		Fig. 2.C1
EXP484	30°	6	½ H	1 H	2 H	X	Figs. 2.2, 2.3, 2.5, 2.6, 2.9, 2.11-15, 2.C1
EXP480	45°	6	½ H	1 H	2 H		Fig. 2.3
EXP476	60°	6	½ H	1 H	2 H	X	Figs. 2.3, 2.5, 6, 9, 11-14
EXP481	75°	6	½ H	1 H	2 H		Fig. 2.3
EXP477	90°	6	½ H	1 H	2 H	X	-

2.2.4. Numerical set-up

As a complement to the analogue experiments, we also model rift interaction using the thermal-mechanical finite-element code SULEC (e.g. Buiter & Ellis 2012; Ellis *et al*. 2011; Naliboff & Buiter 2015). These experiments aim to determine whether deformation driven from sidewalls and for a range of material properties and length scales produces similar structures and processes to those in the analogue models. Our broad approach follows that of Allken *et al*. (2012, 2013), where the crust is represented by a combination of linear viscous and brittle (Drucker–Prager) behaviour.

The numerical setup (Appendix 2A, Fig. 2.A1) is aimed at investigating the brittle upper crust and spans 15 cm along the x- (width) and z- (length) axes, and extends 2 cm to the base of the brittle upper crust along the y-axis (depth). We focus on one seed offset per experiment and the narrow horizontal (x- and z-axes) extent of the model permits a relatively high numerical resolution (120 × 16 × 120 elements of 0.125 cm widths in all directions) that captures first-order processes between interacting rifts. Additional models (Appendix 2B) contain a viscous lower crust

that extends to 4 cm depth or test length scales (km instead of cm) and material properties commonly assigned to the crust in numerical experiments.

The composition of the brittle layer follows the analogue models with alternating layers (0.5 cm) of quartz and corundum sands. Brittle deformation initiates along viscous seeds at the model base that extends 4 cm in the z-direction. In cross-section, seed size is 0.25 × 0.25 cm (along the x- and y-axes). Offsets between the seeds (rift offset) range from 2 to 4 cm (1–2 H). The properties (Appendix 2A, Table 2.1) of the brittle sand layers and viscous seeds follow the analogue material properties (Table 2.1).

Wider shear zones and lower shear zone dip angles (45° versus ca. 60°) in the numerical experiments compared with the analogue experiments produce wider rifts that intersect the surface approximately 1 cm closer to each other than those in the analogue models. The wider shear zones and lower dip angle directly reflect the numerical resolution, which is well established as a first order control on these properties in numerical shear band experiments (e.g. Lemiale *et al*. 2008; Kaus 2010; Buiter 2012). To achieve significantly

thinner shear zones and dip angles approaching those in the analogue experiments (~60°) would likely require ~5× higher resolution in each spatial direction (125 times more elements in total), which is well outside the limits of most numerical codes. The combined effect of wider shear zones at lower dip angles is that numerical seed offsets of 2–4 cm (1–2 H) equate to analogue seed offsets of 0.5–1.5 H. We clarify this by hereby referring to numerical model seed offsets in terms of the exact offset in cm and a term H*, which represents the numerical seed offset adjusted to equivalent analogue model seed offsets.

Fixed outward velocities along the left and right walls drive exten- sional deformation, which is oriented at 0°, 30° or 60° (angle α) relative to the x-axis. The total velocity magnitude is fixed at ca. 3.5 mm/h (ca. 1.75 mm/h on each side), which produces equivalent velocity gradients to those in the wider analogue models. The equivalent velocity gradients reflect a linear relationship between the applied velocity and model width within the numerical experiments, which were selected to match the observed analogue model velocity gradient. The time step is fixed at 225 s. Horizontal velocities along the front and back walls vary linearly between the left and right walls and remain fixed through time in order to maintain constant velocity gradients. The base and top of the model, respectively, maintain free-slip and zero stress (free) velocity conditions. As noted above, the numerical free-slip base contrasts with the mobile base of the analogue models, which drives deformation. Additional details of the numerical methods are given in Appendix 2A.

2.2.5. Model scaling

We apply the standard equations to scale our models up to natural scales. For brittle Mohr-Coulomb type materials, the following equation for stress ratios (σ^*, convention: $\sigma^* = \sigma_m/\sigma_n$ with subscripts m and n representing model and nature, respectively) holds (Hubbert 1937; Ramberg 1981):

$$\sigma^* = \varrho^* h^* g^* \tag{2.1}$$

We use the following values to calculate the density ratio (ϱ^*): $\varrho_m = 1690$ kg/m^3 and $\varrho_n = 2800$ kg/m^3, the length ratio (h^*): $h_m = 4\cdot10^{-2}$ m and $h_n = 4\cdot10^4$ m and the gravity ratio (g^*): $g_m = g_n = 9.81$ m/s^2. The stress ratio for the brittle part of the models is thus ca. $6\cdot10^{-7}$.

Scaling of viscous materials is more complex, since in contrast with brittle materials, their behaviour is time-dependent. The following formulas can be applied for fluids with (near-) Newtonian rheology (Weijermars & Schmeling 1986):

$$\dot{\varepsilon}^* = \sigma^*/\eta^* \tag{2.2}$$

where $\dot{\varepsilon}^*$ is the strain rate ratio as a function of the stress ratio and viscosity ratio (η^*). With $\dot{\varepsilon}^*$ we can derive the velocity ratio (v^*) as well as the time ratio (t^*):

$$\dot{\varepsilon}^* = v^*/h^* = 1/t^* \tag{2.3-4}$$

It follows that, as lower crustal viscosities are generally considered to range from $1\cdot10^{19}$ to $1\cdot10^{23}$ Pa·s (e.g. Buck 1991), 1 hour in our models represents 0.04 to 42 Ma ($\eta_m = 1.5\cdot10^5$ Pa·s). The model extension velocity of 6 mm/h translates to a velocity between 0.14 and $1.4\cdot10^3$ mm/y in nature. Typical extension velocities observed in continental rifts (e.g. East Africa) plot in this range (Stamps *et al.* 2008, Fig. 2.1)

In order to secure dynamic similarity between our models and nature, we consider the ratio R_s between gravitational stress and cohesive strength (or cohesion: C) for the brittle domain in both our models and nature (Ramberg 1981; Mulugeta 1988):

$$R_s = \frac{\text{gravitational stress}}{\text{cohesive strength}} = \frac{\rho \cdot g \cdot h}{C} \tag{2.5}$$

Similarly we use the Ramberg number or R_m for the ratio between gravitational forces and viscous stress in the viscous domain (Weijermars & Schmeling 1986):

$$R_m = \frac{\text{gravitational stress}}{\text{viscous stress}} = \frac{\rho \cdot g \cdot h}{\dot{\varepsilon} \cdot v} = \frac{\rho \cdot g \cdot h^2}{\eta \cdot v} \tag{2.6}$$

57

Finally the Reynolds number or R_e indicates what flow type occurs in the viscous layers (Weijermars & Schmeling 1986):

$$R_e = \frac{\rho \cdot v \cdot L}{\eta} \qquad (2.7)$$

where L represents a distance covered at a certain velocity v. The values we use to calculate these dimensionless numbers are given in Table 2.3. The model R_m value of 25 fits well in the natural range (1 to $1 \cdot 10^4$) and R_s values are 13.8 and 9.2 in the models and nature respectively ($C_{nature} = 6 \cdot 10^7$, after Corti et al. 2004). As the Reynolds numbers are << 1 (indicating laminar flow) for any reasonable value of L, the requirement of dynamic similarity is fulfilled.

Table 2.3. *Parameters used for model scaling.*

	General parameters			Brittle upper crust		Ductile lower crust		Dimensionless values		
	Grav. accel. g (m/s^2)	Crustalt thickness (m)	Extension velocity v (m/s)	Density ϱ (kg/m^3)	Cohesion C (Pa)	Density ϱ (kg/m^3)	Viscosity η (Pa·s)	Ramberg number R_m	Brittle stress ratio R_s	Reynolds number R_e
Model	9.81	0.04	$1.7 \cdot 10^{-6}$	1725[a]	24[b]	1600	$1.5 \cdot 10^5$	25	13.8	<<1
Nature	9.81	$4 \cdot 10^4$	ca. $1 \cdot 10^{-10}$	2800	$6 \cdot 10^7$	2900	$1 \cdot 10^{19\ to\ 23}$	$1 \cdot 10^{0\ to\ 4}$	9.2	<<1

(a)   Average density of both sand types
(b)   Average cohesion of both sand types

2.3. Overview of deformation patterns

2.3.1. Analogue structural surface overview

In all models, faulting initiates above the seeds shortly after the onset of extension. After ca. 1.5 h, enough topographic relief develops above the faults to analyse discrete structures. Final surface deformation patterns after a model duration of 240 min (or 2.4 cm of extension) reveal that significant structural variations occur when the extension direction or seed offset is modified (Figs. 2.3, 2.4). Orthogonal extension produces wide rift basins above the initial seeds (ca. 1.2 H or 2.4 cm for α = 0°, Fig. 2.4), whereas increasing extension obliquity results in narrower rifts (0.6 H or 1.2 cm for α = 60°).

For extension obliquity α ≥ 45° (Fig. 2.3) narrow basins and strike-slip motion characterize the system. Strike-slip motion along the rift bound ary faults can be well traced due to the offset in the surface grid, which increases with extension obliquity (Fig. 2.3a). From α = 15° to 60°, the increasingly narrower rift basins contain oblique-slip normal boundary faults and internal en echelon oblique/strike-slip features. Riedel-type secondary structures develop at the edge of the basins in strike-slip dominated oblique extension (α ≥ 75°), with surface strikes oriented 14–23° oblique with respect to the rift trend. Fault branches that stem from the edges of the initial seeds are present in several models with 2 H seed offset and α ≥ 30°. These faults are strike-slip dominated as shown by their narrow geometry and the surface grid offset (Fig. 2.3).

The initial seed offset and extension obliquity both determine whether rifts connect through a transfer zone (hard linkage, as the rift boundary faults are continuous) or through an accommodation zone (soft linkage, as the rift boundary faults are discontinuous and overlap from rift to rift). All models with a seed offset of ½ H and 1 H produce a connected rift system at the model surface (Fig. 2.3). In contrast, a 2 H seed offset prohibits direct hard linkage for orthogonal and oblique extension models up to 30° extension obliquity. For α ≥ 45°, a continuous transfer zone develops that connects the rifts through hard linkage.
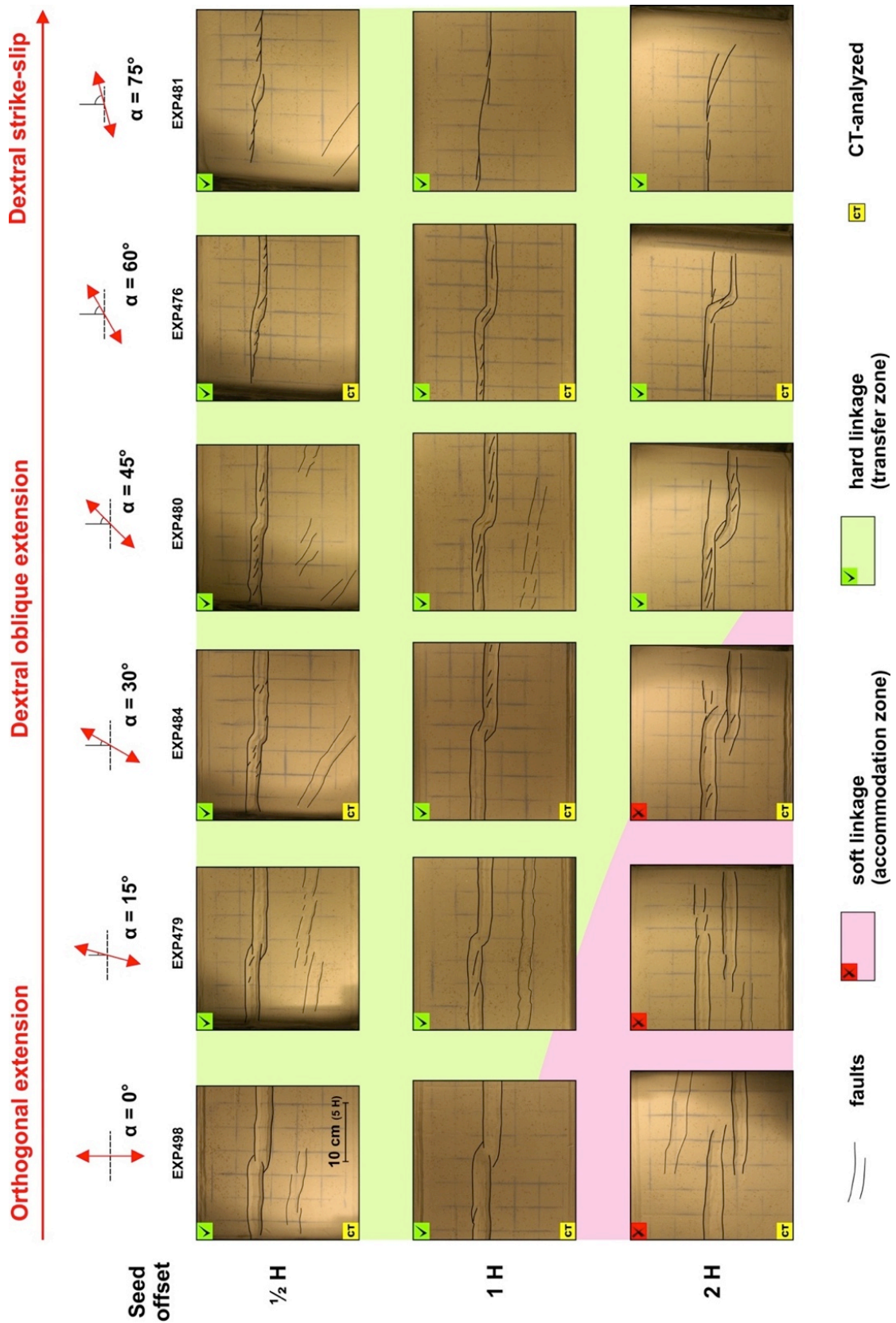
Fig. 2.3. *Overview of final surface deformation patterns in the analogue models as a function of extension obliquity (angle α = 0°–75°) and seed offset, after 240 min or 2.4 cm extension. Colour coding shows rift linkage mode: green for hard linkage (transfer zones) and pink for soft linkage (accommodation zones).*

59

Some top view images show minor additional boundary effects away from the initial seeds and the main rift structures (Fig. 2.3). The ½ H seed offset models develop en echelon rifts striking perpendicular to the extension direction so that with increasing extension obliquity, these small rifts develop more obliquely with respect to the seeds. Similar structures occur in the 1 H seed offset models ($\alpha = 15°$ and $45°$), although there is less correlation with extension obliquity. Only the $\alpha = 15°$ example contains faulting away from the main rift that develop perpendicular to the extension direction. When extension obliquity is $45°$, they have the same orientation as in the experiments with $\alpha = 15°$. Limited normal faulting along the long sidewalls occurs in all models However, neither boundary effect interferes with the rift linkage structures.
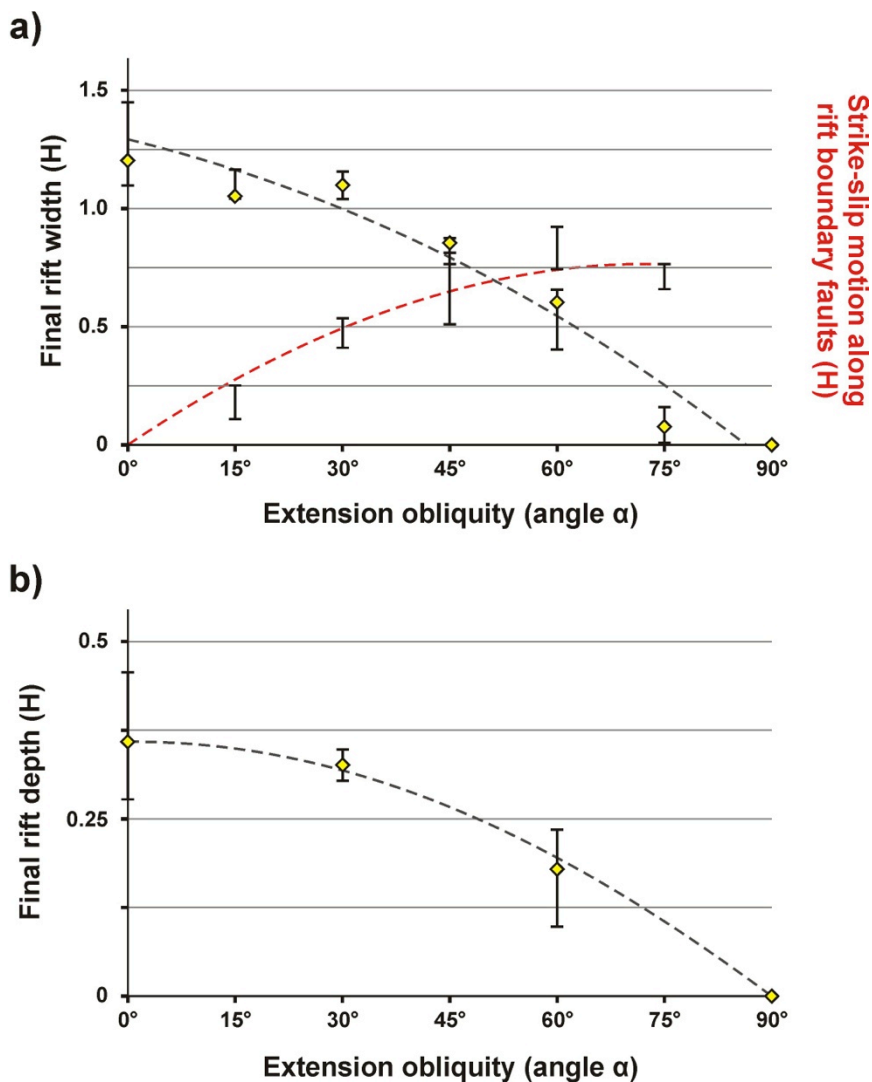
Fig 2.4. *(a) Final rift segment width and strike-slip motion along rift boundary faults as a function of extension obliquity (independent of seed offset), measured on model surface views (Fig. 4). (b) Final rift depth over extension obliquity, measured on CT sections. In both graphs, error bars indicate the ranges of measurements and the yellow dots indicate typical values (mode). All trend lines are 2nd order polynomial, $R^2 = 0.97, 0.93$ and 0.99, respectively.*

2.3.2. Analogue internal deformation

Combining horizontal and vertical CT sections of the final model stage provide 3D insights into the internal model structure as a function of extension obliquity and seed offset (Figs. 2.5, 2.6). The horizontal CT-scan images are taken in the sand ca. ⅙ H (0.3 cm) above the silicone base layer at the end of the model run and show how the rifts propagate away from the initial seeds. The horizontal CT sections cut the initial seeds, but also show where the viscous base layer flows upwards in regions away from the initial seeds (Fig. 2.5a). This vertical displacement reflects decreased loading under the propagating rifts, as the overlying sand layer thins. Vertical CT sections are focussed on zones of rift segment interaction in order to accurately resolve their structural features. The selected models represent 0°, 30° and 60° extension obliquity for ½ H, 1 H and 2 H seed offsets.

All set-ups produce overlapping rift propagation structures stemming from the ends of the initial seeds. The rifts grow towards each other in a direction that tends to become more oblique with increasing extension obliquity (i.e. increasing α). This effect is best seen in the 2 H seed offset models, where rift propagation is oriented perpendicularly to the extension direction (Fig. 2.5c, f, i, i'). The rift segments in models with smaller offsets are likely too close to each other to solely illustrate the influence of extension obliquity. The propagating rift branches seem not to connect at depth in any of the models.

The relationship between structures at depth with those at the model surface (Fig. 2.5) is visible on vertical CT sections (Fig. 2.6). Moving from the back to the front of most models, a single rift segment is initially present (e.g. Fig. 2.6a, section 1). Towards the middle, a second rift segment appears (Fig.

2.6a, sections 2–3) and systematically accommodates more deformation towards the opposite side where the first rift segment subsequently dies out (Fig. 2.6a, sections 4–5). The rift segments do not connect at depth, but rather run along and curve around each other. Both rift segments grow wider towards the surface and consequently merge to form the continuous, well-defined troughs seen on top-view images (Fig. 2.3). In between the interacting rift segments, a horst structure develops. This general structure is typical for models in which the rift segments propagate close to each other (Fig. 2.6a, b, d). With increasing extension obliquity, some variations occur. The rift boundary faults tend to steepen and the trough between the linking rift segments becomes narrower and less deep, from maximum 0.45 H to 0 H in orthogonal extension and strike-slip settings respectively (Figs. 2.4 and 2.10). The trough appears therefore less pronounced on both surface images (Fig. 2.3) and vertical CT sections (Fig. 2.6).

The fault branches in the models with high extension angles that propagate along strike from the edges of the initial seeds (Fig. 2.3) are well resolved on the CT images (Fig. 2.5f, g, h, i). These structures are relatively narrow and steep with respect to the main rifts and represent oblique-slip normal faults (Fig. 6c) or strike-slip faults (Fig. 2.6d), which reflects strain partitioning between the main rifts and these additional transverse structures.

Some boundary effect faults are evident in the CT images, which mostly occur in the models with higher extension obliquity and which are situated at the lower left acute angles of the set-up. The appearance of these boundary effects might be due to a scissoring effect in the lower left corner of the set-up, but they are not considered to have a significant effect on the main model structures.
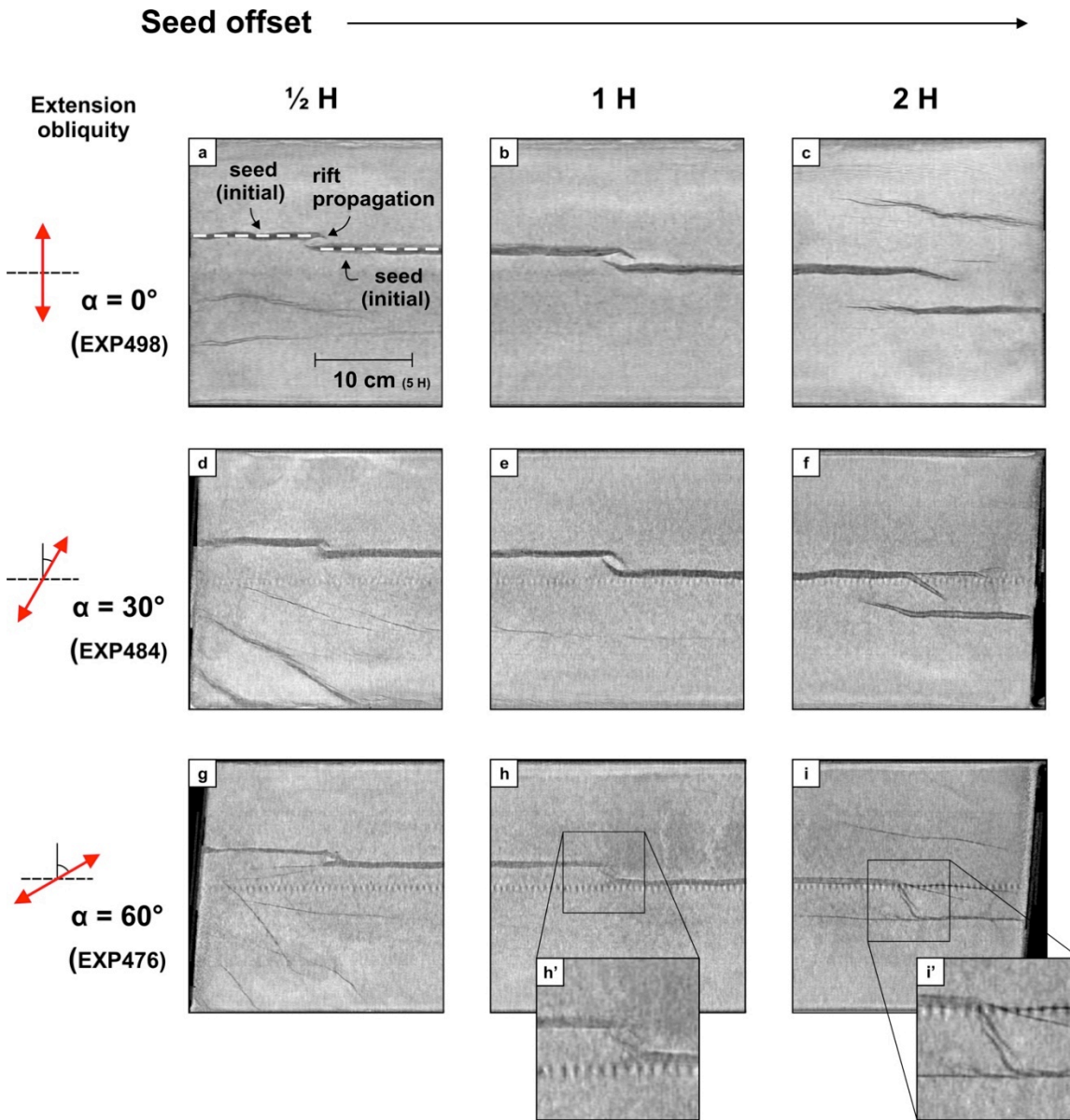
Fig. 2.5. *Overview of final horizontal deformation patterns inside the analogue models as a function of extension obliquity and seed offset. The horizontal CT sections cut the sand ca. ⅙ H (0.3 cm) above the basal silicone layer and are taken after 240 min or 2.4 cm extension. The dark grey linear features represent the original seed and newly developed structures. Striped patterns in the middle of the images (mostly in g–i) are CT-scanning artefacts.*
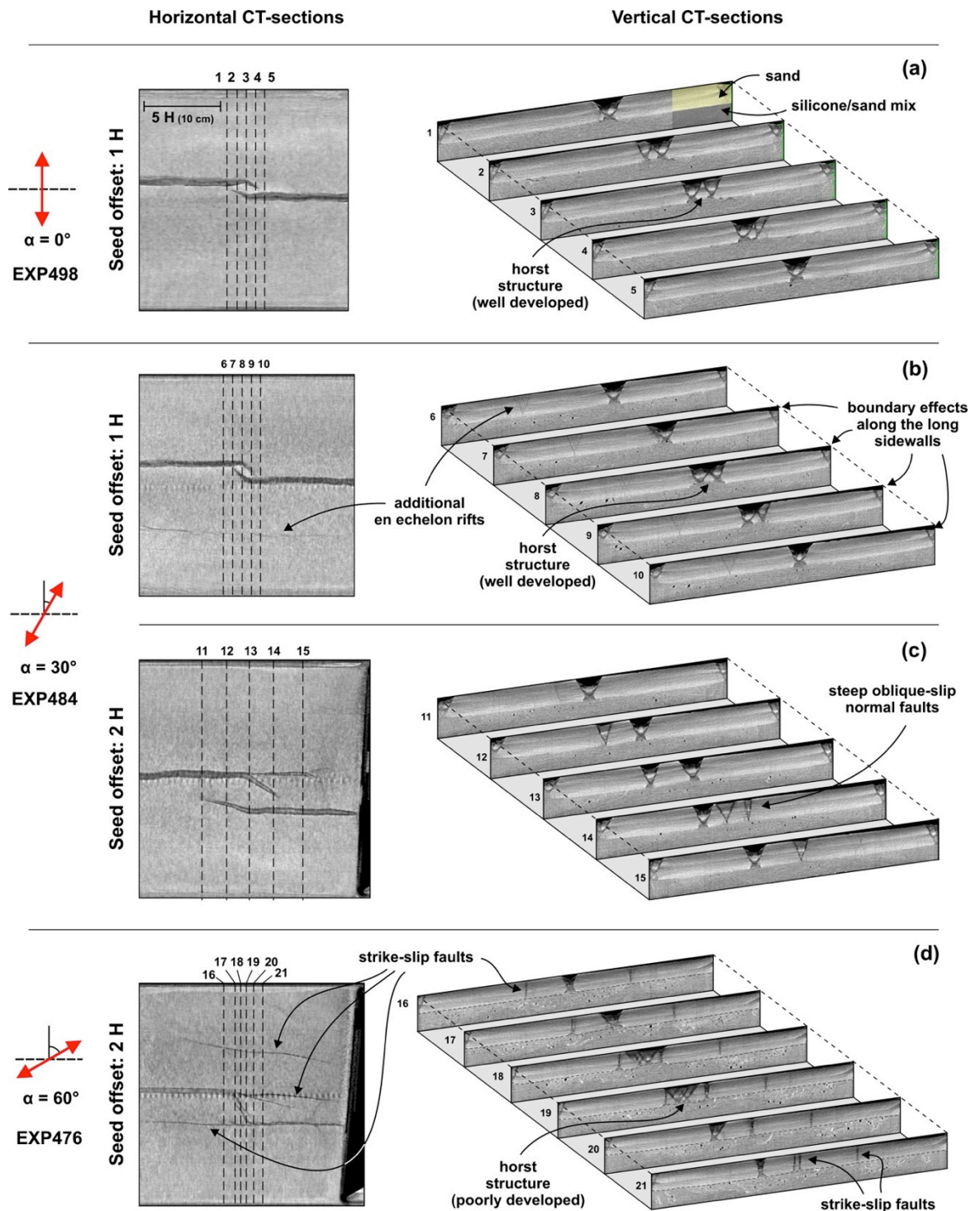
Fig. 2.6. *Final horizontal deformation patterns (left column) and corresponding vertical cross sections (right column) for a selection of analogue models. The horizontal CT sections cut the sand ca. ⅙ H (0.3 cm) above the basal silicone layer and are taken after 240 min or 2.4 cm extension. The locations of the vertical sections are shown in the left column. Striped patterns in the middle of the horizontal sections are CT-scanning artefacts.*

2.3.3. Numerical structural overview and internal analysis

As observed in the analogue experiments, increasing extension obliquity (α) promotes rift linkage (Fig. 2.7), albeit over a comparatively limited range of seed offsets. For an initial seed offset of 0.5 H* (2 cm) propagating shear zones overlap (Figs. 2.7a–c, 2.8_{top}) to produce a connected rift system for all extension angles. Clear rotations of the topographic structures and shear zones towards the extension direction, however, occur with in- creasing extension obliquity. Notably, an extension obliquity of 60° (Fig. 2.7c) generates significantly less topographic development within rift zones as deformation transitions to dominantly strike-slip behaviour.

Increasing the seed offset to 1.0 H* (3 cm) fails to produce rift linkage during orthogonal extension (Fig. 2.7d) at $\varepsilon = 10\%$, although relatively low topography at the rift intersection reflects interaction between the adjacent inner shear zones. This topographic structure (Fig. 2.7d) separating the rifts is

similar in nature to the horsts observed in the orthogonal analogue models. An extension obliquity of 30° fully links the rift systems as

Increasing the seed offset to 1.0 H* (3 cm) fails to produce rift linkage during orthogonal extension (Fig. 2.7d) at e = 10 %, although relatively low topography at the rift intersection reflects interaction between the adjacent inner shear zones. This topographic structure (Fig. 2.7d) separating the rifts is similar in nature to the horsts observed in the orthogonal analogue models. An extension obliquity of 30° fully links the rift systems as the adjacent shear zones connect through a well-defined transfer zone (Fig. 2.7e, Fig. 2.8_{middle}). As with a 0.5 H* (2 cm) offset, increasing the extension obliquity to 60° significantly inhibits development of the rift systems and also fails to produce rift linkage. A seed offset of 1.5 H* (4 cm) (Fig. 2.7g-I, Fig. 2.8_{bottom}) fails to link in all cases, although increasing extension obliquity produces similar topographic and shear zone rotations as in Fig. 2.7b-c,e-f.
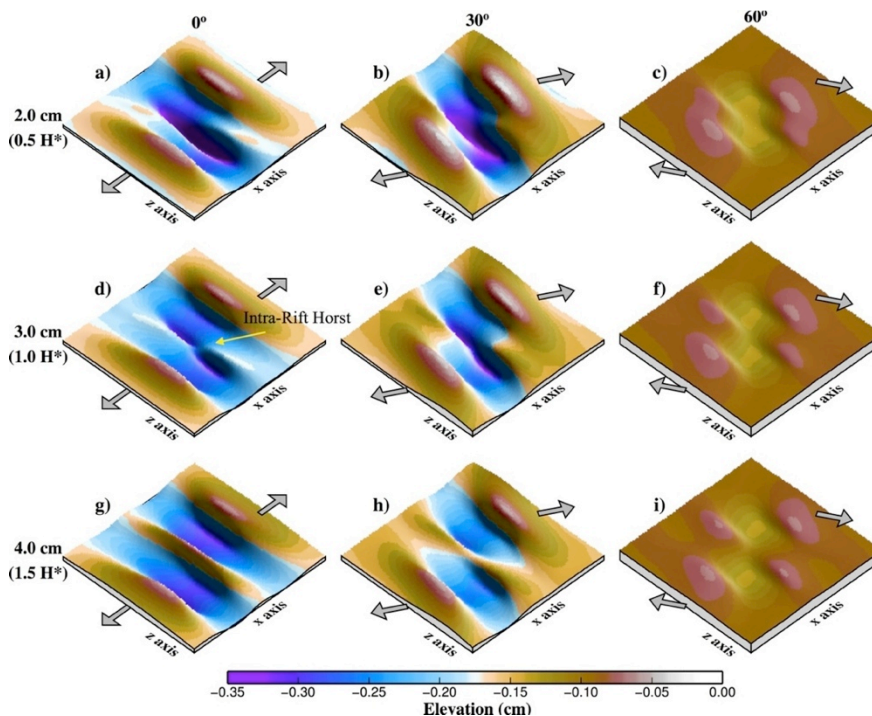
Fig. 2.7. *Overview of the final stages of the numerical models. Surface elevation after 240 min of extension (10% strain) for extension directions of 0°, 30° or 60° and seed offsets of 2, 3 or 4 cm (0.5, 1.0, 1.5 H*). The entire surface extent of the model domain (15 cm × 15 cm) is plotted at a 1:1 scale. The vertical axis (y) is exaggerated by a factor of 10 to illustrate deformation structures. Note the annotated intra-rift horst (panel d).*

The results above reveal that rift linkage only occurs when the rift bounding shear zones, which initiate at the two seeds, initially intersect (Figs. 2.7a-c, 8$_{top}$) or nearly intersect at moderate extension obliquity (~30°, Figs. 2.7e, 2.6$_{middle}$). This contrasts with the analogue experiments, where rift linkage occurs over a wide range of seed offsets and extension obliquities (Fig. 2.3). While the inclusion of a lower crust layer (Appendix 2B, Fig. 2.B1) in models with a 4 cm seed offset (1.5 H*) nearly doubles topographic gradients across the rift zones, they still exhibit similar kinematic behaviour to the models without a lower crust. Similarly, numerical experiments with parameters modified to values typically associated with the continental crust exhibit similar rift interaction for equivalent seed offsets (Appendix 2B, Fig. 2.B2).

These findings indicate that the numerical results are robust at our resolution. However, the analogue experiments undergo distinct internal deformation behaviour not captured in the numerical experiments. We speculate that this may be caused by the limited numerical resolution that does not fully capture the details of the plastic behaviour of sand. Our resolution of 0.125 cm (or 1.25 km) and total number of elements (230,400 or 374,400) is in line with recent 3D numerical brittle-viscous experiments (e.g., Allken *et al.* 2011; 2012; Brune *et al.* 2012; see Table 5 in Thieulot 2014), but is substantially lower than the maximum resolutions typically achieved in high-resolution 2D experiment modelling deformation at the length scales examined here.
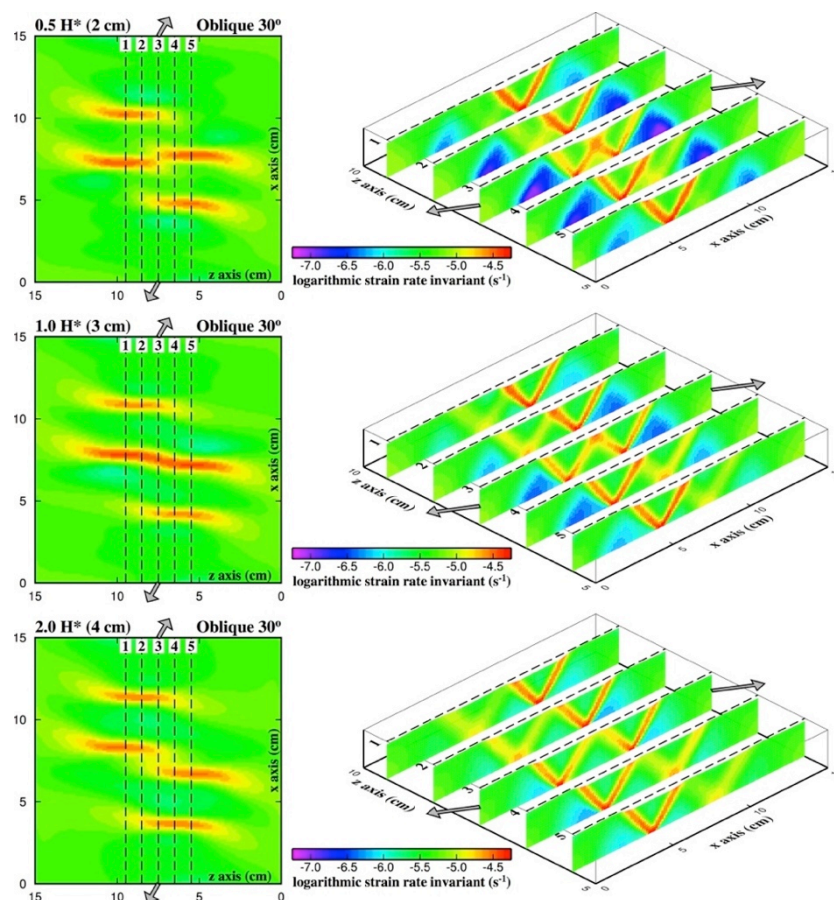
Fig. 2.8. *Final deformation stages of the numerical models. Left: Surface deformation after 240 min of extension (10% strain) for an extension direction of 30° and rift offsets of 2.0 cm (0.5 H*), 3.0 cm (1.0 H*) and 4.0 cm (1.5 H*). Dashed lines indicate the location of plotted cross-sections. Right: Deformation as a function of depth for cross-sections 1-5.*

2.4. Analogue structural evolution

2.4.1. Rift segment evolution

The top view images of final deformation patterns in the previous sections (Fig. 2.4) already show that away from the rift interaction zones, orthogonal extension creates standard rifts along the initial seed. In contrast, oblique extension models produce rift-internal oblique en echelon structures. Horizontal CT sections taken in the sand ½ H (1 cm) above the basal silicone layer provide additional insights (Fig. 2.9). Symmetric rifts develop under orthogonal extension conditions (Fig. 2.9a), while a 30° extension obliquity produces limited en echelon normal faults, oriented more or less perpendicular to the extension direction. The en echelon normal faults eventually link to form a continuous rift structure (Fig. 2.9b). For $\alpha = 60°$ the initial structures are oblique-slip normal- or even strike-slip faults oriented ca. 30° to the extension direction. Subsequently steep (ca. 70°) and there- fore probably oblique-slip normal rift boundary faults develop to create a continuous rift basin (Fig. 2.9c). For 30° and 60° extension obliquities, the en echelon structures are preserved until the end of the model run. A 60° extension obliquity system (Fig. 9c), however, develops significantly more en echelon structures than the 30° extension obliquity equivalent (Fig. 2.9b).

3D internal analysis also allows the quantification of rift geometry evolution (Fig. 2.10). Vertical CT sections show a changing final rift segment geometry with increasing extension obliquity (Fig. 6). The degree of oblique extension also appears to control the initial boundary fault dip angle and initial rift width (Fig. 10a). Fault dip angles increase from ca. 67° under orthogonal extension to ca. 90° in strike-slip settings, while initial rift width decreases from ca. 0.75 H to ca. 0 H respectively. The relation between rift width (W), fault dip angle (β) and thickness of the brittle (sand) layer (T) closely follows the formula $W = 2\ T/\tan\ \beta$ (after Allemand & Brun 1991). Vertical CT sections show that fault dip angles tend to decrease with time, as the model evolves (Fig. 10b). In orthogonal models, the initial ca. 67° boundary fault dip angle decreases to ca. 57° after 240 min. This effect is less pronounced when α is 30° and almost absent when α is 60° (fault dip angles of ca. 72° to 63° and ca. 80° to 77° respectively, Fig. 10b).
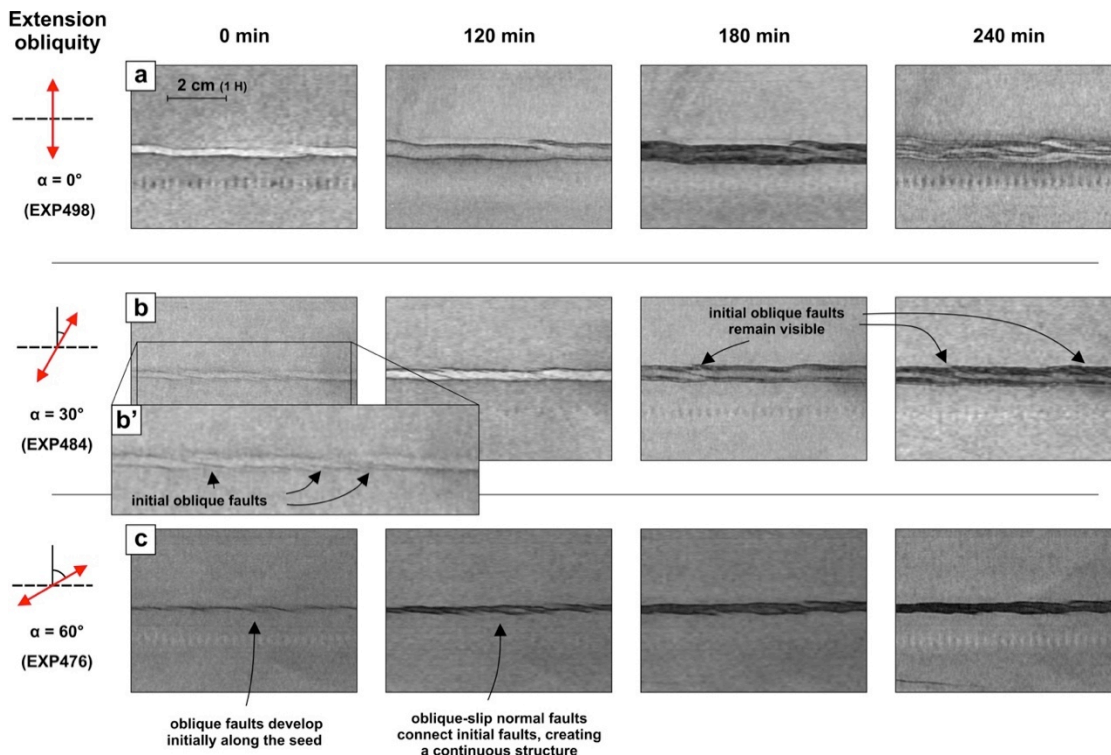
Fig. 2.9. (previous page) *Evolution of horizontal deformation patterns of rift segments away from the rift interaction zones in the analogue models. The CT sections cut the sand ½ H (1 cm) above the silicone layer. Extension obliquities (angle α) are 0°, 30° and 60°. Striped patterns are CT-scanning artefacts.*

_____
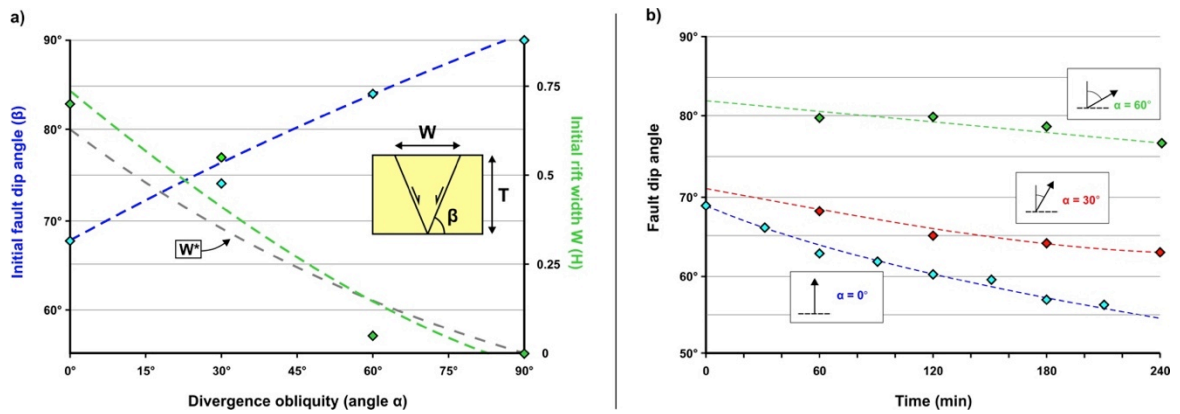
Fig. 2.10. *Measurements of the rift boundary fault dip angles in the analogue models. a) Dip angle of the initial rift boundary fault and rift width as a function of extension obliquity. W* represents the ideal rift width according to the equation W = 2 T/tan β (Allemand & Brun 1991), using the measured fault dip angles (β) and brittle sand layer thickness T = 0.75 H (instead of 1 H, since the brittle layer is thinner above the seeds); b) Decreasing fault dip angle with model evolution for different extension obliquities. The values shown are measured over the entire fault depth along rift boundary faults on representative CT sections throughout the model. Trend lines are 2nd order polynomial, R2 values are >0.9, except for the "angle α = 60°" linear trend line in (b) with $R^2 = 0.83$.*

2.4.2. Analysis of 3D surface evolution

Figs. 2.11-13 show 3D model topography maps that visualize the structural evolution for models with 0°, 30° and 60° extension obliquity and ½ H, 1 H and 2 H seed offsets (Figs. 2.11-13). In all models surface structures are visible after 60 min and become more pronounced with time. Several observations from the top view images of the final model stages (Fig. 2.4) are also well resolved on the 3D model topography images. Wider rifts form in orthogonal settings and narrower rifts occur towards the strike-slip domain. Strike-slip faults stem from the initial rift segments when α ≥ 30°. Additional rift structures in areas away from the seeds are visible and some boundary effects are present.

While poorly resolved on the previous top view images (Fig. 2.4), topography maps (Fig. 2.11-13) clearly show the development of relay ramps and subsequent formation of

transfer zones. These structures occur in the orthogonal extension models with ½ H and 1 H seed offsets (Figs. 2.11a, 2.12a) and in the 1 H offset model with α = 30° (Fig. 2.12b). The relay ramps represent an initial soft-linkage mode of rift interaction, in contrast with the hard-linking transfer zones with continuous boundary faults that form in early stages in other models (e.g. Fig. 2.12c). The relay ramps, however, are breached towards the end of the model run as the rift boundary faults connect to form a continuous transfer zone. The final structure closely resembles the transfer zones in the other models (compare the evolution of Fig. 2.11b with Fig. 2.12b).

A horst structure between both rift segments develops in various models (Figs. 2.6a, b, d, 2.11a, 2.12a and 2.14). The horsts decrease in significance with increasing extension obliquity, as the rift segments propagate more closely to each other and leaving less space for a horst in between.
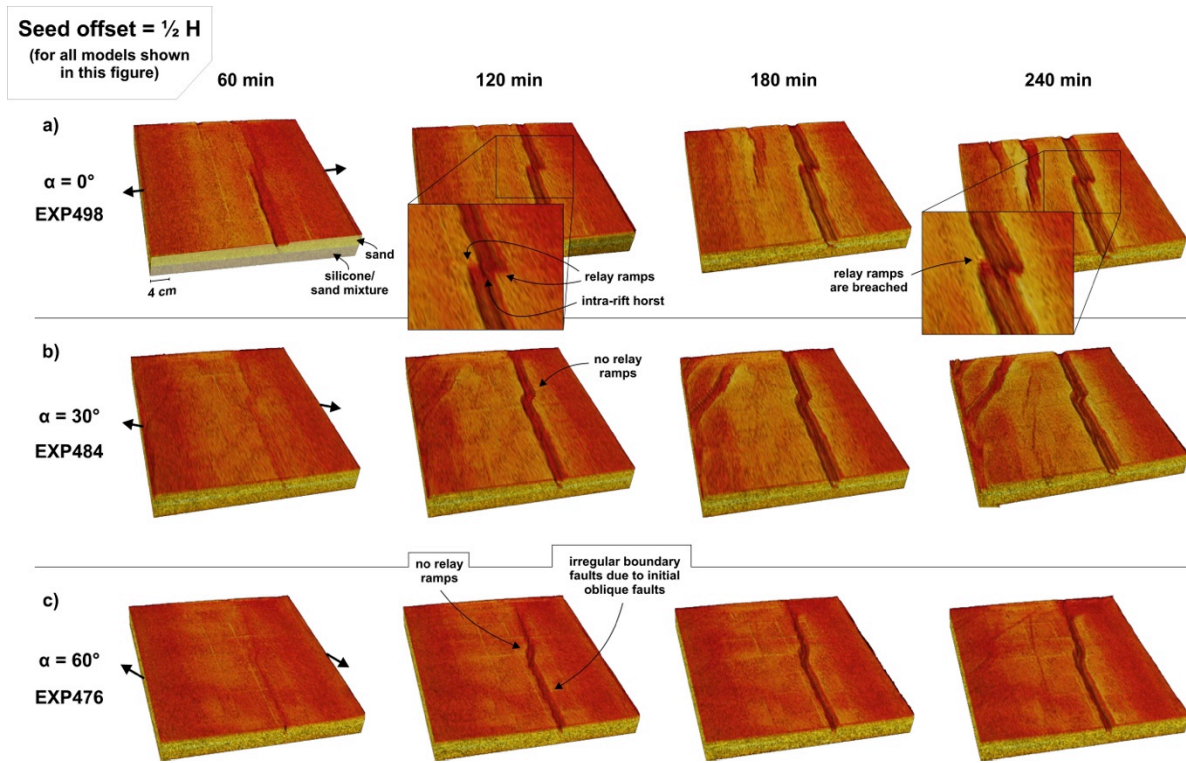
Fig. 2.11. *CT-derived 3D surface topography images, showing the evolution of surface deformation patterns in the analogue models. Seed offset is ½ H and extension obliquities (angle α) are 0°, 30° and 60°.*
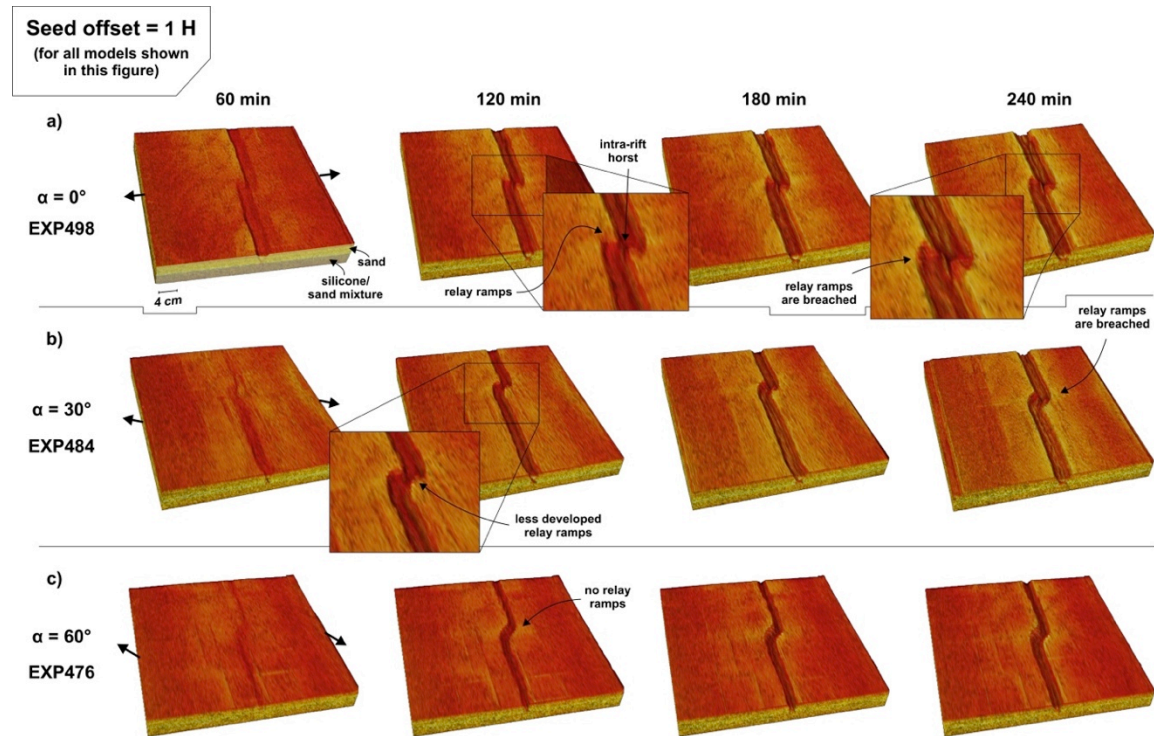
Fig. 2.12. (previous page) *CT-derived 3D surface topography images, showing the evolution of surface deformation patterns in the analogue models. Seed offset is 1 H and extension obliquities (angle α) are 0°, 30° and 60°.*

_____
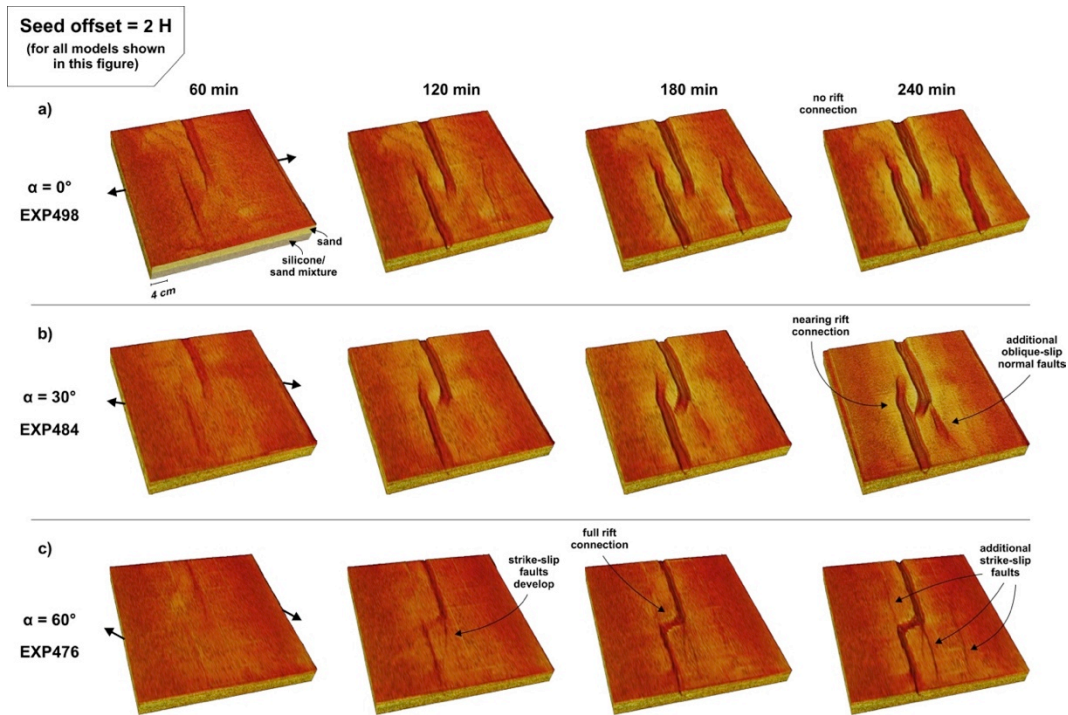
Fig. 2.13. *CT-derived 3D surface topography images, showing the evolution of surface deformation patterns in the analogue models. Seed offset is 2 H and extension obliquities (angle α) are 0°, 30° and 60°.*

2.5. Discussion

2.5.1. Analogue rift segments

A schematic overview (Fig. 2.14) summarizes the range of structures observed in the analogue models. Model rift segment geometries closely follow the formula of Allemand & Brun (1991): W = 2 T/tan β (Fig. 2.10a, insets in Fig. 2.14a, d, g), which indicates that the measurements of rift characteristics are internally consistent. With increasing extension obliquity (α) in the models, rifts become narrower, bound by steeper faults and shallower as basin depth decreases from maximum 0.45 H to 0 H (Fig. 2.4b). These structural changes reflect the increasing strike-slip component in the system, as pure strike-slip faults are normally steep (vertical) structures, while normal faults generally dip ca. 60°. However, the fault dip angle also decreases with time, which is due to both flow within the viscous seed at depth and sand collapse along the rift faults at the surface.

Curved en echelon rift-internal structures that develop with in- creasing extension obliquity are similar to structures observed in both analogue models and nature (McClay *et al.* 2002; Philippon *et al.* 2015; Corti *et al.* 2003 and references therein). Our models show less structural detail due to their smaller physical size, however, hindering a more thorough comparison between our results and previous models and nature. The frequency of en echelon structures increases with increasing extension obliquity, which reflects the increasing amount of distributed strike-slip motion the system must accommodate. These structures tend towards normal fault characteristics at lower extension obliquities and more towards an oblique-slip normal fault or strike-slip fault character for models with higher extension obliquities.

The additional Riedel structures that originate from the rift segments in almost strike-slip settings (α ≥ 75°, Fig. 4) have the same strike-slip nature and orientation as the Riedel faults observed in previous oblique extension models using a similar set-up, but with- out the initial seeds applied in this study (Schreurs & Colletta 1998). As our seeds force faults to nucleate above them, the Riedel fault system seen in the models by Schreurs and Colletta (1998) does not develop and Riedel features only form along the rift boundary faults.

2.5.2. Analogue rift interaction zones

Initial seed offset is a decisive factor controlling whether rift segments initially link through transfer zones or accommodation zones (Le Calvez & Vendeville 2002; Allken *et al.* 2012). Small seed offsets promote the formation of transfer zones, as rifts inherently connect more easily when they are close to each other, whereas larger seed offsets tend to produce accommodation zones (Fig. 2.14). This is because the rifts develop independently from each other when seed offsets are 2 H or larger. However, formation of initial relay ramps in small seed offset models shows that soft linkage can also occur in small seed offset settings (Fig. 2.14a, b, e). These specific relay ramps are subsequently breached to form a continuous transfer zone as deformation progresses, similar to the observations by Acocella *et al.* (2005). Therefore, the absence of relay ramps does not rule out their previous existence.

For a seed offset of 2 H (Fig. 2.14c, f, i), the extension obliquity significantly affects the rift propagation direction. As the propagating parts of the rift segments are not bound to any inherited heterogeneities, they will orient themselves according to the model stress field and propagate perpendicularly to the extension direction (Fig. 2.14f). Similar behaviour is observed in the normal fault experiments of Hus *et al.* (2005). As the extension obliquity increases, propagating rift segments migrate towards each other, facilitating hard linkage (Fig. 14i). In contrast, during orthogonal extension rifts propagate in a parallel fashion and fail to connect. Instead, an accommodation zone develops (Fig. 2.14c). This process is also the reason why initial relay ramps form in orthogonal extension models with low seed offsets (Fig. 14a, b). In the α = 30°, 1 H seed offset model, the rift segments propagate towards each other, but are also far enough away from each other to initially prevent hard linkage (Fig. 2.14e).

This is contrary to the ½ H equivalent model that directly produces a transfer zone (Fig. 2.14d). These variations in early rift linkage styles indicate the delicate interplay between seed offset and extension obliquity in low seed offset settings.

A similar influence of extension obliquity on rift propagation direction can be observed when additional minor rifts develop away from the main rift structures (Fig. 2.3). These rifts also open orthogonally to the extension direction and in the process create an en echelon series of basins. The latter effect only occurs when the extension velocity (and lower crustal viscosity) causes enough brittle-ductile coupling to initiate (limited) wide or distributed rifting (Brun 1999; Allken *et al.* 2012).
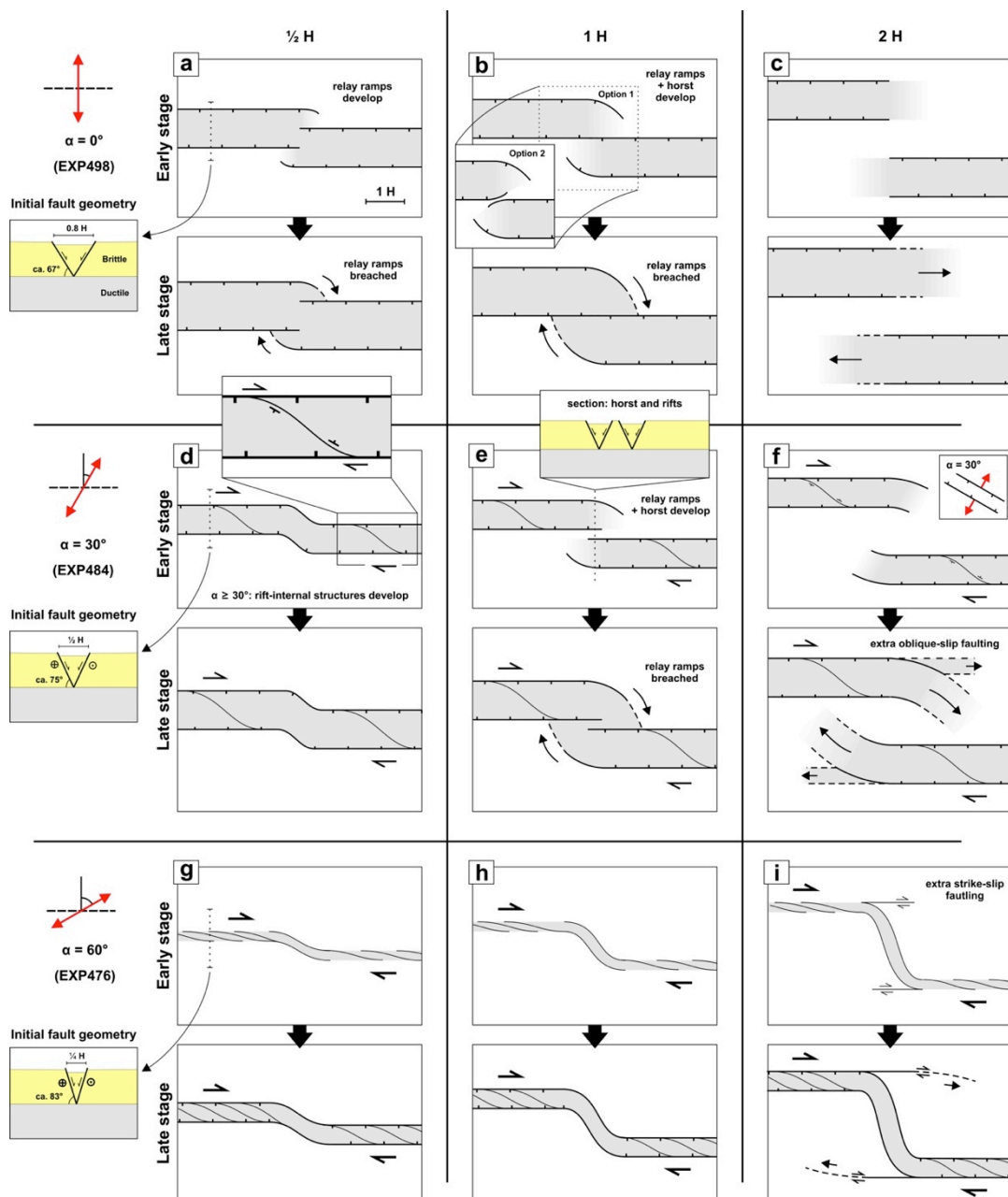
Fig. 2.14. *Graphic overview of observed structures in the analogue models as a function of extension obliquity and seed offset. Note that the vertical cross-sections are idealized (shown without the seed).*

The majority of models produces some type of horst structure at the centre of the rift interaction zone (e.g. Fig. 2.14e, inset). The most pronounced examples are formed in the 1 H models under 30° extension obliquity conditions (Figs. 2.6a, b, 2.11a, b, 2.12a, b). This is a result of the interplay of seed offset and initial rift width, which causes the rifts to propagate along and curve around each other at depth, but also to merge towards the surface. This creates a relatively large horst between the connecting rift segments and causes the formation of relay ramps as previously discussed, features also observed in previous orthogonal extension models by Corti (2004). Higher degrees of extension obliquity (increasing α) lead to direct rift segment connections, which prohibits a well-developed horst (Fig. 2.6d). These intra-rift horsts can provide structural traps for hydrocarbons (Fossen *et al*. 2010) and are observed in this study during orthogonal and oblique (up to 30°) extension. Towards 60° extension obliquity, such horsts are more likely to be poorly developed. Fossen *et al*. (2010) show that such horsts may also develop when the boundary faults curve away from each other in such a setting (Fig. 2.14b, option 2), which is also observed to a limited extent in our models (Fig. 2.3, experiment with α = 0° and offset = ½ H).

Oblique extension also invokes strain partitioning in the form of additional strike-slip faults stemming from and oriented more or less parallel to the rift segments. Similar to the general rift segments, these secondary structures are narrower with more oblique extension as they have to accommodate more transverse motion (ca. 0.3 H and 0.1 H with 30° and 60° extension obliquity respectively). The internal strain partitioning between rift boundary faults and an additional set of strike-slip faults in the transfer zones themselves, as observed by Acocella *et al*. (1999a) is not reproduced in our models, although the general structure with continuous rift boundary faults is quite similar. This is possibly due to the smaller size of our models (2 cm thick brittle sand layers vs. 7 cm thick brittle material), which might prevent us from observing more detailed internal structures, if present.

2.5.3. Numerical models

The numerical models show similar first-order linkage patterns as the analogue experiments and confirm that increasing extension obliquity aids rift linkage. Our tests of model thickness, numerical resolution, and model scaling also show that the numerical results are robust. However, in detail, the series of numerical experiments does not reproduce many of the analogue structures. This discrepancy almost certainly reflects the numerical resolution, which is limited due to the computational requirements of 3D models. While the 3D numerical rift interaction experiments in orthogonal extension of Allken *et al*. (2011, 2012) produce a range of structures similar to those observed in our analogue experiments, these structures developed over much larger total strains and in some case much larger seed offsets. For the small total strains (10%) examined here, the complex rift linkage structures fail to develop in part due to the resolution-controlled broad width of the numerical shear zones, their 45° dip angle and the limited number of elements between offset rifts (~10-20). We speculate that spatial resolutions at least an order of magnitude higher in areas of focused deformation are needed to resolve the analogue features. Future numerical comparisons to 3D analogue experiments will likely require adaptive-mesh refinement techniques (Choi *et al*. 2013) to resolve fine-scale structures while maintaining reasonable computational requirements. Future high-resolution numerical models should also consider the role of initial imperfections (i.e. random variations in strength) in analogue models, which may help facilitate the development of fine-scale structures not present in the comparatively homogeneous numerical experiments.

2.5.4. Comparison with nature

The structures observed in the early stages (t = 120 min, or 5% extension) of the analogue ½ H and 1 H offset orthogonal models and the 1 H offset, 30° extension obliquity model bear resemblance to the graben stepovers in the Utah Canyonlands and the North Sea Viking Graben (Fig. 2.15a). Between the analogue models and the natural exam- ples, rift offsets

are comparable and relay ramps and a horst structure between the rifts are present (Figs. 2.6a, 2.11, 2.12, 2.15a, b, e, f). A similar horst structure occurs in certain numerical models (Figs. 2.7d and 2.B2b). The similarity between our models and the natural examples indicates that oblique extension (up to 30°) could have been involved in the evolution of these natural examples, especially in the Viking Graben (e.g. Zanella & Coward 2003).

At the Western Branch of the East African Rift, the Kivu-Rusizi accommodation zone provides another natural example where rifts grow into each other without merging faults (Fig. 2.15d). More to the north, the accommodation zone (Pakwach Basin) between Lake Albert and Rhino-Camp Basin has a clear oblique extension setting (Fig. 15c, relative locations shown in Fig. 2.1). Extension directions are moderately oblique with respect to the main rift trends of Lake Albert and the Rhino-Camp Basin (α = ca. 7° and ca. 20° respectively). Rift offset is ca. 1.5 H, not enough to isolate both rift segments, as the sediment- filled Pakwach Basin connects both rift segments. We expect the struc- tures to show similarities to our 1 H orthogonal extension model and our α = 30° model (Fig. 2.15e, f). The relay ramps form both in the ana- logue model and nature, but they are best developed at the southern tip of the Rhino-Camp basin, where extension obliquity is lowest. At the northern tip of the Lake Albert rift, where extension obliquity is higher, multiple en echelon normal faults (striking

approximately perpendicular to the extension direction) disrupt and otherwise well-developed relay ramp. Such relay ramp breaching can be observed in our α = 30° model (Fig. 2.15f), the formation of individual en echelon faults is however best expressed in our 1 H, 60° extension obliquity model (Fig. 13c).

Breaching of relay ramps has also been reported in the Utah Canyonlands (Trudgill and Cartwright 1994) as well as along the boundary faults of Lake Albert (Dou *et al.* 2004) and in the Mesozoic North Sea rifts (Roberts *et al.* 1990). In addition, rift segments curving around each other are present in the East African Rift System area and could ultimately lead to the creation of micro-plates (Koehn *et al.* 2008). Further-more, the maximum subsidence of 0.45 H in our models represents a maximum of 9 km subsidence in nature, which is well in the range of subsidence values reported in continental rifts (e.g. Corti *et al.* 2007 and references therein).

Our models produce accommodation zones and transfer zones with rift-connecting boundary faults that strongly resemble natural examples. However, discrete transfer faults do not develop in our models. The 10% maximum extension that we apply is possibly not sufficient to transform the initial structures into discrete transfer faults (Roberts *et al.* 1990; Acocella *et al.* 2005).

Fig. 2.15. (next page) *Comparison of analogue model results with natural examples. (a) Northern part of the right-stepping Viking Graben system (left), shown together with the Devils Lane stepover (Canyonlands, Utah, right). Note the high areas and relay ramps at graben stepovers, associated with oil and/or gas fields in the case of the Viking Graben (GF, GFS, HU, KB, VS and VA). m.b.s.l. = meters below sea level. Modified after Fossen et al. (2010), AAPG© 2010 and reprinted with permission of the AAPG whose permission is required for further use. (b) CT-derived surface image showing the topography of an orthogonal extension (angle α = 0°), 1 H offset model after 120 min or 0.6 H (1.2 cm) extension. One numerical model develops a similar structure (Fig. 7d). (c) Albertine Rift structure with the accommodation zone between Lake Albert and the Pakwach and Rhino-Camp Basins to the north. AN = Albert Nile; BBF = Bunia Border Fault; NTBF = North Toto Bunyoro Fault; RK = River Kafu; TF = Tonya Fault; VN = Victoria Nile. Image modified after Stamps et al. (2008) and PEPD (2012), copyright by the Petroleum Exploration and Production Department, Uganda. (d) Block diagram of the Kivu-Rusizi accommodation zone. Location is shown in Fig. 1b. Image modified after Ebinger (1989). (e, f) CT-derived surface images (zoom-ins of Fig. 12, EXP498 and EXP484 respectively) showing the model topography after 120 min.*

a North Sea Viking Graben — Devils Lane stepover (Utah Canyonlands)

b α = 0°, offset = ½ H

c

d Kivu Rift — Accom. Zone — Rusizi basin

e ca. 1 H — α = 0° offset = 1 H

f ca. 1 H — α = 30° offset = 1 H
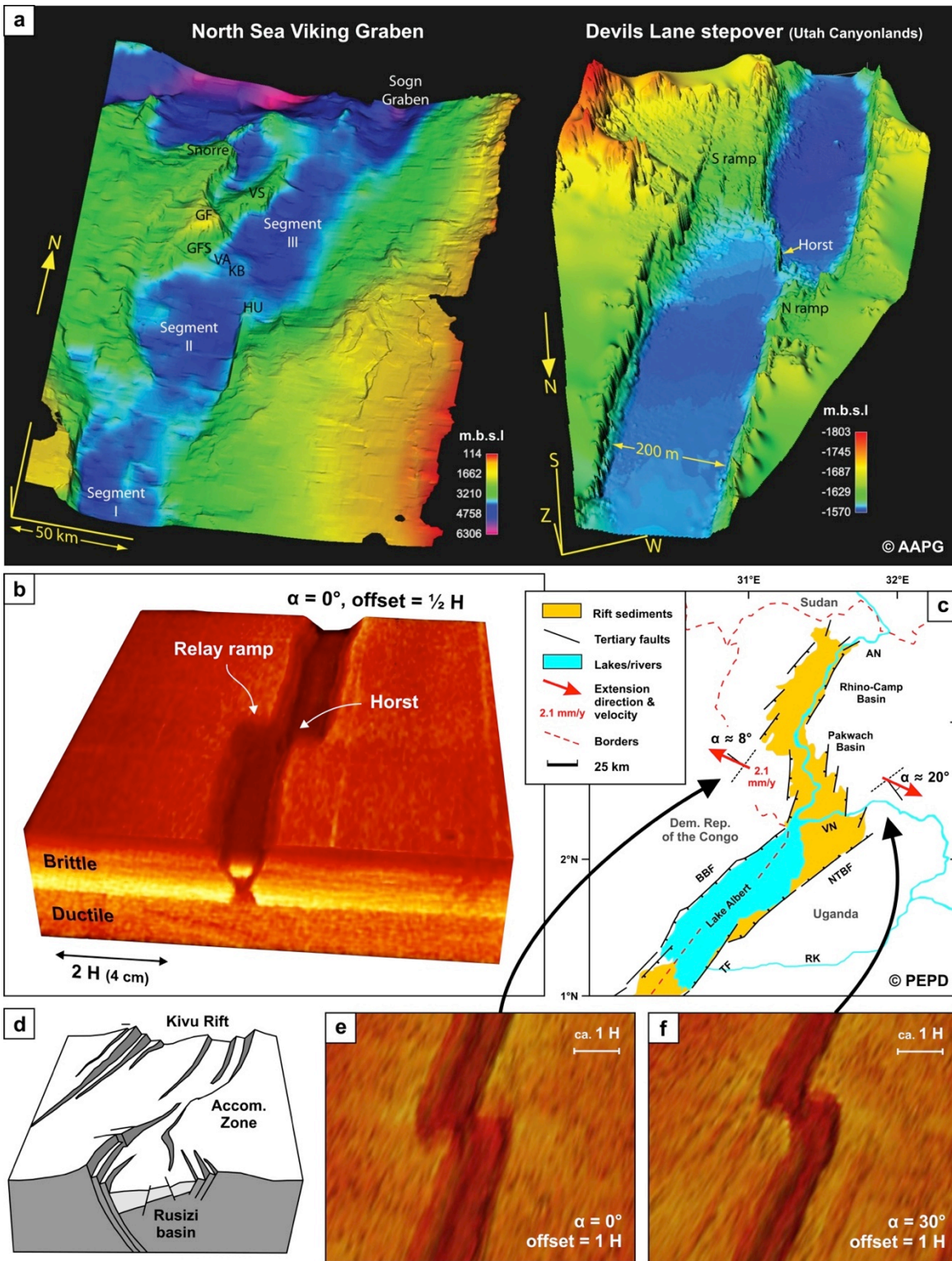
2.6. Conclusions

We present 3D analogue and numerical experiments that investigate the influence of extension obliquity and initial offset between inherited heterogeneities on rift interaction in continental settings. We conclude that:

- Increasing extension obliquity (i.e. increasing angle α) strongly changes rift structures. Orthogonal settings produce wide rifts, while oblique extension settings result in narrower rifts with oblique internal structures. Towards the strike-slip domain, the system is dominated by strike-slip structures;
- Rift linkage can occur through the formation of continuous boundary faults at the surface (hard linkage mode), or through the formation of relay ramps (soft linkage mode). In most cases, initial relay ramps are breached and removed with increasing deformation;
- Transfer zone formation is promoted by both decreasing offsets between initial heterogeneities and increasing extension obliquity, which reflects that rifts tend to align in a direction that is perpendicular to the extension direction;

- Rift bounding faults in the analogue models do not link at depth, but rather curve around each other and merge towards the surface to form a continuous trough. We predict that associated intra-rift horsts, which may provide hydrocarbon traps in nature, are most likely to develop in more orthogonal extension settings;
- We find agreement in rift linkage patterns between analogue and numerical experiments to the very first order, highlighting the variability in structures that can be obtained from using different modelling methods. Future experiments could test techniques for achieving a substantially higher numerical resolution in the rift linkage zones and perhaps different plasticity (brittle behaviour) models;
- Several of the characteristic structures we observe in our orthogonal and oblique extension models are also present in natural rift settings such as the North Sea, the Utah Canyonlands and the East African rift system.

2.7. Acknowledgements

Appendix 2A. Numerical methods and approximations

We model 3D viscous-plastic deformation with the particle-in-cell (Eulerian-Lagrangian) finite element code SULEC (e.g. Ellis *et al*. 2011; Buiter & Ellis 2012; Naliboff & Buiter 2015). SULEC solves for incompressible slow viscous flows through the equations for conservation of mass (2.A1) and momentum (2.A2):

$$\nabla \cdot u = 0 \qquad (2.A1)$$

$$\nabla \cdot \sigma' - \nabla P + \rho g = 0 \qquad (2.A2)$$

Here, u is velocity, σ' is the deviatoric stress tensor, P is dynamic pressure (mean stress), ρ is density and g is gravitational acceleration (-9.81 m/s^2 in the vertical direction and otherwise 0). Determining velocity and pressure with an iterative penalty method (e.g. Pelletier *et al*. 1989) transforms equations (2.A1) and (2.A2) into

$$\nabla \cdot \sigma'^{(i)} - \nabla P^{i-1} + \nabla(K\nabla \cdot u^i) + \rho g = 0 \quad (2.A3)$$

$$P^i = P^{i-1} - K\nabla \cdot u^i \qquad (2.A4)$$

The term K represents the compressibility factor (here $1 \cdot 10^{16}$ Pa), while i represents the pressure iteration number. In order to avoid pressure instabilities (i.e. checker boarding) associated with fixed x- and z- velocities along all vertical walls and Q1P0 elements (linear in velocity, constant in pressure), we fixed the pressure at lithostatic values (P_L), modifying equations (2.A3) and (2.A4) to

$$\nabla \cdot \sigma' - \nabla P_L + \nabla(K\nabla \cdot u) + \rho g = 0 \qquad (2.A5)$$

$$P = P_L \qquad (2.A6)$$

Numerical instabilities associated with numerical overshoots across large density contrasts, mainly at the free surface, are stabilised with the method of Kaus *et al*. (2010) and Quinquis *et al*. (2011).

Material strength reflects a combination of viscous and brittle behaviour, with viscous flow following a linear creep model relating the effective stress (σ'_{eff}), viscosity (μ'_{eff}) and strain rate ($\dot{\varepsilon}'_{eff}$):

$$\sigma'_{eff} = 2\mu'_{eff}\dot{\varepsilon}'_{eff} \qquad (2.A7)$$

Values of μ'_{eff} for sand and PDMS (if present) are, respectively $1 \cdot 10^9$ Pa·s and $1.5 \cdot 10^5$ Pa·s. The effective stress and strain rate are:

$$\sigma'_{eff} = \left(\tfrac{1}{2}\sigma'_{ij}\sigma'_{ij}\right)^{1/2} \qquad (2.A8)$$

$$\dot{\varepsilon}'_{eff} = \left(\tfrac{1}{2}\dot{\varepsilon}'_{ij}\dot{\varepsilon}'_{ij}\right)^{1/2} \qquad (2.A9)$$

Brittle material behaviour follows a Drucker-Prager yield criterion, defining an effective stress limit:

$$\sigma'_{eff} = P\sin\phi + C\cos\phi \qquad (2.A10)$$

Where C is the cohesion and ϕ is the angle of internal friction. We use cohesion values (C) of 21 Pa and 39 Pa for quartz sand and corundum sand respectively. Values of ϕ for quartz (35°-31°) and corundum (37°-32°) sand weaken (Table 1) linearly between plastic strain values of 0.5 and 1.5 (as measured by the second invariant of the strain tensor). Viscosity is limited by imposed maximum ($1 \cdot 10^9$ Pa·s) and minimum ($1 \cdot 10^4$ Pa·s) values. Material properties are tracked through tracers, which initially number 27 per element. Tracer injection and deletion keeps tracer density between 8 and 54 tracers per element throughout the model evolution.
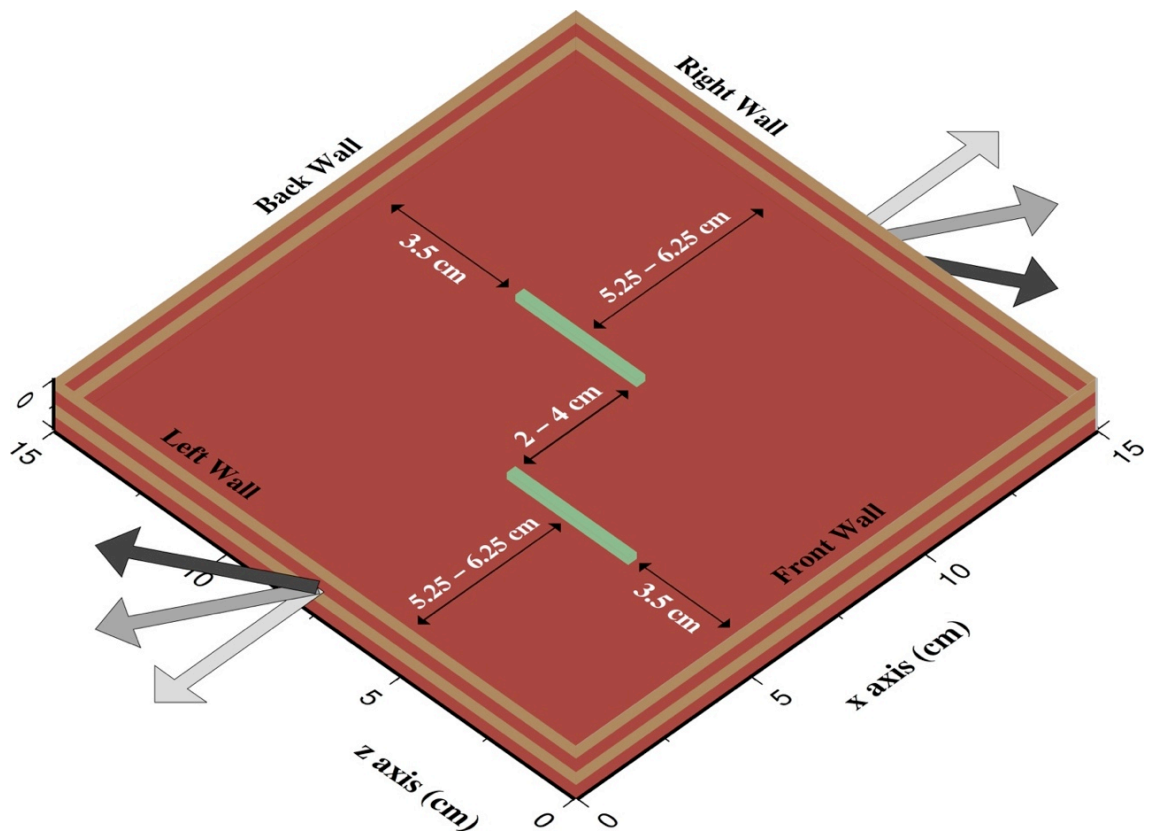
Fig. 2.A1. *Compositional layering and boundary conditions of 3D numerical models. Light and dark tan layers, respectively, represent alternating layers (0.5 cm) of quartz and corundum sand. Rectangular viscous seeds (green) are separated by 2-4 cm (0.5-1.5 H*) along the x-axis. Fixed velocities along the model sides drive deformation. The extension obliquity is 0º (light grey), 30º (grey) or 60º (dark grey).*

Appendix 2B. Additional numerical experiments
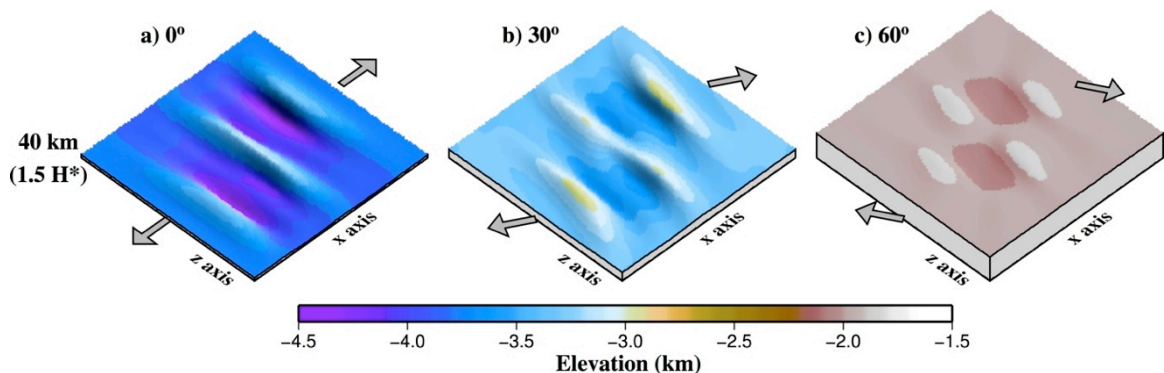
Fig. 2.B1. *Surface elevation of numerical experiments after 240 min (10 % strain) for extension obliquities of 0º, 30º or 60º and a 4.0 cm (1.5 H*) seed offset. In contrast to Figs. 2.7 and 2.8, these experiments contain a 2 cm thick viscous (PDMS) lower crust. The entire extent (15 x 15 cm) of the horizontal domain (x- and z-axis) is plotted at a 1:1 scale. The vertical axis (y) is exaggerated by a factor of 10 to illustrate deformation structures.*
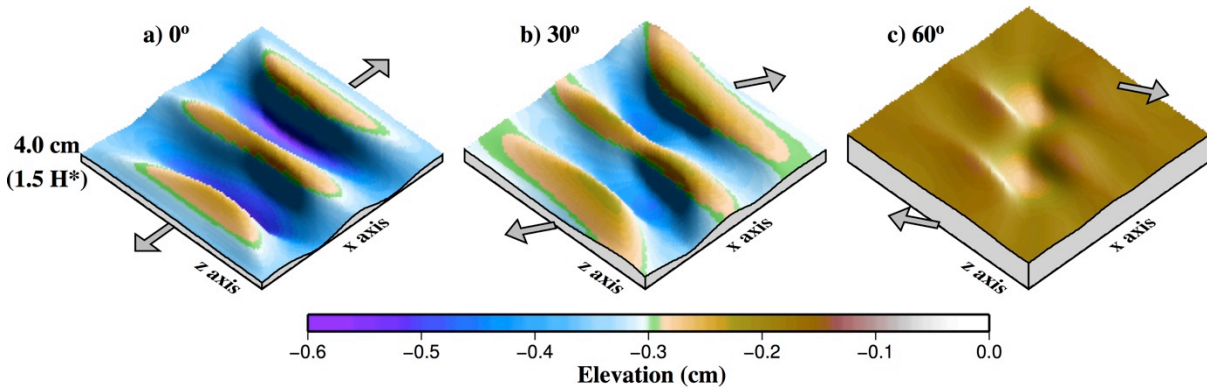
Fig. 2.B2. *Surface elevation after 1.5 Ma (10 % strain) for models containing properties commonly used in numerical studies of continental extension. The surface elevation is shown for extension obliquities of a) 0º, b) 30º or c) 60º and a 40 km (1.5 H*) seed offset. As in Figs. 2.7 and 2.B1, the vertical axis (y) is exaggerated by a factor of 10 to illustrate deformation structures. The model spans 150 x 150 km in the x- and z-directions, with a 20 km thick brittle upper (2800 kg/m³) and a 20 km thick linear viscous lower crust (2900 kg/m³). Grid spacing in the x- and z-directions is fixed at 1.25 km, while the vertical resolution ranges from 1.25 km (upper crust) to 2 km (lower crust). Seed dimensions are 2.5 km (x), 2.5 km (y) and 40 km (z). The crust extends at 10 mm/yr (5 mm/yr on each side) with a fixed time step of 25,000 years. The friction angle and cohesion in the brittle upper crust, respectively, weaken from 20º-10º and 20-10 MPa over a finite plastic strain interval of 0.5-1.5. The upper and lower crust viscosities are, respectively, 10^{26} and 10^{21} Pa·s.*

Appendix 2C. Additional analogue data
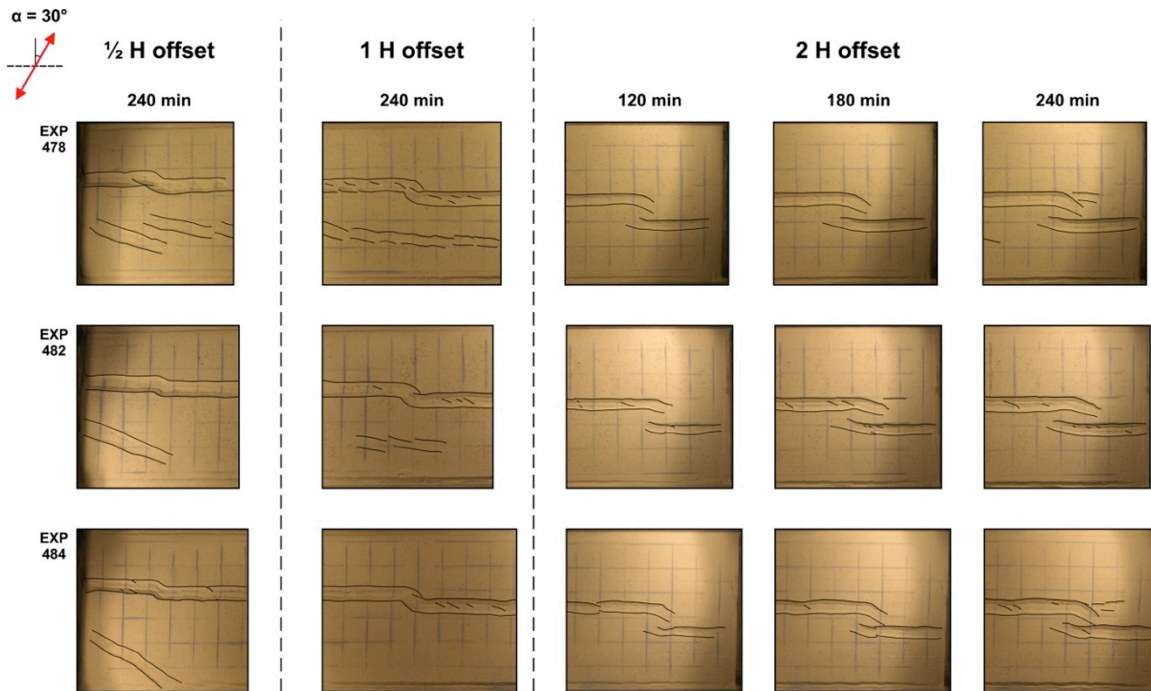
Fig. 2.C1. *Surface views of multiple analogue model runs with identical starting conditions (angle α = 30º) result in similar surface structures, indicating that our model results are reproducible.*

Set-up models 472-474 (shown without sand cover)

Orthogonal extension

weak zone configuration
(offset: 1, 2 and 3 H)

5 H (10 cm)

EXP 471 (divergence: 30 mm/h) t = 1:00h; e = ca. 11%)

EXP 472 (divergence: 20 mm/h) t = 1:30h; e = ca. 11%)

EXP 474 (divergence: 6 mm/h) t = 4:00h; e = ca. 10%)
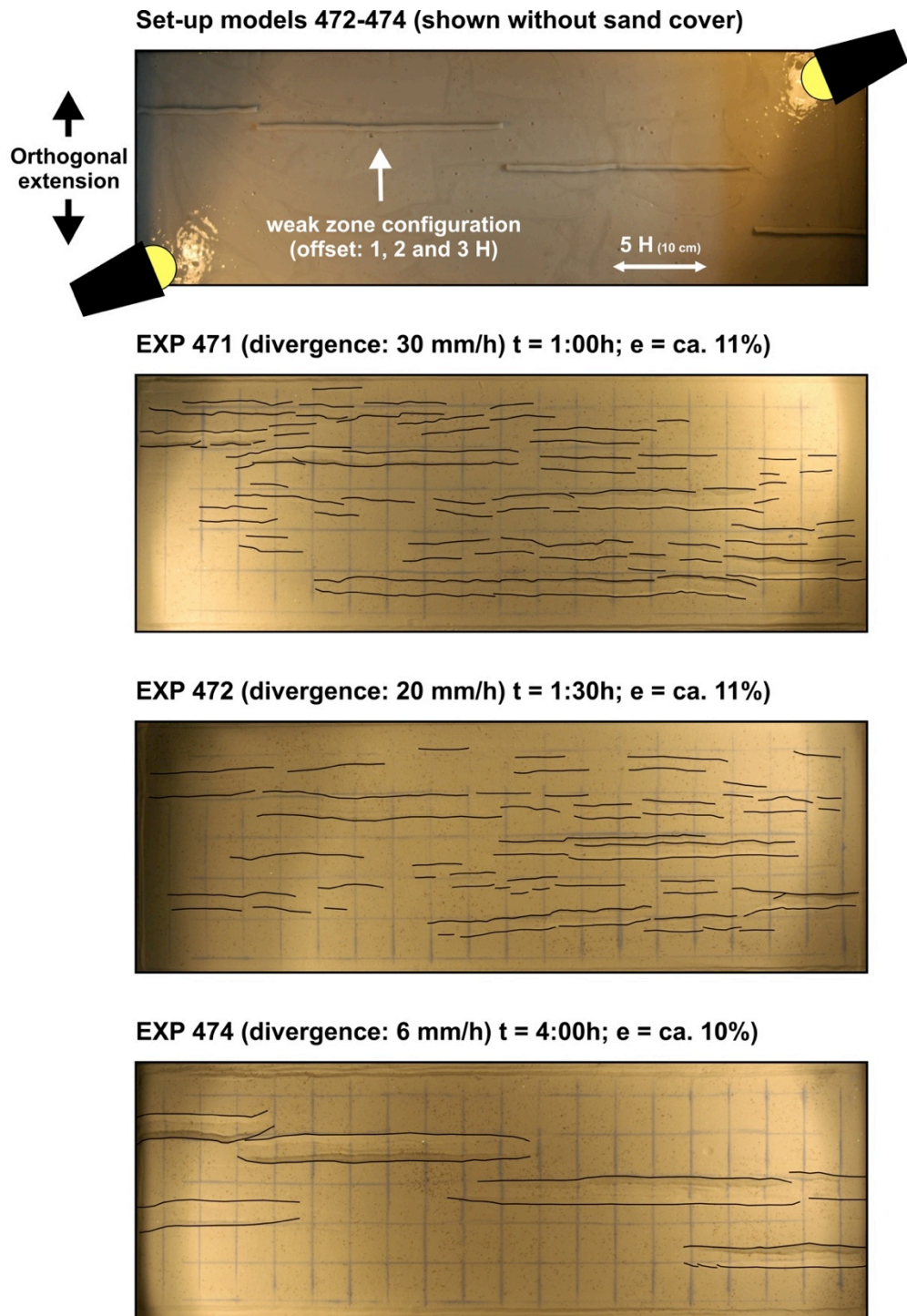
Fig. 2.C2. *Decreasing the overall extension velocity from 30 to 6 mm/h shows that lower extension velocities result in well localized faulting along the pre-defined seeds. Accordingly, we use an extension velocity of 6 mm/h throughout this study.*

Chapter 3

How oblique extension and structural inheritance influence rift segment linkage: Insights from 4D analog models

Frank Zwaan[a] *, Guido Schreurs[a]

a) Institute of Geological Sciences, University of Bern, Baltzerstrasse 1+3, CH-3012 Bern, Switzerland

_____

Abstract

Rifting of the continental lithosphere involves the initial formation of distinct rift segments, often along preexisting crustal heterogeneities resulting from preceding tectonic phases. Progressive extension, either orthogonal or oblique, causes these rift segments to interact and connect, ultimately leading to a full-scale rift system. We study continental rift interaction processes with the use of analog models to test the influence of a range of structural inheritance (seed) geometries and various degrees of oblique extension. The inherited geometry involves main seeds, offset in a right-stepping fashion, along which rift segments form as well as the presence or absence of secondary seeds connecting the main seeds. X-ray computer tomography techniques are used to analyze the 3D models through time, and results are compared with natural examples. Our experiments indicate that the extension direction exerts a key influence on rift segment interaction. Rift segments are more likely to connect through discrete fault structures under dextral oblique extension conditions because they generally propagate toward each other. In contrast, sinistral oblique extension commonly does not result in hard linkage because rift segment tend to grow apart. These findings also hold when the system is mirrored: left-stepping rift segments under sinistral and dextral oblique extension conditions, respectively. However, under specific conditions, when the right-stepping rift segments are laterally far apart, sinistral oblique extension can produce hard linkage in the shape of a strike-slip-dominated transfer zone. A secondary structural inheritance between rift segments might influence rift linkage, but only when the extension direction is favorable for activation. Otherwise, propagating rifts will simply align perpendicularly to the extension direction. When secondary structural grains do reactivate, the resulting transfer zone and the strike of internal faults follow their general orientation. However, these structures can be slightly oblique due to the influence of the extension direction. Several of the characteristic structures observed in our models are also present in natural rift settings such as the Rhine-Bresse Transfer Zone, the Rio Grande Rift, and the East African Rift System.

_____

3.1. Introduction

During the early stages of rifting, rift segments generally form along preexisting lithospheric weaknesses formed during previous tectonic activity (Morley *et al.* 1990; Nelson *et al.* 1992; Corti 2012). Because these weaknesses are often noncontinuous, the initial rift segments distributed in loose and in-line or en echelon arrangements (Morley *et al.* 2004) and need to interact and connect to form a continuous rift system. Associated rift linkage structures are classified as either transfer zones (TZs) when a discrete fault system connects both rift segments (hard linkage) or accommodation zones (soft linkage) when deformation is distributed and faults do not connect (Rosendahl 1987; Larsen 1988; Childs *et al.* 1995; Faulds & Varga 1998; Fig. 2.1e, f). The complex evolution and structuration of rift interaction zones has an important influence on sedimentary facies distribution and the migration and trapping of hydrocarbons (Morley *et al.* 1990; Paul & Mitra 2013). Several hydrocarbon fields are associated with accommodation zones in, e.g., the North Sea Viking Graben (Fossen *et al.* 2010). Interacting rift segments also influence magma migration and vice versa (Corti *et al.* 2004; Minor *et al.* 2013). Other examples of rift interaction zones are found in, e.g., Eastern France (Rhine-Bresse Transfer Zone [RBTZ]; Illies 1977; Ustaszewski *et al.* 2005; Fig. 3.1a), the Utah Canyonlands (accommodation zones, Trudgill & Cartwright 1994; Fossen *et al.* 2010), New Mexico, USA (Santo Domingo Relay [SDR] in the Rio Grande Rift; Aldrich 1986; Minor *et al.* 2013; Fig. 3.1b), and the East African Rift System (various transfer and accommodation zones; Morley *et al.* 1990; Corti 2012; Fig. 3.1c, d).

Data from numerical and analog studies indicate the influence of various parameters on rift interaction, e.g., the presence and geometry of structural heterogeneities, such as fault and shear zones, detachment layers, and magma intrusions that determine what structures develop (Elmohandes 1981; Naylor *et al.* 1994; Acocella *et al.* 1999a, 2005; Basile & Brun 1999; Le Calvez & Vendeville 2002; McClay *et al.* 2002; Tentler & Acocella 2010; Paul & Mitra 2013; Brune 2014; Zwaan *et al.* 2016; Chapter 2). Key factors affecting

the large-scale evolution of rift interaction structures are the rift offset and the degree of brittle-ductile coupling in the system. Larger offsets between rift segments cause TZs to be narrower (Acocella *et al.* 1999a; Dauteuil *et al.* 2002) or even prevent TZs from developing (Le Calvez & Vendeville 2002; Allken *et al.* 2011, 2012; Zwaan *et al.* 2016; Chapter 2). However, initial accommodation zones tend to evolve into TZs with increasing deformation (Acocella *et al.* 2005) and higher strain rates increase transfer zone widths (Dauteuil *et al.* 2002). The overlap or underlap of rift segments (see also Figs. 3.2d, e, i) can result in a variation of rift interaction zone structures and can cause the formation of microcontinents (Müller *et al.* 2001; Tentler & Acocella 2010). In addition, strong brittle-ductile coupling due to either high viscosities in the lower crust or high extension velocities (Brun 1999; Buiter *et al.* 2008) causes distributed deformation (wide rifting) and prevents rift segments from developing discrete transfer zones (Allken *et al.* 2011, 2012; Zwaan *et al.* 2016; Chapter 2).

Recent numerical modeling suggests that oblique extension, i.e., when the extension direction is not orthogonal to the strike of a structure (Fig. 3.2f), is an important factor promoting continent break up (Brune *et al.* 2012; Bennett & Oskin 2014). Although oblique extension has been studied and modeled extensively with respect to the evolution of continuous rifts (Tron & Brun 1991; McClay & White 1995; Clifton & Schlische 2001; McClay *et al.* 2002; Brune 2014; Philippon *et al.* 2015), its effects on interacting rift segments have largely been neglected to date. In our previous analog modeling study (Zwaan *et al.* 2016; Chapter 2), we did apply various degrees of dextral oblique extension and various seed offsets. The offset was of the "staircase" type (no overor underlapping seeds), and the seeds that localize deformation were not linked by any secondary structural weakness. We demonstrated how dextral oblique extension and low seed offsets promote rift linkage, what structures can be expected, and how these evolve. Here, we elaborate on our earlier work by assessing the effects of both the

geometry of inherited structures (linked and not linked with various degrees of underand overlap) and of oblique extension (sinistral and dextral) on rift interaction processes.

Contrary to most previous analog models, we use a model setup with distributed basal deformation that allows us to apply a greater variety of structural inheritance geometry because we do not force deformation along the edges of a baseplate (see also Morley 1999; Le Calvez & Vendeville 2002; Zwaan *et al*. 2016; Chapter 2, and compare with Elmohandes 1981; Acocella *et al*. 1999a; Basile & Brun 1999; Dauteuil *et al*. 2002). Selected models were analyzed by X-ray computer tomography (CT) techniques to reveal their detailed internal and external structures in 4D.
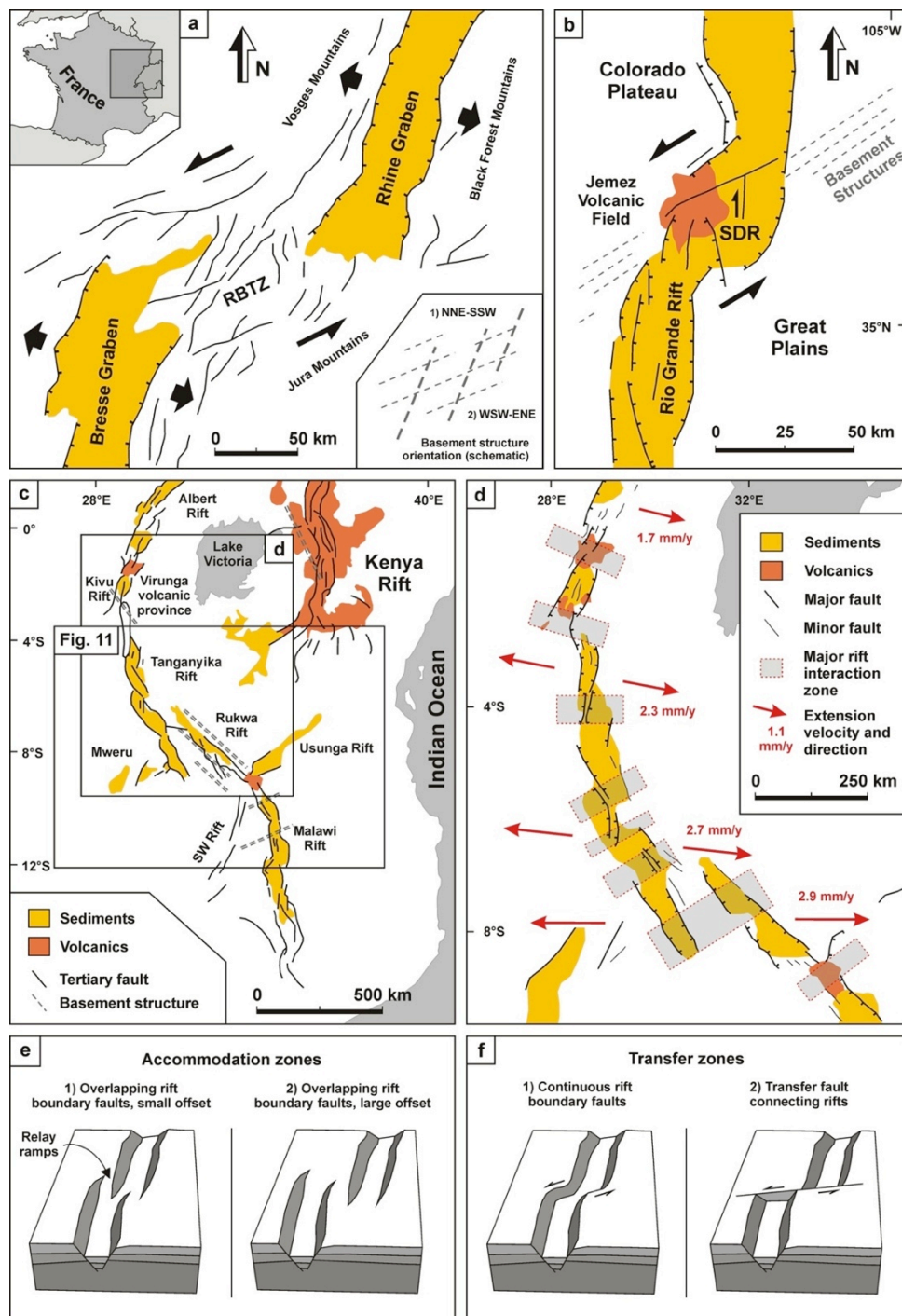
Fig. 3.1. (previous page) *Natural examples of rift interaction structures and accommodation/ transfer zone convention. (a) Rhine-Bresse Transfer Zone (RBTZ) between the Rhine Graben and Bresse Graben in eastern France. Image modified after Illies (1977) and Ustaszewski et al. (2005). (b) Santo Domingo Relay (SDR) within the Rio Grande Rift (USA). Image modified after Aldrich (1986) and Minor et al. (2013). (c) East African Rift System depicting the various rift segments and the occurrence of sediment basins and volcanics. Image modified after Ebinger (1989) and Acocella et al. (1999a). (d) Western branch of the East African Rift System, showing the major rift interaction zones with the associated sediments and volcanics, as well as current extension directions and velocities. Image modified after Saria et al. (2014) and Corti (2012), the location is shown in (c). Hatched lines represent normal faults; the character of faults without motion indications are not specified in the original publications. (e and f) Block diagrams depicting the differences between accommodation and TZs as proposed by Faulds & Varga (1998). (e) Accommodation zones (soft linkage) in which rift boundary faults do not connect, but die out laterally and overlap. Examples are present in the East African Rift System; their locations are shown in (d). (f) TZs (hard linkage) in which the rift boundary faults are continuous from rift to rift, e.g., the Selenga accommodation zone in Lake Baikal (Scholz & Hutchinson 2000) or in which a single transfer fault connects both basins, e.g., the Gulf of Suez or Thailand (Acocella et al. 1999a; Morley et al. 2004).*

_____

3.2. Materials and methods

3.2.1. Model set-up

We use a similar methodology as applied by Zwaan *et al.* (2016; Chapter 2, Fig. 3.2). Our models are designed to represent the continental crust: Alternations of quartz and corundum sand (grain size of 60–250 μm, density of 1560 kg/cm³; grain size of 88–175 μm, density of 1890 kg/cm³, respectively) form the model brittle upper crust. This alternation of sands with different densities serves to create X-ray attenuation variations that permit the visualization of model layers on CT images (Fig. 3.2g). The quartz and corundum sands have an internal peak friction angle of 36.1° and 37° and cohesion values of approximately 9 and 39 Pa, respectively. A near-Newtonian viscous mixture of corundum sand and silicone (SGM-36 PDMS) represents the ductile lower crust onto which the sand layers are sieved from an height of ca. 30 cm. The brittle and ductile model layers are both 2 cm thick, and the total 4 cm layer cake translates to a 40 km thick continental crust. For CT-scanned models, we use a double layer thickness (8 cm total) to better visualize structural details. Further details of the model materials are given in Table 3.1.

Our experimental apparatus contains a 30.5 cm wide base of 20 foam and 21 Plexiglas bars (each 1.0 and 0.5 cm wide, respectively) that is compressed to a 25.5 cm width between two mobile sidewalls (Fig. 3.2a). By moving the sidewalls apart, the foam expands uniformly resulting in a distributed extensional deformation in the overlying model materials. The mechanism can be considered to be the active rifting type because deformation is controlled by extension at the base of the model, rather than by "far-field stresses" due to pull by the opening sidewalls. In addition, one of the baseplates can move laterally. This allows us to model strike-slip settings and, in combination with orthogonal extension, to apply oblique extension. In these oblique extension models, additional transverse sidebars guide the shearing of the foam and Plexiglas bars at the base of the model setup.

On top of the basal PDMS/corundum sand layer, we apply ca. 5 mm wide, 2.5 mm high semicircular bulges (seeds) of the same viscous mixture. These seeds represent the influence of discrete inherited weaknesses (e.g., faults or shear zones) that localize deformation because the strong overlying sand is locally thinner (Fig. 3.2b). Structural weaknesses in nature may also occur as pervasive fabrics, i.e., present over a wide area (e.g., a dominant foliation), which poses an

important challenge to analog modelers (Morley 1999). However, the natural examples we address in this paper can be considered of the discrete type on the crustal scale we are concerned with (examples in Fig. 3.1). The seeds serve to create right-stepping rift segments at the desired locations (Fig. 3.2d, e 2i).

Table 1. *Material properties*

Granular materials	Quartz sand	Corundum sand
Grain size range	60-250 μm	88-175 μm
Density (sieved)	1560 kg/m^3	1890 kg/m^3
Angle of internal peak friction	36.1°	37°
Angle of dynamic-stable friction	31.4°	32°
Cohesion	9 ± 98 Pa	39 ± 10 Pa
Viscous material	**PDMS/corundum sand mixture**	
Weight ratio PDMS : corundum sand	0.965 kg : 1.00 kg	
Mixture density	ca. 1600 kg/m^3	
Viscosity[a]	ca. 1.5·10^5 Pa·s	
Type	near-Newtonian (n = 1.05)[b]	

(a) Holds for model strain rates < 10^{-4} s^{-1}. (b) Stress exponent n (dimensionless) represents sensitivity to strain rate

Table 2. *Model parameters.*

Series 1 (with rift-connecting seed)				Series 2 (without rift-connecting seed)			
Model no.	Extension obliquity (angle α)	Model geometry (angle ϕ)	Shown in	Model no.	Extension obliquity (angle α)	Model geometry (angle ϕ)	Shown in
1	-30°	60°	Fig. 3.4	**27 (C)**	-30°	30°	Fig. 3.9
2	-30°	75°	Fig. 3.4	**28 (D)**	-30°	30°	Fig. 3.9
3	-30°	90°	Fig. 3.4	**29 (E)**	-30°	30°	Fig. 3.9
4	-30°	105°	Fig. 3.4	30	-30°	15°	Fig. 3.8
5	-30°	120°	Fig. 3.4	31	-30°	45°	Fig. 3.8
6	-30°	135°	Fig. 3.4	32	-30°	60°	Fig. 3.8
7 (G)	-30°	30°	Fig. 3.9	33	-30°	90°	Fig. 3.8
8	0°	60°	Fig. 3.4	34	0°	15°	Fig. 3.8
9	0°	75°	Fig. 3.4	35	0°	30°	Fig. 3.8
10	0°	90°	Fig. 3.4	36	0°	45°	Fig. 3.8
11	0°	105°	Fig. 3.4	37	0°	60°	Fig. 3.8
12	0°	120°	Fig. 3.4	38	0°	75°	Fig. 3.8
13	0°	135°	Fig. 3.4	39	0°	90°	Fig. 3.8
14	30°	60°	Fig. 3.4	40	30°	15°	Fig. 3.8, 3.A1
15	30°	75°	Fig. 3.4	41	30°	45°	Fig. 3.8, 3.A1
16	30°	90°	Fig. 3.4	42	30°	90°	Fig. 3.8, 3.A1
17	30°	105°	Fig. 3.4	**43^{CT} (F)**	-30°	30°	Figs. 3.9-11, 3.13
18	30°	120°	Fig. 3.4	44*	30°	90°	Fig. 3.A1
19	30°	135°	Fig. 3.4	45*	30°	± 15°	Fig. 3.A1
20	60°	60°	Fig. 3.4	46*	30°	± 30°	Fig. 3.A1
21	60°	75°	Fig. 3.4	47*	30°	± 55°	Fig. 3.A1
22	60°	90°	Fig. 3.4				
23	60°	105°	Fig. 3.4				
24 (A)	60°	120°	Figs. 3.3, 3.4				
25	60°	135°	Fig. 3.4				
26^{CT} (B)	15°	75°	Figs. 3.5-7				

Bold: Key models, referred to as models A-G when discussed in the text
CT: CT-scannded models
*   Models with a 6 mm/h extension velocity instead of the standard 3 mm/h

a) Experimental apparatus

rubber sidewall

c) CT-scanner

mobile longitudinal sidewalls

25.5 cm

79 cm

surface grid (4 x 4 cm)

seed

pivoting bars, providing transverse confinement of plexiglass and foam bars

mobile base plate

fixed base plate

b) Model layering

seed (weak zone due to thin sand)

brittle quartz and corundum sand (2 cm: 20 km upper crust)

ductile silicone/ corundum sand mix (2 cm: 20 km lower crust)

plexiglass/ foam base (5 cm thick)

d) Series 1 set-up

seed

φ

4 cm offset

φ between 60° and 135°
α between -30° and 60°

e) Series 2 set-up

seed

φ

4 cm offset

no seed connection

φ between 15° and 90°
α between -30° and 30°

f) Oblique extension definition (angle α)

sinistral transtension

α < 0°

orthogonal extension

α = 0°

seed trend

dextral transtension

α > 0°

g) Distributed deformation

X   X'

seed

brittle

viscous

foam/plexiglass base

h) Velocity gradient graph

model width (25 cm)

v (mm/h)

12
0
0
-6
-12

x   x'

double model width (50 cm)

i) Model example

1.3   1.5

φ = 60°
φ = 75°
φ = 90°

10 cm   seed

1.3

Resulting vector: ~ 3 mm/h, α = 30°

Exp. 3

Exp. 1   Exp. 2

v(x) = 1.5 mm/h

v(y) = 2.6 mm/h
(2 x 1.3 mm/h)

α = 30°

v(xy) ≈ 3.0 mm/h

Fig. 3.2. (previous page) *Model setup. (a) Cut-out view of the experimental apparatus depicting its various components. (b) Compositional layering of quartz and corundum sand representing the brittle upper crust and a viscous silicone/corundum sand mixture simulating the ductile lower crust, above a Plexiglas and foam base. (c) Experimental apparatus in the CT scanner during a model run. (d and e) Seed geometry setup for our two model series with a secondary rift-connecting seed (series 1) and without a secondary seed (series 2). (f) Extension obliquity definition for our model series. (g) Distribution basal deformation in the model. As the sidewalls move apart with 3 mm/h, a velocity gradient develops in the foam and Plexiglas base (yellow arrows). The CT image is derived from model B (compare with Fig. 3.6). Layering in the sand is due to the alternations of quartz and corundum sand with different densities. (h) Velocity gradient due to the distributed basal deformation in our setup. The standard 3 mm/h velocity gradient for the normal model width (black line) would have to be quadrupled for a model with double dimensions (red line). However, as our models with double layer thickness have the same width as our standard models, the velocity should only be doubled to obtain the correct velocity gradient (dotted red line). The model velocity is kept at 3 mm/h for the CT-scanned models, but as explained in the text, the model structures are still comparable. For comparison, the blue lines show the velocity profile for basal plate setups with a normal thickness (dotted blue line) and a double thickness (continuous blue line). (i) Example of a model run. (Left) Initial setup of three separate experiments in one model run (without sand cover). (Right) Final surface structures.*

_____

Our rift segments are relatively narrow though, due to the narrow seed and basic rift geometry (Allemand & Brun 1991). Other modelers have often applied wider patches of silicone (Tron & Brun 1991) or a rubber base sheet (McClay & White 1995), of which the edges determine the rift boundaries, producing wider rifts with more detailed structures. However, since we focus on large-scale rift interaction processes instead of detailed structuration, this is acceptable. An advantage over traditional analog setups with baseplates (Elmohandes 1981; Acocella *et al.* 1999a; Basile & Brun 1999; Dauteuil *et al.* 2002) is that our setup allows a large variation of structural inheritance geometries; the seeds can be applied in any desired geometry. We also exploit the length of the experimental apparatus to increase our model efficiency by running three experiments per model run (Fig. 3.2i).

We use the term H that is equal to the thickness of the brittle crust (Allken *et al.* 2011, 2012) to quantify lengths in our models. The brittle crust thickness has a major influence on rift geometry (Allemand & Brun 1991), and this normalized value H enables comparisons between models with different brittle layer thicknesses. The horizontal offset between the seeds is set at 2 H (4 cm in the normal thickness models and 8 cm in the CT-

scanned models), to cancel any rift-proximity effects observed previously by Zwaan *et al.* (2016; Chapter 2). We define seed overand underlap by the angle ϕ between the main seed trend and the orientation of the line between the near ends of the seeds (Fig. 3.2d, e). Extension obliquity is given by the angle α between the normal to the rift trend and the extension direction (Fig. 3.2f). A negative angle α represents a situation with sinistral oblique extension, whereas a positive angle indicates dextral oblique extension. When angle α is 0°, extension is orthogonal.

We apply an extension velocity of 3 mm/h to better localize deformation, eliminating the effects due to high brittle-ductile coupling and the associated wide rifting (Brun 1999; Buiter *et al.* 2008; Fig. 3.A1). As it is standard in most physical rifting models, the extension rate is constant along the whole length of our models. Models run for 8 h, producing 2.4 cm of extension in the given extension direction.

The total 47 of models run for this study are split into two series (Table 3.2). The models in the first series are aimed at investigating the effect of a secondary seed connecting the parallel oriented main lateral seeds. This rift-connecting seed represents a secondary discrete structural inheritance as observed in, e.g., Eastern France (Ustaszewski *et al.* 2005;

Fig. 3.1a), the Santo Domingo Relay (SDR) in the Rio Grande Rift in the USA (Acocella *et al.* 1999a; Fig. 3.1b), and the East African Rift System (Acocella *et al.* 1999a; Corti 2012). In series 1 models, the main seeds are arranged in a right-stepping fashion and we model geometries with under- and overlap (Fig. 3.2d). Next to the dextral oblique extension and orthogonal extension previously applied by Zwaan *et al.* (2016; Chapter 2), we also apply sinistral oblique extension, as observed in for instance the East African Rift System (Saria *et al.* 2014). Note that not all combinations of extension direction and seed geometry are necessarily found in nature, but this way, we create a complete and systematic overview of the structures we can expect as a result of the combined effects of rift under/overlap and various degrees of oblique extension.

The models in the second series consist of parallel-oriented, right-stepping main seeds without secondary rift-connecting seeds, leaving the system more freedom to evolve between the main rifts (Fig. 3.2e). These series 2 models focus on main seeds with underlap only, but they do involve sinistral and dextral oblique extensions as in series 1. Also in this series, not every model should necessarily have an equivalent in nature. Further factors, such as the effects of sedimentation and erosion, are not considered in this study.

The Mohr-Coulomb characteristics of sand enable its use as an analog for the brittle crust. Viscous materials are more complex to apply, as their behavior is time-dependent. We use the density, length and gravity ratios (ϱ^*, h^* and g^* respectively, convention: $\varrho^* = \varrho_{model}/\varrho_{nature}$) to calculate stress ratios σ^*: $\sigma^* = \varrho^* h^* g^*$ (Hubbert 1937; Ramberg 1981). Subsequently we calculate the strain rate ratio $\dot{\varepsilon}^* = \sigma^*/\eta^*$ with the viscosity ratio (η^*): $\dot{\varepsilon}^* = \sigma^*/\eta^*$ (Weijermars & Schmeling 1986). Next, velocity and time ratios (v^* and t^*) are obtained: $\dot{\varepsilon}^* = v^*/h^* = 1/t^*$. Depending on the assumed viscosity of the lower crust, our 3 mm/h model velocity and our 4 cm model representing a 40 km thick continental crust translates to a velocity between ca. $7 \cdot 10^{-2}$ and $7 \cdot 10^2$ mm/y in nature. Velocities measured in natural rift settings plot in this range (e.g. a few mm/y in East Africa, Saria *et al.* 2014).

Further scaling formulas concern the dynamic similarity between models and nature. The ratio R_s between gravitational stress and cohesive strength (cohesion C) applies to the brittle domain: $R_s = \frac{gravitational\ stress}{cohesive\ strength} = \frac{\rho \cdot g \cdot h}{C}$ (Ramberg 1981; Mulugeta 1988). Similarly, the Ramberg number R_m or ratio between gravitational forces and viscous stress relates to the viscous domain: $R_m = \frac{gravitational\ stress}{viscous\ stress} = \frac{\rho \cdot g \cdot h}{\dot{\varepsilon} \cdot \eta} = \frac{\rho \cdot g \cdot h^2}{\eta \cdot v}$ (Weijermars and Schmeling 1986). The R_s value of 13.8 for the model is close to the natural value of 9.2, whereas the model R_m of 50 fits in the natural range (1 to $1 \cdot 10^4$). We therefore consider our standard 4-cm-thick models to be properly scaled. Scaling parameters are summarized in Table 3.3.

The double thickness in the CT-scanned models (8 cm instead of 4 cm) has some consequences for scaling. Following the scaling equations, the model extension velocity should be quadrupled to account for a double layer thickness. This is, however, only valid in a standard rigid baseplate model with a constant extension velocity throughout the model (the blue lines in Fig. 3.2h). In contrast, the extension velocity in our model follows a gradient (Fig. 3.2g, h). As the model width remains the same as in our standard thickness models, the extension velocity at the edge of the model should only be doubled to 6 mm/h (the red lines in Fig. 3.2h). Only when the model width would be doubled too, should the extension velocity be quadrupled (the blue and red lines intersecting in Fig. 3.2h). The extension velocity for the CT models is, however, kept at 3 mm/h instead of raising it to 6 mm/h (the black line in Fig. 3.2h). These 3 mm/h at the edge of the model, or rather the virtual 6 mm/h for a double model width, correspond to an extension velocity between $3.6 \cdot 10^{-2}$ and $3.6 \cdot 10^2$ mm/year in nature. This velocity range still captures natural plate velocities. The R_s and R_m ratios are now 27 and 100, respectively. The former is still close to the natural value, and the latter still fits in the natural range between 1 and $1 \cdot 10^4$. Because the structures we observe with the standard and double model thicknesses are quite similar, we consider them comparable.

Table 3. *Scaling parameters*

	General parameters			Brittle upper crust		Ductile lower crust		Dynamic scaling values	
	Grav. accel. g (m/s^2)	Crustal thickness h (m)	Extension velocity v (m/s)	Density ϱ (kg/m^3)	Cohesion C (Pa)	Density ϱ (kg/m^3)	Viscosity η (Pa·s)	Ramberg number R_m	Brittle stress ratio R_s
Model (normal)	9.81	0.04	$8.3 \cdot 10^{-7}$	1690^a	24^b	1600	$1.5 \cdot 10^5$	25	13.8
Model (CT)	9.81	0.08	$1.7 \cdot 10^{-6\ c}$	1690^a	24^b	1600	$1.5 \cdot 10^5$	100	27
Nature	9.81	$4 \cdot 10^4$	ca. $1 \cdot 10^{-10}$	2800	$7 \cdot 10^{7\ d}$	2900	$1 \cdot 10^{19\ to\ 23}$ $_e$	$1 \cdot 10^{0\ to\ 4}$	9.2

(a)   Average density of both sand types
(b)   Average cohesion of both sand types
(c)   Virtual velocity for a double model width is $1.7 \cdot 10^{-6}$ m/s instead of $8.3 \cdot 10^{-7}$ m/s (see text for explanation)
(d)   Cohesion value after Corti *et al*. (2004)
(e)   Viscosity range after Buck (1991)

3.3. Results series 1

3.3.1. Series 1 general overview

Faults only become visible on top view images after enough topography has formed to cast shadows on the obliquely lit model surface, although CT scanning shows fault formation shortly after model initiation in this type of model (Zwaan *et al*. 2016; Chapter 2). Consequently, the first structures appear on the top-view images after some 6 mm (0.3 H) of extension (model A, Fig. 3.3b) and continue to evolve until the end of the model run when 24 mm (1.2 H) of extension has taken place (Fig. 3.3e).

We present an overview of the final surface structures from series 1, in which the main seeds are connected by a secondary inherited weakness with various orientations (angles φ). We apply a spectrum of extension directions including dextral and sinistral oblique extension, as well as pure orthogonal extension (angle α ranges between -30° and 60°; Fig. 3.4). All 24 models produce well-developed rift segments above the main lateral seeds with a symmetric graben structure whose width decreases with increasing extension obliquity (either sinistral or dextral). Rift width is reduced from approximately 1.5 H (2.9 cm) to 0.95 H (1.9 cm) for angle α increasing from 0° to 60°. We also observe the occurrence of initial en echelon faults that quickly connect with each other to form continuous rift boundary faults when extension is oblique (best visible in Figs. 3.3c-

3e, 3.5c-5f). These rift boundary faults also accommodate increasing amounts of strike-slip motion with increasing degrees of oblique extension: approximately 0.2 H (0.4 cm) for α = ±30° and 0.5 H (1.0 cm) for α = 60°. Within the rift segments, sinistral oblique extension models develop right-stepping en echelon rift-internal faults that accommodate oblique-slip motion (Fig. 3.4a-4f), whereas dextral oblique extension models form left-stepping rift-internal faults (Fig. 3.4m-4x). In some cases, minor (strike-slip) faults develop away from the rift structures (Fig. 3.4s, p, r) or at the tips of the rift segments (Fig, 3.4o, r, s, u, v). These minor structures are not considered to have a large influence on the main structures we are interested in. Boundary effects are mostly restricted to limited normal faulting along the longitudinal sidewalls (Fig. 3.6).

Although every model contains well-developed rift segments along the main seeds, these segments do not connect in all cases: Rifts in -30° (sinistral) oblique extension models propagate subperpendicularly to the extension direction and thus away from each other, regardless of the presence and orientation of the secondary rift-connecting seed (Fig. 3.4a-f). Models with orthogonal extension only show the development of TZs when angle φ is 75°or less (Fig. 3.4g, 4h). Otherwise, the main rift segments propagate in a parallel fashion, subperpendicular to the extension direction (Fig. 3.4i-4l).

In contrast to the sinistral oblique extension models, all dextral oblique extension models exhibit hard linkage and produce TZs (Fig. 4m-x). However, as in the case of their sinistral oblique extension equivalents, the secondary rift-connecting seeds are often not activated. In several cases, they are even crosscut by the propagating rift structures (Figs. 3f, 4o-r, v-x). Only when the extension obliquity (angle α) is between 0° and 60° and angle ϕ is 90° or less (Fig. 3.4g, h, m, n, s-u) can we observe activation of the rift-connection seeds. Otherwise, rifts propagate perpendicular to the extension direction, simply ignoring the presence of any rift-connecting seeds.

When TZs develop, they generally consist of curved rift boundary faults that propagate toward the other rift segment, forming a continuous trough that connects both rift segments. The α = 30° and ϕ ≥ 90° models (Fig. 3.4o-r) exhibit more complex structures as the rifts propagate from the seed tips and curve around and toward each other. Between both propagating rift branches, a "horst" area remains undeformed and is separated from the main rigid blocks in the model.
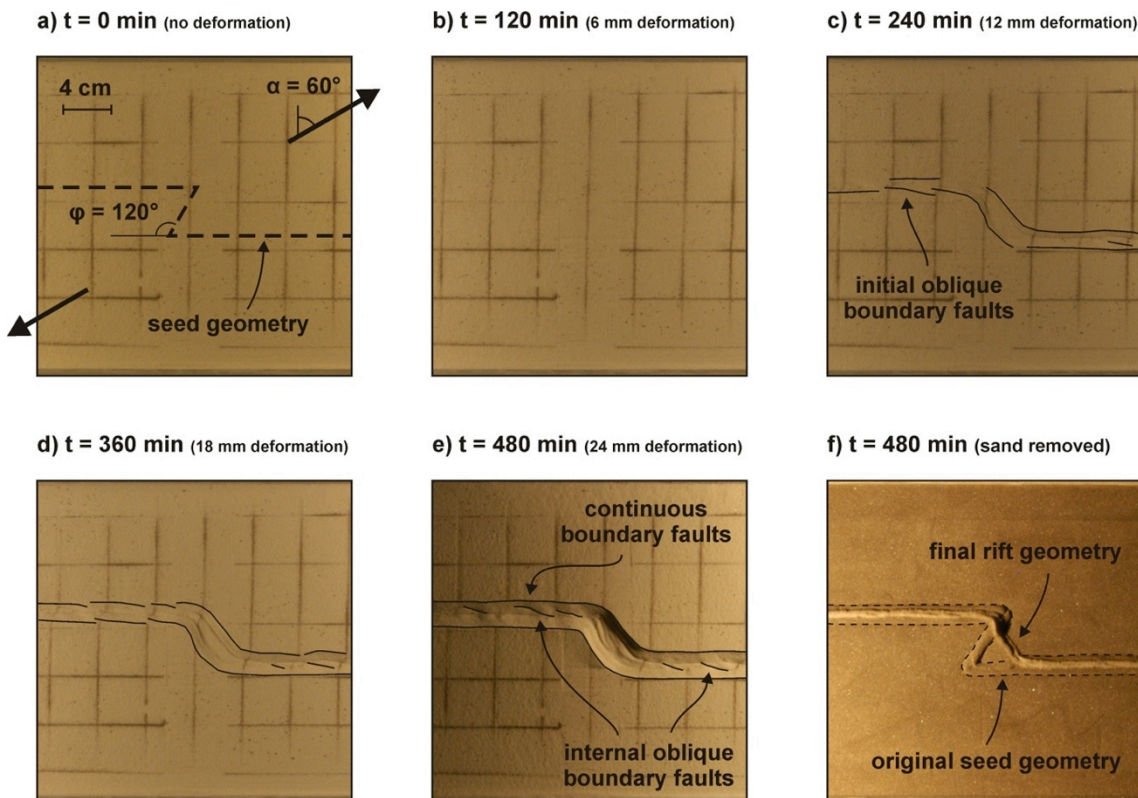
Fig. 3.3. *Top view images depicting the evolution of model A from series 1 (with rift-connecting seed): (a) Initial set-up with seed geometry and extension direction: Angle ϕ = 120° (overlap) and angle α = 60° (dextral oblique extension). The 4 x 4 cm surface grid allows the assessment of surface motion. (b-e) surface evolution of the model; (f) Initial seed geometry (within the dotted lines) and the actual orientation of the transfer zone at the end of the model run and after removal of the sand layers. The transfer zone orientation is visible due to isostatic rising of the viscous layer associated with decreased loading as basin formation thins the overlying sand layer.*
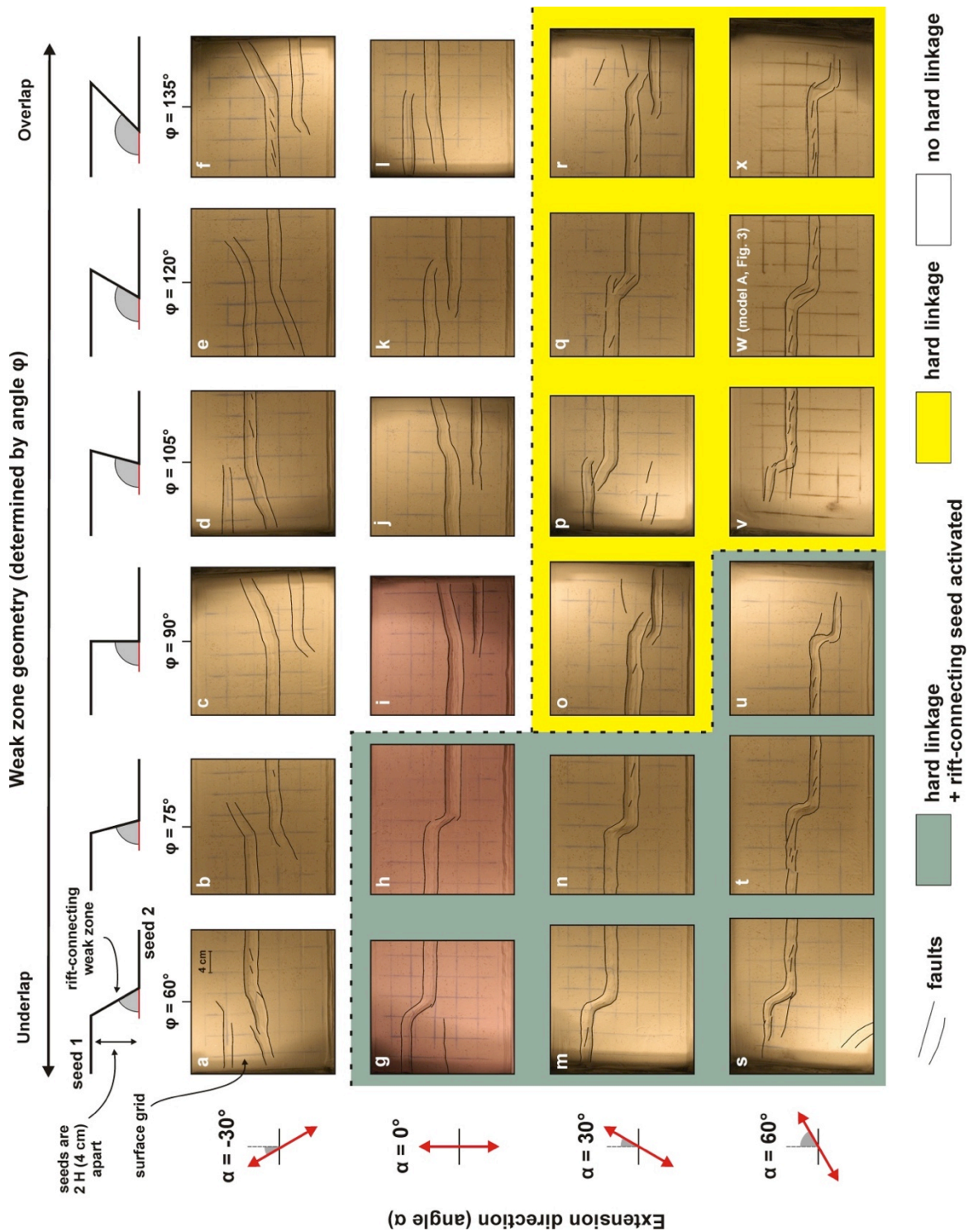
Fig. 3.4. *Overview of final surface structures 24 models from series 1 (with rift-connecting seeds) as a function of extension direction (angle α) and seed geometry (determined by angle φ). The models in the overview are divided in three groups: models without hard linkage, i.e. no transfer zone, models with hard linkage, but without activation of the rift-connecting seed and models with both hard linkage and activation of the rift-connecting seed. Faults are indicated with black lines.*

3.3.2 Series 1 CT-scanned model (Model B)

To further investigate the characteristics of our series 1 models, we ran a $\alpha = 15°$, $\phi = 75°$ model with a rift-connecting seed in the CT-scanner (model B). We apply a double layer thickness to increase resolution on CT images. In general, the surface structures are similar to the previous models with $\phi = 75°$ and $\alpha = 0°$ or 30° (Fig. 3.4b, h), but CT images, both 3D surface scans as horizontal and vertical sections, allow a much more detailed structural analysis (Fig. 5-7).

The first structures to appear on the 3D CT images are normal faults (initial dip angle of approximately 70°) along the main seeds (Fig. 3.5b). These faults initially form at the side of the seed that is closest to the sidewalls creating an asymmetric graben. After approximately 60 min (3 mm of deformation), however, rift boundary faults also develop on the other side of the rift to render the rift symmetric (Fig. 3.5c). The rift boundary faults are not completely continuous structures; initial faults are offset in a left-stepping fashion, and their surface trace strikes are approximately 8° oblique to the main rift trend (Fig. 3.5c). However, they rapidly link up to form continuous boundary faults (Fig. 3.5e, 5f). Within the rift segments, a secondary set of antithetic normal faults develops and a horst develops in the middle of the rift as a result (Figs. 3.5e, 3.6). However, these internal structures are disrupted toward the end of the model run. Also, the seed is deformed as a result of the rift structure above it. We observe tilted fault blocks sinking into the seed (Figs. 3.5f, 3.6).

The horizontal and vertical CT sections allow a better analysis of the transfer zone area (Fig. 3.7). In contrast to the structures along the main rift segments, the transfer zone structures are poorly developed at first. We observe combined strike-slip and oblique-slip normal faulting (initial fault dip angle approximately 90° and 76°, respectively) starting along the rift-connecting seed (Fig. 3.7b, c). The vertical offset along the rift boundary faults is limited. However, the strike-slip fault within the transfer zone is well developed and runs from one rift segment to the other (Fig. 3.7d-f). Throughout the model run, the main rift basins remain wider and deeper than the basin that opens at the transfer zone. The final rift basin width is approximately 2.3 H (4.6 cm) at the main rift segments and 1.6 H (3.2 cm) within the transfer zone. Corresponding maximum basin depths amount to approximately 0.8 H (1.6 cm) and 0.4 H (0.8 cm) along the main rift segments and within the transfer zone, respectively.

Similar to the rift boundary faults along the main rift segments, the transfer zone boundary faults form along the rift-connecting seed trend, but they are offset at several places (Fig. 3.5d). In fact, the individual faults measured at the surface tend to be oriented approximately 20° oblique to the rift-connecting seed at depth. Also, the whole transfer zone structure itself is at the surface some 10° oblique with respect to the rift-connecting seed (Figs. 3.5d, 3.7f). Due to the internal strike-slip faults, the internal transfer zone structure is complex. The vertical CT sections perpendicular to the transfer zone reveal its nature as a transtensional fault zone because it combines strike-slip and normal fault features. We observe a narrow graben with steep boundary faults and vertical strike-slip faults within it (Fig. 3.7, insets).
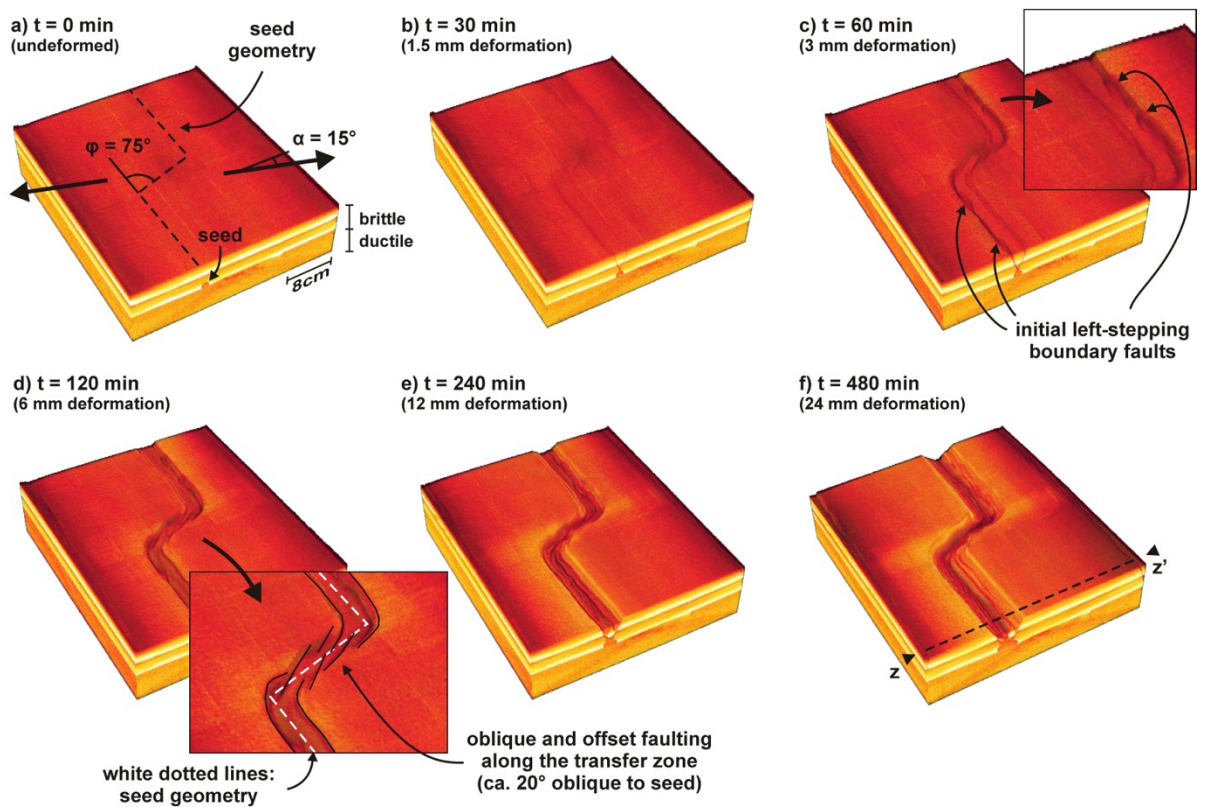
Fig. 3.5. *CT-derived images showing the 3D surface evolution of model B. (a) Initial set-up: rift-connecting seed present, angle $\phi = 75°$ (underlap) and angle $\alpha = 15°$ (dextral oblique extension). (b) Faulting starts along the seeds; (c) Initial boundary faults form oblique due to oblique extension, while a transfer zone forms along the rift-connecting seed; (d) The transfer zone develops distinct oblique faulting; (e-f) initial oblique boundary faults are connecting to form continuous boundary faults. The final transfer zone structure is slightly oblique to the original seed orientation (f). For vertical section z-z', see Fig. 3.6.*

Fig. 3.6. *CT section through a main rift segment in model B, showing rift internal structure at the end of the model run. The layering in the brittle layer is due to the density difference between quartz and corundum sand (see Table 1). Compare with Fig. 3.2g for the initial state. For section location see Fig. 3.5.*
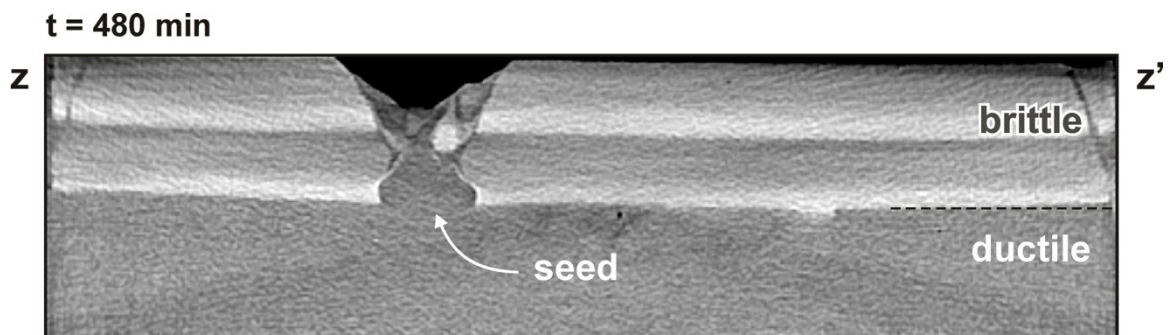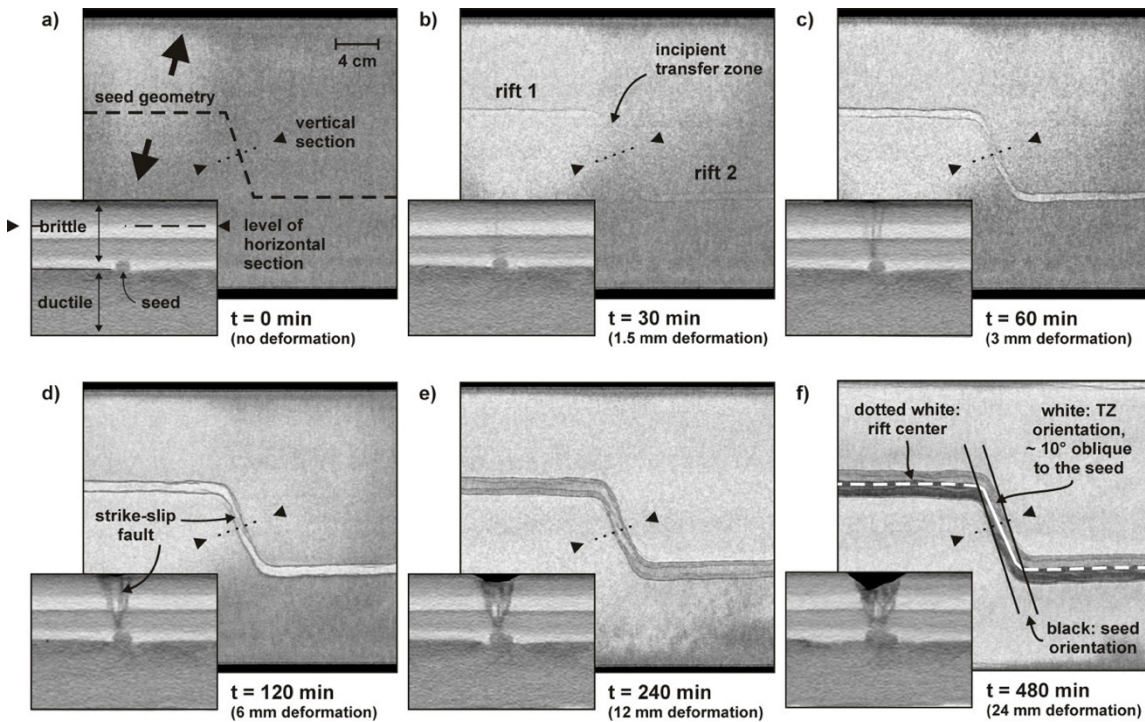
Fig. 3.7. *CT-analysis of model B with horizontal and vertical sections: (a) Initial set-up (rift-connecting seed present, φ = 75°, α = 15°); (b-f) Model evolution, revealing the location and nature of faulting within the model. Horizontal sections are taken ca. 2.5 cm above the brittle-ductile interface, see also the vertical section in (a). Vertical sections are perpendicular to the transfer zone, their location is indicated by a dashed line on horizontal sections. (f) also shows the oblique orientation of the transfer zone with respect to the seed below it.*

3.4. Results series 2

3.4.1. Series 2 general overview

The top view images of series 2 models, in which rift segments are underlapping and not connected by any seed, are presented in Fig. 3.8. The characteristics of the main rift segments are similar to those in series 1, as is the rift propagation behavior. The α = 30° (dextral) oblique extension models in series 2 (Fig. 3.8a-c) develop rift segments along the seeds that propagate approximately perpendicular to the extension direction. For φ = 90° (Fig. 3.8a), the propagating rifts curve around each other. When φ = 45° (Fig. 3.8b), the extension direction makes the segments grow straight toward each other, forming a continuous basin. However, in the φ = 15° case (Fig. 3.8c), the seed underlap is such that the propagation of the segment perpendicular to the extension directions almost causes them to miss each other. When extension is orthogonal (Fig. 3.8d-i), rift propagation is also subperpendicular to the direction of extension. Therefore, the propagating rifts do not lead to hard linkage in the φ= 90°-60° cases (Fig. 3.8d-f). However, in the φ = 45°-15° cases (Fig. 3.8g-i), the rift segments show a tendency to grow toward each other, although for the φ = 15° model (Fig. 3.8i) a full transfer zone does not develop.

94
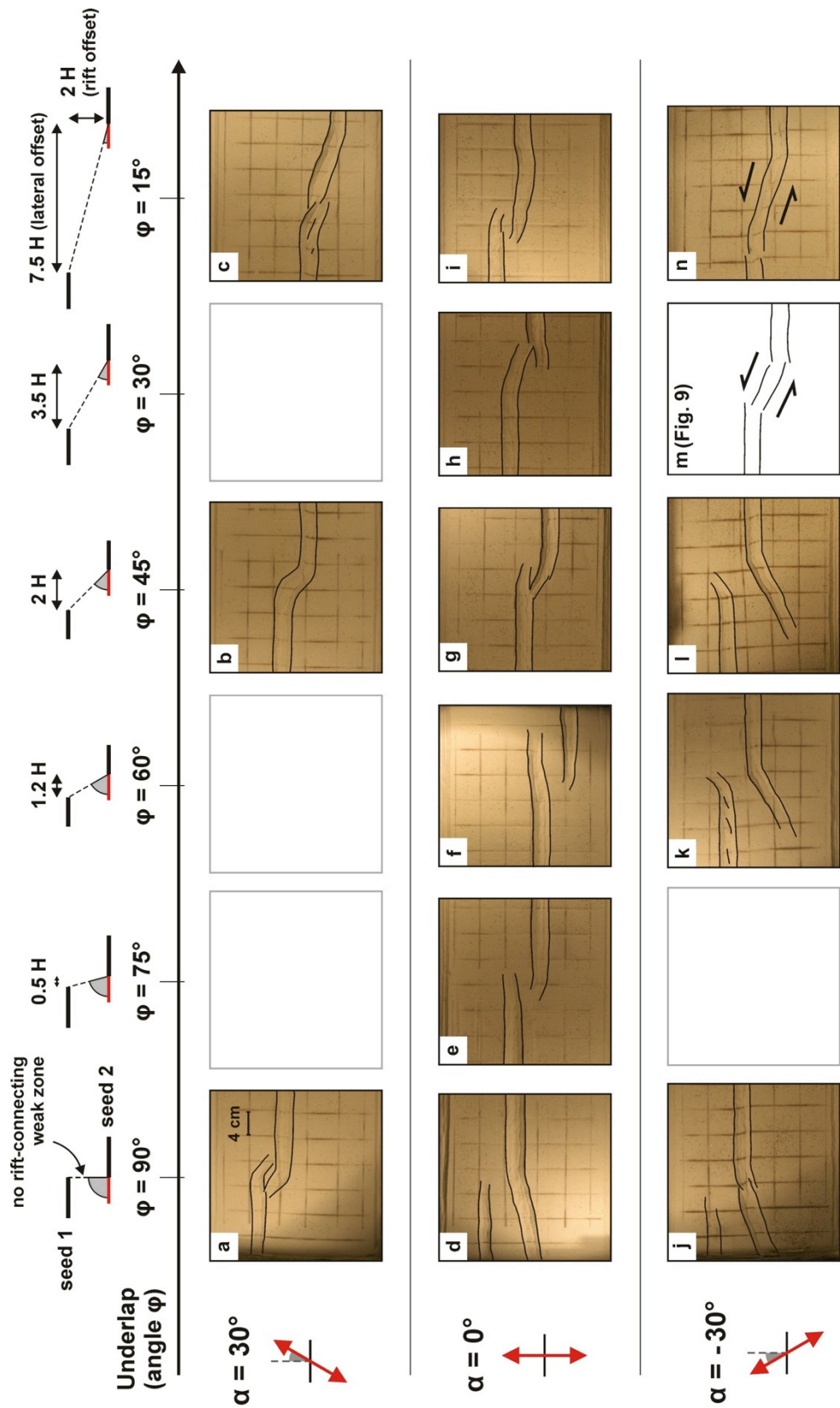
Fig. 3.8. *Top views depicting the final surface structures of 13 models from series 2 as a function of extension direction (angle α) and seed underlap (determined by angle φ). Faults are indicated with black lines. The black and white image (m) is shown in Fig. 3.9.*

95

A similar situation with respect to the relation between the extension direction and rift propagation direction is seen in the -30° sinistral oblique extension models. The ϕ = 90°-45° models (Fig. 3.8j-l) show rift segments propagating away from each other, subperpendicular to the extension direction. However, when ϕ = 30° or 15° (Fig. 3.8m, n), hard linkage occurs as models establish TZs. We ran multiple models with ϕ = 30° and α = -30° to examine this in further detail, and we observed a range of characteristic features (models C-G; Fig. 3.9). During the 480 min or 24 mm (1.2 H) of -30° (sinistral) oblique extension, models C and D develop an initial sinistral strike-slip fault zone (Fig. 3.9b, f) that subsequently evolves in a transfer zone basin connecting the rift segments (Fig. 3.9d, h). This final transfer zone basin is situated between continuous rift boundary faults, along which sinistral normal oblique-slip motion is accommodated. Note that model G (Fig. 3.9q-t) has a rift-connecting seed and technically belongs to series 1, but is shown here for comparison. It is clear that the structures follow the trace of the rift-connecting seed in model G, but the structures are very similar to those seen in models C and D.

The ϕ = 90° and 60° models (Fig. 3.8j, k) show rift segments propagating away from each other, sub perpendicular to the extension direction. However, when ϕ = 30° or 15° (Fig. 3.8m, n), hard linkage occurs with models establishing transfer zones. We ran multiple models with ϕ = 30° and α = -30° to examine this in further detail, and observed a range of characteristic features (models C-G, Fig. 3.9). During the 480 min or 24 mm (1.2 H) of -30° (sinistral) oblique extension, models C and D both develop an initial sinistral strike-slip fault zone (Fig. 3.9b and f) that subsequently evolves in a transfer zone basin connecting the rift segments (Fig. 3.9d and h). This final transfer zone basin is situated between continuous rift boundary faults along which sinistral normal and oblique-slip motion is accommodated. Note that model G (Fig. 3.9q-t) has a rift-connecting seed and technically belongs to series 1, but is shown here for comparison. It is clear that the structures follow the trace of the rift-connecting seed in model G, but the structures are very similar to those seen in models C and D.

In model E (Fig. 3.9i-l) on the other hand, a transfer zone is present, but it is poorly developed and it is essentially strike-slip dominated. Instead of forming a continuous basin structure as in models C and D, model E has one of the rift branches propagating away from the rift, subperpendicular to the extension direction as seen in the other sinistral oblique extension models in series 1 and 2 (Figs. 3.4, 3.8). Model F (Fig. 3.9m, p), which is the CT-scanned model that will be discussed in more detail below, develops similar features as model E: one rift branch propagating away and rift linkage through a sinistral strike-slip-dominated transfer zone.

Note that the characteristics of the strike-slip transfer zone structures in the model E and F examples (Fig. 3.9l, p) resemble the early stages of the transfer zone structures in models C, D, and G (Fig. 3.9b, f, r). But, although all deformation is accommodated by a transfer zone evolving into a continuous trough in models C, D, and G, part of the deformation in models E and F goes into the propagating rift branches. Therefore, the TZs remain shallow and strike-slip dominates in the latter models.

3.4.2. Series 2 CT-scanned (Model F)

To further assess the phenomenon of rift connection by a strike-slip transfer zone under sinistral oblique extension, we ran a α = -30°, ϕ = 30° model with double layer thickness as well as double rift offset and without rift-connecting seed in the CT scanner (model F). The CT data are used to create 3D surface images (Fig. 3.10) and horizontal and vertical sections (Fig. 3.11) that allow more detailed analysis. The model generates two rift segments, of which one propagates subperpendicular to the extension direction and a strike-slip dominated transfer zone between the two rift segments.

In model F, deformation initially takes place along the seeds (Fig. 3.10b). Both rift segments show a tendency to propagate perpendicular to the extension direction. However, at t = 120 min (6 mm of deformation), vertical sinistral strike-slip fault segments start developing between the main rifts (Fig. 3.11b). Some 30 min later, these fault segments form a zone of en echelon

strike-slip faults, all oriented 20° oblique to the rift trend in a Riedel fault configuration (Figs. 3.10c, 3.11c). As deformation progresses, oblique-slip normal faulting becomes more prominent and a negative flower structure develops (sections in Fig. 3.11c-11f). The associated horizontal sections also show how the Riedel faults connect in various orientations.

Meanwhile, the main rift basins continue developing above the seeds and one rift segment propagates toward the side of the model. This propagating rift arm is perhaps partially a boundary effect as its orientation is not perpendicular with respect to the extension direction (compare with model E; Fig. 3.9i-l). The rift branch takes up a large portion of deformation so that the strike-slip dominated transfer zone only accommodates a total of 0.6 cm (0.15 H) sinistral strike-slip motion. Subsidence along the transfer zone is also limited (approximately 1 mm or 0.025 H).
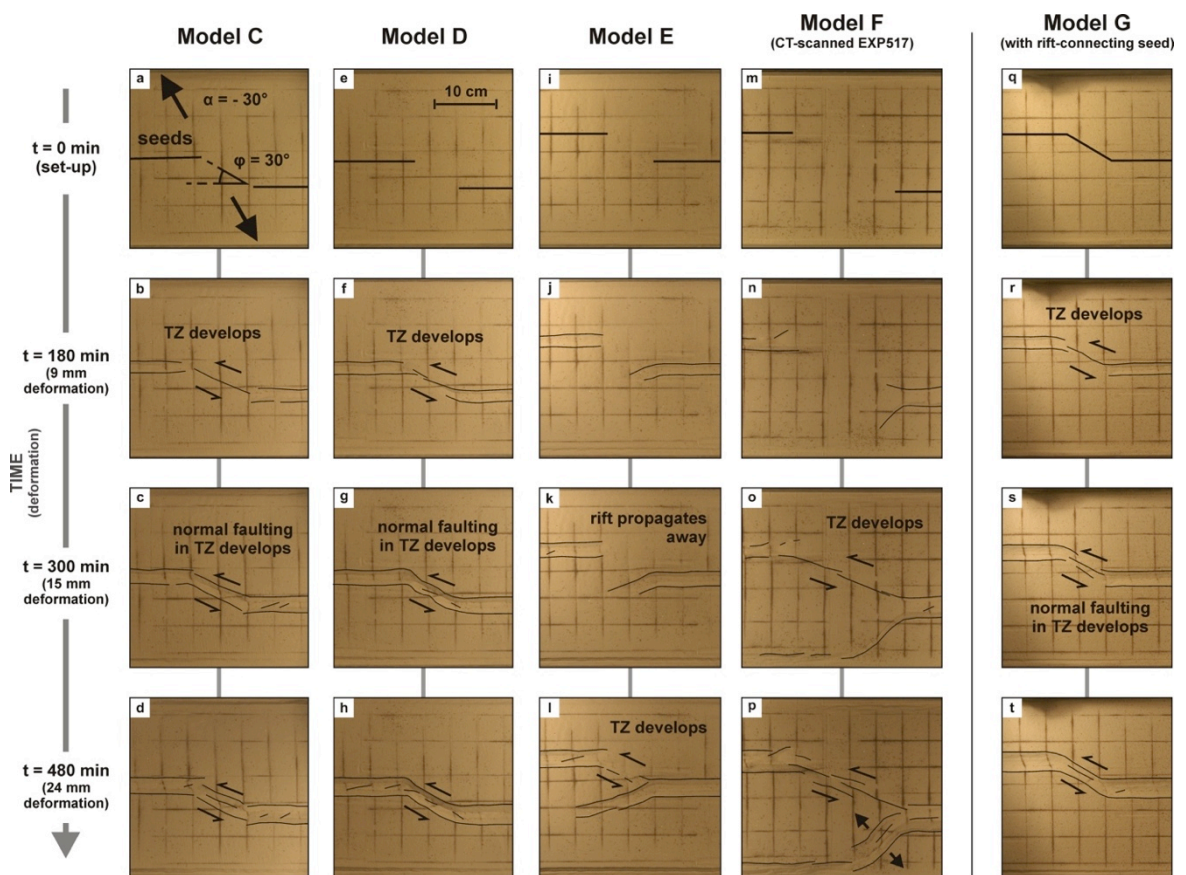
Fig. 3.9. *Surface structure evolution of 5 models with ϕ = 30° and α = -30° to assess the development of sinistral strike-slip transfer zones. Models C (a-d), D (e-h), E (i-l) and G (q-t) have normal layer thickness (a 2 cm ductile and a 2 cm brittle layer). CT-scanned model F (m-p, see also Figs. 3.10-13) has the same basic set-up but double layer thickness and therefore a larger seed offset. Note that model G (q-t) has a rift-connecting seed while the other models do not, and technically belongs to series 1. However, it is included here for comparison. TZ = transfer zone. Faults are indicated with black lines.*
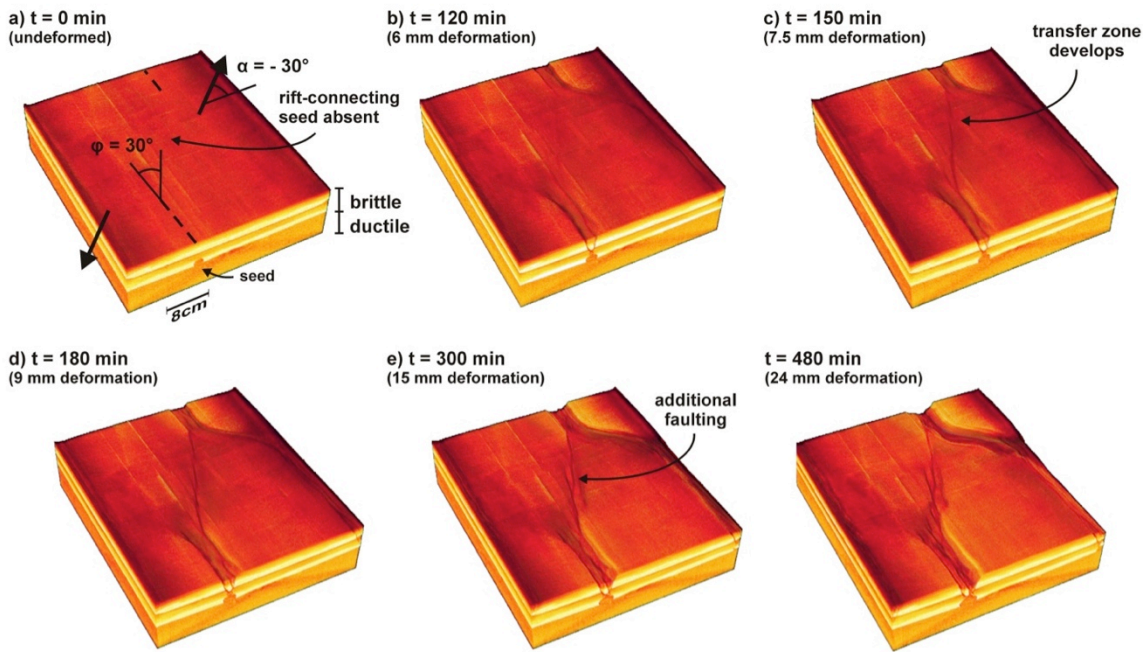
Fig. 3.10. *CT-derived images showing the 3D surface evolution of model F. (a) Initial set-up: rift-connecting seed absent, angle $\phi = 30°$ (underlap) and angle $\alpha = -30°$ (sinistral oblique extension); (b) Faulting initiates along the seeds; (c) a strike-slip transfer zone appears and on rift arm propagates towards the model edge; (d-f) the established structures evolve further: the rift segments and rift branch grow larger the transfer zone develops more expressed strike-slip faults. (f) Shows in addition the orientation of the transfer zone (TZ) with respect to the rift-connecting seed below.*
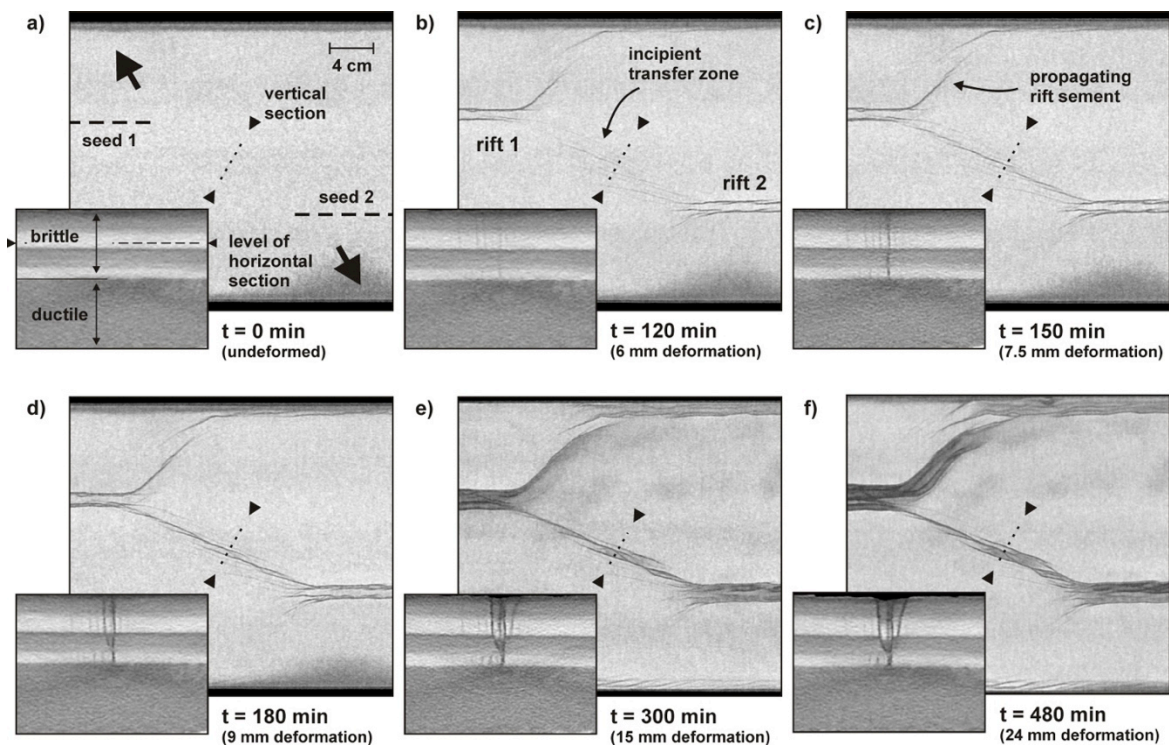
Fig. 3.11. (previous page) *CT-analysis of Model F with horizontal and vertical section (a) Initial set-up (rift-connecting seed absent, φ = 30°, α = -30°); (b-f) Model evolution, revealing the location and nature of faulting within the model. Horizontal sections are taken ca. 2.5 cm above the brittle-ductile interface, see also the vertical section in (a). Vertical sections are perpendicular to the transfer zone, locations are shown by a dashed line on horizontal sections.*

_____

3.5. Discussion

3.5.1. Characteristics of main rift segments

The geometry and evolution of the rift segments away from the rift interaction zones in our models are similar to those observed and described by Zwaan *et al.* (2016; Chapter 2). In general, an increase in extension obliquity (angle α) results in a decrease in graben width and depth as the system becomes less extension dominated. Higher degrees of extension obliquity also result in more features such as en echelon boundary faults and rift-internal oblique structures. The main rift segments propagate roughly perpendicular to the extension direction as previously observed in modeling studies involving oblique extension (Tron & Brun 1991; McClay & White 1995; McClay *et al.* 2002) and in natural settings (Dauteuil & Brun 1993; Morley *et al.* 2004). Our models produce relatively narrow structures with minimal internal details compared with those in previous modelling studies and some natural examples, but this is quite permissible as here we rather focus on rift interaction processes on a regional scale than on detailed internal rift geometries.

3.5.2. Rift propagation and interaction

The models from series 1 and 2 show the extension direction as a dominant factor controlling the propagation direction of rift segments because rift propagation tends to be subperpendicular to it. As a consequence, we observe that the rift linkage of right-stepping rift segments is generally promoted by dextral oblique extension that causes the rifts to propagate toward each other and prevented by sinistral oblique extension that has them grow apart. However, in a mirrored system with rift segments arranged in a left-stepping fashion, dextral and sinistral oblique extension switch places (see also Fig. 3.13). Dextral oblique

extension now should prevent rift linkage because rift segments grow apart under these conditions. In contrast, sinistral oblique extension should cause left-stepping rift segments to connect. Rift segment arrangement is therefore a second important influence on rift interaction, and rift linkage is most likely when the extension direction is such that rift segment propagation is directed toward the other rift segment. Note that the orthogonal extension models from series 2 do not fully fit the general picture. The rift segments in the larger underlap models (φ = 45° and 30°; Fig. 3.8g, h) do partially connect. Possibly the 2 H offset between the rifts is not large enough to prevent them from interacting after all, or rift propagation directions can vary up to a certain degree in our specific setup.

Similar influences of oblique extension on fault orientation and associated rift propagation directions are reported in previous analog models (Hus *et al.* 2005; Zwaan *et al.* 2016; Chapter 2), although sinistral oblique extension was not tested before. The curving of propagating rifts toward each other under orthogonal extension with φ ≥ 90° isolates part of the model between both propagating rift segments, a so-called rift pass (Nelson *et al.* 1992), which is also observed in previous analog models and can lead to microcontinent formation (Müller *et al.* 2001; Tentler & Acocella 2010). We can expect for our specific setup that dextral oblique extension enhances this process because it induces rifts to propagate toward each other, especially when rifts are too far apart to interact under orthogonal extension conditions.

3.5.3. Rift-connecting seeds and rift segment interaction

Our models show limited reactivation of secondary pre-existing weaknesses. The

secondary seeds only activate when they are oriented favorably to the regional tectonic stresses. Furthermore, in our experiments, rift segments in models with angle $\phi = 90°$ under orthogonal extension fail to link. This is in contrast with previous models (Acocella *et al*. 1999a; Dauteuil *et al*. 2002), but it is in accordance with other models such as those completed by Le Calvez & Vendeville (2002), illustrating a fundamental difference between traditional rigid baseplate setups, which force deformation along the plate boundaries, and setups that allow more freedom for the model to evolve.

The notion that inherited structures do not necessarily reactivate has been previously explored, for example, in models run by Nalpas *et al*. (1995), although their study was aimed at initial rifting and subsequent inversion. Note that model series 2 does not cover the whole spectrum of model series 1 and only focuses on the underlap models since we expect the equivalent overlap models in series 2 to have the same characteristics as those in series 1. This is illustrated by the $\phi = 90°$ models from series 1 and 2 that produce very similar structures (compare Fig. 3.4c, i, o with Fig. 3.8a, d, j). However, inherited structures might influence structures in ways that our model setup does not capture, such as creating boundaries for propagating rifts, causing general weakening of the brittle crust, and locally changing the state of stress (Bell 1996; Morley 2010).

3.5.4. Transfer zone details

Strain partitioning accounts for the limited strike-slip faulting that occurs at the tip of rift segments in some models (Fig. 3.4o, s, u, v) as also observed in models by Zwaan *et al*. (2016; Chapter 2). Moreover, strain partitioning can also produce a major strike-slip fault within a transfer zone that runs from one rift segment to the other as seen in model B (with 15° oblique extension; Fig. 3.7). This is similar to observations in orthogonal extension models by Acocella *et al*. (1999a), as is the fact that the whole transfer zone itself might form oblique to the deeper crustal weakness. In previous studies, the surface orientation of transfer zones is expressed with angle ϕ (Acocella *et al*. 1999a; Corti 2012),

but because this is also used to describe the orientation of structural inheritance, we propose to use angle κ (Greek kappa) for the orientation of the transfer zone instead (Fig. 3.12).

3.5.5. Rift segment linkage under sinistral oblique extension conditions

The sinistral oblique extension models ($\alpha = -30°$) of series 2 show the expected rift propagation behavior as a function of extension direction also seen in series 1 (Figs. 3.4a-f, 3.8a-l), except for the $\phi = 30°$ and 15° models (Figs. 3.8m, n, 3.9). These develop a spectrum of TZs between the main rift segments, ranging from a rift structure with a sinistral strike-slip component along the boundary faults (models C and D; Fig. 3.9a-h) to a more discrete sinistral strike-slip zone along with one rift branch propagating away from the rift (models E and F; Fig. 3.9i-p). Although the rift branch orientation in model F is slightly off (not perpendicular to the extension direction), probably due to the influence of faulting at the model edge, it does fit in the general picture. In a way, these different models can be seen as different stages when only the transfer zone evolution is concerned. The strike-slip-dominated TZs in models E and F (Fig. 3.9i-p) then represent the early stages of transfer zone development. In these models, the propagating rift branches take up a part of the deformation resulting in a less evolved transfer zone. In models C and D (Fig. 3.9a-h), deformation is fully accommodated by the transfer zone alone. This concentration of deformation results in basin formation following the initial strike-slip phase that is also captured by models E and F. The final results of models C and D thus illustrate a more advanced stage in transfer zone development.

Our four $\phi = -30°$, $\alpha = -30°$ models (models C-F) without a rift-connecting seed all establish a transfer zone between the main rift segments. However, some models (E and F; Fig. 3.9i-p) develop an additional propagating rift branch similar to those in (most) other $\alpha = -30°$ models (Fig. 3.8j-l). These hybrid features in models E and F indicate that the $\alpha = -30°$, $\phi = 30°$ situation marks a transition between two modes of rift interaction. When

φ > 30°, we should expect accommodation zones to form and rifts to grow apart, which is consistent with our models (Fig. 3.8j-l), whereas φ ≤ 30° settings will produce strike-slip-dominated TZs, as is confirmed by our φ = 15° model (Fig. 3.8n). When we then add a rift-connecting seed as in model G (Fig. 3.9q-t), we observe the exact same structures as in the models without a rift-connecting seed, i.e., models C and D (Fig. 3.9a-h). The transfer zone in model G does follow the trend of the rift-connecting seed, but it is not clear from our models whether the seed is really activated

or whether it just has the same orientation as the transfer zone. However, the fact that model G does not develop any propagating rift branches such as those in models C and D could indicate a localizing effect of the seed, and the absence of a seed could allow the system the freedom to develop propagating rift branches. Our model results thus do not exclude any influence of basement structures on transfer zone formation, but they show that such structures are not strictly necessary to produce rift linkage through a strike-slip-dominated transfer zone.
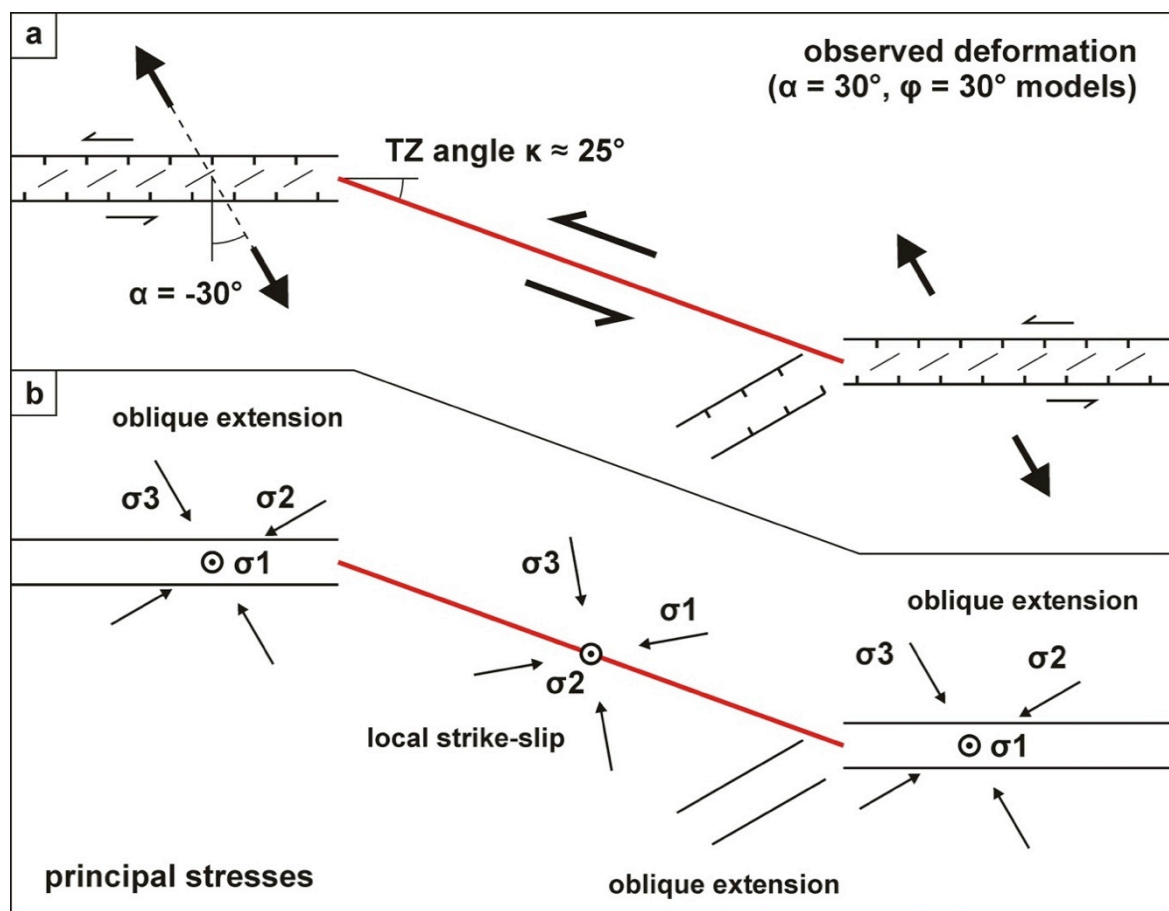
Fig. 3.12. *Schematic overview of (a) observed deformation structures at the model surface and (b) inferred principal stresses at time of transfer zone formation within our φ = 30° models with -30° (sinistral) oblique extension. The general state of stress, present along the rift segments and any propagating rift branch, has σ₁ vertical and σ₃ horizontal in -30° sinistral oblique extension direction. The strike-slip character of the transfer zone indicates a local change in stress: both σ₁ and σ₃ become horizontal (ca. 30° and 60° oblique to the transfer zone respectively) and oblique to the transfer zone, while σ₂ is now vertical.*

The formation of strike-slip TZs in the $\phi \leq 30°$, $\alpha = -30°$ experiments (structures schematically depicted in Fig. 3.12a) indicates strong local changes in the regional stress field (Fig. 3.12b). Throughout the model, sinistral oblique extension causes a state of stress with σ_1 vertical to the surface and σ_3 oriented horizontally, roughly parallel to the direction of extension ("oblique extension" setting; Fig. 3.12b). As the seeds localize deformation and normal faults strike perpendicular to σ_3, this state of stress causes initial oblique faulting along the seeds. When the initial rift segments start propagating away from the seeds, the developing rift branch, free from the localizing influence of the seed, directs itself perpendicular to the regional σ_3. The rift segments should thus simply grow apart, but we observe the formation of strike-slip TZs (Fig. 3.12a). To create a strike-slip fault zone between the rift segments, σ_1 and σ_3 must be reoriented so that they lie within a horizontal plane, some 30° and 60° oblique to the strike-slip zone, respectively. Thus, the local σ_1 is now oriented approximately 25° oblique with respect to the regional σ_2 and the local σ_2 replaces the regional σ_1 as the vertical principal stress ("local strike slip," Fig. 3.12b). Such local stress changes also occur at stepovers in strike-slip fault systems (Okubo & Schultz 2006; De Paola *et al.* 2007). The TZs in our models do resemble releasing bends observed in such settings, yet the kinematics do not fit since releasing bends form in a dextral slip environment (for a right-stepping fault segment arrangement, McClay & Bonora 2001), whereas our models involve sinistral slip.

We suggest that the local change in the state of stress in our $\phi \leq 30°$ models is related to the absence of a seed in the large space between the two underlapping rift segments (Figs. 3.8m, n, 3.9). Models with less space between the underlapping rift segments ($\phi > 30°$) do not form strike-slip TZs (Fig. 3.8j-l). The second factor involved in the formation of a strike-slip fault zone is the occurrence of sinistral deformation along the rift segments. This motion causes a transfer of material toward the rift interaction zone (Fig. 3.12a). Without a seed to localize extensional deformation, and with material being forced

into the rift interaction zone, the development of a strike-slip fault zone between the rift segments probably provides the most efficient way to accommodate deformation.

3.5.6. Comparison with natural examples

Rhine-Bresse TZ and Rio Grande Rift

The early stages of the models from series 1 with an angle ϕ of 60° or 75° and a 0°-30° extension obliquity produce similar structures as those the RBTZ (Figs. 3.1a, 3.4g, h, m, n, 3.5-7). As in the natural example, the secondary structural grain is reactivated (Ustaszewski *et al.* 2005), which is well visible in the CT scanned model B (Figs. 3.5-7) and we observe two rift segments analogous to the Rhine Graben and the Bresse Graben with a transfer zone in between (Fig. 3.1a). The normal component of the modeled transfer zone border faults is in agreement with an interpretation of the RBTZ being an extension-dominated feature with minor strike-slip motion (Madritsch *et al.* 2009). The rift segment widths of some 2 H in the model translate to some 30-40 km in nature, which is similar to the dimensions of the natural example. The modeled transfer zone in between the rift segments remains shallow and contains limited internal oblique faulting with respect to the main rift segments (Fig. 3.5b, c).

The SDR within the Rio Grande Rift (Fig. 3.1b) represents possibly a more advanced stadium of a similar system as the RBTZ, with near-orthogonal regional extension (Minor *et al.* 2013). It also accommodates sinistral motion and forms a continuous sediment-filled basin system comparable with the transfer zone that follows the secondary seed in model B (Fig. 3.5d-f). An alternative interpretation involves sinistral oblique extension on a region scale (Chapin & Cather 1994), which would qualify our sinistral oblique extension models for comparison. The structures in models C, D, and G (Fig. 3.9a-h, q-t) bear a resemblance to the SDR. We observe a continuous basin within the transfer zone with sinistral oblique-slip motion. However, the orientation of the transfer zone is slightly different: Angle κ is 25° in the models against 45° in nature. This might indicate some

influence of the structural inheritance present in the natural example.

Tanganyika-Rukwa-Malawi fault zone

The strike-slip TZs observed in the sinistral oblique extension models from series 2 bear resemblance to the situation in East Africa according to the "oblique-opening model" put forward by Chorowicz (2005). Within the Western Branch of the East African Rift System lies the Tanganyika-Rukwa-Malawi (TRM) fault zone (Rosendahl *et al*. 1992; Chorowicz 2005), an overall dextral strike-slip zone that connects the left-stepping rift branches currently in a dextral oblique extension system with α = -30° (Saria *et al*. 2014; Figs. 3.1c, d, 3.13). When we compare this natural example with model F, mirrored to mimic this natural example, there are more similarities: The strike-slip zone is oriented at a low angle (κ = 20°-25°) to the rift segment orientation in the model and in nature. Also, the Tanganyika part of the TRM fault zone seems to propagate slightly away from the Malawi rift, as we observe with one rift segment in our model F (Fig. 3.13). However, the latter is (partially) a boundary effect due to the normal faulting at the model edge.

Our ϕ = 30°, α = -30° models thus seem to fit the natural example, but the interpretation of the TRM fault zone as a dextral strike-slip zone is challenged by an orthogonal opening model, in which all rift basins form due to extension perpendicular to the rift trends (Morley 2010; Delvaux *et al*. 2012). Field

evidence indicates that the steep rift boundary faults of the Rukwa Basin are indeed rather normal or dip-slip faults instead of strike-slip faults. Their apparent strike-slip character is proposed to derive from an earlier phase of strike-slip tectonics in the early Mesozoic after which they were reactivated during late Cenozoic NE-SW extension in the area. Yet our α = -30°, ϕ = 30°, models without propagating rift branches do clearly develop initial strike-slip fault zones that evolve into graben-like structures toward the end of the model run (models C, D, and G; Fig. 3.9a-d, f-h, q-t). It would thus be possible to fit the field observations in the oblique-opening model, although the dip-slip-dominated boundary faults along the Rukwa Basin do not fully correspond with the significant strike-slip character of our modeled TZs.

The reason for this could be the absence of crustal strength variations in our models as analog modeling and field studies have pointed out that these can cause local changes in the extension direction (Morley 2010; Corti *et al*. 2013a; Philippon *et al*. 2015). Michon & Sokoutis (2005) suggest that such processes influence the TRM fault zone because it is situated in a mobile orogenic belt along the Tanzania Craton (Fig. 3.13). The fact that our modeled TZs and the Rukwa Basin do not fully correlate could thus be due to the absence of such crustal strength variations in our model setup, preventing a full reconstruction of the TRM fault zone characteristics.
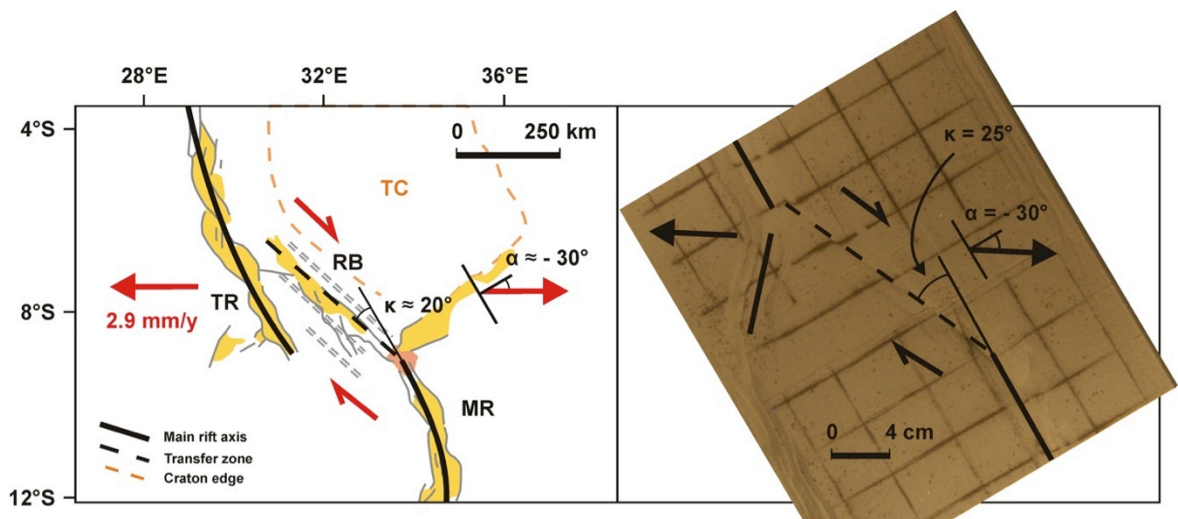
Fig. 3.13. (previous page) *Comparison between the Tanganyika-Rukwa-Malawi fault zone (left) and a final top view of Model F (right). Note that the model image is mirrored to fit the natural example. We observe: (1) a similar extension direction (angle α), (2) a strike-slip transfer zone with the same motion with (3) a similar orientation to the main rifts (angle κ) and (4) rift segments that grow apart. MR = Malawi Rift, RB = Rukwa Basin, TR = Tanganyika Rift, TC = Tanzania Craton. Image modified after Ebinger (1989), Acocella et al. (1999a), Corti et al. (2007) and Saria et al. (2014). For location, see Fig. 3.1c.*

_____

3.6. Conclusions

Our models examining the effects of oblique extension and structural inheritance on rift interaction lead to the following conclusions:

- Extension direction is a key influence on rift linkage; right-stepping rift segments are more likely to connect with dextral oblique extension because they tend to grow and propagate toward each other. This mechanism could promote micro-continent formation. In contrast, orthogonal extension and sinistral oblique extension generally do not result in rift linkage because the right-stepping rift segments propagate in a parallel fashion or grow apart, respectively;

- Although sinistral oblique extension generally prevents rift linkage between right-stepping rift segments, it can lead to linkage in the shape of a strike-slip-dominated transfer zone when the rift segments are laterally far apart;

- The previous two points are also valid for a mirrored system; left-stepping rift segments form TZs as sinistral oblique extension makes the rift segments propagate toward each other. In contrast, orthogonal and dextral oblique-extension result in parallel rift propagation or rifts growing apart, respectively, preventing transfer zone formation. Underlapping left-stepping rift segments can form a strike-slip transfer zone under dextral extension conditions;

- Secondary structural inheritance might influence rift linkage, but only when the extension direction is favorable for reactivation. Otherwise, propagating rifts will simply align approximately perpendicular to the extension direction;

- When secondary structural inheritances are reactivated, the resulting transfer zone and internal faults commonly follow their general orientation. Mild obliquity does occur as these structures attempt to align perpendicular to the extension direction;

- Several of the characteristic structures we observe in our models are also present in natural rift settings, such as the Rhine-Bresse Transfer Zone, the Rio Grande Rift, and the East African Rift System.

3.7. Acknowledgements

Appendix 3A. Effect of extension velocity on rift localization
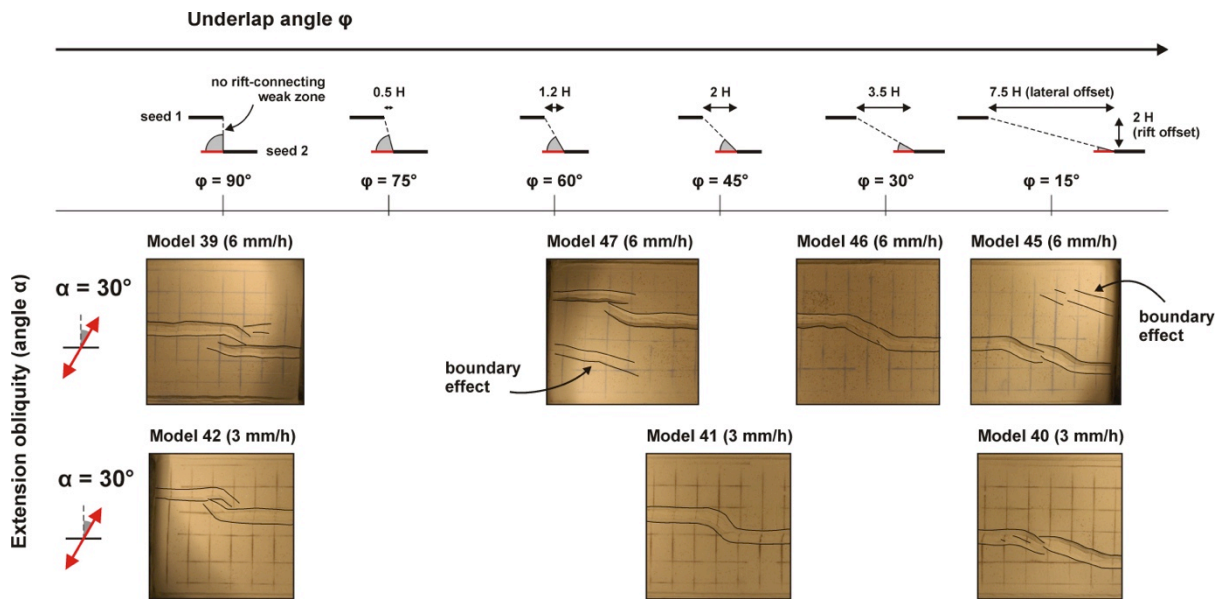
Fig. 3.A1. *Velocity comparison, depicting how lowering extension velocity from 6 mm/h as applied by Zwaan et al. (2016; Chapter 2) to 3 mm/h in this study decreases boundary effects, i.e. additional faulting, without hindering the development of the main rift structures.*

Chapter 4

Effects of sedimentation on rift segment and transfer zone evolution in orthogonal and oblique extension settings: insights from analogue models analysed with 4D X-ray CT and digital volume correlation techniques

Frank Zwaan[a] *, Guido Schreurs[a], Jürgen Adam[b]

a) Institute of Geological Sciences, University of Bern, Baltzerstrasse 1+3, CH-3012 Bern, Switzerland
b) Department of Earth Sciences, Royal Holloway, University of London, Egham, Surrey, TW20 0EX, U. Kingdom

_____

Abstract

During the early evolution of rift systems, individual rift segments often develop along pre-existing crustal weaknesses that are frequently non-continuous and laterally offset. As extension progresses, these initial rift segments establish linkage in order to develop a continuous rift system that might eventually lead to continental break-up. Previous analogue and numerical modelling efforts have demonstrated that rift interaction structures are influenced by structural inheritances, detachment layers, magma bodies, rate and direction of extension, as well as distance between rift segments on rift interaction structures. Yet to date, the effects of syn-tectonic sediments have been largely ignored or only modelled in 2D. In this study we therefore assess the influence of sedimentation on rift segment and rift transfer zone evolution in orthogonal and oblique extension settings, by means of 3D brittle-ductile analogue models, analysed with 4D X-ray computed tomography (XRCT or CT) methods and 3D digital volume correlation (DVC) techniques. Our models show that syn-rift sedimentation does not significantly influence the large-scale evolution of rift and transfer zone structures. Nevertheless, syn-rift sedimentation can strongly affect rift-internal structures: sedimentary loading reinforces the rift wedge, decreasing rift wedge faulting and increases subsidence within the rift basin. These effects are strongest in areas where most accommodation space is available, that is, along the main rift segments. In contrast, rift segments that undergo high degrees of oblique extension develop less accommodation space and are therefore less influenced by sedimentary loading. Rift interaction structures are least affected by sediment influx, as they experience relatively low amounts of subsidence and little accommodation space is available. Our conclusions are valid for the early stages of rift development, when a high sediment influx could delay continental break-up, as other processes are likely to become dominant during later stages of continental extension. Finally state-of-the-art DVC analysis of CT data proves to be a powerful tool to extract and fully quantify 3D internal model deformation in great detail and could be useful for comparing and calibrating analogue and numerical models.

_____

4.1. Introduction

Early rifting of the continental lithosphere involves the formation of rift segments, usually along the trace of pre-existing tectonic fabrics (e.g. Dunbar & Sawyer 1988; Versfelt & Rosendahl 1989; Morley *et al.* 1990). As the system evolves, these rift segments, which are often non-continuous and offset, must grow laterally, interact and connect in order to create a continuous rift basin on the way to continental break-up, (e.g. the East African Rift System, Fig. 4.1a, b). The associated rift interaction structures include transfer zones (hard linkage), where continuous fault zones connect rift segments, or accomm-odation zones (soft linkage), where rift boundary faults do not yet connect (Rosendahl 1987; Larsen 1988; Childs *et al.* 1995; Faulds & Varga 1998, Fig. 4.1c, d). The evolution of rift interaction structures during early rift development is of importance because of its control on melt migration and the localization of volcanic activity, and a better under-standing may improve seismic risk assessment (Lambiase & Bosworth 1995; Faulds & Varga 1998 and references therein; Acocella *et al.* 1999a,b, Corti *et al.* 2004). Developing rift interaction zones are also known to influence hydrocarbon systems, by controlling the drainage and sedimentation patterns leading to source rock and reservoir rock deposition (Roberts *et al.* 1990; Faulds & Varga 1998). Furthermore, the complex structuration affects the migration of hydrocarbons (Nelson *et al.* 1992; Acocella *et al.* 1999a,b; Corti *et al.* 2004) and facilitates formation of hydrocarbon traps as observed in the North Sea Viking Graben and the East African Rift System (Morley *et al.* 1990; Fossen *et al.* 2010).

Previous analogue and numerical modelling studies have demonstrated the influence of inherited structures, detachment layers and magma bodies, as well as distance between rift segments on rift interaction structures (e.g. Basile & Brun 1999; Le Calvez & Vendeville 2002; Paul & Mitra 2013; Zwaan *et al.* 2016; Chapter 2). Other important factors are the rate and direction of extension. High strain rates strengthen the ductile parts of the lithosphere (Brun 1999; Buiter *et al.* 2008). Associated high brittle-ductile coupling effects generate distributed or wide rifting, hindering rift linkage whereas, low strain rates/ viscosities tend to localize extension in narrow rift zones, favouring transfer zone formation (Allken *et al.* 2011, 2012; Zwaan *et al.* 2016; Chapter 2). Recent studies demonstrate that oblique extension has an important influence on rift linkage as it causes rift segments to either propagate toward each other or to grow away from each other, depending on the initial rift segment configuration (Zwaan & Schreurs 2017; Chapter 3). Within the context of oblique extension facilitating continental break-up by lowering the lithospheric plastic yield strength (Brune *et al.* 2012) and en-hancing magmatism (Keir *et al.* 2015), oblique extension may also assist break-up on a crustal scale through connecting rift segments.

Surface processes are also known to affect tectonic systems. Erosion for instance can significally increase orogenic topography (Simpson 2006) and localize crustal de-formation (Stolar *et al.* 2007), while syn-collisional sedimentation may cause sub-duction plate retreat and diffused crustal deformation (Gray & Pysklywec 2012). Similarly, erosion and syn-rift sedimentation affect extensional systems as well, for instance prolonging fault activity and increasing rift subsidence (Burov & Cloetingh 1997; Burov & Poliakov 2001; Corti *et al.* 2010, 2013b; Olive *et al.* 2014), suppressing salt diapirism (Thomas 1994; Brun & Fort 2008), causing rifting to shift to a narrow rifting mode (Bialas & Buck 2009) or even delaying continental break-up (Martín-Barajas *et al.* 2013).

However, previous attempts to model the coupling between surface processes and rift tectonics have predominantly been based on 2D simulations. In this study we therefore assess the influence of sedimentation on rift and rift interaction structures in orthogonal and oblique extension settings in 3D, by means of three series of crustal scale brittle-ductile analogue models that are analysed with state-of-the-art 4D X-ray Computer Tomo-graphy (XRCT or CT) methods and 3D Digital Volume Correlation (DVC) methods.
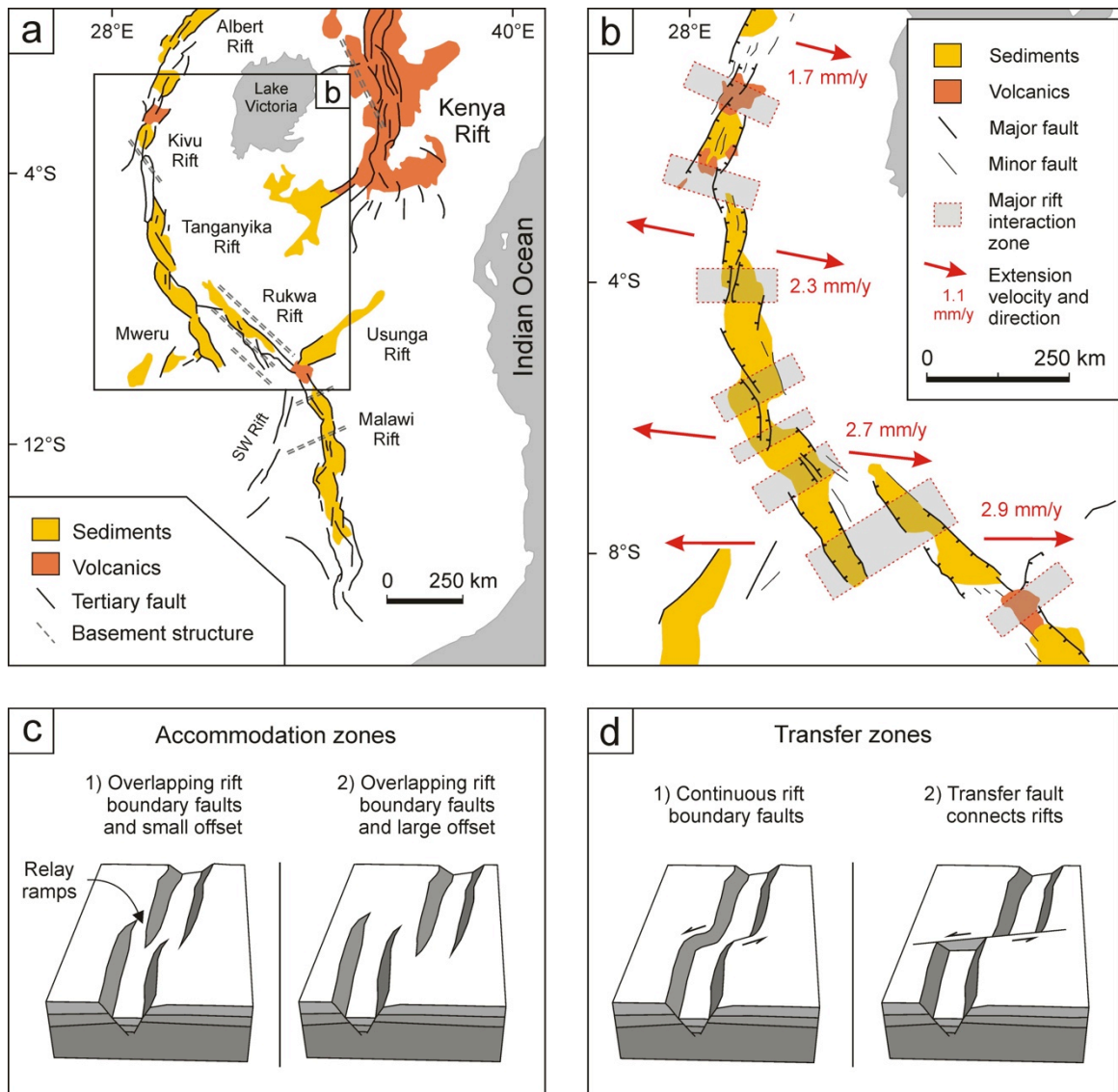
Fig. 4.1 *Natural examples of rift interaction structures and accommodation/transfer zone convention: (a) Rift segments and distribution of sedimentary basins and volcanics in the East African Rift System. Image modified after Ebinger (1989) and Acocella et al. (1999a); (b) Western branch of the East African Rift System with major rift interaction zones with associated sediments and volcanics (modified after Corti 2012), as well as current extension directions and velocities (modified after Saria et al. (2014). Location and names are shown in (a). Hatched faults represent normal faults, the character of faults without motion indications are not specified in the original publications; (c-d) Block diagrams depicting the differences between accommodation and transfer zones as proposed by Faulds & Varga (1998). (c) Accommodation zones (soft linkage) in which rift boundary faults do not connect, but die out laterally and overlap. Examples are found in the East African Rift System (b). (d) Transfer zones (hard linkage) in which the rift boundary faults are continuous from rift to rift, e.g. the Selenga Accommodation Zone in Lake Baikal (Scholz & Hutchinson 2000) or in which a single transfer fault connects both basins, e.g. the Gulf of Suez or Thailand (Acocella et al. 1999a; Morley et al. 2004). Modified after Zwaan et al. (2016; Chapter 2).*

4.2. Materials and methods

4.2.1 Material properties

We use both brittle and viscous materials to simulate the brittle and ductile parts of the continental crust, respectively. A 4 cm thick layer of fine quartz sand (ø = 60-250 μm), sieved from ca. 30 cm height into the model to ensure a constant density of ca. 1560 kg/m^3, acts as a 20 km thick brittle upper crust. The sand is also flattened with a scraper at every cm during model construction, which creates slight density differences. This "layering" subsequently appears on CT images but is not considered to have a significant influence on subsequent material behaviour (Fig. 4.2h). Sedimentary infill is modelled with alternations of fine corundum and quartz sand as the density differences between both sand types is visible on CT images (ϱ = 1890 kg/m^3 and ø = 88-175 μm for corundum sand, Panien *et al*. 2006; Klinkmüller 2011).

We apply a 4 cm thick viscous layer to simulate a 20 km thick lower crust. The viscous material is a mixture of the same corundum sand mentioned above with SGM-36 Polydimethylsiloxane (PDMS) silicone (weight ratio PDMS : corundum sand = 0.965 : 1.00). Its behaviour is near-Newtonian (η = ca. 1.5·10^5 Pa·s; n = 1.05) and the viscous mixture has a similar density as the overlying quartz sand (ca. 1600 kg/m^3). This results in a more natural density profile than pure PDMS would allow (ϱ = ca. 965 kg/m^3) and it prevents undesirably strong buoyancy effects.

Small quantities of Zirshot ceramic microbeads (ϱ = ca. 2300 kg/m^3 and ø = 150-210 μm, CBAG 2017) are mixed with the quartz and corundum sands in a 1:50 weight ratio to generate a volumetric pattern on CT scans, allowing DVC analysis (Adam *et al*. 2013; Paragraph 4.2.4). Note that the 1:50 weight ratio corundum/Zirshot mixture is itself mixed with the PDMS, so that the actual Zirshot weight ratio is ca. 1:100 in the viscous layer. The Zirshot spheres are not considered to have a significant effect on the behaviour of the main model materials (Lohrmann *et al*. 2003, Panien *et al*. 2006, Klinkmüller 2011). Further material properties are summarized in Table 4.1.

Tabel 4.1. *Material properties*

Granular materials	Quartz sand[a]	Corundum sand[b]	Zirshot[c]
Grain size range	60-250 μm	88-175 μm	150-210 μm
Bulk density (sieved)	1560 kg/m^3	1890 kg/m^3	ca. 2300 kg/m^3
Angle of internal peak friction	36.1°	37°	-
Angle of dynamic-stable friction	31.4°	32°	-
Cohesion	9 ± 98 Pa	39 ± 10 Pa	-

Viscous material	PDMS/corundum sand mixture[a]		
Weight ratio PDMS : corundum sand	0.965 kg : 1.00 kg		
Mixture density	ca. 1600 kg/m^3		
Viscosity[d]	ca. 1.5·10^5 Pa·s		
Type	near-Newtonian (n = 1.05)[e]		

(a) Quartz sand and viscous mixture characteristics after Zwaan & Schreurs (2016)
(b) Corundum sand characteristics after Panien *et al*. (2006) and Klinkmüller (2011)
(c) Zirshot properties after Carlo AG (2017)
(d) The viscosity value holds for model strain rates < 10^{-4} s^{-1}
(e) Stress exponent n (dimensionless) represents sensitivity to strain rate

4.2.2. Experimental set-up

The experimental apparatus consists of a 36 cm wide base of foam and Plexiglass bars between two longitudinal sidewalls, which is compressed to a 30.5 cm width before model materials are applied (Fig. 4.2a, c, g, l). As precise computer-controlled motors drive the sidewalls apart during an experiment, the foam expands, which causes distributed extension that is transferred to the overlying model materials with minimal boundary effects (Fig. 4.2g). One base plate can move laterally, which in combination with the outward motion of the longitudinal sidewalls, allows the application of any required degree of oblique extension (Figs. 4.1b, 4.2a, d-f, k, m). At both ends of the model, pivoting plastic bars control the model base when oblique extension is applied by forcing the Plexiglass bars with the foam stacked in between sideways, into a parallelogram shape (Fig. 4.2a, d-f). Rubber sidewalls contain the model ends and accommodate distributed deformation, reducing boundary effects (Fig. 4.2a). Every component of the machine around the model consists of X-ray transparent materials to allow for CT-scanning and various models are analysed with CT-techniques to reveal their 3D internal evolution (Fig. 4.2b, g, l).

Thin rods (1 cm thick, semi-cylindrical) of the PDMS/corundum sand mixture are applied on top of the basal viscous layer (Fig. 4.2a). These "seeds" act as linear weak zones, representing discrete crustal weaknesses; the strong sand layers above the seeds are locally thinner and thus weaker, causing deformation to localize (Fig. 4.2c, g, h-i, l, m). We use a disconnected "staircase offset" seed geometry for model series 1 ($\phi = 90°$, no seed over- or underlap, Fig. 4.2h, m). Series 2 and 3 both involve a secondary rift-connecting seed, representing a secondary structural grain as for instance observed in the Rhine-Bresse transfer zone (Ustaszewski et al. 2005) and the East Africa Rift System (Acocella et al. 1999a and references therein, Figs. 4.1a, 4.2i, j). The seed offset is 2 H in all set-ups (Fig. 4.2h-j, m), H being equivalent to the brittle layer thickness, in order to avoid rift proximity effects (Zwaan et al. 2016; Chapter 2). A 4x4 cm grid allows tracking of surface deformation (Fig. 4.2a).

Extension obliquity is defined by the angle α between the normal to the seed orientation and the extension direction (Fig. 4.2k). When α is zero, extension is orthogonal, a positive angle α indicates dextral oblique extension and a negative angle α implies sinistral oblique extension. We apply orthogonal extension and various degrees of dextral oblique extension for series 1 ($\alpha = 0°$, 30° or 60°). Series 2 involves slight dextral oblique extension ($\alpha = 15°$), whereas we use sinistral oblique extension ($\alpha = -30°$) for series 3 (Table 4.2).

Every model run takes 4 hours, and with an extension rate of 7.5 mm/h results in a total of 30 mm extension in the specified direction (Fig. 4.2i). Most models were run twice: once with and once without syn-rift sedimentation for comparison. Sedimentation is implemented by filling the rift basins with alternating layers of quartz and corundum sand. This is done by hand at fixed time steps, (t = 1h, 2h and 3h, Fig. 4.2l, m), with the use of a small funnel, after which a slight amount (ca. 0.5 mm) of quartz sand was sieved on the surface to cover the brown corundum sand for better top view quality and subsequently a new grid was put in place. Sedimentation in our models is thus not a continuous process. This is in rough accordance with the observation that sedimentation in natural rift settings generally occurs in cyclothems, that is pulses associated with recurring periods of fault reactivation (Martins-Neto & Catuneanu 2012). Although the application of sediment is instantaneous and therefore not completely realistic, the periodicity (and thus magnitude) of cyclotems in rifts is 2-15 Ma (Blair & Bilodeau 1988), fitting well with the scaled timeframe of our experiments (Paragraph 4.3), providing us with a useful first-order comparison between the system with and without sedimentation.

We applied 20 min time steps (2.5 mm of extension) for CT-scanning, to acquire a detailed record of the 3D model evolution. During these scans, the model was halted (ca. 5 min) to acquire multiple CT datasets per time step, improving data quality for subsequent DVC analysis. The model was also stopped during sediment application, allowing a small timeframe (ca. 10 min) in which the model deforms slightly, as revealed by DVC results between the pre- and post-sediment

scans of the same time step. This deformation is however insignificant with respect to the displacements induced by the experimental apparatus when the model is running. We completed 14 experiments in total, of which further details are shown in table 4.2.

Fig. 4.2. *Model set-up. (a) Cut-out view of the experimental apparatus depicting its various components. (b) Experimental apparatus in the CT-scanner during a model run. (c) Compositional layering of quartz and corundum sand representing the brittle upper crust and a viscous silicone/corundum sand mixture reproducing the ductile lower crust, overlying a foam base. (d-f) Schematic surface view showing the initial state (d) and subsequent deformation of the empty apparatus (e) orthogonal extension and (f) oblique extension, respectively. (g) Distribution of basal deformation in the model. As the sidewalls move apart with 7.5 mm/h, a velocity gradient develops in the foam and plexiglass base (yellow arrows). The darker x-shape in the image is a CT-artefact that appears in all CT sections. CT image derived from model G.*

Fig. 4.2. (continued) *(h-j) Seed geometries for our three model series in map view. (k) Extension obliquity definition. (l) Sediment application as seen on CT images. Left: rift basin after 60 min. Right: the basin is filled to model syn-rift sedimentation. (m) Model run example (Model G). Left: initial set-up top view (without sand cover to show the seed geometry). Middle: surface structures (t = 60 min). Right: basins are filled to simulate syn-rift sedimentation.*

Tabel 4.2. Model parameters

	Model	Extension obliquity (alpha)	Seed geometry (phi)	Secondary seed	Sediment ation	CT- scanned	Shown in
Series 1	A	0°	90°	-	-	-	-
	B	0°	90°	-	-	X	Figs. 4.3-4.6, 4.8-4.9
	C	0°	90°	-	X	X	Figs. 4.4-4.6, 4.10, 4.A1
	D	30°	90°	-	-	-	-
	E	30°	90°	-	X	-	-
	F	30°	90°	-	-	X	Figs. 4.4, 4.5, 4.7
	G	30°	90°	-	X	X	Figs. 4.2, 4.4, 4.5, 4.7
	H	60°	90°	-	-	-	Fig. 4.4
S2	I	15°	75°	X	-	X	Fig. 4.11
	J	15°	75°	X	X	X	Fig. 4.11
Series 3	K	-30°	25°	-	-	-	-
	L	-30°	25°	X	X	-	-
	M	-30°	25°	X	-	X	Fig. 4.12
	N	-30°	25°	X	X	X	Fig. 4.12

4.2.3. Model scaling

In order to correctly represent crustal deformation, our models need to be properly scaled. Stress ratios (σ^*, convention: $\sigma^* = \sigma_{model}/\sigma_{nature}$) can be calculated with the following equation (Hubbert 1937; Ramberg 1981): $\sigma^* = \rho^* \cdot h^* \cdot g^*$, where ϱ^*, h^* and g^* represent the density, length and gravity ratios respectively. The strain rate ratio $\dot{\varepsilon}^*$ can be calculated with the stress ratio σ^* and the viscosity ratio η^* (Weijermars & Schmeling 1986): $\dot{\varepsilon}^* = \sigma^*/\eta^*$, which allows us to derive the velocity ratio v^* and time ratios t^* using the following equations: $\dot{\varepsilon}^* = v^*/h^* = 1/t^*$. Depending on the assumed natural lower crustal viscosity ($\eta = 10^{19}\text{-}10^{23}$, e.g. Buck 1991) 1 hour in our models represents 0.008-84 Ma in nature, so that our model velocity of 7.5 mm/h translates to 0.05-500 mm/y. Typical rift extension velocities plot in this range (a few mm/y, e.g. Saria *et al*. 2014, Fig. 4.1b). The values we use for our scaling calculations are listed in Table 4.3.

To ensure dynamic similarity between brittle materials in our models and nature, we apply the ratio R_s as a function of gravitational stress and cohesive strength or cohesion C (Ramberg 1981; Mulugeta 1998): $R_s = $ *gravitational stress/cohesive strength* $= \rho \cdot g \cdot h/C$. Furthermore, we use the Ramberg number R_m for viscous materials (Weijermars & Schmeling 1986): $R_m = $ *gravitational stress/viscous stress* $= \rho \cdot g \cdot h^2/(\eta \cdot v)$. The R_m value of 80 plots in the natural range of 1.2-1200 and the R_s values are quite similar with values of 27.6 and 9.2 in the models and nature respectively.

4.2.4. Digital Volume Correlation (DVC)

General DVC methodology

Besides revealing the internal structures of our models in great detail at various time steps, the use of CT techniques also allows the application of digital volume correlation (DVC) to quantify 3D internal model deformation. DVC analysis, which is based on cross correlation of intensity patterns in time-series voxel (voxel = volume pixel) data, has a significant advantage over preceding techniques (e.g. 3D PIV, Boutelier *et al*. 2012; Strak & Schellart 2014) as it enables a full quantification of 3D displacement fields and the derived 3D strains and strain rates within otherwise opaque model materials. Furthermore, DVC does not trace individual particles, but particle patterns, which makes it an ideal technique to analyse larger 4D datasets with strong deformation gradients (Adam *et al*. 2005; Adam *et al*. 2013).

We use the DVC module of the commercial DaVis image correlation software package (version 8.4, © LaVision). The DVC algorithm calculates model displacement fields by cross correlating intensity patterns in small voxel sub-volumes of the time-series experiment volume. For small sub-volumes, local displacement vectors are determined by identifying similar intensity patterns of individual voxel sub-volumes in subsequent time steps of the experiment volume (Fig. 4.3a, b). The digital cross correlation of the 3D intensity patterns is executed by Fast Fourier Transform (FFT) algorithm, which provides the spatial average of the local displacement vectors over the size of the voxel sub-volume (Fig. 4.3c). Subsequently, the incremental displacement field is constructed by assembling the 3D vectors of all sub-volumes in the voxel space.

Although DVC analysis does not require the identification of individual particles in voxel sub-volumes, small-scale intensity variations caused by identifiable particle clusters are essential for the calculation of a high-resolution displacement field. In order to improve the texture on the CT-data, the models were scanned multiple (five) times for every 20 min time step and the intensity values of the voxel data are subsequently stacked. This reduces the noise caused by the high X-ray reflectivity of the Zirshot ceramic beads, significantly improving the clarity of the intensity patterns and consequently the quality of the DVC results. Furthermore, pre-processing image filters serve to enhance the image texture and to further eliminate background noise.

With the incremental displacement field, displacement components (v_x, v_y, v_z) and the derived strain tensor $E_{ij} = \partial V_i = \partial_j$ (with i $\in$

{x, y, z} and j ∈ {x, y, z}) can be calculated. Subsequently, the strain tensor E_{ij} allows us to determine incremental shear strain (ε_{xy}, ε_{xz}, ε_{yz}) and the 3D Shear ($3Ds = |\vec{\varepsilon}_x - \vec{\varepsilon}_z|$). The incremental displacement and strain data describe material transport and deformation between successive scans, as well as their spatial and temporal variation in the experiments. Moreover, the total displacement field and finite strain in the experiment volume can be determined by Lagrangian summation of the incremental displacement data (e.g. geological strain, Fig. 4.3e, f).

Vector resolution

The spatial resolution or density of the vector field depends on the voxel size, sub-volume size and overlap of the sub-volumes. The voxel size depends on the XRCT scanner resolution (voxel size = 0.6 mm in this study). The sub-volume and overlap of the sub-volumes are DVC analysis parameters depending on the combination of scanner resolution and the quality of intensity patterns in the granular material.

The sub-volumes must remain large enough to include characteristic elements of the image texture for a reliable correlation between successive time-series images of the experiment volume. A robust identification of distinct intensity patterns in the experiment volume was achieved with sub-volumes of 32*32*32 voxels (sub-volume size = 32 voxels) and consequently each 3D displacement vector represents the spatial

average of a discrete experiment volume with the size of 19.2 x 19.2 x 19.2 mm or 7.1 cm3.

The high spatial vector resolution was achieved by calculating vectors for overlapping sub-volumes. In our experiments with a sub-volume size of 32 voxels and a 75% overlap the vector resolution is 8 voxels. Consequently, the resulting vector resolution is 4.8 mm or approximately 32 times D50 for the given voxel size (0.6 mm) of the scanner and mean grain size of the silica sand (grain size = 60-250 micron with D50 ~ 0.15 mm). The small sub-volumes and high vector resolution enable the observation of inhomogeneous translation and deformation in the experiment volumes.

Vector accuracy

Modern DVC cross-correlation algorithms achieve vector accuracies significantly smaller than 0.1 voxel with ranges from 0.05 to 0.1 voxel depending on the sub-volume size, image quality and image texture (Liu & Morgan 2007; Pannier *et al.* 2010). The use of FFT algorithm in combination with the multi-pass approach in the local correlation used in the StrainMaster DVC system (DaVis 8.4, © LaVision) allowed displacement un-certainties ranging between 0.006 voxel and 0.02 voxel (Madi *et al.* 2013). However, these error margins not only depend on the accuracy of the mathematical correlation procedures but also on the quality of the volume data. Assuming the higher error margin of 0.1 voxel, the vector accuracy for the DVC analysis of the experiments is ±0.06 mm (±0.4 D50).

Tabel 4.3. *Scaling parameters*

	General parameters			Brittle upper crust		Ductile lower crust		Dynamic scaling values	
	Gravitational acceleration g (m/s²)	Crustal thickness h (m)	Extension velocity v (m/s)	Density ϱ (kg/m³)	Cohesion C (Pa)	Density ϱ (kg/m³)	Viscosity η (Pa·s)	Ramberg number R_m	Brittle stress ratio R_s
Model	9.81	0.08	2.1·10⁻⁶	1560	9	1600	1.5·10⁵	7.8	25.5
Nature	9.81	4·10⁴	1·10⁻¹⁰	2800	7·10⁷ [a]	2900	1·10¹⁹ to 23 [b]	1.2·10⁰ to 4	9.2

(a) Cohesion value after Corti *et al.* (2004)
(b) Viscosity range after Buck (1991)

Fig. 4.3. *Analysis of CT scanned analogue experiment using Digital Volume Correlation (DVC) techniques. (a) Voxel data of time-series experiment scans are subdivided into sub-volumes (Model B example). (b) Pattern search by cross-correlation of sub-volumes in reference and deformed volume yields the spatial average displacement (3D displacement vector) over the size of the sub-volume. (c) Pattern correlation with Fast Fourier Transformation cross correlation function does not require tracking single particles. (d-d') CT sections from Model B used for DVC analysis. Intensity variations due to Zirshot ceramic beads in the brittle and viscous layers produce a random 3D image texture (i.e. marker particle pattern), necessary for DVC analysis. The image is optimized by stacking multiple CT sections, which reduces noise. (e) Finite displacement vectors (projected in xy-section) with colour map of horizontal displacement component (v_x); (f) Finite displacement vectors with colour map of longitudinal strain along the x-axis (e_{xx}) showing contraction and extension (cold and warm colours, respectively). Modified after Adam et al. (2013).*

4.3. Model results

4.3.1. Series 1 models

Top view analysis

A surface overview of models from series 1 is presented in Fig. 4.4. Deformation initially localizes above the seeds where rift segments start to form. Our models demonstrate the dominant influence of the extension direction on the propagating rift segments. When extension is orthogonal, the rifts propagate slightly towards each other (Fig. 4.4a). An extension obliquity of 30° causes the rifts to propagate towards each other in a more acute angle (ca. 40° oblique with respect to the rift trend, Fig. 4.4b, e). This effect is even more pronounced in the case of 60° extension obliquity with respect to the rift trend, Fig. 4.4c, f). The curved character of the rift propagation creates a horst or "rift pass" structure (Nelson *et al*. 1992) between the propagating rift branches, although its size diminishes with increasing extension obliquity (Fig. 4.4a-c).

This rift pass represents a zone of elevated viscous material as revealed by the topography of the viscous layer after sand removal (Fig. 4.4d-f), and undergoes some sinistral rotation around a vertical axis (Fig. 4.4a). Final rift width decreases with increasing extension obliquity from ca. 4.5 cm in orthogonal extension models to ca. 2.4 cm in the 60° oblique extension case, Fig. 4.A1a). Simultaneously, a higher degree of oblique extension promotes the formation of oblique rift-internal structures (Fig. 4.4c).

The above-mentioned general features also occur in models with syn-rift sedimentation (Fig. 4.4g-j). However, the regular filling of the rift basins results in significantly less pronounced rift topography. In models without sedimentation the seed below the rift segments rises as is visible after sand removal (Fig. 4.4d-e). In models with sedimentation the same "diapirism" occurs but an additional trough structure develops within the seed, which continues partially into the propagating rift branch (Fig. 4.4i, j).

CT-analysis

The use of X-Ray CT techniques allows a more detailed analysis of our models (Figs. 4.5-7). Almost immediately after experiment initiation faults localize above the seed (Figs. 4.6d, j, 4.7d, j) and subsequently rift basins develop after some 40 to 60 min, or 5 to 7.5 mm of extension (Figs. 4.5b, f, j, n, 4.6e, k, q, w). These grabens remain separated in the orthogonal extension cases, but the oblique extension models establish rift linkage early on (after some 120 min or 15 mm extension, Fig. 4.5k, o). As the model run proceeds and the rift branches propagate, the developing rift pass areas undergo relative uplift. The latter is highlighted in Fig. 4.5c, d, g, h, k, l, o, p, since the most elevated parts of the model form a lesser barrier for X-rays and are subsequently brighter (see also Fig. 4.6a, b, sections 3-5 and 9-12, and Fig. 4.7a, b, sections 3-5 and 10-13). The same bright colours suggest rift shoulder uplift along the main rift boundary faults (Fig. 4.5).

117
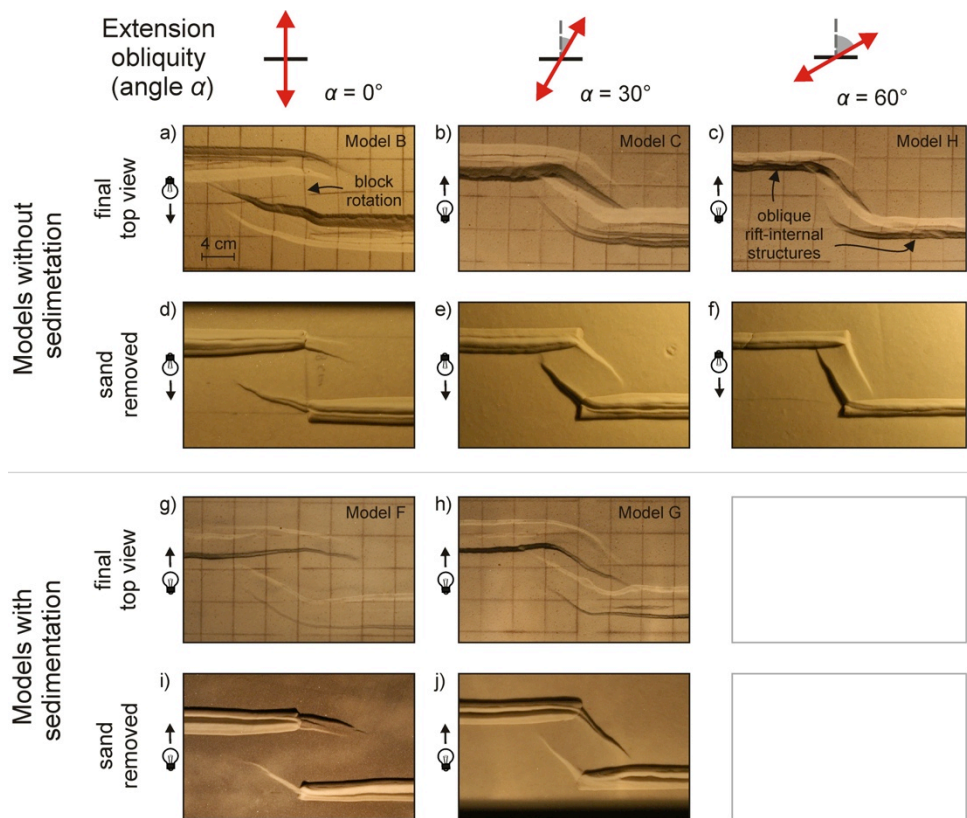
Fig. 4.4. *Top view analysis of series 1 (Models B, C, F, H, and G), illustrating the influence of extension obliquity on transfer zone formation. Removing the sand cover reveals the deformation at the top of the viscous layer. Lighting directions are indicated to the left of each model.*

2D CT sections provide a detailed insight into the internal structuration and evolution (Figs. 4.6 and 4.7). By combining these 2D sections, the internal structural variation can be shown in 3D (Figs. 4.6a, b and 4.7a, b). Under orthogonal extension and independently from the presence of syn-rift sediments, the sections indicate that the rifts are most complex above the initial seeds (Fig. 4.6a, b). The propagating parts of the rift segments have similar characteristics, although they are less developed than the sections above the initial seeds. In both models, the rift structure is bounded by two major boundary faults that have accumulated less slip towards the propagating rift tip (Fig. 4.6a, b). However, the features within the rifts are strongly influenced by the presence of sedimentation, which can be best observed in the main rift segments, where most deformation is accommodated (Fig. 4.6o-t and u-z).

The topography of the rift valley floors is quite distinct. Without syn-rift sediments (Model B), the rift valley floors exhibit a deep bowl-like shape (Fig. 4.6a, h and n), whereas the topography is rather flat when sedimentation is applied (Model C, Fig. 4.6b, t and z) Furthermore, the rift wedge is much more deformed and faulted in Model B, as shown by the dark grey colours (Fig. 4.6a, h and n) and its rift boundary faults angle decrease with time (from initially ca. 70° to ca. 60° towards the end of the model run, see Fig. 4.6e-h, k-n and measurements plotted in Appendix 4A, Fig. 4.A1e). In contrast, Model C develops localized deformation along fewer large faults within the rift wedge (Fig. 4.6b, t and z) and its rift boundary fault angle remains the same throughout the model run (ca. 70°, Fig. 4.A1f). An additional feature is the geometry of the seed underneath the rift structure. As already seen on top view images (Fig. 4.4d-f, i and j), the seeds rise under the rifts in all models, but the rift wedge sinks deeper into the seed when sediments are applied, causing the viscous layer to rise less and form a deep V-shaped depression on the

seed crest (Fig 4.6h', n', t' and z'). Syn-rift sedimentation thus results in stronger subsidence: the earliest syn-rift sediments in Model C subside deeper than the rift valley floor does in Model B (compare h' and n' with t' and z' in Fig. 4.6, Fig 4.8b).

Under 30° oblique extension conditions, the rifts connect, creating a complex transfer zone with a fully-developed rift pass in between (Fig. 4.7a and b). However, the overall picture is rather similar to the orthogonal extension situation. Again, the main rift segments along the seeds contain the best-developed structures, which become less complex towards the propagated tips, where they may merge with the adjacent rift segment (seen in Figs. 4.5i-l, m-p and 4.7b, section 14). The rift segments show the same response to syn-rift sedimentation as seen in the previous orthogonal extension models. We obtain a flatter rift valley topography, the rift wedge exhibits a strongly localized deformation along major faults instead of a shattered appearance, and significantly more subsidence occurs (compare Fig. 4.7 h, h', n, n' with Fig. 4.7t, t', z, z'). In comparison to the orthogonal extension case, however, the rift boundary faults are steeper, the rift basins are narrower and less subsidence occurs (observations summarized in Appendix 4A, Fig. 4.A1).
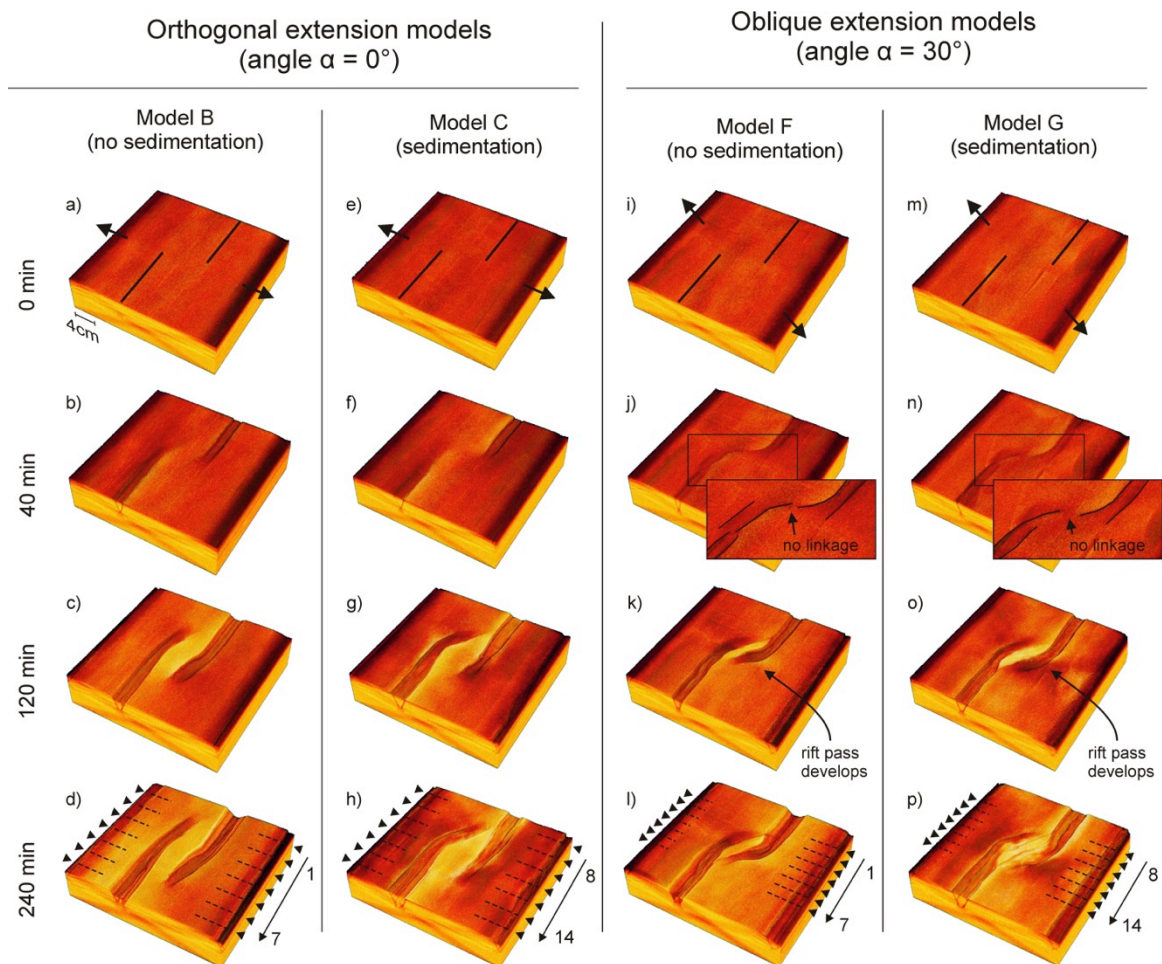
Fig. 4.5. *3D CT-derived topography evolution of Models B, C, F and G (series 1). Brighter colours on the model surface represent higher parts of the model, which are therefore more transparent for X-rays and show up as a lighter colour. This provides a qualitative insight into vertical displacement.*
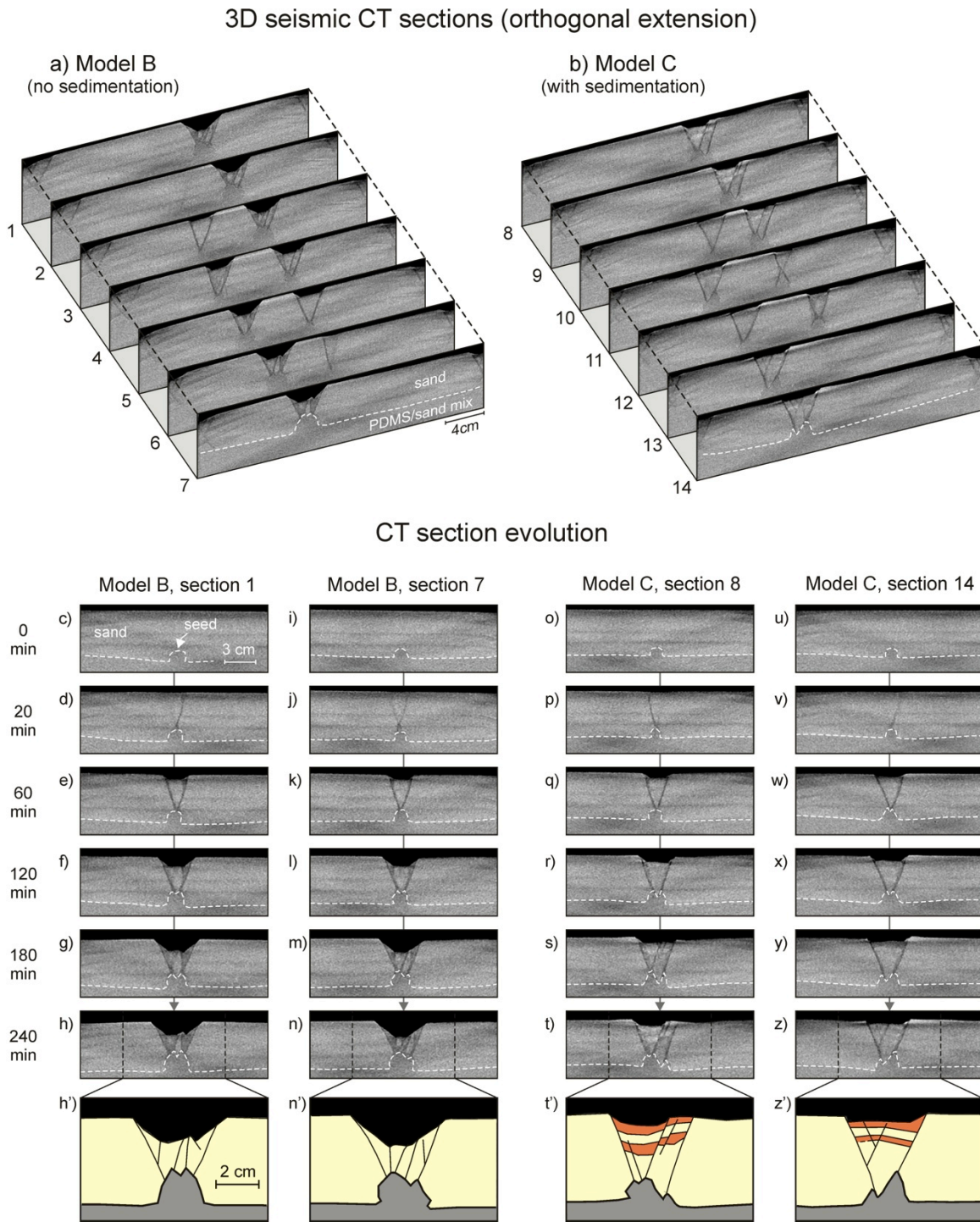
Fig. 4.6. *CT-derived sections illustrating the internal structure and evolution of orthogonal extension Models B and C (series 1). Location of sections is shown in Fig. 4.5. Insets: grey represents the viscous layer, light yellow the sand and the red/light yellow alterations the syn-rift sediments.*
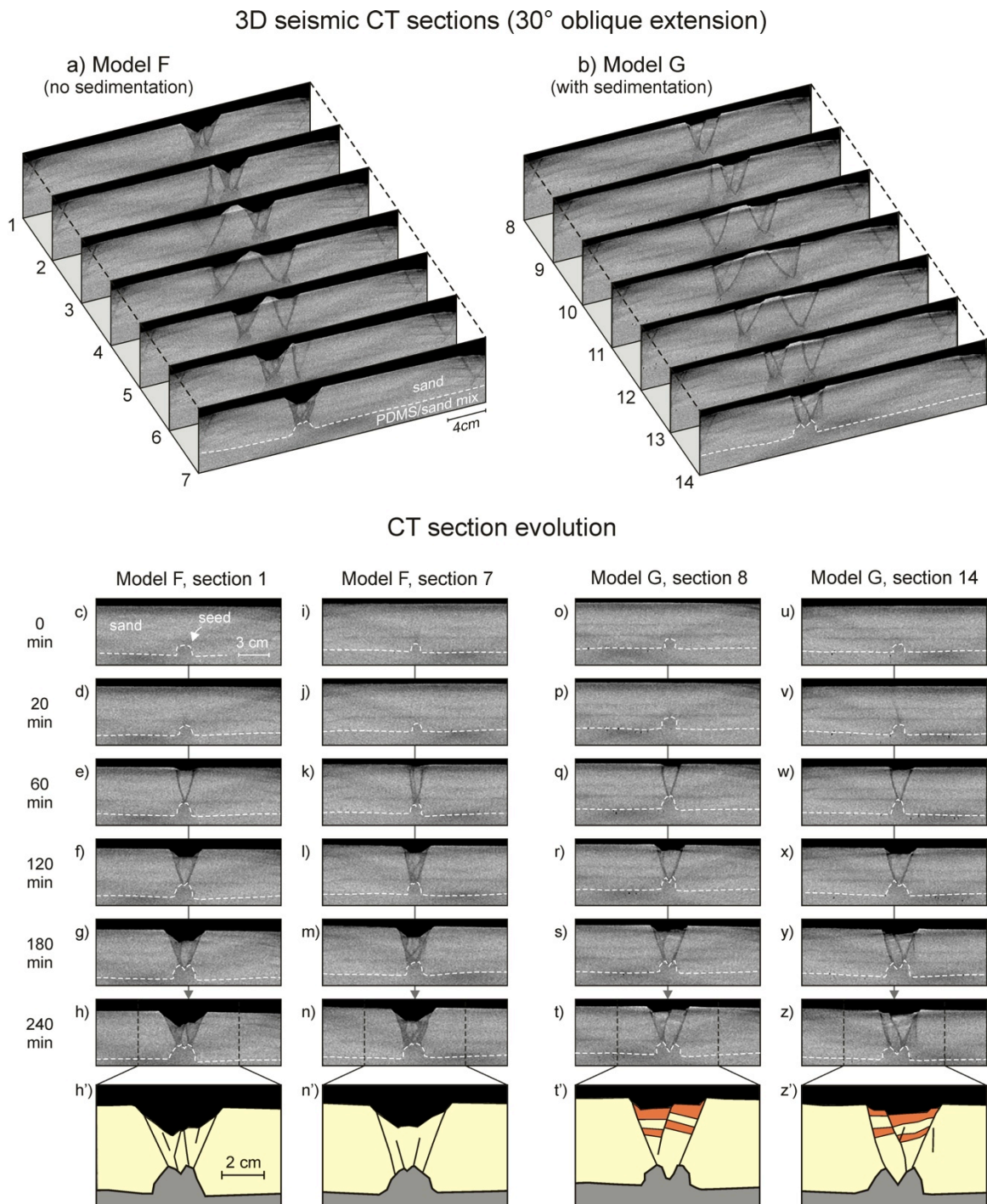
Fig. 4.7. *CT-derived sections illustrating the internal structure and evolution of 30° oblique extension Models F and G (series 1). Location of sections is shown in Fig. 4.5. Insets: grey represents the viscous layer, light yellow the sand and the red/light yellow alterations the syn-rift sediments.*

Digital Velocity Correlation (DVC) analysis of Model B

The use of DVC techniques allows us to fully quantify the internal model displacement field and related deformation processes. We present the first DVC results in a range of colour charts that display the various displacement (Fig. 4.8) and strain components (Fig. 4.9) for Model B, as it is the least complex model (orthogonal extension, no sedimentation). The finite displacement and strain results are visualised in three sections (xy - normal to rift zones) that represent sections 2, 4 and 6 of Model B (see Figs. 4.5d, 4.6a for their locations), quantifying the sum displacement and strain of the model at the end of the experiment.

Fig. 4.8a-c shows the finite 3D displacement field (v_l, the colour chart shows finite 3D displacement and white arrows represent the 3D vectors projected in xy-plane). The three displacement components in x, y and z-directions illustrate the horizontal displacement parallel to the sections (v_x: Fig. 4.8d-f), the vertical displacement (v_y: Fig. 4.8g-i) and the horizontal out-of-plane displacement perpendicular to the xy-plane (v_z: Fig. 4.8j-l). The 3D displacement chart (Fig. 4.8a-c) illustrates the contrasting deformation styles in the brittle sand layer and viscous layer as well as the localised deformation in the rift basins, whereas the central horst structure between the rift segments is characterised by small displacements, reflecting its relative stable position. The high displacement zone in the viscous layer near the left model boundary is probably due to boundary effects (limited normal faulting, Fig. 4.7a, d).

The horizontal displacement chart (v_x) illustrates model extension normal to the rift segments with the left-hand and right-hand halves of the model roughly moving in opposite directions (Fig. 4.8d-f). Horizontal displacement is strongest in the silicone layers close to the sidewalls and different displacement patterns are noticeable in the brittle and ductile layers. In the sand layer the

pronounced displacement continuity is located in the most active rift segment materials moves differencly whereas in the silicone layer beneath the central horst structure (Fig. 4.8d, f). The brittle part of the horst behaves as a solid block, as indicated by the continuous colour, and moves away from the dominant rift, yet slower than the adjacent brittle units (Fig. 4.8d-f). Below the horst, parts of the viscous layer flow towards the most dominant rift (xy-plane parallel motion shown by thick white arrows in Fig. 4.8d-f).

The vertical displacement chart (v_y, Fig. 4.8g-i) displays areas of subsidence and uplift in the xy-plane. It is dominated by general subsidence throughout the model because of the overall stretching of the viscous layer. Yet subsidence is strongest in the rift basins and toward the sides of the model, whereas the central horst remains relatively stable. In addition, below the large rift structures, the viscous layer shows strong upward flow due to thinning and unloading of the overlying sand layers in the rift segments (Fig. 4.8g and i). This phenomenon is also present, although less pronounced, in the central section of the model, where the two rifts in the overlap zone are comparable in size (Fig. 4.8h).

Horizontal displacement perpendicular to the xy-plane (v_z) and parallel to the rift axis is less pronounced than observed for the x and y directions (max. 4 mm instead of up to 10 mm) and is strongest in the viscous layer of the left-hand side of the model (Fig. 4.8j-k). Here, material moves out of section, towards the observer. Out-of-section displacement is most prominent in the central section of the model, away from all boundary walls (Fig 4.8j-l). In the viscous layer to the right of the central horst a counter flow occurs (Fig 4.8k, left side towards and right side away from observer). These dominant flow directions are also observable in the respective overlying rift segments, between which a displacement gradient indicates a small strike-slip component (oblique-slip rift faults: dextral in left rift; sinistral in right rift as seen in Fig. 4.8k) caused by minor rotation of the central horst block about a vertical axis (Fig. 4.4a).
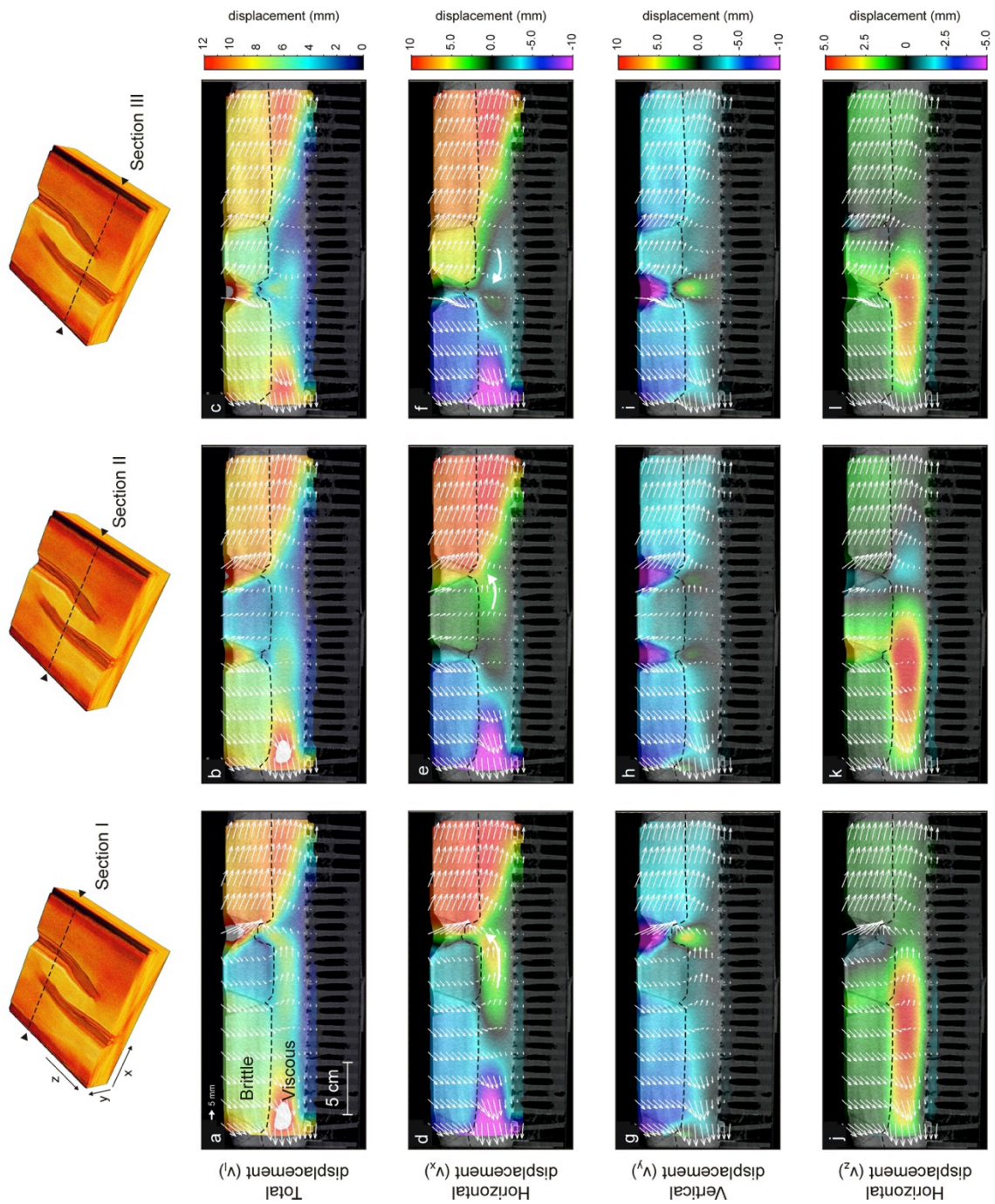
Fig. 4.8. *DVC total displacement analysis of Model B (orthogonal extension, no sedimentation). (a-c) 3D displacement; (d-f) Horizontal displacement in the xy-plane, parallel to the extension direction. Warm colours represent displacement to the right, cold colours represent displacement to the left; (g-i) Vertical velocities. Warm colours represent upward displacement, cold colours represent downward displacement; (j-l) Horizontal velocities in the xz-plane (normal to section and extension direction). Warm colours represent displacement towards the observer, cold colours represent displacement away from the observer. The locations of sections I, II and III are close to those of sections 3, 4 and 6 in Figs. 4.5d and 4.6a.*

From the 3D displacement field, the 3D strain field and related strain components can be derived (Fig. 4.9a-c). Similar to the displacement components, the strain data are shown in xy-sections colour charts. In addition to the overall 3D shear strain (Fig. 4.9a-c), we show the longitudinal strain (e_{xx}) indicating extension and contraction in x-direction normal to the rift segments (Fig. 4.9d-f), shear strain (e_{xy}) indicating sinistral and dextral shear in the xy-plane (Fig. 4.9g-i), and longitudinal strain (e_{zz}) visualising extension and contraction along the z-axis normal to the xy-section and parallel to the rift segments (Fig. 4.9d-f). The total 3D shear strain plots show a strong contrast between the lower viscous layer and the upper brittle layer; the strain is distributed along the top and basal interface of the viscous layer, whereas strain in the brittle sand layer is strongly localized along the major rift fault zones with shear strains up to 30% (Fig. 4.9a-c).

An important contributor to the 3D strain field is the longitudinal strain along the x-axis (e_{xx}, Fig. 4.9d-f). Extension strain values up to 25% characterise the main rift segments, while the rising viscous material below the rifts indicate convergent flow and contraction with strain values around -10%. Along the sidewalls, slight boundary effects are visible. In the other parts of the model, the viscous layer shows a generally distributed extension with maximum finite strain values of approximately 10% in

the centre of the viscous layer indicating channel flow.

Planar shear strain (e_{xy}) charts indicate areas of sinistral and dextral shear in the xy plane (warm colours and cold colours, respectively; Fig. 4.9g-i). The conjugate rift boundary faults show contrasting shear sense with right-dipping faults exhibiting dextral shear (blue) and left-dipping faults showing sinistral shear (red) which is in agreement with the normal fault conditions. This configuration is not restricted to the brittle parts of the model as the faults extend into differential flow zones in the viscous layer with conjugate flow regimes. The best example is illustrated in Fig. 4.9i, in which two additional dextral and sinistral shear flow zones develop, accommodating the rise of viscous material below the rift as seen in Fig. 4.8i. The shear pattern observed near the sidewalls is probably due to boundary effects as seen on displacement field charts (Fig 9d-f).

In contrast to the e_{xx} and e_{xy} results, the longitudinal strain in z-direction (e_{zz}) is less structured (Fig. 4.9j-l). The longitudinal strain (e_{zz}) is very small in comparison to the perpendicular longitudinal horizontal strains in the extension direction (maximum $e_{zz} \sim 1\%$ and maximum $e_{xx} \sim 25\%$, respectively) We generally observe strain localization in the rift structures within the brittle layer and more distributed strain in the viscous part of the model.
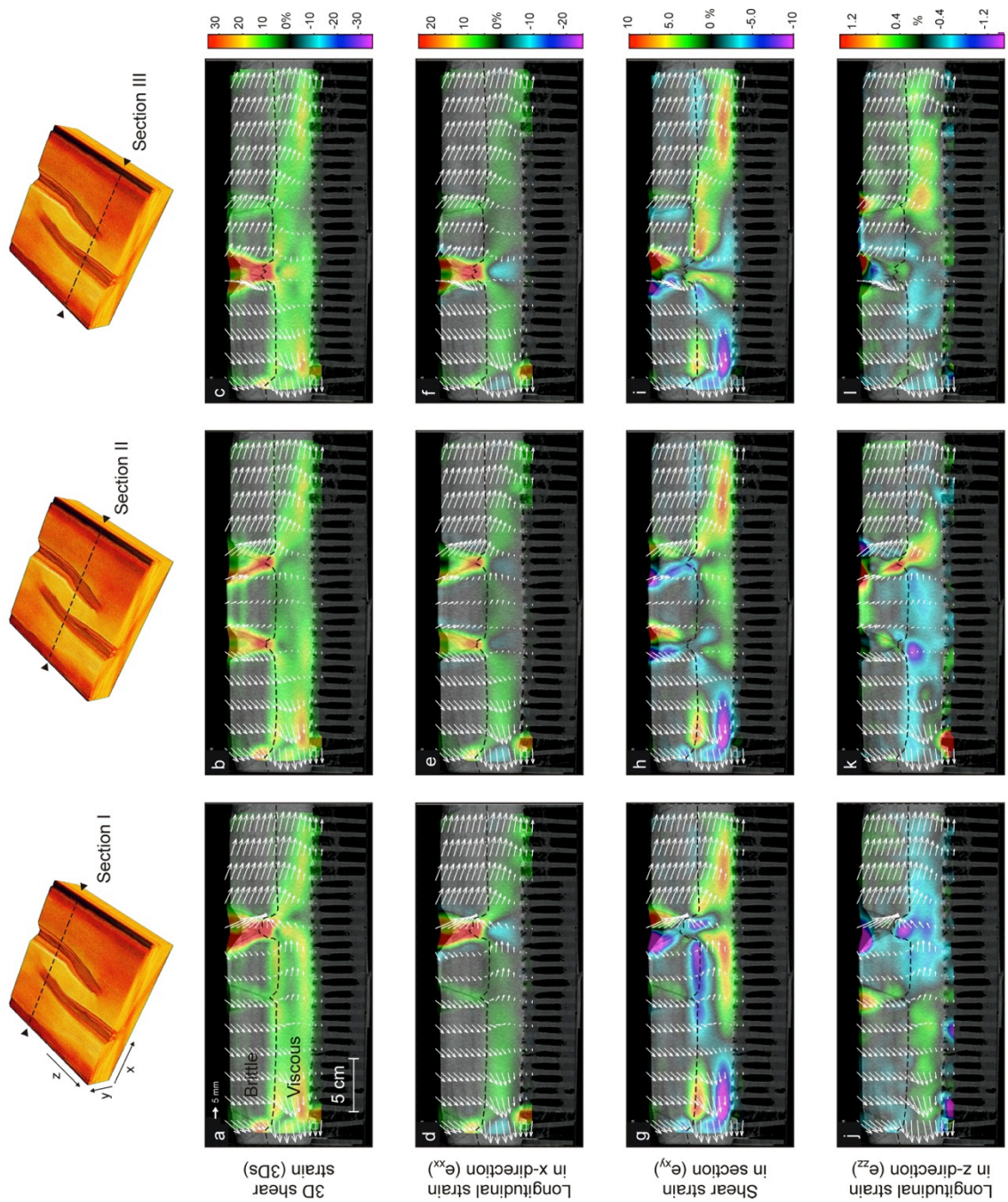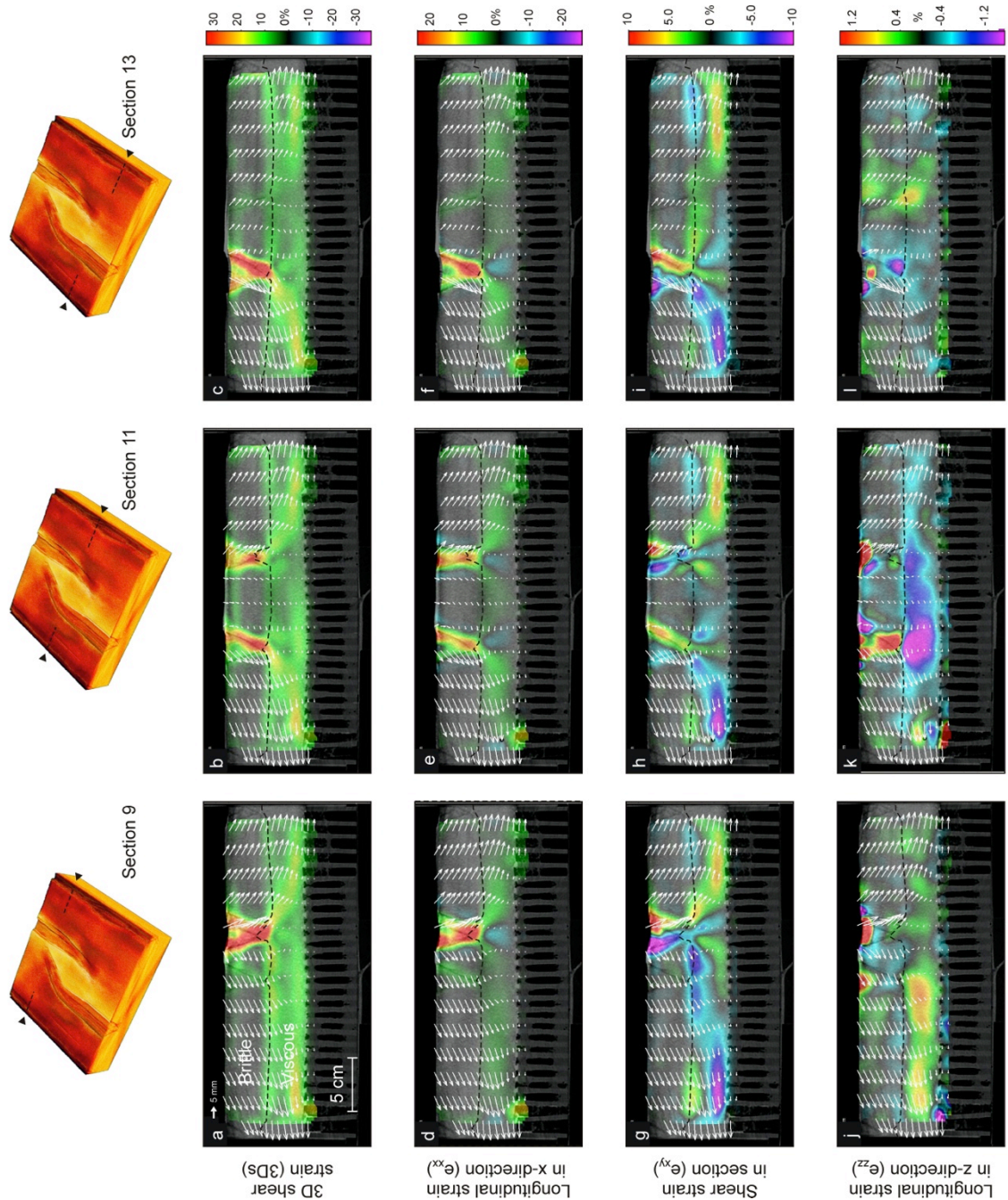
Fig. 4.9. *Strain charts of xy-sections derived from finite 3D strain fields of Model B (orthogonal extension, no sedimentation) obtained through DVC analysis. (a-c) 3D shear strain (positive values only): Higher values show more deformed areas (localised shear in sand layer, differential flow in viscous layer; (d-f) Longitudinal strain in the x-direction (e_{xx}): warm colours represent extension, cold colours represent contraction; (g-i) Shear strain (e_{xy}) in the xy-section plane: Warm colours represent sinistral shear, cold colours represent dextral shear; (j-l) Longitudinal strain in z-direction (e_{zz}): Warm colours represent extension, cold colours represent contraction. The locations of sections I, II and III are close to those of sections 3, 4 and 6 in Figs. 4.5d and 4.6a.*

Digital Volume Correlation (DVC) analysis of Model C

Similar to Model B, DVC analysis was applied to Model C (orthogonal extension, with sedimentation) in order to allow a quantitative comparison between models with and without sedimentation (Fig. 4.10). The displacement fields are rather comparable to those of Model B, with displacement concentrated towards the sides of the model, while the horst block or rift pass in the middle of the model remains relatively stable (4.11a-f). Model C also shows the same type of boundary effects (strong displacement near the model edge). Displacement magnitudes are however slightly higher than those observed in Model B (Fig. 4.8a-f) as a consequence of the additional loading by syn-rift sediments, causing both sides of the model to slide away faster from the relatively stable central horst block.

Vertical displacement in Model C (Fig. 4.10g-h) has a similar character as seen in Model B (Fig. 4.10g-h). Overall subsidence occurs throughout the model, with localized uplift and subsidence at the developing rift basins. However, uplift of viscous material below the rifts is less intense under the main rift segments in Model C than in Model B (Figs. 4.8g, i, 4.10g, i) due to the synkinematic sediment loading. Yet, the rise of material below the rifts at the central horst block appears to be slightly stronger than observed in Model B (Fig. 4.8h and Fig. 4.10h). Another difference is visible in the areas adjacent to the main rift structures, where the darker colours and steeper vectors in Model C (Fig. 4.10g-h) indicate stronger subsidence than for the same areas in Model B without sedimentation (Fig. 4.8g-h).

Comparing the more detailed differences in total displacements and total strains within the rift wedges is not feasible at this stage, because the Lagrangian summation of the incremental displacement data is only possible for the pre-kinematic material present at the start of the experiment and cannot be applied to newly applied material. We must therefore refrain from discussing these parts of the model in detail, although subsidence is obvious (Fig 4.11g-i). Furthermore, material is moving out of plane, most importantly on the left-hand side of the mode, an observation previously also made in Model C (Fig. 4.8j-l and Fig. 4.10j-l). However, dynamics of faulting and the effect of synkinematic sedimentation could be analysed using the incremental displacement data, but the DVC vector resolution does not allow a more detailed interpretation.

Overall, the results of the DVC analysis of Model C are rather comparable to those of Model B. The main differences lie in the higher displacement values that occur when syn-rift sedimentation is applied. As the results of the strain analysis for Model C are almost identical to those of Model B, they are not further discussed here. For the Model C strain chart, the reader is referred to Appendix 4B (Fig. 4.B1)
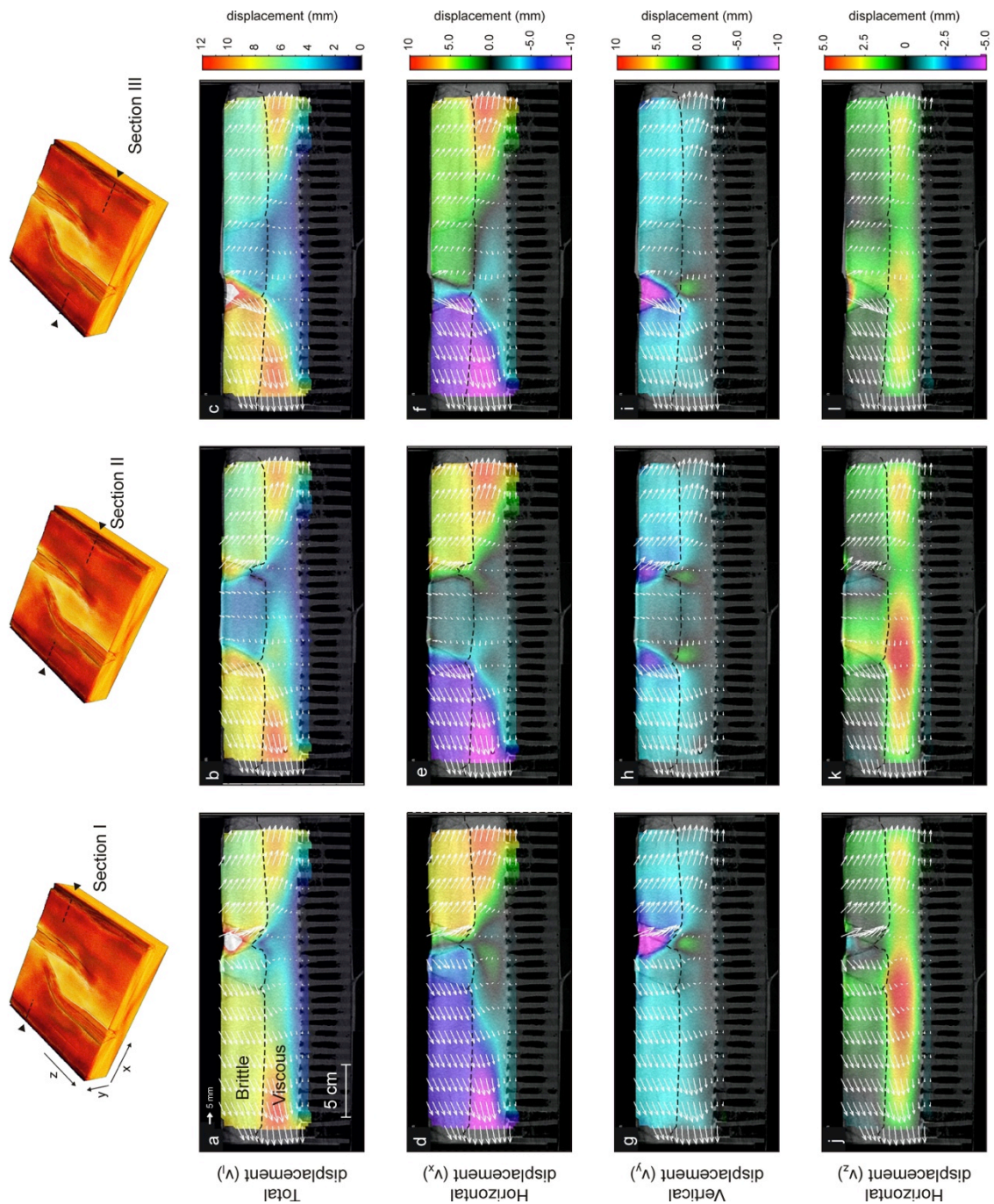
Fig. 4.10. *DVC total displacement analysis of Model C (orthogonal extension, sedimentation) (a-c) 3D displacement; (d-f) Horizontal displacement in the xy-plane, parallel to the extension direction. Warm colours represent displacement to the left, cold colours represent displacement to the right; (g-i) Vertical velocities. Warm colours represent uplift, cold colours represent subsidence; (j-l) Horizontal displacement in the z-direction (normal to section and extension direction). Warm colours represent displacement towards the observer, cold colours represent displacement away from the observer. The locations of sections I, II and III are close to those of sections 9, 11 and 13 in Figs. 4.5dh and 4.6b.*

4.3.2. Additional transfer zone models (Series 2 and 3)

As the models of series 1 did not produce a single, continuous transfer zone, possibly because the total extension was not sufficient to do so (Acocella *et al.* 2005), we ran two additional model series with different set-ups (Table 4.2). The additional model series involve a secondary seed (representing a secondary structural grain to localize a transfer zone), rift segment underlap (angle $\phi = 75°$ and 25° for series 2 and 3 respectively) and oblique extension (angle $\alpha = 15°$ and -30° for series 2 and 3 respectively, Fig. 4.2e-g). These set-ups are similar to those tested by Zwaan & Schreurs (2017; Chapter 3): the minor underlap and dextral transtension favours transfer zone formation by directing rift propagation towards the other rift segment in series 2, whereas the significant underlap combined with sinistral oblique extension produces a strike-slip dominated transfer zone in series 3.

Series 2 models

The series 2 models show the development of a continuous transfer zone basin with connected boundary faults between the rift segments, all situated above the secondary seed (Fig. 4.11). As previously observed in model series 1, syn-rift sedimentation does not significantly affect the large-scale structures so that rift segments as well as the transfer zone have a very similar geometry in both models. However, the structures within the rift segments and transfer zone are strongly influenced when syn-rift sedimentation is applied (Model J) or absent (Model I). Compared to Model I, Model J has a flatter rift topography, less faulting and more subsidence within the rift basin (Fig. 4.11i, j). Because the transfer zone consists of a continuous basin, flanked by oblique slip-normal faults, it behaves as an obliquely opening rift segment. The transfer zone shows a similar architecture to the main rift rift segments between which it is situated (Fig. 4.11i, j). In Model I the surface within the transfer zone basin is subsiding more as compared to the transfer zone basin in Model J. The transfer zone also experiences by more internal deformation structures, while the viscous layer has risen closer to the surface. However during the early model phases, both models show the innermost rift boundary faults connecting via a strike-slip fault within the developing transfer zone (Fig. 4.11b, b', f, f'). In later stages, this structure evolves in a series of right-stepping en-echelon faults (Fig. 4.11d, d', h, h'). As a result, the transfer zones have a much more complexly faulted appearance than the main rift segments.

Series 3 models

Similar to the dextral oblique extension models of series 2, the sinistral oblique extension models of series 3 also form distinctive main rift segments and a transfer zone along the primary and secondary seeds, respectively (Fig. 4.12). Again, on a large scale the rift segments are not much affected by syn-rift sedimentation (Fig. 4.12d, d', h, h'), although internal structures are (Fig. 4.12i and j). Synkinematic sediments in Model N (Fig. 4.12, left column) results in a flatter rift topography, a less faulted rift structure and overall more subsidence than Model N without sedimentation (Fig. 4.12j).

The transfer zone initiates as a sinistral strike-slip zone in both models (Fig. 4.12b, b' and f, f'). Subsequently Model M develops a single large basin within the transfer zone, which has a right-stepping en-echelon arrangement with respect to the main rift segment (Fig. 4.12c, c'). In contrast, Model N develops a more fragmented structure with multiple small right-stepping basins in an en-echelon configuration (Fig. 4.12g, g'). Finally, in both models the transfer zone evolves into a continuous trough between rift-boundary faults (Fig. 4.12d, d', h, h', i and j), in which syn-rift sedimentation has a comparable effect on internal structures as in the main rift segments, although the latter are less faulted (Fig 13i, j).

128
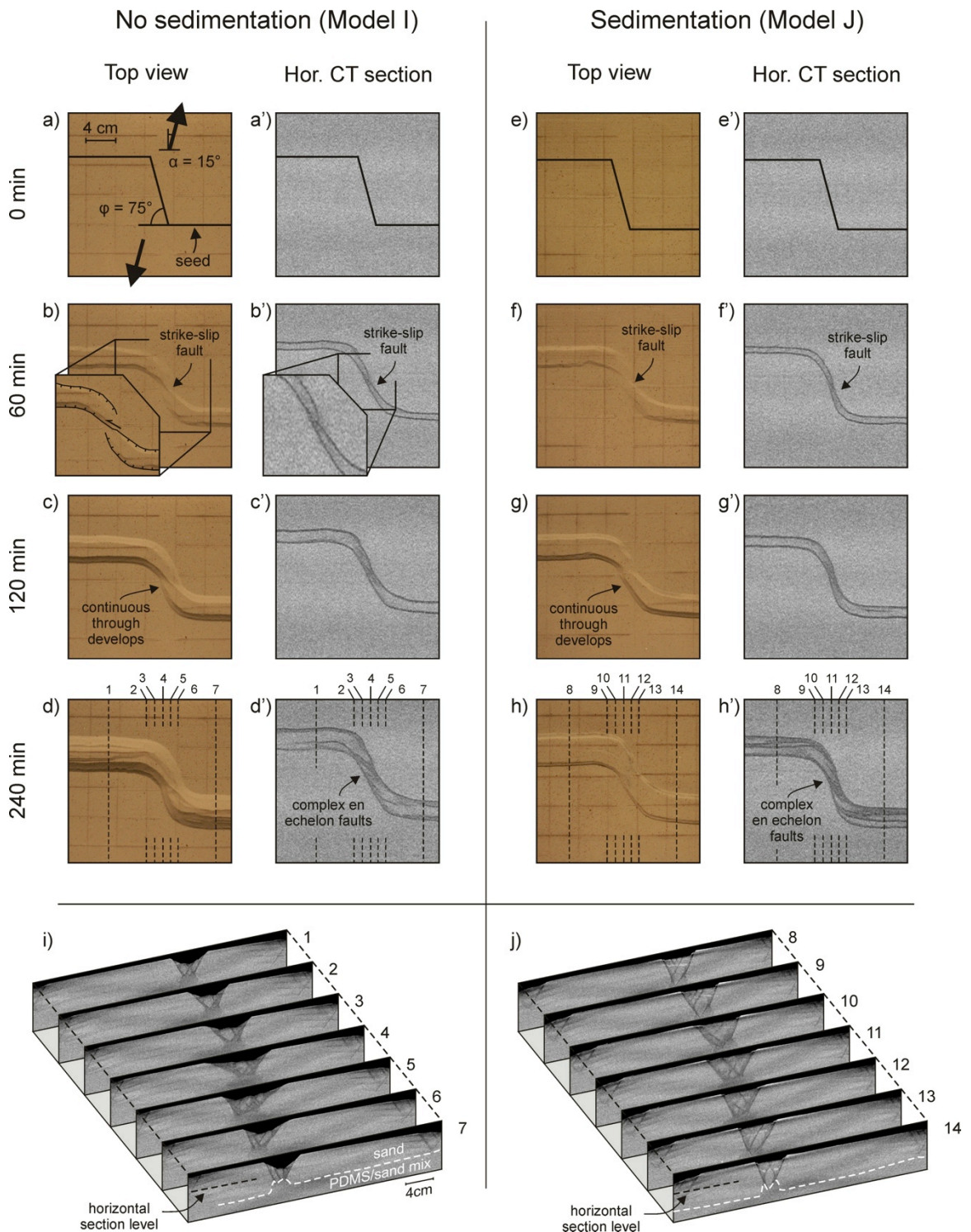
Fig. 4.11. *Overview of Model I (without sedimentation) and Model J (with sedimentation) from series 2. Set-up: 15° oblique extension, secondary seed and rift underlap ($\phi = 75°$). (a-d and e-h) Top view results with time. (a'-d' and e'-h') Horizontal CT sections, at 2 cm depth (see i). (i-j) CT sections, illustrating the final internal model structure. Section locations are shown in d-d' and h-h' for Models I and J respectively.*
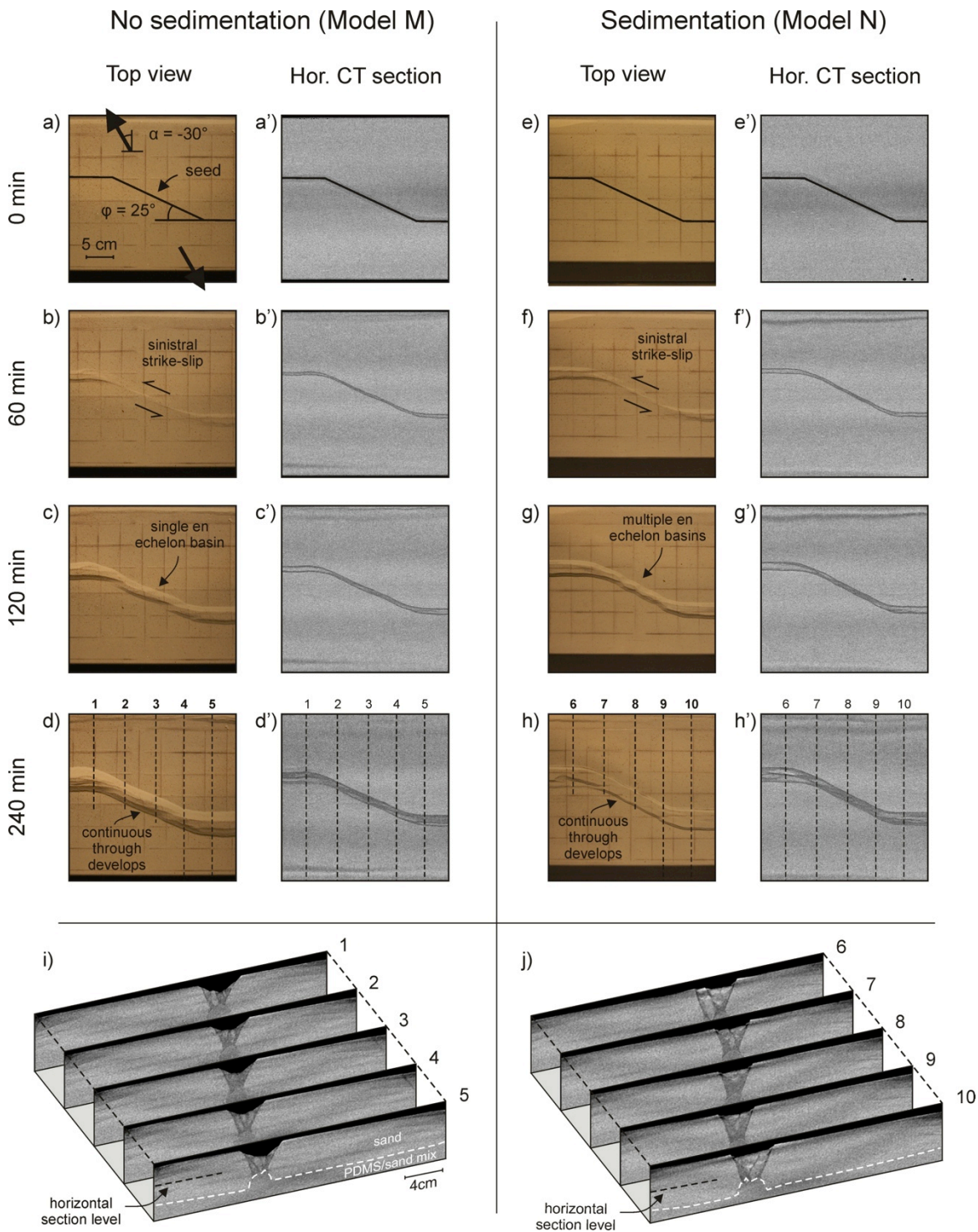
Fig. 4.12. *Overview of Model M (without sedimentation) and Model N (with sedimentation) from series 3. Set-up: -30° (sinistral) oblique extension, secondary seed and rift underlap ($\phi = 25°$). (a-d and e-h) Top view results with time. (a'-d' and e'-h') Horizontal CT sections, at 2 cm depth (see i). (i-j) CT sections, illustrating the final internal model structure. Section locations are shown in d-d' and h-h' for Models M and N respectively.*

4.4. Discussion

4.4.1. Large-scale rift and rift interaction zones

The overall evolution of rift segments and rift interaction zones as a function of extension obliquity in our models are similar to those described by Zwaan *et al.* (2016; Chapter 2) and Zwaan & Schreurs (2017; Chapter 3). Early rift segments develop above the seeds, revealing the important influence of structural weaknesses on the initial position of rift segments. The narrower and shallower rifts with steeper rift boundary faults that develop with increasing degrees of oblique extension (Fig. 4.A1a-c) are logical, as the system becomes more strike-slip dominated, strike-slip faults being vertical. Furthermore, the development of en-echelon boundary faults and rift-internal structures (Fig. 4.4c) is a common feature in oblique extension settings (e.g. Tron & Brun 1991; McClay & White 1995; Morley *et al.* 2004) as extensional structures tend to develop approximately perpendicular to the extension direction (e.g. Hus *et al.* 2005).

The latter process also has a dominant influence on the rift interaction structures in our series 1 models. Orthogonal extension with a 2 H staircase rift offset causes the rift segments to propagate roughly parallel to each other, while increasing degrees of dextral oblique extension promote linkage of right-stepping rift segments. This rule also holds for the opposite case: sinistral oblique extension in combination with left-stepping rift segments promotes rift linkage (Zwaan & Schreurs 2017; Chapter 3). However, the presence of secondary weaknesses results in a more complex evolution. In the series 2 models, the transfer zone is much more localized with respect to the rift pass structures forming in the series 1 models due to the presence of a rift-connecting seed (compare Fig. 4.7 and Fig. 4.11). Yet, the 15° dextral oblique extension in series 2 models also favours rift linkage since the general stress field induces the rifts to propagate toward each other. On the other hand, the series 3 set-up with 30° sinistral oblique extension could cause the propagating rifts to grow apart by the same principle. Though in these models, the seed localizes deformation, producing an initial sinistral strike-slip dominated transfer zone that evolves into a series of basins and finally forms a continuous trough (Fig. 4.12). However, Zwaan & Schreurs (2017; Chapter 3) have noted that the same set-up without a rift-connecting seed may also produce a similar transfer zone due to local stress field modifications.

These general results are not significantly altered when we incorporate syn-kinematic sedimentation. Our models suggest that syn-rift sedimentation does not have a significant influence on the large-scale rift and transfer zone development in our model parameter space. This first-order observation, is of importance for previous model studies with the same basic set-up, but without sedimentation (e.g. Le Calvez & Vendeville 2002; Zwaan *et al.* 2016; Zwaan & Schreurs 2017; Chapters 2 and 3), since it validates their large-scale model results.

4.4.2. Sedimentary loading and basin architecture

The large-scale rift setting might not be significantly affected by sedimentation, but a close-up view on the rift-internal structures shows that there are significant differences between models with and without sedimentation. The flat topography seen in syn-rift sedimentation models is a logical consequence of sedimentation (as we fill the rift basins to rift shoulder level). The other striking differences that occur when sedimentation is applied (less faulting within the rift wedge, higher subsidence and less uplift of the viscous lower crust) are due to the effects of sedimentary loading (Fig. 4.13b and b').

The influx of sediments causes an increased gravitational load on the rift wedge, which subsequently subsides deeper into the viscous layer below, simultaneously preventing the viscous material from rising (compare Model B with Model C, Figs. 4.8g-l and 4.10g-l). Sedimentary loading also affects footwall segments of the rift boundary faults, as Model C, including syn-rift sedimentation, shows a

more pronounced subsidence of the footwall segments than observed in Model B without sedimentary loading was applied (Figs. 4.8g-l and 4.10g-l). The infill and loading effects due to sedimentation also increase the strength of the sand and the shear zones with depth so that faulting is more localized and fault displacement increases (Fig. 4.13a, b), a feature also observed in previous numerical models (Olive *et al*. 2014). In contrast, a lack of sedimentation in the models thins and weakens the rift wedge, which is then easily deformed and broken up to spread over the widening gap (Fig. 4.13b), similar to the simulations of Burov & Poliakov (2001). Furthermore, the pronounced isostatic rise of the viscous lower crust (Figs. 4.8g-I, 4.9g-l) enhances internal rift wedge deformation, while hanging wall unloading supports

relative rift shoulder uplift (Fig. 4.5a-d, i-l, Weissel & Karner 1989).

Sedimentary infill also supports the stability of the rift shoulders so that rift boundary faults do not collapse and decrease fault dip angle as readily as in the models without sedimentation (Fig. 4.A1d-f). However, this effect diminishes with increasing extension obliquity. Probably, the rift basin becomes more extension-dominated with progressive deformation, so that the initial steep rift boundary faults acquire an increasingly stronger dip-slip component and tilt towards the shallower fault angles typical for pure normal faults (Fig. 4.7b, o-z). The rise of the viscous layer below the rift might also cause rotation of the rift boundary faults.
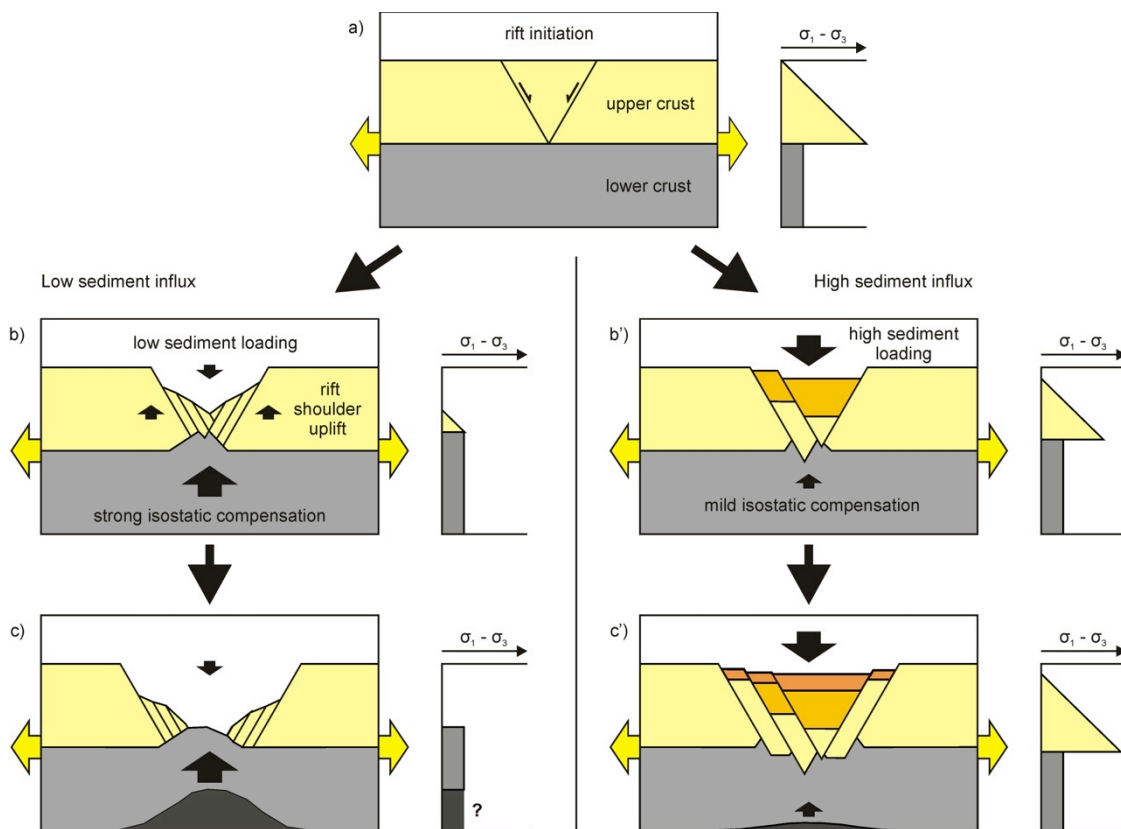
Fig. 4.13. *Schematic overview summarizing the influence sedimentation could have on rift evolution, based on our models. A strength profile is shown to the right of each image. (a) Rift initiation: extension and normal faulting in the undeformed upper crust. (b-c) Rift evolution without sediment influx: deep topography, high fault density due to weakening of the upper crust, rising lower crust (and mantle?) and early rupture of the upper crust. (b'-c') Rift evolution with sediment influx: strong subsidence, but rift basin fills up to form flat topography, low fault density due to upper crust strengthening, limited rising of the lower crust (and mantle?) and postponed rupture of the upper crust.*

However, the role of syn-rift sedimentation during the evolution of a rift segment depends on the amount of accommodation space that is created over time. We observe the most significant influence of sedimentation in the main rift segments of our models, where most extension and subsidence is focused. These effects grow stronger towards the end of the model run, when most sediment loading has accumulated. In contrast, the impact of sedimentation is limited along the propagating rift branches from series 1 (Figs. 4.5-7), as these structures undergo much less subsidence during the model run. The models from series 2 and 3 (Figs. 4.11, 4.12) do develop rift-dominated transfer zones, but these are less developed than the main rift segments. It follows that within our parameter space, syn-rift sedimentation has a minor effect on internal structuration of rift interaction zones and is most influential in the main rift segments and becomes more important with progressive rifting.

4.4.3. Oblique extension and strike-slip faulting

Another factor influencing the development of accommodation space is the degree of oblique extension. Our models indicate, in line with previous findings (e.g. Zwaan et al. 2016; Chapter 2), that increasing degrees of oblique extension decrease basin widths, as rift boundary faults steepen due to the stronger strike-slip component (Fig. 4.A1a). In combination with less subsidence in the rift basin, high degrees of oblique extension decrease the amount of accommodation space available (Fig. 4.A1b) and thus repress the effects of syn-rift sedimentation. This is the case with Model H (60° dextral oblique extension, Fig. 4.4c, f), which did not produce enough accommodation space during the early stages to apply sedimentation. Model N provides another example (Fig. 4.12), in which a strike-slip zone establishes the earliest rift connection, allowing little sedimentary infill during the initial phases. This is a specific model with a specific set-up, but transfer fault zones connecting rift segments are often observed in nature (e.g. Morley et al. 2004, Fig. 4.1d) and are probably little affected by syn-kinematic sedimentation. However, in the Model N case, the transfer

fault does subsequently develop into a rift basin, similar to the Rukwa Basin in the Tanganyika-Rukwa-Malawi fault zone in East Africa (Rosendahl et al. 1992; Chorowicz 2005; Zwaan & Schreurs 2017; Chapter 3). Thus, an initial strike-slip transfer fault system can in later stages evolve into a rift-type sediment-filled basin.

4.4.4. Basin architecture: model vs nature

Although sedimentation is shown not to have a strong effect on initial rift and rift interaction structures, it has significant influence on rift-internal model structures. In nature, we often find thick sedimentary infill within rift basins, for instance in the Rhine Graben, (Derer et al. 2005), East African Rift System (Morley 1988; Ebinger 1989), North Sea (Erratt et al. 1999) and Baikal Rift (Hutchinson et al. 1992; Hus et al. 2012). The curved rift valley floor topography seen in our models without sedimentation is rather unlike the geometries observed in young continental rift settings, as is the model basin depth of ca. 10 mm, which translates to ca. 5 km or more in nature; the deepest continental rift basin, Lake Baikal, is 1,600 m deep (Hutchinson et al. 1992) and even the mean ocean depth on Earth only amounts to some 3.7 km (Charette & Smith 2010). Although our crustal scale sedimentation experiments do not capture factors as lithospheric flexure and isostasy or mantle upwelling, which might mitigate the degree of subsidence, they provide a more realistic rift geometry and topography. It is therefore desirable to apply (at least a degree of) sedimentation when modelling extensional tectonics.

4.4.5. Rift pass structures

The propagating rift tips in the models from series 1 lead to the formation of a horst or rift pass structure between both rift segments that can eventually lead to microcontinent formation (Nelson et al. 1992; Koehn et al. 2008), especially in oblique extension conditions (Figs. 4.4-7). DVC analysis demonstrates that the relative uplift of the central horst or rift pass block, within a regionally subsiding area, is due to hanging wall unloading as a result of rift activity on both sides (Figs. 4.8g-I, 4.10g-l). Furthermore,

the slight rotation of the rift pass block is a logical result of the extension gradient along the propagating rift segments (Figs. 4.4a, 4.8j-l, 4.11j-l, 4.14a). This extension gradient also causes the flow of viscous material towards the most developed part of the rift, where the strongest isostatic compensation occurs (Figs. 4.8, 4.10, 4.14b).

Similar structural highs as those in our experiments occur in the North Sea Central Graben, situated between Late Jurassic-Early Cretaceous left-stepping rift segments (Fig. 4.15) that opened along pre-existing tectonic lineaments inherited from the Caledonian orogeny (Bartholomew *et al.* 1993). A first rift phase in the Triassic formed the rough Central Graben structure that is reactivated during subsequent Late Jurassic-Early Cretaceous extension, probably under orthogonal or near-orthogonal extension conditions (Erratt *et al.* 1999, 2010). While deep rift basins formed during these rifting events, leading to the deposition of world-class Upper Jurassic hydrocarbon source rocks (Gautier 2005), the intervening highs remained emergent and subjected to erosion. The highs were only flooded following regional post-rift thermal subsidence initiated in Late Cretaceous times, occasionally interrupted by local pulses of inversion that continued into the Cenozoic (Cartwright 1989; Johnson *et al.* 2005).

An excellent example of such a rift pass block in the North Sea Central Graben is provided by the Mandal High at the Norwegian-Danish Border, situated between the Feda Graben in the west and the Søgne Basin in the east (Fig. 4.16). It remained a stable and exposed structural high from Permian times until the Late Cretaceous, while the adjacent Feda Graben and Søgne Basin experienced significant amounts of tectonic subsidence and sediment infill during the two major rift phases (Fig. 4.16b, c). Note the effect of the Upper Permian (Zechstein) evaporites on the structural style. Post-rift thermal sag resulted in the deposition of thick layers of chalk sediments (Surlyk *et al.* 2003), that are slightly deformed due to Late Cretaceous-Cenozoic inversion and associated salt motion (diapirism) and he whole structure is nowadays overlain by several kilometres of Cenozoic infill (Fig. 4.16e).
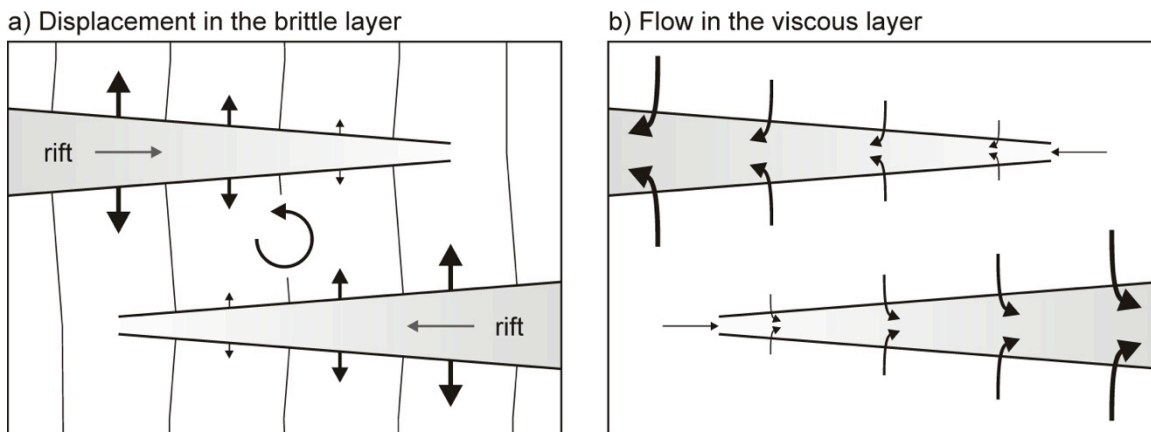
Fig. 4.14. *Schematic depiction of the brittle and viscous deformation in a rift pass setting as observed in our models (compare with Fig. 4.4a). (a) Map view of brittle displacement, involving an extension gradient occurring along both propagating rift basins causing a rotation of the rift pass block as indicated by the deformed lines that were initially parallel. (b) Material flow in the viscous layer beneath the brittle cover. Material moves towards the developing rifts. Motion is dominantly perpendicular to the rift, but it contains also a rift-parallel component, from the rift tip to the more developed sections of the rift.*
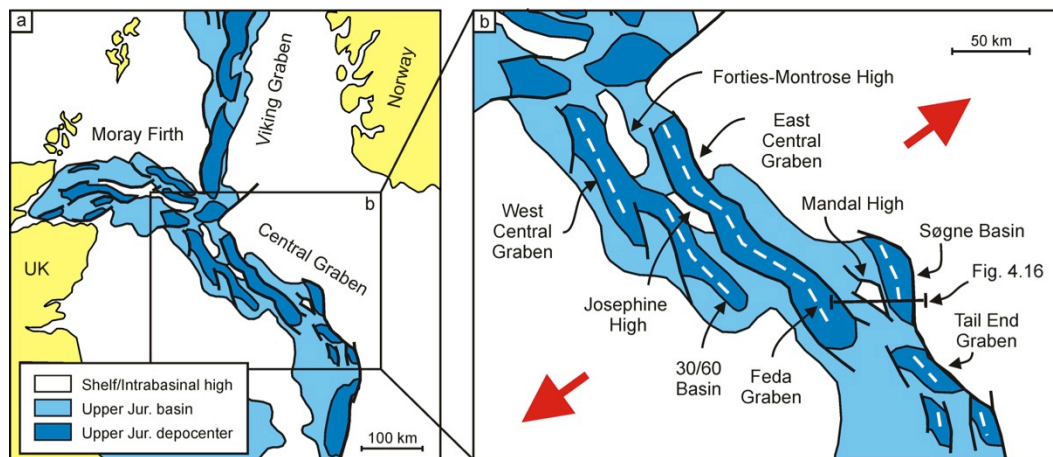
Fig. 4.15. *(a) North Sea Jurassic rifts. (b) En-echelon left-stepping basins and intra-basin horsts and rift passes in the Central Graben. Approximate extension direction is shown by red arrows. White dotted lines illustrate rift basin orientation. Modified after Erratt et al. (1999)*
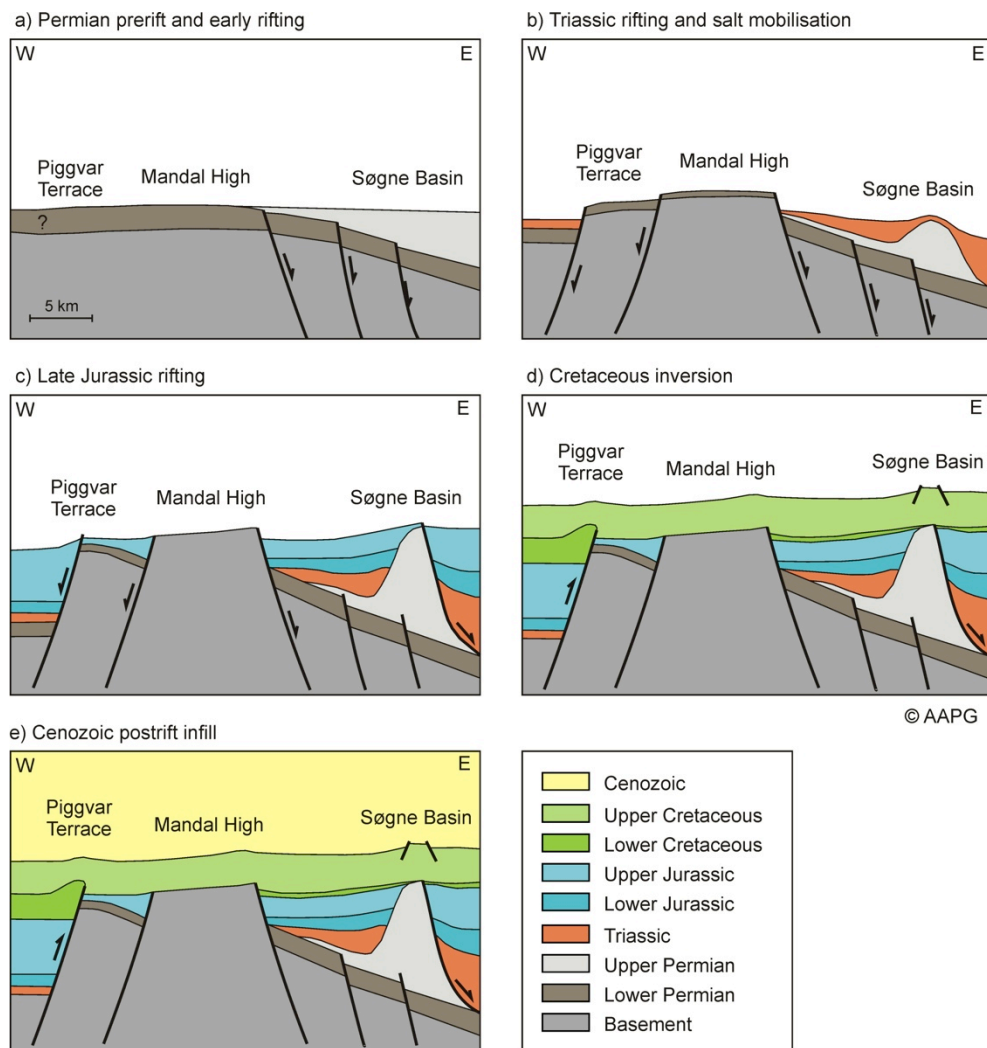
Fig. 4.16. *Evolution of the Mandal High in the North Sea in (a) the Permian, (b) Triassic, (c) Late Jurassic, (d) Cretaceous and (e) Cenozoic. Modified after Rossland et al. 2013. Location indicated in Fig. 4.15. AAPG©2013, reprinted by permission of the AAPG, whose permission is required for further use.*

4.4.6. Additional insights from DVC analysis

Although CT scanning provides a very useful non-destructive method to monitor the internal 3D structural evolution of our models, the CT images alone only allow a predominantly qualitative structural analysis (Figs. 4.6-8, 4.11-13). With the use of DVC analysis, we can now for the first time reveal and quantify the complex 3D displacement and strain patterns in both the brittle and viscous parts of our experiments (Figs. 4.8-11). The results indicate the clear distinctions between brittle and viscous behaviour, where deformation is either strongly localized or distributed (Fig. 4.9). Especially the distributed deformation within the viscous layer is demonstrated to be complex (Fig. 4.9g-I). Furthermore, the minor boundary effects near the sides of the models (best visible on Fig. 4.8a-f and 10g-i) are shown to influence material flux in the viscous layer. The 3D aspect of the DVC analysis also reveals the flow of viscous material out of section in orthogonal extension models, and the rotation of the rigid rift pass block about a vertical axis (Figs. 4.8j-l, 4.9j-l, 4.14). Therefore, a 2D crustal-scale restoration of an orthogonally extended system may be flawed if such effects are not taken into account.

Altogether, DVC analysis of CT data allows a much more thorough and detailed understanding of our models and the possibility to map small distributed and large localized deformation and displacements could be a powerful tool for analogue-numerical comparison and calibration.

4.4.7. Implications for continental break-up

Our models demonstrate that syn-rift sedimentation does not have an important influence on early large-scale rift and rift interaction zone evolution. Yet, sedimentation might be of importance on a longer timescale. We see how models without sedimentation develop a strongly thinned upper crust, which can be expected to break apart when further extension occurs. On the other hand, constant infill of the rift basin could constantly strengthen the upper crust and potentially prevent any break-up from occurring (Fig. 4.13c'). The amounts of material needed for the latter scenario are rather enormous and

therefore unlikely to be available, but a steady influx of sediment could significantly delay continental break-up, as seen in the Gulf of California (Martín-Barajas *et al.* 2013). In contrast, a low sediment supply leading to starved basins is quite common (e.g. the Jurassic North Sea rifts, Fraser *et al.* 2003) facilitating continental break-up (Fig. 4.13c).

However, the processes associated with rifting and eventual break-up are numerous. For instance the lithospheric strength profile and the degree of brittle-ductile coupling within the system has a strong influence on fault localization and the style of rifting (e.g. Dunbar & Sawyer 1989; Brun 1999; Buiter *et al.* 2008). Isostatic compensation and flexure on a lithospheric scale as well as mantle plume emplacement commonly modifies rift zone topography significantly (Weissel & Karner 1989; Underhill & Partington 1993; Moucha & Forte 2011). Mantle plume-induced thermal variations also influence the lithospheric strength profile and the associated magmatism and magmatic intrusion (diking) are known to promote break-up (Buck 2004; Ebinger 2012). Furthermore, the bottom of the lithosphere (e.g. cratonic roots) directs the flow of mantle plume material and thermal variations (Fouch *et al.* 2000). Thermal blanketing by sediments may modify the thermal profile and strength of the lithosphere (Stephenson 2009). Another thermal effect may occur during pauses in rift activity, causing cooling and strengthening of the rising asthenosphere below the rift so that with renewed extension, rifting may initiate elsewhere (Naliboff & Buiter 2015).

As a matter of fact, most rifts fail to split a continent, emphasizing the complexity of continental breakup (Ebinger 2012). Although syn-sedimentary loading may influence the process, we should consider it in the larger context of the complete extensional system and the larger-scale processes mentioned above, which determine the long-term rift evolution. These processes are however not included in our crustal-scale analogue models. Lithospheric-scale analogue models involving syn-sedimentation would allow a better constraint on the mechanical behaviour of the system (lithospheric flexure, isostacy), whereas numerical models would enable the simulation of chemical and thermal influences.

4.5. Conclusion

We conducted various crustal-scale analogue tectonic models to investigate the effects of syn-rift sedimentation on rift and rift interaction zone development in continental settings and come to the following conclusions:

- On a large scale, syn-rift sedimentation does not significantly influence the development of rift and rift interaction structures;
- Syn-rift sedimentation can however strongly affect rift-internal structures: sedimentary loading reinforces the rift wedge, decreasing rift wedge faulting, and increasing subsidence of the rift wedge;
- These effects are strongest in areas where most accommodation space is available, that is, along the main rift segments. In contrast, rift segments that undergo high degrees of oblique extension develop less accommodation space and can be expected to be significantly less affected by sedimentary loading;
- Rift interaction structures are least affected by sediment influx, as they undergo relatively low amounts of subsidence so that little accommodation space is available;
- We advisee to apply sedimentation in models of extensional tectonic settings, as our rift basins with syn-rift sedimentation develop more realistic features than the models without;
- Novel 3D DVC analysis allows a much more thorough understanding of our models than surface images or CT scans alone can provide. It enables the highly detailed monitoring and quantification of material displacement and deformation, revealing the complex behaviour of both the brittle and viscous model materials;
- The 3D DVC analysis demonstrates that material can move out of plane in orthogonal extension settings due to viscous flow or block rotation about a vertical axis, which has to be taken in account when conducting structural reconstructions;
- The above conclusions are valid for the early stages of rift development, when a high sediment influx could delay continental break-up. However, the long-term evolution of the rift system is dominated by other, lithospheric-scale processes.

4.6. Acknowledgements

Appendix 4A

Fig. 4.A1. *Measurements on models, showing the influence of extension obliquity (angle α) and sedimentation on rift geometry. (a) Rift width, decreases with increasing extension obliquity and is consistently lower in models with sedimentation; (b) Subsidence (height difference between rift shoulders and rift valley floor; for models with sedimentation the height difference between rift shoulders and the base of the oldest sediments is measured), decreases with increasing extension obliquity and is consistently higher with sedimentation; (c) Initial boundary fault angle, which increases with higher extension obliquity (d) Final rift boundary angle, which is stable in models with sedimentation, but increases with higher extension obliquity; (e) change in rift boundary fault angle with time for models without sedimentation; (f) change in rift boundary fault angle for models with sedimentation.*

Appendix 4B

Fig. 4.B1. *Strain charts of xy-sections derived from finite 3D strain of Model C (orthogonal extension, sedimentation) obtained through DVC analysis. (a-c) 3D shear strain (positive values only): Higher values show more deformed areas (localised shear in sand layer, differential flow in viscous layer; (d-f) Longitudinal strain in the x-direction (e_{xx}): Warm colours represent extension, cold colours represent contraction; (g-i) Shear strain (e_{xy}) in the xy-section plane: Warm colours represent sinistral shear, cold colours represent dextral shear; (j-l) Longitudinal strain in z-direction (e_{zz}): Warm colours represent extension, cold colours represent contraction.*

Chapter 5

Rift propagation under orthogonal and scissor extension conditions: insights from analogue models analysed with 4D X-ray computed tomography

Frank Zwaan[a] *, Guido Schreurs[a]

a) Institute of Geological Sciences, University of Bern, Baltzerstrasse 1+3, CH-3012 Bern, Switzerland

_____

Abstract

In natural rift settings, extension rates often increase or decrease along strike, due to the rotation about a vertical axis for small-scale settings or about an Euler pole for global scale systems, associated with the propagation of rift structures or whole ocean basins. Analogue (and numerical) modellers traditionally use a constant along-strike deformation rate, although some have applied rotational motion in their experiments. To date, however, a vigorous comparison between these two fundamentally different modelling approaches is lacking. We therefore apply a novel experimental apparatus to systematically compare rift development and rift propagation in either a traditional orthogonal extension set-up (involving constant extension velocity along strike) or a scissor extension set-up (involving an extension gradient along strike), analysed with surface scanning and X-Ray computed tomography (XRCT or CT) techniques. The results indicate that significant localization of deformation is required in order to create a rift structure that subsequently propagates. Furthermore, scissor extension appears to be of high importance for rift propagation and even in the orthogonal extension models that produce rift propagation, slight scissor motion seems to be involved. CT analysis also indicates that rifts in scissor extension develop early after which the parts of the system farther away from the scissor axis evolve faster so that the rift appears to propagate on the surface. Finally we observe that regional subsidence is caused by stretching and thinning of the lower crust in the extensional systems.

_____

5.1. Introduction

In natural rift settings, extension rates often increase or decrease along strike, due to the rotation about a rotation axis for small-scale settings or about an Euler pole for global scale systems, associated with the propagation of rift structures or whole ocean basins (e.g. Martin 1984; Van der Pluijm & Marshak 2004, Fig. 5.1). Examples are found in the Gulf of Aden and the Red Sea, associated with the counter clockwise rotation of the Arabian plate (Fig. 5.1a) and possibly the East African Rift System (EARS), where various crustal blocks are pivoting eastward (Fig. 5.1c).

In the Arctic, the slowly extending Gakkel Ridge also contains an extension gradient towards the North Atlantic. The associated plate boundary enters the Eurasian continent at the Laptev Margin, where extension is diffused (e.g. Franke *et al*. 2001; Van Wijk & Blackman 2005; Franke & Hinz 2009). Similar settings are found in the Havre Trough, New Zealand (Benes & Scott 1996) and the Woodlark Basin off Papua New Guinea (Benes *et al*. 1994). In the case of the Laptev Margin, the plate boundary continues into Siberia and enters a compressive regime at the Chersky Range on the opposite side of the Euler pole (Fujita *et al*. 2009; Imaeva *et al*. 2016), completing a full "scissor tectonic system" (Fig. 5.1c).

Yet analogue (and numerical) modellers traditionally use a constant along-strike deformation rate (e.g. Withjack & Jamison 1986; Michon & Merle 2000; Philippon *et al*. 2015). The few authors who present analogue models with along-strike extension rate variations focussed on the rotation of the Danakil Block associated with extension propagation in the Afar (Souriot & Brun 1992), the continuation of the Havre Trough into New Zealand (Benes & Scott 1996), subduction rollback in the Pacific Kuril Basin (Schellart *et al*. 2002; 2003) and the opening of the South China Sea (Sun *et al*. 2009). Recently, Molnar *et al*. (2017) described different models of the Red Sea, testing the influence of large-scale mantle weaknesses with various obliquities to the extension direction on propagating rift evolution.

To date, however, a vigorous comparison between these two fundamentally different modelling approaches is lacking. In this paper, we therefore present a systematical comparison effort between rift development and rift propagation in either a traditional orthogonal extension set-up (involving constant extension velocity along strike) or a scissor extension set-up (involving an extension gradient along strike, for which a novel experimental apparatus was developed).

The basal deformation mechanism of both set-ups is similar to the method applied by Zwaan *et al*. (2016; Chapter 2) and Zwaan & Schreurs (2017; Chapter 3), which allow a high degree of freedom for the rifts and transfer zones to develop. Selected models are scanned with the use of X-ray computed tomography (XRCT or CT) techniques to reveal their 3D internal evolution. Additional surface scanning is applied to trace topography evolution. The model results are subsequently compared with previous models and natural examples.
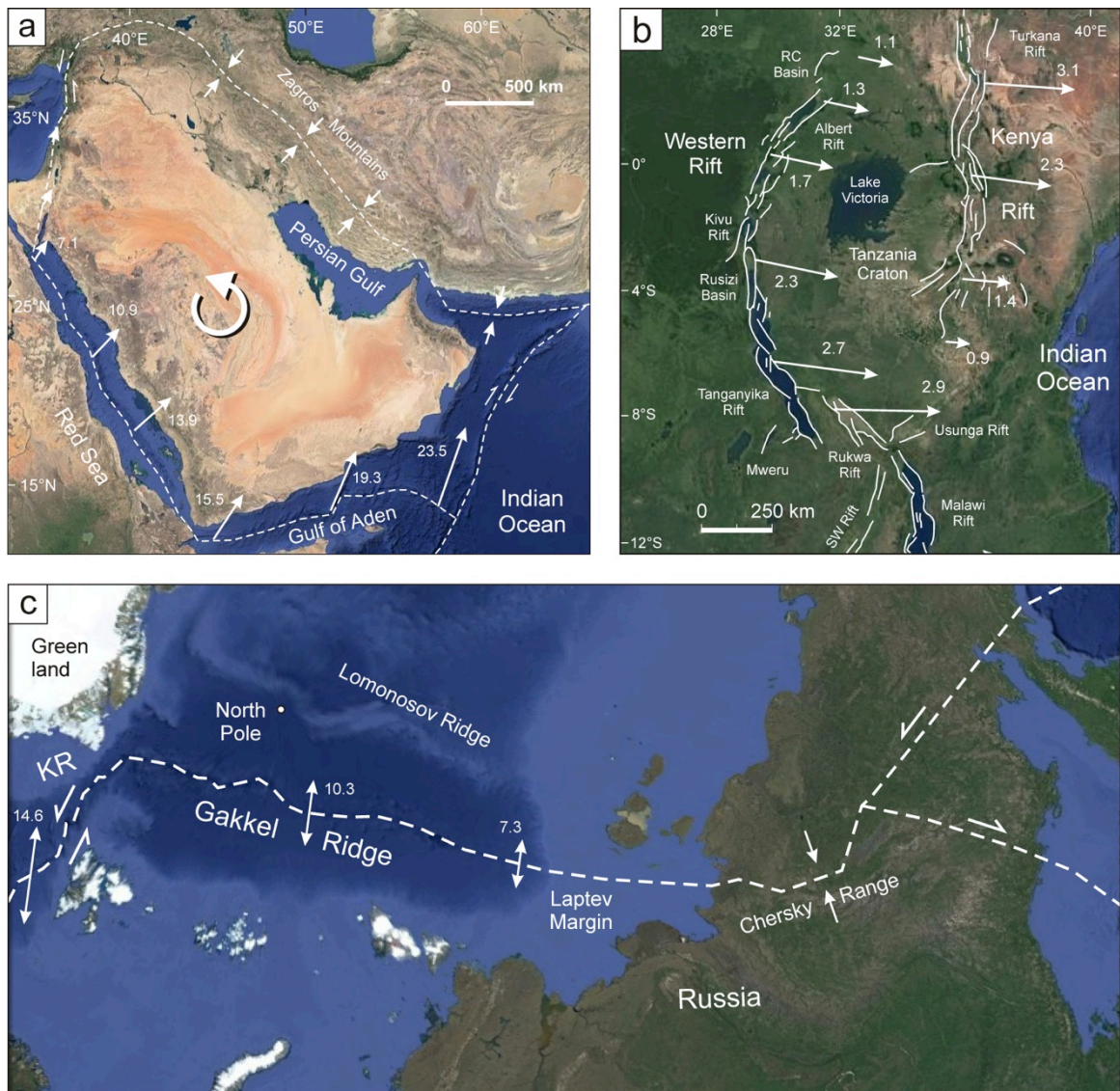
Fig. 5.1. *Natural examples of extension gradients. (a) Red Sea and the Gulf of Aden (due to the counterclockwise block rotation of Arabia. Dotted limes indicate plate boundaries, extension velocities are derived from GPS measurements. Image modified after after Bellahsen et al. (2003) and ArRajehi et al. (2010). (b) Distribution of rift basins and extension gradients in the East African Rift system. RC Basin: Rhino-Camp Basin. Extension velocities are derived from GPS measurements (Image modified after Ebinger (1989), Acocella et al. (1999a) and Saria et al. (2014). (c) Artic region, showing an increasing extension velocity along the Gakkel ridge, and the compressive domain at the Siberian Chersky Range. KR: Knipovitch Ridge. Image modified after Dick et al. (2003), Imaeva et al. (2016) and Fujita et al. (2009). Background images are added from Google Earth, velocities in mm/h.*

5.2. Materials and methods

5.2.1 Model materials

We apply a brittle-viscous model layering, representative of the upper and lower continental crust, respectively (Fig. 5.2). The uppermost, brittle part of the model consists of a 4 cm thick layer of fine quartz sand (ø = 60-250 μm). The sand is sieved from ca. 30 cm height into the experimental apparatus to maintain a constant sand density of ca. 1560 kg/m³. During application, the sand is scraped and flattened at every cm, causing slight density differences. This layering is captured on CT images (Fig. 5.8). A 4 cm thick viscous basal layer represents the 20 km thick ductile lower crust. It consists of a mixture of near-Newtonian (η = ca. 1.5·10⁵ Pa·s; n = 1.05) SGM-36 Polydimethylsiloxane (PDMS) silicone with dense corundum sand ($\varrho_{specific}$ = 3950 kg/m³ and ø = 88-175 μm, Panien *et al.* 2006; Klinkmüller 2011; Carlo AG 2017). The resulting density (ca. 1600 kg/m³) ensures a realistic density profile than pure silicone would allow (ϱ = ca. 960 kg/m³), avoiding unrealistic buoyancy effects. An overview of the material properties is provided in table 5.1.

5.2.2. Model set-up

For this study we apply two experimental machines with the same basic method to induce deformation in the overlying model materials. Both machines contain a 8 cm thick (5 cm for model M13) compressed foam base squeezed between two longitudinal sidewalls (Fig. 5.2a, b). On this base, the viscous and brittle model materials are applied. During a model run, the sidewalls are driven apart by precise computer-controlled motors, causing uniform expansion in the foam (Zwaan *et al.* 2016; Chapter 2). This distributed extension is then transmitted to the overlying model materials.

In order to model orthogonal extension, the sidewalls of the orthogonal extension apparatus are merely moving apart in a perpendicular fashion (Fig. 5.2a, c). The subsequent extension is constant along strike, as in most previous studies of extensional

tectonics (e.g. Withjack & Jamison 1986; Michon & Merle 2000; Philippon *et al.* 2015).

In contrast, the scissor extension set-up involves rotation of the sidewall about an axis, dividing the model in a 65 cm long extensional and a 25 cm compressional domain (Fig. 5.2b, d), similar to the scissor tectonic setting in the Arctic (Fig. 5.1c). In both domains, deformation increased away from the scissor axis, where no deformation takes place. The far end of the scissor extension domain opens with the same velocity as the sidewalls in the orthogonal extension set-up (both 4 mm/h for a total of 8 mm, although M13 was run with half the velocity). Thin rods (1 cm thick, semi-cylindrical "seeds") of the PDMS/corundum sand mixture put on top of the basal viscous layer act as linear weak zones that simulate discrete crustal weaknesses (Fig. 5.2a, b, e, f). Here, deformation is localized since the overlying sand is locally thinner and thus weaker. The seeds are situated along the axis of the model and we applied different seed lengths (¼, ½, ¾ and 1 L (L being the equivalent of the extension domain length, Fig. 5.2e) to test the degree of localization the models need to produce propagating rift structures.

Except for one model (M13), the duration of every model run amounts to 5 hours for a total of 40 mm of extension at the end of the model run (ca. 13% extension, as all models were 30 cm wide at the start of the model run, Fig. 5.2c, d). We applied 30 min time steps for CT-scanning (a scan for every 4 mm of extension), yielding a detailed record of the 3D model evolution. Additional model surface measurements with a TRITOP ATOS III surface scanner on model M13 (Fig. 5.2g) enables topography evolution analysis. No sedimentation is implemented in this study, which is permissible since we are not comparing the detailed rift-internal structures (Zwaan *et al.* submitted; Chapter 4). We completed 13 experiments in total, of which further details are listed in table 5.2.
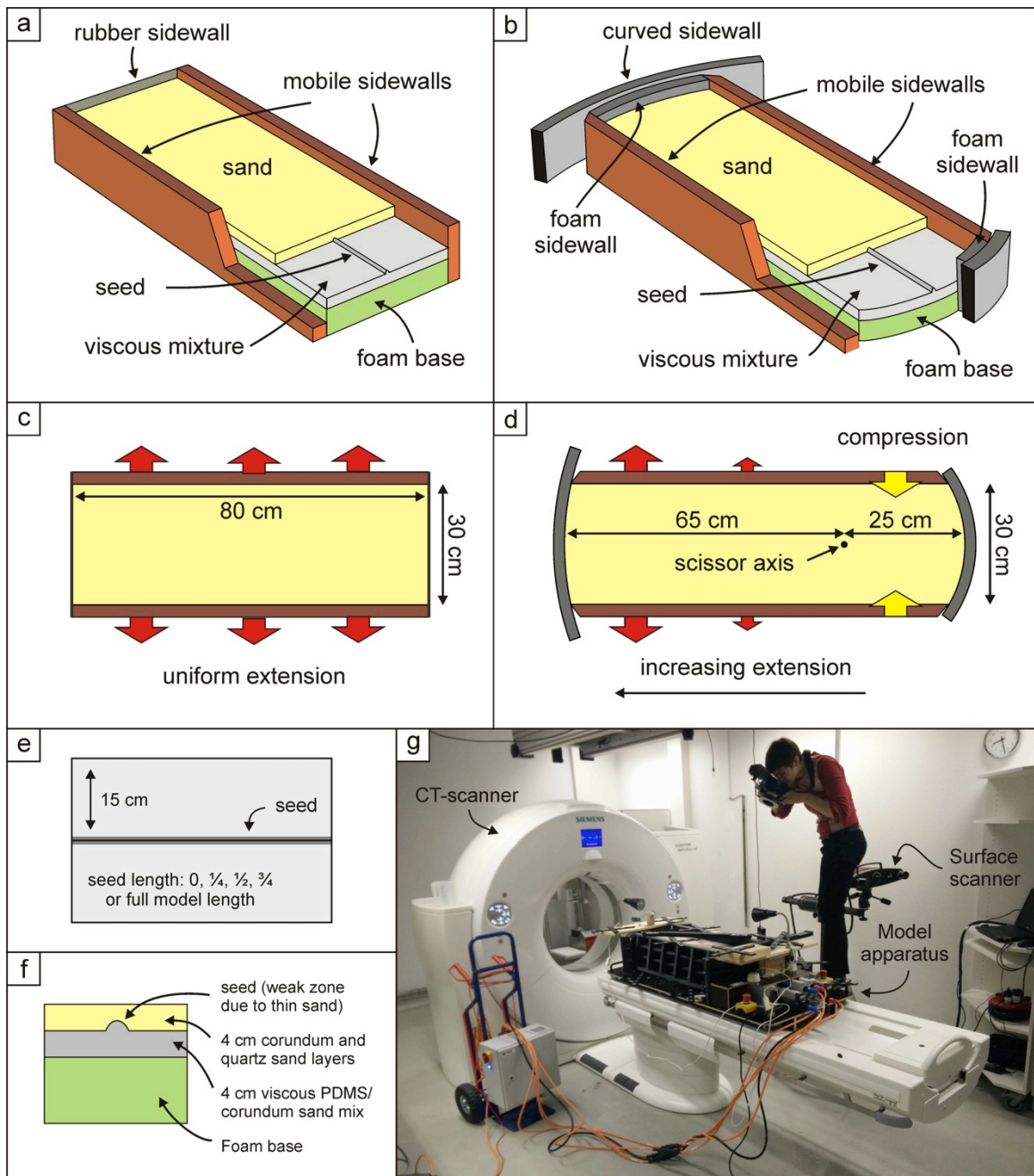
Fig. 5.2. *Model set-ups. (a) 3D set-up for the orthogonal extensional models. (b) 3D set-up for the scissor extensional models. (c) Top view depicting orthogonal extension deformation. (d) Top view illustrating scissor extension deformation. (e) Seed geometries. (f) Model layering. (g) example of a model (M13) scanned with XRCT and surface scanning techniques (photo by Jakub Fedorik).*

Table 5.1. *Material properties*

Granular materials	Quartz sand[a]	Corundum sand[b]
Grain size range	60-250 µm	88-175 µm
Density (specific)[c]	2650 kg/m^3	3800 kg/m^3
Density (sieved)	1560 kg/m^3	1890 kg/m^3
Angle of internal peak friction	36.1°	37°
Angle of dynamic-stable friction	31.4°	32°
Cohesion	9 ± 98 Pa	39 ± 10 Pa

Viscous material	PDMS/corundum sand mixture[a]	
Weight ratio PDMS : corundum sand	0.965 kg : 1.00 kg	
Mixture density	ca. 1600 kg/m^3	
Viscosity[d]	ca. 1.5·10^5 Pa·s	
Type	near-Newtonian (n = 1.05)[e]	

(a)   Quartz sand and viscous mixture characteristics after Zwaan & Schreurs (2016; Chapter 2)
(b)   Corundum sand characteristics after Panien *et al*. (2006) and Klinkmüller (2011)
(c)   Zirshot properties and specific densities of the sands after Carlo AG (2017)
(d)   The viscosity value holds for model strain rates < 10^{-4} s^{-1}
(e)   Stress exponent n (dimensionless) represents sensitivity to strain rate

Table 5.2. *Model characteristics*

Series	Model	Seed length	CT scanned	Surface scanned	Shown in
Orthogonal extension	M1	-			Fig. 5.3
	M2	¼ L (20 cm)			Fig. 5.3
	M3	½ L (40 cm)			Figs. 5.3, 5.4
	M4	¾ L (60 cm)			Figs. 5.3, 5.5
	M5	1 L (80 cm)			-
	M6	1 L (80 cm)	X		Figs. 5.3, 5.6-8
Scissor extension	M7	-			Fig. 5.3
	M8	¼ L (16.25 cm)			Fig. 5.3
	M9	½ L (32.5 cm)			Figs. 5.3, 5.4
	M10	¾ L (48.75 cm)			Figs. 5.3, 5.6
	M11	1 L (65 + 25 cm)			-
	M12	1 L (65 + 25 cm)	X		Figs. 5.3, 5.6, 5.9, 5.10.
	M13*	1 L (65 + 25 cm)	X	X	Figs. 5.11

* Model with 4 mm/h extension and 3 cm total extension

5.2.3. Model scaling

For a correct model scaling we calculate stress ratios (σ*, convention: σ* = σ$_{model}$/ σ$_{nature}$) with the following equation (Hubbert 1937; Ramberg 1981): $\sigma^* = \rho^* \cdot h^* \cdot g^*$, where ϱ*, h* and g* represent the density, length and gravity ratios respectively. The strain rate ratio $\dot{\varepsilon}^*$ is acquired from the stress ratio σ* and the viscosity ratio η* (Weijermars & Schmeling 1986): $\dot{\varepsilon}^* = \sigma^*/\eta^*$. Then, the velocity ratio v* and time ratios t* are derived with the following equations: $\dot{\varepsilon}^* = v^*/h^* = 1/t^*$. Since the lower crust has a wide viscosity range, (η = 10^{19}-10^{23}, e.g. Buck 1991), 1 hour in our models scales up to 0.008-0.8 Ma in nature and our model velocity (8 mm/h) translates to 0.05-500 mm/y. Typical rift extension velocities fit in this range (several mm/y, e.g. ArRajehi *et al*. 2010, Fig. 5.1b). All scaling parameters are listed in Table 5.3.

In order to ensure dynamic similarity between the brittle model materials and their natural equivalents in the upper crust, we derive the ratio R$_s$, from the gravitational stress and cohesive strength or cohesion C (Ramberg 1981; Mulugeta 1998): R$_s$ = *gravitational*

stress/cohesive strenght $= \rho \cdot g \cdot h/C$. For viscous materials, the Ramberg number R_m applies (Weijermars & Schmeling 1986): $R_s =$ *gravitational stress/viscous strenght* $= \rho \cdot g \cdot h^2/(\eta \cdot v)$. The R_m value of 74 plots in the natural range of 1.2-1200 and the

R_s values are quite similar with values of 25.5 and 9.2 for the model and natural materials respectively. Also the R_m value of Model M13 is in accordance with the natural values. Therefore we consider our model adequately scaled.

Table 5.3. *Scaling parameters*

	General parameters			Brittle upper crust		Ductile lower crust		Dynamic scaling values	
	Gravitational acceleration g (m/s^2)	Crustal thickness h (m)	Extension velocity v (m/s)	Density ϱ (kg/m^3)	Cohesion C (Pa)	Density ϱ (kg/m^3)	Viscosity η (Pa·s)	Ramberg number R_m	Brittle stress ratio R_s
Model	9.81	0.08	2.2·10^{-6} (1.1·10^{-6})[a]	1560	9	1600	1.5·10^5	74 (147)[a]	25.5 (25.5)[a]
Nature	9.81	4·10^4	1·10^{-10}	2800	7·10^{7} [b]	2900	1·10$^{19 \text{ to } 23}$ [c]	1.2·10$^{0 \text{ to } 4}$	9.2

(a)   Between brackets: values for Model M13 (different extension velocity)
(b)   Cohesion value after Corti *et al*. (2004)
(c)   Viscosity range after Buck (1991)

5.3. Model results

5.3.1. Top view model analysis

We present an overview of the experimental results in Fig. 5.3. Both model set-ups have in common that without a seed, deformation is concentrated along the longitudinal sidewalls (Fig 5.3. a, f). When a ¼ L is applied, a modest rift basin forms and limited rift propagation occurs (Fig. 5.3b, g), which is deflected towards the lower sidewall in the orthogonal extension set-up (M2, Fig. 5.3b). Most of the deformation is however taken up by boundary effects along the sidewalls.

A ½ L seed produces significantly more rift localization than the previous models (Figs. 5.3c, h, 5.4). After ca. 30 min, faulting initiates along the seeds (Fig. 5.4b, g). Subsequently the rifts propagate away from the seed, along the full model length in orthogonal extension model M3 (Fig. 5.3c, 4e) and about half the distance between the seed tip and the rotation axis in model M9 (Fig. 5.3h, 4j). The final rift propagation distance seems to be established relatively early during the model run: after ca. 60 min for M3 (Fig. 5.4c) and ca. 120 min for M9 (Fig. 5.4i). Instead of the orderly, symmetric rift structures above the seeds, the propagating rift parts of the rifts in both set-ups exhibit curved

and more random fault geometries. Also the boundary effects in model M3 (Fig. 5.3c) are more significant in the right-hand sided half of the model, towards which the rift propagates.

In the ¾ L case (Fig. 5.3d, i), we observe a similar result as with the ½ L models (Figs. 5.3c, h, 5.4). Also here, the seed localizes early faulting (after some 30 min, Fig. 5.5b, g), forming a symmetric rift structure while the propagating part of the rift develops later on (after 60-120 min, Fig 5.4c, i) and tends have a more random configuration. There are slightly stronger boundary effects visible along the sidewalls perpendicular to the propagating rift. For orthogonal extension model M4 (Figs. 5.3d, 5.5a-e), the rift propagates along the entire length of the model, similar to the ½ L equivalent (M3, Figs. 5.3c, 5.4e). Yet the rift in model M10 (Fig. 5.3i, 5.5j) propagates further towards the scissor axis than seen in model M9 (Fig. 5.3h, 4j) and compared to orthogonal extension model M4 (Fig. 5.3d), model M10 contains a along-strike structural gradient involving a well-developed rift structure to the left that dies out towards the scissor axis to the right.

A full model length seed generates rift localization along the central axis of the model

in both set-ups (Fig. 5.3e, j, Fig. 5.6). The orthogonal extension model M6 (Fig. 5.3e) develop a continuous and symmetric rift basin along the full length of the model. This structure is formed early on (at t = 30 min, Fig. 5.6b) and subsequently grows in scale as extension progresses. The scissor extension equivalent model M12 also contains an early rift basin after some 30 min (Fig. 5.6g). Yet this basin progressively propagates towards the scissor axis with on-going extension and almost reaches the axis at the end of the model run (Figs. 5.3j, 5.6j). Within the compressional domain on the other side of the scissor axis in model M12 and unique to this model set-up, a thrust develops, due to the presence of a seed in that part of the model (Figs. 5.3f-j, 5.6f). It should be noted that every modelops a limited degree of boundary effects along the longitudinal sidewalls.
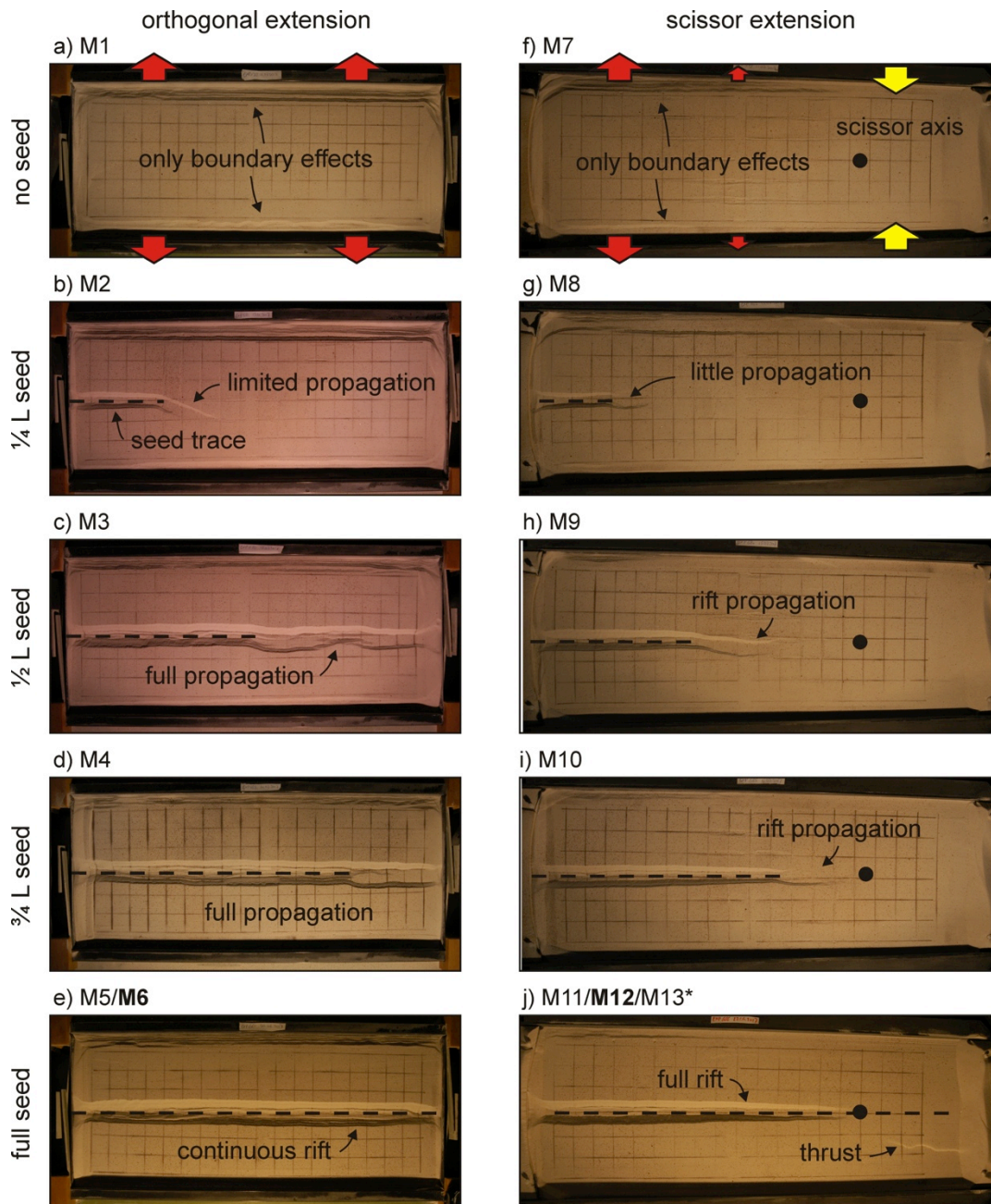
Fig. 5.3. *Overview depicting the final surface structures of both model series and their relations to the initial seed geometries and scissor axis locations. *model M13 has a slightly different set-up (see Table 2), yet very similar structures as models M11 and M12, the latter is shown here.*
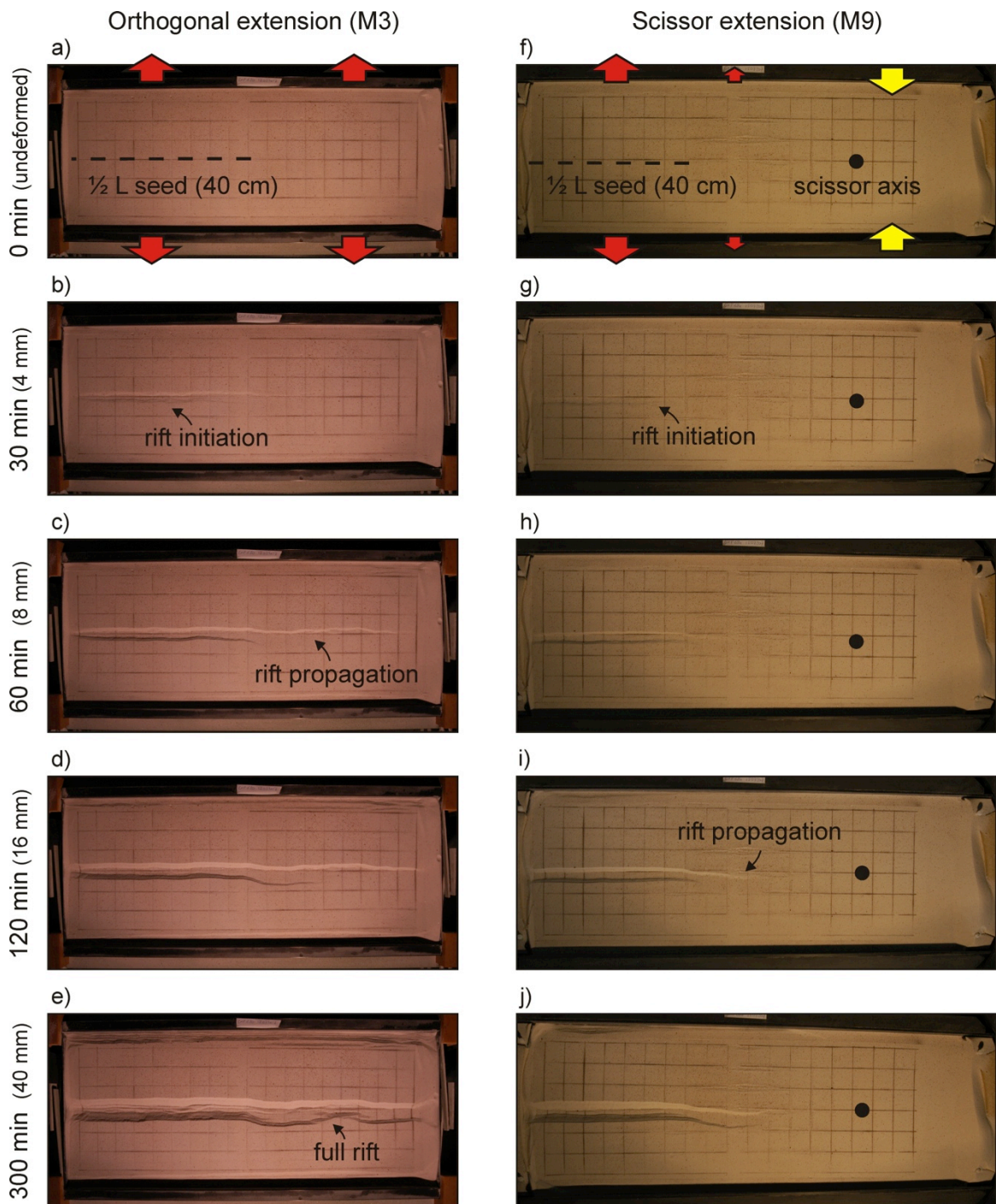
Fig. 5.4. *Top view images depicting the surface evolution of models M3 and M9 (½ L seed).*
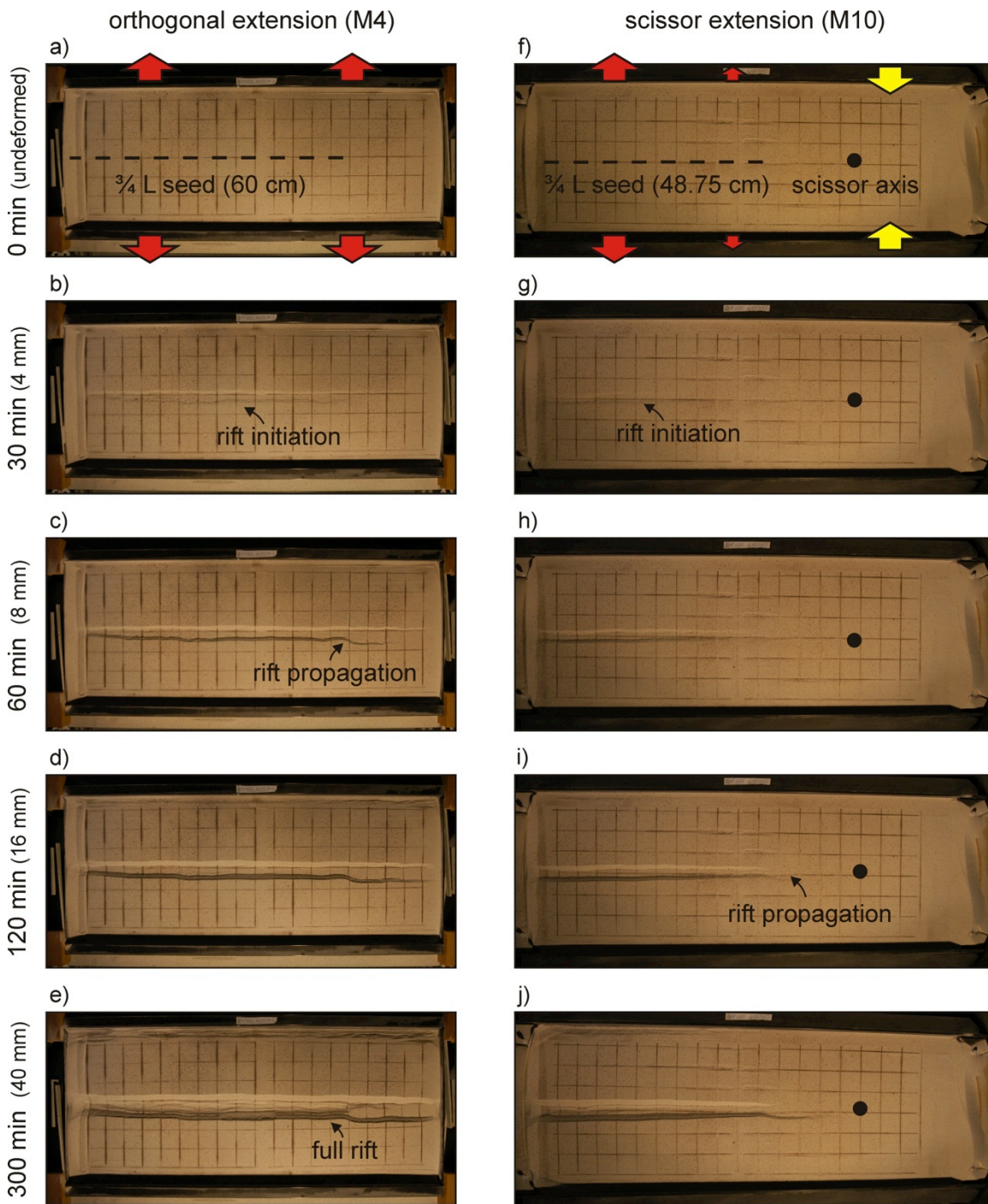
Fig. 5.5. *Top view images depicting the surface evolution of models M4 and M10 (¾ L seed).*
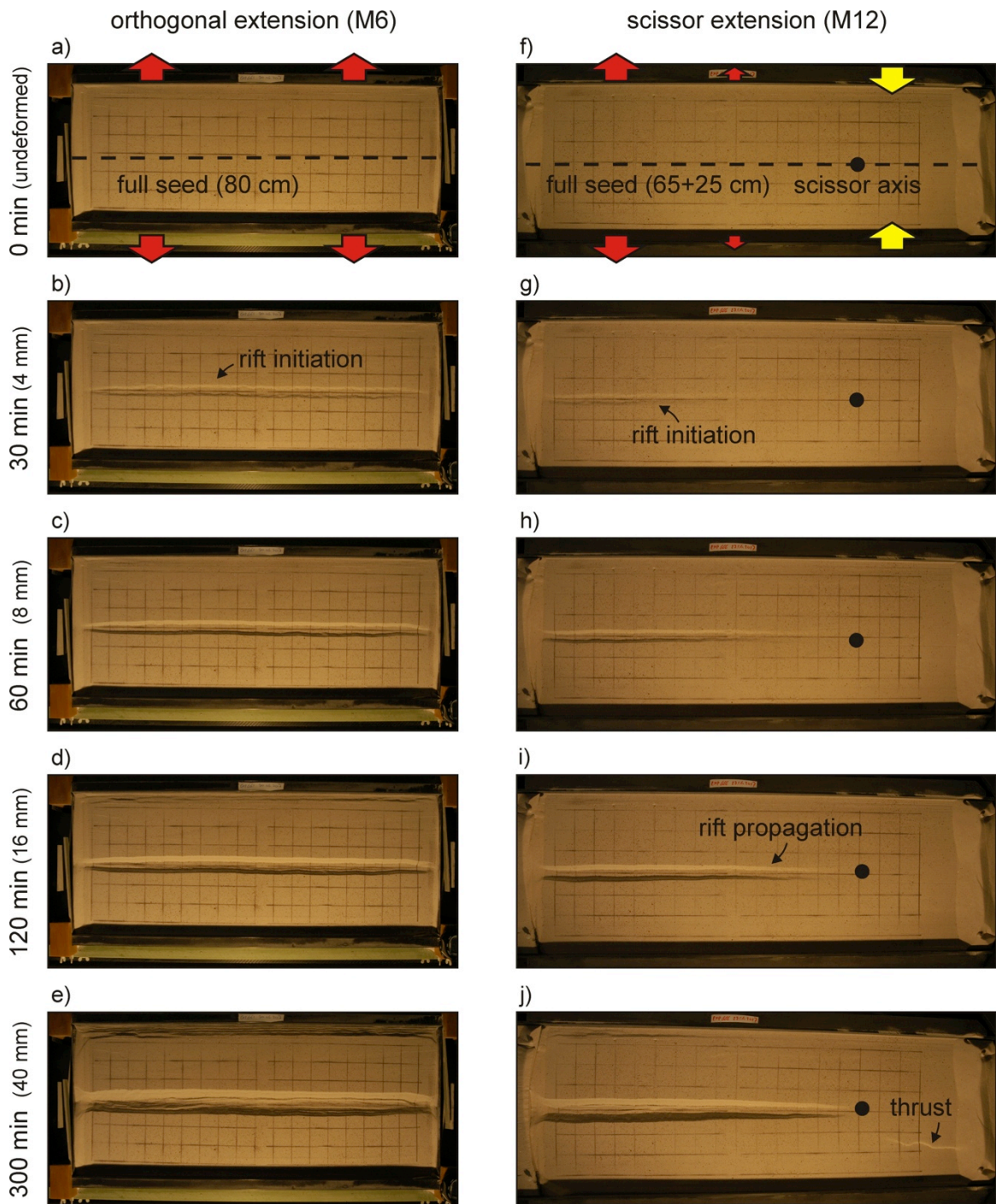
Fig. 5.6. *Top view images depicting the surface evolution of models M6 and M12 (1 L seed).*

5.3.2. 3D CT analysis of models M6 and M12

The full-length seed models seem to have produced the most distinct model results and the most outspoken differences between both set-ups and were therefore selected for a rerun (M6 and M12). The scissor machine was applied another time with a slightly different set-up (M13, details in Table 5.2 and sections 2.2) but yielded very similar results as M12 and will be discussed in Paragraph 5.3.3.

The 3D CT-derived topography snapshots and horizontal/vertical CT sections depicting the 40 cm central segment of orthogonal extension experiment M6 illustrate the model internal evolution and the links with the model surface (Figs. 5.7, 5.8). Early on (t = ca. 30 min, Figs. 5.7b, 5.8b), a symmetric graben establishes itself above the full length of the seed and the rift wedge starts subsiding between the rift boundary faults. Yet after 120 min (Fig. 5.7d, 5.8d), the rift wedge starts to break up. Meanwhile, the viscous layer rises below the rift. These combined processes cause the viscous layer to reach the model surface at t = 300 (Fig. 5.8f) with on both sides the remains of the rift wedge, while the two major boundary faults flank the overall graben structure. The along-strike structural continuity the model develops is outstanding.

In contrast to scanning only the model centre as for model M6, we scanned the whole of scissor extension model M12 to capture its structural evolution along its full deformation gradient (Figs. 5.9, 5.10). As with its orthogonal extension equivalent, a symmetric graben structure appears after ca. 30 min (Figs. 5.9c, 5.10b). As seen on the model, (Figs. 5.3, 5.6), the CT images reveal the effect of the deformation gradient from the initiation of the model run on, with the more developed rift structures in the outer part of the extension domain (Figs. 5.9c, 5.10b). The extension gradient causes more deformation and subsidence away from the axis, resulting in the propagation of rift-related faulting as the less evolved parts of the rift attain the deformation stages the outer parts of the rift already went trough (Figs. 5.9, 5.10). The model thus contains a deformation gradient in both time (compare any section in Fig 10 and its equivalent during the model run) and space (e.g. compare section 1 from Fig. 5.10c with section 2 and section 3 from Fig. 5.10d and Fig. 5.10e, respectively). The other striking feature in model M6 is the development of a thrust on the opposite side of the rotation axis after ca. 120 min (Fig. 5.10c). It is clearly rooted in the seed (Fig. 5.10c, d, e) and causes relative uplift of the hanging wall highlighted by the bright coloration in Fig. 5.9d-f.
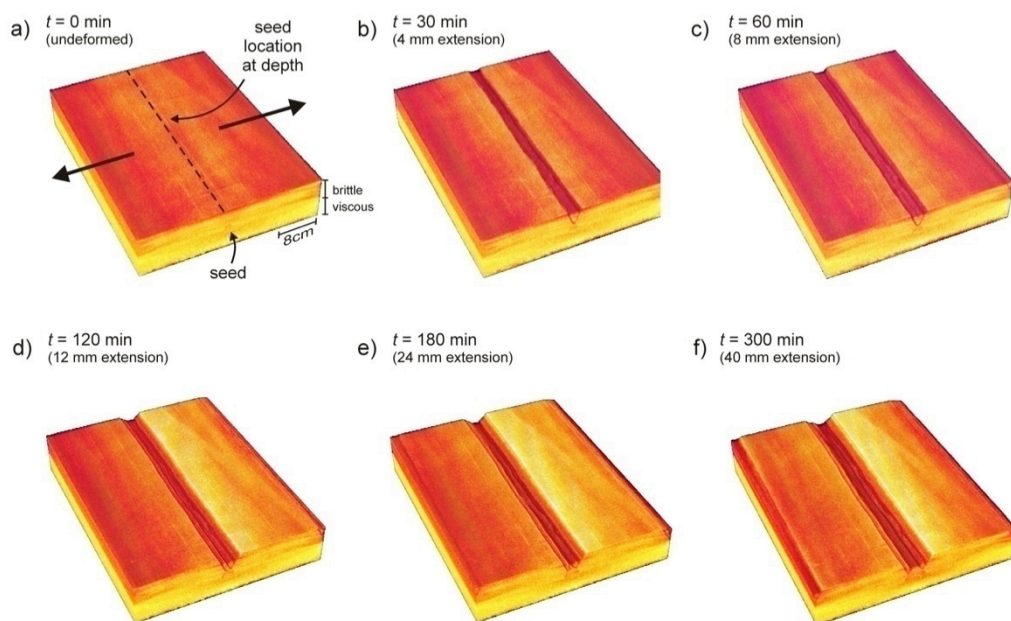
Fig. 5.7. *CT-derived 3D topography evolution of model M6 (orthogonal extension, 1 L seed).*
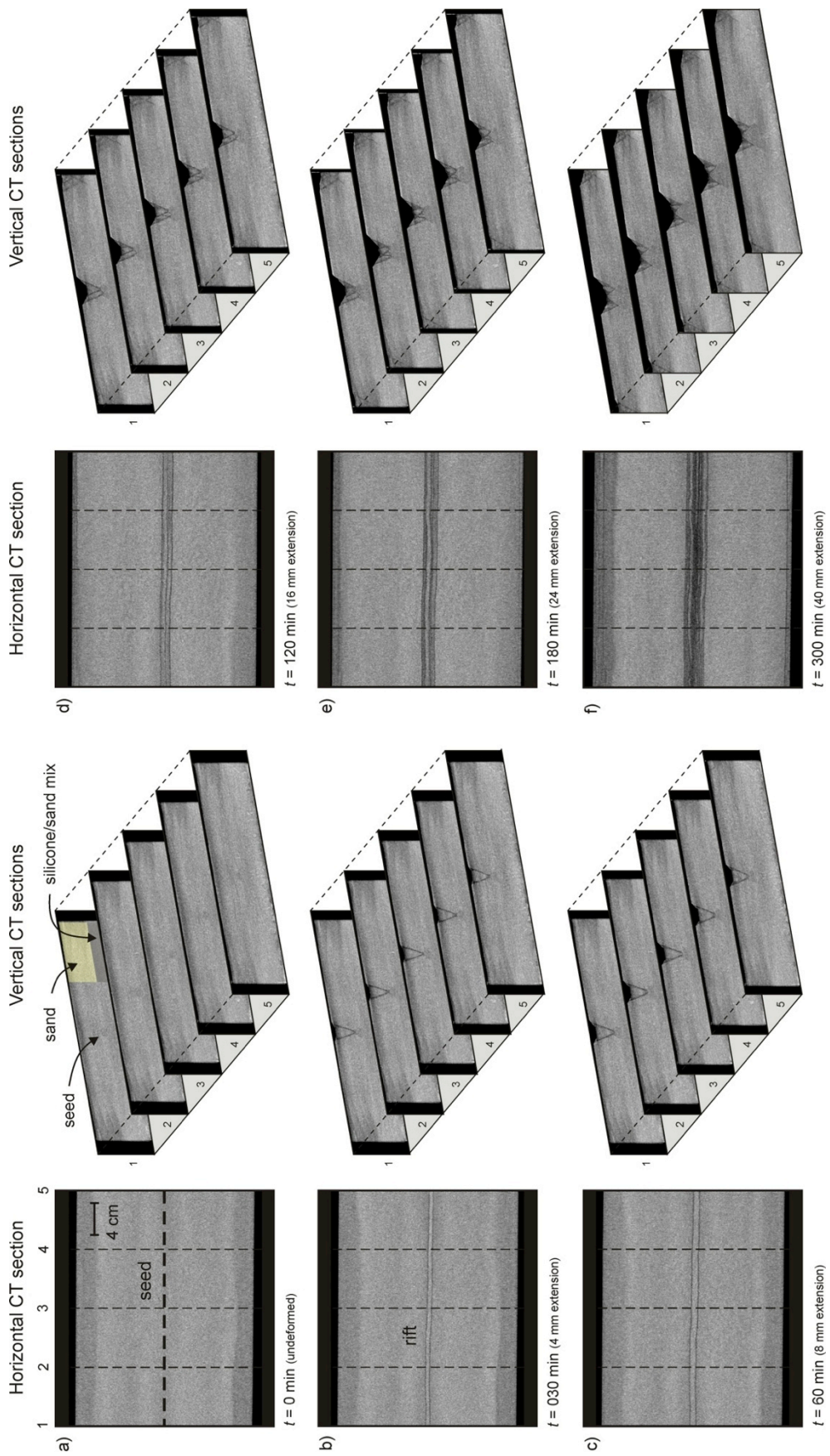
Fig. 5.8. *CT-derived 3D internal evolution of model M6 (orthogonal extension, 1 L)*
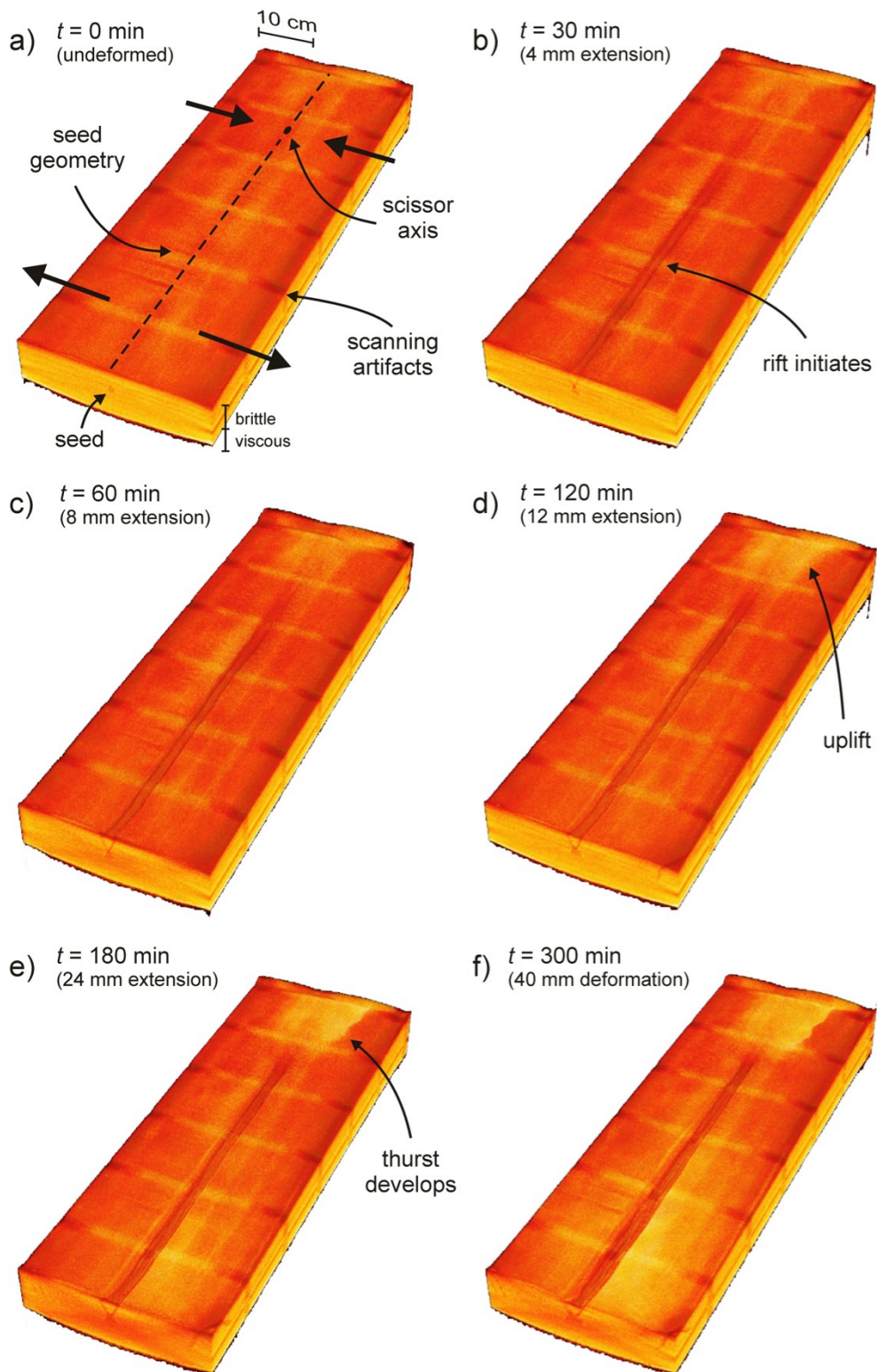
Fig. 5.9. *CT-derived 3D topography evolution of model M12 (scissor extension, 1 L seed).*

154
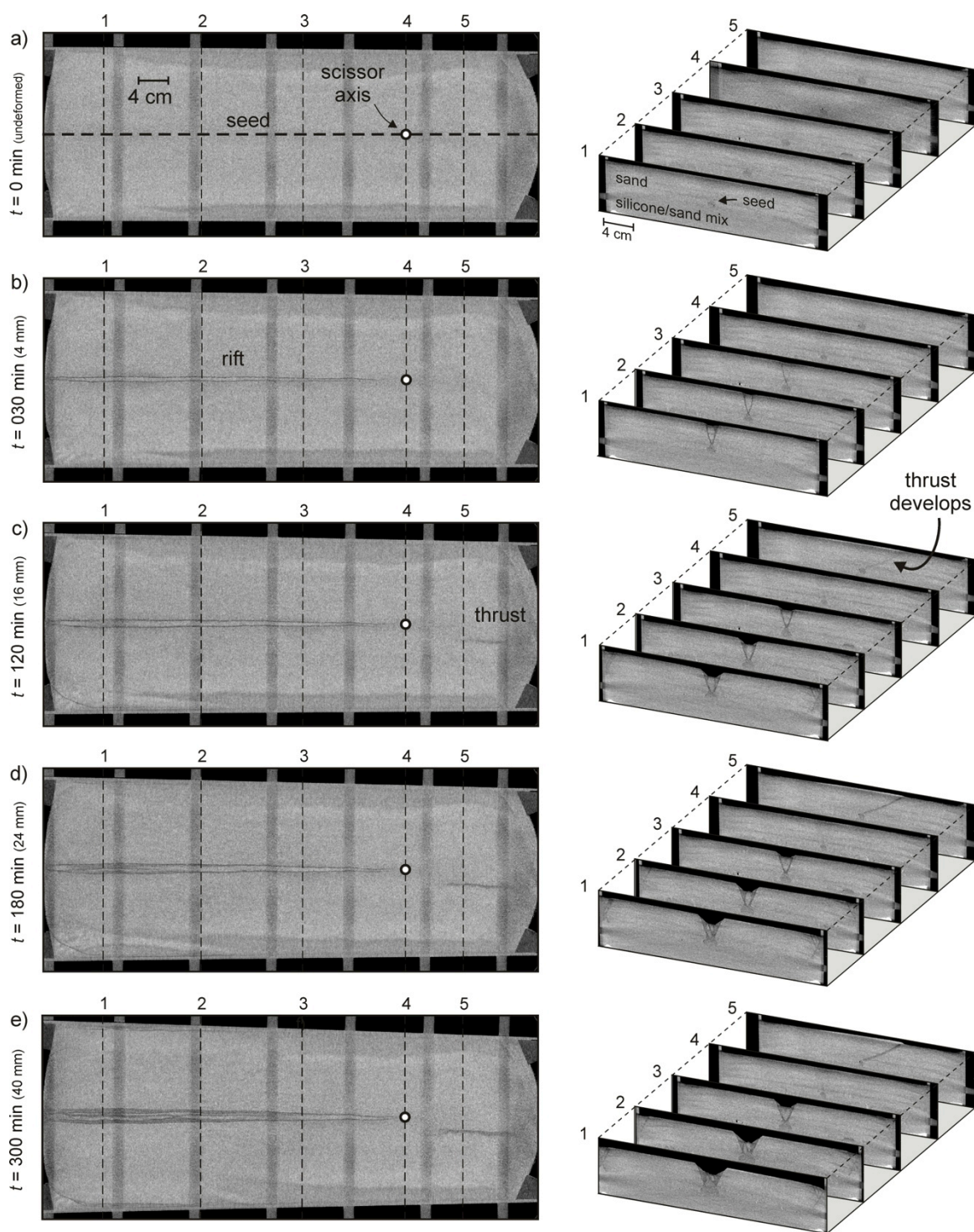
Fig. 5.10. *CT-derived 3D internal evolution of model M12 (scissor extension, 1 L seed).*

5.3.3. 3D Topography and CT analysis of model M13

Model M13 has the same basic set-up as model M12 (full seed length, Fig. 5.11). The lower extension velocity with respect to the other models (4 mm/h instead of 8 mm/h for a total of 30 mm extension) is not expected to have an important influence on the model structures as these are already well localized due to low brittle-ductile coupling, an effect only favoured by lower strain rates (e.g. Zwaan *et al*. 2016; Chapter 2).

The use of surface scanning techniques allows a detailed model topography analysis, revealing a similar evolution as model M12 (Fig. 5.11a, b). Rifting initiates above the seed after 180 min (12 mm extension, equivalent to 90 min in model M12), causing subsidence that propagates towards the scissor axis with increasing extension (Fig. 5.11a, b). In the mean time, thrusting and uplift occurs in the compressional domain and the initial basin steadily deepens. The vertical motion analysis (Fig. 5.11b) also reveals the "regional subsidence" that occurs in the extensional domain, while the compressional domain shows thrusting and significant uplift. CT-scans (Fig. 5.11c, d) illustrate how this uplift is due to the formation of two thrusts in a pop-up configuration.

a) 3D topography evolution
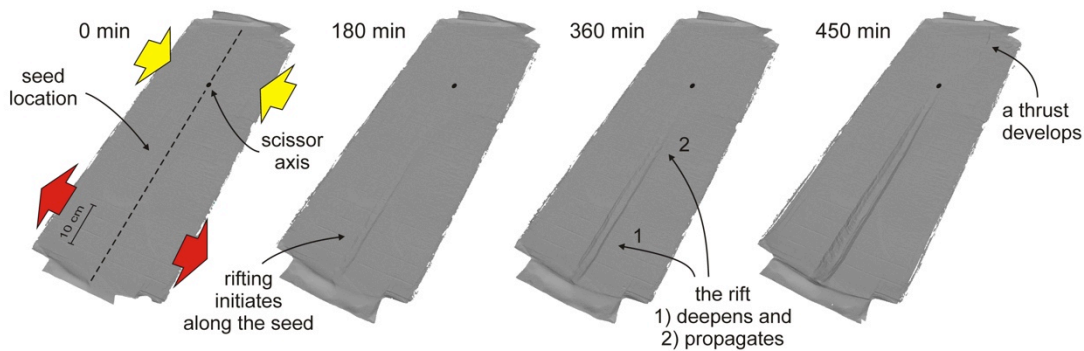
b) Vertical motion analysis
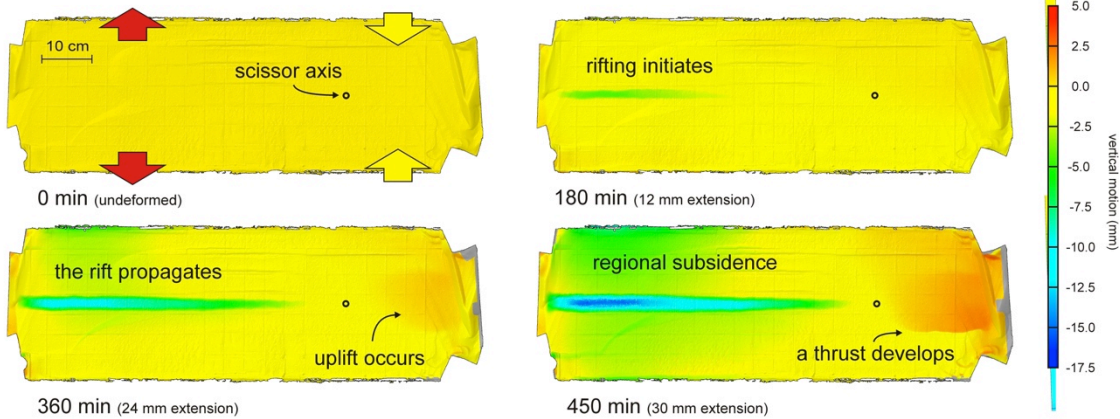
c) Horizontal CT-section (final stage, t = 450 min)
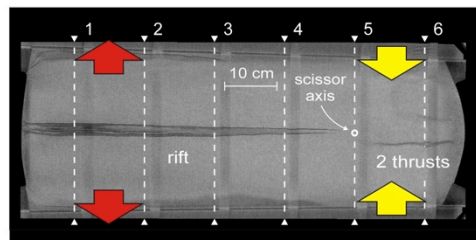
d) Vertical CT-section
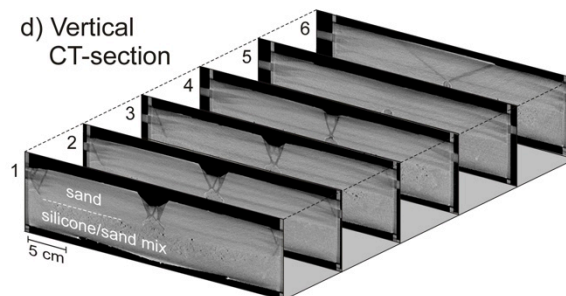
Fig. 5.11. (previous page). *Topography and internal analysis of M13. (a) 3D surface scanner results, depicting the model evolution. (b) Vertical motion analysis, indication sunsidence and uplift in the model with respect to the intial topography. (c) Horizontal section through the brittle part of the model and (d) vertical sections through the model, depicting the internal structures at the end of the model run.*

_____

5.4. Discussion

5.4.1. Rift propagation

The models with no or short seeds (Fig. 5.3a, b, f, g) show no or little rift propagation. Instead, strong boundary effects along the sidewalls take up most of the deformation. It appears that our model set-up requires a certain minimum seed length in order to localize a rift structure that can subsequently propagate. This critical seed length lies between ¼ and ½ L, as all models with a seed length of ½ L or larger form propagating rifts that develop freely as they are not strongly controlled by the presence of a seed (Figs. 5.3c-e, h-j, 5.4, 5.5).

The orthogonal extension models with rift propagation pose a problem, as one would expect the structure to open simultaneously along the full length of the model, considering the rigid behaviour of sand above a viscous layer (Zwaan *et al.* submitted; Chapter 4) and the constant extension rate along-strike, as seen in 1 L model M6 (Fig. 5.3e, 5.6a-e, see also Fig. 1.8). However, part of the extension seems to be taken up by stronger boundary effects perpendicular to the propagating rift so that the latter develops more slowly, potentially inducing some rotation effects (Figs. 5.4a-e, 5.5a-e), suggesting that pure orthogonal extension alone does not lead to rift propagation. A similar rotation associated with rift propagation occurs in the near-orthogonal extension models by Mart & Dauteuil (2000). It is logical that the most developed rift segments in our scissor extension models are found away from the scissor axis, where most extension takes place, and that deformation propagates towards the scissor axis with increasing extension (Fig. 5.3, 4f-j, 5f-j). This is also true for a full seed length scissor extension model, while in contrast the orthogonal extension equivalent forms a continuous rift (Figs. 5.3e, j, 5.6).

5.4.2. Propagating rift details

The propagating rift structures are different from those forming above the seed, as the former have more freedom to evolve (Figs. 5.3b-d, 5.4, 5.5). This is best seen in model M3 (Figs. 5.3c, 5.4a-e), which develops curvy boundary faults and strong rift width variations, but similar effects are present in the other models as well. Most interesting are the increased rift width combined with the tendency to deflect slightly. These effects are probably the result of the thicker sand cover at the edge of the seed; as the sand becomes thicker and the boundary fault angles remains constant, the rift geometry relations demand a wider rift (e.g. Allemand & Brun 1991; Zwaan *et al.* 2016; Chapter 2, Fig. 1.5f). The rift deflection also resembles the models by Benes & Scott (1996) in which a propagating oceanic rift enters a continental lithosphere and is widened and (slightly) deflected. Natural analogues of this setting would be the Havre Trough in New Zealand (Benes & Scott), the Woodlark Basin in Papua new Guinea (Benes *et al.* 1994) and the Laptev Margin in the Arctic (Drachev *et al.* 1998; Van Wijk & Blackman 2005, Fig. 5.1c).

5.4.3. Full seed models

In contrast to the models with a seed that does not cover the full model length, models M6, M12 and M13 fully localize deformation throughout the model. The CT-scans of these models clearly reveal the differences between both set-ups: while pure orthogonal extension in model M6 created a continuous graben with nearly identical structures along-strike (Figs. 5.7, 5.8), the extension gradient in scissor extension models M12 and M13 produce a graben with a clear structural gradient (Figs. 5.9-11), which also changes with time as deformation and the rift basin structures

propagate towards the less developed parts of the rift closer to the scissor axis.

The surface scans of model M13 furthermore quantify vertical changes on the model surface, clearly indicating the formation of a rift depocenter and its propagation toward the scissor axis as well as a general subsidence in the extensional domain (Fig. 5.11b). This general subsidence is due to the extending and simultaneously thinning viscous layer, similar to the behaviour of the lower crust in passive rifting settings (Huismans *et al*. 2001). This would fit with our set-up that does not take the lithospheric mantle and the asthenosphere into account, which can have important influences on the regional topographies (e.g. doming due to mantle plume emplacement, Underhill & Partington 1993; Moucha & Forte

2011). Similar regional subsidence as in the scissor tectonics setting occurs throughout the orthogonal extension models as well (compare the sections from Fig. 5.8a' with those from Fig. 5.8f', where the black part of the section represents the free air).

In contrast, the compressional domain either remains at a stable level or is uplifted above the pop-up structure (yellow and orange-red in Fig. 5.11b, respectively). Together with the extensional domain, this forms a complete scissor-tectonic system, as seen in the Arctic (Fig. 5.1c). Yet there are some differences as the Gakkel Ridge is an oceanic basin and the Laptev margin represents a continent-ocean boundary (e.g. Franke *et al*. 2001), while our model only simulates the continental crust.

5.5. Conclusion and outlook

We ran various analogue tectonic experiments to assess the differences in rift development and propagation under orthogonal extension and scissor extension conditions, providing the following insights:

- Our model method require significant localization of deformation in order to create a rift that subsequently propagates;
- Scissor extension is a key factor in rift propagation, even in the orthogonal extension models, slight rotational motion seems to be involved in the actual rift propagation;
- Stretching of the viscous lower crust is expected to cause regional subduction.
- Overall, the fundamental difference between both set-ups is that orthogonal extension results in a full symmetrical and continuous rift structures, while scissor extension has rifting initiating at the far end of the model before propagating to the scissor axis with increased deformation.

In order to further investigate this model series, the following steps are planned:

- All models were sprinkled with coffee grains to create a pattern for particle image velocimetry (PIV) analysis (e.g. Molnar *et al.* 2017), which might reveal the exact horizontal motions in the models, in order to better understand the mechanics involved in rift propagation in our orthogonal extension models;
- The CT data from models M6 and M12 allows the extraction of their topography for every time step, enabling 1) a similar 4D subsidence/uplift analysis as done for model M13 and 2) a 4D comparison between the topography evolution of orthogonal and scissor extension models;
- As the model materials are mixed with small amounts of zirshot, it would be possible to apply Digital Volume Correlation (DVC, Adam *et al.* 2013; Zwaan *et al.* submitted; Chapter 4) to the CT data from models M6 and M12, for a highly detailed assessment of 4D (internal) model deformation;
- Future modelling efforts could focus on reproducing the Arctic scissor tectonic system.

5.7. Acknowledgements

Chapter 6

Evolution of rift linkage zones in orthogonal and scissor extension settings: insights from analogue models analysed with 4D X-ray computed tomography

Frank Zwaan[a] *, Guido Schreurs[a]

a) Institute of Geological Sciences, University of Bern, Baltzerstrasse 1+3, CH-3012 Bern, Switzerland

_____

Abstract

When simulating rift systems, analogue and numerical modellers often apply a continuous extension rate along the strike of a rift or rift system. Yet in nature, significant extension velocity variations are observed along strike, as the natural consequence of tectonic plates moving apart about a pole of rotation, resulting in scissor extension and rift propagation. Such extension gradients may have an effect on developing rift interaction structures, therefore we present various analogue tectonic experiments to assess the differences between rift linkage zones forming in orthogonal extension settings versus scissor extension settings, involving various degrees of rift underlap. Our modelling efforts give the following results: 1) Although scissor extension and orthogonal extension produce quite different large-scale structures, local features in a scissor extension systems can be regarded as evolving in an orthogonal extension setting since the extension gradient between the two rifts are often negligible. 2) Various degrees of underlap produce three basic modes of rift linkage structures. Low underlap distance (high angle ϕ) experiments develop rift pass structures. With increasing underlap distance (ϕ = ca. 40°), transfer zone basins develop. High degrees of underlap ($\phi \leq 30°$), tend to result in sub-basins. 3) Several of these structures are found in previous model studies and in nature. Yet a direct comparison is challenging, as various parameters might modify their structural development significantly.

_____

6.1. Introduction

When simulating rift systems, analogue and numerical modellers often apply a continuous extension rate along the strike of a rift or rift system (e.g. Michon & Merle 2000; Van Wijk & Blackman 2005). This is true for models of both orthogonal and oblique extension, where the direction of extension is at an angle with the extensional structure (e.g. McClay & White 1995; Van Wijk 2005; Philippon *et al*. 2015). Even in models involving changing extension obliquities along strike, the extension velocity remains constant (e.g. Corti *et al*. 2007).

Yet in nature, we often observe significant extension intensity variations along strike, as the natural consequence of tectonic plates moving apart about a pole of rotation (e.g. Martin 1984; Van der Pluijm & Marshak 2004), resulting in rift propagation. Such extension gradients exist in the Red Sea and the Gulf of Aden oceanic basins (Fig. 6.1a), caused by the anticlockwise rotation of the Arabian peninsula (Bosworth *et al*. 2005; ArRajehi *et al*. 2010). Other examples may befound in the East African Rift System (EARS), where the Western branch of the EARS and the Kenya Rift curve around the Tanzania Craton (Fig. 6.1b), and in the Arctic, where the Gakkel Ridge displays an increasing extension velocity towards the North Atlantic (Dick *et al*. 2003, Fig. 6.1c).

The few analogue modelling studies involving such extension gradients focussed on the transition from a localized spreading centre into deformation-dissipating continental crust as observed at the Havre Trough, New Zealand (Benes & Scott 1996) and the Laptev Margin (Fig. 6.1c). Other studies involve subduction rollback in the Pacific Kuril Basin (Schellart *et al*. 2002; 2003) and the opening of the South China Sea (Sun *et al*. 2009). A recent study by Molnar *et al*. (2017) assesses the influence of large-scale lithospheric weaknesses on rift propagation in the Red Sea. Chapter 5 of this Thesis illustrates how rift propagation in scissor extension settings is distinctly different from the orthogonal extension equivalent.

Another important feature that is commonly associated with rift structures is their tendency to develop along structural inheritances such as old faults or shear zones, locally thinned lithosphere or old orogenic belts (e.g. Corti 2012 and reference therein). As a result, the initial rift basins are often poorly aligned and need to link up to form a continues rift structure, as currently observed in the EARS (e.g. Corti 2012, Fig. 6.1b) or the Gulf of Suez (e.g. Corti 2004). These rift linkage structures are classified as transfer zones when hard linkage occurs trough fault linkage, while in an accommodation zone soft linkage takes occurs, i.e. faults do not connect but overlap each other and deformation is distributed (Rosendahl 1987; Larsen 1988; Childs *et al*. 1995; Faulds & Varga 1998). A proper understanding of linkage zone evolution is of importance to describe rift evolution towards continent break-up, as these structures may represent the predecessor of later transform structures in the oceanic domain (Bellahsen *et al*. 2013). In addition, linkage zones can influence the migration of melts and hydrocarbons (Corti *et al*. 2004; Minor *et al*. 2013), providing complex structural traps (Paul & Mitra 2013) in e.g. the Norwegian Viking Graben (Fossen *et al*. 2010) and rift and passive margin settings in general.

Various modelling studies have focussed on the evolution of such structures, highlighting the importance of primary and secondary structural inheritances and their geometry, the influence of extension velocity and direction (e.g. Elmohandes 1981; Acocella *et al*. 1999a; Tentler & Acocella 2010, Brune *et al*. 2012; Zwaan *et al*. 2016; Zwaan & Schreurs 2017; Chapters 2, 3). Yet to date, none has explored the influences of along-strike extension gradients on the development of rift interaction zones. Therefore, we here compare the development of rift linkage structures in either orthogonal extension settings (constant extension velocity along strike) or scissor extension settings (extension gradient along strike) as observed in our laboratory experiments. For a more detailed comparison between both settings, we apply various degrees of underlap in our analogue models as

well (comparable to Tentler & Acocella 2010; Allken *et al.* 2011, 2012).

The model techniques are similar to those described in Chapter 5, involving a distributed type of deformation, allowing more freedom for the rifts and transfer zones to develop.

Selected models are scanned with the use of X-ray computed tomography (XRCT or CT) techniques to reveal their 3D internal evolution. The model results are subsequently compared with previous models and natural examples.
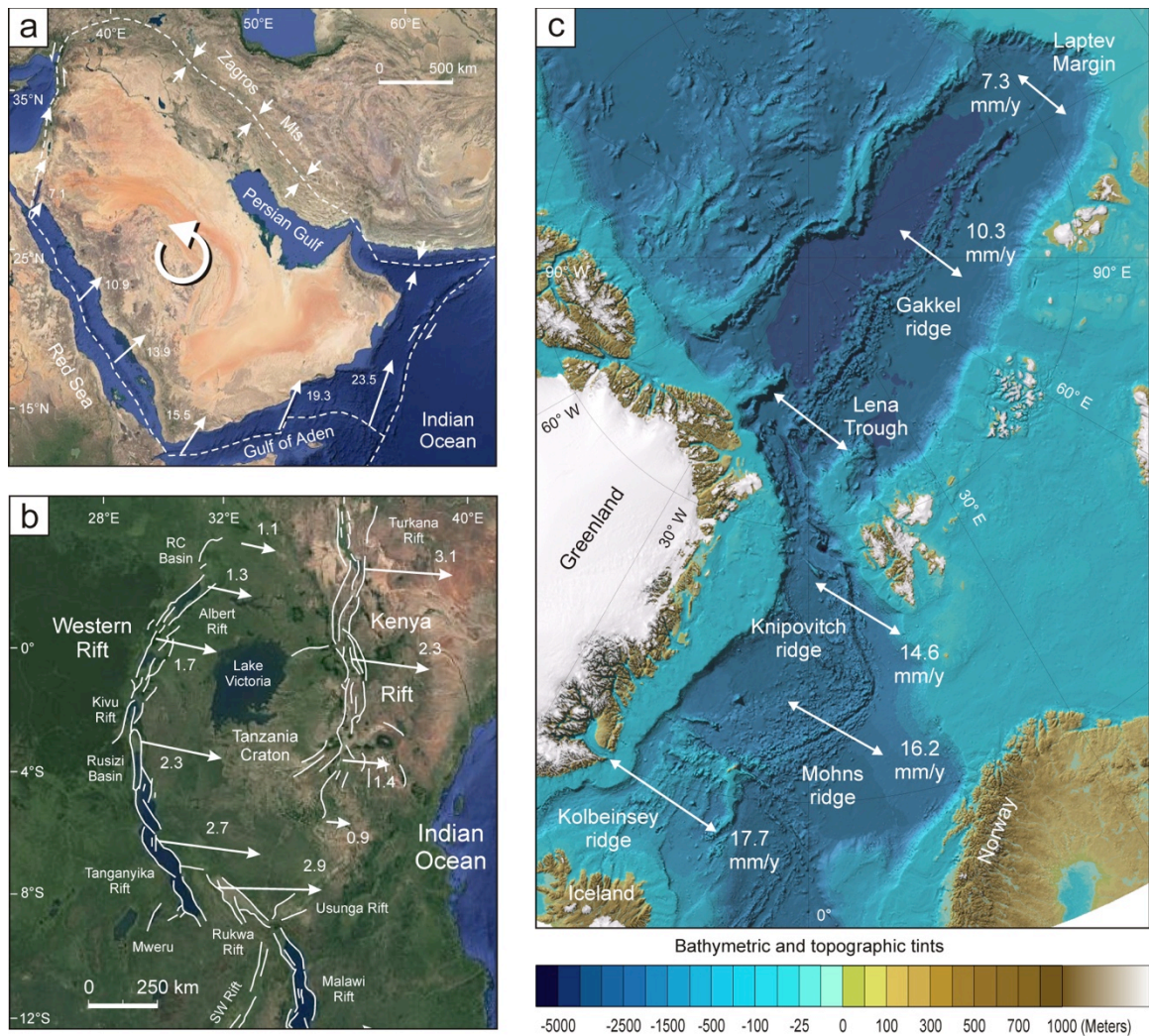
Fig. 6.1. *Natural examples of extension gradients. (a) Block rotation of the Arabian peninsula, causing along-strike extension gradients in the Red Sea and the Gulf of Aden oceanic basins. Dotted limes indicate plate boundaries. Image modified after Bellahsen et al. (2003), Bosworth et al. (2005) and ArRajehi et al. (2016). Satellite images after Google Earth. (b) Distribution of rift segments, transfer zones and associated sediments basins in the East African Rift System, as well as current extension directions and velocities. RC Basin: Rhino-Camp Basin. Image modified after Ebinger (1989), Acocella et al. (1999a) and Saria et al. (2014) Satellite images after Google Earth. (c) Artic region, showing an increasing extension velocity along the Gakkel Ridge towards the North Atlantic. Image modified after Dick et al. (2003) and Jakobsson et al. (2012). Velocities in mm/h.*

6.2. Materials and methods

6.2.1 Material properties

Both brittle and viscous materials are applied in our models, representing the brittle and ductile parts of the continental crust, respectively. The 20 km brittle upper crust is modelled by a 4 cm thick layer of fine quartz sand (ø = 60-250 μm), sieved from ca. 30 cm height into the experimental apparatus, ensuring a constant sand density of ca. 1560 kg/m^3. We also flatten the sand using a scraper at every cm during the build-up of the model, to create slight density differences. This "layering" subsequently appears on CT images (Fig. 6.6).

We apply a 4 cm thick viscous layer to simulate a 20 km thick lower crust. The viscous material is a mixture of near-Newtonian (η = ca. 1.5·10^5 Pa·s; n = 1.05) SGM-36 Polydimethyl-siloxane (PDMS) and dense corundum sand ($\varrho_{specific}$ = 3950 kg/m^3 and ø = 88-175 μm, Panien *et al*. 2006; Klinkmüller 2011; Carlo AG 2017) following a 0.965 : 1.00 weight ratio. The density of this viscous mixture is close to that of the overlying quartz sand (ca. 1600 kg/m^3), yielding a density profile that is closer to the natural situation than pure low density PDMS (ϱ = ca. 960 kg/m^3) would have it, simultaneously preventing strong buoyancy effects. Further material properties are presented in Table 1.

6.2.2. Experimental set-up

We use 2 different machines with the same basic deformation mechanism, involving a compressed foam base between two longitudinal sidewalls on which the model materials are applied (Fig. 6.2a, c). During a model run, precise computer-controlled motors drive the sidewalls apart. Consequently, the foam expands uniformly, causing distributed extension that is transferred to the overlying model materials.

The main difference between both set-ups lies within the sidewall motion. In the orthogonal extension set-up (M-series, Fig. 6.2a, c), the sidewalls move apart in a perpendicular fashion, producing uniform extensional deformation along strike applied in most rifting model studies. For the scissor tectonic setting however, the sidewalls pivot around a scissor axis that divides the model in a 65 cm long extensional and a 25 cm long compressional sector (S-series, Fig. 6.2b, d), although we shall ignore the structures developing in the compressional domain in this paper as they have no influence on the extensional domain (Chapter 5). Both sectors develop a deformation gradient away from the scissor axis, where no faulting takes place. The far end of the extensional domain in the scissor set-up moves with the same velocity as the sidewalls in the orthogonal extension set-up (both 4 mm/h for a total of 8 mm/h).

In order to contain the model materials and to diminish boundary effects, we use either rubber or curved foam sidewalls at the short ends of the models (Fig. 6.2b). These uniformly deforming materials decrease boundary effects at the model edges while the curvature of the foam is necessary to allow for a smooth pivoting of the sidewalls in the scissor extension set-up. A 4 x 4 cm grid on the model surface yields a first-order impression of surface deformation. Furthermore, every component of the machine around the model consists of X-ray transparent materials to allow for CT-scanning and selected models are analysed with CT-techniques to reveal their 3D internal evolution (Fig. 6.2g).

Thin rods (1 cm thick, semi-cylindrical "seeds") of the viscous PDMS/corundum sand mixture on top of the basal viscous layer (Fig. 6.2a, b, e, f), act as linear weak zones and represent discrete crustal weaknesses since the strong sand cover is locally thinner and thus weaker above the seeds, causing deformation to localize (Fig. 6.2f). Seed offset is 2 H for all models (Fig. 6.2f), equivalent to twice the brittle layer thickness (8 cm), in order to avoid rift proximity effects (Zwaan *et al*. 2016; Chapter 2). Various degrees of seed underlap (measured by angle φ) are applied (similar to Zwaan and Schreurs 2017; Chapter 3)

The duration of every model run amounts to 5 hours, for a total of 40 mm of extension. We applied 30 min time steps (4 mm of extension) for CT-scanning of selected experiments, yielding a detailed record of the 3D model evolution. No sedimentation is implemented for our models. We completed 29 experiments in total, the details of which are summarized in table 6. 2.
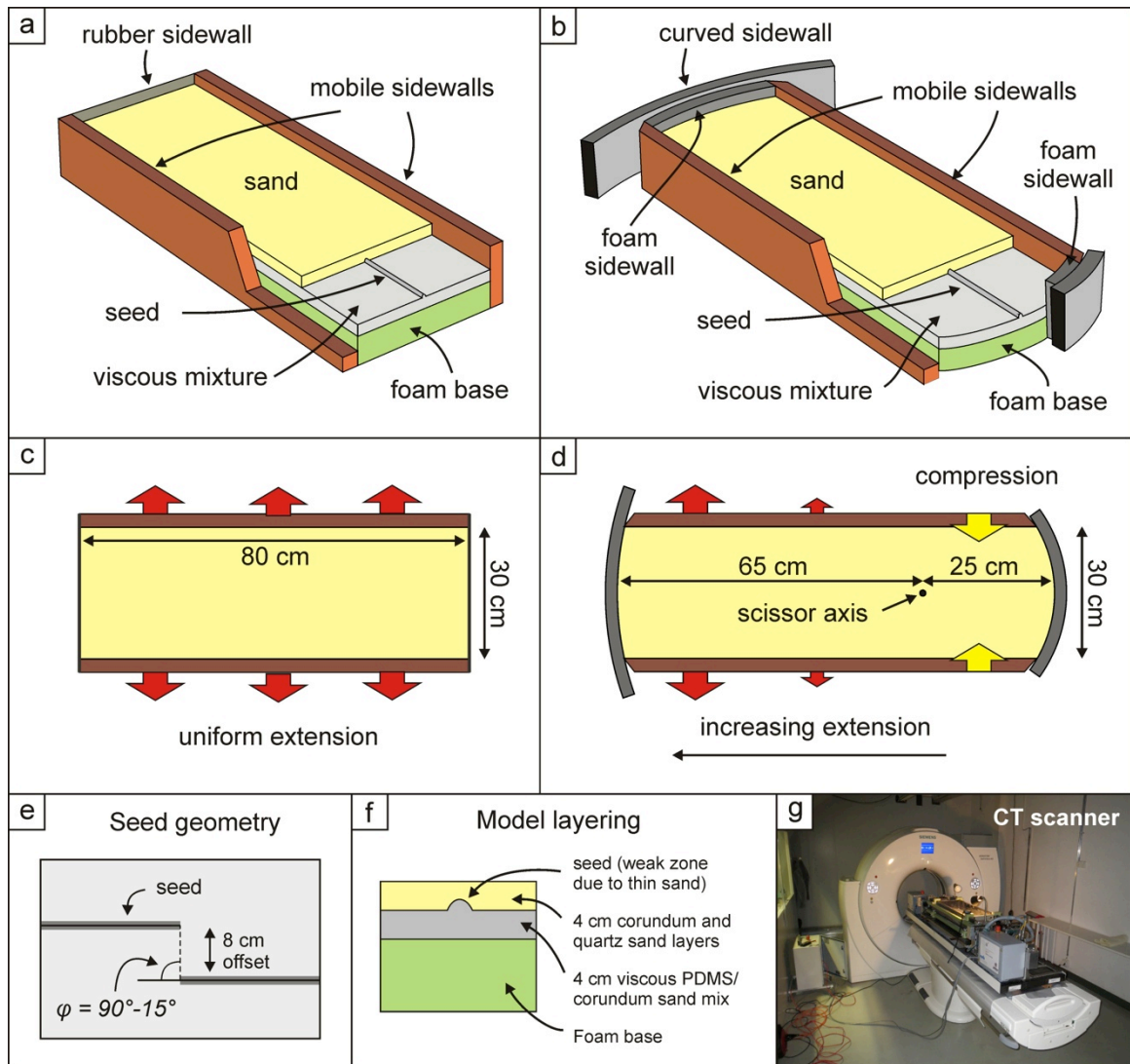
Fig. 6.2. *Model set-up. (a-b) Cut-out views of the normal extension apparatus (a) and scissor extension apparatus (b), depicting their various components. (c-d) Top views of the deformation applied in the normal extension set-up (c) and the scissor extension set-up (d). (e) Seed geometry definition. Angle φ is the angle between the seed strike and the horizontal line connecting the two seed tips, ranging between 90° and 15° in this paper. (f) Model layering, showing the brittle-ductile parts of the models, on top of the foam base, as well as the seed. (g) Example of a model run in the CT scanner.*

Table 6.1. *Material properties*

Granular materials	Quartz sand[a]	Corundum sand[b]
Grain size range	60-250 µm	88-175 µm
Density (specific)[c]	2650 kg/m^3	3800 kg/m^3
Density (sieved)	1560 kg/m^3	1890 kg/m^3
Angle of internal peak friction	36.1°	37°
Angle of dynamic-stable friction	31.4°	32°
Cohesion	9 ± 98 Pa	39 ± 10 Pa

Viscous material	PDMS/corundum sand mixture[a]
Weight ratio PDMS : corundum sand	0.965 kg : 1.00 kg
Mixture density	ca. 1600 kg/m^3
Viscosity[d]	ca. 1.5·10^5 Pa·s
Type	near-Newtonian (n = 1.05)[e]

(a) Quartz sand and viscous mixture characteristics after Zwaan & Schreurs (2016; Chapter 2)
(b) Corundum sand characteristics after Panien *et al.* (2006) and Klinkmüller (2011)
(c) Dpecific densities of the sands after Carlo AG (2017)
(d) The viscosity value holds for model strain rates < 10^{-4} s^{-1}
(e) Stress exponent n (dimensionless) represents sensitivity to strain rate

Table 6.2. *Model parameters*

	Model	Seed (angle ϕ)	Shown in		Model	Seed (angle ϕ)	Shown in
Orthogonal extension models	M1	90°	Fig. 6.3, 6.13	Scissor extension models	S1	90°	Fig. 6.3
	M2	90°			S2	90°	
	M3	60°	Fig. 6.3		S3	60°	Fig. 6.3
	M4	50°	Fig. 6.3		S4	50°	Fig. 6.3
	M5	45°	Fig. 6.3		S5	45°	Fig. 6.3
	M6	40°			S6	45°	
	M7	40°	Figs. 6.3, 6.13		S7	40°	Fig. 6.3
	M8	30°	Fig. 6.4		S8	30°	Figs. 6.3, 6.7, 6.9
	M9[CT]	30°	Fig. 6.3-6		S9	30°	Fig. 6.7-9
	M10	30°	Fig. 6.4		S10[CT]	30°	Fig. 6.7
	M11	20°	Figs. 6.3, 6.11		S11[a]	30°	Fig. 6.8
	M12	15°	Fig. 6.3		S12[b]	30°	Fig. 6.8
					S13[c]	30°	Fig. 6.9
					S14	20°	Fig. 6.10
					S15[CT]	20°	Figs. 6.10-12
					S16	20°	Figs. 6.3, 6.10
					S17	15°	Fig. 6.3

(CT) CT-scanned model
(a) Transfer zone center 5 cm to the left
(b) Transfer zone center 5 cm to the right
(c) Thicker seed test

Table 6.3. *Scaling parameters*

	General parameters			Brittle upper crust		Ductile lower crust		Dynamic scaling values	
	Gravitational acceleration g (m/s^2)	Crustal thickness h (m)	Extension velocity v (m/s)	Density ϱ (kg/m^3)	Cohesion C (Pa)	Density ϱ (kg/m^3)	Viscosity η (Pa·s)	Ramberg number R_m	Brittle stress ratio R_s
Model	9.81	0.08	2.1·10^{-6}	1560	9	1600	1.5·10^5	78	25.5
Nature	9.81	4·10^4	1·10^{-10}	2800	7·10$^{7\ a}$	2900	1·10$^{19\ to\ 23\ b}$	1.2·10$^{0\ to\ 4}$	9.2

(a) Cohesion value after Corti *et al.* (2004)
(b) Viscosity range after Buck (1991)

6.3. Model results

6.3.1. Overview of model results

We present a selection of the final model results in Fig. 6.3, an overview depicting the various structures that develop under normal (orthogonal) extension and scissor extension conditions (Fig. 6.3a and 3b, respectively).

In the normal extension set-up (Fig. 6.3a), rift basins form above the initial seeds in all experiments. For models with underlap angle ϕ down to 45°, rifts propagate roughly parallel to each other. In most cases, one of the rift branches is dominant and can (almost) reach the other rift structures (e.g. $\phi = 50°$, M4 in Fig. 6.3a). Only in the $\phi = 90°$ case, both rifts are propagating equally, creating a rift pass structure (Nelson *et al.* 1992) between them, involving slight rotation as indicated by the deformed surface grid (M1 in Fig. 6.3). Similar rotation occurs in all models with 90° > $\phi \geq 45°$.

However, the $\phi = 40°$ setting (M7 in Fig. 6.3) marks a distinct change in structural style, as the main rift segments connect by forming continuous rift boundary faults and a transfer zone basin with some oblique internal faults in between. When the rift underlap distance increases (i.e., decreasing angle ϕ), these oblique structures form en echelon rift basins between the main rift segments (M11 and 12 in Fig. 6.3a). The larger the underlap distance, the larger the intermediary basin. Some block rotation is involved as well, best visible in the $\phi = 20°$ case (M11 in Fig. 6.3a).
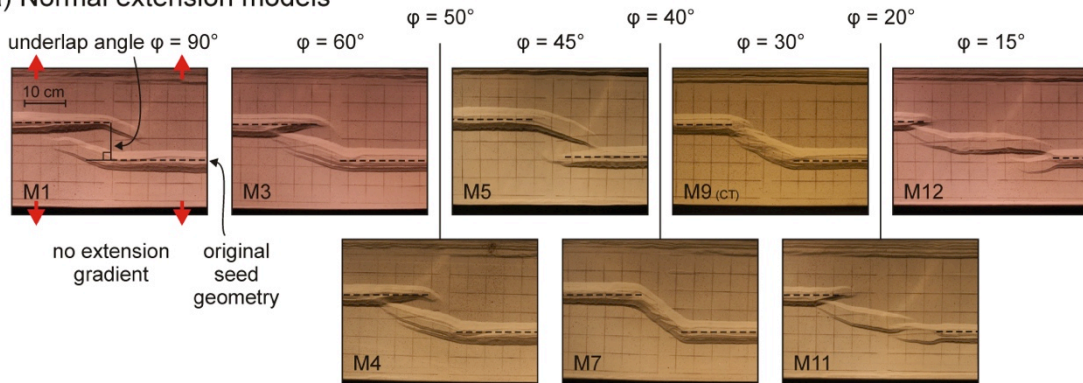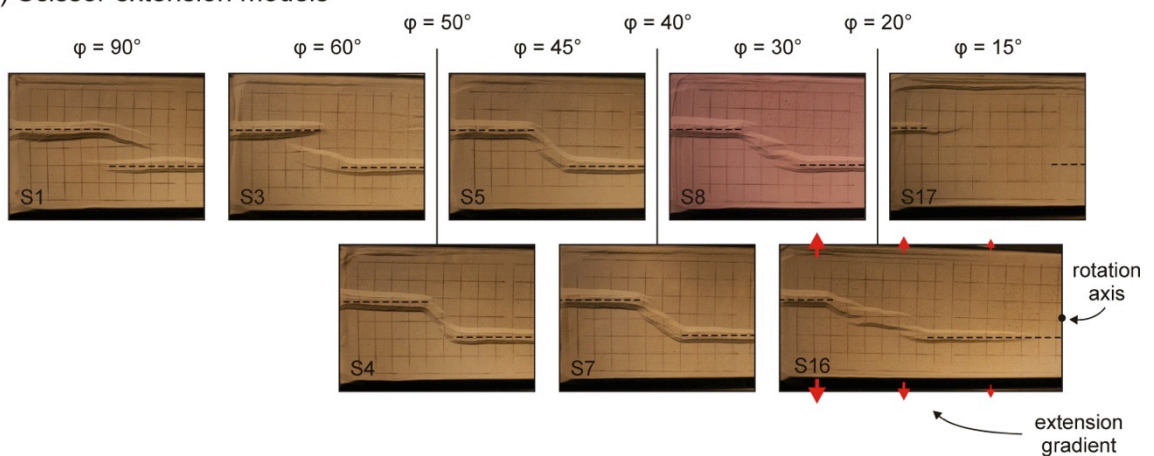
Fig. 6.3. *Surface structure overview of model results from both (a) the orthogonal extension models and (b) the scissor extension models as a function of rift underlap (angle ϕ).*

When scissor extension is applied, the results are quite similar to those of the orthogonal extension experiment (Fig. 6.3b). Also here, we observe propagating rift segments when angle ϕ is high. However, the transition from rift pass and accommodation zone geometries to a continuous transfer zone structure occurs a bit earlier than in the normal extension models, with ϕ = 50° and continues to ϕ = 40° (S6 and S7 in Fig. 6.3b, respectively). When angle ϕ decreases to 30° (S8 in Fig. 6.3b), the transfer zone becomes segmented and with ϕ = 20° (S16 in Fig. 6.3b) a full intermediary basin develops. In both cases, the system develops slight block rotation.

A significant difference with the orthogonal extension models however, is the width of the rift segments. In the scissor extension experiments, rift width is largest to the left, where most extension is concentrated and most narrow towards the scissor axis to the right, where deformation is less intense (best visible in the uncropped top view S16 in Fig. 6.3b). The extension gradient causes the model to develop almost no structures in the ϕ = 15° model (S17 in Fig. 6.3b). Instead, most deformation is directed to the sidewalls.

6.3.2. Linkage zone variability (orthogonal extension, ϕ = 30°)

An important observation is that the models exhibit a certain structural variability; Fig. 6.3 displays the models that provide a best fit, i.e. a logical order of structures. Yet some models have been repeated, occasionally yielding results that seem more typical of models with a slightly lower or higher underlap angle. For example, the ϕ = 30° orthogonal extension setting can either produce a continuous transfer zone basin (M8, Fig. 6.4a, b), an accommodation zone with an en echelon basin between both main rifts (M10, Fig. 6.4e, f) or an intermediate form (M9 in Figs. 6.3a, 6.4c, d). In effect, the surface structure of model M9 seems closer to the continuous transfer zone basin observed in model M8. Yet when the sand is removed to reveal the topography of the deformed viscous layer (Fig. 6.4b, d, f), the deeper structure shows more affinity with that of model M10 than the clean continuous trace of the M8 transfer zone. Furthermore, the transfer zone from model M8 is quite

similar to the one in model M7 (ϕ = 40°, Fig. 6.3a), as is the accommodation zone from model M10 quite similar to the one in M11 (ϕ = 20°, Fig. 6.3a), so that the ϕ = 30° model setting might indicate a transition between different rift linkage modes.

The CT data from transitional model M9 reveal the structural evolution of such a transitional rift linkage structure (Figs. 6.5, 6.6). Early after model initiation, simple symmetric rifts develop above the seeds and start propagating towards each other (Figs. 6.5b, 6.6b, b'). These rift branches do not directly link, but grow past each other, while one of them develops a small-scale sub-basin (Figs. 6.5c, d, 6.6c, c', d, d'). As deformation progresses and rift-internal structures grow more complex, the barriers between these rift arms dwindle and a continuous transfer zone basin develops (Figs. 6.5e, 6.6e, e'). Yet the internal structures, however complex, remain separated at depth until the end of the model run (Fig. 6.6f, f').

6.3.3. Linkage zone variability (scissor extension, ϕ = 30°)

Also the ϕ = 30° scissor extension models have a significant variety in their rift linkage structures (Fig. 6.7). Model S8 (Figs. 6.3, 6.7a, b) is quite similar to its orthogonal equivalent model M9 (Figs. 6.3a, 6.4c, d, 6.5, 6.6). Yet models S9 and M10 (Fig. 6.7c-f) both develop a dominant rift basin on the left-hand seed, which propagates towards the right-hand, underdeveloped rift basin. The underdevelopment of these rift basins is probably related to the scissor extension set-up, in which less deformation takes place towards the right, where the scissor axis is situated in our experiments (e.g. S16 in Fig. 6.3). However, in model S8 (Figs. 6.3b, 6.7a, b) this secondary rift arm is considerably more developed.

A hint is provided by a test in which the linkage zone centre is either shifted 5 cm to the left or 5 cm to the right with respect to the normal set-up (S11, S12 and S9 in Fig. 6.8, respectively). It appears that the normal and set-up (S9) and the right-shifted model (S12), in which rift linkage is not established, see a relatively late development of the second rift

(Fig. 6.8g,l). In contrast, model S11 does develop early localization of the second rift, and subsequent rift linkage (Fig. 6.8a-e). Another test was done with a thicker seed (1.5 mm diameter compared to the standard 1 mm) on the right-hand seed (S13 in Fig. 6.9e, f). This additional model also establishes early localization and rift linkage.
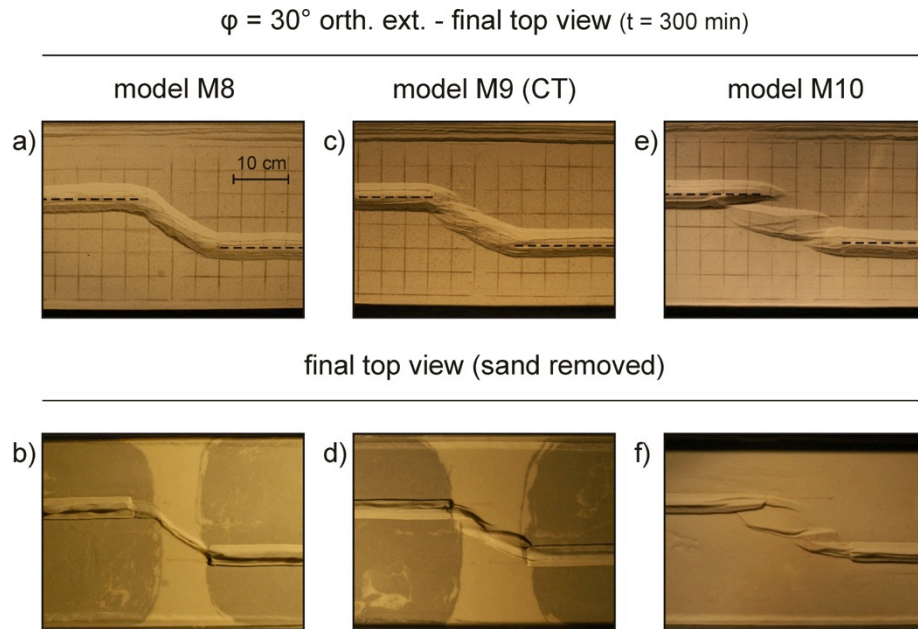
Fig. 6.4. *Structural variation within φ = 30° models M8-10 (orthogonal extension).*
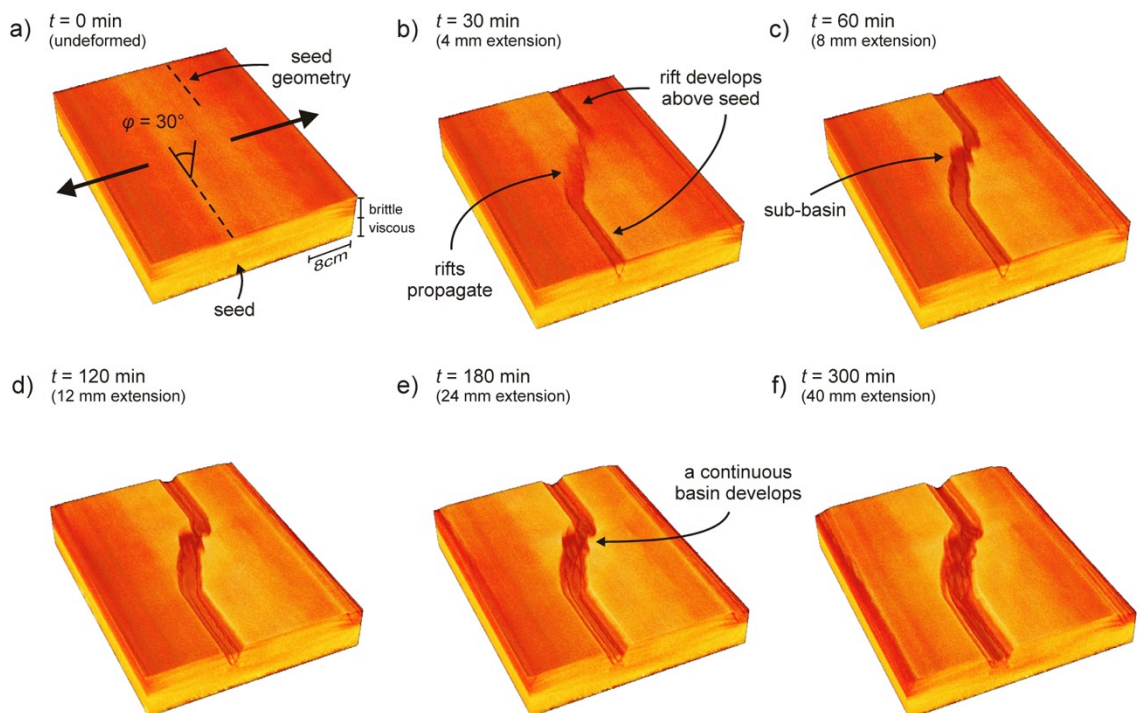
Fig. 6.5. *CT-derived 3D topography evolution of model M9 (orthogonal extension, φ = 30°).*
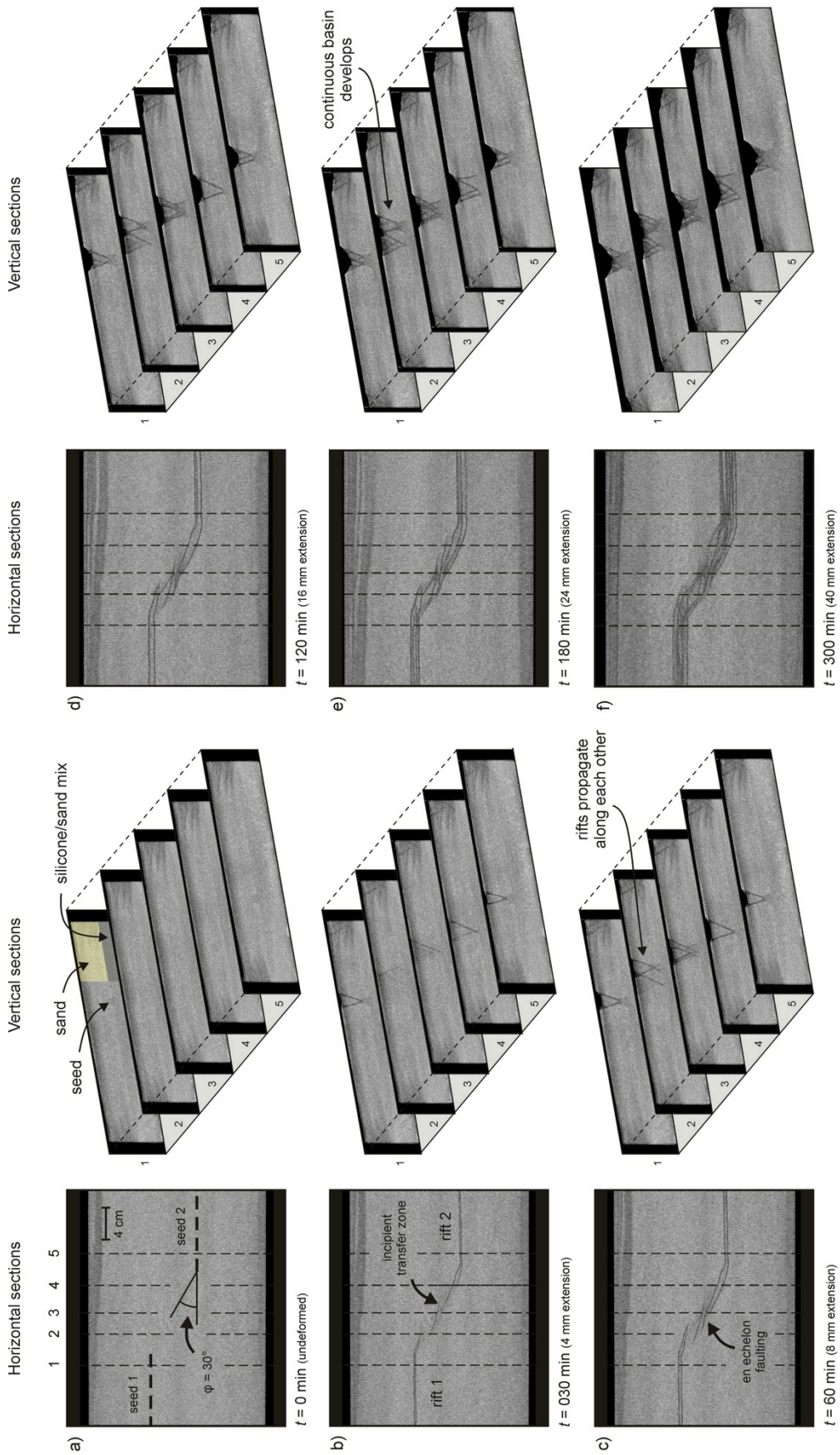
Fig. 6.6 *CT-derived 3D internal evolution of model M9 (orthogonal extension, $\phi = 30°$).*
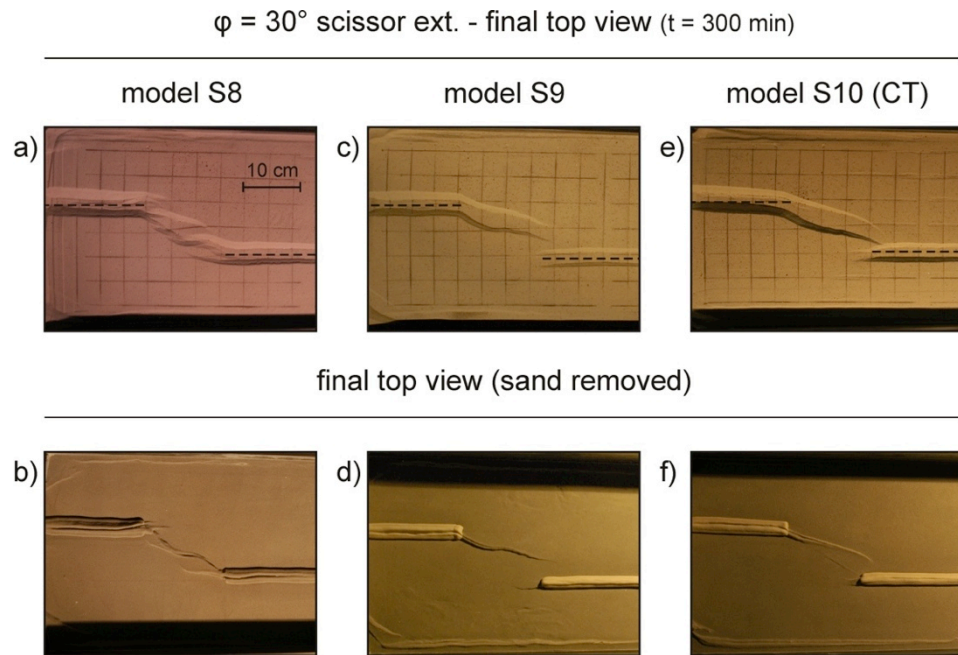
Fig. 6.7. *Structural variation within φ = 30° models S8-10 (scissor extension) after 300 min.*
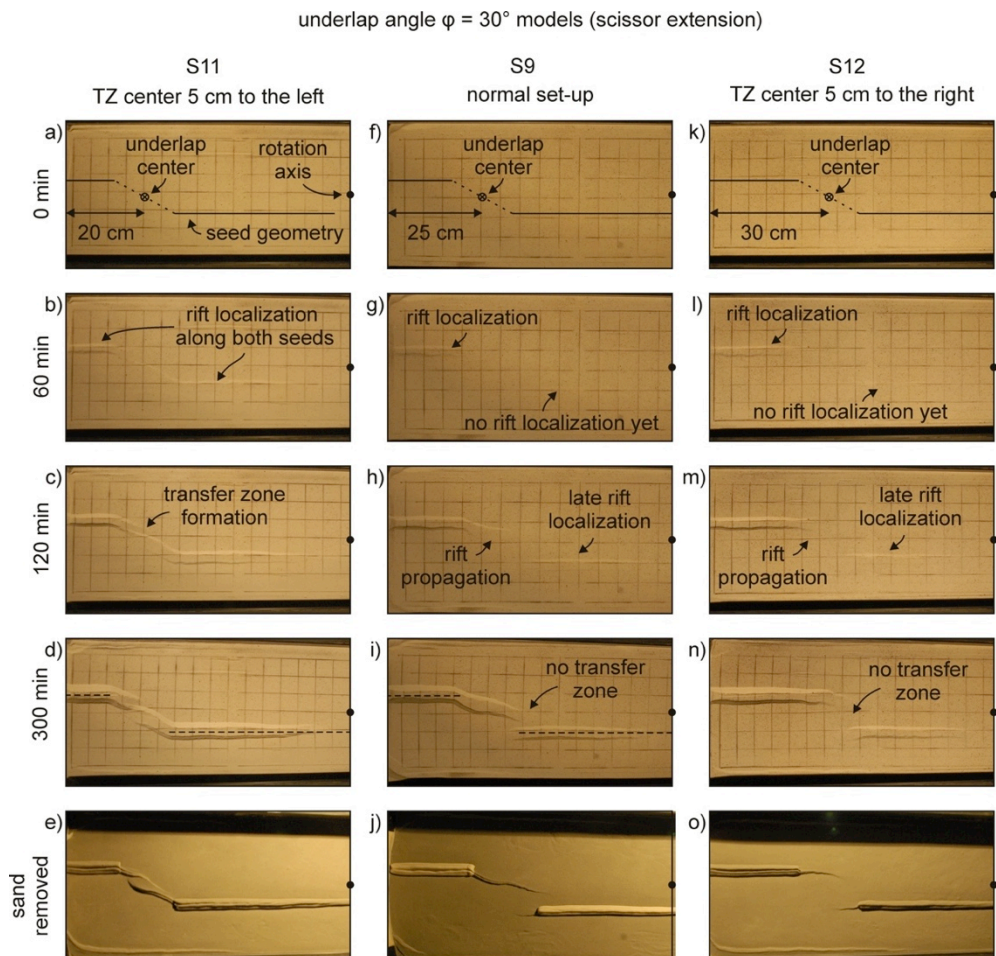
Fig. 6.8. *Comparative evolution of φ = 30° models (scissor extension) with different transfer zone centre locations.*
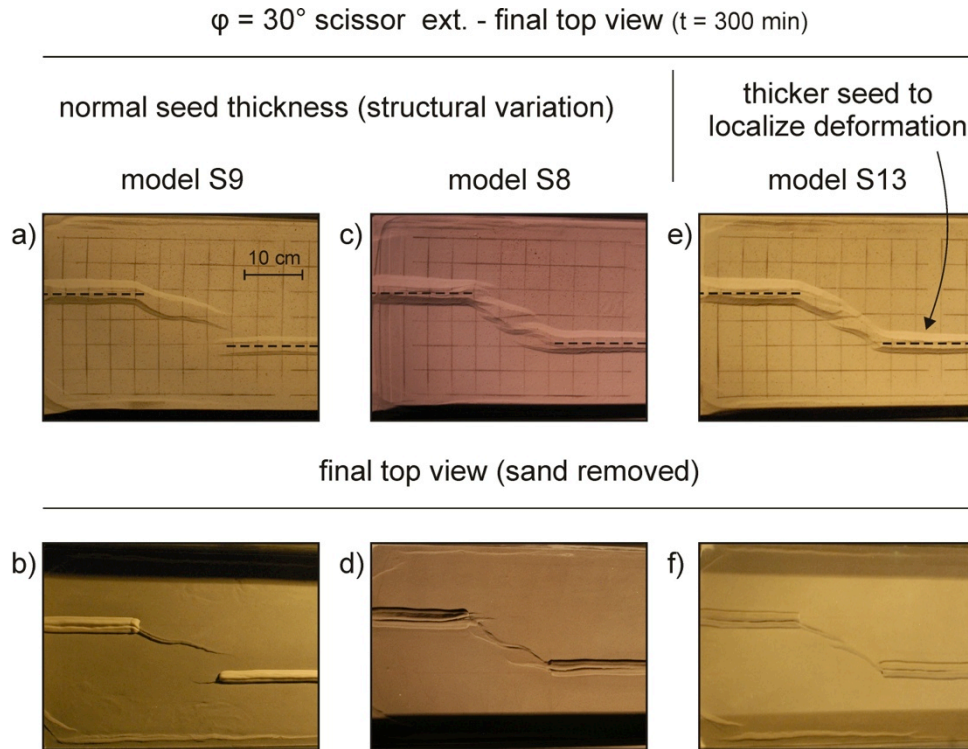
Fig. 6.9. *Seed thickness influence on transfer zone formation for $\phi = 30°$ scissor extension models at the end of the model run (300 min).*

6.3.4. Linkage zone variability (scissor extension $\phi = 20°$)

Similar to the $\phi = 30°$ models described above, we ran multiple versions of the $\phi = 20°$ scissor extension set-up. Also here, a range of structures occurs. Limited rift basins with limited propagation may develop (S14, Fig. 6.10a, b), or a well-developed accommodation zone with en echelon rift basins forms (S16, Figs. 6.3b, 6.10e, f). Model S15 forms a hybrid between these two modes, developing a limited inter-rift basin. As with the $\phi = 30°$ scissor models that fail to establish linkage (Figs. 6.7-9), the right-hand rifts in both models S14 and S15 localize relatively late and deflect slightly towards the nearest sidewall (Fig. 6.10a-d).

These processes can best be described with the use of the CT data from model S15 (Figs. 6.11, 6.12). Early after the start of the model run and not yet visible on the surface, faulting initiates along the right-hand seed 1 (Fig. 6.12b, b'). Only after 60 min, slight faulting is apparent along seed 2, while the rift along seed 1 has grown significantly and starts propagating towards seed 2 (Figs. 6.11c, 6.12c, c'). As deformation proceeds, the dominant rift propagates further initiating a secondary inter-rift basin. Meanwhile, the second rift arm starts to deflect towards the sidewall, where boundary effects are developing (Figs. 6.11d, 6.12d, d'). After 120 min, the principle structural elements are emplaced, which continue developing with ongoing extension, yet no final linkage occurs between the rift branches in model S15 (Figs. 6.11f, 6.12f, f').
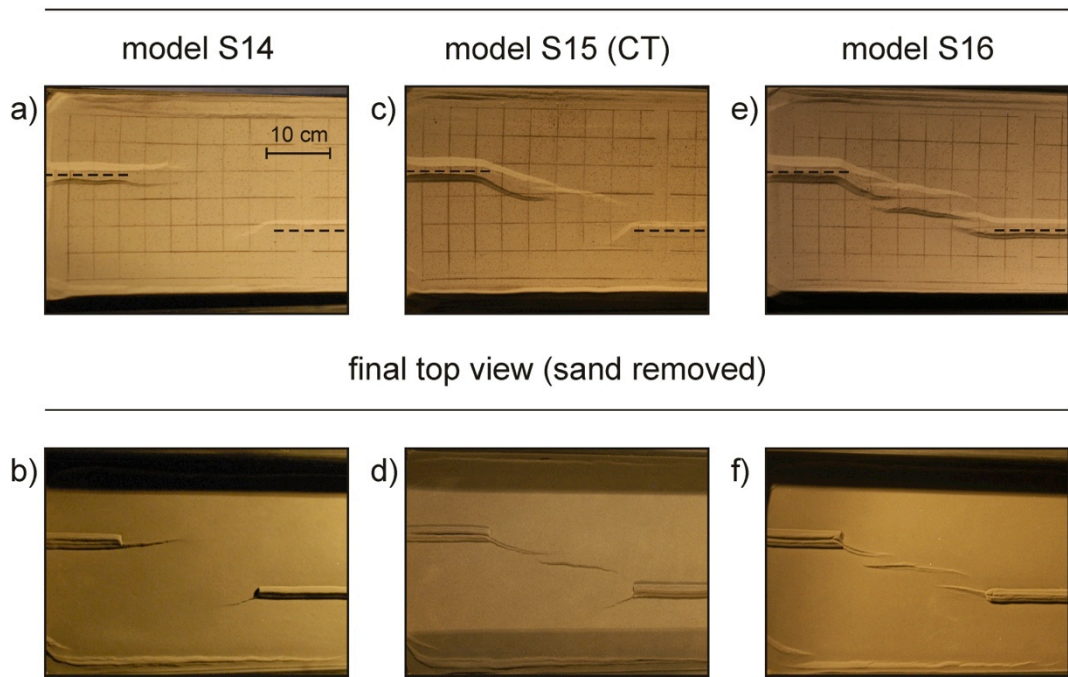
Fig. 6.10. *Structural variation within φ = 20° models S14-16 (scissor extension) after 300 min.*
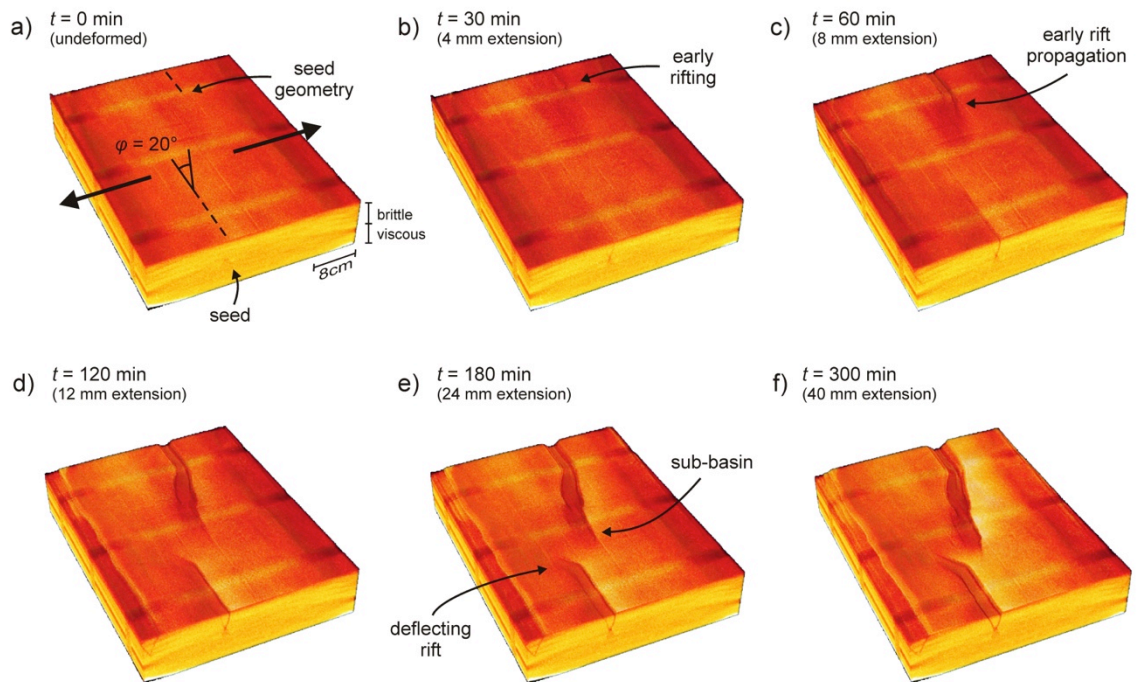
Fig. 6.11. *CT-derived 3D topography evolution of model S15 (scissor extension, φ = 20°).*
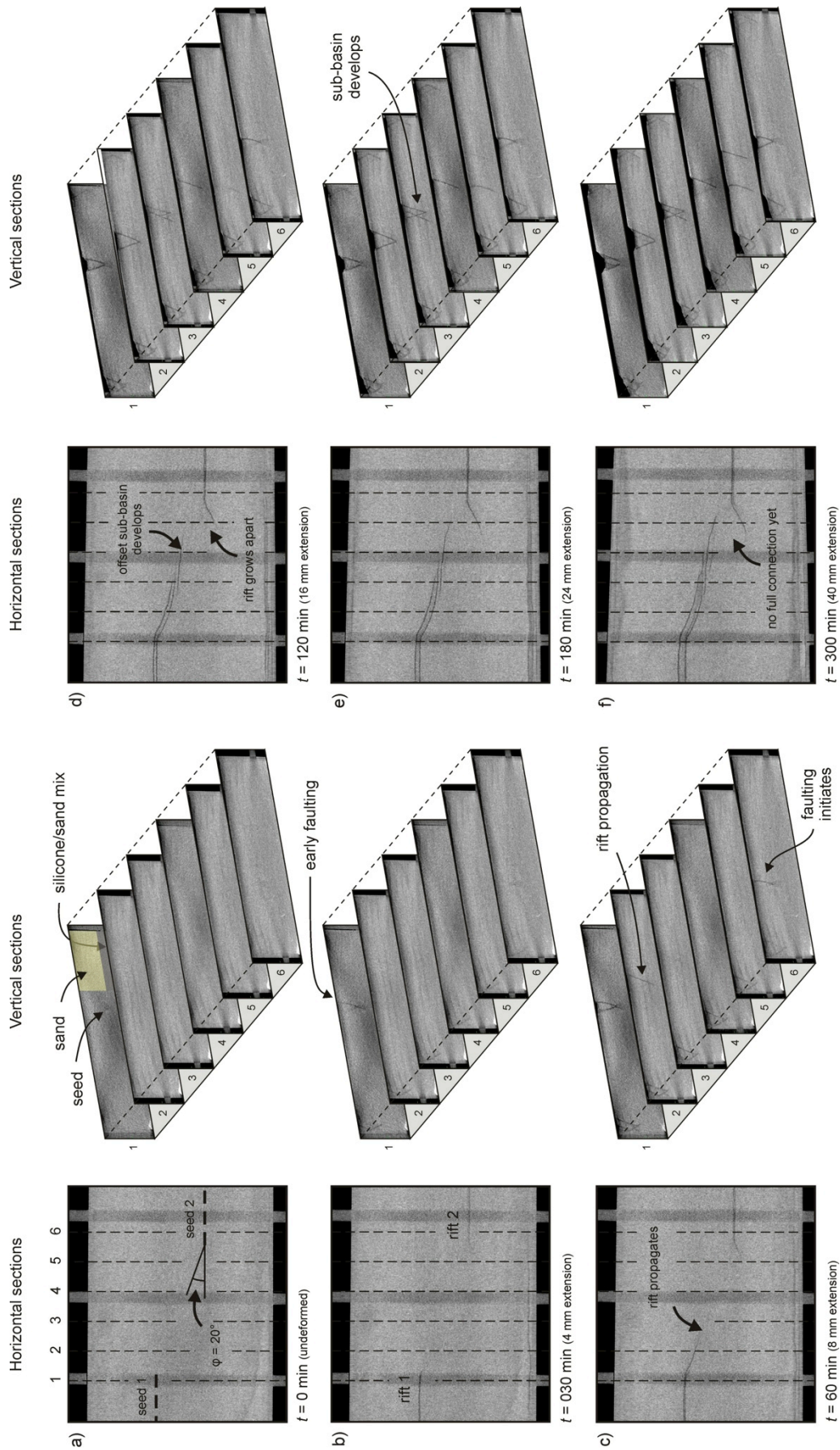
Fig. 6.12 *CT-derived 3D internal evolution of model S15 (scissor extension, φ = 20°).*

6.4. Discussion

6.4.1. Large-scale rift and rift interaction zones

Although orthogonal extension models and scissor extension models show large-scale differences in along-strike rift development (Chapter 5, S16 in Fig. 6.3b), both model set-ups develop very similar rift linkage structures, depending on the degree of underlap (Fig. 6.3). This can be explained by the fact that even in our scissor extension experiments, the extension direction is approximately perpendicular to the seeds. Only the magnitude of extension changes along strike and a high underlap angle ϕ results in an insignificant difference in extension rate between the seed tips, so that on a small scale, the system can be regarded as subjected to orthogonal extension.

The degree of underlap has a significant influence on the rift linkage structures in both set-ups. The rift pass structures typical for the $\phi \gtrsim 45°$ models in both set-ups (Fig. 6.3) are similar to the features described by Zwaan *et al*. (submitted; Chapter 4). However, as already remarked by these authors, the tendency of the rifts to grow toward each other suggests that a 2 H distance between rifts is not enough to prevent them interacting under orthogonal extension conditions, which contradicts the findings by Zwaan *et al*. (2016; Chapter 2), but is in accordance with similar slightly erratic models with high underlaps (small angles ϕ) by Zwaan and Schreurs (2017; Chapter 3, Fig. 6.8g-i).

The transfer zone basins developing in the $\phi \approx 45°$ and 30° experiments (Fig. 6.3) are probably a consequence of both the seed geometry and the rift propagation direction, as shown by model M9 (Fig. 6.5), but perhaps best demonstrated by model S11 (Fig. 6.8a-e). Similar behaviour, enforced by increasing degrees of dextral oblique extension, is observed by Zwaan & Schreurs (2017; Chapter 3). Both propagating rift branches almost directly grow into each other, forming a continuous transfer zone basin. However, the occurrence of sub-basins in several of the $\phi = 30°$ experiments indicates the transition to a third type of rift linkage structures: accommodation zones.

Model M10 with $\phi = 30°$ (Fig. 6.4e, f) already represents an accommodation zone, which is characterized by the presence of a large right-stepping sub-basins between the main rift segments and typically develop in models with $\phi \leq 20°$ (Fig. 6.3). The occurrence of these sub-basins is probably related to the presence of the two main rift segments. As shown in Chapter 4 and model S17 (Fig. 6.3), faulting will concentrate along the model sidewalls when not sufficiently concentrated along seeds in our foam-base set-up. But it appears that when both main rift basins are well-developed, deformation is directed to the middle of the model. Since the regional extension field is (near-)orthogonal to the seeds, these en echelon basins develop approximately along-strike, as illustrated in model M12 (Fig. 6.3a).

6.4.2. Rift localization in scissor extension models

In most models, faulting localizes well along the seeds. Yet several scissor extension experiments fail to develop early faulting along the right-hand seed, which is closest to the scissor axis (Fig. 6.8). This phenomenon occurs mostly in models with considerabel rift underlap ($\phi \leq 20°$) and in some cases, there is almost no localization at all (model S17, Fig. 6.3). The late development of faulting on the near-scissor axis seed is shown to obstruct rift linkage (Fig. 6.8) and is probably linked to the low amount of extension in the parts of the model near to the scissor axis, compared to the more stretched parts of the model further away from the scissor axis. In the cases that this near-scissor axis rift segment fails to develop early on, the boundary effects along the sidewalls account for most if not all deformation in that sector. In nature however, such boundary effects would not occur and we can safely state the models with more localized deformation and subsequent rift linkage zone development fits best with natural settings.

6.4.3. Structural variability

Specific set-ups show a degree of structural variability (Figs. 6.4, 6.7-10, 6.13a-c section 4.1). This is a result of the foam base set-ups we use, in which the experiments are not strongly controlled by for example moving base plates and a velocity discontinuity (e.g Brun & Tron 1993; Michon & Merle 2000). Therefore, the models might have slightly deviant structures that might originate in minor differences in sand or viscous layer thickness, sand compaction, temperature and other external variabilities. Yet the fact that these structures are always close to those seen in set-ups with slightly higher or lower angle ϕ and the fact that our experiments produce a logical sequence of results (Figs. 6.3, 6.13a-c), illustrates the general robustness of our modelling method.

6.4.4. Comparison with other models/nature

A direct comparison with previous models is challenging, as the specific boundary conditions vary. The numerical models involving rift underlap and orthogonal extension by Allken *et al.* (2011) for instance, develop rift pass structures, sub-basins as well as transfer zone basins, which are comparable to structures in the Utah Canyonlands and the North Sea Viking Graben. However, these models only concern the upper crust and their rift offset is significantly larger (3 H to develop a sub-basin, 5 H for a continuous transfer zone basin and 6 H for a rift pass structure, Fig. 6.13d-f), yet the underlap associated with these structures is quite similar to our ϕ = 20°, 40° and 90° models (Fig. 6.13a-c). However, strain weakening effects and variations in final yield value might however influence the development of these structures (Allken *et al.* 2011).

Other numerical simulations by Allken *et al.* (2012) do incorporate the lower crust and produce similar structures as described by Allken *et al.* (2011). Yet also these experiments illustrate the added influence of various other factors, such as viscosity, brittle-ductile coupling, which may produce a variety of structures for the same geometrical set-up. Therefore, caution is advised when directly comparing rift linkage structures and inferring their development without accurate knowledge of the kinematics involved.

Tentler & Acocella (2010) present an analogue modelling study on the influence of both rift offset and underlap in an oceanic setting, using a set-up that involves a rising asthenosphere. Similar to our models they develop sub-basins with high underlap angles (ca. 30°, Fig. 6.13g), while transfer zones develop around 45° angles (Fig. 6.13h) and rift pass features (referred to as overlapping spreading centres in oceanic settings, e.g. Hieronymus 2004) occur when ϕ equals 90° (Fig. 6.13i), of which examples are found along various mid-oceanic ridges around the globe (Tentler & Acocella 2010 and references therein, Fig. 6.13j, k).

Indeed, Tentler & Acocella (2010) simulate oceanic spreading centres, while our models focus on the early stages of continental rifting. Therefore a direct comparison might be precarious. However, since oceanic settings basically involve a brittle upper lithosphere (oceanic crust) and a ductile lower lithosphere (e.g. Benes & Scott 1996), similar to our brittle-ductile experiments, such a comparison is feasible.

Another feature in the low offset, low underlap set-ups by Tentler & Acocella (2010) is the development of transform faults. These do not form in our models, possibly due to the large rift offset, but they neither occur in low offset, low underlap models by Zwaan *et al.* (2017; Chapter 2). Another reason might be the relatively low total stretching in our models; studies have shown that transfer faults, potential precursors of oceanic transform faults, may form with higher degrees of stretching (Acocella *et al.* 2005).
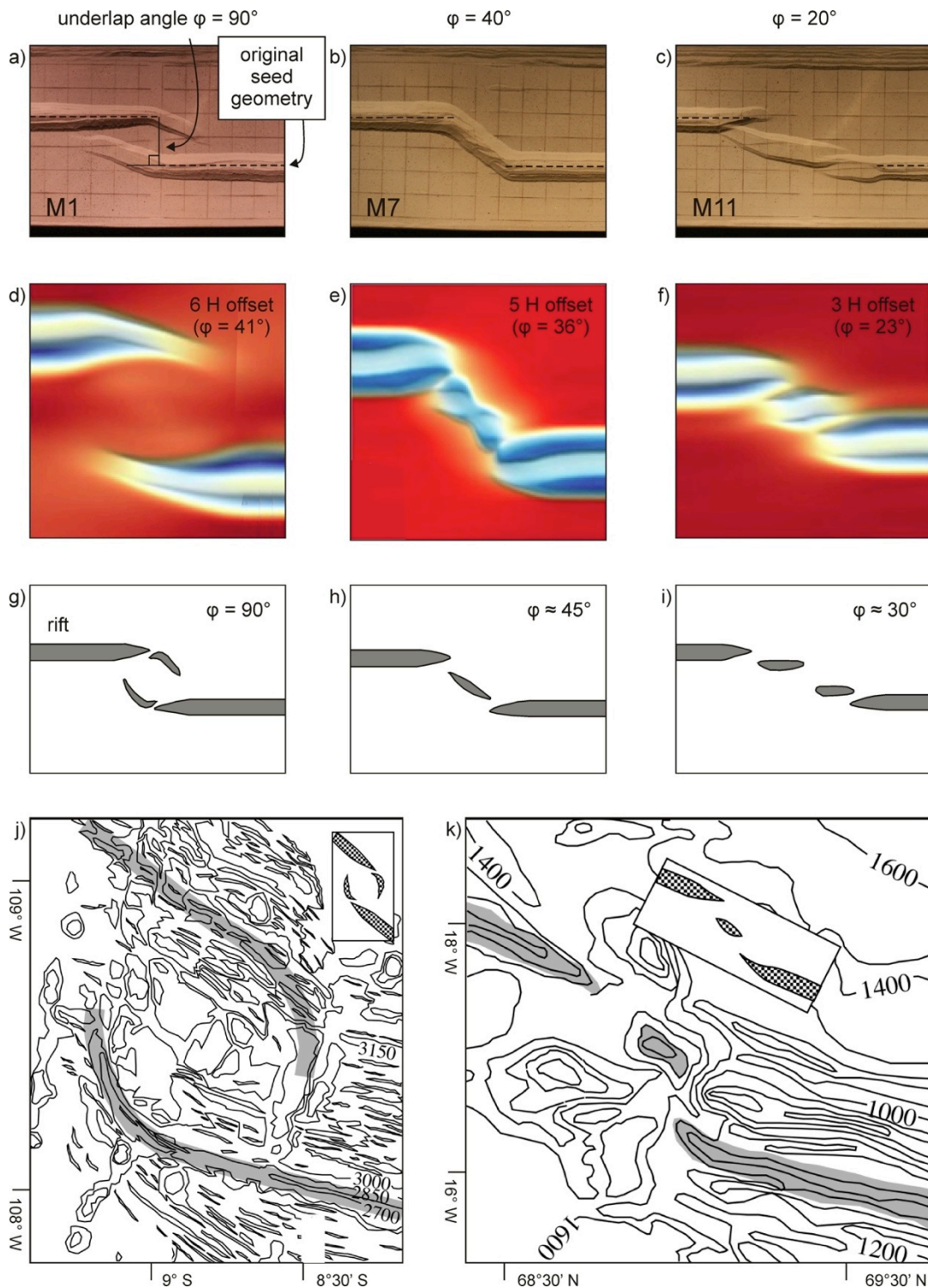
Fig. 6.13. *Comparison with other models and nature. (a-c) Top views of our orthogonal extension models M1, M7 and M11 with 2 H offset and φ = 90°, 40° and 20°, respectively. (d-f) Top views of numerical simulations by Allken et al. (2011), with φ = 41°, 36° and 23°, respectively. (g-i). Top view interpretations of analogue models by Tentler & Acocella (2010) with φ = 90°, 45° and 30°. (j) Overlapping spreading centre at the East Pacific Rise. Image modified after Wang and Cochran (1993). (k) En echelon basin along the Kolbeinsey Ridge at the Mid Atlantic Ridge. Image modified after Devey et al. (1994). Contours indicate depth and grey areas represent deep troughs.*

6.5. Conclusion

In this paper we describe various analogue tectonic experiments to assess the differences between transfer zones forming in orthogonal extension settings versus scissor extension settings. The model results allow the following conclusions:

- Although scissor extension and orthogonal extension produce quite different large-scale structures, local features in a scissor extension systems can be regarded as forming in an orthogonal extension setting;
- Various degrees of underlap produce three basic modes of rift linkage structures. Low underlap (high angle ϕ) experiments develop rift pass structures. With increasing underlap (ϕ = ca. 40°), transfer zone basins develop. High degrees of underlap ($\phi \leq 30°$), tend to result in sub-basins;
- Several of these structures are found in previous model studies and in nature. Yet a direct comparison is challenging, as various parameters might modify their structural development;
- We do not observe any transform structures, potentially due to the limited amount of extension in our experiments.

In order to further investigate this model series, the following steps are planned:

- All models are sprinkled with coffee grains to create a pattern for Particle Image Velocimetry (PIV) analysis (e.g. Molnar *et al.* 2017), which might reveal the exact horizontal motions in the models, in order to better constrain e.g. the rotation of the rift pass structures;
- As the model materials are mixed with small amounts of zirshot, it would be possible to apply Digital Volume Correlation (DVC) analysis (Adam *et al.* 2013; Zwaan *et al.* submitted; Chapter 4) to the CT data from models M6 and M12, for a highly detailed assessment of 4D (internal) model deformation;

Chapter 7

Comparing crustal-scale analogue extension model set-ups using X-ray computed tomography (XRCT) techniques

Frank Zwaan[a] *, Guido Schreurs[a], John Naliboff[b], Susanne J.H. Buiter[c,d], Jürgen Adam[e]

a) Institute of Geological Sciences, University of Bern, Baltzerstrasse 1+3, CH-3012 Bern, Switzerland
b) Department of Geology, University of California, One Shields Avenue, Davis, CA 95616, USA
c) Team of Solid Earth Geology, Geol. Survey of Norway (NGU), Leiv Eirikssons vei 39, 7040 Trondheim, Norway
d) The Centre for Earth Evolution and Dynamics, University of Oslo, Sem Sælands vei 2A, 0371 Oslo, Norway
e) Department of Earth Sciences, Royal Holloway, University of London, Egham, Surrey, TW20 0EX, UK

_____

Abstract

Analogue modellers have historically applied various methods, involving a range of experimental machines and model materials, in order to investigate a wide variety of experimental tectonic settings. Set-ups have involved (a combination of) rigid base plates, rubber, moving sidewalls and foam to deform the model materials such as sand, clay, microbeads, silicone and paraffin wax. Although these methods have provided the scientific community with highly valuable insights in tectonic processes and the evolution of structures, comparing the results of these various models is challenging. In this paper we therefore present a comparison between crustal-scale analogue models with a range of different set-ups constituting of either a rubber base, a foam base or rigid base plates to deform brittle-only or brittle-viscous models. We use X-ray computed tomography (XRCT or CT) and digital volume correlation (DVC) for a highly detailed 3D analysis of internal and external model evolution. Our modelling efforts provide the following results: There is a strong difference between brittle-only models with either a base plate or a foam/rubber base set-up; Rubber base and foam base set-ups are very much alike, with the migration of faulting towards the rift axis, resembling the situation in the Ethiopian Rift. To avoid strong boundary effects in rubber base set-ups, a low width/length ratio is advised. Plate base brittle-only experiments should not involve too much extension to remain realistic. Of the brittle-viscous experiments we tested, the results with the least boundary effects were obtained through a foam base and seed set-up. This is partially due to the use of a rubber sidewall, which could also be applied for a rubber base set-up in order to decrease boundary effects. High extension rates can produce flexural basins and marginal grabens in a plate base set-up, as for example observed in the Ethiopian Rift.

_____

7.1. Introduction

Tectonic analogue modelers have historically applied several distinct methods, involving various different experimental machines and different model materials to investigate a broad range of tectonic settings. Numerous authors have for instance performed experiments with set-ups involving (a combination of) rigid base plates, rubber base sheets, moving sidewalls and foam to deform their model materials (e.g. Allemand *et al.* 1989; Acocella *et al.* 1999a; Amilibia *et al.* 2005; Bahroudi *et al.* 2003; Alonso-Henar *et al.* 2015; Phillippon *et al.* 2015). Other experiments rely on (enhanced) gravity to drive deformation (e.g. Gartell 1997; Fort *et al.* 2004; Corti *et al.* 2004; Acocella *et al.* 2005).

The materials used in these models include (mixtures of) quartz or feldspar sand, silica flour, microbeads, (kaolinite) clay to simulate the brittle parts of the crust or lithosphere (Hubbert 1937, Elmohandes 1981; Serra & Nelson 1988; Clifton & Schlische 2001; Autin *et al.* 2010; Abdelmalak *et al.* 2016). Viscous silicone putties are commonly used for the ductile parts of the lithosphere (Basile & Brun 1999; Michon & Merle 2000; Sun *et al.* 2009), whereas in asthenosphere-scale models, the behaviour of the astheno-spheric mantle is imitated with low viscosity materials such as honey, glucose syrup or even pure water (Mart & Dauteuil 2000; Chemenda *et al.* 2002; Schellart *et al.* 2002; 2003; Molnar *et al.* 2017). Further examples of these and other analogue model materials can be found in an extensive review by Schellart & Strak (2016).

Although these methods have provided the scientific community with highly valuable insights in tectonic processes and the evolution of structures, a robust comparison between these various models is challenging. Therefore, efforts have been made to investigate the influence of different set-ups and materials on resulting structures. For instance, Schreurs *et al.* (2006; 2016) and Graveleau *et al.* (2012) compare results of thrust wedge experiments. Similar efforts concerning analogue modelling of lithospheric extension are published by Vendeville *et al.* (1987), Brun (1999) and Bahroudi *et al.*

(2003). Yet new methods and analysis techniques are developed since and we consider an update is desirable.

The aim of this paper is therefore to describe and compare a compilation of analogue models involving various crustal-scale, normal-gravity set-ups. We either apply a rubber base, a foam base or rigid base plates to deform the brittle or brittle-viscous model materials for a total of 6 basic different set-ups. The use of X-ray computed tomography (XRCT or CT) and digital volume correlation (DVC) allows a highly detailed 3D view of internal and external model evolution.

7.2. Materials and methods

7.2.1 Material properties

We ran both brittle and brittle-viscous experiments to simulate a 20 km thick upper crust and a complete 40 km brittle-ductile crustal succession, respectively. For the brittle-only models, we apply a 4 cm thick layer of fine quartz sand (ø = 60-250 μm). The sand is sieved from a ca. 30 cm height into the experimental apparatus to guarantee a sand density of ca. 1560 kg/m^3. The sand is flattened using a scraper at every cm during model preparation, causing slight density variations, which subsequently appears on CT images as "layering" (Fig. 7.4).

The models involving a brittle-ductile set-up include a 4 cm thick viscous layer, consisting of a mixture of near-Newtonian (η = ca. 1.5·10^5 Pa·s; stress exponent (n) = 1.05) SGM-36 Polydimethylsiloxane (PDMS) silicone oil with dense corundum sand ($\varrho_{specific}$ = 3950 kg/m^3, Panien *et al.* 2006; Klinkmüller 2011; Carlo AG 2017) following a 0.965 : 1.00 weight ratio. Its density (ca. 1600 kg/m^3) is close to that of the 4 cm thick overlying quartz sand layer (1560 kg/m^3), resulting in a density profile that is closer to the natural state than pure low density PDMS (ϱ = ca. 960 kg/m^3) would permit, avoiding boundary effects due to unrealistic buoyancy effects. Further material properties are listed in table 7.1.

Table 7.1. *Material properties*

Granular materials	Quartz sand[a]	Corundum sand[b]
Grain size range	60-250 μm	88-175 μm
Density (specific)[c]	2650 kg/m^3	3800 kg/m^3
Density (sieved)	1560 kg/m^3	1890 kg/m^3
Angle of internal peak friction	36.1°	37°
Angle of dynamic-stable friction	31.4°	32°
Cohesion	9 ± 98 Pa	39 ± 10 Pa

Viscous material	PDMS/corundum sand mixture[a]
Weight ratio PDMS : corundum sand	0.965 kg : 1.00 kg
Mixture density	ca. 1600 kg/m^3
Viscosity[d]	ca. 1.5·10^5 Pa·s
Type	near-Newtonian (n = 1.05)[e]

a	Quartz sand and viscous mixture characteristics after Zwaan & Schreurs (2016; Chapter 2)
b	Corundum sand characteristics after Panien *et al*. (2006) and Klinkmüller (2011)
c	Specific densities after Carlo AG (2017)
d	The viscosity value holds for model strain rates < 10^{-4} s^{-1}
e	Stress exponent n (dimensionless) represents sensitivity to strain rate

7.2.2. Experimental set-up

The basic model apparatus consist of a fixed base and two sidewalls which can move inward and outward independently from each other, controlled by precise computer-guided motors. This machine can subsequently be modified for a total of 6 basic model set-ups and various sub-set-ups (Fig. 7.1, Table 7.2). We use three different basic deformation mechanisms to transfer deformation in the overlying model materials: a rubber sheet base, a foam base or a base of rigid plates.

For the rubber base set-up a 1.5 mm thick Neoprene rubber sheet is spanned between the two sidewalls. When the sidewalls open, the rubber sheet is stretched and extends uniformly along a constant velocity gradient, causing distributed deformation (Fig. 7.1c, d). The sides of the set-up are free, that is, not confined by any sidewalls, for the model with only a brittle layer. The short ends of the brittle-ductile rubber base models are enclosed by sand so that the viscous material cannot escape from the model set-up.

Also the foam base produces distributed deformation (Zwaan *et al*. 2016, Zwaan & Schreurs 2017; Chapters 2, 3), but in an opposite way, since the 8 cm thick RG 50 Polyurethane foam is first compressed between the sidewalls and extends uniformly as the sidewalls move apart during extension (Fig. 7.1a, e, f). Rubber sidewalls at the short ends of the set-up confine the model materials, with the distributed extension of the rubber decreasing boundary effects there

For the last set-up, 3 mm thick rigid plastic base plates that may represent the strong brittle mantle (Tron and Brun 1993, Fig. 1.12) are fixed to the mobile sidewalls (Fig. 7.1g, h). When these plates move apart a velocity discontinuity (VD) develops between them, focussing deformation. Additional plates border the short ends of the model. These move along secondary plates during extension, so that no gaps open and the model materials cannot escape from the set-up. In contrast to the other distributed extension set-ups, the rigid base plates allow both symmetric and asymmetric extension.

Both brittle and brittle-viscous model layering is applied for every set-up (both 4 cm thick), as well as seeds to localize deformation in several models (Fig. 7.1). These seeds consist of 1 cm thick, semi-cylindrical rods of the PDMS/corundum sand mixture on top of the basal viscous layer, where they act as weak zones localizing deformation, since the strong sand cover is locally thinner and thus weaker.
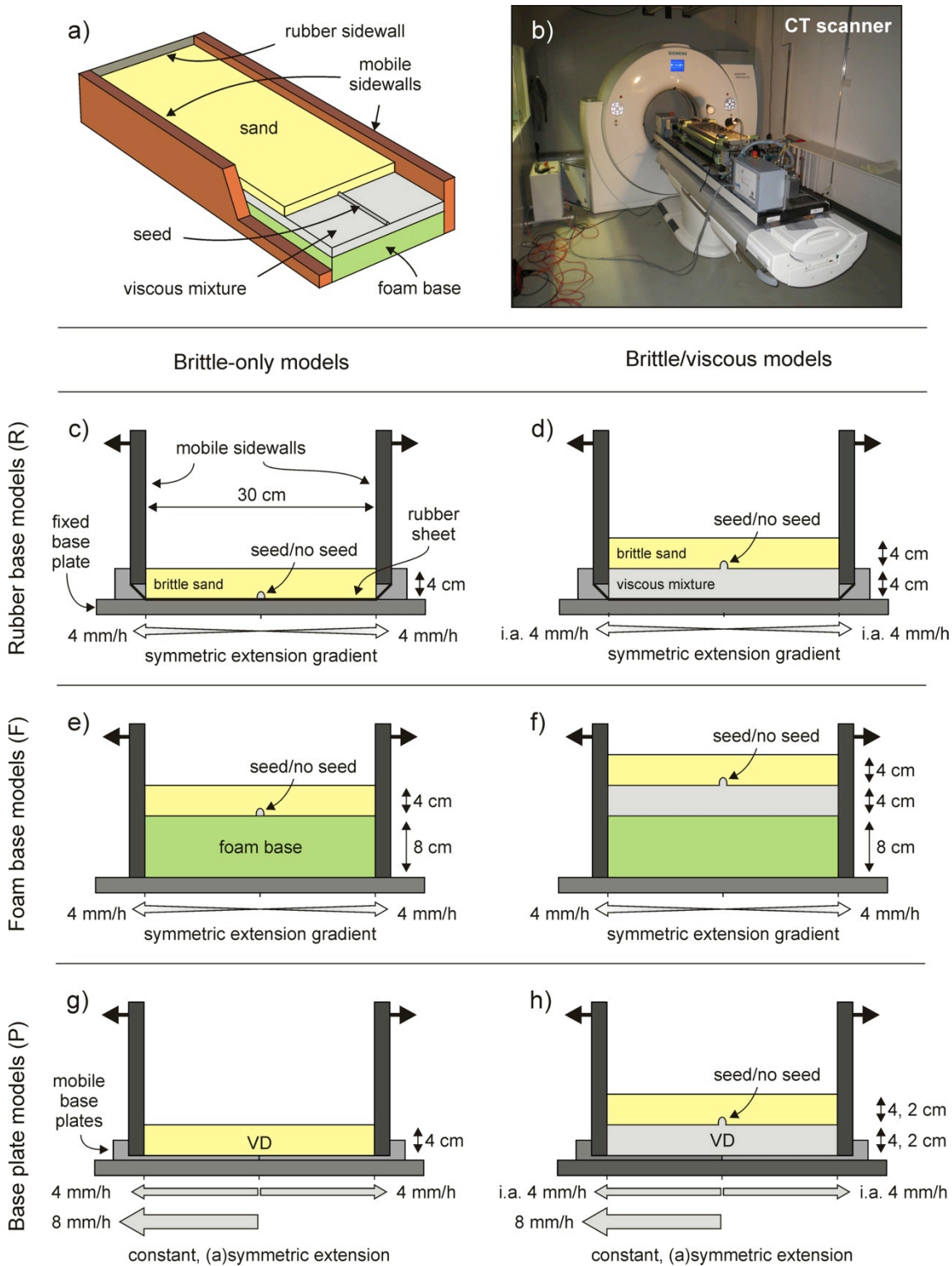
Fig. 7.1. *Model set-ups used for this study. (a) 3D cut-out sketch of a foam base model with brittle-viscous layering and a seed. (b) The experimental apparatus in the CT scanner of the University of Bern Institute of Forensic Medicine. (c-d) Rubber base set-ups for symmetric distributed extension: (c) brittle-only with or without seed, (d) brittle-viscous with or without seed. (e-f) Foam base set-ups for symmetric distributed extension: (e) brittle-only with or without seed, (f) brittle-viscous with or without seed. (g-h) Base plate set-ups controlled by a basal velocity discontinuity (VD) for symmetric and asymmetric extension. (g) brittle-only with or without seed, (f) brittle-viscous with or without seed. VD: velocity discontinuity.*

During most model runs, extension velocities amount to 8 mm/h with both sidewalls moving 4 mm/h for symmetrical extension or a single sidewall moving 8 mm/h for asymmetrical extension (Fig. 7.1g, h). Considering a model run of 5 h, the total extension equals 40 mm (or ca. 13%, given an initial width of ca. 31 cm). Several models had a different extension velocity and total extension, as listed in Table 2 and described in the results and discussion sections. A 4 x 4 cm grid on the model surface yields a first-order impression of surface deformation. Furthermore, every component of the machine around the model consists of X-ray transparent materials to allow for CT-scanning and various models are analysed with CT-techniques to reveal their 3D internal evolution (Fig. 7.1b). For one model (R4), a preliminary digital volume correlation (DVC) test was performed, for which the reader is referred to Appendix 7A, Fig. 7.A1. For more background concerning this novel analysis technique, the reader is referred to Chapter 4 of this Thesis.

Table 7.2. *Model parameters*

	Model	Layering	Seed	Extension	Extension velocity	Shown in:
Rubber base	R1	B	-	S	8 mm/h, 20 mm/h[a]	Fig. 7.2
	R2[b]	B	X	S	10 mm/h	-
	R3[b]	B	X	S	20 mm/h	-
	R4[CT, DVC, b]	B	X	S	20 mm/h[c]	Fig. 7.A1
	R5[CT,b]	B	X	S	10 mm/h	Fig. 7.2
	R6[CT]	B	X	S	20 mm/h[d]	Figs. 7.2-4
	R7	BV	-	S	8 mm/h , 20 mm/h[a]	Fig. 7.5
	R8	BV	X	S	8 mm/h	Fig. 7.5
	R9	BV	-	S	80 mm/h	Fig. 7.A2
	R10	BV	-	S	480 mm/h	Fig. 7.A2
Foam base	F1	B	-	S	8 mm/h	Fig. 7.6
	F2	B	X	S	8 mm/h	-
	F3	B	X	S	8 mm/h	-
	F4[CT]	B	X	S	8 mm/h	Figs. 7.6-8
	F5	BV	-	S	8 mm/h	Fig. 7.9
	F6	BV	X	S	8 mm/h	-
	F7[CT]	BV	X	S	8 mm/h	Figs. 7.9-11
Plate base	P1	B	-	S	8 mm/h	Fig. 7.12
	P2	B	-	AS	8 mm/h	Fig. 7.12
	P3	BV	-	S	8 mm/h	Fig. 7.13
	P4	BV	-	S	2 mm/h	Fig. 7.15
	P5	BV	-	S	40 mm/h	Fig. 7.15
	P6	BV	-	AS	8 mm/h	-
	P7	BV	-	AS	8 mm/h	Fig. 7.13
	P8[e]	BV	-	S	2 mm/h	-
	P9[e]	BV	-	S	80 mm/h	-
	P10	BV	X	S	8 mm/h	Fig. 7.14

B   Brittle-only layering
BV   Brittle-viscous layering
X   Seed applied
S   Symmetric extension
AS   Asymmetric extension

Notes:

CT   CT-scanned models
DVC   (preliminary) DVC analysis applied
a   Two-phase models, 40 mm extension in phase 1, followed by 20 mm extension in phase 2
b   Initial model width 25 cm instead of 35 cm
c   54 mm extension, but the rubber sheet ripped after ca. 2 h (40 mm extension)
d   60 mm total extension
e   Models thickness 40 mm (20 mm brittle, 20 mm viscous) and 20 mm total extension

7.2.3. Model scaling

For model scaling we use the standard equations. We calculate stress ratios (σ^*, convention: $\sigma^* = \sigma_{model}/\sigma_{nature}$) using the following equation (Hubbert 1937; Ramberg 1981): $\sigma^* = \rho^* \cdot h^* \cdot g^*$ where ϱ^*, h^* and g^* represent the density, length and gravity ratios respectively. The strain rate ratio $\dot{\varepsilon}^*$ is derived with the stress ratio σ^* and the viscosity ratio η^* (Weijermars & Schmeling 1986): $\dot{\varepsilon}^* = \sigma^*/\eta^*$. Subsequently, the velocity ratio v* and time ratios t* can be obtained with the following equations: $\dot{\varepsilon}^* = v^*/h^* = 1/t^*$. As the natural lower crustal viscosity has a wide range ($\eta = 10^{19-}10^{23}$, e.g. Buck 1991), 1 hour in our models translates to 0.008-84 Ma in nature and our standard model velocity (8 mm/h) converts to a velocity of 0.05-500 mm/y in nature.

Typical rift extension velocities plot in this range (several mm/y, e.g. Saria *et al.* 2014). The scaling parameters are summarized in Table 3.

To ensure dynamic similarity between brittle natural and model materials, we calculate the ratio R_s, which is a function of gravitational stress and cohesive strength (C) (Ramberg 1981; Mulugeta 1998): $R_s = gravitational$ $stress/cohesive$ $strength = = \rho \cdot g \cdot h/C$. For viscous materials, the Ramberg number R_m applies (Weijermars & Schmeling 1986): $R_m = gravitational$ $stress/viscous$ $strength = \rho \cdot g \cdot h^2/(\eta \cdot v)$. The R_m value of 75 plots in the natural range of 1.2-1200 and the R_s values are quite similar with values of 34 or 68 versus 9.2 for the standard model and natural settings respectively.

Table 7.3. *Scaling parameters*

	General parameters			Brittle upper crust		Ductile lower crust		Dynamic scaling values	
Model	Grav. Accel. g (m/s^2)	Upper crustal thickness h (m)	Extension velocity v (m/s)	Density ϱ (kg/m^3)	Cohesion C (Pa)	Density ϱ (kg/m^3)	Viscosity η (Pa·s)	Ramberg number R_m	Brittle stress ratio R_s
Standard	9.81	0.04	$2.2 \cdot 10^{-6}$	1560	9	1600	$1.5 \cdot 10^5$	75	68
P5	9.81	0.04	$1.1 \cdot 10^{-5}$	1560	9	1600	$1.5 \cdot 10^5$	15	68
R1, R3, R4, R6	9.81	0.04	$5.5 \cdot 10^{-6}$	1560	9	1600	$1.5 \cdot 10^5$	30	68
R2, R5	9.81	0.04	$2.8 \cdot 10^{-6}$	1560	9	1600	$1.5 \cdot 10^5$	60	68
R10	9.81	0.04	$1.3 \cdot 10^{-4}$	1560	9	1600	$1.5 \cdot 10^5$	1.3	68
P4	9.81	0.04	$5.6 \cdot 10^{-7}$	1560	9	1600	$1.5 \cdot 10^5$	30	68
P8	9.81	0.02	$5.6 \cdot 10^{-7}$	1560	9	1600	$1.5 \cdot 10^5$	75	34
P9	9.81	0.02	$2.2 \cdot 10^{-5}$	1560	9	1600	$1.5 \cdot 10^5$	1.9	34
Nature	9.81	$4 \cdot 10^4$	$1 \cdot 10^{-10}$	2800	$7 \cdot 10^{7}$ [a]	2900	$1 \cdot 10^{19 \text{ to } 23}$ [b]	$1.2 \cdot 10^{0 \text{ to } 4}$	9.2

a   Cohesion value after Corti *et al.* (2004)
b   Viscosity range after Buck (1991)

7.3. Results

7.3.1. Rubber base set-up (brittle-only)

The surface evolution of a selection of rubber base models with only a brittle sand cover is depicted in Fig. 7.2. In model R1 (Fig 7.2a-d), without a seed to localize deformation, deformation focuses along the sidewalls during the model run. In addition, remarkable conjugate faults are visible at the end of the standard model run (300 min, 40 mm of extension). A second, faster phase of extension helps to emphasize this phenomenon (Fig. 7.2d). This faster extension rate does however not influence the structures, as sand deformation is a time-independent process.

In contrast to model R1, models R5 and R6 contain a viscous seed to focus faulting along the central axis of the model (Fig. 7.2e, h). As a result, both models develop a central graben structure. The different extension velocities do not have a significant influence on the final structures. Similar to model R1 however, well-defined conjugate faults occur also in models R5 and R6 (Fig. 7.2g, k).
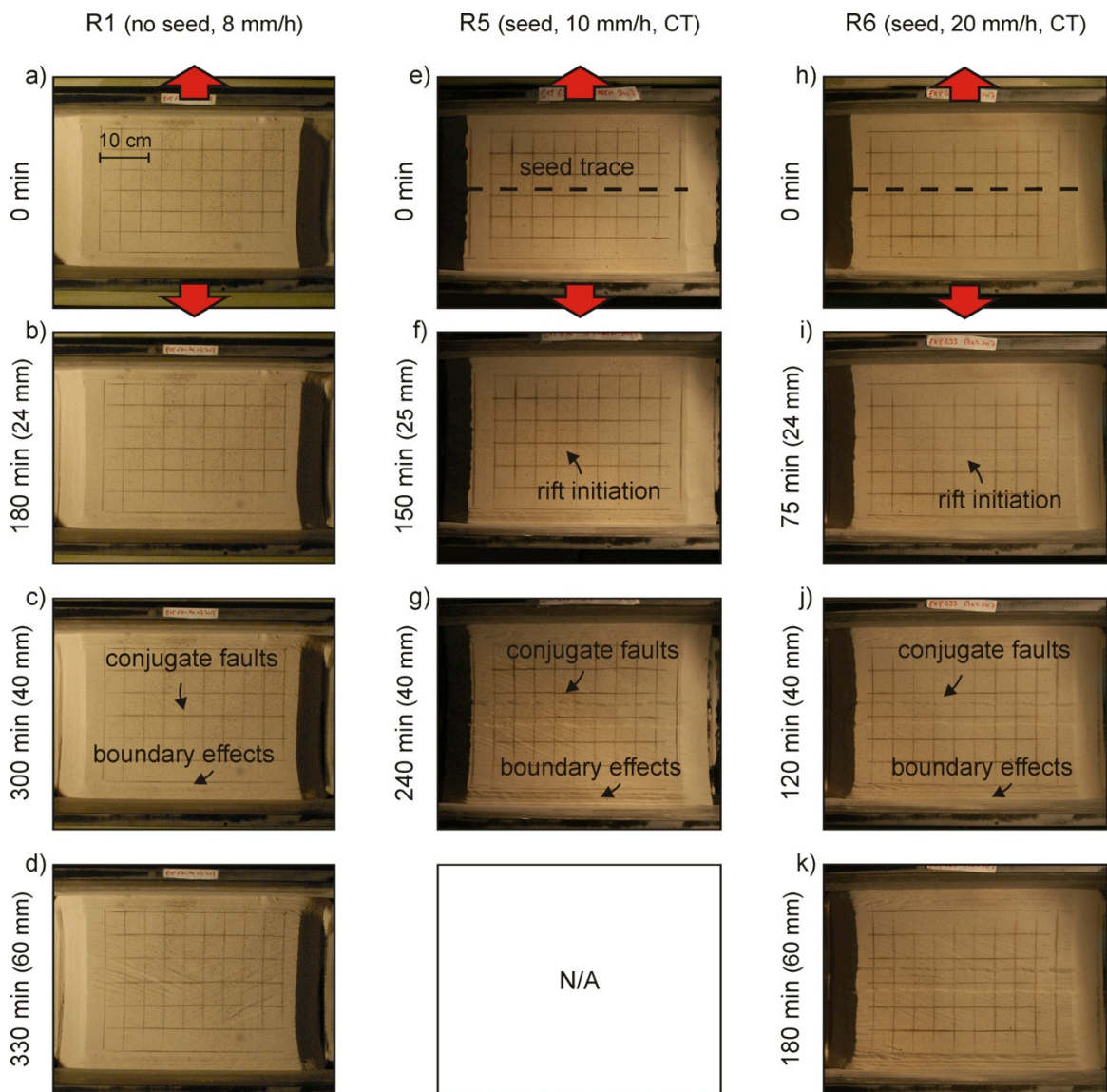
Fig. 7.2. *Surface evolution overview of brittle-only rubber base models R1 (without seed) and R5 and R6 (both with seed). Model R1 is illuminated from the left, Models R5 and R6 from the right.*

The evolution of these structures is best visible on the CT scans of model R6 (Figs. 7.3, 7.4). The CT-derived 3D images reveal how deformation localizes along the seed and the sidewall in the initial stages of experiment R6, forming a cylindrical rift structure (Figs. 7.3b, c, 7.4b, c). However, after some 20-25 mm of extension, conjugate sets of vertical strike-slip faults start developing (Figs. 7.3d, 7.4d), becoming a dominant, pervasive structure toward the model end (Figs. 7.3f, 7.4f). This feature is the result of along-strike compression, as the orthogonally extending rubber sheet contracts along-strike, forcing sand to wedge into the model. Nevertheless, the rift structures continue to evolve, and the initial defor-mation along the sidewall starts migrating towards the model centre (Figs. 7.3f, 7.4f). Also the bright coloration in Fig. 7.3f indicates rift shoulder uplift, because more elevated parts of the model form less of a boundary to X-rays.

In addition, a preliminary digital volume correlation (DVC) analysis of a section through the centre of Model R4 (similar set-up as Model R5) reveals a horizontal displacement gradient imposed by the distributed extension of the rubber base (Appendix A, Fig. 7.A1a-f, m). The analysis also shows the concentration of subsidence in the rift structure above the seeds and along the sidewalls (Fig. 7.A1g-l, n).
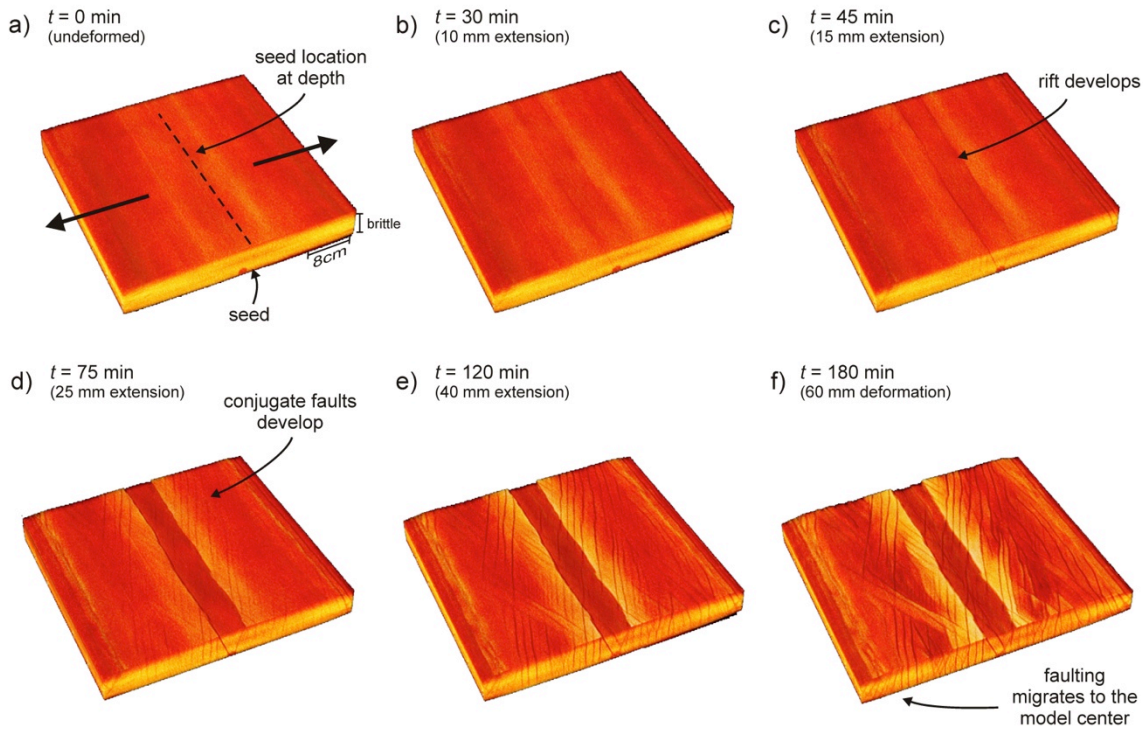
Fig. 7.3. *CT-derived 3D topography evolution of brittle-only rubber base model R6 (with seed).*
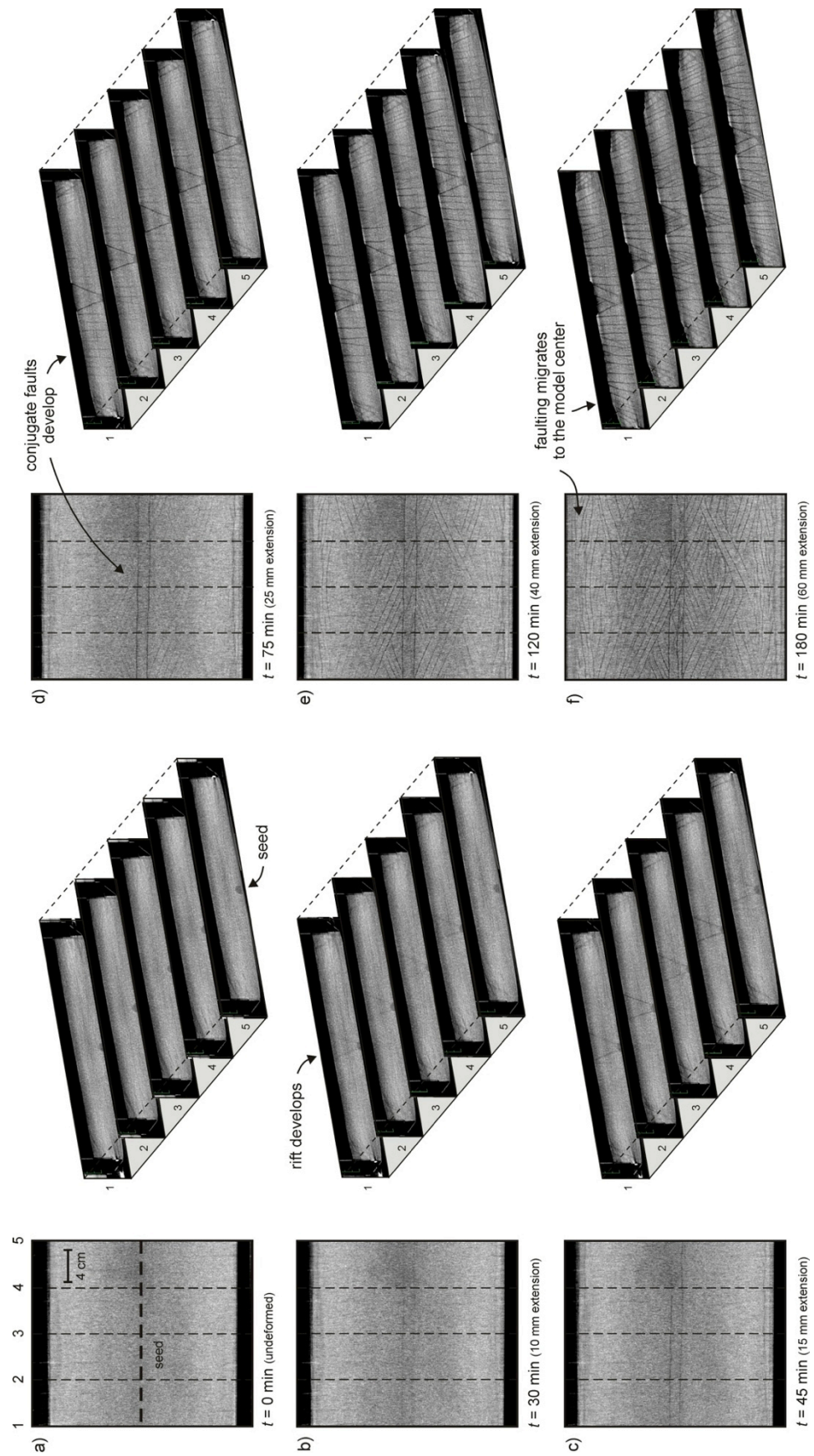
Fig. 7.4. *Internal structural evolution as seen on CT images of brittle-only rubber base model R6 (with seed).*

7.3.2. Rubber base set-up (brittle-viscous)

We present the results of brittle-ductile rubber base models R7 and R8 in Fig. 7.5. Model R7, which contains no seed, produces no clear surface structures except for the strong boundary effects along the sidewalls (Fig. 7.5a-d). In contrast, Model R8 in which a seed is present, experiences early fault localization (after 30 min a rift becomes visible at the surface, Fig. 7.5f) and continues evolving towards the end of the model run (Fig. 7.5h). However, also this experiment develops strong boundary effects along the sidewalls and at the corners, where some viscous material flows into the gap between the original sand buffer and the retreating sidewall. The rift structure is also best developed in the centre of the model, while it dies out towards the sides (Fig. 7.5h). This may be caused by increased friction along the confining sand and the structural gradient involves slight block rotation of the sand layer in the corners of the model.

We also ran two models with highly increased extension velocities (Appendix 7B, Fig. 7.B1). Model R9 with 80 mm/h extension (7.B1a-d) does produce a central rift that is quite similar to the one in model R8 (Fig. 7.5e-h), even though no seed is included. Higher extension velocities (480 mm/h in model R10) result in strongly distributed deformation with multiple rifts (Fig. 7.B1e-h).
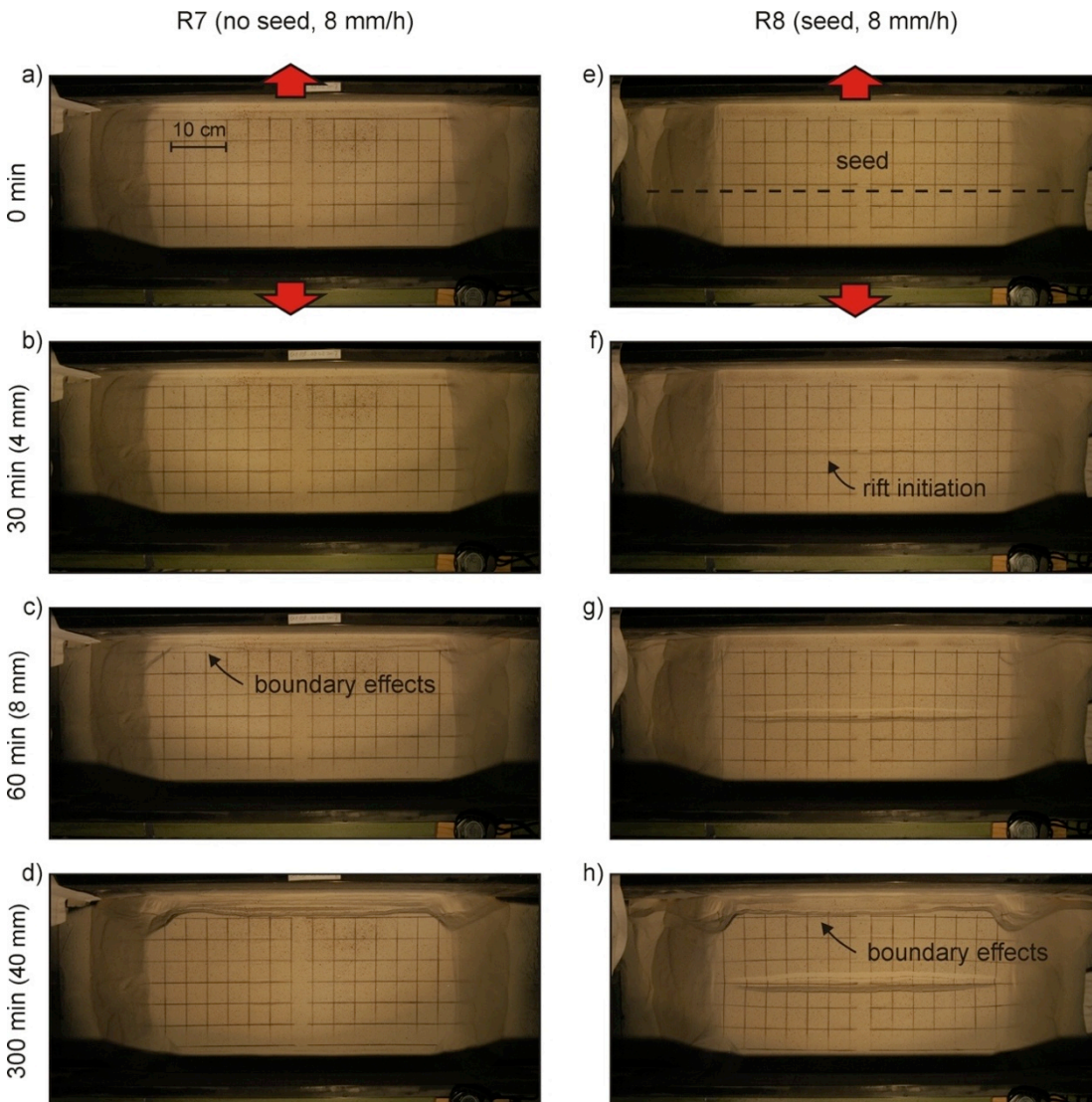
Fig. 7.5. *Surface evolution overview of brittle-viscous rubber base models R7 (without seed) and R8 (with seed). Both models are illuminated from below.*

7.3.3. Foam base set-up (brittle-only)

Two foam base models, both brittle-only, are shown in Fig. 7.6. Experiment F1 (without seed) develops no distinct features except for significant boundary effects along the longitudinal sidewalls towards the end of the model run (Fig. 7.6d). In contrast, the seed in model F4 localizes deformation in the centre of the model, although strong faulting along the sidewalls is also visible at the surface (Fig. 7.6h).

The CT data from experiment F4 (with seed) reveals the evolution of these structures in more detail (Figs. 7.7, 7.8). Some 60 min after model initiation, a graben develops above the seed (Figs. 7.7c, 7.8c), which continues to develop towards the end of the model (Figs. 7.7f, 7.8f). Next to the main rift structure, boundary effects initiate along the sidewalls (Figs. 7.7c, 7.8c) and start propagating toward the centre of the model. At the end of the model run, pervasive sidewall-parallel striking normal faulting is omnipresent throughout the experiment, yet no conjugate sets of strike-slip fault occur (Figs. 7.7f, 7.8c). The bright coloration of the rift shoulders indicates local uplift.
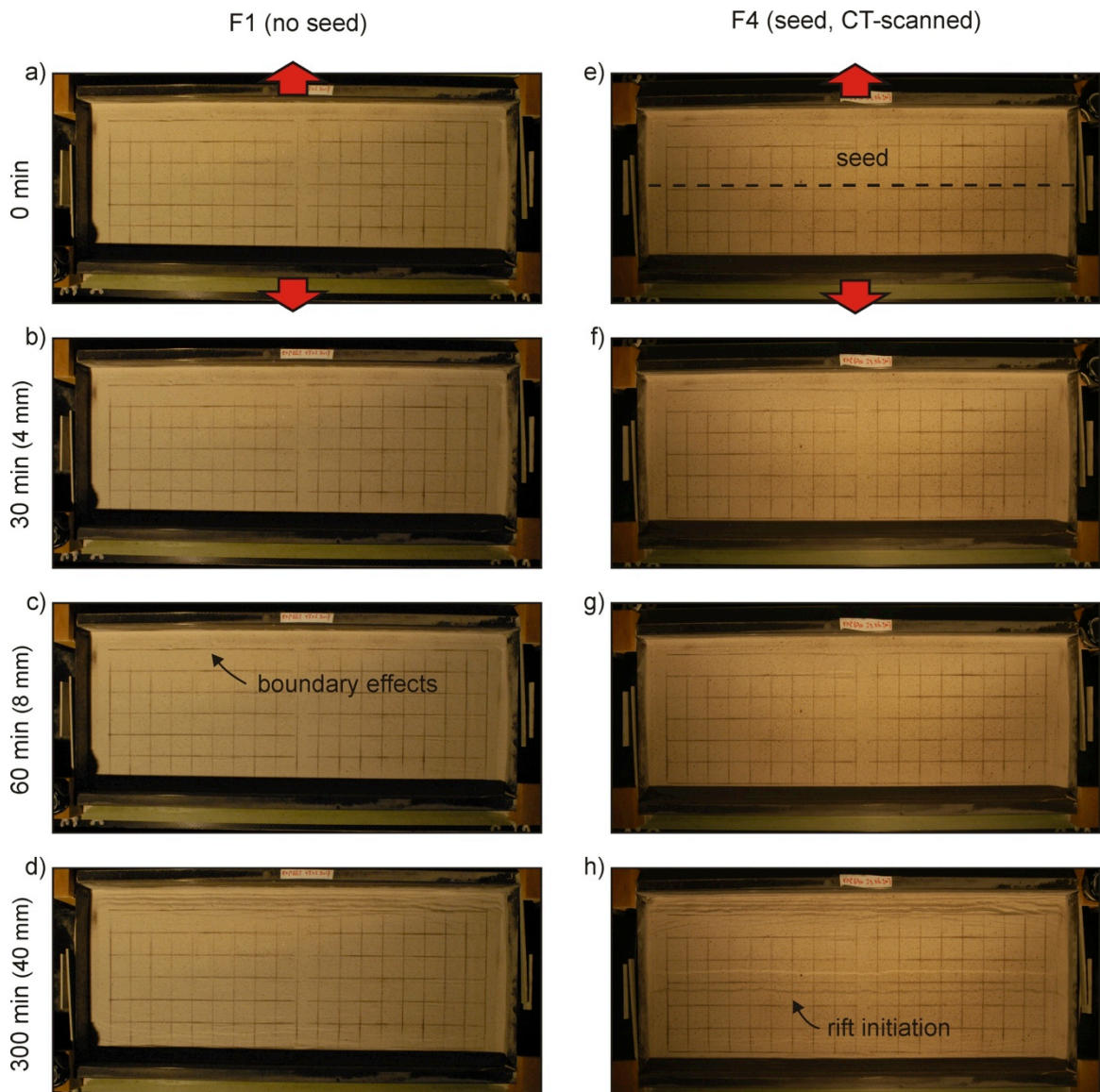
Fig. 7.6. *Surface evolution overview of brittle-only foam base models F1 (without seed) and F4 (with seed). Both models are illuminated from below.*
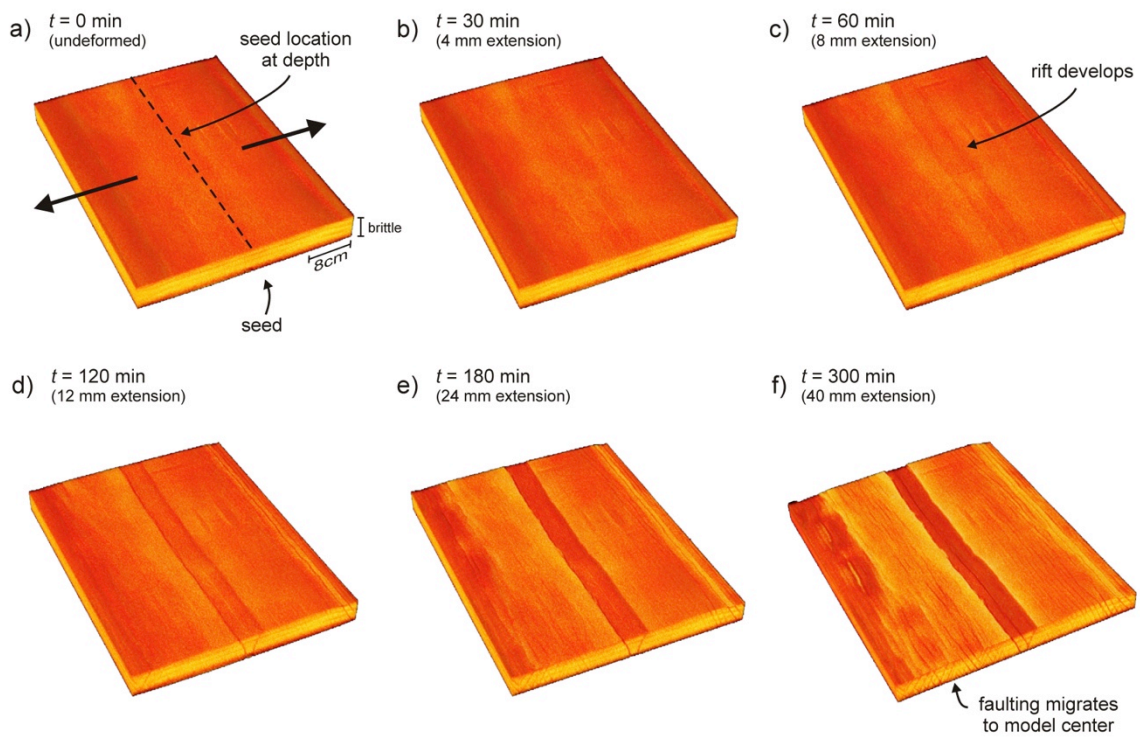
Fig. 7.7. *CT-derived 3D topography evolution of brittle-only foam base model F4 (with seed).*
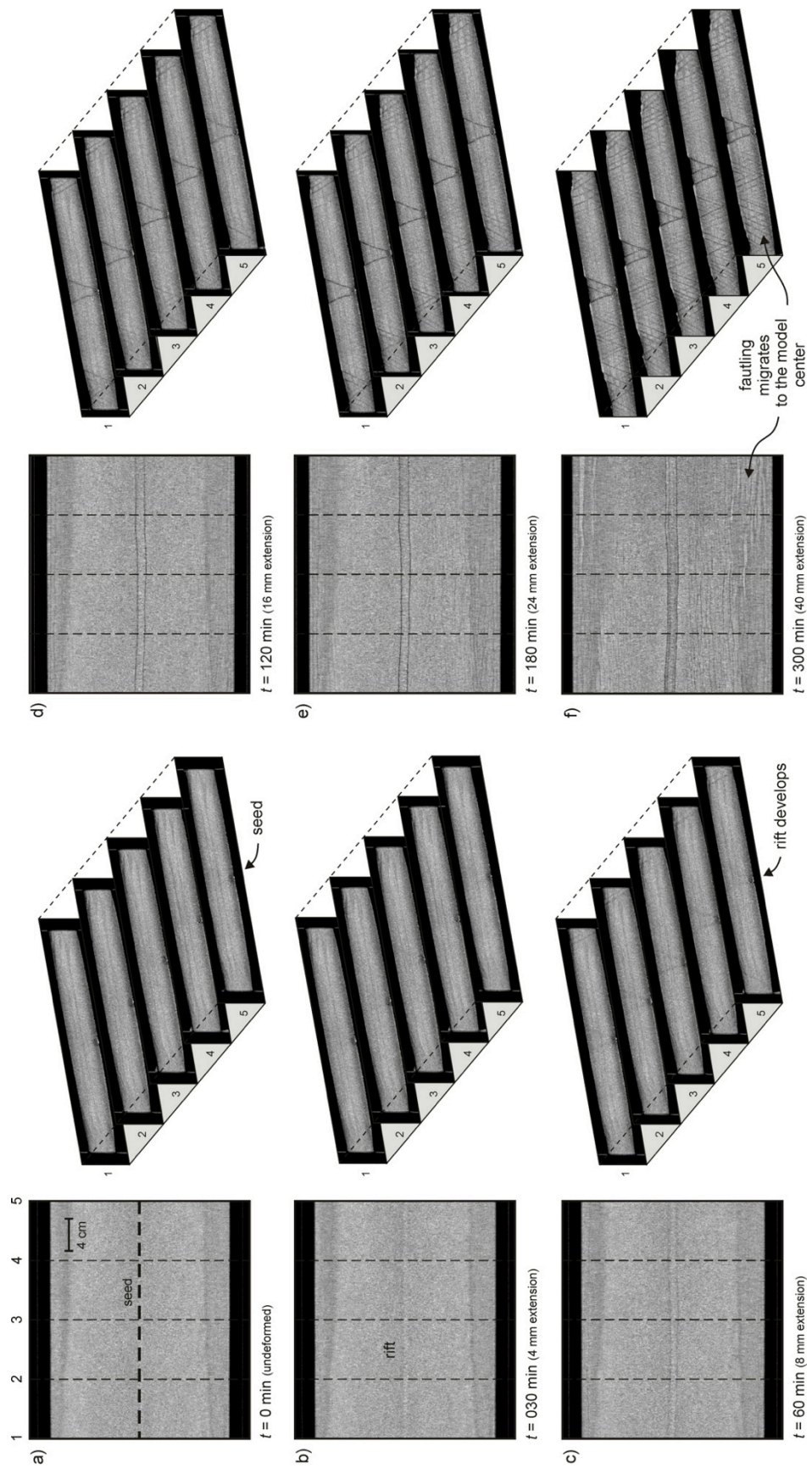
Fig. 7.8. *Internal structural evolution as seen on CT images of brittle-only foam base model F4 (with seed)*

191

7.3.4. Foam base set-up (brittle-viscous)

The evolution of foam base experiments with a brittle-viscous layering is summarized in Fig. 7.9. When no seed is applied (model F6, Fig. 7.8a-d), no central graben forms. Instead, all deformation is concentrated in the boundary effects along the sidewalls. By contrast, model F7 (with a seed) produces a well-developed symmetric graben structure. Yet also this set-up produces some minor faulting along the sidewalls.

CT images illustrate the detailed 3D evolution of model F7 (Figs. 7.10, 7.11). Soon after model initiation (30 min, Figs.

7.10b, 7.11b), a central graben develops above the seed. As the experiment progresses this structure continues to evolve: the rift basin grows deeper with increased subsidence and the rift wedge starts breaking up due to internal faulting (Figs. 7.10d, 7.11d). Some boundary effects develop, but are relatively insignificant with respect to the central graben (Figs. 7.10e, 7.11e): towards the end of the model run the brittle sand is almost breached by the upwelling viscous layer (Figs. 7.10f, 7.11f). In this model, deformation is strongly focussed on the rift structure and no distributed faulting can be distinguished. This model develops rift shoulder uplift as well (Fig. 7.10d-f).
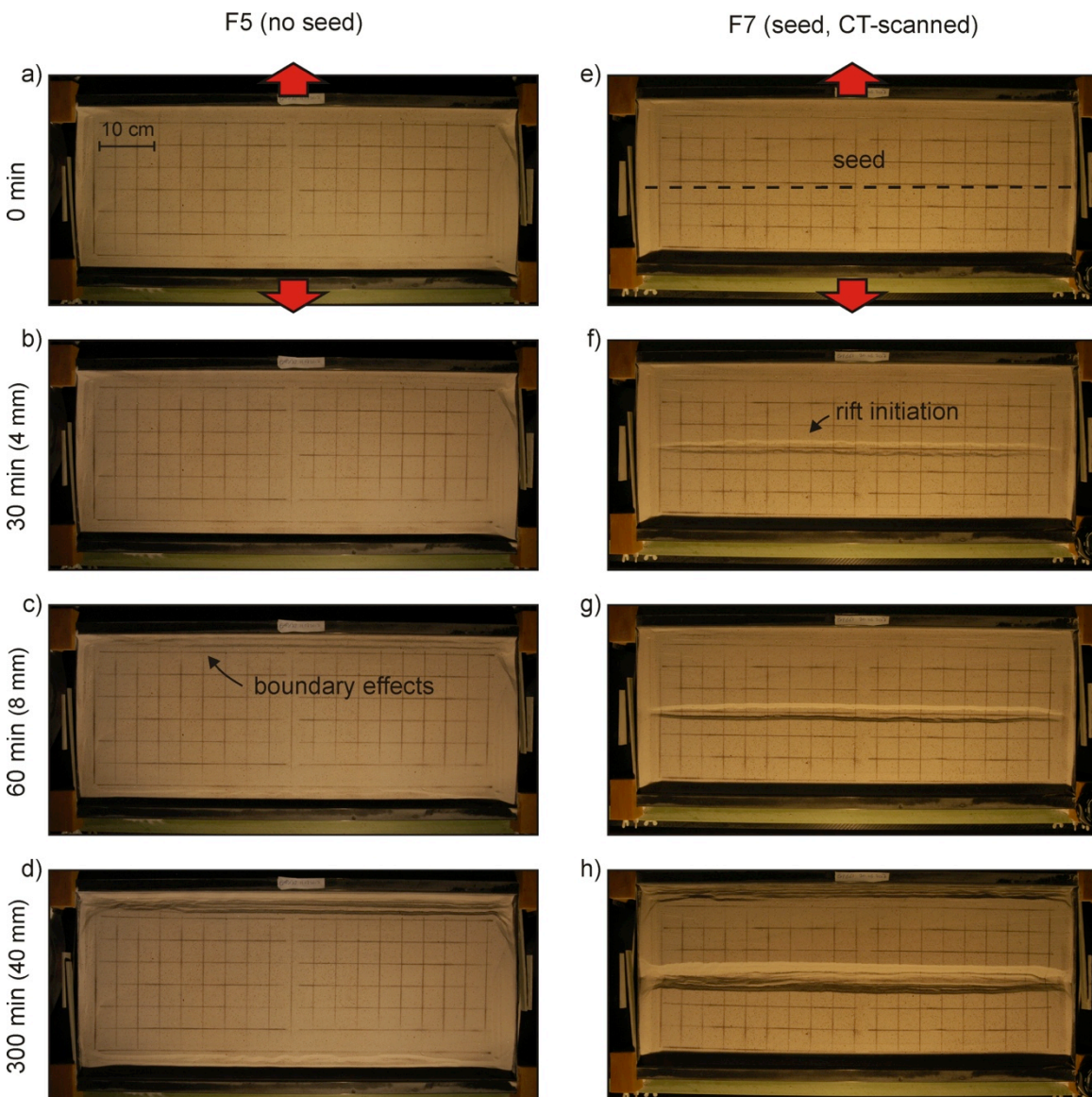
Fig. 7.9. *Surface evolution overview of brittle-viscous foam base models F5 (without seed) and F7 (with seed). Both models are illuminated from below.*
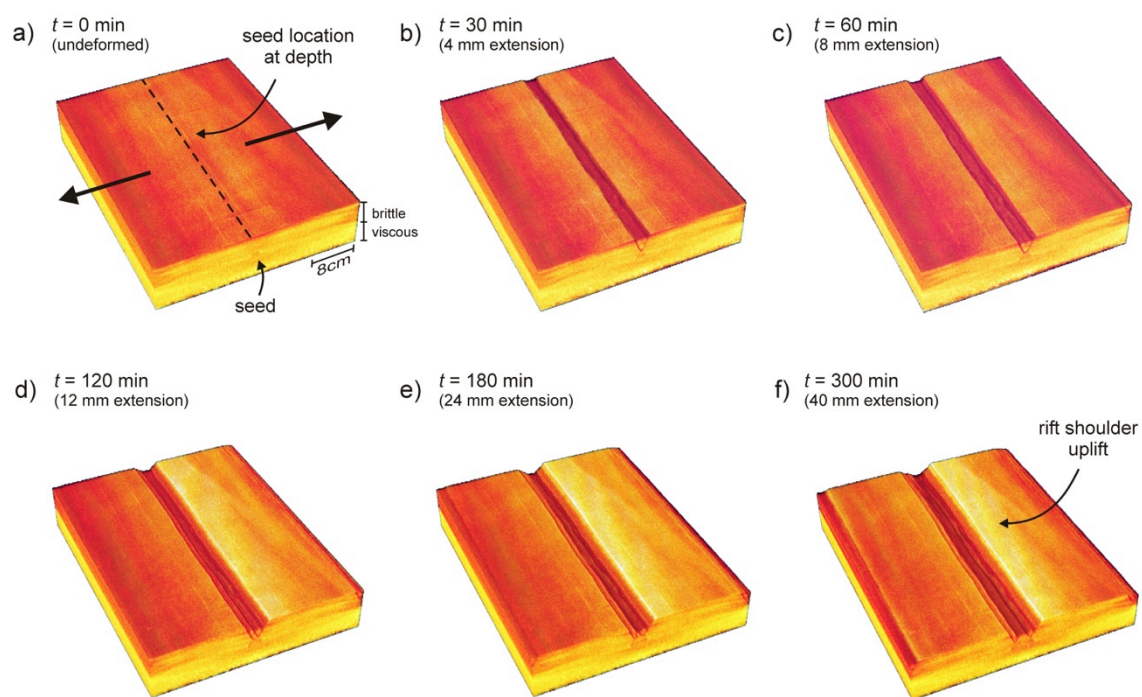
Fig. 7.10. *CT-derived 3D topography evolution of brittle-viscous foam base model F7 (with seed).*
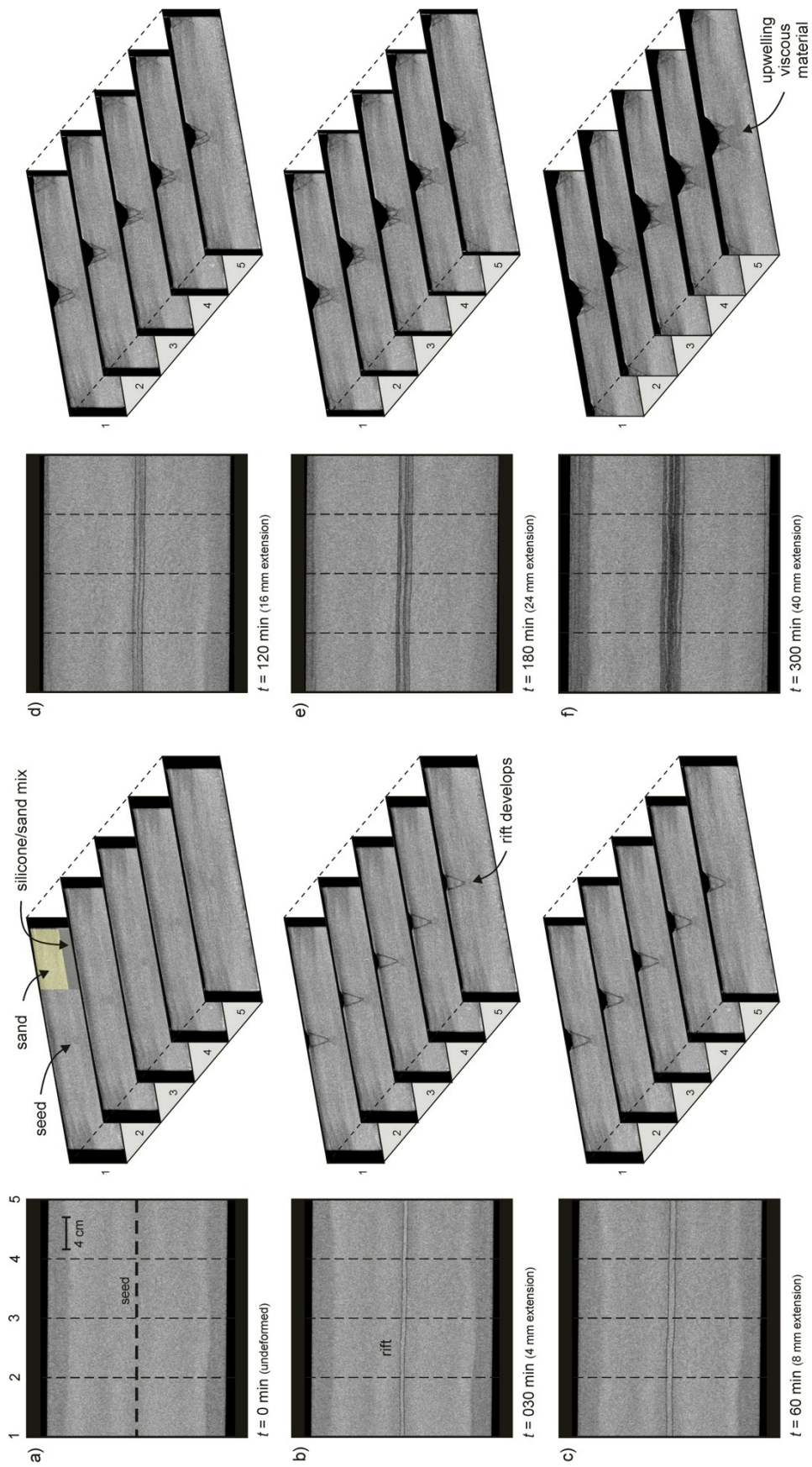
Fig. 7.11. *Internal structural evolution as seen on CT images of brittle-viscous foam base model R6 (with seed).*

7.3.5. Plate base (brittle-only)

A more traditional experimental set-up involves rigid base plates, which is applied for models P1 and P2, both consisting of a brittle sand layer on top of the moving base plate(s) (Fig. 7.12). Early on, both experiments develop a rift above the velocity discontinuity (VD, Fig. 7.12a, g). However, after some 120 min, a difference occurs as model P1 (symmetrical extension) contains a symmetrical graben, while the graben in model P2 (asymmetrical extension) collapses (Fig. 7.12c, h). As deformation continues, model P1 develops a graben with a central horst block in the middle, which is missing in model P2 (Fig. 7.12e, j). Otherwise, both structures have the same width and no boundary effects occur along the sidewalls.
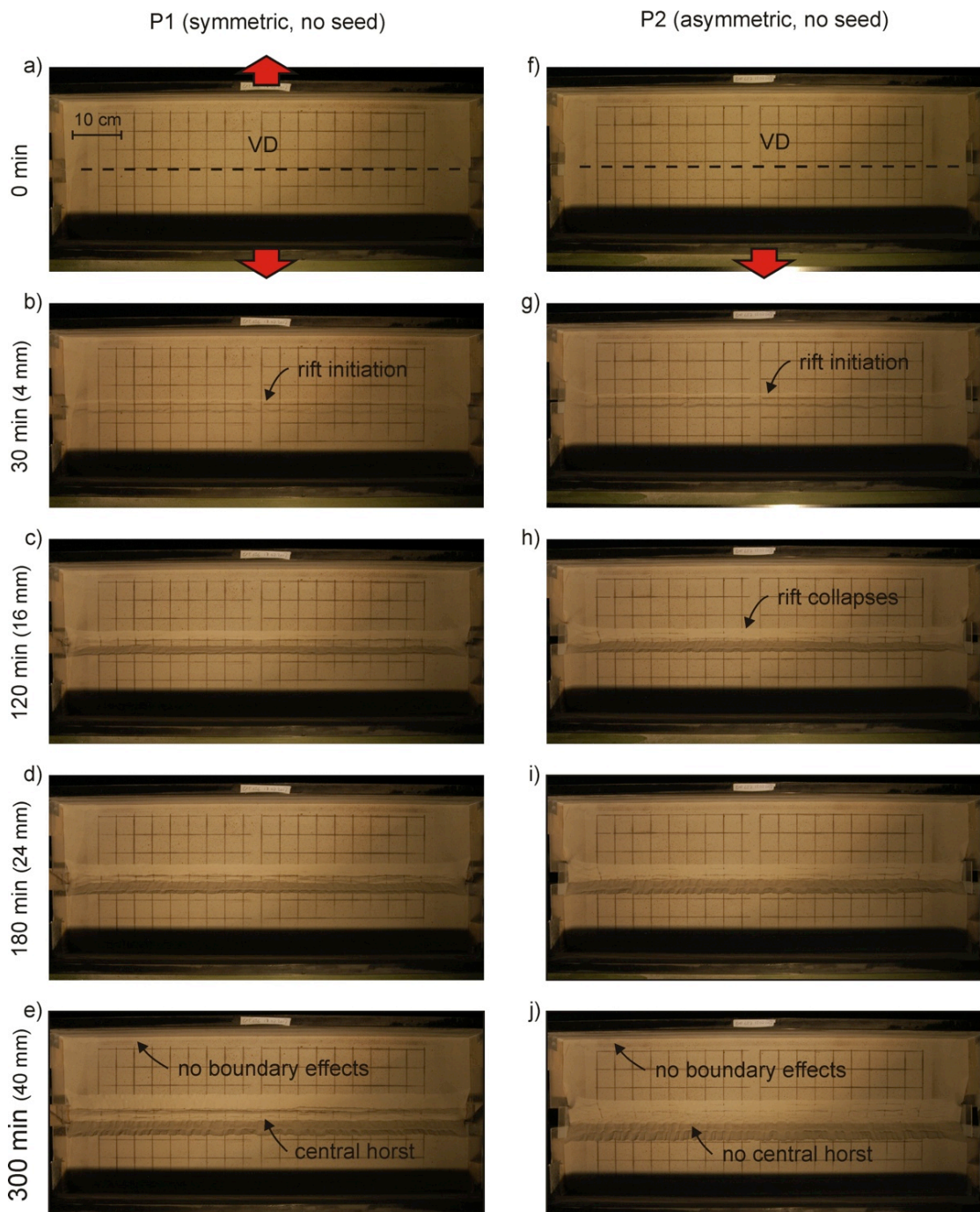
Fig. 7.12. *Surface evolution overview of brittle-only base plate models P1 (symmetric extension) and P2 (asymmetric extension). Both models are illuminated from below.*

7.3.6. Plate base (brittle-viscous)

Applying a brittle-ductile layering to the base plate set-up produces the surface structures shown in Figs. 7.13 and 7.14. In experiments P3 and P7 (symmetrical and asymmetrical extension, respectively, both without a seed), rifting initiates at the short edges of the model, where the confining plates are moving apart (Fig. 7.3b, f). These rifts propagate slightly towards the centre of the model, but strong boundary effects along the sidewalls take up much of the extension there (Fig. 7.13d, h). As a result, block rotation takes place on both sides of the propagating rifts. The surface structures are basically the same in both models, suggesting that the application of symmetric or asymmetric extension does not have a significant influence in this set-up.

Extension velocity is of little consequence it seems, since experiments with 40 mm/h and 2 mm/h extension velocities (P4 and P5, Table 1.2) do produce very similar structures as models P3 and P7. However, the application of a seed on top of the viscous layer (model P10, Fig. 7.14) does result in the early localization and rift development (Fig. 7.14b). This structure continues developing towards the end of the model run, yet the ends are more evolved than the middle section, where boundary effects along the sidewall account for a larger part of the deformation, similar to models P3 and P7 (Figs. 7.13d, h, 7.14d).
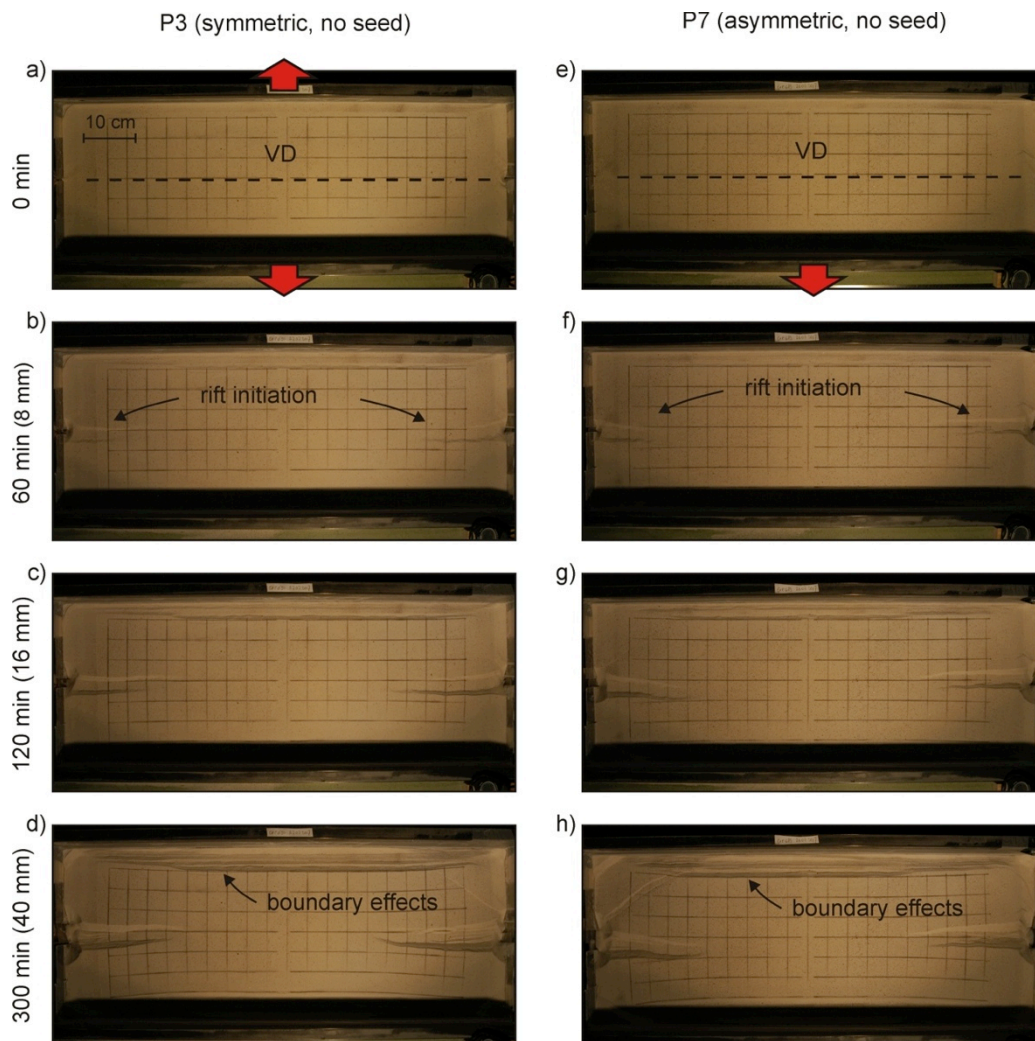
Fig. 7.13. *Surface evolution overview of brittle-viscous base plate models P3 (symmetric extension) and P7 (asymmetric extension). Both models are illuminated from below.*

Further tests with half the layer thickness as the standard models (2 cm brittle and 2 cm viscous, without seed, models P8 and P9, Fig. 7.15) produce a continuous rift above the VD neither. Model P8, with an extension velocity of 2 mm/h (properly scaled down with respect to the standard 8 mm/h), produces the same surface structures as models P3 and P7 (Figs. 7.13, 7.15a). However, model P9, with an 80 mm/h extension rate (translating to 160 mm/h

in the standard set-up), does produce some striking structures (Fig. 7.15b, c). No central rift structure develops. Instead the viscous layer directly above the VD is stretched, creating a flexural depression with continuous flexural rift basins at its margin. Secondary graben structures develop further away from the VD indicating distributed deformation and notably, no boundary effects occur along the sidewalls.
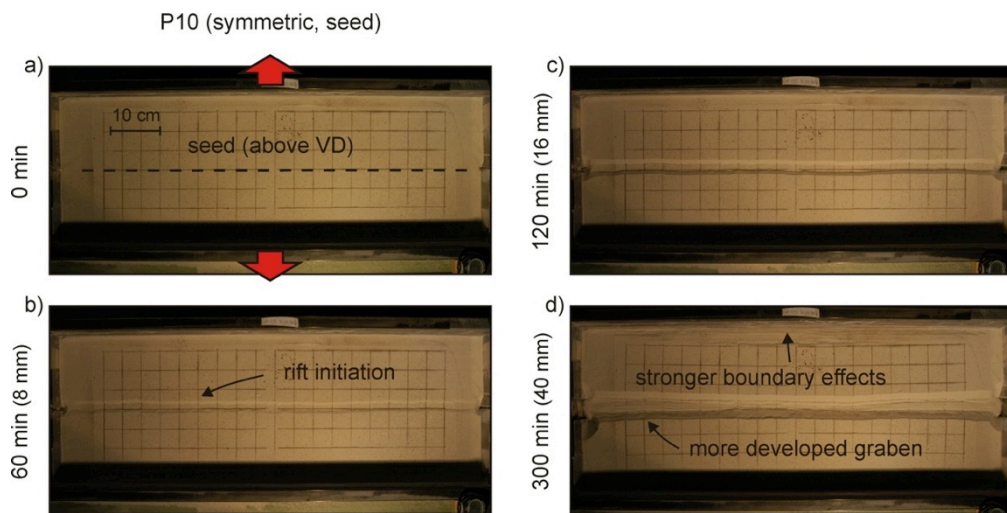
Fig. 7.14. *Surface evolution overview of brittle-viscous base plate model P10 (symmetric extension and with seed). The model is illuminated from below.*

197
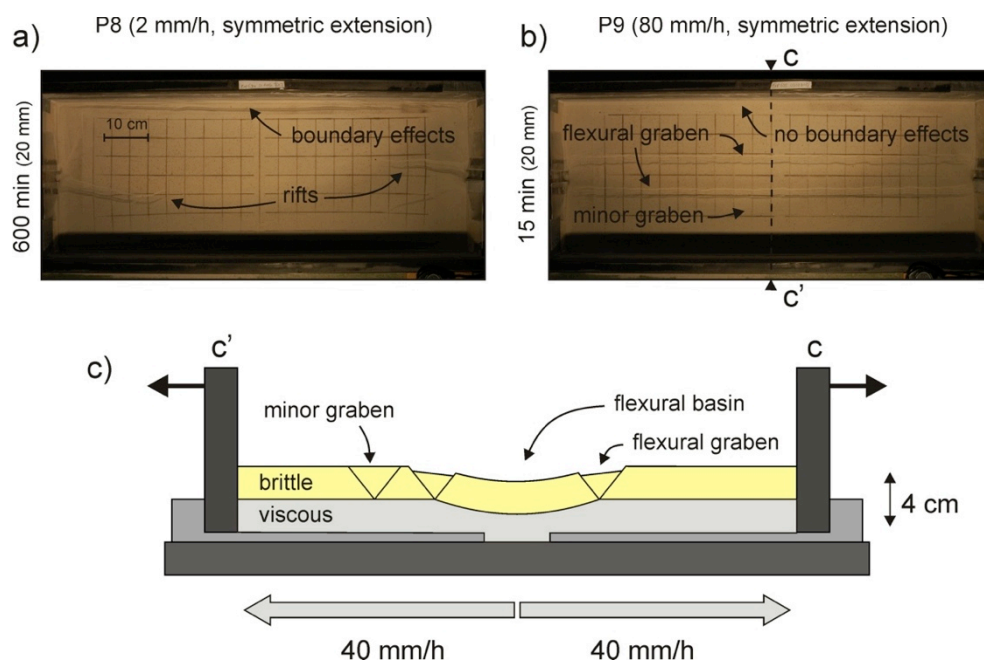
Fig. 7.15. (previous page) *Final top view images of two brittle-viscous base plate models with half the standard layer thickness (40 mm total instead of 80 mm), symmetric extension, no seed but different extension rates: (a) Model P8 (2 mm/h) and P9 (80 mm/h). (c) Interpreted section through model P9, showing the formation of flexural basins. Section location is shown in (b).*

_____

7.4. Discussion

7.4.1. General structures

The three set-ups produce various results, of which a schematic overview is provided in Fig. 7.16, depicting the general structures in map view and section. A clear distinction exists between the brittle-only models (left-hand half in Fig. 7.16) and the brittle-viscous models (right-hand side in Fig. 7.16) since the viscous layer seems to act like a buffer between the deformation-inducing base and the overlying sand. In the brittle models, no buffer exists and deformation is directly transmitted to the overlying sand cover.

7.4.2. Brittle-only experiments

In the rubber base models, the lack of a viscous layer causes a distributed type of deformation and faulting throughout the model (Figs. 7.2-4, 7.16a, a', b, b', 7.B1), including the curious conjugate fault sets due to the along-strike contraction of rubber base that is stretched parallel to the extension direction. Major deformation initiates at the long sidewalls and faulting migrates towards the model axis with progressive stretching. Seeds do localize rift basins, but the formation of this structure only accounts for a minor part of the extension and experiences little subsidence with respect to most other models (e.g. P1 and P2 in Fig. 7.12).

The brittle-only foam base models produce very similar structures as the brittle-only rubber base experiments: distributed deformation that migrates towards the model centre and a minor axial rift when a seed is applied (Figs. 7.6-8, 7.16e, e', f, f'). However, the foam base models do not develop any conjugate strike-sip faults. This may be due to the lower width/length ration of the foam base we use (ca. 0.3) with respect to that of its rubber base equivalent (ca. 0.6). Rubber base models by McClay & White

(1995) and McClay *et al*. (2002) have much lower ratios (0.17 and 0.25, respectively) and do not undergo visible contraction perpendicular to the extension direction, whereas a model by Bahroudi *et al*. (2003) has a ratio of 1.2 and develops strong conjugate strike-slip faulting, even with a viscous basal layer.

The migration of fault activity from the sidewalls to the model centre in both the brittle-only rubber and foam base models may also occur in the Ethiopian Rift, where deformation was initially focussed along the main boundary faults, but since ca. 2 Ma migrated to along-axis rift centres (Ebinger & Casey 2001; Corti 2009). This shift of rift activity is however associated with intense volcanism and continental break-up, so that this comparison may not be completely valid.

Contrary to their rubber and foam base equivalents, a strong localization of the faulting along the velocity discontinuity (VD) occurs in the brittle-only base plate models (Figs. 7.12, 7.16i, j). The continuous motion of the base plate causes the strong concentration of faulting since none of the deformation is lost on distributed deformation and boundary effects, resulting in deep rift basins. As a matter of fact, the centre of the rift basins in both the asymmetric and symmetric experiment lies practically at the same level as the base plates at the end of the model run (4 cm, translating to a 20 km deep basin. This does not seem to provide any meaningful insights in rift formation and this set-up might only provide useful results when smaller amounts of extension are applied (e.g. maximum half the thickness of the brittle crust H, Fig. 7.12c, d, h, i). The small horst structure along the axis of the symmetric extension experiment (Figs. 7.12e, 7.16i, i') is likely formed as both plates move away leaving a small quantity of material behind in the middle.
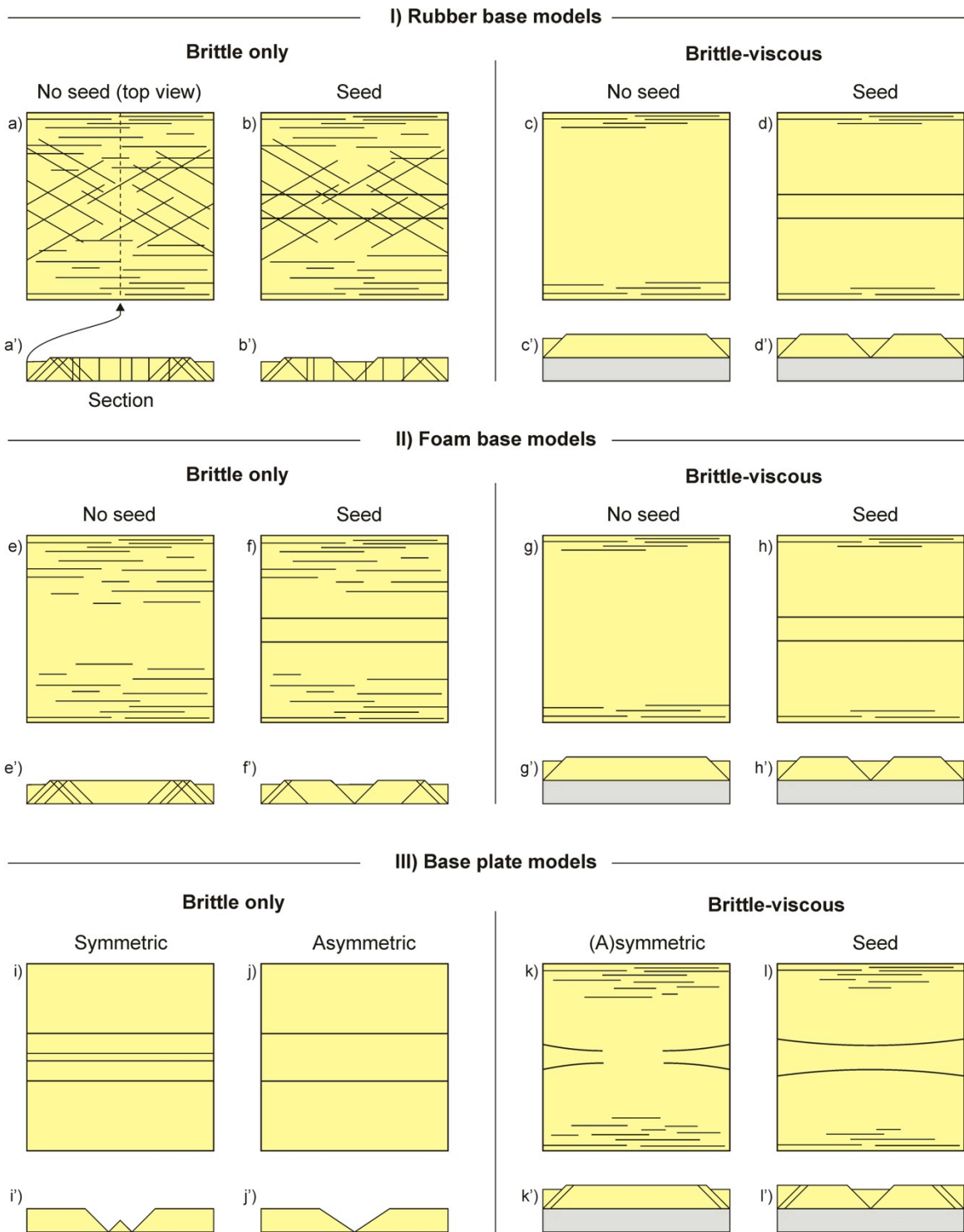
Fig. 7.16. *Schematic overview of all model results in top view (a-l) and in a central section parallel to the extension direction (a'-l'). For all models, extension is parallel to the section indicated in (a).*

7.4.2. Brittle-viscous experiments

The presence of a viscous layer produces quite different structures with comparison to the brittle-only results (Fig. 7.16. Both the brittle-viscous rubber and foam base cases (Figs. 7.5, 7.16c, d and Figs. 7.9-11, 7.16g, h), produce basically the same structures: when no seed is present, faulting occurs along the sidewalls, whereas a seeds concentrate deformation, resulting in a rift structure. The decoupling from the rubber or foam base allows the brittle cover to behave as a rigid block, floating on the viscous layer, whereas the brittle-only models were directly coupled to the base, forcing a pervasive type of faulting (Fig. 7.16a, b, e, f). Such strong coupling can be achieved in the brittle-viscous models as well, by using a material with a higher viscosity or by increasing the extension rate as in models R9 and R10, leading to distributed or wide rifting (Brun 1999; Buiter et al. 2008; Zwaan et al. 2016; Chapter 2, Fig. 7B1). Note that the central rift in model R9 is not localized due to a seed (Fig. 7.B1a-d), but probably due to a wide rift periodicity: the higher the extension rate, the smaller the periodicity and the more rifts develop, as illustrated by model R10 (Fig. 7.B1e-h). It is furthermore important to mention that no conjugate fault sets occur in the brittle-viscous rubber or foam base experiments. The fact that the rifts in the rubber base models are less developed towards the short ends of the model is due to the application of sand to contain the viscous material, causing friction, and could potentially be solved by using a rubber sidewall, as is done for the foam set-up.

In contrast to brittle-only model results, the brittle-viscous base plate model results are quite similar to those of the rubber and foam base experiments (Fig. 7.12-14, 7.16k, l). Without a seed to focus rifting and independent of the symmetry or asymmetry of extension, as the viscous layer accommodates the stretching, minor rifting initiates at the short sides of the model due to the parting rigid sidewalls there. However, these rifts do not fully propagate toward the centre of the model, so that boundary effects along the sidewalls are stronger (Figs. 7.13, 7.16 k). Even with a seed, this boundary effect causes the rifts to be more developed at the short ends of the model (Figs. 7.14, 7.16j).

The fact that our brittle-viscous rigid base plate set-ups fail to produce proper rift basins without a seed to localize deformation is in remarkable contradiction with previous studies that produce well-developed rifts above the VD (e.g. Allemand & Brun 1991; Bonini et al. 1997; Keep & McClay 1997; Tron & Brun 1993).

At close examination however, Allemand & Brun (1991) apply a different brittle-viscous thickness ratio of ca. 2/1 instead of our 1/1, which probably increases brittle-ductile coupling and rift localization. Whether this thickness ratio is realistic depends heavily on the specific tectonic setting, as lithospheric rheological profiles are known to vary considerably over the globe (Brun 1999). The models by Tron & Brun (1993) have a high brittle-viscous thickness ratio as well (2/1 instead of our 1/1). Together with their relatively high extension rates (15 cm/h), these models are more related to experiment P9 discussed in the following section. This might also be the case for the models by Allemand & Brun (1991), but no extension rates are provided.

Other authors (e.g. Bonini et al. 1997; Keep & McClay 1997) produce rift structures by applying only a small patch of viscous material along the VD, opposed to the full viscous layer used for our models. In these experiments, the borders of these viscous patches form rheological contrasts, strongly focussing deformation, whereas the outer brittle regions remain unaffected. The resulting rift structures are therefore strongly controlled by the width of the viscous patch instead of by the VD.

7.4.3. Flexural basins

Although model P9, which develops flexural marginal basins may not strictly be part of the model comparison due to its excessive extension velocity compared to the standard set-up, its intriguing structures should not be omitted (Fig. 7.15b, c). Its high extension velocity causes strong coupling between the

brittle and viscous layer resulting in intense stretching (necking) above the velocity discontinuity and subsequent downward bending of the sand cover. Similar effects are seen in the high-extension velocity models by Brun & Tron (1993) and Tron & Brun (1993), although their relatively thick brittle cover develops considerably more faulting. This may be promoted by the higher degree of total extension in their models (4 and 5 cm), which amounts to 2 and 2.5 times their 2 cm brittle layer thickness, respectilvely (i.e. 2 or 2.5 H, Allken et al. 2011). In our models, we only apply 4 cm or 1 H total extension, given our brittle layer thickness of 4 cm.

They do however not produce the flexure at the edge of the system, which causes local extension and the formation of marginal basins in our model P9. Similar structures can be observed along the Western Escarpment of the Afar (northernmost sector of the East African Rift System) in Ethiopia (e.g. Chorowicz *et al*. 1999), possibly caused by loading due to massive diking and underplating occuring in the adjacent rift basin (Corti *et al*. 2015). Our models suggest that a rapid extension could also cause such geometries.

7.5. Conclusion

In this paper we present a comparison between crustal-scale analogue models with a range of different set-ups, leading us to the following conclusions:

- There is a strong difference between brittle-only models with either a base plate or a foam/rubber base set-up;
- Rubber base and foam base set-ups are much alike and the migration of fault activity towards the rift axis might resemble the situation in the Ethiopian Rift;
- To avoid strong boundary effects in rubber base set-ups, applying a low width/length ratio is advised;
- Plate base brittle-only experiments should not involve too much extension to remain realistic;
- Of the brittle-viscous experiments we tested, the least boundary effects were were obtained with a foam base and seed set-up. This is partially due to the use of a rubber sidewall, which could also be applied for a rubber base set-up in order to minimize boundary effects;
- The seemingly poor results obtained with the brittle-ductile rigid base plate set-up is probably due to the low brittle-ductile thickness in our models;
- High extension rates could produce flexural basins and marginal grabens, as e.g. observed in Ethiopia.

In order to further investigate this model series, the following steps are planned:

- All models are sprinkled with coffee grains to create a pattern for particle image velocimetry (PIV) analysis (e.g. Molnar *et al.* 2017), which might reveal the exact horizontal motions in the models, in order to better constrain e.g. the compressive deformation of the rubber-base models;
- Various models could be rerun in the CT-scanner to allow a detailed 4D analysis of the model structures;
- Some models could be rerun with thinner viscous layers to thest the influence of brittle/viscous ratios;
- As the model materials are mixed with small amounts of Zirshot, it is possible to apply further digital volume correlation (DVC) analysis (Adam *et al.* 2013; Zwaan *et al.* submitted; Chapter 4) for a quantified assessment of 4D (internal) model deformation;
- This model series can serve as a base for a future detailed analogue-numerical comparison effort, similar to e.g. Buiter *et al.* (2006; 2016).

7.6. Acknowledgements

Appendix 7A

vx (incremental horizontal displacement)   vy (incremental vertical displacement)
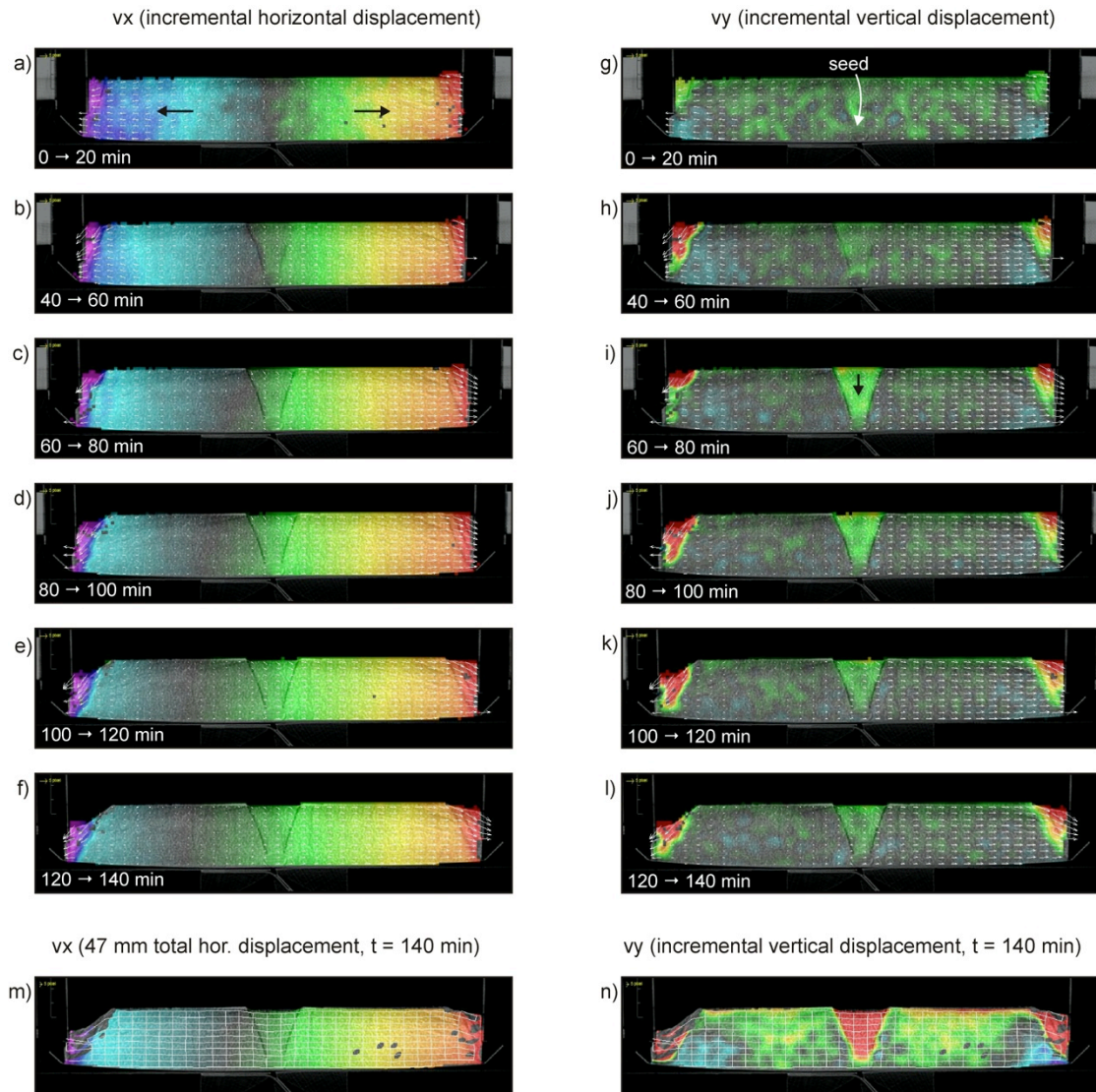
Fig. 7.A1. *Preliminary (uncalibrated) digital volume correlation (DVC) analysis of CT-scanned brittle-only rubber base model R4 with 20 mm/h extension velocity (similar set-up as Model R6, shown in Figs. 2-4), illustrating horizontal and vertical internal displacement. (a-f) Incremental horizontal displacement between time steps and (m) total horizontal displacement. Cool colours indicate leftward motion, warm colours rightward motion. (g-l) Incremental vertical displacement between time steps and (n) total vertical displacement. Cool colours indicate upward motion, warm colours downward motion. The section is taken through the center of the model, parallel to the extension direction. NB: the rubber base sheet started tearing at t = ca. 140 min. The model total extension is 54 mm. For an explanation of the DVC technique, the reader is referred to Chapter 4 of this Thesis.*

Appendix 7B
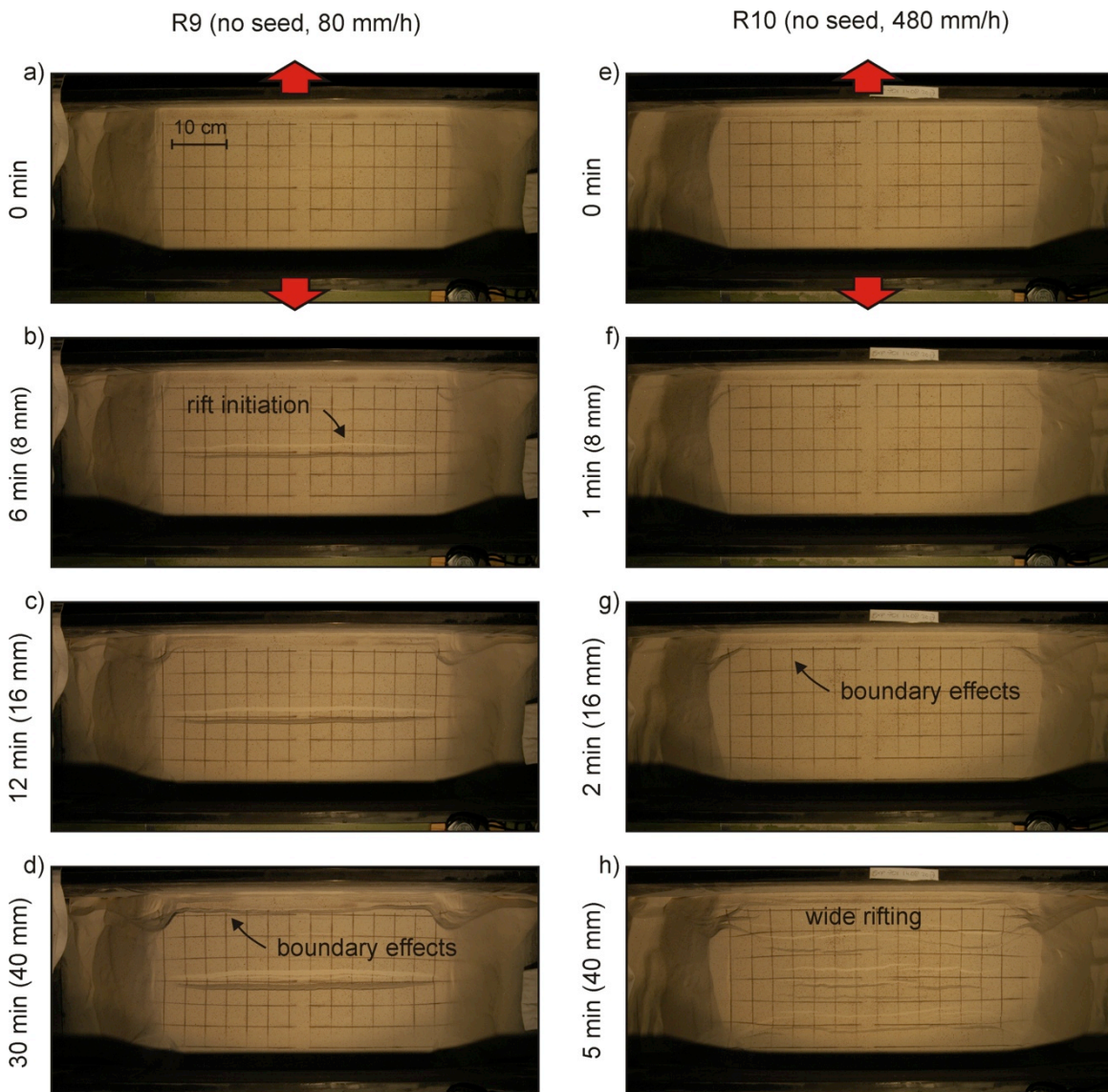
Fig. 7.B1. *Surface evolution overview of high-extension rate brittle-viscous rubber base models R9 (80 mm/h) and R10 (480 mm/h, both without seed). The wide rifting leads to either a central rift (R9) or multiple rifts that distribute deformation (R10). The models are illuminated from below.*

Chapter 8

Conclusion and Outlook

The experiments performed for this Thesis and described in the previous 7 chapters have provided a better insight in the development and propagation of rift basin and rift linkage zones in various extensional regimes, how they might be influenced by various structural inheritance geometries and syn-tectonic sedimentation, and how our basic methodology compares to different other model set-ups. A summary of the results is provided below, as well as an outlook for future modelling opportunities.

8.1. Choice of set-up

The defining factor in analogue modelling is the model set-up. Throughout this Thesis, a brittle-ductile foam base configuration with seeds is applied to localize deformation in the brittle top layer. Numerous other methods have been used in previous modelling studies, of which a selection was tested for a thorough comparison in Chapter 7.

It appears that structural inheritance, either in the shape of a velocity discontinuity (VD) or a seed, is key to focus deformation in our models. In the rubber and foam base set-ups, a viscous basal layer facilitates fault localization as it buffers distributed deformation, and reduces coupling, allowing the brittle cover to behave as rigid blocks. It simultaneously prevents the strong and probably exaggerated concentration of faulting along the VD as seen with the rigid plate set-up. The experiments illustrate furthermore that the standard brittle-ductile foam set-up with a seed focussing deformation produces the least amount of boundary effects and thus provides the best results among the tested set-ups. A rubber sheet base model could in theory be similarly efficient, yet a rubber or foam sidewall will be necessary to reduce boundary effects. The brittle-ductile base plate models for instance develop too much friction along the sidewalls, a problem that could partially be resolved by applying a lubricant between the short sidewalls and the model materials.

Another consideration is the simulation of oblique extension as in Chapters 2-4 using a foam base model configuration, which may be feasible for the rubber base set-up as well, but will causes spatial problems when applied to the base plate set-up. Therefore, the standard methodology used throughout chapters 2-6 is confirmed to be appropriate for this study, yet the other set-ups may be of use for studies involving analogue models of other tectonic settings.

8.2. Factors controlling rift basin development

Various factors are shown to be of influence on the evolution of a rift basin. Firstly, the application of a linear seed, simulating a linear type of structural inheritance in the upper crust, produces a narrow rift basin, where previous authors have often applied wider patches of viscous material or rubber sheets to create a wider rift zone. Furthermore, the rate of extension is shown to control the degree of brittle-ductile coupling (Chapter 2), either producing a localized rift along the seed or multiple rift basins throughout the model. Also the amount of extension determines the type of structures present in a rift: only minor deformation along boundary faults or additional faulting within the rift wedge, potentially accompanied by a rising viscous layer may occur. The amount of extension is

also a factor of the extension direction, since oblique extension produces narrower basins, with steeper boundary faults and oblique internal structures.

Moreover, along-strike variations in extension rate in both time and space may lead to a complex structural configuration, as illustrated by scissor extension models (Chapters 5 and 6). It appears that such gradients in the rate (and thus amount) of extension are a crucial factor in rift propagation.

A final factor is syn-rift sedimentation, as described in Chapter 3. The presence of sediments in the rift basin does not affect the initial rift configuration set by large-scale tectonic forces, but its additional weight does influence the structural style within the rift basin, concentrating deformation along a set of major faults instead of a myriad of minor faults and causing increased total subsidence, preventing the viscous layer from rising. High syn-rift sediment influx might even delay continental break-up, but large-scale plate tectonic processes determine whether a continent is actually broken up eventually.

8.3. Factors controlling rift interaction

Most of the factors that influence the evolution of individual rift segments, affect the interaction and linkage between them as well. For instance, a seed may localize deformation, but a high extension rate and associated brittle-ductile coupling results in the development of multiple rift basins with little amounts of extension each, limiting their capacity to interact. Instead, low extension rates focus deformation along a single rift segment, allowing it to propagate and interact with other segments.

However, it is shown that large rift offsets hinder rift linkage, especially when the extension direction is such that the segments propagate parallel to each other or even apart (orthogonal extension and sinistral extension in Chapters 1-3), although in some cases strike-slip transfer zone development may occur (sinistral extension models for right-

stepping rift segments in Chapters 2 and 3). The interplay between initial seed geometry and extension direction proves to be a crucial factor for rift linkage establishment.

Within this context, secondary seeds, connecting the main rifts, are of minor importance and only activate when oriented favourably to the regional extension direction (Chapter 3). The presence of sedimentation, although of importance for internal rift structures, does not significantly affect the large-scale rift linkage zone formation, especially since these zones experience relatively little subsidence, thus less accommodation space is available for sediment deposition (Chapter 4). In contrast to the situation with large-scale rift structures, along-strike extension gradients associated with scissor extension have no strong impact on rift interaction zones, since the extension gradient between two rifts is generally minor (Chapter 6).

8.4. Additional remarks

Although top view photographs and CT data allow a thorough insight into the 3D external and internal model evolution, 4D DVC analysis has provided an unprecedented understanding of 3D internal displacement and deformation within the brittle and viscous parts of the models (Chapter 4). These results illustrate the strong difference between brittle behaviour, the sand behaving as rigid blocks interrupted by discrete zones of faulting, floating on the viscous layer that shows a distributed flow pattern. Not only does the DVC analysis capture the rising viscous material beneath the rift basins, it also reveals out-of-plane flow of viscous material due to the interacting rift segments. This last observation is crucial for 2D structural reconstructions of orthogonal extension settings, as both viscous and brittle material can move out of section.

The models are compared with natural examples of continental rifts and rift interaction structures, resembling various structures observed in e.g. the East African Rift System, the North Sea Viking Graben and the Cenozoic European Rift System. However,

a comparison with previous models and natural examples also shows a reasonable fit with the geometries of oceanic spreading centres, suggesting that these brittle-viscous set-ups can also be used for the modelling of oceanic settings.

8.5. Outlook

This work has involved the use of the good old Namazu apparatus and the newly designed Xissor machine, which together with the ready access to a CT scanner have yielded spectacular footage of the internal model evolution. Combined with the use of 4D DVC techniques, new PIV surface analyses and a recently acquired David 5 structured light scanner (SLS) for detailed topography scans, the UniBern TecLab now provides unique opportunities for future analogue modelling projects.

As shown in Chapter 6, the Namazu machine is easy to customize for a variety of different set-ups from (oblique) extension to (oblique) compression that can subsequently be run in the CT scanner, as was readily done for a collaboration with researchers from the University of Pavia (Fedorik *et al*. in prep.). Although less flexible, the Xissor machine allows a fair degree of tinkering as well and could be used for various different set-ups as well.

The Namazu machine could even be adjusted for lithosphere-scale models. Similar to the Xissor design process, a BSc student Y. Pöltinger from the IPEK/HSR Technische Hochschule Rapperswil provided a conceptual design for a totally new machine for (oblique) extension/compression, including the option to include mantle convection, with codename the "Honeypot" (Appendix VI). Financial constraints prevented its construction, but inspired by the versatility of the Namazu and

discussions with Y. Nestola (then Univeristy of Roma TRE), I sketched a new lithosphere-scale model set-up that may be more readily realized in the future by a handy hobbyist (Appendix VII). CT-scanned models of this type are rare, providing an opportunity for new breakthroughs, especially in combination with DVC techniques.

Other possibilities might lie in importing the CT datasets into 3D structural interpretation software. Fedorik *et al*. (in prep) have applied Move™, which proved to be a rather cumbersome undertaking since the software does not allow one to freely scroll through the dataset, moving in all possible directions as is possible in OsiriX. Researchers from the IFP Energies nouvelles (Paris) are known to be able to import their data into GOCAD® and have in collaboration with the University of Lorraine applied this technique for the calibration of 3D structural reconstruction software, normally used on seismic datasets (Chauvin *et al*. in press). Rumours have it that it will also be possible to import CT datasets in 3D seismic interpretation software Petrel, providing the software's complete toolbox for structural interpretation and georeferencing that the medical software OsiriX lacks dearly.

The current planning is to prepare the last three chapters of this Thesis, rerunning specific models in the CT scanner and using DVC analysis for a quantitative deformation assessment. Chapter 7 is also planned as a basis for an analogue-numerical comparison study to calibrate computer simulations and combine the strengths of both modelling approaches (see Paragraph 1.5). Furthermore, a BSc student (M. Bühler) is now starting promising work on models of multiphase rifting in the Mozambique Channel with the use of the Namazu apparatus and the new SLS surface scanner for topography analysis, ensuring the continuation of this work in the UniBern TecLab.
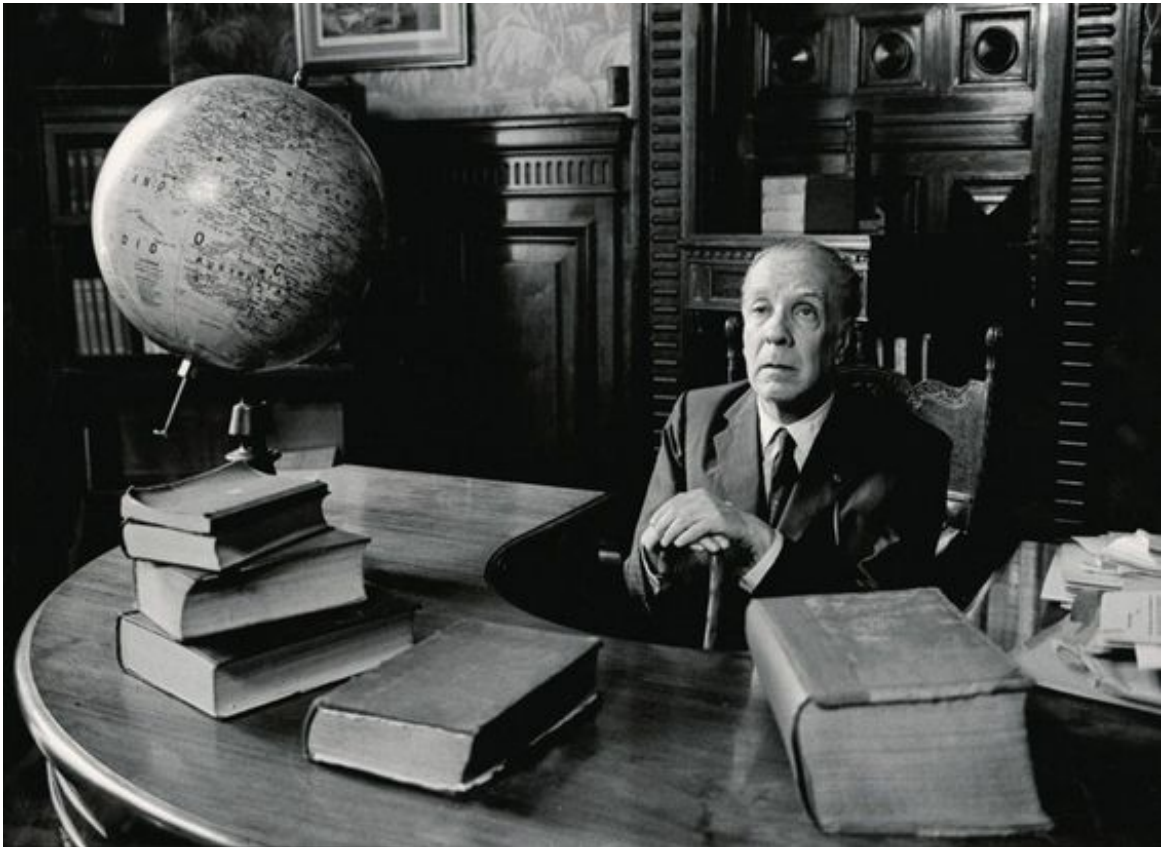
Photo: Eduardo Comesaña

Bibliography

Abdelmalak, M.M., Bulois, C., Mourgues, R., Galland, O., Legland, J.-B., Gruber, C. 2016. Description of new dry granular materials of variable cohesion and friction coefficient: Implications for laboratory modeling of the brittle crust. Tectonophysics 684, 39-51.

Acocella, V., Faccenna, C., Funiciello, R., Rossetti, F. 1999a. Sand-box modelling of basement-controlled transfer zones in extensional domains. Terra Nova 11 (4), 149-156.

Acocella, V., Salvini, F., Funiciello, R., Facenna, C. 1999b. The role of transfer structures on volcanic activity at Campi Flegrei (Southern Italy). Journal of Volcanology and Geothermal Research 91, 123-139.

Acocella, V., Faccenna, C., Funiciello, R., Rossetti, F. 2000. Analogue modelling of extensional transfer zones. Italian Journal of Geoscience 119, 85-96.

Acocella, V., Morvillo, P., Funiciello, R. 2005. What controls relay ramps and transfer faults within rift zones? Insights from analogue models. Journal of Structural Geology 27, 397-408.

Adam, J., Urai, J.L., Wieneke, B., Oncken, O., Pfeiffer, K., Kukowski, N., Lohrmann, J., Hoth, S., van der Zee, W., Schmatz, J. 2005. Shear localisation and strain distribution during tectonic faulting - new insights from granular-flow experiments and high-resolution optical image correlation techniques. Journal of Structural Geology 27, 2, 283-301.

Adam, J., Klinkmüller, M., Schreurrs, G., Wieneke, B. 2013. Quantitative 3D strain analysis in analogue experiments simulating tectonic deformation: Integration of X-ray computed tomography and digital volume correlation techniques. Journal of Structural Geology 55, 127-149.

Agostini, A., Corti, G., Zeoli, A., Mulugeta, G. 2009. Evolution, pattern, and partitioning of deformation during oblique continental rifting: Inferences from lithospheric-scale centrifuge models. Geochemistry, Geophysics, Geosystems 10 (11), Q11015.

Aldrich, M. J. 1986. Tectonics of the Jemez Mountains and Rio Grande Rift. Journal of Geophysical Research 91 (B2), 1753-1762.

Allemand, P., Brun, J.-P., Davy, P., Van der Driessche, J. 1989. Symétrie et asymétrie des rifts et mécanismes d'amincissement de la lithopshère. Bulletin de la Société Géologique de France 8 (3), 445-451.

Allemand, P., Brun, J-.P. 1991. Width of continental rifts and rheological layering of the lithosphere. Tectonophysics 188, 63-69.

Allken, V., Huismans, R.S., Thieulot, C. 2011. Three-dimensional numerical modeling of upper crustal extensional systems. Journal of Geophysical Research 116, B10409.

Allken, V., Huismans, R.S., Thieulot, C. 2012. Factors controlling the mode of rift interaction in brittle-ductile coupled systems: A 3D numerical study. Geochemistry, Geophysics, Geosystems 13, Q05010.

Alonso-Henar, J., Schreurs, G., Martinez-Díaz, J.J., Álvarez-Gómez, J.A., Villamor, P. 2015. Neotectonic development of the El Salvador Fault Zone and implications for the deformation in the Central America Volcanic Arc: Insights from 4-D analog modeling experiments. Tectonics 34, 133-151.

Amilibia, A., McClay, K.R., Sàbat, F., Muñoz, J.A., Roca, E. 2005. Analogue Modelling of Inverted Oblique Rift Systems. Geologica Acta 3 (3), 251-271.

ArRajehi, A., McClusky, S., Reilinger, R., Daoud, M., Alchalbi, A., Ergintav, S., Gomez, F., Sholan, J., Bou-Rabee, F., Ogubazghi, G., Haileab, B., Fisseha, S., Asfaw, L., Mahmoud, S., Rayan, A., Bendik, R., Kogan, L. 2010. Geodetic constraints on present-day motion of the Arabian Plate: Implications for Red Sea and Gulf of Aden rifting. Tectonics 29, TC3011.

Autin, J., Bellahsen, N., Husson, L., Beslier, M.-O., Leroy, S., d'Acremont, E. 2010. Analog models of oblique rifting in a cold lithosphere. Tectonics 29, TC6016.

Autin, J., Bellahsen, N., Leroy, S., Husson, L., Beslier, M.-O., d'Acremont, E. 2013. The role of structural inheritance in oblique rifting: Insights from analogue models and application to the Gulf of Aden. Tectonophysics 607, 51-64.

Bahroudi, A., Koyi, H.A., Talbot, C.J. 2003. Effect of ductile and frictional décollements on style of extension. Journal of Structural Geology 25, 1401-1423.

Balestrieri, M.L., Bonini, M., Corti, G., Sani, F., Philippon, M. 2016. A refinement of the chronology of rift-related faulting in the Broadly Rifted Zone, southern Ethiopia, through apatite fission-track analysis. Tectonophysics 671, 42-55.

Bartholomew, I.D., Peters, J.M., Powell, C.M. 1993. Regional structural evolution of the North Sea: oblique slip and the reactivation of basement lineaments. Petroleum Geology Conference series 4, 1109-1122.

Basile, C., Brun, J.-P. 1999. Transtensional faulting patterns ranging from pull-apart basins to transform continental margins: an experimental investigation. Journal of Structural Geology 21, 23-37.

Bell, J.S. 1996. In situ stresses in sedimentary rocks (part 2): applications of stress measurements. Geoscience Canada 23, 135-153.

Bellahsen, N., Facenna, C., Funiciello, F., Daniel, J.M., Jolivet, L. 2003. Why did Arabia separate from Africa? Insights from 3-D laboratory experiments. Earth and Planetary Science Letters 216, 365-381.

Bellahsen, N., Husson, L., Autin, J., Leroy, S., d'Acremont, E. 2013. The effect of thermal weakening and buoyancy forces on rift localization: Field evidences from the Gulf of Aden oblique rifting. Tectonophysics 607, 80-97.

Beniest, A., Koptev, A., Burov, E. 2017. Numerical models for continental break-up: Implications for the South Atlantic. Earth and Planetary Science Letters 461, 176-189.

Benes, V., Scott, S.D., Binns, R.A. 1994. Tectonics of rift propagation into a continental margin: Western Woodlark Basin, Papua New Guinea. Journal or Geophysical Research 99 (B3), 4439-4455.

Benes, V., Scott, S.D. 1996. Oblique Rifting in the Havre Trough and Its Propagation into the Continental Margin of New Zealand: Comparison with Analogue Experiments. Marine Geophysical Researches 18, 189-201.

Bennett, S.E.K., Oskin, M.E. 2014. Oblique rifting ruptures continents: Example from the Gulf of California shear zone. Geology G34904.1.

Beyene, A., Abdelsalam, M.G. 2005. Tectonics of the Afar Depression: A reviw and synthesis. Journal of African Earth Sciences 41, 41-59.

Bialas, R.W., Buck, W.R. 2009. How sediment promotes narrow rifting: Applications to the Gulf of California. Tectonics 28, TC4014.

Blair, T.C., Bilodeau, W.L. 1998. Development of tectonic cyclothems in rift-pull-apart, and foreland basins: Sedimentary response to episodic tectonism. Geology 16, 517-520.

Bonini, M., Souriot, T., Boccaletti, M., Brun, J.-P. 1997. Successive orthogonal and oblique extension episodes in a rift zone: Laboratory experiments with application to the Ethiopian Rift. Tectonics 16 (2), 347-362.

Bonini, M., Corti, G., Innocenti, f., Manetti, P., Mazzarini F., Abebe, T., Pecskay, Z. 2005. Evolution of the Main Ethiopian Rift in the frame of Afar and Kenya rifts propagation. Tectonics 24, TC1007.

Bosworth, W., Huchon, P., McClay, K. 2005. The Red Sea and Gulf of Aden Basins. Journal of African Earth Sciences 43, 334-378.

Boutelier, D., Chemenda, A., Burg, J.-P. 2003. Subduction versus accretion of intra-oceanic volcanic arcs: insight from thermo-mechanical analogue experiments. Earth and Planetary Science Letters 212, 31-45

Boutelier, D., Oncken, O., Cruden, A. 2012. Fore-arc deformation at the transition between collision and subduction: Insights from 3-D thermomechanical laboratory experiments. Tectonics 31, TC2015.

Bruel, D. 2002. Impact of Induced Thermal Stresses During Circulation Tests in an Engineered Fractured Geothermal Reservoir: Example of the Soultz-Sous-Forêts European Hot Fractured Rock Geothermal Project, Rhine Graben, France. Oil & Gas Science and Technology - Rev. IFP 57 (5), 459-470.

Brun, J.-P. 1999. Narrow rifts versus wide rifts: inferences for the mechanics of rifting from laboratory experiments. Philosophical Transactions of the Royal Society London A 357, 695-712.

Brun, J.-P. 2002. Deformation of the continental lithosphere: Insights from brittle-ductile models. Geological Society, London, Special Publications 200, 355-370.

Brun, J.-P., Tron, V. 1993. Development of the North Viking Graben: inferences from laboratory modelling. Sedimentary Geology 86, 31-51.

Brun, J.-P, Nalpas, T. 1996. Graben inversion in nature and experiments. Tectonics 15 (2), 677-687.

Brun, J.-P. Fort, X. 2008. Entre sel et terre. Structures et mécanismes de la tectonique salifère. Collection Interactions, Vuibert, Paris.

Brun, J.-P., Fort, X. 2011. Salt tectonics at passive margins: Geology versus models. Marine and Petroleum Geology 28, 1123-1145.

Brune, S. 2014. Evolution of stress and fault patterns in oblique rift systems: 3-D numerical lithospheric-scale experiments from rift to breakup. Geochemistry, Geophysics, Geo-systems 15, 3392-3415.

Brune, S., Popov, A.A., Sobolev, S.V. 2012. Modeling suggests that oblique extension facilitates rifting and continental break-up. Journal of Geophysical Research 117, B08492.

Buck, W.R. 1991. Models of Continental Litho-spheric Extension. Journal of Geophysical Research 96, 20,161-20,178.

Buck, W.R. 2004. Consequences of Astheno-spheric Variability on Continental Rifting. In: Karner, G., Taylor, B., Driscoll, N., Kohlstedt, B. (eds.) Rheology and Deformation of the Lithosphere at Continental Margins. Columbia University Press, New York, 92-137.

Buiter, S.J.H. 2012. A review of brittle compressional wedge models. Tectono-physics 530-531, 1-17.

Buiter, S.J.H., Babeyko, A.Y., Ellis, S., Gerya, T.V., Kaus, B.J.P., Kellner, A., Schreurs, G., Yamada, Y. 2006. The numerical sandbox: comparison of model results for a shortening

and an extension experiment. Geological Society, London, Special Publications 253, 29-64.

Buiter, S.J.H., Huismans, R.S., Beaumont, C. 2008. Dissipation analysis as a guide to mode selection during crustal extension and implications for the styles of sedimentary basins. Journal of Geophysical Research 113, B06406.

Buiter, S.J.H., Ellis, S. 2012. SULEC: Benchmarking a new ALE finite-element code. Geophysical Research Abstracts 14, EGU2012-7528.

Buiter, S.J.H., Torsvik, T.H. 2014. A review of Wilson Cycle plate margins: a role for mantle plumes in continental break-up along sutures? Gondwana Research 26, 627-653.

Buiter, S.J.H., Schreurs, G., Albertz, M., Gerya, T.V., Kaus, B., Landry, W., Le Pourhiet, L., Mishin, Y., Egholm, D.L., Cooke, M., Maillot, B., Thieulot, C., Crook, T., May, D., Souloumiac, P., Beaumont, C. 2016. Benchmarking numerical models of brittle thrust wedges, Journal of Structural Geology 92, 140-177.

Burov, E., Cloetingh, S. 1997. Erosion and rift dynamics: new thermomechanical aspects of post-rift evolution of extensional basins. Earth and Planetary Science Letters 150, 7-26.

Burov, E., Poliakov, A. 2001. Erosion and rheology controls on synrift and postrift evolution: Verifying old and new ideas using a fully coupled numerical model. Journal of Geophysical Research 106 (B8), 16,461-16,481.

Butler, R.W.H., Tavarnelli, E., Grasso, M. 2006. Structural inheritance in mountain belts: An AlpineeApennine perspective. Journal of Structural Geology 28, 1893-1908.

Byerlee, J.D. 1978. Friction of rocks. Pure and Applied Geophysics 116, 615-626.

Cadell, H.M. 1888. Experimental researches in mountain building. Royal Society of Edinburgh Transactions 35, 337-360.

Carlo AG (Carlo Bernasconi AG, Switzerland) 2017. Company website: www.carloag.ch

Cartwright, J.A. 1989. The kinematics of inversion in the Danish Central Graben. In: Cooper, M.A., Williams, G.D. (eds.) Inversion Tectonics. Geological Society, London, Special Publications 44, 153-175.

Chapin, C.E., Cather, S.M. 1994. Tectonic setting of the axial basins of the northern and central Rio Grande rift. In: Keller G.R., Cather, S.M. (eds.) Basins of the Rio Grande Rift: Structure, Stratigraphy, and Tectonic Setting: Geological Society of America Special Paper 291, 5-25.

Charette, M.A., Smith, W.H.F. 2010. The Volume of Earth's Ocean. Oceanography 23 (2), 112-114.

Chauvin, B.P, Stockmeyer, J.M, Lovely, P.J., Plesch, A., Caumon, G., Shaw, J.H. in press. Consistent boundary conditions in 3D mechanics-based restoration: validation on an extensional sandbox model. AAPG Bulletin

Chemenda, A., Déverchère, J., Calais, E. 2002. Three-dimensional laboratory modelling of rifting: application to the Baikal Rift, Russia. Tectonophysics 356, 253-273.

Childs, C., Watterson, J., Walsh, J.J. 1995. Fault overlap zones within developing normal fault systems. Journal of the Geological Society, London 152, 535-549.

Choi, E., Buck, W.R., Lavier, L.L., Petersen, K.D. 2013. Using core complex geometry to constrain fault strength. Geophysical Research Letters 40, 3863-3867.

Chorowicz, J. 2005. The East African rift system: Journal of African Earth Sciences 43, 379-410.

Chorowicz, J., Bernard, C., Bonavia. F. 1999. Left-lateral strike-slip tectonics and gravity induced individualisation of wide continental blocks in the western Afar margin. Eclogae Geologicae Helvetiae 92, 149-158.

Clifton, A.E., Schlische, R.W. 2001. Nucleation, growth and linkage of faults in oblique rift zones: Results from experimental clay models and implications for maximum fault size. Geology 29 (5), 455-458.

Colletta, B., Letouzey, J., Pinedo, R., Ballard, J.F., Balé, P. 1991. Computerized X-ray tomography analysis of sandbox models: Examples of thin-skinned thrust systems. Geology 19, 1063-1067.

Corti, G. 2004. Centrifuge modelling of the influence of crustal fabrics on the development of transfer zones: insights into

the mechanics of continental rifting architecture. Tectonophysics 384, 191-208.

Corti, G. 2008. Control of rift obliquity on the evolution and segmentation of the main Ethiopian rift. Nature Geoscience 1, 259-262.

Corti, G. 2009. Continental rift evolution: From rift initiation to incipient break-up in the Main Ethiopian Rift, East Africa. Earth-Science Reviews 96, 1-53.

Corti, G. 2012. Evolution and characteristics of continental rifting: Analog modeling-inspired view and comparison with examples from the East African Rift System. Tectonophysics 522-523, 1-33.

Corti, G., Bonini, M., Conticelli, S., Innocenti, F., Manetti, P., Sokoutis, D. 2003. Analogue modelling of continental extension: a review focused on the relations between the patterns of deformation and the presence of magma. Earth-Science Reviews 63 (3-4), 169-247.

Corti, G., Bonini, M., Sokoutis, D., Innocenti, F., Manetti, P., Cloetingh, S., Mulugeta, G. 2004. Continental rift architecture and patterns of magma migration: A dynamic analysis based on centrifuge models. Tectonics 23, TC2012.

Corti, G., Manetti, P. 2006. Asymmetric rifts due to asymmetric Mohos: An experimental approach. Earth and Planetary Science Letters 245, 315-329.

Corti, G., Van Wijk, J., Cloetingh, S., Morley, C.K. 2007. Tectonic inheritance and continental rift architecture: Numerical and analogue models of the East African Rift system. Tectonics 26, TC6006.

Corti, G., Ranalli, G., Mulugeta, G., Agostini, A., Sani, F., Zugu, A. 2010. Control of the rheological structure of the lithosphere on the inward migration of tectonic activity during continental rifting. Tectonophysics 490, 165-172.

Corti, G., Philippon, M., Sani, F., Keir, D., Kidane, T. 2013a. Re-orientation of the extension direction and pure extensional faulting at oblique rift margins: comparison between the Main Ethiopian Rift and laboratory experiments. Terra Nova 25, 396-404.

Corti, G., Ranalli, G., Agostini, A., Sokoutis, D. 2013b. Inward migration of faulting during continental rifting: Effects of pre-existing

lithospheric structure and extension rate. Tectonophysics 594, 137-148.

Corti, G., Agostini, A., Keir, d., Van Wijk, J., Bastow, I.D., Ranalli, G. 2015. Magma-induced axial subsidence during final-stage rifting: Implications for the development of seaward-dipping reflectors. Geosphere 11 (3), 563-571.

Coskun, B. 1997. Oil and gas fields-transfer zone relationships, Thrace basin, NW Trukey. Marine and Petroleum Geology 14 (4), 401-16.

Coward, M. P., Dewey, J. F., Hempton, M., Holroyd, J. 2003. Tectonic evolution. In: Evans, D., Graham, C., Armour, A., Bathurst, P. (eds.) 2003. The Millennium Atlas: Petroleum Geology of the Central and Northern North Sea, Geological Society, London, 17-33

Devey, C.W., Garbe-Schönberg, C.-D., Stoffers, P., Chauvel, C., Mertz, D.F. 1994. Geochemical effects of dynamic melting beneath ridges: Reconciling major and trace element variations in Kolbeinsey (and global) mid-ocean ridge basalt. Journal of Geophysical Research 99 (B5), 9,077-9,095.

Di Giuseppe, E., Corbi, F., Funiciello, F., Massmeyer, A., Santimano, T.N., Rosenau, M., Davaille, A. 2015. Characterization of Carbopol® hydrogel rheology for experimental tectonics and geodynamics. Tectonophysics 642, 29-45.

Dick, H.J.B., Lin, J., Schouten, H. 2003. An ultra-slow spreading class of oceanic ridge. Nature 426, 405-412.

Dou, L, Wang, J., Cheng, D., Ran, X., Rubondo, E.N.T., Kasande, R., Byakagaba, A., Mugisha, F. 2004. Geological Conditions and Petroleum Exploration Potential of the Albertine Graben of Uganda. Acta Geologica Sinica 78 (4), 1002-1010.

Daubrée, G.A. 1879. Etudes synthétiques de Géologie Expérimentale. Dunot, Paris.

Dauteuil, O., Brun, J.-P. 1993. Oblique rifting in a slow-spreading ridge. Nature 361, 145-148.

Dauteuil, O., Bourgeois, O., Mauduit, T. 2002. Lithosphere strength controls oceanic transform zone structure: insights from analogue models. Geophysical Journal International 150, 706-714.

Delvaux, D., Moeys, R., Stapel, G., Petit, C., Levi, K., Miroshnichenko, A., Ruzich, V., San'kov, V. 1997. Paleostress reconstructions and geodynamics of the Baikal region, Central Asia, Part 2. Cenozoic Rifting. Tectono-physics 282, 1-38.

Delvaux, D., F. Kervyn, A.S. Macheyeki, Temu, E.B. 2012. Geodynamic significance of the TRM segment in the East African Rift (W-Tanzania): Active tectonics and paleostress in the Ufipa plateau and Rukwa basin. Journal of Structural Geology 37, 161-180.

De Paola, N., Woldsworth, R.E., Collettini, C.K., Mccaffrey, J.W., Barchi, M.R. 2007. The structural evolution of dilational stepovers in regional transtensional zones. In: Cunningham, W.D., Mann, P. (eds.) Tectonics of Strike-Slip Restraining and Releasing Bends. Geological Society, London, Special Publications 290, 433-445.

Derer, C.E., Schumacher, M.E., Schäfer, A. 2005. The northern Upper Rhine Graben: basin geometry and early syn-rift tectono-stratigraphic evolution. International Journal of Earth Sciences (Geologische Rundschau) 94, 640-656.

Dewey, J.F. 1975. Finite plate implications: some implications fro the evolution of rock masses at plate margins. American Journal of Science 275-A, 260-284.

Dewey, J.F., Holdsworth, R.E., Strachan, R.A. 1998. Transpression and transtension zones. In: Hodsworth, R.E., Strachan, R.A., Dewey, J.F. (eds.) Continental Transpressional and Transtensional Tectonics. Geological Society, London, Special Publications 135, 1-14.

Drachev, S.S., Savostin, L.A., Groshev, V.G., Bruni, I.E. 1998. Structure and geology of the continental shelf of the Laptev Sea, Eastern Russian Arctic. Tectonophysics 298, 357-393.

Dunbar, J.A., Sawyer, D.S. 1988. Continental rifting at pre-existing lithospheric weaknesses. Nature 333, 450-452.

Dunbar, J.A., Sawyer, D.S. 1989. How Pre-existing Weaknesses Control the Style of Continental Breakup. Journal of Geophysical Research 94 (B6), 7278-7292.

Dziewonski, A.M., Anderson, D.L. 1981. Preliminary reference Earth model. Physics of the Earth and Planetary Interiors 25, 297-356.

Ebinger, C.J. 1989. Tectonic development of the western branch of the East African rift system. Geological Society of America Bulletin 101, 885-903.

Ebinger, C. 2005. Continental breakup: the East African perspective. Astronomy and Geophysics 46, 2.16–2.21.

Ebinger, C.J. 2012. Evolution of the Cenozoic East African rift system: Cratons, plumes, and continental break-up. In: Roberts, D.G., Bally, A.W. (eds.) Regional Geology and Tectonics: Phanerozoic Rift Systems and Sedimentary Basins 1B, Elsevier, 132-162.

Ebinger, C.J., Casey, M. 2001. Continental breakup in magmatic provinces: an Ethiopian example. Geology 29, 527-530.

Ebinger, C., Ayele, A., Keir, D., Rowland, J., Yirgu, Wrigth, T., Belachew, M., Hamling, I. 2010. Length and Timescales of Rift Faulting and Magma Intrusion: The Afar Rifting Cycle from 2005 to Present. Annual Review of Earth and Planetary Sciences 38, 439-466.

Ellis, S.M., Little, T.A., Wallace, L.M., Hacker, B.R., Buiter, S.J.H. 2011. Feedback between rifting and diapirism can exhume ultrahigh-pressure rocks. Earth and Planetary Science Letters 311 (3-4), 427-438.

Elmohandes, S.-E. 1981. The Central European Graben System: Rifting Imitated by Clay Modelling. Tectonophysics 73, 69-78.

Erbello, A., Corti, G., Agostini, A., Sani, F., Kidane, T., Buccianti, A. 2016. Modeling along-axis variations in fault architecture in the Main Ethiopian Rift: Implications for Nubia-Somalia kinematics. Journal of Geodynamics 102, 24-38.

Erratt, D., Thomas, G.M., Wall, G.R.T. 1999. The evolution of the Central North Sea Rift, Petroleum Geology Conference series 5, 63-82.

Erratt, D., Thomas, G.M., Hartley, N.R., Musum, R., Nicholson, P.H., Spisto, Y. 2010. North Sea hydrocarbon systems: some aspects of our evolving insights into a classic hydrocarbon province. In: Vining, B.A., Pickering, S.C. (eds.) Petroleum Geology: From Mature Basins to New Frontiers - Proceedings of the 7th Petroleum Geology Conference, 37-56.

Faulds, J.E., Varga, R.J. 1998. The role of accommodation zones and transfer zones in the regional segmentation of extended terranes, in: Faulds, J.E., Stewart, J.H. (eds.) Accommodation Zones and Transfer Zones: The Regional Segmentation of the Basin and Range Province. Geological Society of America Special Paper 323, 1-46.

Fedorik., J., Zwaan, f., Schreurs, G., Toscani, G., Bonini, L., Lodolo, E., Civile, D., Seno, S. in preparation. 4D analogue modelling of transcurrent fault structures interacting with a trust belt

Fort, X., Brun, J.-P., Chauvel F. 2004. Salt tectonics on the Angolan margin, synsedimentary deformation processes. AAPG Bulletin 88 (11), 1523-1544.

Fossen, H., Schultz, R.A., Rundhovde, E., Rotevatn, A., Buckley, S.J. 2010. Fault linkage and graben stepovers in the Canyonlands (Utah) and the North Sea Viking Graben, with implications for hydrocarbon migration and accumulation. AAPG Bulletin 94 (5), 597-613.

Fouch, M.J., Fischer, K.M., Parmentier, E.M., Wysession, M.E., Clarke, T.J. 2000. Shear wave splitting, continental keels, and patterns of mantle flow. Journal of Geophysical Research 105 (B3), 6255-6275.

Franke, D., Hinz, K., Oncken, O. 2001. The Laptev Sea Rift. Marine and Petroleum Geology 18, 1083-1127.

Franke, D., Hinz, K. 2009. Geology of the Shelves surrounding the New Siberian Islands, Russian Arctic. Stephan Mueller Special Publication Series 4, 35-44.

Fraser, S., Robinson, A., Johnson, H., Underhill, J., Kadolsky, D. 2003. Upper Jurassic. In: Evans, D., Graham, C., Armour, A., Bathurst, P. (eds.) The Millennium Atlas: Petroleum Geology of the Central and Northern North Sea. Geological Society, London, 155-189.

Fujita, K., Koz'min, B.M., Mackey, K.G., Riegel, S.A., McLean, M.S., Imaev, V.S. 2009. Seismotectonics of the Chersky Seismic Belt, eastern Sakha Republic (Yakutia) and Magadan District, Russia. Stephen Mueller Special Publication Series 4, 117-145.

Gartell, A.P. 1997. Evolution of rift basins and low-angle detachments in multilayer analog models. Geology 25 (7), 615-618.

Gautier, D.L. 2005. Kimmeridge Shales Total Petroleum System of the North Sea Graben Province. U.S. Geological Survey Bulletin, 2204-C.

Graveleau, F., Malavieille, J., Dominguez, S. 2012. Experimental modelling of orogenic wedges: A review. Tectonophysics 538-540, 1-66.

Gray, R., Pysklywec, R.N. 2012. Influence of sediment deposition on deep lithospheric tectonics. Geophysical Research Letters 39, L11312.

Gudmundsson, A. 1995. Ocean-ridge discontinuities in Iceland. Journal of Geological Society London 152, 1011-1015.

Gupta, A., Scholz, C.H. 2000. A model of normal fault interaction based on observations and theory. Journal of Structural Geology 22, 865-879.

Hall, J. Sir. 1815. On the vertical position and convolutions of certain strata and their relation with granite. Royal Society of Edinburgh Transactions, 7,79-108.Hubbert, M.K., 1937. Theory of scaled models as applied to the study of geological structures. Geological Society of America Bulletin 48, 1459-1520.

Hey, R., Martinez, F., Höskuldsson, Á., Benediktsdóttir, Á. 2010. Propagating rift model for the V-shaped ridges south of Iceland. Geochemistry, Geophysics, Geosystems 11 (3), Q3011.

Hieronymus, C.H. 2004. Control on seafloor spreading geometries by stress- and strain-induced lithospheric weakening. Earth and Planetary Science Letters 222, 1, 177-189.

Huismans, R.S., Podladchikov, Y.Y., Cloetingh, S. 2001. Transition from passive to active rifting: Relative importance of asthenospheric doming and passive extension of the lithosphere. Journal of Geophysical Research 106 (B6), 11,271-11,291.

Hubbert, M.K. 1937. Theory of scaled models as applied to the study of geological structures. Geological Society of America Bulletin 48, 1459-1520.

Hubbert, M.K. 1951. Mechanical basis for certain familiar geological structures. Geological Society of America Bulletin 6 (2), 355-372.

Hus, R., Acocella, V., Funiciello, R., De Batist, M. 2005. Sandbox models of relay ramp structure and evolution. Journal of Structural Geology 27, 459-473.

Hus, R., Poort, J., Charlet, F., Naudts, L., Khlystov, O., Klerkx, J., De Batist, M. 2012. Lake Baikal. In: Roberts, D.G., Bally, A.W. (eds.) Regional Geology and Tectonics: Phanerozoic Rift Systems and Sedimentary Basins 1B, Elsevier, 258-276.

Hutchinson, D.R., Golmshtok, A.J., Zonenshain, L.P., Moore, T.C., Scholz, C.A., Klitgord, K.D. 1992. Depositional and tectonic framework of the rift basins of Lake Baikal from multichannel seismic data. Geology 20, 589-592.

Illies, J.H. 1977. Ancient and recent rifting in the Rhinegraben. In: Frost, R.T.C., Dikkers, A.J. (eds.) Fault tectonics in N.W. Europe. Geologie en Mijnbouw 56, 329-350.

Imaeva, L.P., Imaev, V.S., Koz'min, B.M. 2016. Structural-dynamic model of the Chersky seismotectonic zone (continental part of the Arctic-Asian seismic belt). Journal of Asian Earth Sciences 116, 59-68.

Jackson, M.P.A., Talbot, C.J. 1986. External shapes, strain rates, and dynamics of salt structures. Geological Society of America Bulletin 97 (3), 305-323.

Jakobsson, M., Mayer, L., Coakley, B., Dowdeswell, J.A., Forbes, S., Fridman, B., Hodnesdal, H., Noormets, R., Pedersen, R., Rebesco, M., Schenke, H.-W., Zarayskaya Y., Accettella, D., Armstrong, A., Anderson, R.M., Bienhoff, P., Camerlenghi, A., Church, I., Edwards, M., Gardner, J.V., Hall, J.K., Hell, B., Hestvik, O.B., Kristoffersen, Y., Marcussen, C., Mohammad, R., Mosher, D., Nghiem, S.V., Pedrosa, M.T., Travaglini, P.G., Weatherall, P. 2012. The International Bathymetric Chart of the Arctic Ocean (IBCAO) Version 3.0. Geophysical Research Letters 39, L12609.

Johnson, H., Leslie, A.B., Wilson, C.K., Andrews, I.J., Cooper, R.M. 2005. Middle Jurassic, Upper Jurassic and Lower Cretaceous of the UK Central and Northern North Sea. Britisch Geological Survey Research Report RR/03/11.

Kaus, B.J.P. 2010. Factors that control the angle of shear bands in geodynamic numerical models of brittle deformation. Tectono-physics 484, 36-47,

Kaus, B.J.P, Mühlhaus, H., May, D.A. 2010. A stabilization algorithm for geodynamic numerical simulations with a free surface. Physics of the Earth and Planetary Interiors 181, 12-20.

Keep, M., McClay, K.R. 1997. Analogue modelling of multiphase rift systems. Tectonophysics 273, 239

Keir, D., Stuart, G.W., Jackson, A., Ayele, A. 2006. Local Earthquake Magnitude Scale and Seismicity Rate for the Ethiopian Rift. Bulletin of the Seismological Society of America 96, 2221-2230.

Keir, D., Bastow, I.D., Corti, G., Mazzarini, F., Rooney, T.O. 2015. The origin of along-rift variations in faulting and magmatism in the Ethiopian Rift. Tectonics 34, 464-477.

Klinkmüller, M. 2011. Properties of analogue materials, experimental reproducibility and 2D/3D deformation quantification techniques in analogue modeling of crustal-scale processes. PhD Thesis, University of Bern, Switzerland.

Koehn, D., Aanyu, K., Haines, S., Sachau, T. 2008. Rift nucleation, rift propagation and the creation of basement micro-plates within active rifts. Tectonophysics 458, 105-116.

Koyi, H. 1997. Analogue modelling: from a qualitative to a quantitative technique - a historical outline. Journal of Petroleum Geology 20 (2), 223-238.

Lambiase, J.J., Bosworth, W. 1995. Structural controls on sedimentation in continental rifts. In: Lambiase, J.J. (ed.) Hydrocarbon Habitat in Rift Basins. Geological Society, London, Special Publications 80, 117-133.

Larsen, P.-H. 1988. Relay structures in a Lower Permian basement-involved extension system, East Greenland. Journal of Structural Geology 10, 3-8.

Le Calvez, J.H. 2002. Physcial modelling of normal faults and graben relays above salt. PhD Thesis, University of Texas, Austin.

Le Calvez, J.H., Vendeville, B.C. 2002. Experimental designs to model along-strike fault interaction. In: Schellart, W.P., Passchier, C. (eds.) Analogue modelling of large-scale tectonic processes. Journal of the Virtual Explorer 7, 1-17.

Lemiale, V., Mühlhaus, H.B., Moresi, L., Stafford, J. 2008. Shear band analysis of plastic models formulated for incompressible viscous flows. Physics of the Earth and Planetary Interiors 171, 177-186.

Liu, L., Morgan, E.F. 2007. Accuracy and Precision of Digital Volume Correlation in Quantifying Displacements and Strains in Trabecular Bone. Journal of Biomechanics 40, 3516-3520.

Lohrmann, J., Kukowski, N., Adam, J., Oncken, O. 2003. The impact of analogue material properties on the geometry, kinematics, and dynamics of convergent sand wedges. Journal of Structural Geology 25, 1691-1711.

Lund, J.W., Boyd, T.L. 2016. Direct utilization of geothermal energy 2015 worldwide review. Geothermics 60, 66-93.

Lyell, C. 1871. The Student's Elements of Geology. John Murray, London.

Madi, K., Tozzi, G., Zhang, Q.H., Tong, J., Cossey, A., Au, A., Hollis, D., Hild, F. 2013. Computation of full-field displacements in a scaffold implant using digital volume correlation and finite element analysis. Medical Engineering & Physics 35 (9), 1298-1312.

Madritsch, H., Kounov, A., Schmid, S.M., Fabbri, O. 2009. Multiple fault reactivations within the intra-continental Rhine-Bresse Transfer Zone (La Serre Horst, eastern France). Tectonophysics 471, 297-318.

Mann, P., Gahagan, L., Gordon, M.B. 2003. Tectonic Setting of the World's Giant Oil and Gas Fields. In: Halbouty, M.T. (ed.) Giant oil and gas fields of the decade 1990-1999, AAPG Memoir 78, 15-105.

Mart, Y., Dauteuil, O. 2000. Analogue experiments of propagation of oblique rifts. Tectonophysics 316, 121-132.

Martin, A.K. 1984. Propagating rifts: Crustal extension during continental rifting. Tectonics 3 (6), 611-617.

Martín-Barajas, A., González-Escobar, M., Fletcher, J.M. Pacheco, M., Oskin, M., Dorsey, R. 2013. Thick deltaic sedimentation and detachment faulting delay the onset of continental rupture in the Northern Gulf of California: Analysis of seismic reflection profiles. Tectonics 32, 1294-1311.

Martins-Neto, M.A., Catuneanu, O. 2012. Roberts, D.G., Bally, A.W. Rift sequence stratigraphy. In: Roberts, D.G., Bally, A.W. (eds.) Regional Geology and Tectonics: Phanerozoic Rift Systems and Sedimentary Basins 1B, Elsevier, 58-70.

Mauduit, T., Dauteuil, O. 1996. Small-scale models of oceanic transform zones. Journal of Geophysical Research 101 (B9), 20,196-20,209.

McClay, K.R., White, M.J. 1995. Analogue modelling of orthogonal and oblique rifting. Marine and Petroleum Geology 12 (2), 137-151.

McClay, K., Khalil, S. 1998. Extensional hard linkages, eastern Gulf of Suez, Egypt. Geology 26, 563-566.

McClay, K. Bonora, M. 2001. Analog models of restraining stepovers in strike-slip fault systems. AAPG Bulletin, 85, no. 2, 233-260.

McClay, K.R., Dooley, T., Whitehouse, P., Mills, M. 2002. 4-D evolution of rift systems: Insights from scaled physical models. AAPG Bulletin 86 (6), 935-959.

Mezger, T.G. 2006. The Rheology Handbook: For users of rotational and oscillatory rheometers. 2nd revised edition. Vincentz Network GmbH & Co. KG, Hannover.

Michon, L., Merle, O. 2000. Crustal structures of the Rhinegraben and the Massif Central grabens: An experimental approach. Tectonics 19 (5), 896-904.

Michon, L., Sokoutis, D. 2005. Interaction between structural inheritance and extension direction during graben and depocentre formation: An experimental approach. Tectonophysics 409, 125-146.

Milani, E.J., Davison, I. 1988. Basement control and transfer tectonics in the Recôncavo-Tucano-Jatobá rift, Northeast Brazil. Tectonophysics 154, 41-70.

Minissale, A., Corti, G., Tassi, F., Darrah, T.H., Vaselli, O., Montegrossi, G., Montanari, D., Yirgu, G., Selmo, E., Teclu, A. 2017. Geothermal potential and origin of natural thermal fluids in the northern Lake Abaya area (Main Ethiopian Rift, East Africa). Journal of volcanology and Geothemal Research 336, 1-18.

Minor, S.A., Hudson, M.R., Caine J.S., Thompson, R.A. 2013. Oblique transfer of extensional strain between basins of the middle Rio Grande rift, New Mexico: Fault kinematic and paleostress constraints. In: Hudson M.R., Grauch, V.J.S. (eds.) New Perspectives on Rio Grande Rift Basins: From Tectonics to Groundwater. Geological Society of America Special Paper 494, 345-382.

Molnar, N.E., Cruden, A.R., Betts, P.G. 2017. Interactions between propagating rotational rifts and linear rheological heterogeneities: Insights from three-dimensional laboratory experiments. Tectonics 36, 420-443.

Montanari, D., Agostini, A., Bonini, M., Corti, G., Del Ventisette, C. 2017. The Use of Empirical Methods for Testing Granular Materials in Analogue Modelling. Materials 10, 635.

Morley, C.K. 1988. Variable extension in Lake Tanganyika. Tectonics 7, No. 4, 785-801.

Morley, C.K. 1999. How successful are analogue models in addressing the influence of pre-existing fabrics on rift structure? Journal of Structural Geology 21, 1267-1274.

Morley, C. K. 2010. Stress re-orientation along zones of weak fabrics in rifts: An explanation for pure extension in 'oblique' rift segments. Earth and Planetary Science Letters 297, 667-673.

Morley, C.K., Nelson, R.A., Patton, T.L., Munn, S.G. 1990. Transfer zones in the East African Rift System and their relevance to hydrocarbon exploration in rifts. AAPG Bulletin 74, 1234-1253.

Morley, C.K., Haranya, C., Phoosongsee, W., Pongwapee, S., Kornsawan, A., Wonganan, N. 2004. Activation of rift oblique and rift parallel pre-existing fabrics during extension and their effect on deformation style: examples from the rifts of Thailand. Journal of Structural Geology 26, 1803-1829.

Moucha, R., Forte, A.M. 2011. Changes in African topography driven by mantle convection. Nature Geoscience 4, 707-712.

Müller, R.D., Gaina, C., Roest, W.R., Hansen, D.L. 2001. A recipe for microcontinent formation. Geology 29, 203-206.

Mulugeta, G. 1988. Squeeze box in the centrifuge. Tectonophysics 148, 323-335.

Naliboff, J., Buiter, S.J.H. 2015. Rift reactivation and migration during multiphase extension. Earth and Planetary Science Letters 421, 58-67.

Nalpas, T., Le Douaran, S., Brun, J.-P., Unternehr, P., Richert, J.-P. 1995. Inversion of the Broad Fourteens Basin (offshore Netherlands), a small-scale model investigation. Sedimentary Geology 95, 237-250.

Naylor, M.A., Laroque, J.M., Gauthier, B.D.M. 1994. Understanding Extensional Tectonics: Insights from Sandbox Models. In: Roure, F., Ellouz, N., Shein, V.S., Skvortsov, I. (eds.) Geodynamic Evolution of Sedimentary Basins. Proceedings of the International Symposium, Moscow 1992, Éditions Technip, Paris, 69-83.

Nelson, R.A., Patton, T.L., Morley, C.K. 1992. Rift-Segment Interaction and Its Relation to Hydrocarbon Exploration in Continental Rift Systems. AAPG Bulletin 76, 1153-1169

Okubo, C.H., Schultz, R.A. 2006. Near-tip stress rotation and the development of deformation stepover geometries in mode II. Geological Society of America Bulletin 118 (3/4), 343-348.

Olive, J.-A., Behn, M.D., Malatesta, L.C. 2014. Modes of extensional faulting controlled by surface processes. Geophysical Research Letters 41, 6725-6733.

Panien, M. 2004. Analogue modelling experiments of basin inversion using well-characterised granular materials and comparisons with numerical models. PhD Thesis, University of Bern, Switzerland.

Panien, M., Schreurs, G, Pfiffner, A. 2005. Sandbox experiments on basin inversion: testing the influence of basin orientation and basin fill. Journal of Structural Geology 27, 433-445.

Panien, M., Schreurs, G, Pfiffner, A. 2006. Mechanical behaviour of granular materials used in analogue modelling: insights from grain characterisation, ring-shear tests and analogue experiments. Journal of Structural Geology 28, 1710-1724.

Pannier, Y., Lenoir, N., Bornert, M. 2010. Discrete volumetric digital image correlation for the investigation of granular type media at microscale: accuracy assessment. EPJ Web of Conferences 6, 35003.

Paul, D., Mitra, S., 2013. Experimental models of transfer zones in rift systems. AAPG Bulletin 97 (5), 759-780.

PEPD. 2012. Petroleum Exploration and Investment Opportunities in Uganda. Petrol. Exploration Exploration and Production Department Publication, Uganda.

Philippon, M., Willingshofer, E., Sokoutis, D., Corti, G., Sani, F., Bonini, M., Cloetingh, S. 2015. Slip re-orientation in oblique rifts. Geology 43, 147-150.

Philippon, M., Corti, G. 2016. Obliquity along plate boundaries. Tectonophysics 693, 171-182.

Powers, M.C. 1953. A new roundness scale for sedimentary particles. Journal of Sedimentary Petrology 23 (2), 117-119.

Quinquis, M.E.T., Buiter, S.J.H., Ellis, S. 2011. The role of boundary conditions in numerical models of subduction zone dynamics. Tectonophysics 497 (1-4), 57-70.

Rattey, R.P., Hayward, A.B. 1993. Sequence stratigraphy of a failed rift system: the Middle Jurassic to Early Cretaceous basin evolution of the Central and Northern North Sea. Petroleum Geology Conference series 4, 215-249.

Ramberg, H. 1981., Gravity, Deformation and the Earth's Crust. Academic Press, London.

Ritter, M., Leever, K., Rosenau, M., Oncken, O. 2016. Scaling the sandbox—Mechanical (dis) similarities of granular materials and brittle rock. Journal of Geophysical Research. Solid Earth 121, 6863-6979.

Roberts, A.M., Price, J.D., Olsen, T.S. 1990. Late Jurassic half-graben control on the siting and structure of hydrocarbon accumulations: UK/Norwegian Central Graben. Geological Society, London, Special Publications 55, 229-257.

Rosendahl, B.R. 1987. Architecture of Continental Rifts with Special Reference to East Africa. Annual Review of Earth and Planetary Sciences 15, 445-503.

Rosendahl, B.R., Kilembe, E., Kaczmarick, K. 1992. Comparison of the Tanganyika, Malawi, Rukwa and Turkana Rift zones from analyses of seismic reflection data. Tectonophysics, 213, 235-256.

Rossland, A., Escalona, A., Rolfsen, R. 2013. Permian–Holocene tectonostratigraphic evolution of the Mandal High, Central Graben, North Sea. AAPG Bulletin 97 (6), 923-957.

Rudolf, M., Boutelier, D., Rosenau, M., Schreurs, G., Oncken, O. 2016. Rheological benchmark of silicone oils used for analog modeling of short- and long-term lithospheric deformation. Tectonophysics 684, 12-22.

Saria, E., Calais, E., Stamps, D.S., Delvaux, D., Hartnady, C.J.H. 2014. Present-day kinematics of the East African Rift. Journal of Geophysical Research. Solid Earth 119, 3584-3600.

Schellart, W.P., Lister, G.S., Jessell, M.W. 2002. Analogue modelling of asymmetrical back-arc extension. In: Schellart, W.P., Passchier, C. (eds.) Analogue modelling of large-scale tectonic processes. Journal of the Virtual Explorer 7, 25-42.

Schellart, W.P., Jessell, M.W., Lister, G.S. 2003. Asymmetric deformation in the backarc region of the Kuril arc, northwest Pacific: New insights from analogue modelling. Tectonics, 22 (5), 1047.

Schellart, W.P., Strak, V. 2016. A review of analogue modelling of geodynamic processes: Approaches, scaling, materials and quantification, with an application to subduction experiments. Journal of Geodynamics 100, 7-32.

Schreurs, C., Colletta, B. 1998. Analogue modelling of faulting in zones of continental transtension and transpression. In: Holdsworth, R.E., Strachan, R.A., Dewey, J.F. (eds.) Continental Transpressional and Transtensional Tectonics. Geological Society, London, Special Publications 135, 59-79.

Schreurs, G., Hänni, R, Vock, P. 2002. Analogue modelling of transfer zones in fold and thrust belts: a 4-D analysis. In: Schellart, W.P. and Passchier, C. (eds.) Analogue modelling of large-scale tectonic processes. Journal of the Virtual Explorer 7, 67-73.

Schreurs, G., Buiter, S.J.H., Boutelier, D., Corti, G., Costa, E., Cruden, A.R., Daniel, J.-M., Hoth, S., Koyi, H.A., Kukowski, N., Lohrmann, J., Ravaglia, A., Schlische, R.W., Withjack, M.O., Yamada, Y., Cavozzi, C., Delventisette, C., Brady, J.A.E., Hoffmann-Rothe, A., Mengus, J.-M., Montanari, D., Nilforushan, F. 2006. Analogue benchmarks of shortening and extension experiments. In: Buiter, S.J.H., Schreurs, G. (eds.) Analogue and Numerical Modelling of Crustal-Scale Processes. Geological Society, London, Special Publications 253, 1-27.

Schreurs, G., Buiter, S.J.H., Boutelier, J., Burberry, C., Callot, J.-P. Cavozzi, C., Cerca, M., Chen, J.-H., Cristallini, E., Cruden, A.R., Cruz, L., Daniel, J.-M., Da Poian, G., Garcia, V.H., Gomes, C.J.S., Grall, C., Guillot, Y., Guzmán, C., Hidayah, T.N., Hilley, G., Klinkmüller. M., Koyi, H.A., Lu, C.-Y., Maillot, B., Meriaux, C., Nilfouroushan, F., Pan, C.-C., Pillot D., Portillo, R., Rosenau, M, Schellart, W.P., Schlische, R.W., Take, A., Vendeville, B., Vergnaud, M., Vettori, M., Wang, S.-H., Withjack, M.O., Yagupsky, D., Yamada, Y. 2016. Benchmarking analogue models of brittle thrust wedges. Journal of Structural Geology 92, 116-139.

Scholz, C.A., Hutchinson, D.R., 2000. Stratigraphic and structural evolution of the Selenga Delta Accomodation Zone, Lake Baikal Rift, Siberia. International Journal of Earth Sciences 89, 212-228.

Serra, S., Nelson, R.A. 1988. Clay modeling of rift asymmetry and associated structures. Tectonophysics 153, 307-312.

Shearer, S.A., Hudson, J.R. Fluid Mechanics: Stoke's Law and Viscosity. Measurement Laboratory Investigation (3), EGR 101.

Simpson, G., 2006. Dynamic interactions between erosion, deposition, and three-dimensional deformation in compressional fold belt settings. Journal of Geophysical Research, 109, F03007.

Souriot, T., Brun, J.-P. 1992. Faulting and block rotation in the Afar triangle, East Africa: The Danakil "crank-arm" model. Geology 20, 911-914.

Stamps, D.S., Calais, E., Saria, E., Hartnady, C., Nocquet, J-.M., Ebinger, C.J., Fernandez, R.M. 2008. A kinematic model for the East African Rift. Geophysical Research Letters 35, L05304.

Stephenson, R., Egholm, D.L., Nielsen, S.B., Stovba, S.M. 2009. Nature Geoscience 2, 290-293.

Stolar, D., Roe, G., Willet, S. 2007. Controls on the patterns of topography and erosion rate in a critical orogen. Journal of Geophysical Research 112, F04002.

Strak, V., Schellart, W.P. 2014. Evolution of 3-D subduction-induced mantle flow around lateral slab edges in analogue models of free subduction analysed by stereoscopic particle image velocimetry technique. Earth and Planetary Science Letters 403, 368-379.

Sun., Z., Zhong, Z., Keep, M., Zhou, D., Cai, D., Li, X., Wu, S., Jiang, J. 2009. 3D analogue modelling of the South China Sea: A discussion on breakup pattern. Journal of Asian Earth Sciences 34, 544-556.

Surlyk, F., Dons, T., Clausen, C. K., Higham, J. 2003. Upper Cretaceous. In: Evans, D., Graham, C., Armour, A., Bathurst, P. (eds.) The Millennium Atlas: Petroleum Geology of the Central and Northern North Sea. Geological Society, London, 213-233.

Tentler, T. Acocella, V. 2010. How does the initial configuration of oceanic ridge segments affect their interaction? Insights from analogue models. Journal of Geophysical Research 115, B01401.

Thieulot, C. 2014. Elefant: a user-friendly multi-purpose geodynamics code. Solid Earth Discussion Paper 6, 1949-2096.

Thomas, E. 1994 Diapirisme salifère induit par l'extension. Mémoire de DEA, Université de Rennes 1.

Torres Acosta, V., Bande, A., Sobel, E.R., Parra M., Schildgen, T.F., Stuart, F., Strecker, M.R. 2015. Cenozoic extension in the Kenya Rift from low-temperature hermochronology: Links to diachronous spatiotemporal evolution of rifting in East Africa. Tectonics 34, 2367-2386.

Tron, V. Brun, J.-P. 1991, Experiments on oblique rifting in brittle-ductile systems. Tectonophysics 188, 71-88.

Trudgill, B., Cartwright, J. 1994. Relay-ramp forms and normal-fault linkages, Canyon-lands National Park, Utah. Geological Society of America Bulletin 106, 1143-1157.

220

Turrini, C., Toscani, G., Lacombe, O., Roure, F. 2016. Influence of structural inheritance on foreland-foredeep system evolution: An example from the Po valley region (northern Italy). Marine and Petroleum Geology 77, 376-398.

Underhill, J.R., Partington, M.A. 1993. Jurassic thermal doming and deflation in the North Sea: implications of the sequence stratigraphic evidence. In: Parker, J.R. (ed.) Petroleum Geology: North-West Europe and Global Perspectives - Proceedings of the 4th Petroleum Geology Conference. Geological Society, London, Petroleum Geology Conference series 4, 337-345.

Ustaszewski, K., Schumacher, M.E., Schmid, S.M., Nieuwland, D. 2005. Fault reactivation in brittle-viscous wrench system-dynamically scaled analogue models and application to the Rhine-Bresse transfer zone. Quaternary Science Reviews 24, 365-382.

Van der Pluijm, B.A., Marshak, S. 2004. Earth Structure. W.W. Norton & Company Ltd., New York.

Van Wijk, J.W. 2005. Role of weak zone orientation in continental lithosphere extension. Geophysical Research Letters 32, L02303.

Van Wijk, J.W., Blackman, D.K. 2005. Dynamics of continental rift propagation: the end-member modes. Earth and Planetary Science Letters 229, 247-258.

Vendeville, B., Cobbold, P.R., Davy, P., Brun, J.-P., Choukroune, P. 1987. Physical models of extensional tectonics at various scales. In: Coward, M.P., Dewey, J.F., Hancock, P.L. (eds.) Continental Extensional Tectonics. Geological Society, London, Special Publications 28, 95-107.

Versfelt, J., Rosendahl, B.R. 1989. Relationships between pre-rift structure and rift architecture in Lakes Tanganyika and Malawi, East Africa. Nature 337, 354-357.

Vink, G.E. 1982. Continental Rifting and the Implications For Plate Tectonic Reconstructions. Journal of Geophysical Research 87 (B13), 10,667-10,688.

Wang, X., Cochran, J.R. 1993. Gravity anomalies, isostasy, and mantle flow at the East Pacific Rise crest. Journal of Geophysical Research 98 (B11), 19,505-19,531.

Wang, J.N., Hobbs, B.E., Ord, A., Shimamoto, T., Toriumi, M. 1994. Newtonian Dislocation Creep in Quartzites: Implications for the Rheology of the Lower Crust. Science 265 (5176), 1204-1206.

Weijermars, R. 1986. Flow behaviour and physical chemistry of bouncing putties and related polymers in view of tectonic laboratory applications. Tectonophysics 124, 325-358.

Weijermars, R., Schmeling, H. 1986. Scaling of Newtonian and non-Newtonian fluid dynamics without inertia for quantitative modelling of rock flow due to gravity (including the concept of rheological similarity). Physics of Earth and Planetary Interiors 43, 316-330.

Weissel, J.K., Karner, G.D. 1989. Flexural uplift of rift flanks due to mechanical unloading of the lithosphere during extension. Journal of Geophysical Research 94 (B10), 13,919-13,950.

Withjack, M.O., Jamison, W.R. 1986. Deformation produced by oblique rifting. Tectonophysics 126, 99-124.

Zanella, E., Coward, M.P. 2003. Structural framework. In: Evans, D., Graham, C., Armour, A., Bathurst, P. (eds.) The Millennium Atlas: petroleum geology of the central and northern North Sea. Geological Society London, 45-59.

Zwaan, F., G. Schreurs, J. Naliboff, Buiter, S.J.H. 2016. Insights into the effects of oblique extension on continental rift interaction from 3D analogue and numerical models. Tectonophysics 693, 239-260.

Zwaan, F., Schreurs, G. 2017. How oblique extension and structural inheritance influence rift segment interaction: Insights from 4D analog models. Interpretation 5 (1), SD119-SD138.

Zwaan, F., Schreurs, G. Adam, J., submitted. Effects of sedimentation on rift segment and transfer zone evolution in orthogonal and oblique extension settings: insights from analogue models analysed with 4D X-ray CT and digital volume correlation techniques. Global and Planetary Change.

Appendix I. Article Geotectonic Research (2015)

Effects of transtension on continental rift interaction: a 4D analogue modeling study

Zwaan, F. and Schreurs, G.

Institute of Geological Sciences, University of Bern, Baltzerstrasse 1+3, 3012, Bern, Switzerland; frank.zwaan@geo.unibe.ch

Introduction

The interaction of individual rift segments during rifting determines the evolution of a rift system and eventually continental break-up. Inherited heterogeneities are an important factor as they control where initial rifts will form. Since these heterogeneities are often not properly aligned, rift segments form separately and need to interact in order to develop a full-scale rift system. A second important factor is the degree of oblique divergence or transtension in the system, ultimately promoting continental break-up (Brune et al. 2012).

Both analogue and numerical modeling have been used to study rift interaction, mostly focusing on transform faults in the oceanic domain. Some analogue work (Acocella et al. 1999) and some recent numerical work (Allken et al. 2012) concern rift interaction in the continental domain. However, traditional rigid base-plate set-ups limit analogue models. Numerical models allow more freedom, but are restricted by low resolutions and difculties for modeling in 3D. Finally, no transtension was involved in all previous studies concerning rift interaction .

Here we present a rst-order study that elaborates upon earlier studies by (1) applying transtension to test its effect on continental rift interaction; and (2) using an improved analogue set-up with distributed deformation that allows more freedom in inherited structure geometry.

Methods

The experimental set-up (Fig. 1) consists of two sidewalls with a base of compressed foam and plexiglass bars stacked in between. Decompressing this base results in distributed deformation of the overlying model materials. Deforming the model laterally with a mobile base plate produces the strike-slip component for a range of transtension set-ups. Divergence velocities are in the order of 6 mm/h, translating to ca. 6 mm/y in nature. A 2 cm thick layer of a viscous silicone/sand mixture represents a 20 km thick ductile lower crust and a 2 cm quartz sand layer represents a 20 km brittle upper crust. Inherited structures are created with thin lines of silicon (seeds) laid down on top of the basal silicone layer. Here the relatively strong sand layer is thinner, creating a weak zone. The offset between adjacent seeds is 1, 2 or 4 cm (10, 20 or 40 km in nature). X-Ray Computer Tomography (CT) was used to reveal and analyze the 3D evolution of internal structures with time (hence 4D).

Results and discussion

An overview of top view results (Fig. 2) shows the nal surface structures as a function of rift offset and degree of transtension. A rst observation is that the seed lines do localize deformation well and that the rifts develop where they should. Furthermore, the rift character changes with increasing divergence obliquity: orthogonal extension
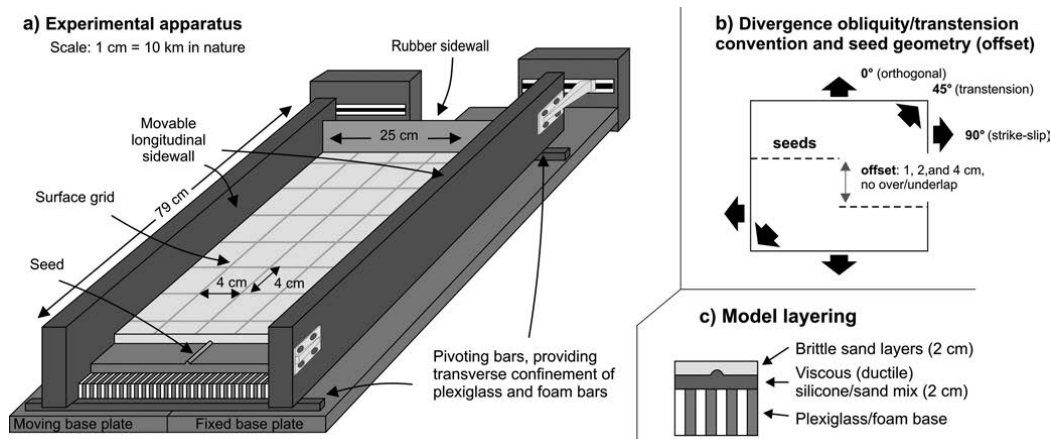
Fig. 1. Model set-up. (a) 3D schematic drawing of the experimental apparatus. (b) Seed geometry and transtension convention (top view). (c) Brittle-ductile layering for this model series.
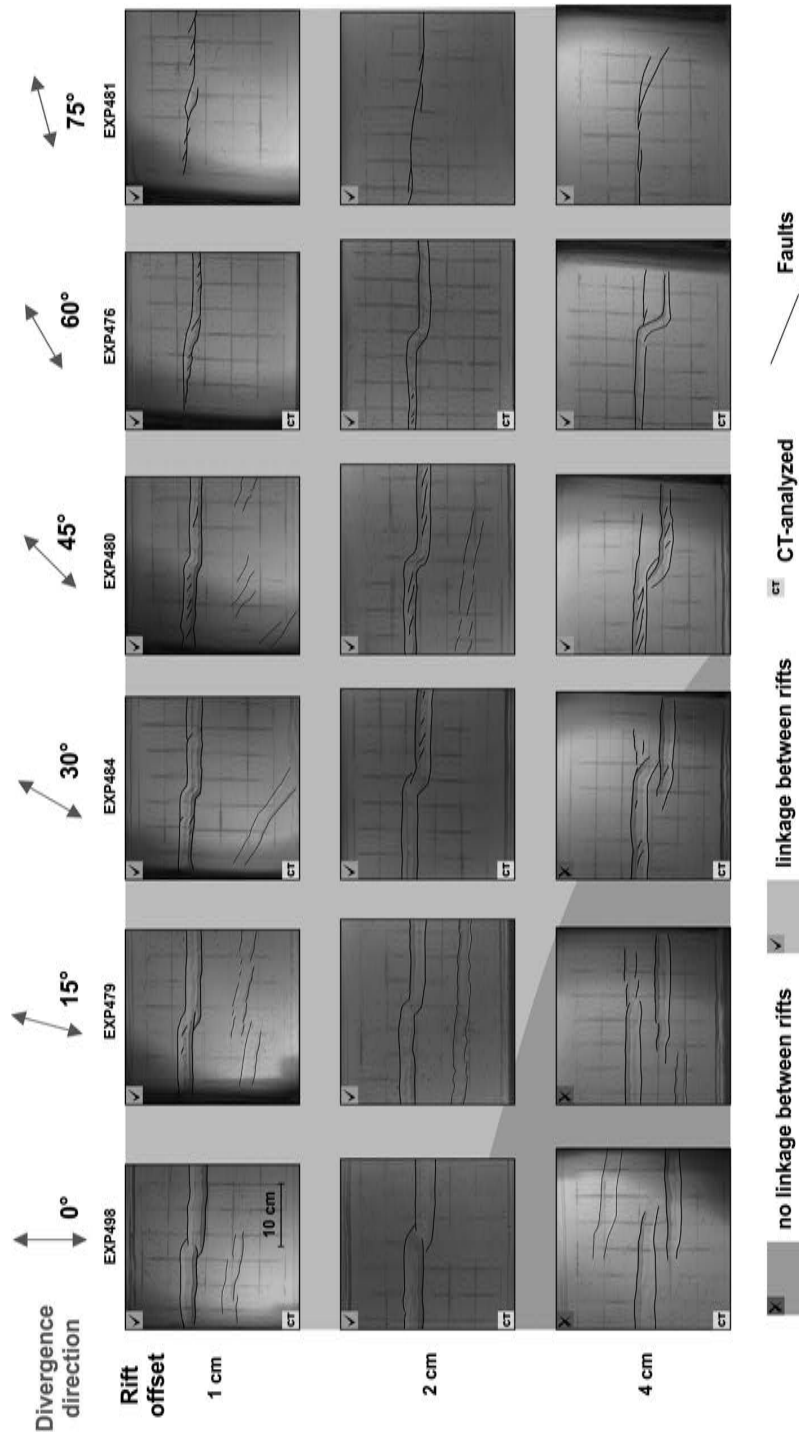
Fig. 2. Top views after 4 hours, showing influence of rift offset and divergence obliquity.

118
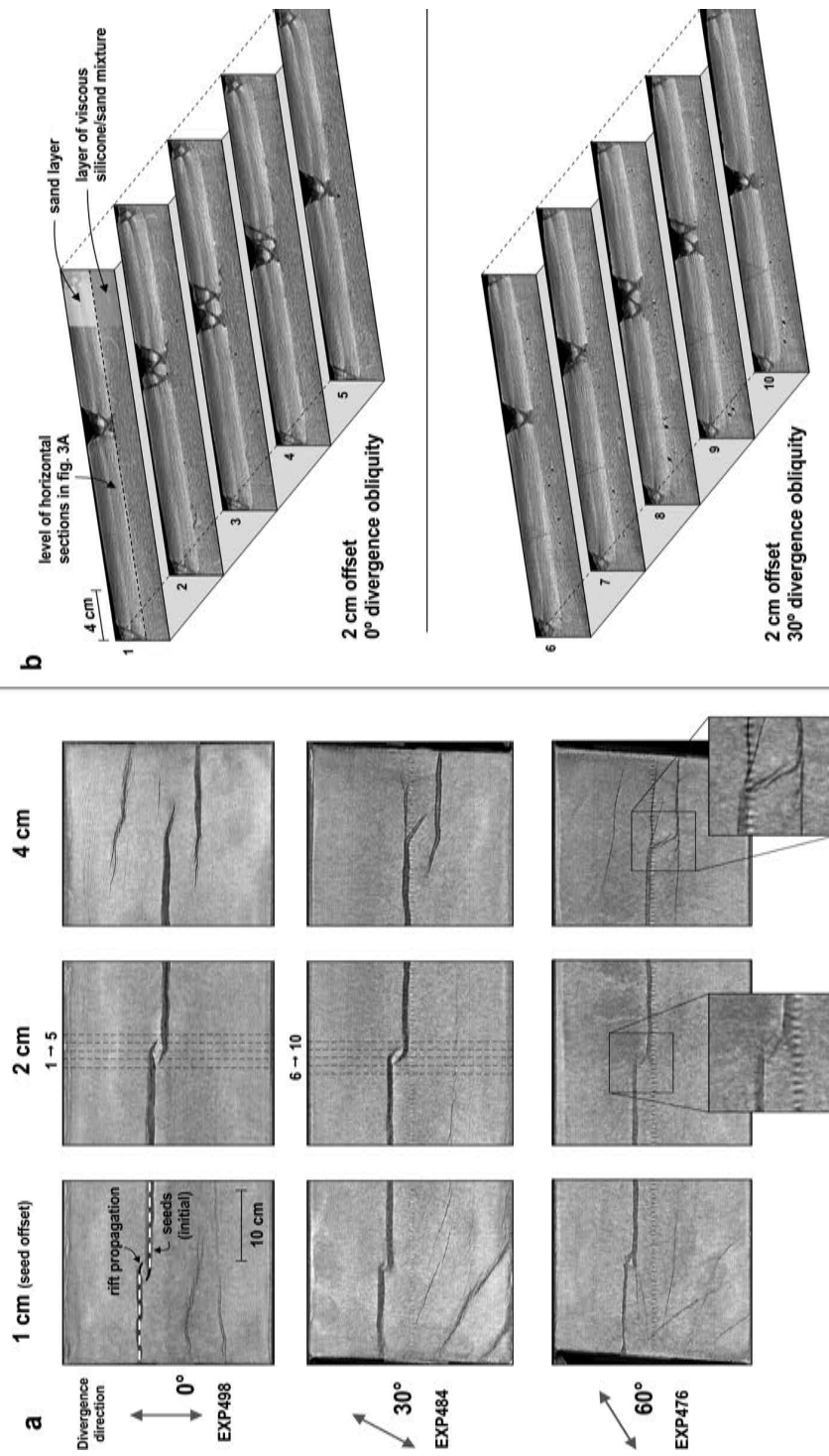
Fig. 3. (a) Horizontal CT-sections ca. 3 mm above the viscous silicone/sand layer; showing the initial seeds and rift propagation after 4 hours as a function of seed offset and divergence obliquity. (b) Vertical sections through two models. Locations of sections are indicated in Fig. 3a.
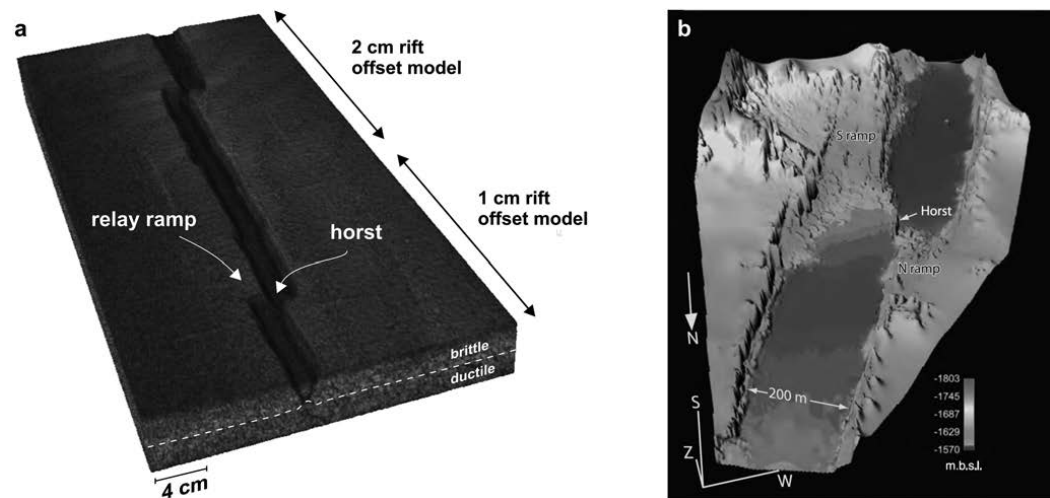
Fig. 4. Comparison of model results with a natural example. (a) CT-derived surface image of EXP498 after 2 hours, showing the topography of 1 and 2 cm offset models. (b) Topography of the Devils Lane stepover (Canyonlands, Utah). Modified after Fossen et al. (2010).

yields wide rift structures, while more transtensional set-ups produce narrower rifts with a strike-slip component along the boundary faults. Towards the strike-slip domain (at 75° divergence obliquity), the structures are almost completely strike-slip dominated. In more detail, the transtensional models also create rift-internal structures that are oriented more or less perpendicular to the divergence direction.

A next key observation is that most of the rifts connect to form a continuous trough at the surface. This is true for all 1 and 2 cm offset models, but not for all 4 cm offset models. In the latter model series, the 4 cm offset is too far a distance for rift connection under orthogonal extension conditions. However, when > 45° divergence obliquity is applied, rifts do merge again.

CT-sections show how this works within the models (Fig. 3a). The horizontal sections, ca. 3 mm above the viscous silicone/sand layer, reveal the location of the initial seeds and the propagation of the rifts. In all models, the rift propagation direction is oblique; the rifts curve towards each other, an effect that is related to the divergence obliquity. This is most clear in the 4 cm offset models, where the propagation directions are almost perpendicular to the divergence direction. The 1 cm offset models in Figure 3 (0° to 45° divergence obliquity) have similar features with minor additional echelon graben structures, perpendicular to the divergence direction.

The horizontal CT-sections also indicate that none of the rifts actually merge at depth. This last feature can be well traced in 3D (Fig. 3b). The horizontal sections reveal that the structure consists of two rifts that run along each other and curve around each other, only to widen and subsequently merge towards the surface. There they create the continuous troughs seen in Figure 2.

Finally, when compared with natural examples from the Canyon Lands in Utah and the North Sea Viking Graben (Fossen et al. 2010), the models produce quite similar structures (Fig. 4), including relay ramps and a horst between both rifts (also visible in Fig. 3b, sections 3 and 8).

Conclusion

- Increasing divergence obliquity strongly changes rift structures from wide rifts in orthogonal settings to narrower rifts with oblique internal structures under transtensional conditions to narrow strike-slip dominated systems towards the strike-slip domain;
- Rift interaction is promoted by (1) decreasing rift offset and (2) increasing divergence obliquity because rift propagation tends to align ca. perpendicular to it;
- The rifts in these models do not link at depth. Instead they curve around each other at depth and merge towards the surface to form a continuous trough there;
- The model results are consistent with natural examples.

References

Acocella et al. 1999. Sand-box modelling of basement-controlled transfer zones in extensional domains. – Terra Nova 11: 149–156.

Allken, et al. 2012. Factors controlling the mode of rift interaction in brittle-ductile coupled systems: A 3D numerical study. – Geochem. Geophys. Geosyst. 13: Q05010.

Brune et al. 2012. Modeling suggests that oblique extension facilitates rifting and continental break-up. – Journal of Geophysical Research 117: B08402

Fossen et al. 2010. Fault linkage and graben stepovers in the Canyonlands (Utah) and the North Sea Viking Graben, with implications for hydrocarbon migration and accumulation. – AAPG Bulletin 94: 597–613.

Appendix II. Article Geopanorama (2015)

Plattentektonik im Sandkasten

La tectonique des plaques dans un bac à sable

Der Prozess der Plattentektonik erklärt, weshalb die Oberfläche der Welt langsam, aber stetig in Bewegung ist. In Echtzeit lassen sich diese grossräumigen Veränderungen in der Erdkruste nicht untersuchen. Mithilfe eines Sandkastenmodells und eines Röntgentomographen ist es Geologen der Universität Bern jedoch gelungen, tektonische Entwicklungen im Labor zu simulieren.

La tectonique des plaques explique pourquoi la surface de la Terre se déplace lentement mais continuellement. Ces transformations de la croûte terrestre à grande échelle ne peuvent pas être étudiées en temps réel. Mais des géologues de l'Université de Berne ont réussi à simuler des évolutions tectoniques en laboratoire à l'aide d'un bac à sable et d'un appareil à rayons X.

FRANK ZWAAN

Im Laufe von Millionen von Jahren verschoben sich Kontinente über die ganze Erde, Gebirgsketten erhoben sich, Ozeane öffneten und schlossen sich wieder. Die Plattentektonik fasziniert Geologen seit langem und stellt sie immer wieder vor neue Herausforderungen. So fehlen beispielsweise viele Daten: Oft sind die Gesteine, die wichtige Hinweise liefern könnten, nicht sichtbar, weil sie entweder unter einer Sedimentschicht verborgen liegen oder schon längst erodiert worden sind.

Zudem ist die Dimension des tektonischen Systems gewaltig: Es umfasst die gesamte Erde und reicht in eine Tiefe von bis zu 200 Kilometer. Geologen versuchen, mit seismischen Untersuchungen und Bohrungen die tiefen Strukturen sichtbar zu machen. Trotzdem sind selbst die geologischen Strukturen der Alpen heute noch nicht genau bekannt.

Eine weitere Knacknuss ist die Zeit: Die Platten bewegen sich sehr langsam, mit höchstens einigen Zentimetern pro Jahr. Dieser Effekt ist nicht direkt beobachtbar, ausser vielleicht bei einem Erdbeben oder einem Vulkanausbruch. Verglichen mit der

Des continents ont migré, des chaînes de montagnes ont surgi et des océans se sont ouverts puis refermés sur toute la Terre au cours de processus qui s'étendent sur des millions d'années. Il y a longtemps que la tectonique des plaques fascine les géologues et leur pose régulièrement de nouveaux défis. Mais certaines données leur font défaut: les roches susceptibles de fournir d'importantes indications sont souvent invisibles car enfouies sous une strate sédimentaire ou érodées depuis longtemps.

Le système tectonique revêt en outre des dimensions gigantesques: il englobe toute la Terre jusqu'à 200 kilomètres sous la surface. Les géologues tentent de visualiser les structures profondes à l'aide d'investigations sismiques et de forages. Mais même ainsi, les structures géologiques des Alpes ne sont pas encore connues avec précision.

La dimension temporelle présente aussi un sérieux problème: les plaques se déplacent très lentement, à raison de quelques centimètres au plus par année. Ce mécanisme n'est pas observable directement, sauf peut-être lors d'un tremblement de terre ou d'une éruption volcanique. Mais ce ne sont que des phénomènes locaux, à pe-

5

226

gesamten Plattentektonik sind dies jedoch nur kleinräumige, lokale Phänomene.

Um die Plattentektonik trotz dieser Einschränkungen untersuchen zu können, greifen die Forscher auf Modelle zurück. Damit wollen sie die heutigen geologischen Strukturen besser verstehen und gleichzeitig herausfinden, wie diese entstanden sind. Computerberechnungen — sogenannte numerische Modelle — sind eine Möglichkeit, dies zu erreichen. Die Forscher des Strukturgeologischen Labors der Universität Bern haben sich jedoch für eine andere Methode entschieden: Sie modellieren die Plattentektonik physisch mit dem Sandkastenmodell.

Simulation mit Sand und Silikon

Um ein System im Labor korrekt modellieren zu können, sind Materialien nötig, die im kleinen Massstab und in kürzerer Zeit — also in Zentimetern statt Kilometern und in Stunden statt Jahrmillionen — genauso reagieren wie die Gesteine in der Erdkruste. Um die obersten Erdschichten nachzuahmen, die sich spröde verformen, setzten die Berner Forscher Sand ein. Daher der Name «Sandkastenmodell». Tiefere und weichere Schichten modellierten sie mit Silikon, einer zähen, sehr langsam fliessenden Flüssigkeit.

Ist der Sandkasten einmal mit verschiedenen Schichten gefüllt, wird er verformt: Mit Hilfe einer Maschine haben die Geologen das Modell zusammengeschoben, um eine Gebirgskette zu bilden. Oder sie haben es auseinandergezogen und so einen Graben entstehen lassen. Während der Verformung fotografierten sie die Oberfläche im Sandkasten immer wieder, um festzuhalten, wie sie sich verändert.

Schwieriger ist es, die internen Strukturen zu beobachten. Eine Möglichkeit ist,

tite échelle, en regard de l'ensemble de la tectonique des plaques.

Les chercheurs appliquent des modèles pour étudier la tectonique des plaques en dépit de ces limitations. Ils comptent sur eux pour mieux comprendre les structures géologiques actuelles et pour découvrir les secrets de leur formation. Une manière d'atteindre cet objectif consiste à réaliser des calculs par ordinateur, nommés modèles numériques. Mais les scientifiques du laboratoire de géologie structurale de l'Université de Berne ont opté pour une autre approche : ils modélisent la tectonique des plaques physiquement, en se servant d'un bac à sable mécanique.

Simulation avec du sable et du silicone

Pour être à même de modéliser correctement un système tectonique en laboratoire, il faut utiliser des matériaux qui se comportent exactement de la même manière que les roches de la croûte terrestre à petite échelle spatio-temporelle — et donc compter en centimètres et en heures au lieu de kilomètres et de millions d'années. Les chercheurs utilisent du sable pour imiter les niveaux supérieurs, qui se déforment de manière cassante, d'où le nom de «modèle du bac à sable». Et ils modélisent les couches profondes, tendres, en recourant à du silicone, un liquide visqueux qui s'écoule très lentement.

Le bac à sable est déformé après avoir été rempli avec les différentes couches : les géologues le compriment avec une machine pour constituer une chaîne de montagnes ou l'écartent pour générer un fossé. Ils photographient continuellement la surface des matériaux contenus dans le bac à sable pendant l'opération afin de docu-

6
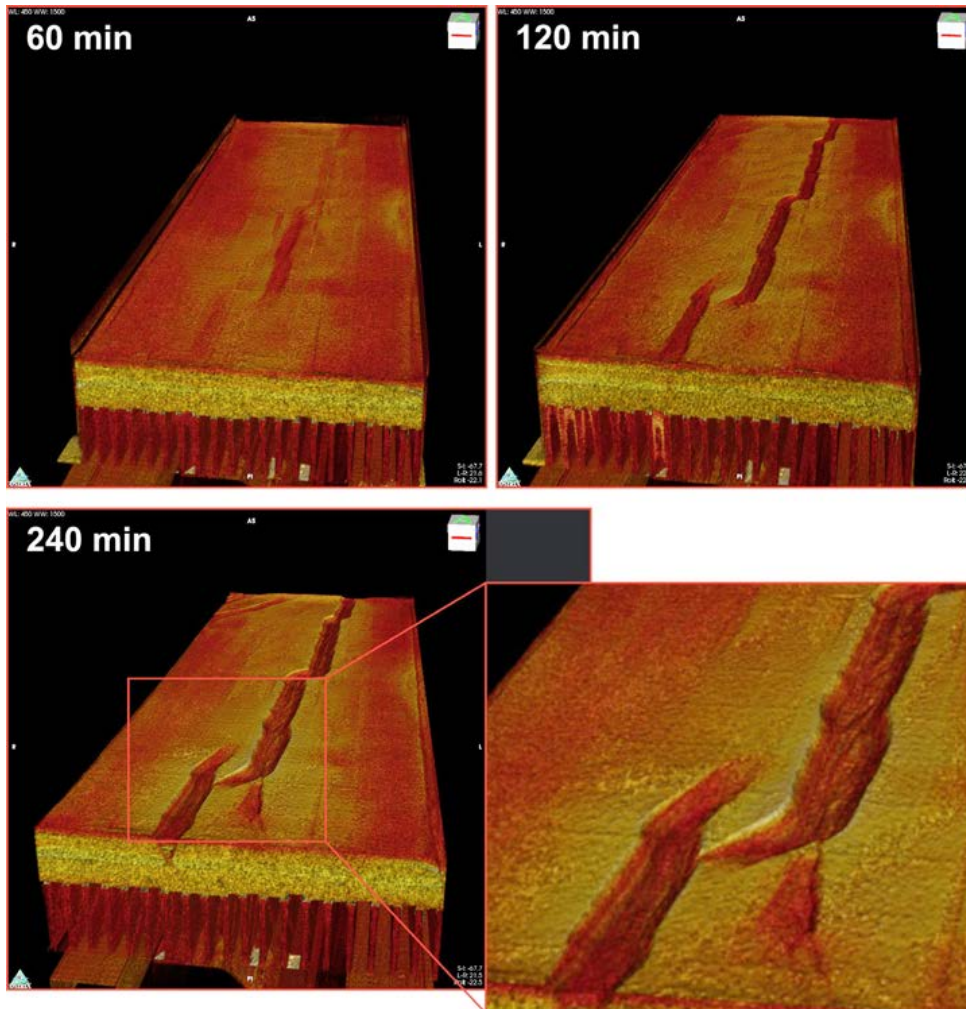
Ergebnisse eines Dehnungsmodells zu verschiedenen Zeitpunkten. Die 3D-Bilder sind Resultate der Röntgenaufnahmen. | Résultats d'un modèle d'extension à différents instants. Ces images 3D proviennent d'un scanner à rayons X. (Foto: F. Zwaan)

das Modell zu befeuchten und anschliessend wie einen Kuchen aufzuschneiden. Da das Modell dabei zerstört wird, macht man dies erst am Ende eines Experiments. Durch das Aufschneiden lässt sich erkennen, welche Strukturen entstanden sind. Allerdings kann man den dynamischen Prozess nicht nachvollziehen, in dem diese Strukturen entstanden sind.

menter son évolution. Il est plus difficile d'observer les structures internes. Une possibilité consiste à mouiller le modèle, puis à le découper comme un gâteau. Mais comme il est alors détruit, les chercheurs ne le font qu'à la fin d'une expérience. Ils voient ainsi les structures engendrées, mais sans pouvoir appréhender le processus qui les a formées.

7

Da die Entwicklung im Innern des Modells ein zentraler Teil der Forschung ist, haben die Berner Geologen eine andere Lösung gefunden, um die verborgenen Prozesse sichtbar zu machen: Sie scannten den Sandkasten während der Verformung mit dem Röntgentomographen des Instituts für Rechtsmedizin. Mit dieser Methode analysierten sie die Modelle nicht nur in den drei räumlichen Dimensionen, sondern noch dazu in einer vierten Dimension: der Zeit.

Geometrie von Grabenstrukturen

Zurzeit entwickeln die Berner Geologen Dehnungsmodelle, mit denen sie die Entstehung von Grabenstrukturen, wie etwa des Rheingrabens zwischen den Vogesen und dem Schwarzwald, zu simulieren versuchen. Bei Gräben sinkt ein Gebiet zwischen Randbrüchen ab. Dauert dieser Prozess lange genug an, können sich Kontinente trennen, und dazwischen öffnet sich ein Ozean. Die Berner Forscher interessiert dabei insbesondere das Phänomen der Transfer-Zonen, auch Verbindungszonen genannt. Wenn Erdplatten auseinander gezogen werden, bilden sich Dehnungsstrukturen (Gräben). Sie entstehen bevorzugt dort, wo die Kruste aufgrund früherer Verformungsphasen bereits geschwächt ist. Die Schwächezonen verlaufen im Untergrund meist nicht geradlinig. Deshalb entwickeln sich mehrere Gräben versetzt zueinander. Dazwischen entstehen mit der Zeit Transferzonen, welche die Gräben verbinden. Auf diese Weise bildet sich ein durchgehendes Dehnungssystem.

Die Berner Geologen führten einige Experimente durch, um dieses System zu testen. Ziel war es, zwei Gräben entstehen zu lassen und dann zu beobachten, was ge-

L'évolution de l'intérieur du modèle est un élément essentiel de la recherche, aussi les géologues bernois ont-ils trouvé une autre solution pour visualiser les mécanismes cachés : ils scannent le bac à sable pendant la déformation en utilisant le tomodensitomètre à rayons X de l'Institut de médecine légale. Cette méthode leur permet d'analyser les modèles non seulement dans les trois dimensions de l'espace, mais en plus dans la quatrième dimension, celle du temps.

Géométrie de structures d'affaissement

Les géologues bernois sont en train de développer un modèle d'extension avec lequel ils comptent simuler la création de structures d'affaissement, comme le Fossé rhénan, situé entre les Vosges et la Forêt noire. Dans ce cas, un compartiment de la croûte terrestre s'enfonce entre deux failles. Si ce processus dure assez longtemps, il arrive que des continents se séparent et qu'un océan s'ouvre entre eux. Les chercheurs de l'Université de Berne s'intéressent en particulier au phénomène des zones de transfert, aussi nommées zones de liaison. Lorsque des plaques tectoniques s'écartent, des structures d'extension (fossés) apparaissent. Elles surviennent de préférence là où la croûte terrestre avait déjà été affaiblie par des phases de déformation antérieures. Les zones de faiblesse affectant le sous-sol ne sont habituellement pas rectilignes, d'où la génération de plusieurs fossés décalés. Des zones de transfert les reliant se forment petit à petit entre eux. C'est ainsi que naît un système d'extension continu.

Les chercheurs bernois ont réalisé quelques expériences pour tester ce système. Leur but consistait à créer deux fos-

8
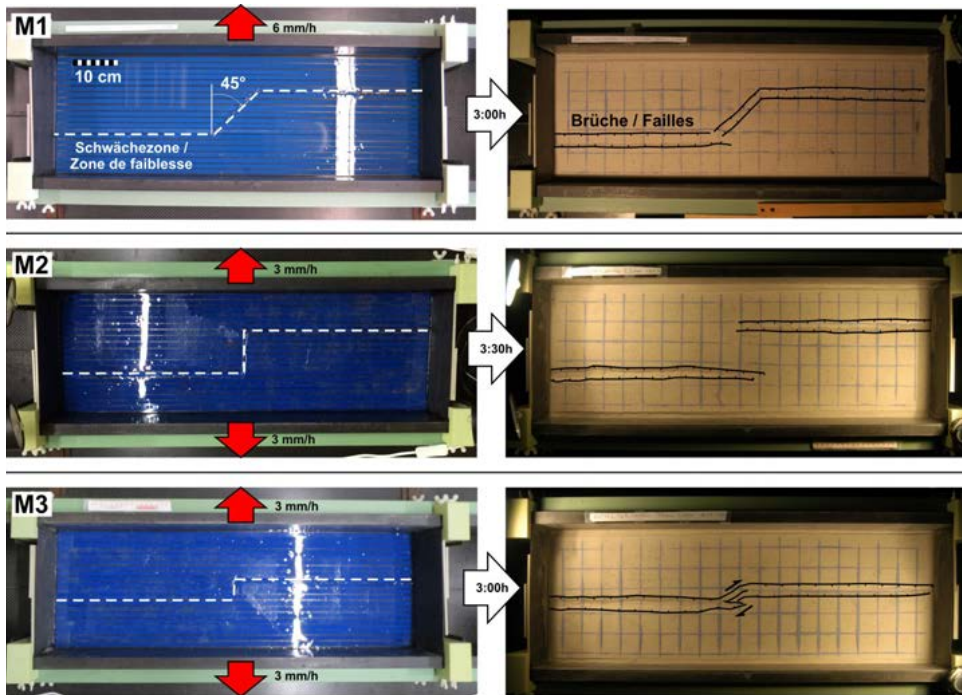
Oberflächenresultate einiger Experimente. Links: Die Ausdehnungsrichtung und -geschwindigkeit sowie die Geometrie der Schwächezonen in den drei Modellen vor dem Experiment (hier noch ohne Sandschichten). Rechts: Oberflächenstrukturen im Sand nach dem Experiment. | Résultats obtenus en surface dans plusieurs expériences. A gauche : conditions initiales (encore sans couche de sable) : direction et vitesse d'extension ainsi que géométrie de la zone de faiblesse. A droite : structures observables en surface au terme de l'expérience. (Foto: Frank Zwaan)

schieht, wenn etwas im System verändert wird. Um die Lage der Gräben zu steuern, legten die Forscher zwei parallel liegende schwache Zonen an. Dazwischen befand sich eine weitere schwache Zone, deren Geometrie je nach Experiment abgeändert wurde. So wollten die Forscher herausfinden, welche Parameter für die Entwicklung einer Transfer-Zone wichtig sind.

Die Resultate der ersten Modellierung zeigten, dass sich zwischen den zwei Gräben im Abstand von neun Zentimetern eine deutliche Verbindung entwickelt, wenn die dazwischen liegende, schwache Zone in einem Winkel von 45 Grad verläuft. Hingegen entstand bei einem Winkel von 90 Grad (Modell 2) gar keine Verbindung. In einer dritten Modellierung verringerten die Geo-

sés, puis à observer ce qui se passe lorsqu'on modifie l'un ou l'autre paramètre. Ils ont donc placé deux zones de faiblesse parallèles pour fixer la position des fossés. Entre elles se trouvait une autre zone de faiblesse, dont la géométrie variait d'une expérience à l'autre. Les scientifiques voulaient découvrir ainsi quels sont les paramètres importants dans l'évolution d'une zone de transfert.

Les résultats de la première modélisation ont montré qu'une zone de liaison bien visible se forme entre les deux fossés lorsqu'ils sont distants de neuf centimètres et que la zone de faiblesse intercalaire forme un angle de 45 degrés avec eux. Aucune zone de liaison n'est en revanche apparue sous un angle de 90 degrés (modèle 2). Dans un

9

230

logen den Abstand zwischen den Gräben auf drei Zentimeter, wodurch wieder eine Verbindung entstand. Daraus folgerten die Forscher, dass für die Entstehung einer Verbindung einerseits der Abstand zwischen den Strukturen wichtig ist, andererseits aber auch der Winkel der schwachen Zone zwischen den Gräben.

Geduld und Technik

Die Berner Geologen werden nun ihre Experimente verfeinern, um die Details besser zu verstehen, insbesondere die Geometrie und Kinematik der Transfer-Zonen. Dafür arbeiten sie mit Forschern aus dem Ausland zusammen, analysieren deren Ergebnisse und vergleichen die eigenen Resultate mit Computermodellen. Darüber hinaus entwickeln sie neue Maschinen, um andere Versuchsanordnungen modellieren zu können. Mit viel Geduld und raffinierten Techniken bringen sie damit immer mehr über die Plattentektonik und die Entwicklung der Erde ans Licht.

Frank Zwaan
Institut für Geologie der Universität Bern
frank.zwaan@geo.unibe.ch

Weitere Informationen, eine Broschüre und ein Video des Schweizer Radio und Fernsehens SRF gibt es im Internet auf http://www.geo.unibe.ch/people/schreurs/schreurs.php?PID=29341736

troisième modèle, la distance entre les fossés a été réduite à trois centimètres et une zone de liaison a de nouveau été engendrée. Les géologues en ont conclu qu'aussi bien la distance entre les structures que l'angle de la zone de faiblesse jouent un rôle crucial dans la formation d'une zone de liaison.

De la patience et de la technique

Les géologues bernois vont maintenant affiner leurs expériences pour mieux comprendre les détails, notamment la géométrie et la cinématique des zones de transfert. Dans ce but, ils collaborent avec des chercheurs étrangers, analysent leurs résultats et comparent ceux qu'ils ont eux-mêmes obtenus avec des modèles informatiques. Ils développent également de nouvelles machines pour modéliser d'autres configurations. Ils en apprennent ainsi toujours davantage au sujet de la tectonique des plaques et de l'évolution de la Terre — au prix d'une grande patience et en appliquant des techniques raffinées.

Traduction:
Christian Marro
TRADUCTONET
chmarro@traductonet.ch

Des informations supplémentaires, une brochure et une vidéo de la chaîne suisse alémanique de radio et télévision SRF sont disponibles sur Internet (en allemand): http://www.geo.unibe.ch/people/schreurs/schreurs.php?PID=29341736

10

Appendix III. Article GeoBrief (2015)

afgestudeerd en dan...

Promoveren in het buitenland
Plaattektoniek in de zandbak van de Universiteit Bern

Ruim een jaar geleden ben ik bij de Universiteit Bern aanbeland voor een promotieonderzoek onder supervisie van Guido Schreurs, een alumnus van de UU die al 20 jaar in de pittoreske Zwitserse hoofdstad werkt. Het onderzoeksthema sprak mij persoonlijk sterk aan: het modelleren van plaattektoniek door middel van analoge (sandbox) modellen. Meer specifiek het modelleren van extensietektoniek, een ironisch onderwerp, zo met de Alpen als een prachtig voorbeeld van compressietektoniek in de achtertuin. Desondanks heeft het onderzoek intussen de nodige resultaten geproduceerd.

De plaattektoniek verklaart hoe in de loop van vele miljoenen jaren het aardoppervlak in beweging is geweest, een proces dat geologen sinds lang fascineert en uitdaagt. Maar je vergeet snel dat de mooie afbeeldingen in tekstboeken op verrassend weinig en indirecte data zijn gebaseerd. Het is immers onmogelijk om werkelijk in de diepte kijken, dus is het behelpen met een boring hier, een veldobservatie daar en eventueel een seismische sectie. Daarnaast is de maat van het systeem enorm, want het is wereldomvattend en de structuren gaan vele honderden kilometers de diepte in.

Waarom (analoog) modelleren?
Een ander probleem is de geologische tijdschaal. Gedurende een mensenleven is, op een eventuele aardbeving na, weinig te merken van de plaattektoniek. Zodoende zijn interpretaties van diepe geologische structuren altijd een momentopname en ont-

breekt het dynamische overzicht, iets wat van groot belang is voor bijvoorbeeld olie- en gasexploratie. De aanwezigheid van olie en gas heeft er inmiddels voor gezorgd dat de Nederlandse ondergrond relatief goed in kaart is gebracht, maar in de Alpen zijn er nog steeds veel onduidelijkheden. Er is dus in Bern, waar de Alpen een belangrijk onderzoeksthema vormen, nog altijd veel werk te doen.

Een manier om deze problemen gedeeltelijk op te lossen, is het maken van dynamische tektonische modellen. Deze helpen om de geologische structuren in de diepte en hun ontwikkeling door de tijd beter te begrijpen. Het is mogelijk om met computers (numerieke) modellen te maken, maar in het structureel-geologische laboratorium in Bern wordt een andere methode toegepast. Hier modelleren we de plaattektoniek fysiek (analoog) met sandbox-machines.
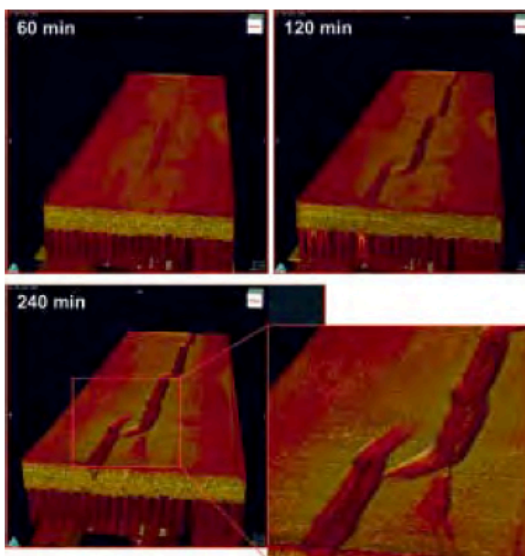
Resultaten van een extensiemodel door de tijd heen. De 3D-beelden zijn verkregen via computertomografie.

Tektoniek in een zandbak
Om in het laboratorium de plaattektoniek correct te modelleren zijn materialen nodig die op kleinere schaal (centimeterschaal i.p.v. kilometerschaal) en in kortere tijd (uren i.p.v. miljoenen jaren) hetzelfde reageren als de gesteenten waaruit de aardschollen bestaan. (Kwarts)zand wordt gebruikt om de bovenste korst en ondiepe gesteenten – lagen die breken tijdens deformatie – te modelleren. Om het op geologische tijdschaal viskeuze gedrag van de onderste korst en bijvoorbeeld zoutlagen te modelleren, worden siliconen of 'silicon putty' gebruikt, een zeer langzaam stromende vloeistof.

Als de sandbox-machine met de nodige zand- en siliconenlagen gevuld is, kunnen motoren de zijkanten bewegen zodat de lagen deformeren. Zo kan het systeem worden gecomprimeerd om een gebergteketen te scheppen. Andersom kan het model uitgerekt worden om een riftvallei, of zelfs een oceaan, te creëren.

De voordelen van CT-analyse
Er zijn meerdere methodes om een model te analyseren. Zolang het model loopt, worden de oppervlaktestructuren in intervallen gefotografeerd om de ontwikkelingen te kunnen volgen. Het is moeilijker om de interne structuren in de gaten te houden. Een van de mogelijkheden is om het model nat te maken en doorsnedes te maken. Helaas wordt het model dan vernietigd; dit is dus alleen een optie aan het einde van een experiment. Het is duidelijk dat het op deze manier onmogelijk is om de evolutie van interne structuren te bestuderen.

Omdat dit toch een belangrijk onderdeel van het onderzoek is, hebben we in Bern een manier gevonden om dit probleem te omzeilen. We mogen gebruik maken van de röntgenscanner van het Forensisch Instituut om de modellen te scannen. Met deze computertomografie (CT)-beelden wordt het mogelijk om de modellen niet alleen in 3D, maar ook door de tijd heen, dus in 4D, te analyseren.

De sandbox-machine in de röntgenscanner gedurende een experiment.

232

Een voorbeeld: transfer zones

Mijn promotieonderzoek richt zich op het modelleren van extensietektoniek. De afgelopen tijd heeft het onderzoek zich geconcentreerd op de evolutie van 'transfer zones', zones die twee uit elkaar liggende grabenstructuren verbinden. Een bekend voorbeeld zijn de transfer zones in het Oost-Afrikaanse riftsysteem. Dichter bij huis ligt de Rhine-Bresse transfer zone tussen de Rijnslenk langs de Frans-Duitse grens en het Rhônedal in Frankrijk. Deze structuren ontstaan doordat deformatie zich bij voorkeur concentreert langs oude zwaktezones in de korst, vaak overblijfselen van eerdere deformatiefasen. Aangezien deze beginnende structuren niet altijd in het verlengde van elkaar liggen, trachten ze zich bij aanhoudende deformatie te verbinden, om een grootschalig riftsysteem te openen. Zo vormen zich transfer zones, die zelf vaak ook weer oudere, zwakke structuren in de korst volgen.

De modellen die op de afbeeldingen te zien zijn, zijn opgebouwd uit een 2-cm-dikke basislaag van siliconen om 20 km onderste korst te simuleren en een 2-cm-dikke toplaag van fijn kwartszand als de bijbehorende 20 km aan bovenste korst. Zwakke zones worden gemaakt door lijnen van siliconen in de gewenste geome-

trie op de basislaag aan te brengen. Daarbovenop worden de zandlagen gezeefd. Omdat op deze plekken het relatief sterke zand dunner is, bevinden zich hier zwaktezones. Door de zij-wanden van de sandbox langzaam uit elkaar te bewegen, wordt het model uitgerekt en ontstaan structuren langs de siliconenlijnen. De snelheden liggen rond de 6 mm/h, wat in de natuur overeenkomt met ca. 6 mm/Ma, een uur in het lab vertaalt zich dus naar ca. 1 Ma.

Resultaten

Uit mijn experimenten blijkt dat de geometrie van de zwaktezones in het systeem een behoorlijke invloed heeft op de resulterende structuren. In het eerste model, met een 45° hoek tussen de twee zwakke zones, ontstonden twee duidelijke grabens met een goed ontwikkelde verbinding ertussen. Toen de hoek tussen de twee zwakke zones naar 90° werd gebracht, vormde zich geen verbinding. Maar toen de oorspronkelijke afstand van 9 cm tussen de beide grabens werd teruggebracht naar 3 cm, zoals in het derde model, kwam er weer een verbinding tot stand tussen de beide structuren. Deze resultaten wijzen erop dat zowel de geometrie van de zwakke zones, als de afstand tussen de grabens van
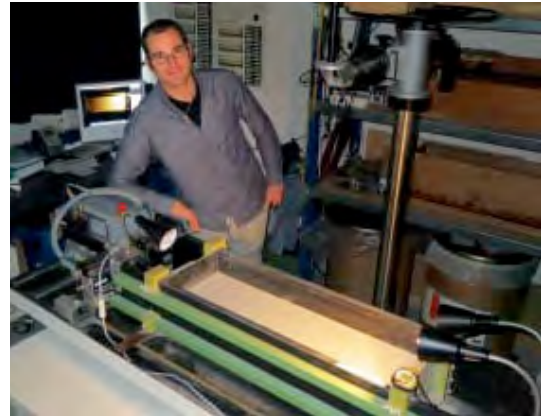
Promovendus Frank Zwaan bij een experiment in het tektonieklaboratorium aan de Universiteit van Bern.

belang zijn voor het ontstaan van transfer zones. Om het systeem beter te begrijpen zijn we nu bezig met om stelselmatig te testen wat de invloed is van bepaalde parameters op het systeem. Dit betreft zaken als de afstand tussen de grabens, extensie met een laterale deformatiecomponent ('oblique extension'), verschillende geometrieën, etc.

De toekomst

Het moge duidelijk zijn dat het analoog modelleren van plaattektoniek een hoop mogelijkheden biedt. In de toekomst zijn we van plan om bij-voorbeeld nog een nieuwe machine in gebruik te nemen. Verder wordt er samengewerkt met collega's in Noor-wegen die zich richten op computer-modelleren. Het doel is om de analo-ge resultaten te vergelijken met numerieke resultaten en vervolgens bepaalde aspecten toe te voegen die niet te modelleren zijn in het lab. Denk aan de invloeden van tempera-tuur, isostasie en continent break-up (het openen van een oceaan). Met collega's uit Engeland proberen we de deformatie in de CT-beelden te kwantificeren door middel van com-puterprogramma's die bewegingen in 3D kunnen traceren. Een laatste aspect is dat de modellen natuurlijk nog ter verificatie met fenomenen in

de natuur moeten worden vergeleken. Het resultaat in de zandbak kan vaak erg aansprekend zijn, maar hoeft niet geheel realistisch te zijn. Al met al is er nog volop werk te verzetten in de komende jaren; een mooie uitdaging voor een beginnend onderzoeker.

Tot slot zou ik studenten die geïnteres-seerd zijn in een wetenschappelijke carrière sterk willen adviseren eens om te kijken naar een MSc- of PhD-project in Zwitserland, een prachtig en fascinerend land. Persoonlijk heb ik hier erg goede ervaringen gehad. Een langer verblijf in het buitenland verruimt je horizon en er zijn hier volop middelen en mogelijkheden aan de vele universiteiten die zich met aardwetenschappen bezig houden.

Frank Zwaan, Universiteit Bern
frank.zwaan@geo.unibe.ch
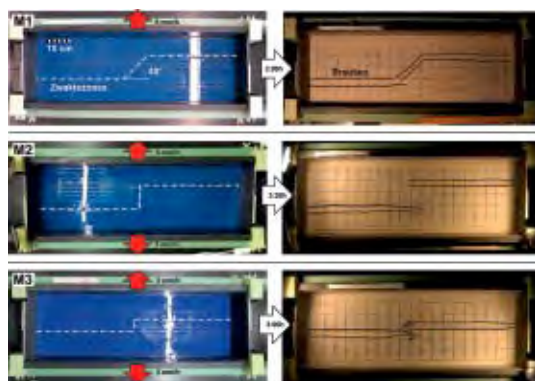
Oppervlakteresultaten van enkele experimenten. Links staan de begin-condities (nog zonder zandlagen) aangegeven zoals de extensierichting en –snelheid, alsmede de geometrie van de zwakke zones. Rechts zijn de resulterende oppervlaktestructuren zichtbaar.

Appendix IV. Blueprints new sidewall parts Namazu apparatus

Allgemeintoleranzen ISO 2768-m in mm

über	0	3	6	30	120	400	1000	2000	4000
bis	3	6	30	120	400	1000	2000	4000	---
Norm ±	0,1	0,1	0,2	0,3	0,5	0,8	1,2	2	3

1 Paar = Gem. Zeichnung und 1x gespiegelt

$\sqrt{Ra3,2}$ ($\vee$)

WERKSTOFF

GEZEICHNET	22.01.2014	ZM	MASSSTAB
GEPRÜFT			BLATT-NR
FREIGEGEBEN			

EP GL 201

BEM/ PA		
1 : 1		
01 / 01		

HSR
HOCHSCHULE FÜR TECHNIK
RAPPERSWIL
FHO Fachhochschule Ostschweiz
INSTITUT FÜR PRODUKTDESIGN,
ENTWICKLUNG UND KONSTRUKTION

IPEK

ZCHNG-NR

762.1950_P0001

d-762.1950_P0001.01-a-2

Klemme unten

BLATT-INDEX a 2 A3

Allgemeintoleranzen ISO 2768-m in mm

über	0	3	6	30	120	400	1000	2000	4000
bis	3	6	30	120	400	1000	2000	4000	----
Norm ±	0,1	0,1	0,2	0,3	0,5	0,8	1,2	2	3

Begrenzungswand

762.1950_P0004

ZCHNG-NR: d-762.1950_P0004_201-b-1

M 1:2

Allgemeintoleranzen ISO 2768-m in mm								
über	0	3	6	30	120	400	1000	2000	4000
bis	3	6	30	120	400	1000	2000	4000	---
Norm ±	0,1	0,1	0,2	0,3	0,5	0,8	1,2	2	3

Führungsschiene

ZNG-NR. 762.1950_P0005

d-762.1950_P0005_z01-a--2

HSR
HOCHSCHULE FÜR TECHNIK
RAPPERSWIL

IPEK INSTITUT FÜR PRODUKTDESIGN, ENTWICKLUNG UND KONSTRUKTION

WERKSTOFF PP

GEZEICHNET 22.01.2014 ZM MASSSTAB 1:1

GEPRÜFT BLATT-NR. 01/01

FREIGEGEBEN

A3

100

170

4

DIE AUF DER ZEICHNUNG ENTHALTENEN MASSE SIND FERTIGMASSE

Allgemeintoleranzen ISO 2768-m in mm								
über	0	3	6	30	120	400	1000	2000
bis	3	6	30	120	400	1000	2000	4000
Norm ±	0.1	0.1	0.2	0.3	0.5	0.8	1.2	2	---

WERKSTOFF		PP		BEM/ FA
GEZEICHNET	22.01.2014	ZM	MASSSTAB	
GEPRÜFT			BLATT-NR.	1:1
FREIGEGEBEN				01 / 01

HSR
HOCHSCHULE FÜR TECHNIK
RAPPERSWIL
FHO Fachhochschule Ostschweiz

IPEK INSTITUT FÜR PRODUKTDESIGN, ENTWICKLUNG UND KONSTRUKTION

Stützplatte

ZCHNG-NR. d-762.1950_P0006_z01-a-2

762.1950_P0006

MODELL-NUMMER

BLATT-INDEX	a
MODELL-INDEX	a
MODELL-VERSION	2
FORMAT	A4

Supportstütze

100

50

45,5

40

13

M 1:2

Ra3,2

$\frac{-0.2}{-0.4}$

+0.5

WERKSTOFF					BEM / FA	ZCHNG-NR.	α-762.1950_P0010_z01-α--1		BLATT-INDEX	α
GEZEICHNET	27.01.2014	ZM	MASSTAB	1 : 1						
GEPRÜFT			BLATT-NR.	01 / 01		762.1950_P0010			1	A4
FREIGEGEBEN						MODEL-NUMMER	MODEL-INDEX	MODEL-VERSION	FORMAT	

HSR
HOCHSCHULE FÜR TECHNIK
RAPPERSWIL
IPEK Produktdatenbank
IPEK
INSTITUT FÜR PRODUKTDESIGN,
ENTWICKLUNG UND KONSTRUKTION

EP GC 201

DIE AUF DER ZEICHNUNG ENTHALTENEN MASSE SIND FERTIGMASSE

Allgemeintoleranzen ISO 2768-m in mm								
über	0	3	6	30	120	400	1000	2000
bis	3	6	30	120	400	1000	2000	4000
Norm ±	0,1	0,1	0,2	0,3	0,5	0,8	1,2	2

								3

239

Appendix V. Design and blueprints Xissor apparatus

BSc project Claude Grau (IPEK/HSR Technische Hochschule Rapperswil, 2014)

The initial concept provided by the student (V.1) was later worked out and assembled by Rudolf Kamber and Michael Ziltener at IPEK Rapperswil (see final plate design, V.2). The construction was funded by the Swiss National Science Foundtion, Prof. Marco Herwegh (University of Bern) and Berne University Science Foundation.

_____

V.1. Conceptual design (Claude Grau)

3D Xissor apparatus design
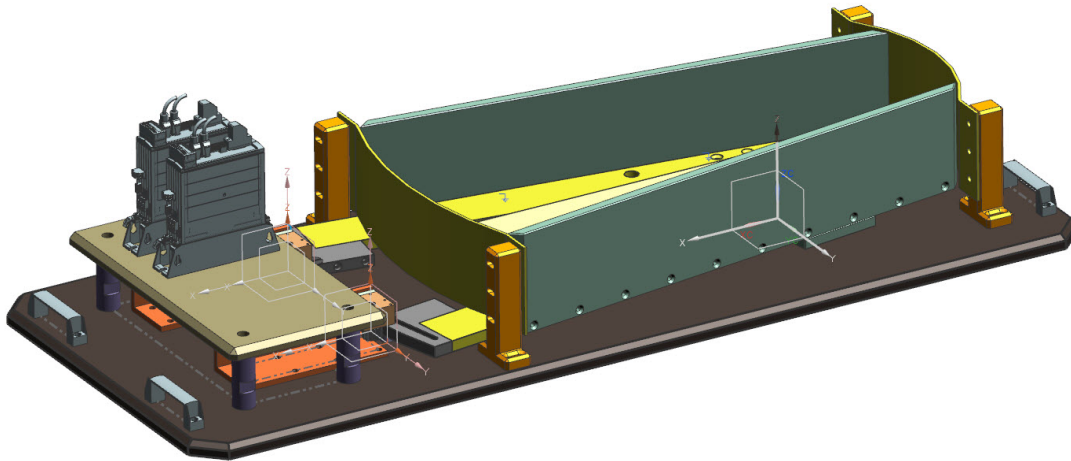
Xissor apparatus frame design (without foam/base plate components)
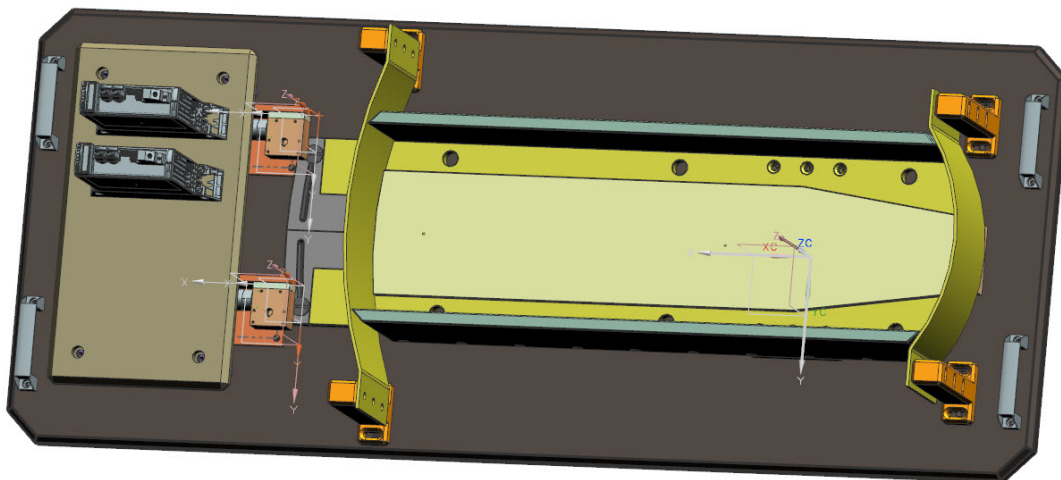
Xissor apparatus frame design (with base plate components)
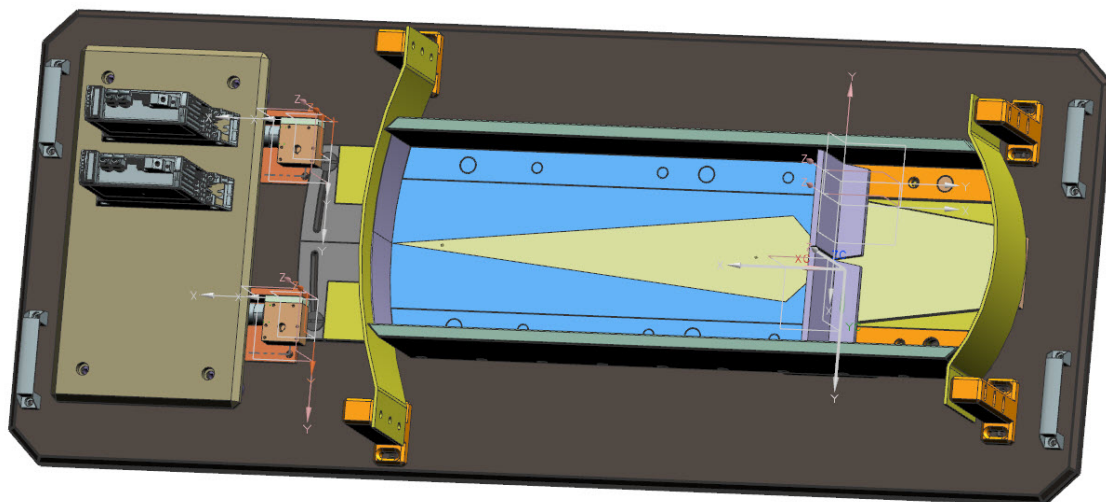
Xissor apparatus frame design (with foam base components)
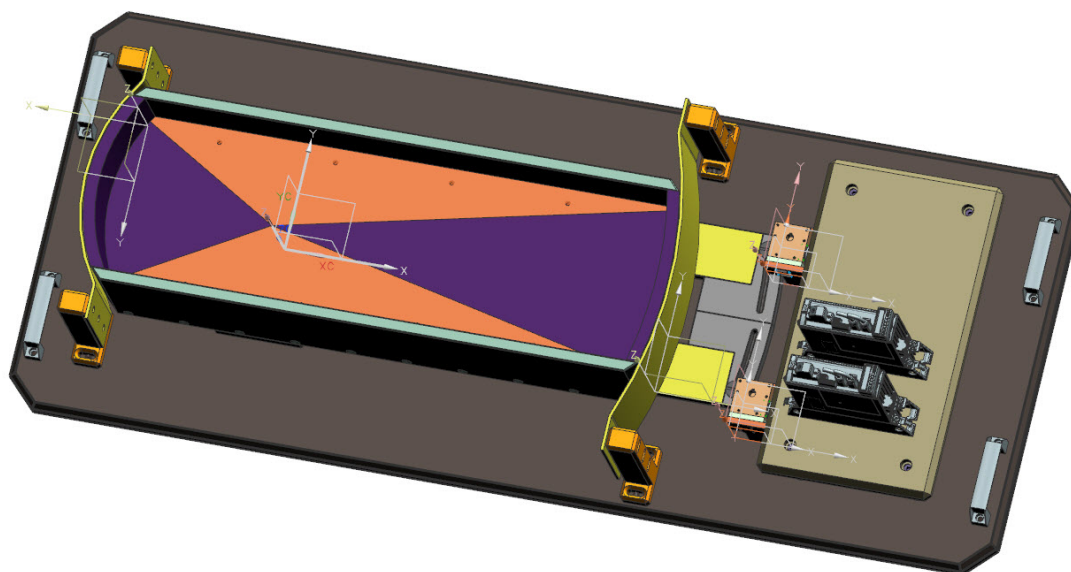
Map view Xissor apparatus design (starting position)
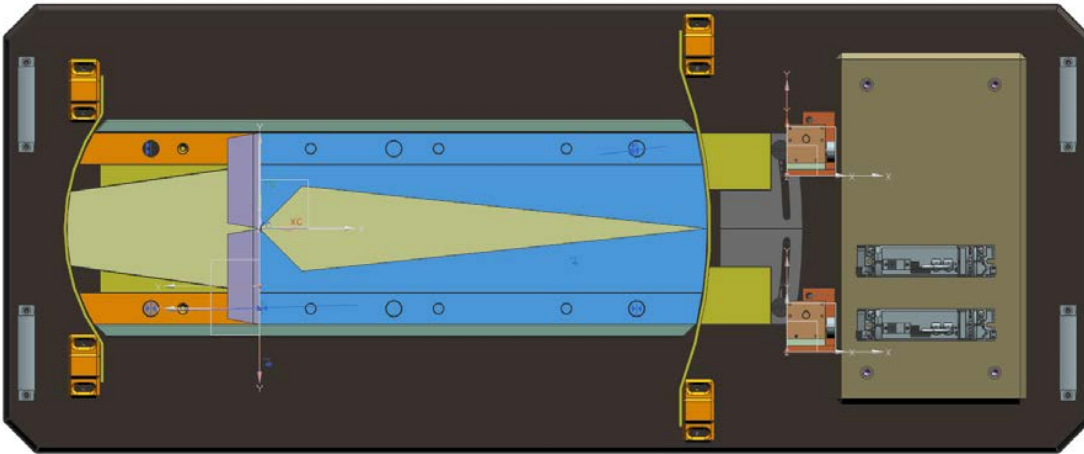
Map view Xissor apparatus design (asymmetric extension)
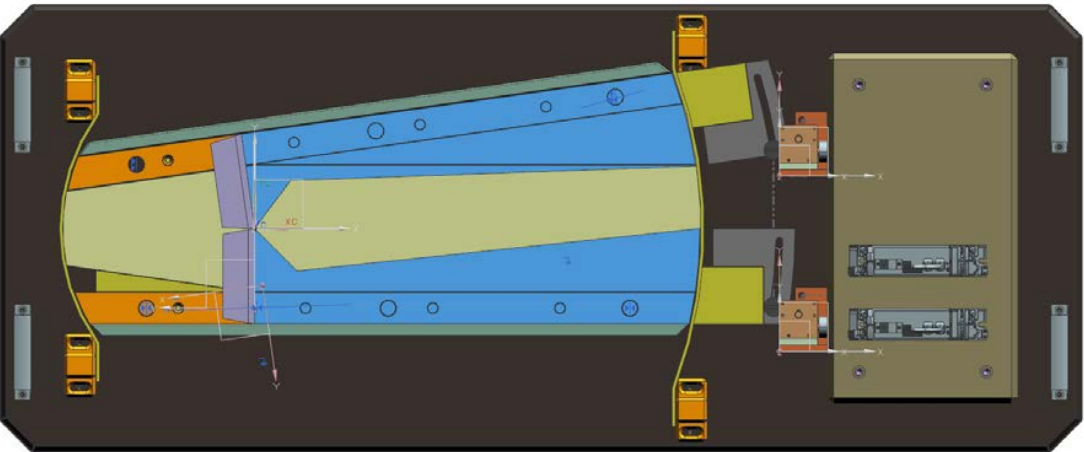
Map view Xissor apparatus design (symmetric extension)
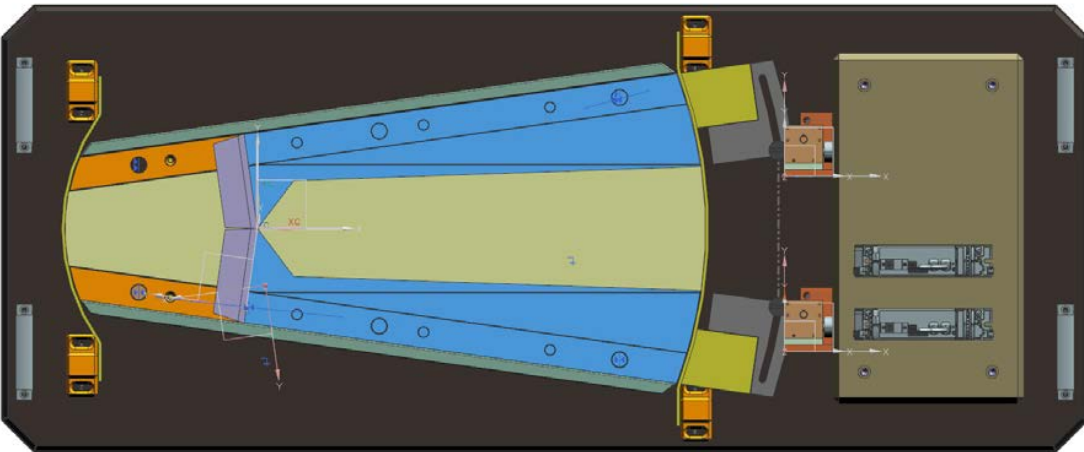
V.2. Final Xissor design blueprints (Rudolf Kamber and Michael Ziltener)

2.1. Base plate set-up
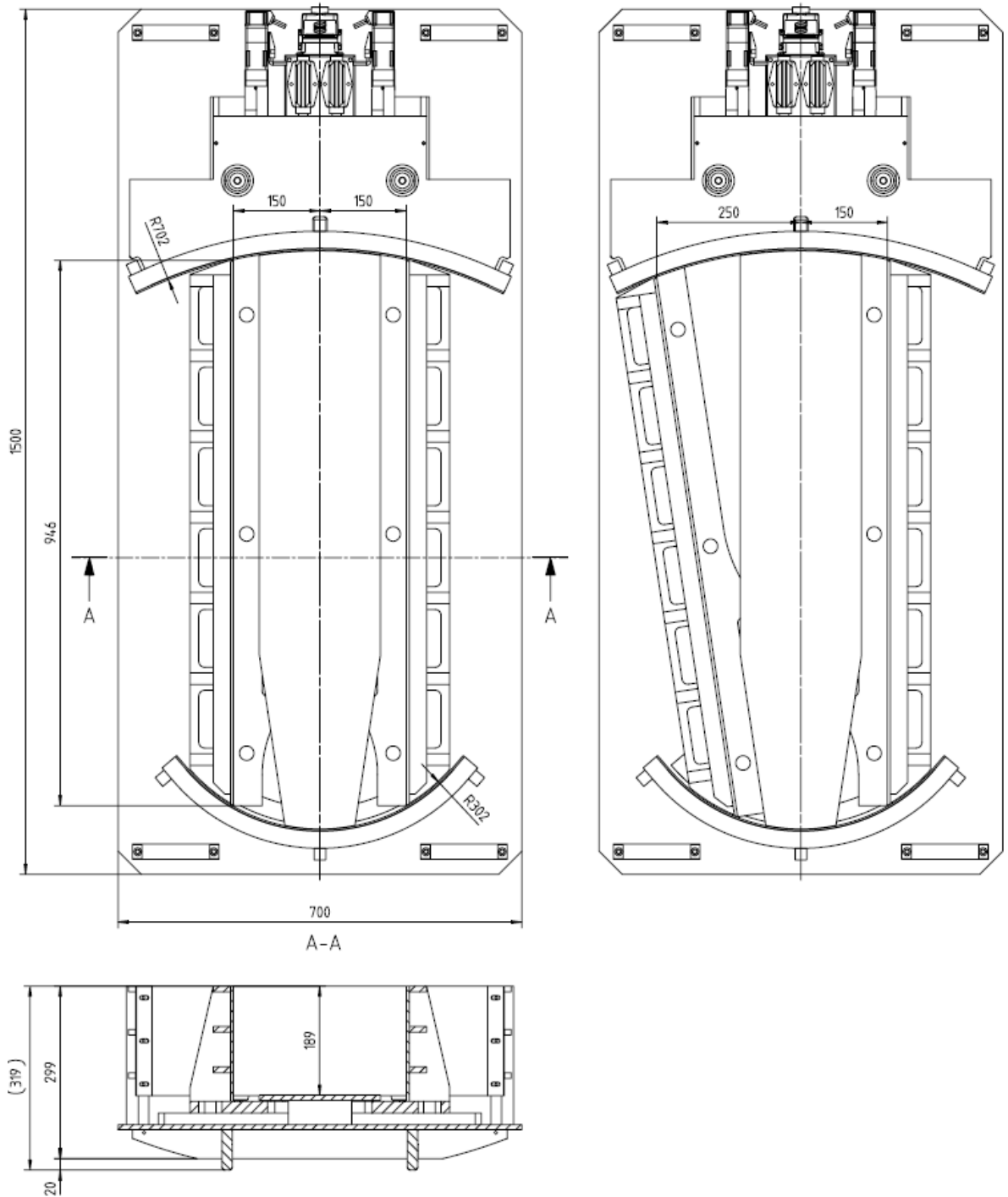
Fig. 1: Dimensions (fixed inserts)

2.2 Foam base plate set-up

B-B
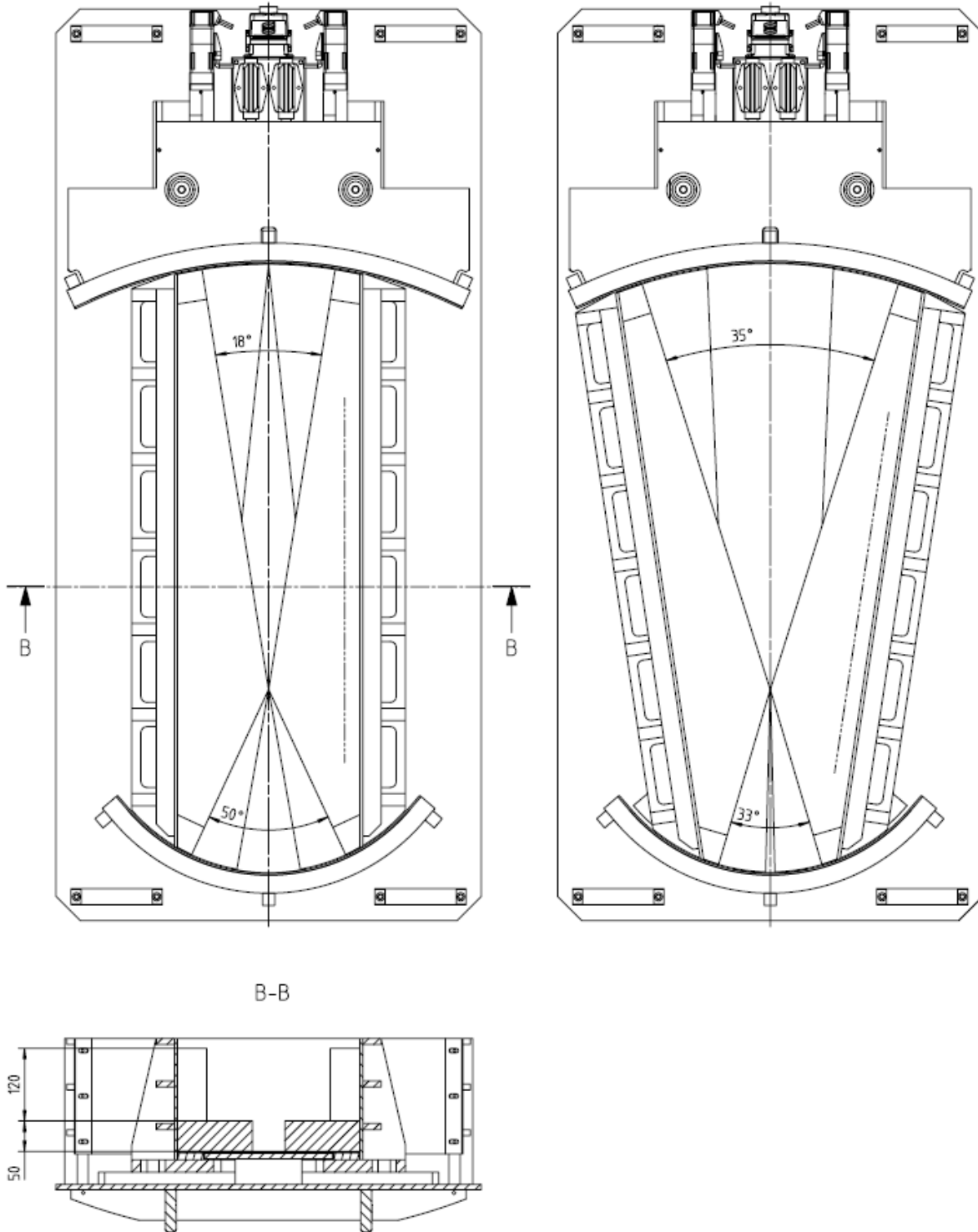
Fig. 2: Dimensions (foam inserts)

Appendix VI. Design Honeypot apparatus

BSc project Yves Pöltinger (IPEK/HSR Technische Hochschule Rapperswil, 2015)

The initial concept, including a convection test with honey and a heating element, was provided by the student but has not been worked out and realized to date.

Diplomanden/-innen	Yves Pöltinger
Examinatoren/-innen	Prof. Theodor Wüst
Experten/-innen	Livio Selm, Ingenieurbüro, Berg, SG
Themengebiet	Produktentwicklung
Projektpartner	Geologisches Institut der Universität Bern, Bern, BE

Yves
Pöltinger

Honeypot

Entwicklung einer 'Sandkasten-Maschine'
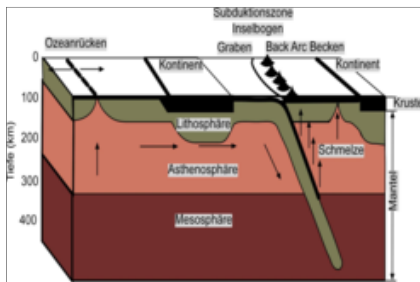
Die Versuchsmaterialien simulieren bestimmte Mantelschichten. Sand: Obere Lithosphäre, Silikon: Untere Lithosphäre, Honig: Asthenospähre
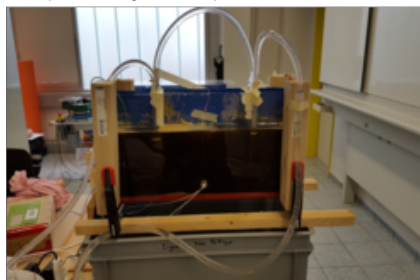
Querschnittsaufbau für Honigkonvektionsversuche mit einem Heizelement und einem Wasserkühlkreislauf.
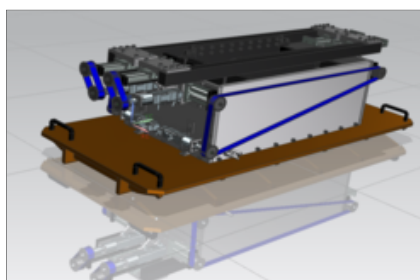
Sandkasten III

Problemstellung: Für eine möglichst realitätsnahe Simulation von Bewegungen in der Erdkruste, verwenden die Forscher Modelle, welche die Schichten der Erdoberfläche mit Sand, Silicon und Honig nachbilden. Zur Beobachtung wird diese Experimentiervorrichtung («Sandkasten») in einen Computertomographen gesteckt. Es soll ein Konzept erarbeitet werden, bei welchem Sand und Silikon auf einer Honigschicht schwimmt. Durch das Verschieben der Seitenplatten am Versuchsaufbau sollen die Bewegungen der tektonischen Platten simuliert werden. Die Werkstoffe im Versuchsbereich müssen radiotransparent sein, damit die Auswertung im CT erfolgen kann. Zusätzlich müssen die Dimensionen an den Lift im Institut und an den CT angepasst werden. Ebenfalls soll überprüft werden, ob mit einer punktuellen Heizung eine Konvektion im Honig erzeugt werden kann.

Ziel der Arbeit: Im Gegensatz zu den bereits bestehenden Esperimentiervorrichtungen, soll bei diesem neuen Konzept der Versuchsaufbau aus Sand und Silikon auch noch auf einer Honigschicht schwimmen und zusätzlich zu Dehnung und Kompression, sollen sich die Längsseiten des Aufbaus parallel zueinander in Längsrichtung verschieben können.

Ergebnis: Das Konzept wurde in intensiver Zusammenarbeit mit dem Auftraggeber und den Spezialisten für die Umsetzung erarbeitet und optimiert. Eine für den Kunden nützliche Konvektion im Honig konnte leider nicht umgesetzt werden. Es stellte sich heraus, dass Honig als Medium zur Simulation von diesem konkreten Strömungsfall ungeeignet ist.

3D View Honeypot machine design
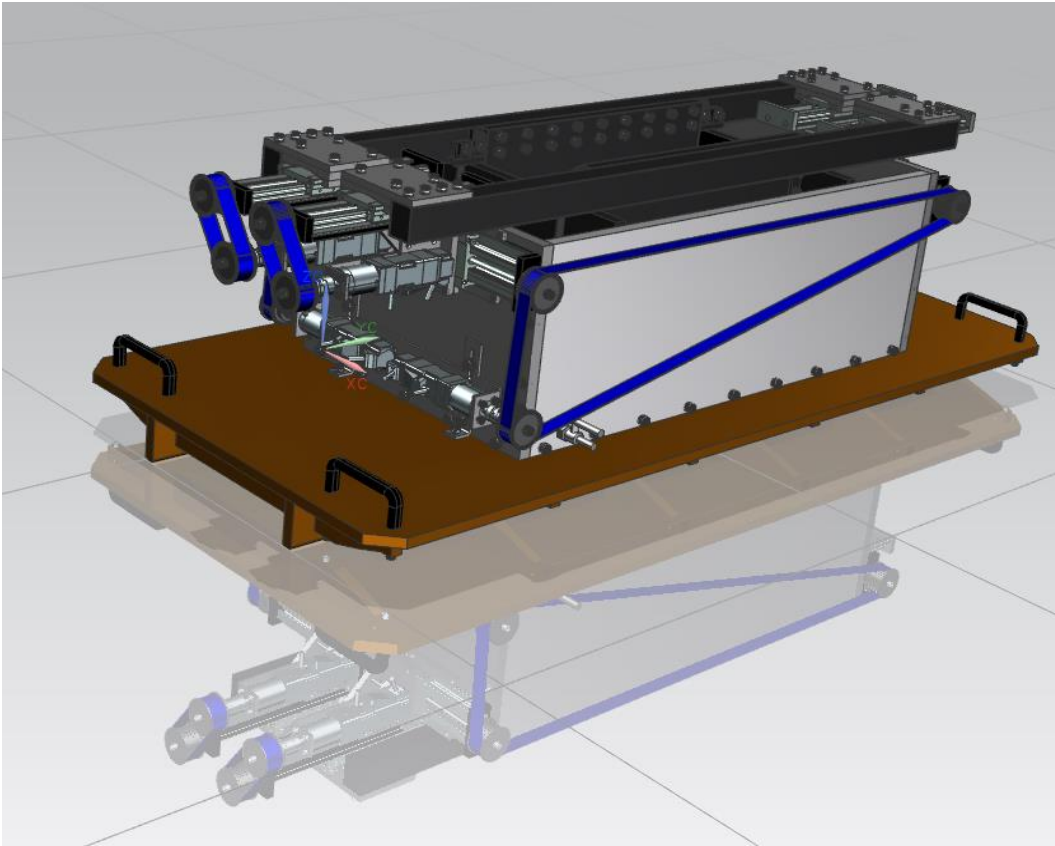
2D Side view Honeypot machine design (long side)
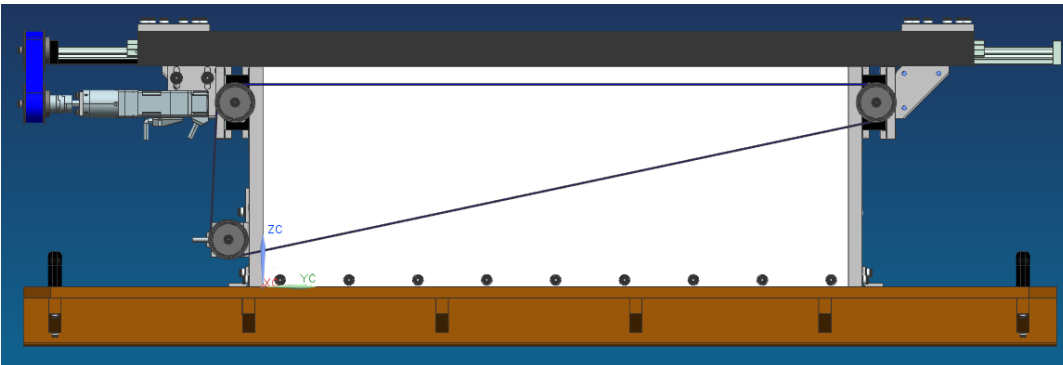
2D Side view Honeypot machine design (short side)
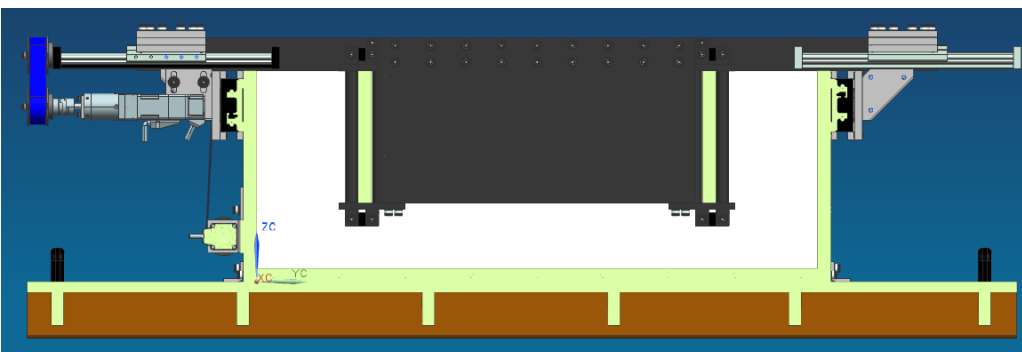
Map view Honeypot machine design (starting position)
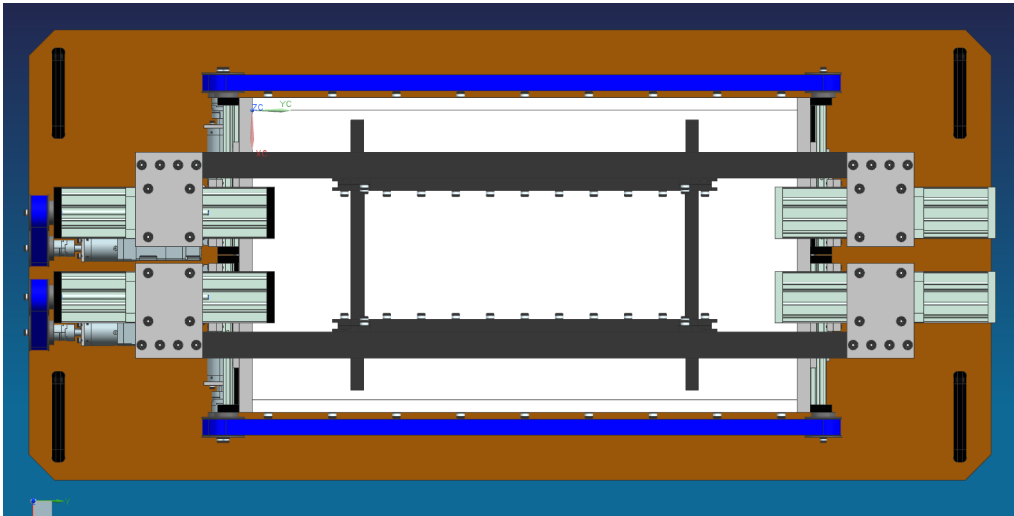
Map view Honeypot machine design (orthogonal extension)
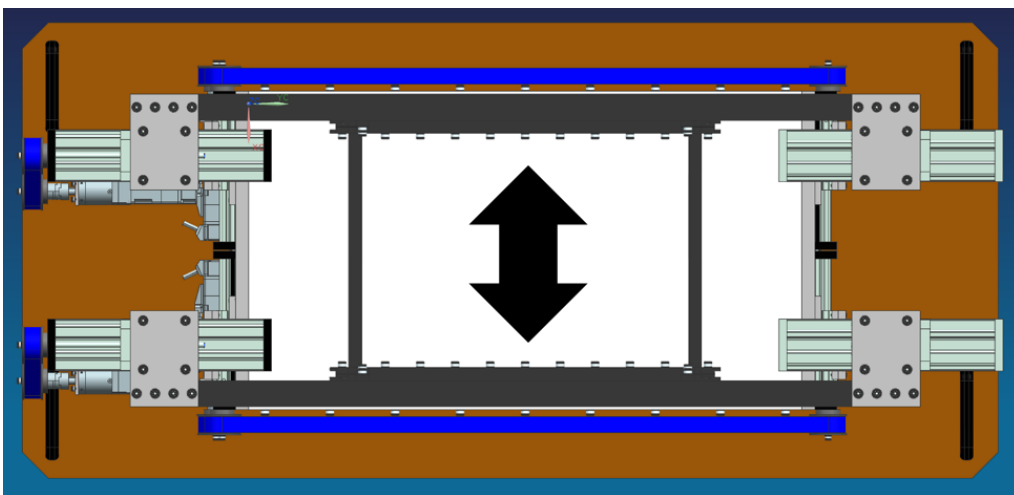
Map view Honeypot machine design (orthogonal compression)
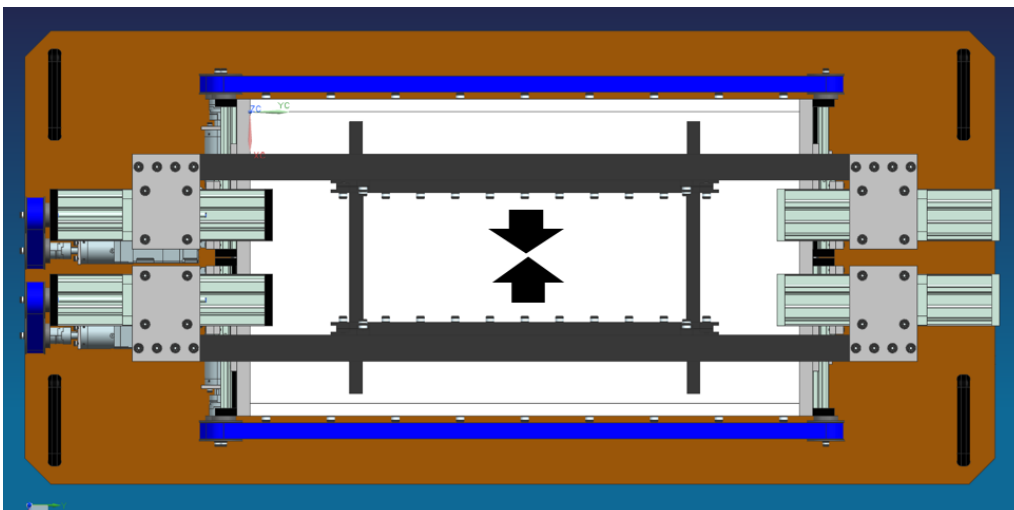
Map view Honeypot machine design (oblique extension)
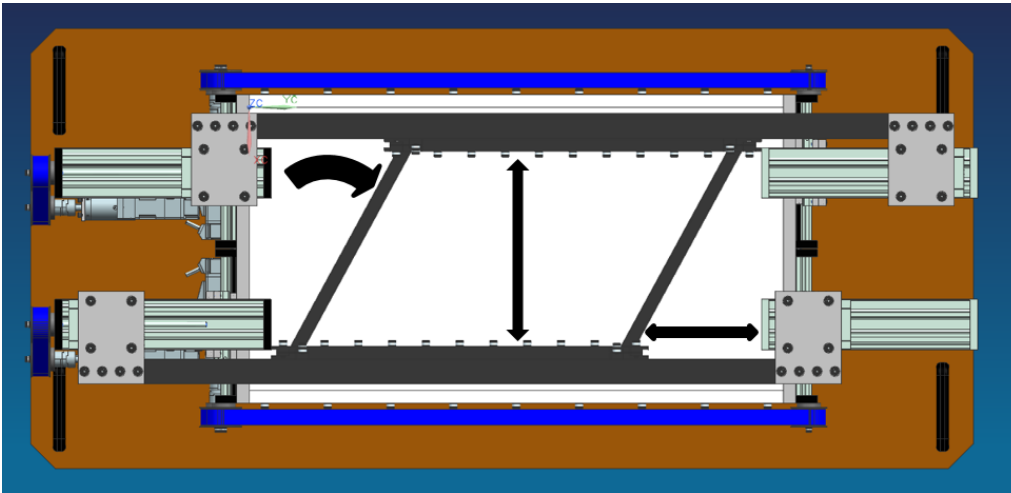
Map view Honeypot machine design (maximal lateral motion)
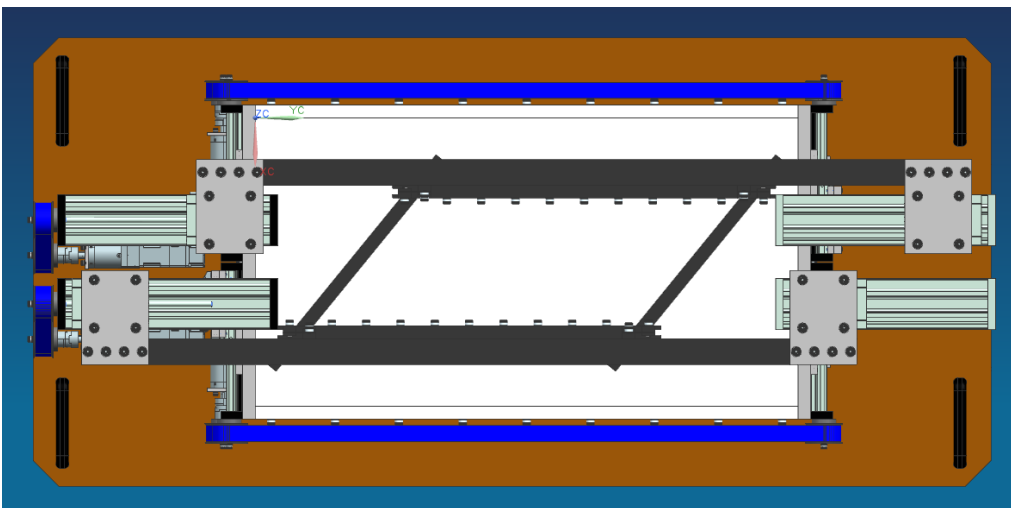
Kurzbericht der Versuche   **Honey convection test by Y. Pöltinger**

Zirkulation:

Der beim Heizelement erwärmte Honig steigt senkrecht an die Oberfläche und verteilt sich dort. Bei einer durchschnittlichen Honigtemperatur von 20 - 50°C kühlt der Honig jedoch nicht schnell genug um abzusinken und so eine Zirkulation zu erzeugen.
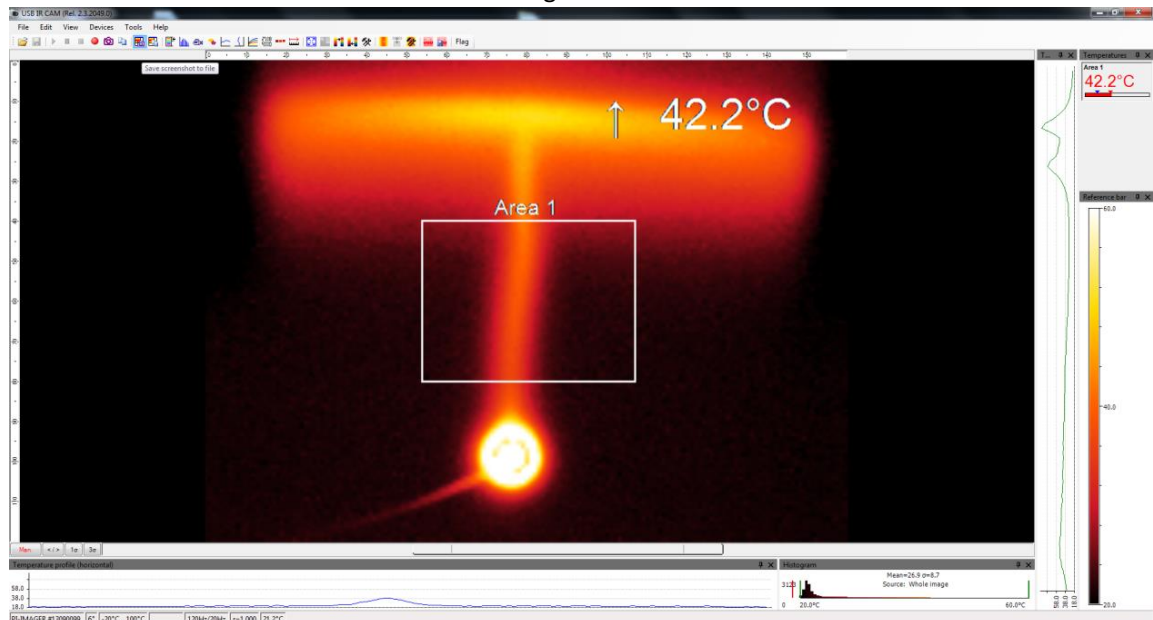
Abbildung 1: Verteilung der Wärme nach 30 min

Erst ab einer Temperatur von circa 70°C im gesamten Honig, entsteht eine Zirkulation. Wenn der Honig bei 70° C konstant gehalten wird kommt die Zirkulation zum Erliegen. Um die Zirkulation zu erhalten, muss das Heizelement mit einer höheren Temperatur betrieben werden. Ich habe dabei mit einer Heizelementtemperatur von 95°C gearbeitet wodurch sich der Honig insgesamt weiter erhitzt.
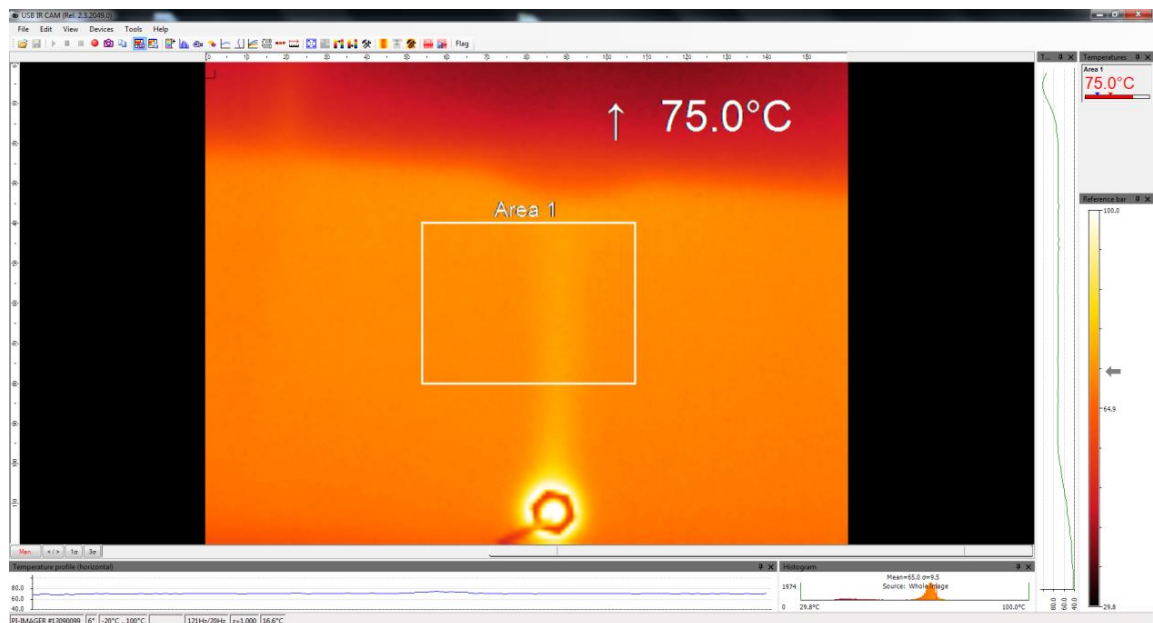
Abbildung 2: Homogene Verteilung der Temperatur bei 70° C nach 3 h
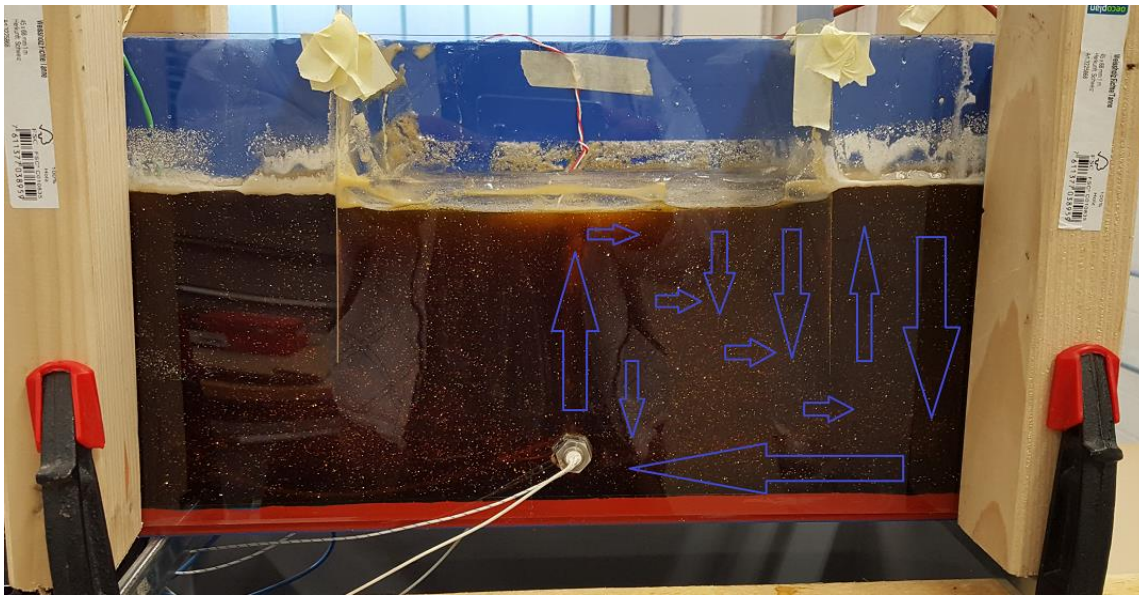
Abbildung 3: Fliesswege des Honigs bei 70°C / Heizelement 95°C

Kühlung:

Ich habe die Seiten ausserhalb des Versuchbereichs gekühlt. Dies hat den Prozess der Zirkulation zum Stillstand gebracht.
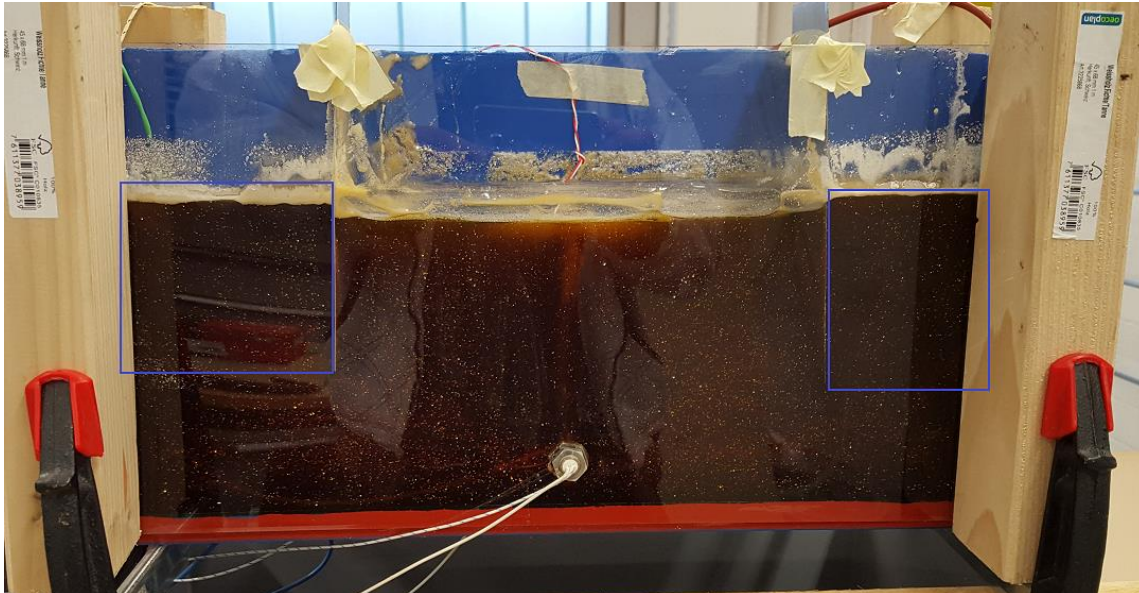
Abbildung 4: Bereich der gekühlt wurde

Der Honig wird durch die Temperaturen dünnflüssig. Ich kann nicht beurteilen ob er in diesem Zustand noch den gewünschten Eigenschaften entspricht.

Schaumbildung:

Ein weiteres Problem ist die Schaumbildung. An der Oberfläche bildet sich ein sehr hartnäckiger Schaum welcher sich nicht von selbst auflöst und sich von der Zirkulation des Honigs auch nicht aufspalten lässt. Direkt über der Wärmequelle bildet sich eine Anhäufung. Die Schaumbildung entsteht bei jeder Temperatur. Je höher die Temperatur ist, desto mehr Schaum entsteht.
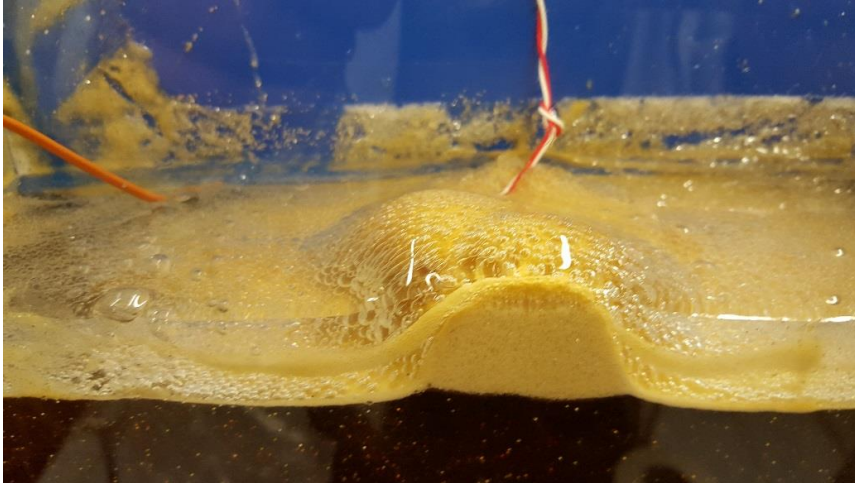
Abbildung 5: Schaumanhäufung unter dem Silikon

Es ist möglich, dass wir mit einer anderen Heizung weniger Schaumbildung hätten. Eine andere Flüssigkeit könnte besser funktionieren.

Konstante Temperatur:

Um den Honig auf eine konstante Temperatur von genau 40°C zu erhitzen, sind mehrere Stunden nötig, da der Honig eine sehr schlechte Wärmeleitfähigkeit hat. Das bedeutet, wenn eine Heizung mit einer Temperatur von 100°C in den Honig eingetaucht wird, sammelt sich der auf circa 80°C erwärmte Honig an der Oberfläche. Dadurch entstehen zwei Schichten. Der erhitzte Honig sammelt sich oben und der Honig mit Zimmertemperatur bleibt unten. Bis diese Schichten sich angeglichen haben und eine gleichmässig verteilte Temperatur von 40°C erreichen benötigt es mehrere Stunden. Wenn das Heizelement auf 40°C eingestellt ist, dauert es noch länger.

Fazit:

Ich glaube nicht, dass wir in geeigneter Frist eine funktionierende Lösung finden mit welcher wir die gewünschte Zirkulation im Honig ohne negative Nebeneffekte erzeugen können. Ich vermute, da das Silikon durch die erhöhte Temperatur an Viskosität verliert, dass die geringen Einflüsse des zirkulierenden Honigs vom Silikon absorbiert werden und keinen Einfluss auf die Sandschicht mehr haben.

Appendix VII. Concept for a lithosphere-scale model set-up

DESIGN NEW HONEY MODEL COMPONENTS TO FIT ON THE EXISTING NAMAZU MACHINE
Frank Zwaan, 2 July 2016

a) Existing machine

blue: mobile plate (can move laterally)

grey: motorblocks that move in and outwards

green: fixed plate
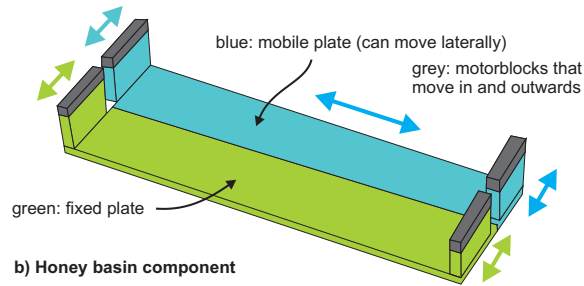
b) Honey basin component

basin to contain honey
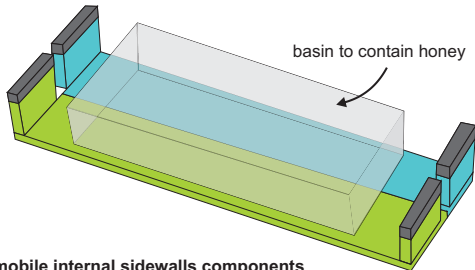
c) mobile internal sidewalls components

dark green: rigid mobile sidewalls

black: rubber sidewalls
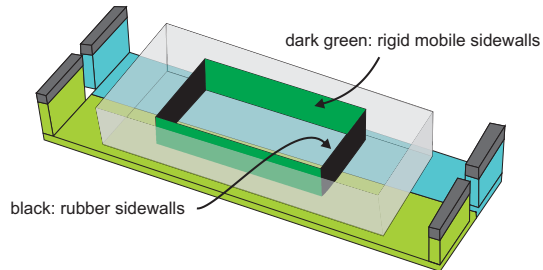
d) connection to motors (bar components)

black: additional bars to fix the red bars to the motor

red: bars fixed to the rigid mobile sidewalls (dark green) that can be fixed to the basin edge to keep their place secure while building the model (the honey basin must be removable to put in a freezer)

e) model materials

yellow: silicone and sand layers that float on the honey layer

orange: honey infill
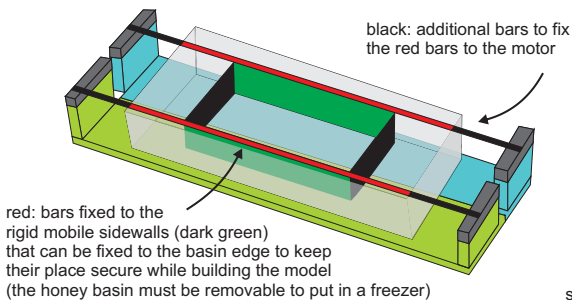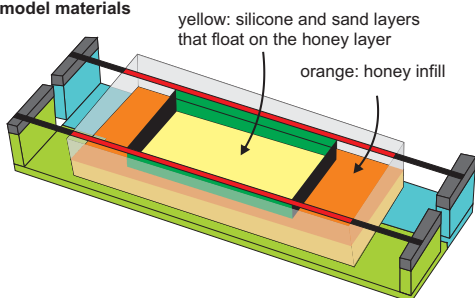
f) possible deformation 1: pure extension
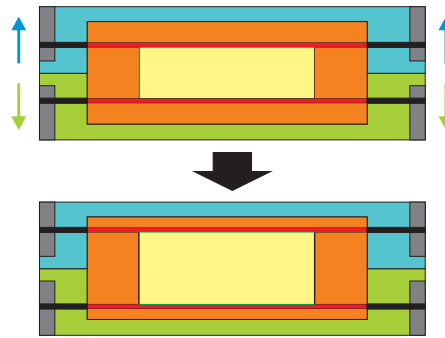
g) possible deformation 2: pure strike-slip
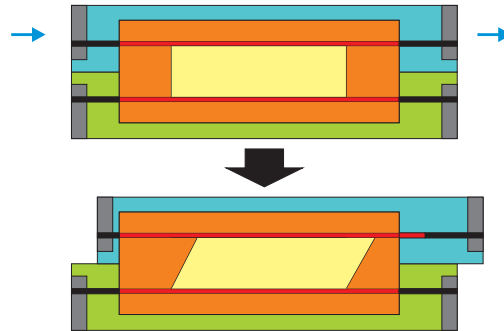
h) possible deformation 2: oblique extension

i) section

space for honey to flow below sidewalls

model materials (float on honey)

honey
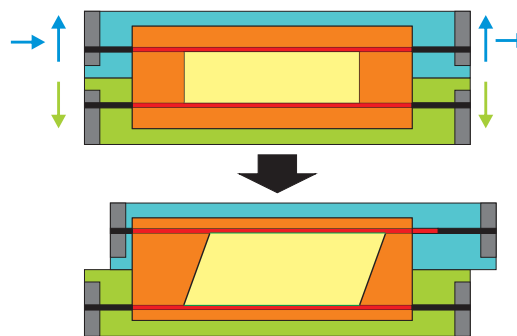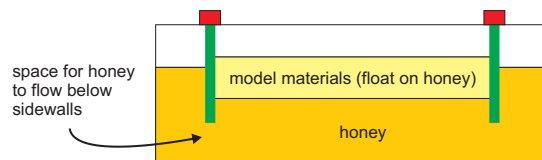
j) rubber sidewall attachment (top view)

dark grey: rubber sidewall (to allow uniform deformation)

screw to fix parts together

model

yellow: mobile plate through slit in the rigid sidewalls to support the rubber sidewalls

dark green: rigid sidewalls

252
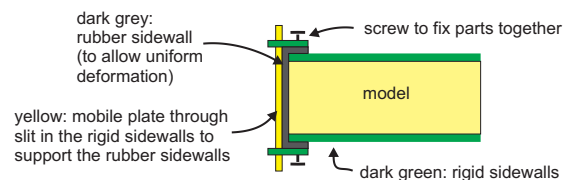
Appendix VIII. Complete overview models 2013-2017

Series 1. Triple-junction models

EXP452_Trj_Test

_____

Set-up
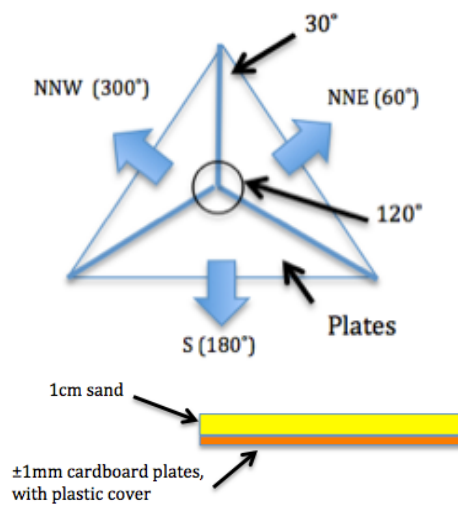
Details

Test for a symmetrical triple junction setting with a purely brittle set-up (qz sand)

The 3 cardboard plates were moved to produce extension in a triple-junction fashion. The rates of extension were not effectively monitored, but one of the (plates pulled by hand)

The model produced nice extensional structures and a recognizable triple point

The structures seemed to be highly controlled by the basal "Velocity Discontinuity"

Asymmetrical extension seems to create a more "natural" rift basin, while symmetrical extension seems to leave some kind of "bulge" in the middle of the rift structure

Start (no sand)
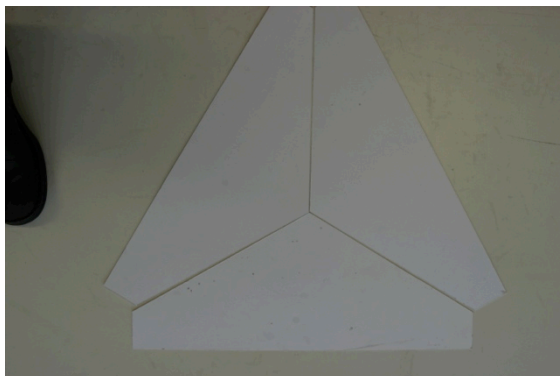
t = 0
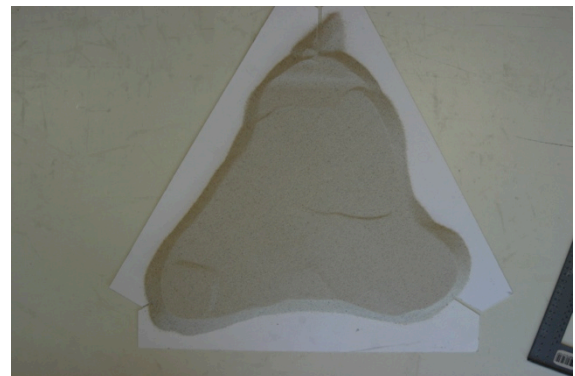
t = 1

t = 1

EXP453_Trj_Test

Set-up
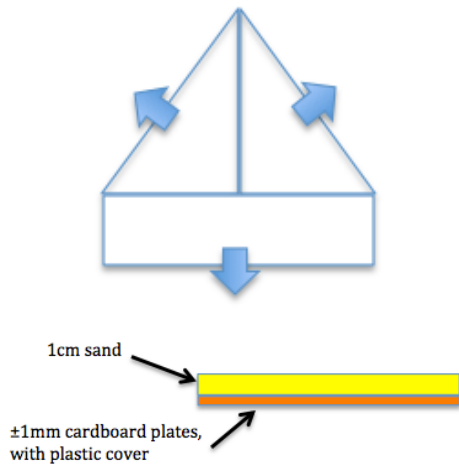
1cm sand

±1mm cardboard plates, with plastic cover

Details

Test for a symmetrical triple junction setting with a purely brittle set-up (qz sand)

The 3 cardboard plates were moved to produce extension in a triple-junction fashion. Check the photographs for more details, but it was attempted to create symmetrical and asymmetrical extension by not moving one of the. The rates of extension were not effectively monitored (plates pulled by hand)

The model produced nice extensional structures and a recognizable triple point

The structures seemed to be highly controlled by the basal "Velocity Discontinuity"

Start (t = 0)
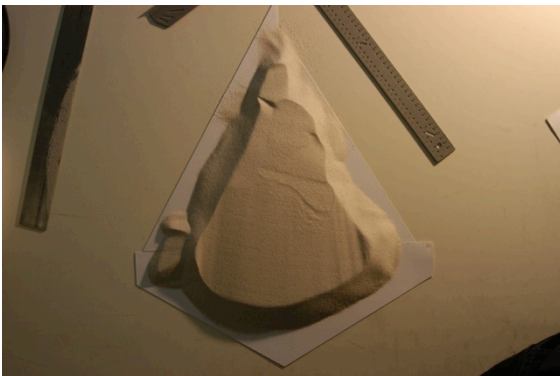
t = 1
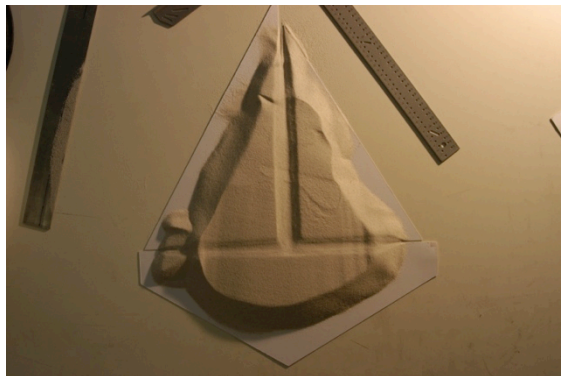
t = 2
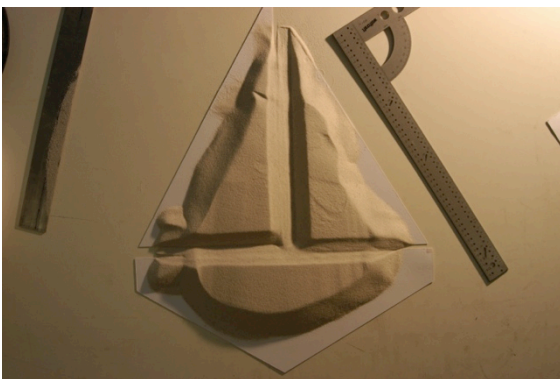
t = 3
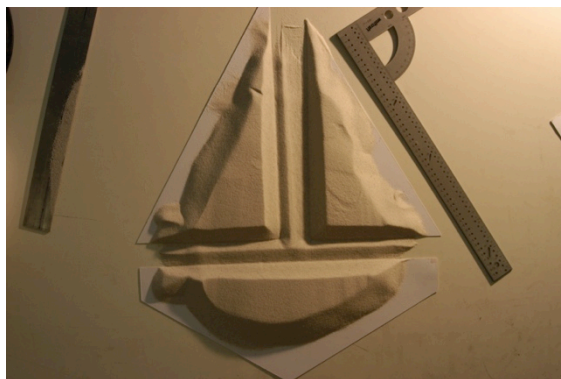
EXP454_Trj_Test

_____

Set-up
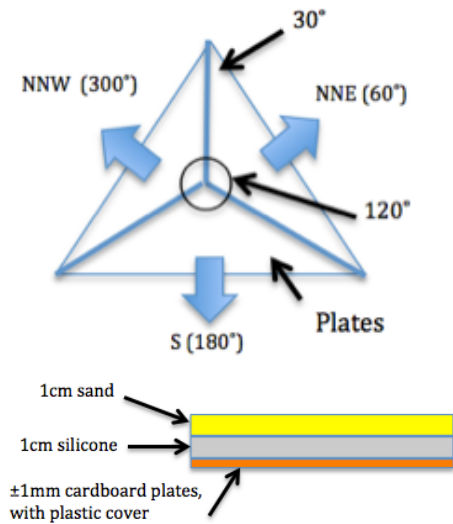
Details

Test for a symmetrical triple junction setting with a brittle-viscous set-up (qz sand and pure PDMS)

The 3 plates were pulled away from each other by means of manual traction, in several pulses (about 5mm per pulse in circa 20sec, total of circa 10 pulses). Every plate moved with the same speed, in 120° opposite directions. The whole set-up was ± 50x50cm large.

The model produced nice structures and the plate movement was easily established

The model seemed to produce more or less the same structures as previous brittle tests (Experiments 452 and 453), maybe the speed of deformation (about 1cm in 30sec) is too high to have decent decoupling between the silicone and the sand → a more or less brittle model

In order to make a good model, deformation rates have to be decreased and to be constant. This can probably only be achieved by building a model machine. Furthermore, it might be best to focus on the structures at the triple point itself because the adjacent rifting has already been studies in previous studies → thicker layers would create a focus on the triple point structures

Start (no sand)

t = 0

t = 1
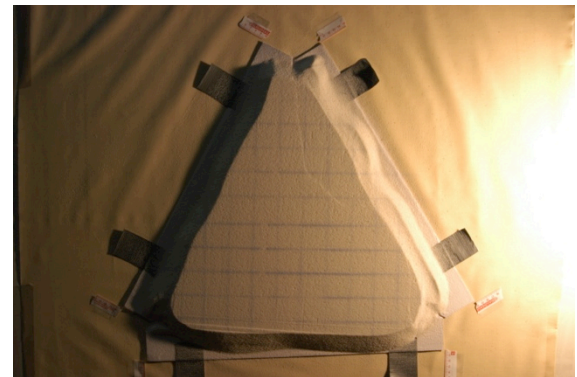
t = 1

Series 2. Rhine-Bresse Transfer Zone model

EXP455_RBTZ_NAM

_____

Set-up
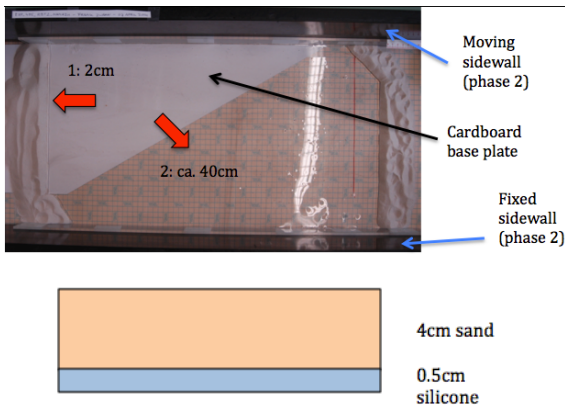
Start (t = 0)
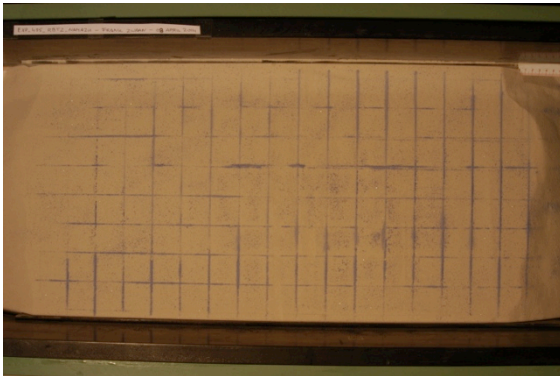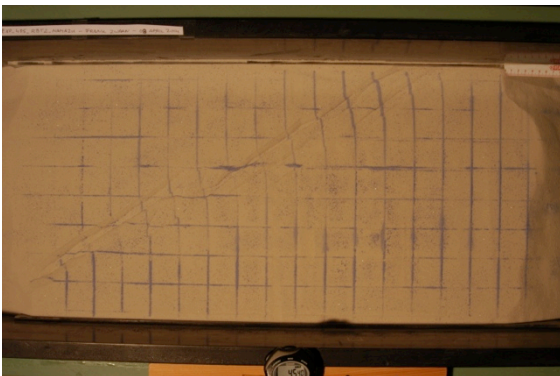
Details

The model is build to improve upon the modeling of the Rhine-Bresse Transfer Zone (RBTZ) in France, close to the Jura Mountains, as was done by Ustazewski et al. (2005). The transfer zone between the two graben systems develops above a detachment layer of Triassic evaporates. The improvement of this model lies in the change of direction during the 2nd (transpressional) deformation phase, which better resembles nature and was not applied in the Ustazewski et al. (2005) models. The other model parameters were kept the same as much as possible as in their model run OR5, to allow comparison (see their table 1 and fig. 9+10).

Set-up: brittle-viscous with qz sand and pure PDMS

The model produced nice structures, more or less as expected.

1. There was a problem with the reactivation phase mechanism: not more than 2cm of compression was possible in the initial setting. After phase 1, a quick adjustment was made that allowed more compression.

2. The cardboard baseplate started folding during compression, it is not clear at what point and it seems to be more extreme at the moving wall side (where it is longest) than on the stabile wall side

3. The cardboard baseplate was not well controlled by the lond pushing sidewall (it went underneath the latter), decreasing the amount of compression (up to 2cm towards the 30° tip of the plate).

The movement of the cardboard base plate along the long sidewall should be better fixed to avoid it to flex and to avoid it to go underneath the sidewall instead of moving into the model.

End of extension phase

End of compression phase

Series 3. Rift interaction models (tests)

Series 3. General set-up
_____
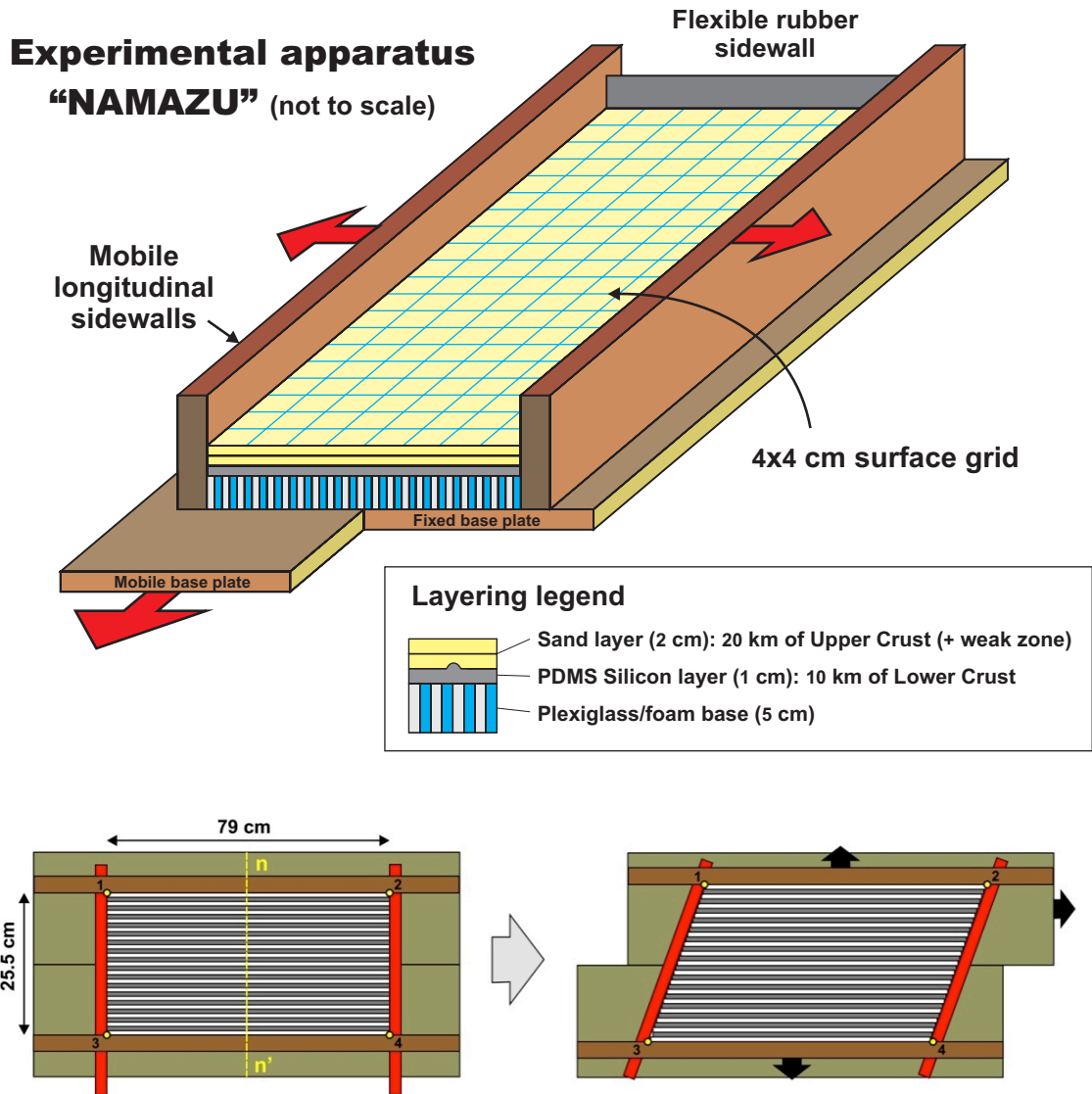
Set-up of the analogue experiments of series 3. a) Cut-out view of the experimental apparatus; b) Schematic surface view showing the initial set-up and subsequent deformation of the empty apparatus.

EXP456_TZ1

_____

Set-up
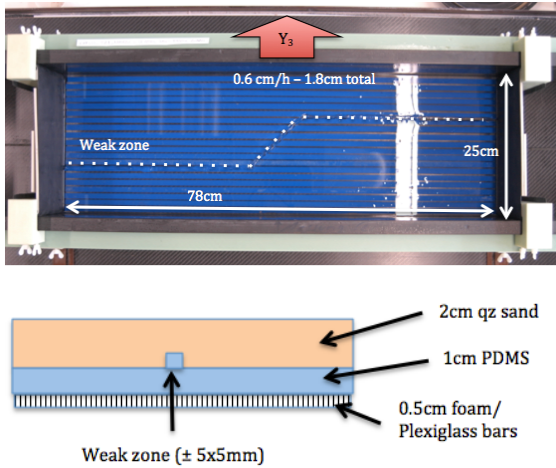
Start (t = 0)

t = 120 min
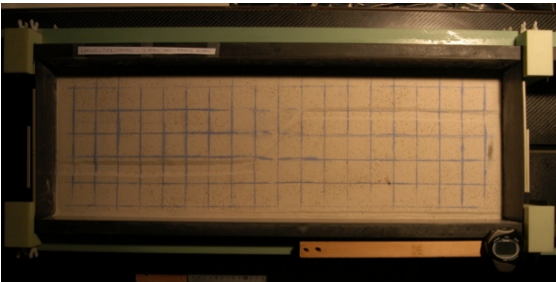
Section locations
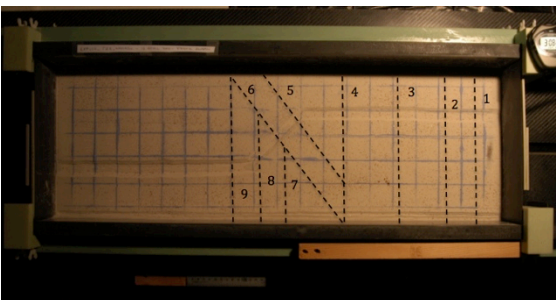
Details

The purpose of the model is to improve (and expand upon) the models previously done by Acocella et al. (1999). In this model, two continental rift segments and a transfer zone in between aresimulated (angle phi: 45°, as for model 02 from Acocella et al. 1999). The improvements are: a distributed extensional base (foam and plexiglass), and the modeling of Lower Crust (PDMS). The "Velocity Discontinuity" is created by applying a 0,5x0,5 PDMS line (see image). The deformation speed is chosen to be rather slow (0.6cm/h).

The building of the model went pretty well, no major obstacles. The weak zones clearly controlled the formation of the rift and transfer zone structures. Not much border effects, except for some extensional faulting along both rigid sidewalls. These did probably not really effect the major rift structures in the middle of the model.

The referencing of the 2 axis Y1 and Y2 blacked out. Since these were needed for the motions involved, the appropriate set-up was not possible. Therefore, it was attempted to create deformation with Axis Y3.

The referencing of the axes could be improved, maybe the speed of deformation. The current velocity creates on first sight the same structures as shown by Acocella et al. (1999a). → it almost looks like a purely brittle model with pure rift structures as observed in the tripe-junction models (EXP452-454). Furthermore, the lighting could be better, in order to increase the visibility of the faults (maybe 2 lamps?).

End (t = 180 min)
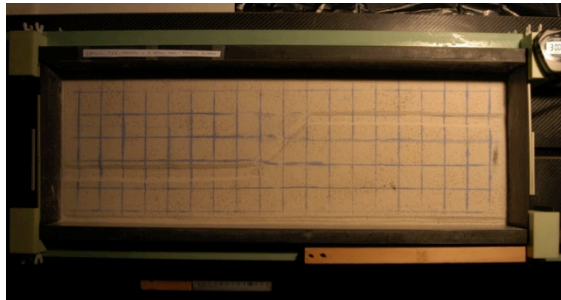
Section 3

EXP457_TZ2

_____

Set-up
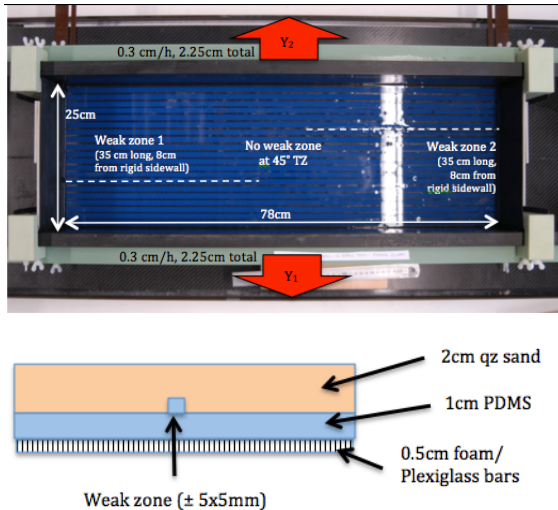
Start t = 0
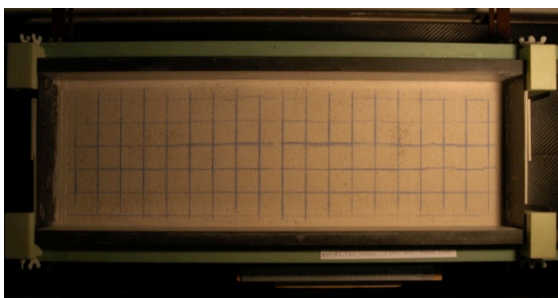
t = 120 min
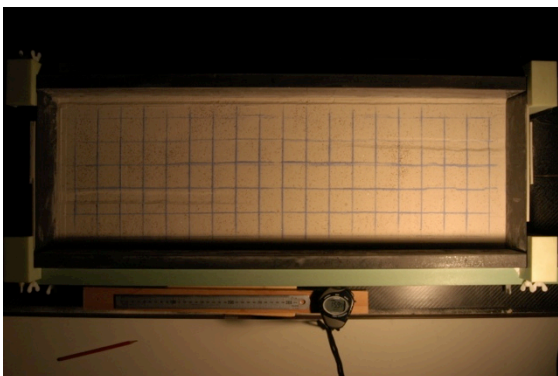
Section locations
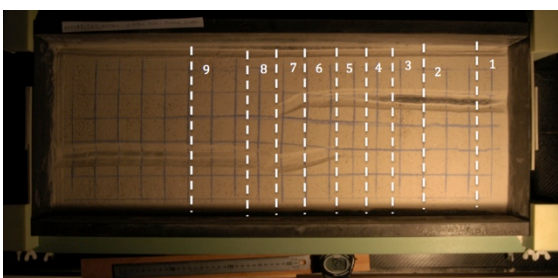
Details

This model is an elaboration on model EXP456_TZ2. It represents a rift setting with two parallel oriented inherited weak zones and a transfer zone in between. In contrast with the EXP456, the 45° oriented transfer zone is not represented by an initial weak zone to test the development of structures under these circumstances.

Both Y1 and Y2 axis did work initially; this might be the correct starting set-up to prevent the previously occurring referencing problems.

The first graben initiated in the down left corner, long before the other graben developed. This could be due to differences in weak zone thickness (which is difficult to really control).

The silicon breached trough the rift base, the model should have ben stopped earlier, but I was away for dinner. Now it looks a bit like salt diapirism in an extensional setting such as the North Sea rift system (which is by the way a possibility for modeling).

Too much water disrupts the possibility of making X-sections, 1-1.5 liter should be enough for a 2cm thick sand layer.

The lighting, to better show the development of the graben structures, now the light does not really allow good observations in the first part of the model run. Also it would be nice to avoid the formation of extensional structures in along the rigid sidewalls. How we could do this is however unclear

t = 180 min
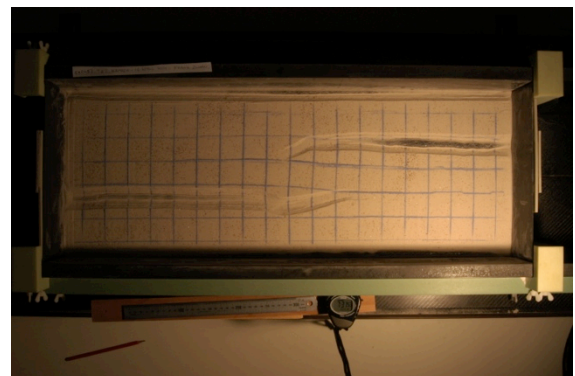
Section 3

EXP465_TZ3

_____

Set-up
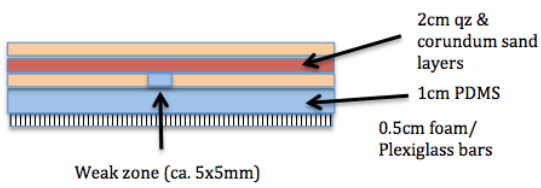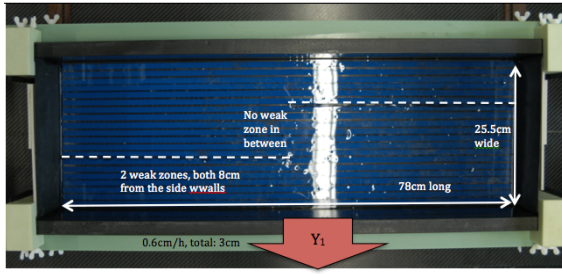
Start t = 0
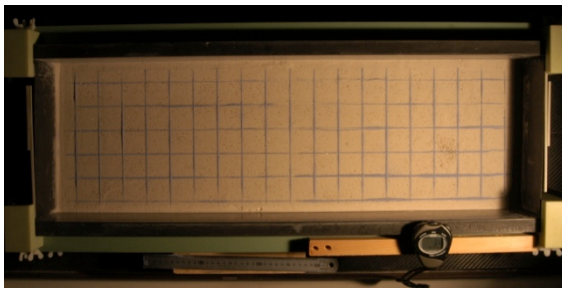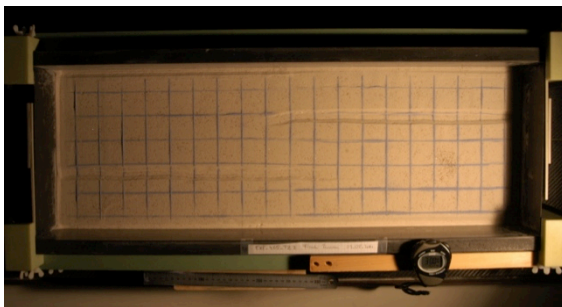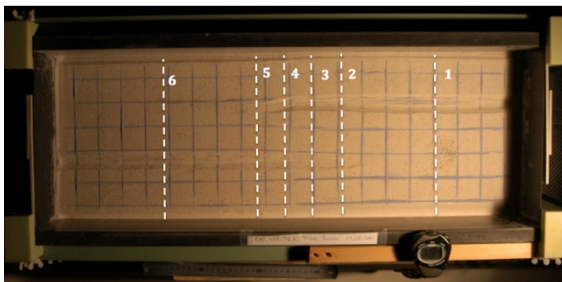
Details

This continental Transfer zone model is a modification of model EXP_457_TZ2, the parallel oriented inherited structures both end at the middle of the model (instead of ending at the 45˚ weak zone line of EXP_456_TZ1). Between both rifts, a Transfer zone might (or might not) develop to connect them, creating 1 major rift system.

Building the model went fairly straightforward, no problems until the start of the model run (see below). The model produced structures similar to those seen in EXP457_TZ2_NAMAZU, the distance between both rifts seems to be to large to produce a linkage. Also, the silicon started rising at the center of the model, starting after about 4:30h.

The Y2 axis failed again, as in EXP456_TZ1_NAMAZU. It would have been possible to use he Y3 axis instead, but this would create a hole under the foam/plexiglass base. Therefore, it was decided to have the Y1 axis (which was still operational) moving at double speed (6mm/h instead of both walls moving 3mm/h). The foam/plexiglass base should still create a more or less distributed deformation.

It also seems that the model is a bit wider than usual. The coordinates are still the same as in previous models (see section II), maybe the motors need referencing.

The motor control system has to be improved, it has already failed twice in 4 model runs

t = 120 min

End (t = 300 min)

Section locations
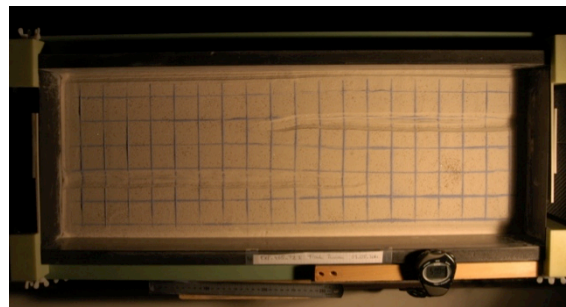
Section 3
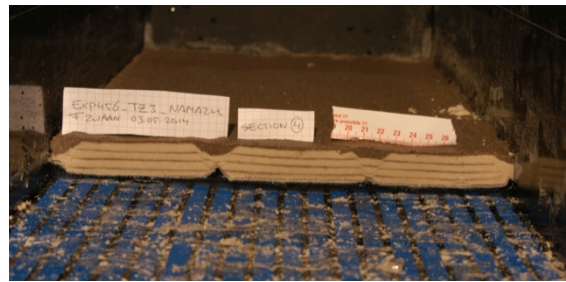
EXP466_TZ4_CT-scanned

_____

Set-up
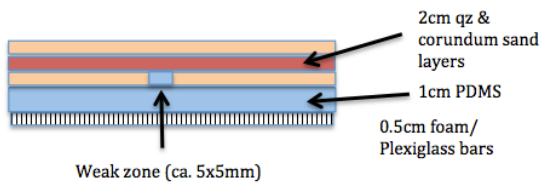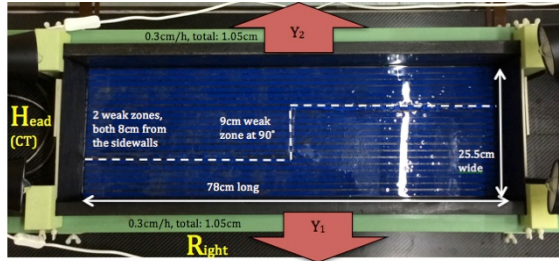
Start t = 0
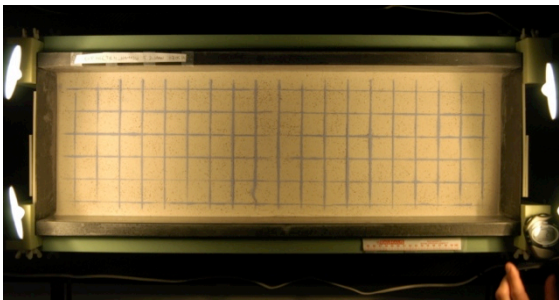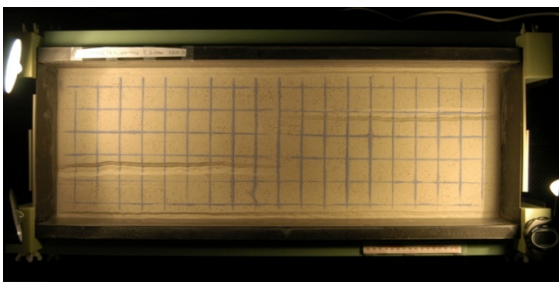
Details

The model purpose is to model a transfer zone between 2 rift systems. It is similar to EXP465_TZ3_NAMAZU, except that a weak zone should control the transfer zone in this model, as are the rifts in both models.

All mechanical stuff went well, the procedure is not very difficult and the CT scanner works fine. The new IKEA lamps worked fine too (see IX)

A little problem occurred laying down the weak zones →? Wrong side of foil used, this was too sticky and so the weak zones were not as smooth as they were in previous models. The big problem was that the Transfer zone between both rifts did not develop. The CT images showed that from the start of the model run, faulting occurred deep in the model along the weak zones, but nothing happened at the Transfer zone, the results were basically similar to those in EXP465_TZ3_NAMAZU, except that we have now CT images of the model. Therefore, it was decided to stop the model relatively quickly, since nothing new would appear. Also, the corundum/quartz sand layering was not very visible on the CT scans.

To create an actual transfer zone, both rift systems should probably be situated more closely together, as is actually the case in the Acoccella et al (1999) paper. This will be done for the next model EXP467_TZ5_NAMAZU. Also the layers of sand will be thicker (ca 7mm or so) to improve visibility on the CT scanner, with a quartz sand layer above the silicon instead of corundum sand.

t = 120 min

End (t = 210 min)
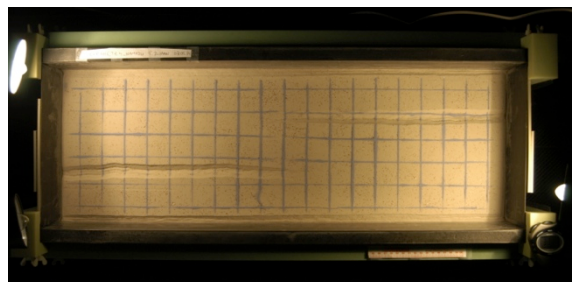
EXP467_TZ5_CT-scanned

_____

Set-up

Start t = 0
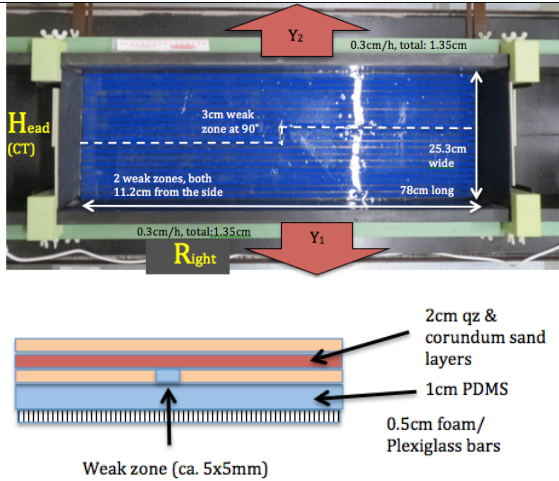
Details

This model aims to create a continental transfer zone to connect two rift systems. Previous TZ models failed to do so, probably because the distance between the 2 rifts was to large (9cm). In this model, the parameters are identical to EXP466_TZ4_NAMAZU, except that the 9cm distance has been reduced to 3cm. Hopefully, a TZ will now develop.

No motor problems, quick and efficient build-up. Only I forgot to compress the foam again, this I corrected at 8:00 in the morning. This might have had an effect on the development of boundary effects… (Apparently a bit less normal faulting along the borders, but this is not very clear).

Some problems occurred creating the sand layering, need to be more careful next time. Also, use less blue sand for the grid…

More importantly, the Transfer Zone did not directly initiate at the weak zone → is the model set-up just wrong or does this say something important about the system in nature? (sand does not have cohesion, so that the sand "plates" are not strong enough. Maybe this is the problem?

We could try to increase the cohesion by **wetting the sand**?

Ultimately, the both rift systems came together, not due to the weak zone, but merely because the prograding deviation of the one dominant rift arm, already observed in the previous models (EXP456, EXP457 and EXP466) progressed in the other rift, connecting both systems. The weak zone does not show any activity, maybe due to the lack of cohesion in sand? It is clear that the distance hypothesis is not working.
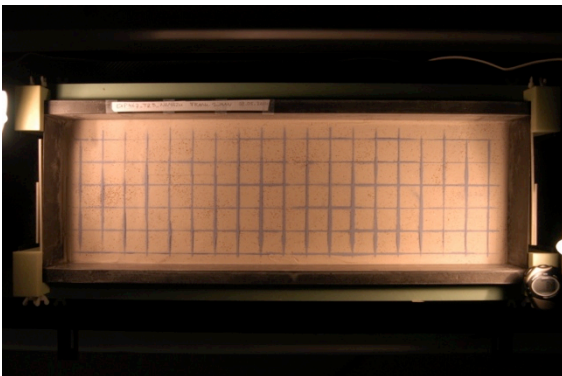
t = 120 min
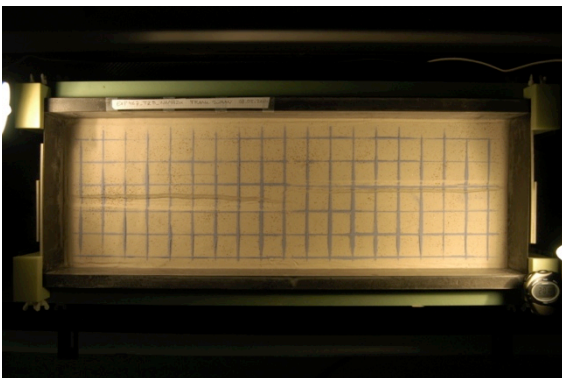
End (t = 270 min)

EXP468_TZ6_CT-scaned

_____

Set-up
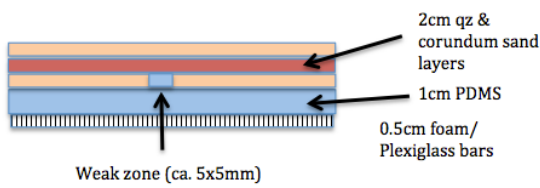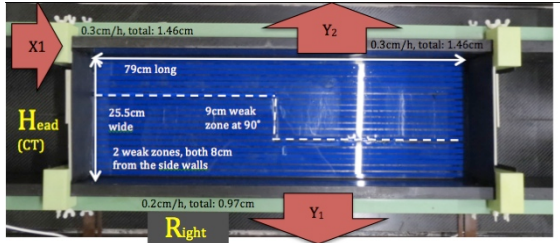
Details

This model is to try to activate the weak/transfer zone that should have formed in the previous experiments, but didn't (EXP465-EXP467), this model attempts to do so by applying oblique extension at 30˚ to the normal orthogonal extension direction. To do so, 3 axes were uses (X_1, Y_1 and Y_2) NB: to keep the deformation speed at ca. 6mm/h, both Y-axes have a slightly different speed. This means the model is slightly asymmetrical, but not big problems are expected since deformation should be distributed. Also, the model is mirrored due to the motor set-up of the machine.

No transfer zone along the weak zone

The connection between the computer and the machine failed at ca. 1h25 for ca. 20 minutes. We need to check out what happened exactly and how long it took before we analyze the results.

The symmetry of the model could be tested to see if it as dominant as it seems here.

Start t = 0

End (t = 270 min)
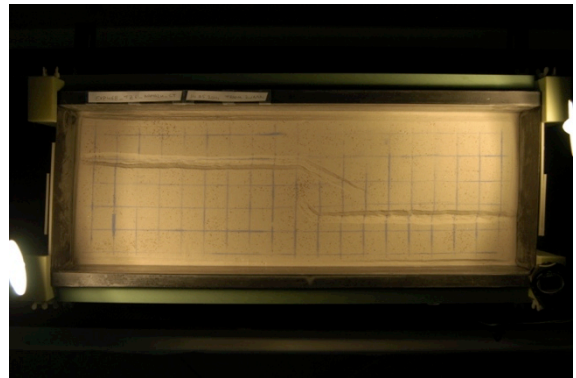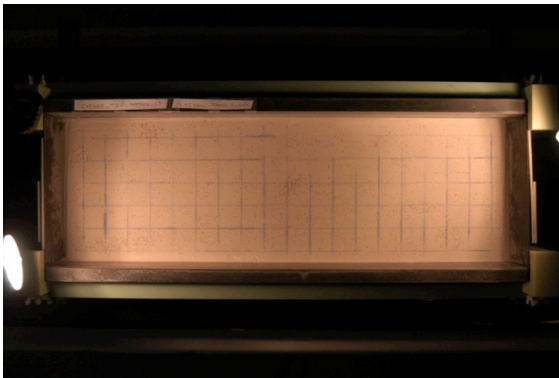
EXP469_TZ7_CT-scanned

_____

Set-up
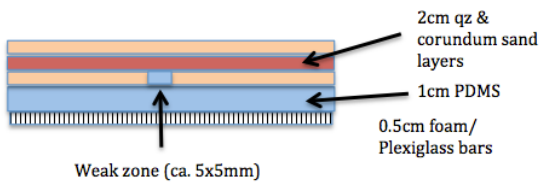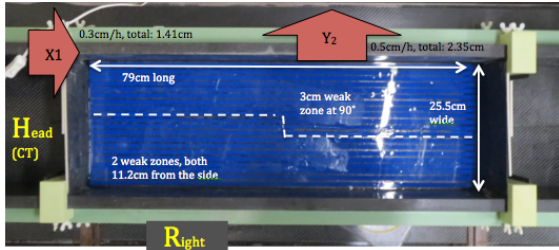
Details

This model reproduces the basic weak zone set-up from EXP467_TZ5_NAMAZU_CT, but with the motor settings from EXP468_TZ6_NAMAZU_CT. In other words, a short 90° oriented weak zone between two rifts that will be deformed transtensionally. The goal is to create the 30° transtensional rifts from EXP468, but to have them connecting. The weak zone in between the rifts is not expected to have much influence.

The graben structures connected quite nicely, although the grabens did not create the strongly oblique structures as observed in one graben from the previous experiment (EXP468_TZ6)

The Y_1 axis failed at the start of the experiment, therefore, the Y_2 Axis had to do all the extension → asymmetrical extension.

The connecting between the both grabens did not really involve the weak zone (although, check CT data), and deformation there seemed to propagate from the surface down, different from the normal deformation propagation (from bottom to top).

Start (t = 0)
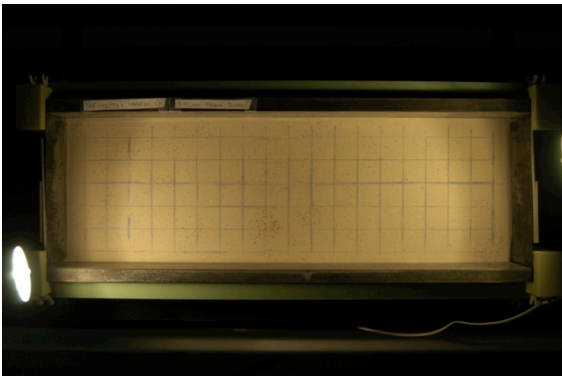
End (t = 270 min)
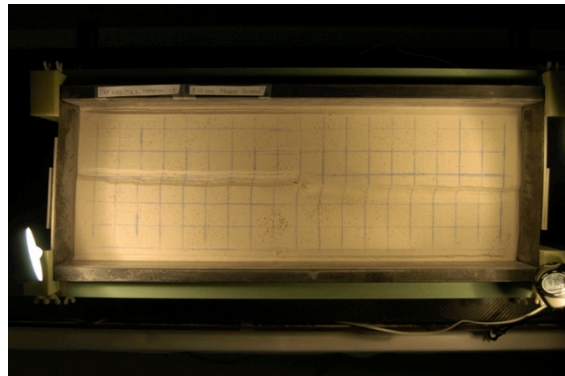
CT images

A: 3D views and X-sections (0 min)   **(60 min)**   **(140 min)**
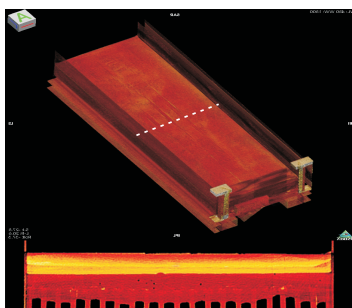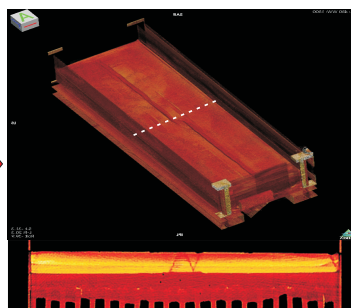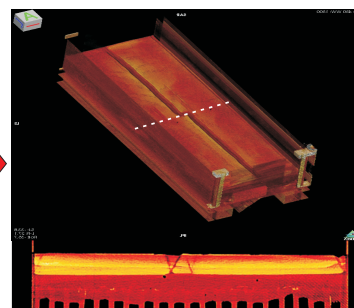
B: X-section only (180 min)   **(240 min)**   **Legend (t = 0)**
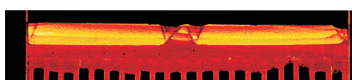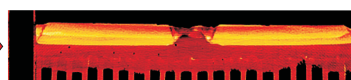
EXP470_TZ8_wet test

_____

Set-up
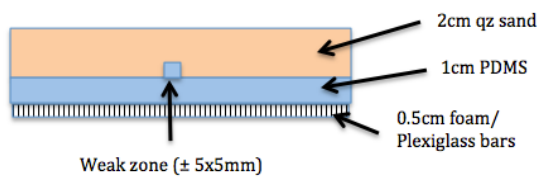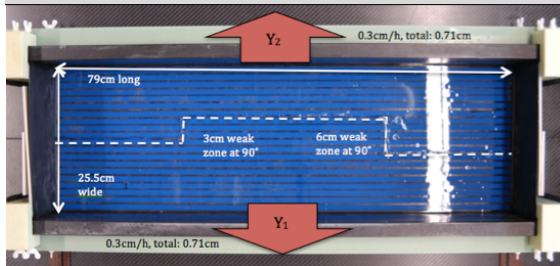
Details

The previous transfer zone models have not produced the expected transfer zone along the prepared weak zones between the rifts. The reason for this could be the lack of cohesion within the sand. Therefore, this model will be wetted, the sand will be wetted to increase the cohesion.

(this should not alter the angle of friction to much (Van Mechelen, 2004), although the sand density will increase.

The model was wetted and a thin layer of dry sand was sieved on top to better visualize the grid. The wetting of the sand was difficult, 1.6L of water proved to soak the sand, but after an hour it was OK

The wet sand is not able to create normal faults. Maybe decreasing the water content could decrease cohesion and allow normal faulting? → dry sand is better?

The initial experiment did not produce a rift at all. The wet sand acted as a strong rigid plate and only produced boundary effects (without faulting, just a steep gap between the sand and the sidewall. So after 2:20h, the experiment was stopped, as it did not change at speeds of 60cm/h (10x initial) or even at 60cm/h (100x initial).

Start t = 0

However, when the sand itself was cut, the cuts acted as plate boundaries and went apart very nicely, even without boundary effects. **However, the (normal) faults are not at all realistic.** Some different geometries were tested and worked well and strike slip compressional movements showed that thrusting works in wet sand.

It seems that wet sand has indeed more cohesion that could solve some problems of the dry sand, but it does not produce normal faults and is therefore rather useless.
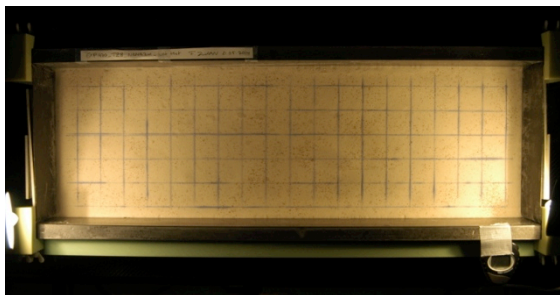
Before cutting
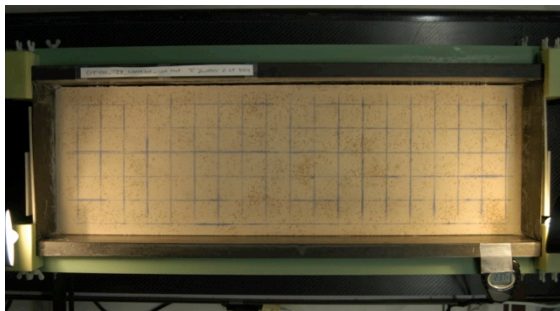
After cutting (oblique extension applied)
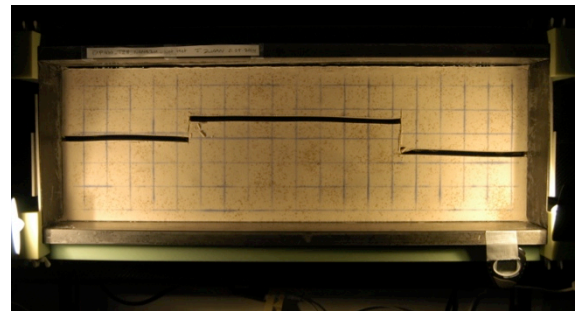
Thrust fault in wet sand at the end of the experiment, location in picture above

Overview Series 3

_____

Tz1 — 6 mm/h — 10 cm — 45° — weak zones — 3:00h — Movement: 1.8 cm

Tz2 — 3 mm/h — 10 cm — 45° — 3 mm/h — 5:30h — Movement: 3.3 cm

Tz3 — 10 cm — 6 mm/h — 5:00h — Movement: 3.0 cm

Tz4 — 3 mm/h — 10 cm — 3 mm/h — 3:30h — Movement: 2.1 cm

Tz5 — 3 mm/h — 10 cm — 3 mm/h — 3:00h — Movement: 1.8 cm

Tz6 — 3 mm/h — 3 mm/h — 10 cm — 2 mm/h — 4:30h — Movement: 2.6 cm at 31°

Tz7 — 3 mm/h — 5 mm/h — 10 cm — 4:00h — Movement: 2.3 cm at 31°
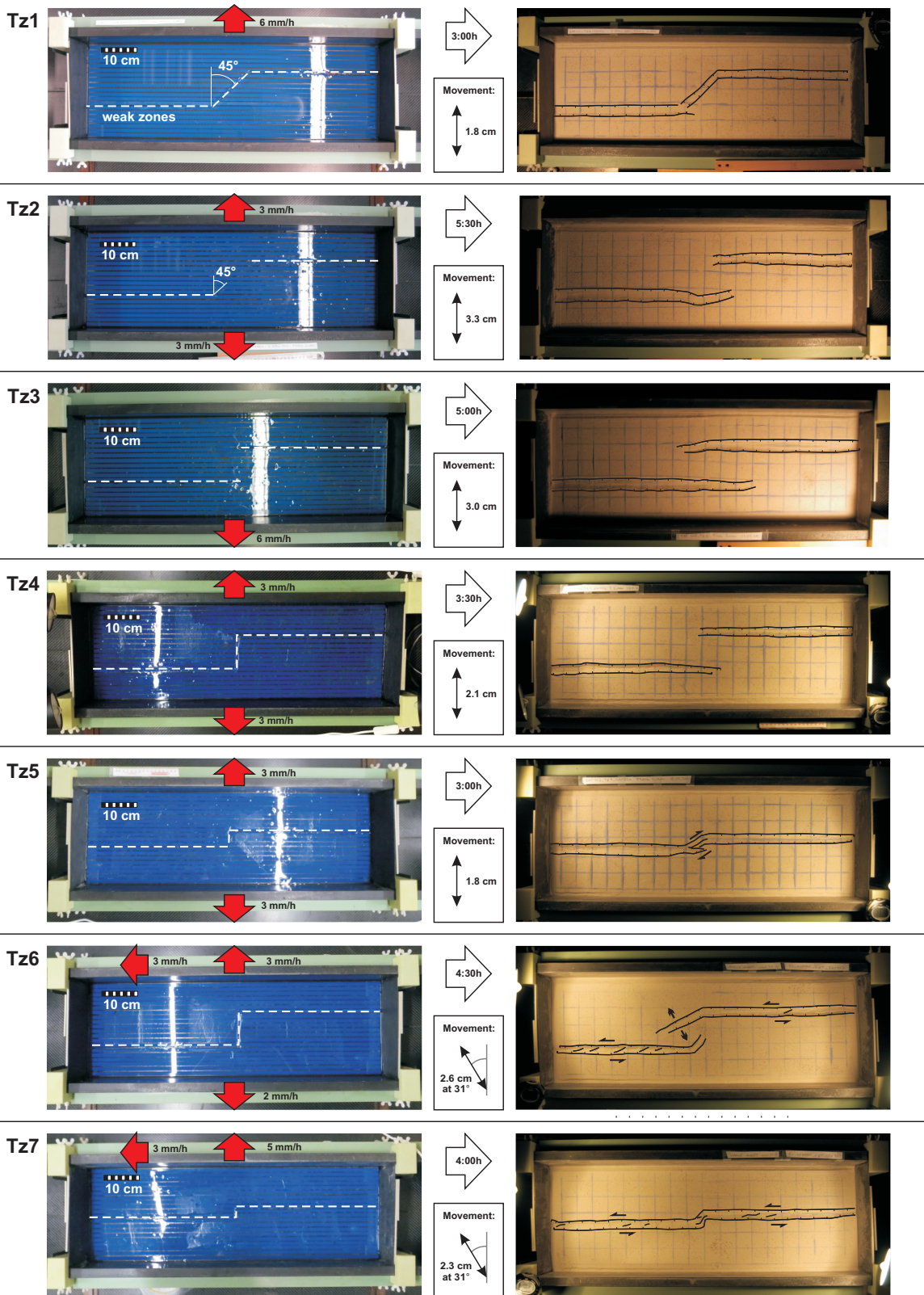
Series 4. Rift interaction models 2 (Chapter 2)

General set-up series 4
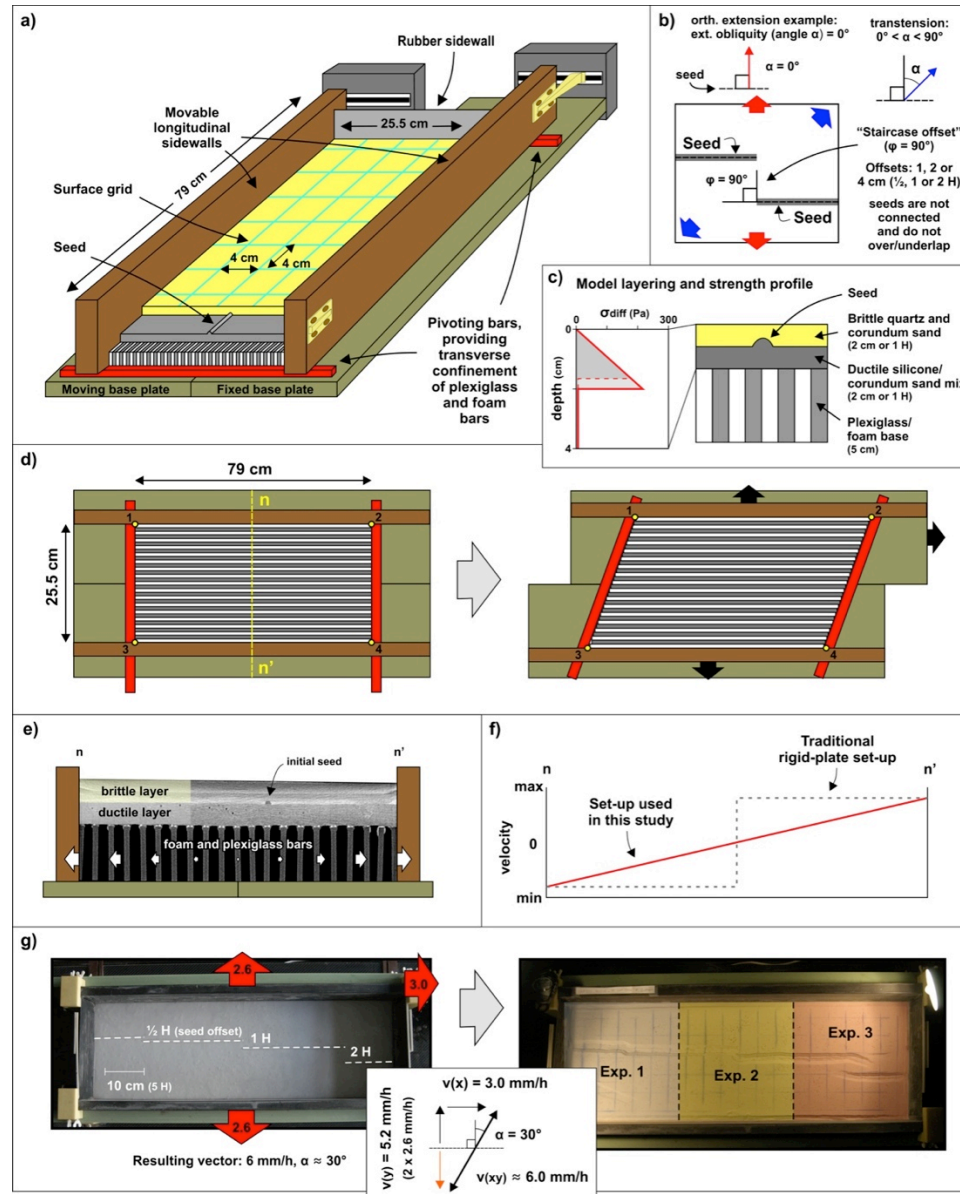
Set-up of the analogue experiments of series 4 (Chapter 2). a) Cut-out view of the experimental apparatus; b) Surface view showing the definition of extension obliquity (angle α) and seed geometry; c) Compositional layering and associated strength profile. The dotted line indicates the strength profile at the seed, where the brittle layer is thinner. Calculated after Brun (2002); d) Schematic surface view showing the initial set-up and subsequent deformation of the empty apparatus; e) Example of a CT-derived cross-section (n–n', see (d)), showing the initial model layering and seed geometry. White arrows indicate the velocity gradient at the model base; f) Velocity profile (perpendicular to extension direction, see (e)) in current and traditional set-ups; g) Left: Surface view of the PDMS/corundum sand mixture with seed geometry before adding the sand cover. Note that the seeds are not connected. Middle: applied extension obliquity. Right: Top view of the example model showing final surface deformation of three simultaneous experiments.

1) EXP472

_____
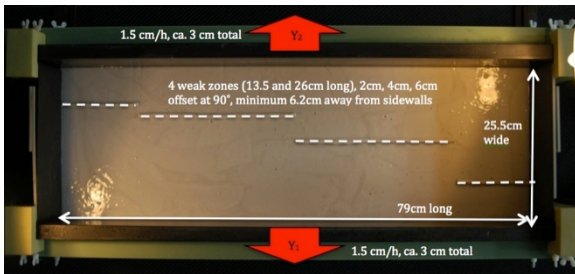
Set-up   Final top view image (after 2h30)
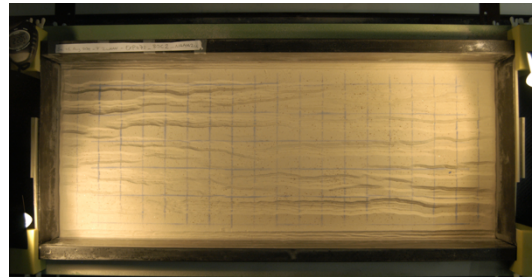
The coupling between the sand and silicone was too high, rifting just happened all over the place, in order to localize rifting, we need to deform more slowly.

2) EXP473 (CT-scanned)

_____
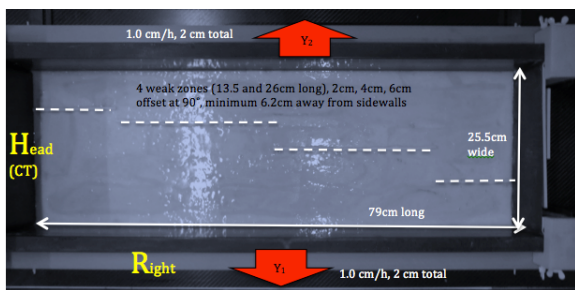
Set-up   Final top view image (after 2h00)
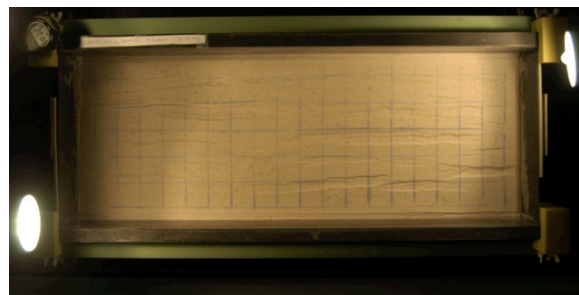
Again, coupling was too strong, the rifting did start at the weak zones, but then rifting started all over the place again (as in the previous model)

3) EXP474 (CT-scanned)

_____
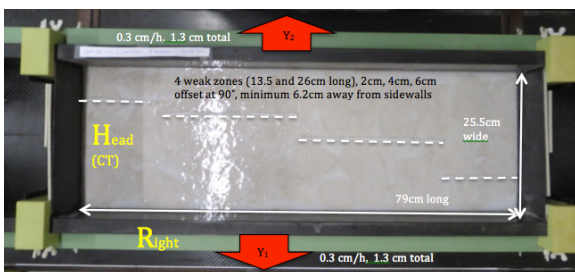
Set-up   Final top view image (after 4h00)
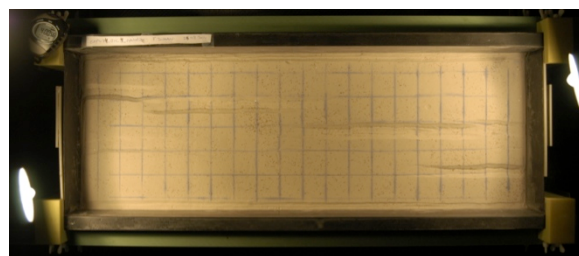
Well localized rifts, with no linkage, not even at the smallest (2 cm) offset!, which is very clear on the CT imaging.

4) EXP475 (CT-scanned)

_____

Set-up   Final top view image (after 4h00)
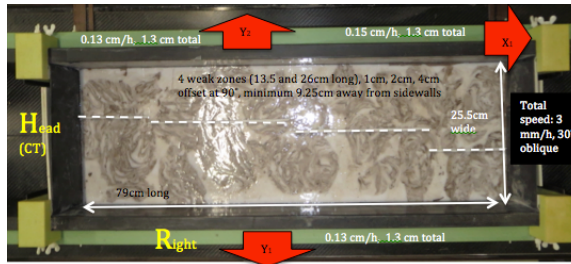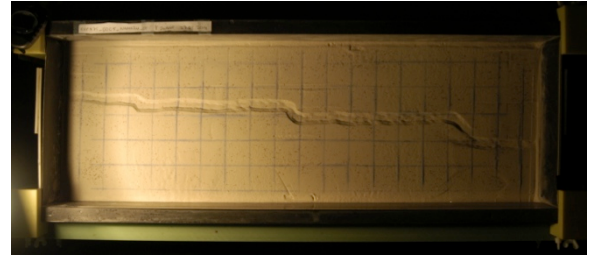
30° oblique model, offsets are 1, 2 and 4 cm here. (instead of 2, 4, 6 cm in previous models). The rifts were nicely connected and also a link starts to develop at the largest (4 cm) offset. The CT data show this last linkage is not fully complete yet though. NB1: smaller offsets than before (1, 2 & 4 cm), NB2: speed was half what it should have been (human error)

5) EXP476 (CT-scanned)

_____
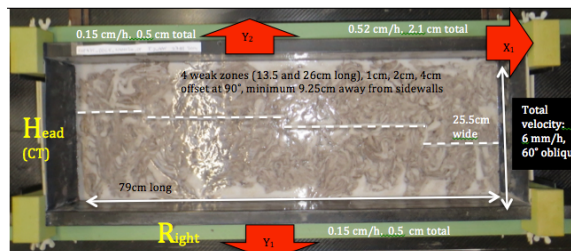
Set-up   Final top view image (after 4h00)
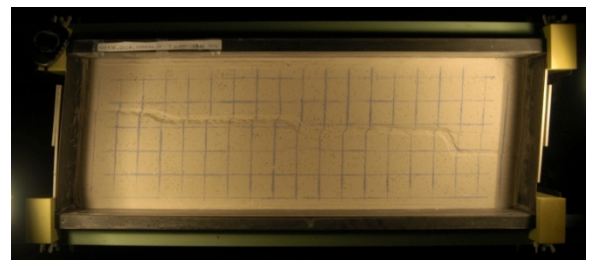
60° oblique model, offsets are 1, 2 and 4 cm. The localization worked very well, only some boundary effects developed near the rubber walls, probably due to space problems as the model is compressed there.

6) EXP477 (CT-scanned)

_____
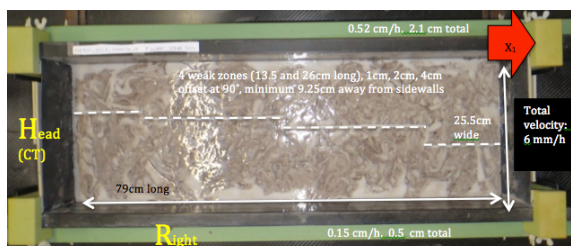
Set-up   Final top view image (after 5h00)
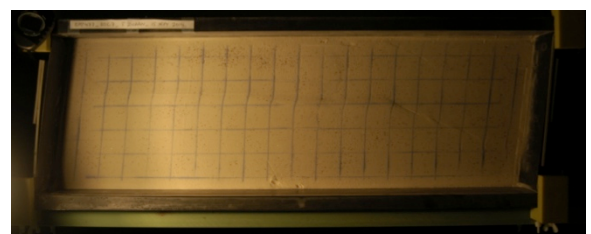
90° oblique model/pure strike-slip, offsets are 1, 2 and 4 cm. The localization seems to have worked reasonably well, some boundary effects developed near the rubber walls, probably due to space problems as the model is compressed there. Also, some "riedel faults" have developed

7) EXP478

_____

Set-up | Final top view image (after 4h00)
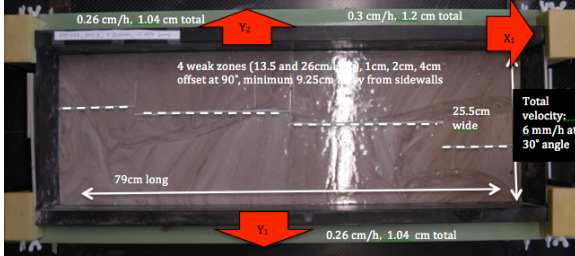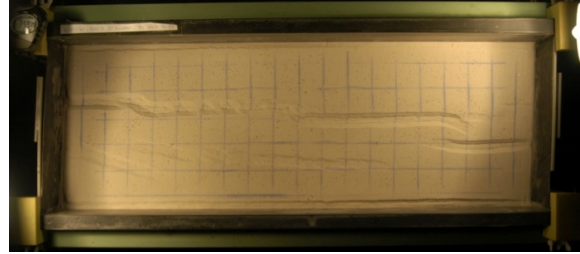
30° oblique model, offsets are 1, 2 and 4 cm. Additional rifting started along the lower longitudinal wall, perpendicular to the extension direction. Wide rifting → more coupling → too much sand in the mixture after the series of model runs?

8) EXP479

_____
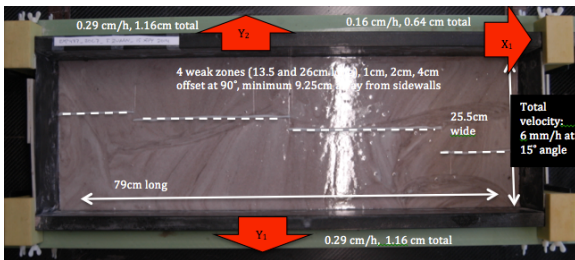
Set-up | Final top view image (after 4h00)
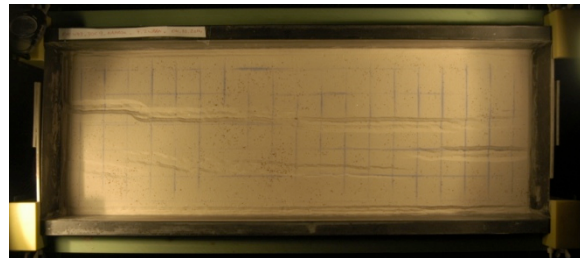
15° oblique model, offsets are 1, 2 and 4 cm. Additional rifting started along the lower longitudinal wall, perpendicular to the extension direction. Wide rifting → more coupling → too much sand in the mixture after the series of model runs?

9) EXP480

_____
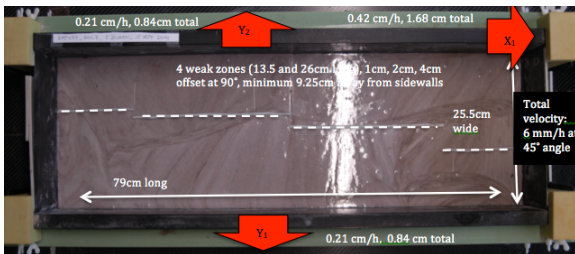
Set-up | Final top view image (after 4h00)
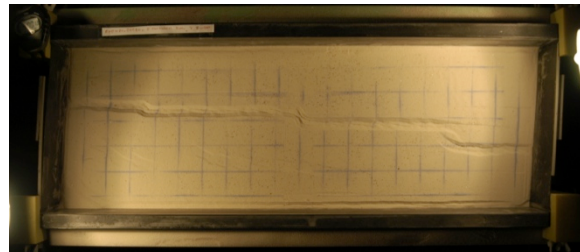
45° oblique model, offsets are 1, 2 and 4 cm. Additional rifting started along the lower longitudinal wall, perpendicular to the extension direction. Wide rifting → more coupling → too much sand in the mixture after the series of model runs?

10) EXP481

_____
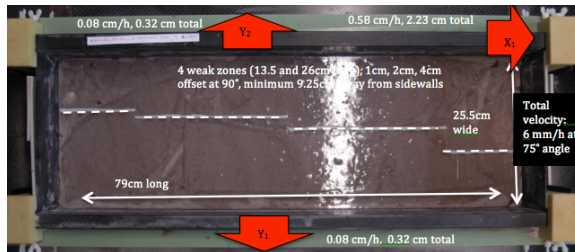
Set-up   Final top view image (after 4h00)
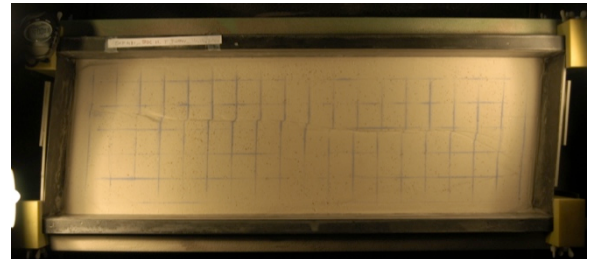
75° oblique model, offsets are 1, 2 and 4 cm. Nice structures, activation of weak zones. Not much boundary effects in this model!

11) EXP482_BOC12_NAMAZU

_____

Set-up   Final top view image (after 4h00)
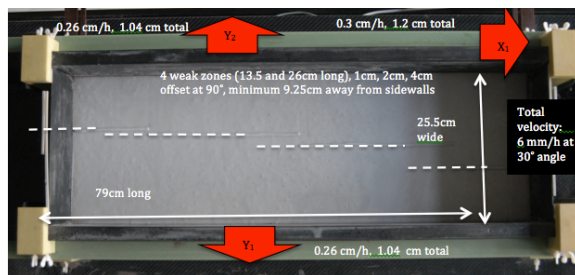
30° oblique model, Fresh putty mix, offsets 1, 2 and 4 cm, new Silicon/sand mix! Nice structures, activation of weak zones. Additional rifting started along the lower longitudinal wall, perpendicular to the extension direction. → too high extension rate after all?

12) EXP483

_____
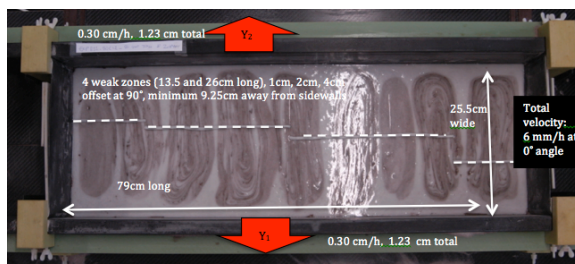
Set-up   Final top view image (after 4h00)
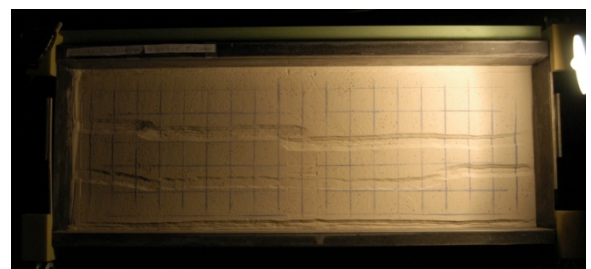
0° oblique model, Fresh putty mix, offsets 1, 2 and 4 cm (to have a 1cm offset model and complete the series). Nice structures, activation of weak zones. Additional rifting started along the lower longitudinal wall, perpendicular to the extension direction. → too high extension rate after all?

13) EXP484 (CT-scanned)
_____

Set-up   Final top view image (after 4h00)
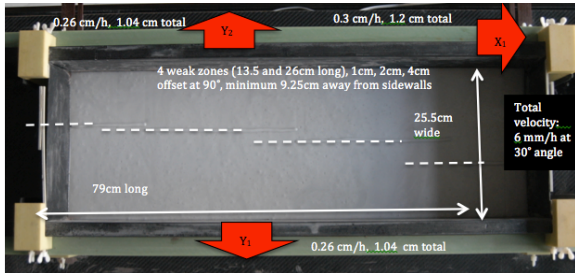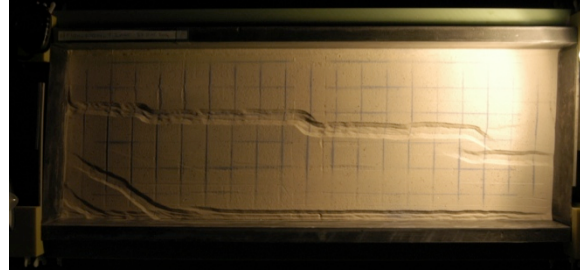
30° oblique model, Fresh putty mix, offsets 1, 2 and 4 cm. (to have a 1cm offset model and complete the series). Nice structures, activation of weak zones. Additional rifting started along the lower longitudinal wall, perpendicular to the extension direction. New silicone mix

14) EXP485 (CT-scanned)
_____
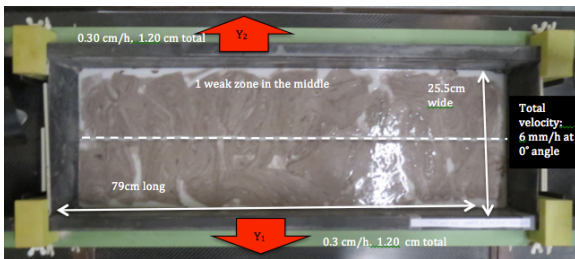
Set-up   Final top view image (after 4h00)
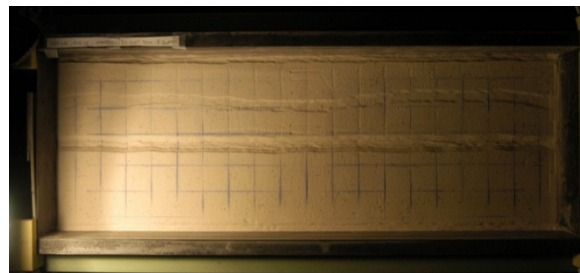
One central seed, benchmark model for numerical modeling. Nice structures, activation of weak zones. Additional rifting started along the lower longitudinal wall…

15) EXP498 (CT-scanned)
_____
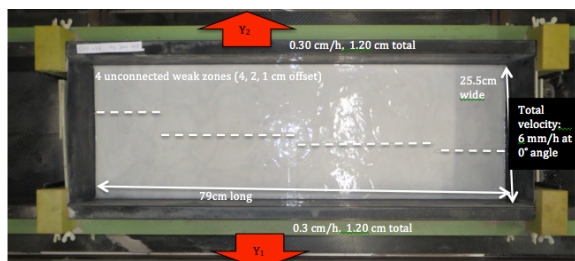
Set-up   Final top view image (after 8h00)
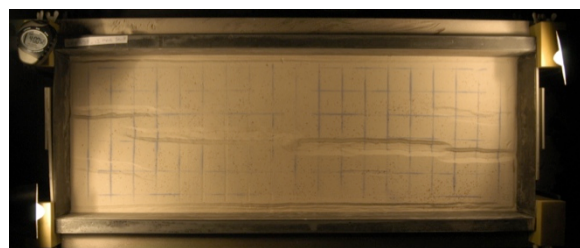
Orthogonal extension. CT-scanned experiment to fill the 1cm offset gap in the CT model serie

272

Series 5. Rift interaction models 3 (Chapter 3)

General set-up series 4

_____

Model setup. (a) Cut-out view of the experimental apparatus depicting its various components. (b) Compositional layering of quartz and corundum sand representing the brittle upper crust and a viscous silicone/corundum sand mixture simulating the ductile lower crust, above a Plexiglas and foam base. (c) Experimental apparatus in the CT scanner during a model run. (d and e) Seed geometry setup for our two model series with a secondary rift-connecting seed (series 1) and without a secondary seed (series 2). (f) Extension obliquity definition for our model series. (g) Distribution basal deformation in the model. As the sidewalls move apart with 3 mm/h, a velocity gradient develops in the foam and Plexiglas base (yellow arrows). The CT image is derived from model B (EXP16). Layering in the sand is due to the alternations of quartz and corundum sand with different densities. (i) Example of a model run. (Left) Initial setup of three separate experiments in one model run (without sand cover). (Right) Final surface structures.

EXP486
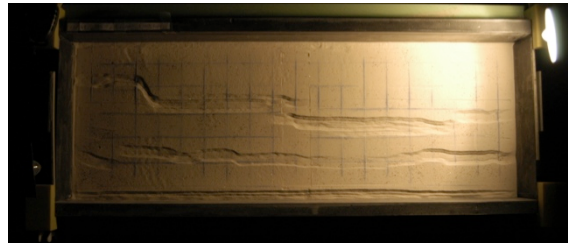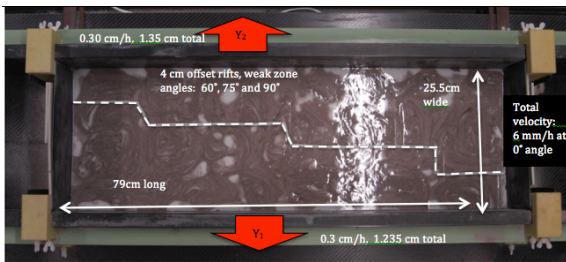
Connection depends on angle of connecting weak zones

EXP487
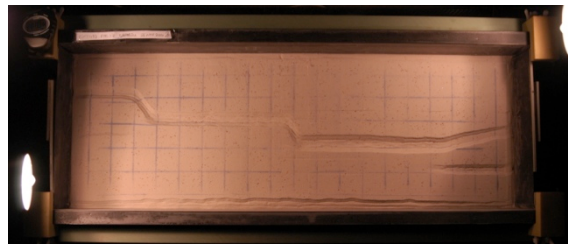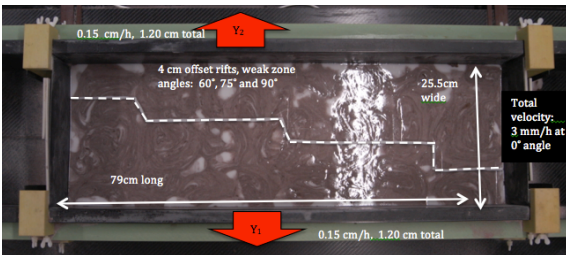
Same set-up as EXP486, half the speed (3 mm/h) → less boundary effects, better linkage as deformation is concentrated

EXP488
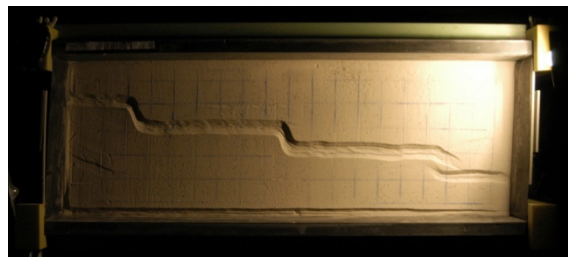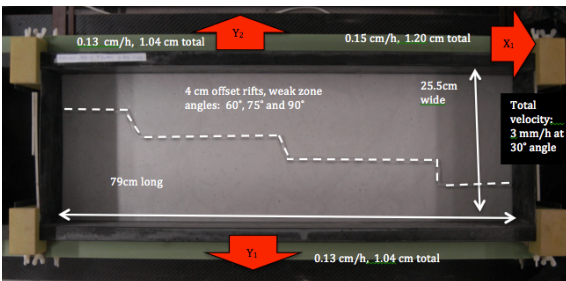
30° oblique extension gives here almost complete linkage, but the 4cm offset will not allow it yet, as observed in previous models. It will do at ca. 45° oblique extension. Fresh silicone mix!

EXP489
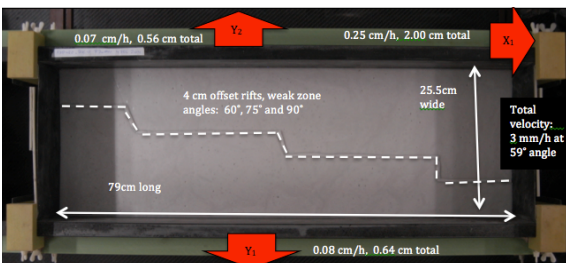
60° oblique extension gives here complete linkage, as predicted.

EXP490
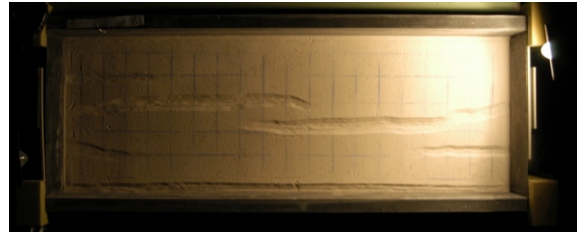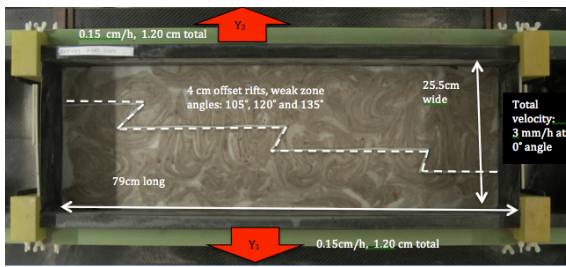
Overlapping weak zones with differently oriented connecting weak zones under orthogonal extension. No weak zone activation, maybe under oblique extension?

EXP491
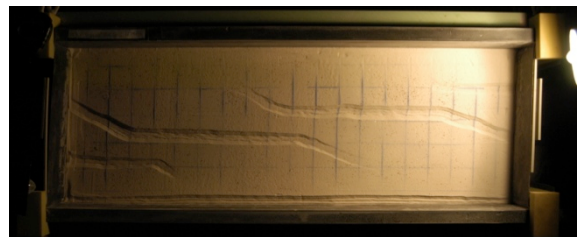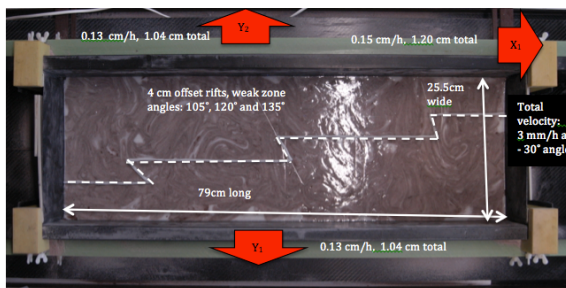
-30° obliquity does not help linkage, but created intriguing en echelon structures

EXP492
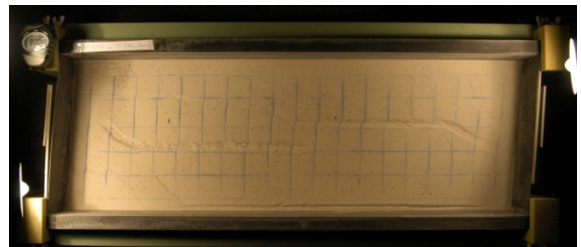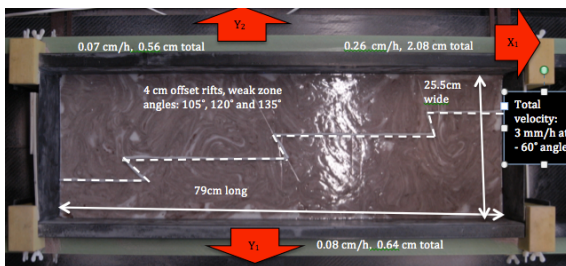
-60° obliquity does not help linkage, but created intriguing en echelon structures and some extra boundary effects

EXP493
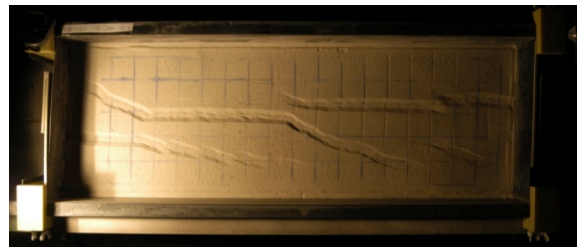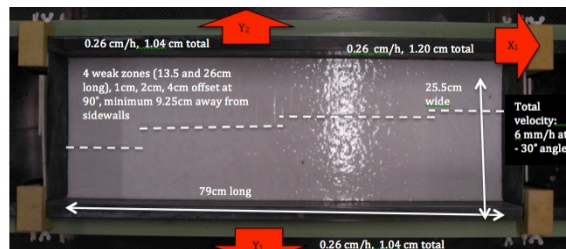
-30° version of series 2.1, shows same type of structures as the negative oblique extension models (EXP491 and 492). New silicone mix

EXP494
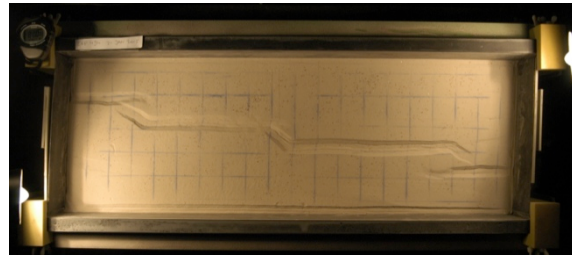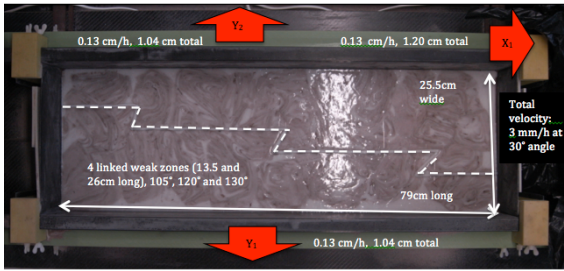
30° extension, no reactivation of connecting weak zones. -30° extension, no reactivation of connecting weak zones.

EXP495
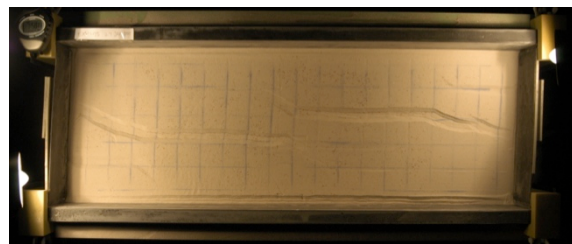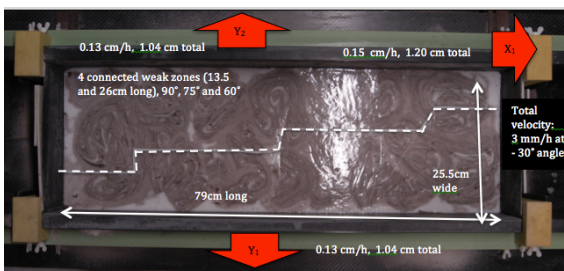
Test with underlapping seeds → orthogonal extension

EXP496
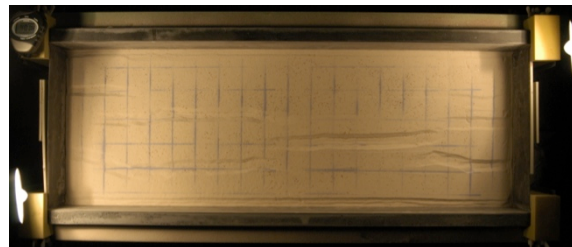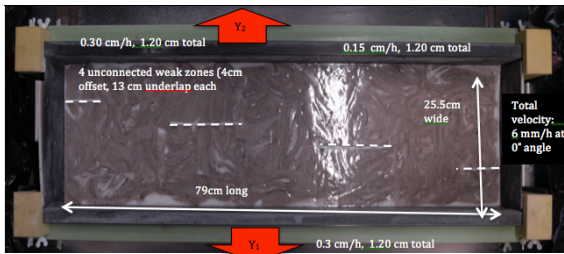
This model tests the influence of 30° oblique extension on different cases of underlap

EXP497
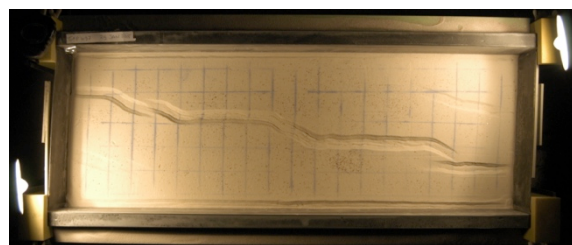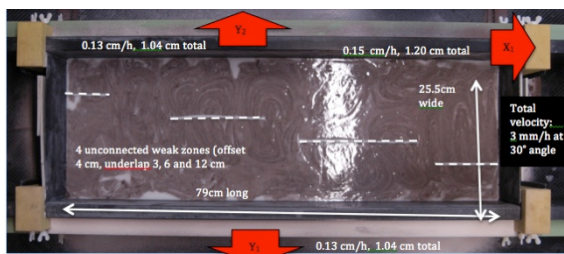
Orthogonal extension. CT-scanned experiment to fill the 1cm offset gap in the transfer zone model series 1.

EXP499
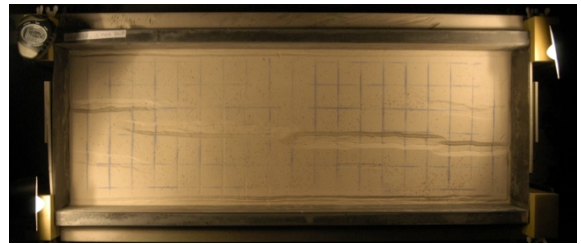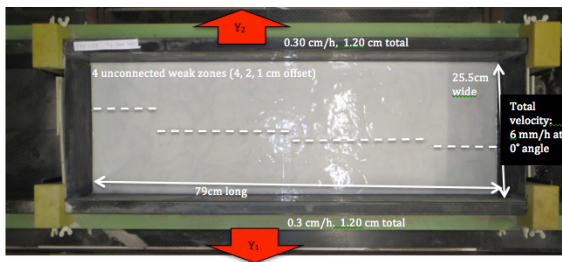
Experiment to test the minimal seed size to localize deformation in orthogonal divergence. A 3 mm/h divergence velocity was applied, to maximize localization

EXP500
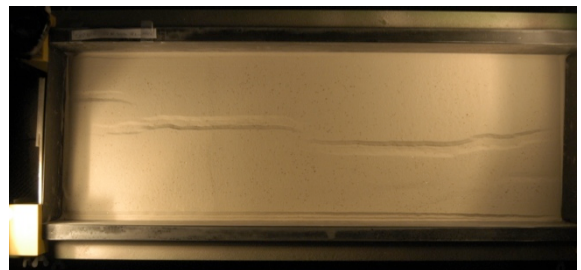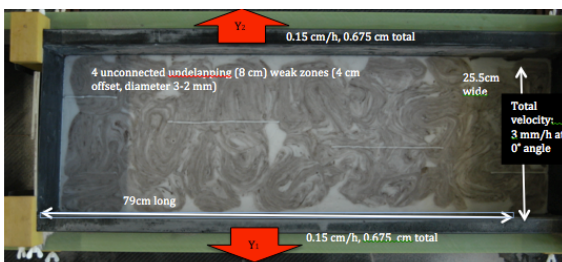
Test if 2.5-3mm seed diameter is always enough to localize. All seeds localized rifting, although the lower right one section is dominated by the propagating rift closer to the middle of the model. An interesting result is the interaction between the rifts, they seem to grow towards each other. Effect of lower divergence velocity? (3 mm/h vs 6 mm/h in series 2.1)

EXP501
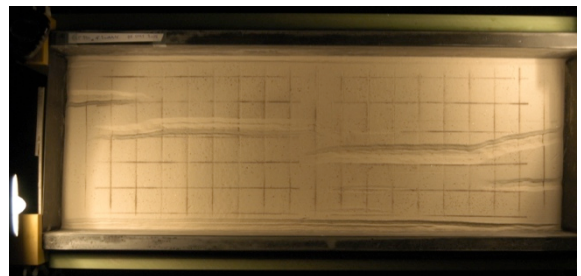
Test influence of underlap (90°, 75° and 60°) on rift interaction since it seemed to matter in EXP 500. However, here nothing happens. Maybe when overlap is larger?

EXP502
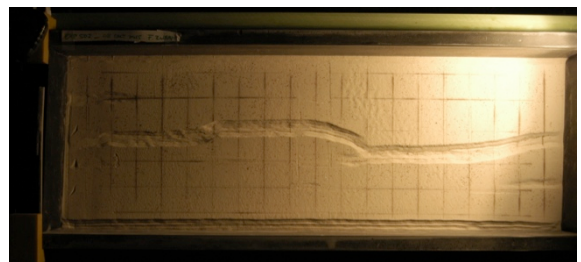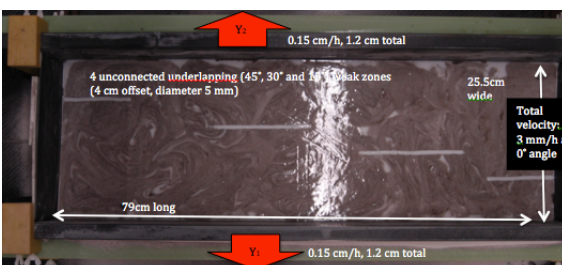
Test influence of underlap (45°, 30° and 15°) on rift interaction since it seemed to matter in EXP 500. Continuation of model EXP501 (90°, 75° and 60°). Poor activation of small weak zones, maybe they are too small?

EXP503
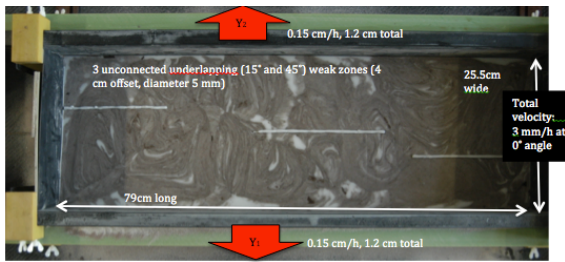
New model with 3 seeds instead of 4, focusing on the 45˚ and 15˚ experiments that failed in EXP502

EXP508
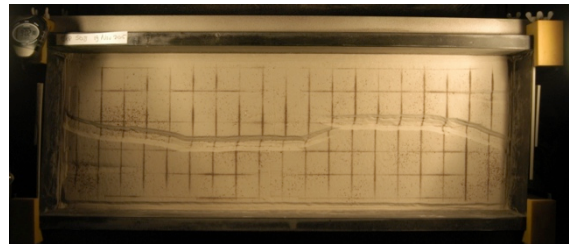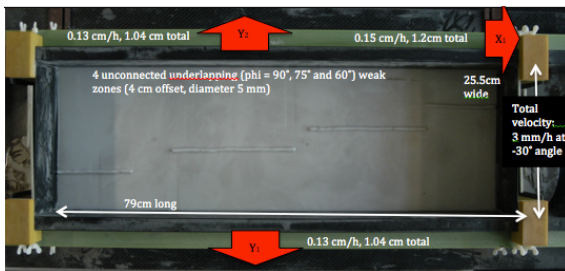
-30˚ oblique extension models. Angle phi = 90˚, 60˚ and 30˚.

EXP509
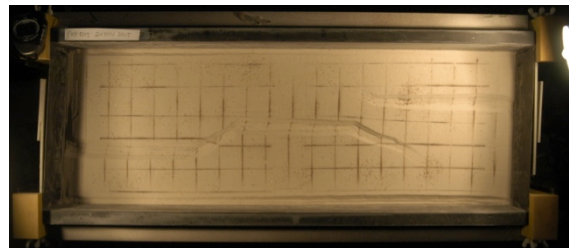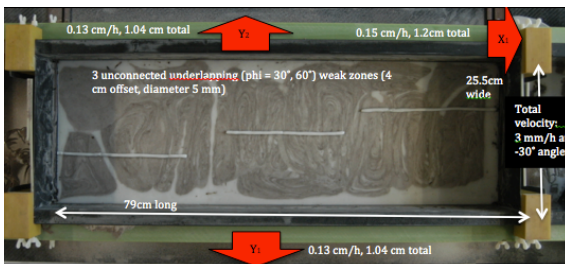
-30˚ oblique extension models. Angle phi = 90˚, 60˚ and 30˚.

EXP510
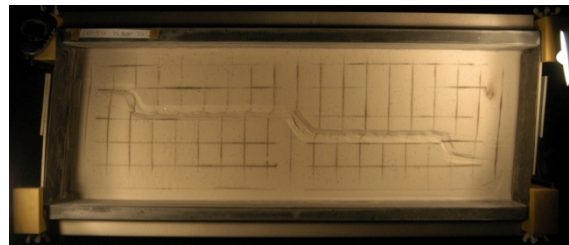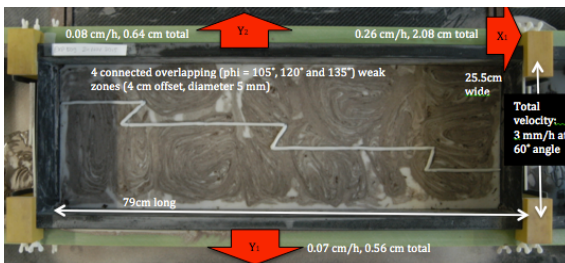
60˚ oblique extension models. Angle phi = 105˚, 120 and 135˚ connected weak zones!

EXP511
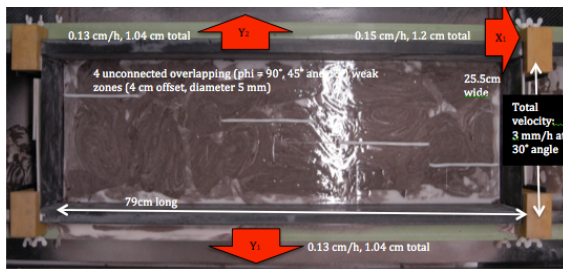
30° oblique extension models. Not connected

EXP512
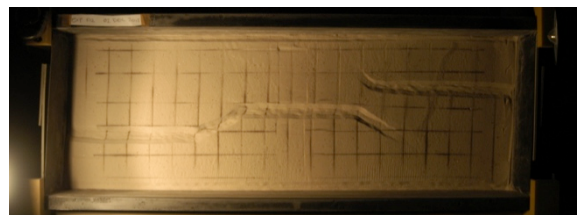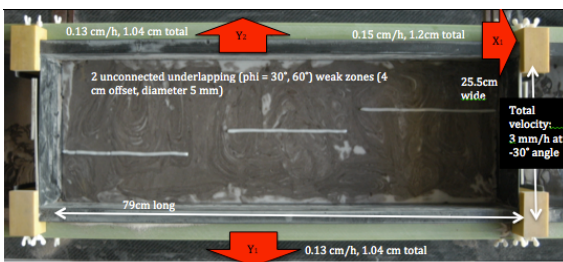
-30° oblique extension models. Angle phi = 60°, and 30°. Rerun of EXP509, since we had strange linkage (parallel to extension direction), which happened again in this model.

EXP513
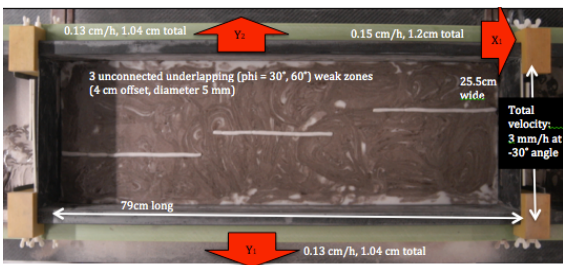
-30° oblique extension models. Angle phi = 60°, and 30°. Rerun of EXP509, since we had strange linkage (parallel to extension direction), which happened again in this model (for the phi = 30° model). No coherent results, the rift even propagated even towards the other rift.

EXP514
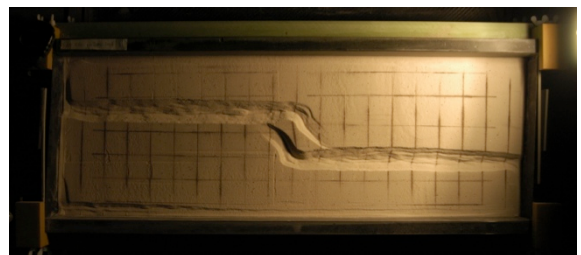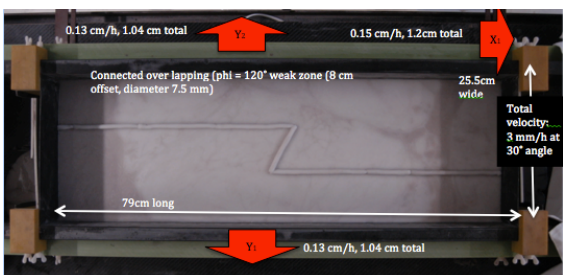
30° oblique extension models. Angle phi = 120°. Double layer thickness for better resolution. Worked well. No reactivation of rift-connecting weak zone

279
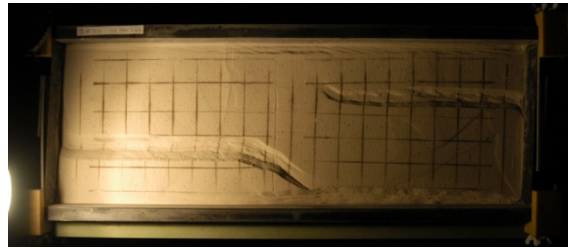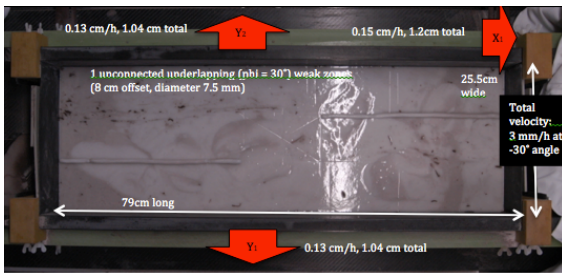
EXP515

-30° oblique extension models. Angle phi = 30°, not connected. Double layer thickness for better resolution. Worked not as we wanted → no connection as expected from previous 4 cm thick models

EXP516 (CT-scanned)
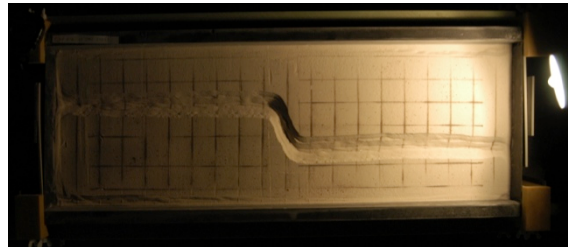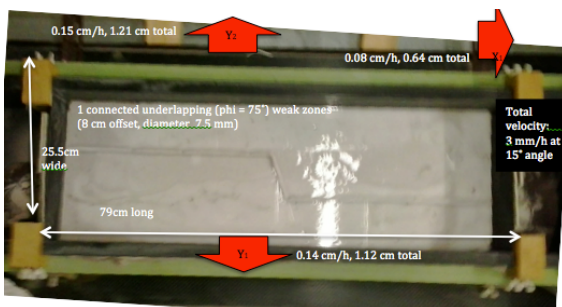
Double layer thickness for better resolution. 15° oblique extension models. Angle phi = 75°, not connected. Nice connection between rift segments, as expected.

EXP517 (CT-scanned)
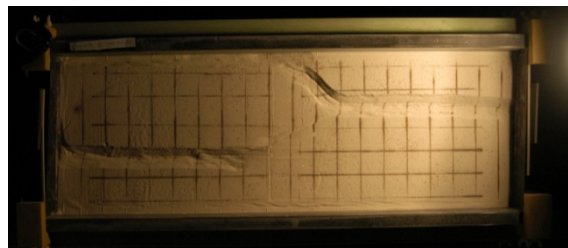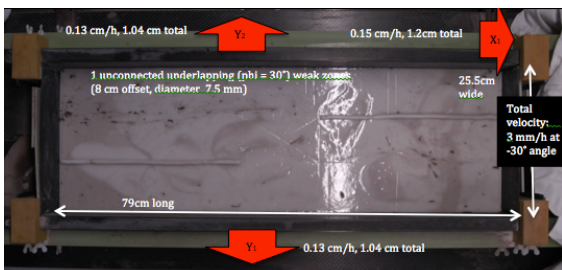
Double layer thickness for better resolution. -30° oblique extension models. Angle phi = 30°, not connected. Extra scan to test better resolution scan. Eff mAs 721 instead of standard 300.

EXP518
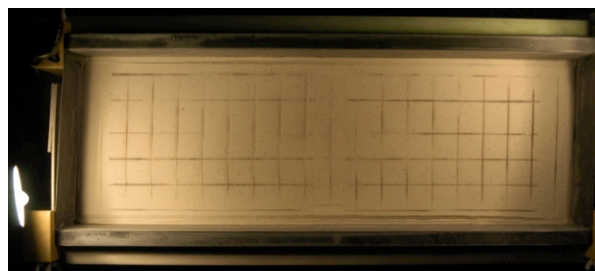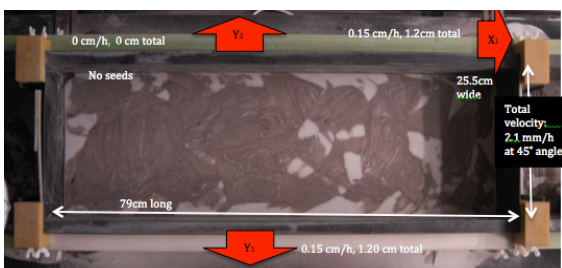
45° oblique extension. (Wrong settings). No seed to test model behaviour

EXP519
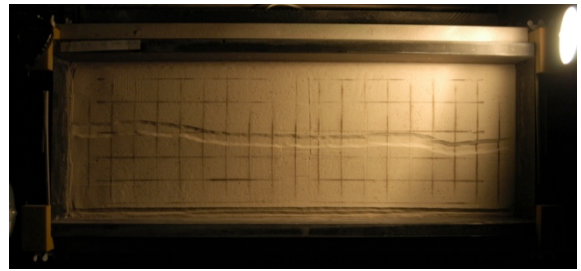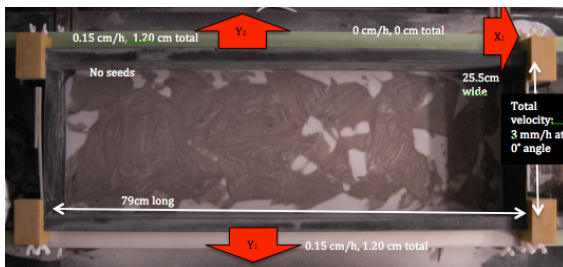
Orthogonal extension, test to see how model behaves without seeds. A rift forms in the middle of the model

EXP520
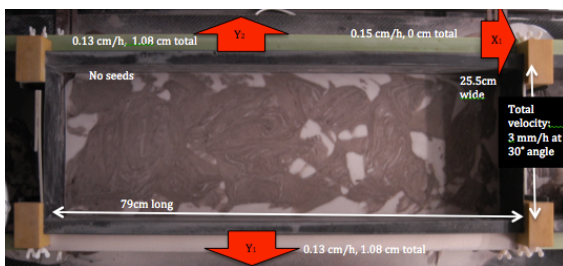
30° oblique extension, test to see how model behaves without seeds

EXP563
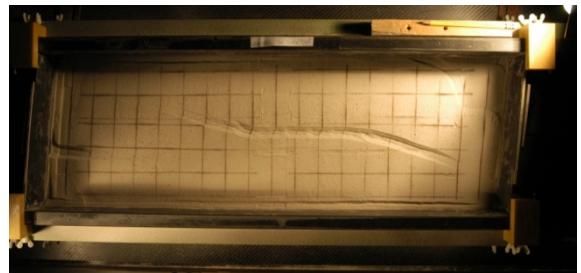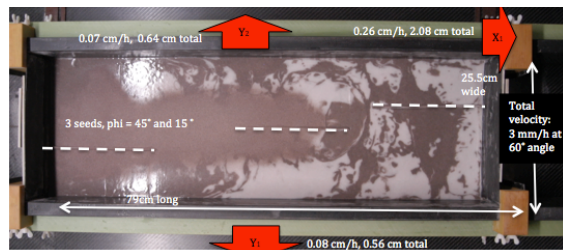
Models to complete series 2 for the interpretation paper. 60° oblique extension (ERROR, 30° was the goal), it has to be rerun. One of the seeds is not activated and no TZ forms.

EXP564
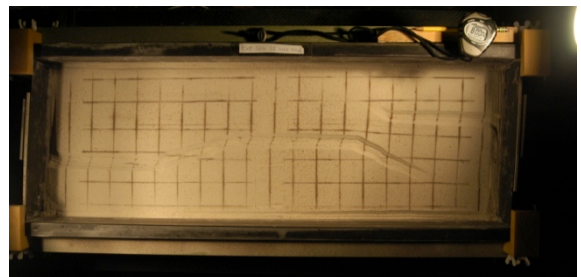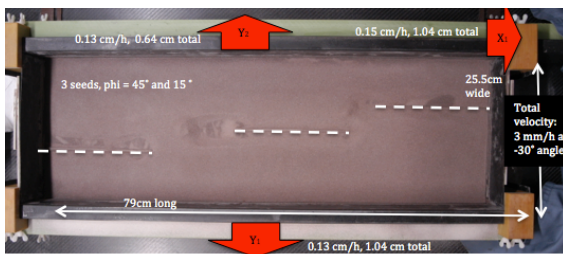
Models to complete series 2 for the interpretation paper
-30° oblique extension and phi = 15° and 45°

EXP565
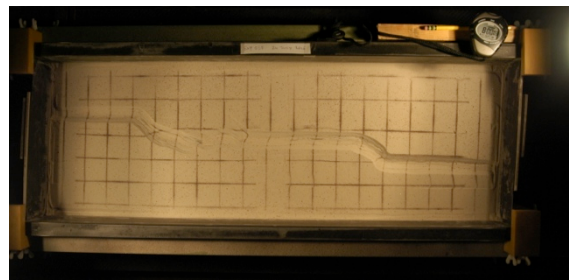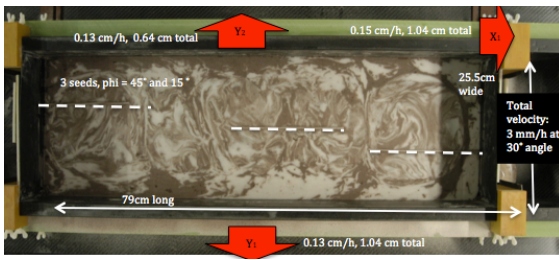
Models to complete series 2 for the interpretation paper. 30˚ oblique extension and phi = 15˚ and 45˚ 45˚ results seems ok, the 15˚ result is rather strange. This one has to be rerun.

EXP566
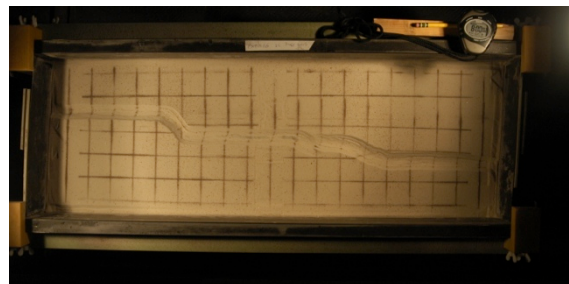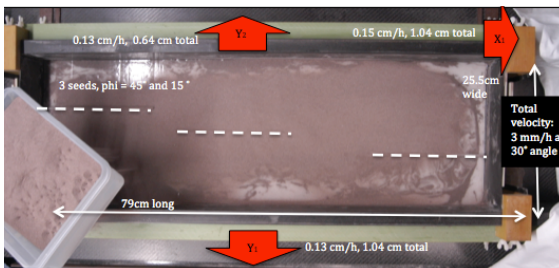
Models to complete series 2 for the interpretation paper, 30˚ oblique extension and phi = 15˚ and 45˚ rerun of model EXP565, to see how the phi = 15˚ model behaves

EXP567
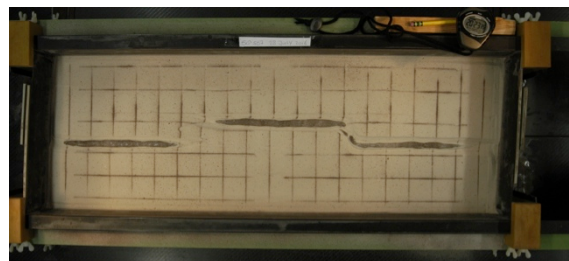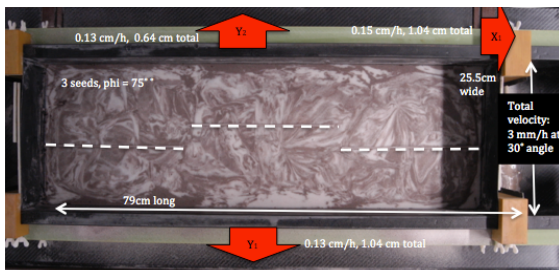
Models to complete series 2 for the interpretation paper. Both phi = 75˚ and alpha = 30˚ and -30˚. Unexpected structures and the Mac stopped taking pictures after 120 min. Especially the alpha = -30˚ is different form other models. After the end of the model, the viscous layer started moving to the surface.

EXP568
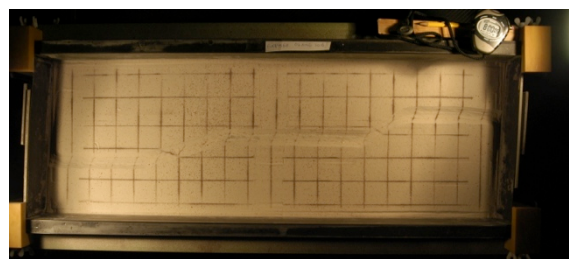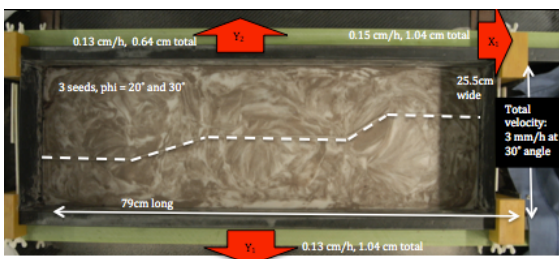
Models to test the sinistral extension creating a TZ with a rift-connecting seed and (phi = 30˚ and 20˚) and alpha = -30˚

EXP569
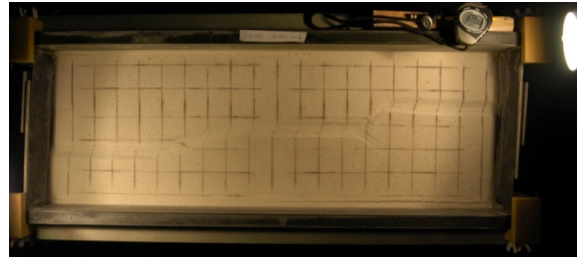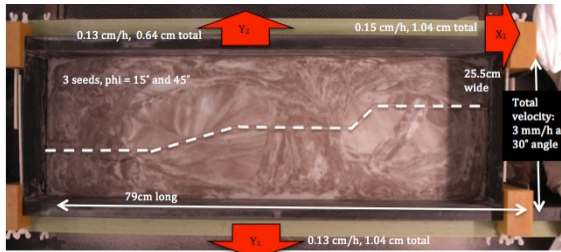
Models to test the sinistral extension creating a TZ with a rift-connecting seed and (phi = 45˚ and 15˚) and alpha = -30˚.

Series 6. Sedimentation models (Chapter 4)

General set-up series 6

Model set-up. (a) Cut-out view of the experimental apparatus depicting its various components. (b) Experimental apparatus in the CT-scanner during a model run. (c) Compositional layering of quartz and corundum sand representing the brittle upper crust and a viscous silicone/corundum sand mixture reproducing the ductile lower crust, overlying a foam base. (d-f) Schematic surface view showing the initial state (d) and subsequent deformation of the empty apparatus (e) orthogonal extension and (f) oblique extension, respectively. (g) Distribution of basal deformation in the model. As the sidewalls move apart with 7.5 mm/h, a velocity gradient develops in the foam and plexiglass base (yellow arrows). The darker x-shape in the image is a CT-artefact that appears in all CT sections. CT image derived from model G.

Model set-up. (h-j) Seed geometries for our three model series. (k) Extension obliquity definition for our models. (l) Sediment application as seen on CT images. Left: rift basin opens after 60 min. Right: the basin is filled to model syn-rift sedimentation. (m) Example of a model run (Model G). Left: initial set-up top view (without sand cover to show the seed geometry). Middle: surface structures after 60 min. Right: basins are filled to simulate syn-rift sedimentation.

EXP605 (Model A)
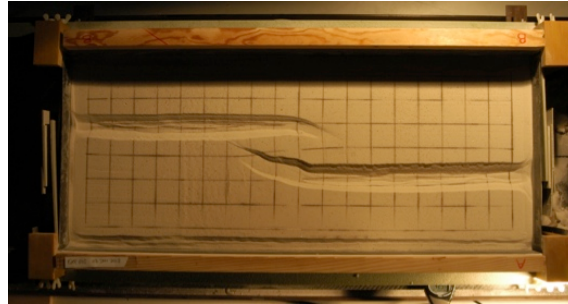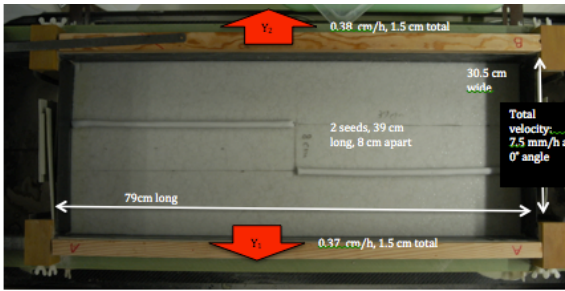
Test with model for Sedimentation series. Orthogonal extension, no sediment

Nice localization, little boundary effects, rifts grow a bit towards each other.

Similar results as Le Calvez (same set-up basically)

EXP606 (not used in Chapter 4)
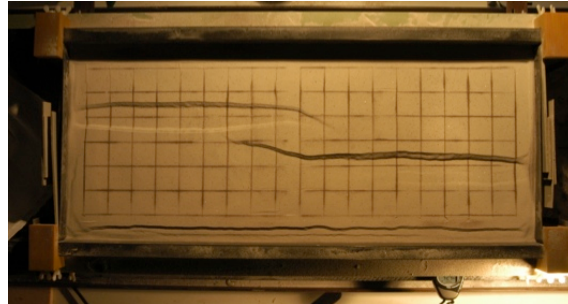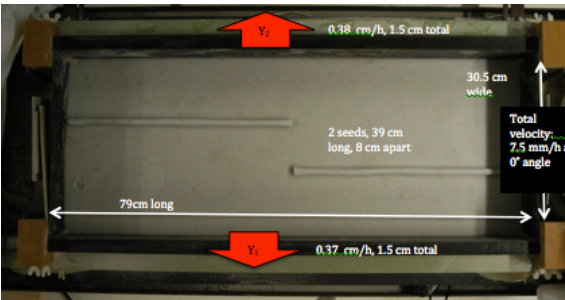
sedimentation. (**2.5 mm qz or cor sand every hour**) Nice localization, little boundary effects, rifts grow a bit towards each other.

Similar results as Le Calvez (same set-up basically) and EXP605. However, toward the end, 1 rift becomes asymmetric and seeds are much more deformed than without sedimentation.

EXP607 (Model E - Sedimentation)
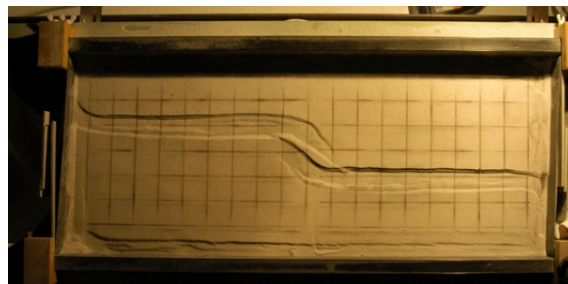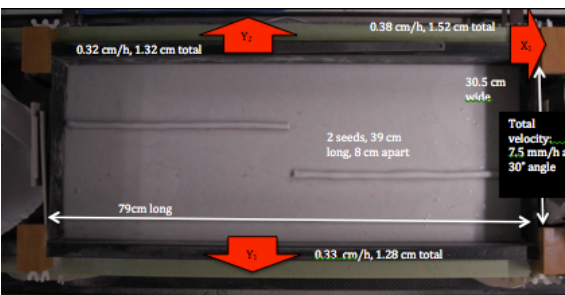
Including sedimentation. (Filling in rift segment qz or cor sand every hour)

30° extension obliquity (dextral)Nice localization, little boundary effects, rifts grow towards each other.

EXP608 (Model D)
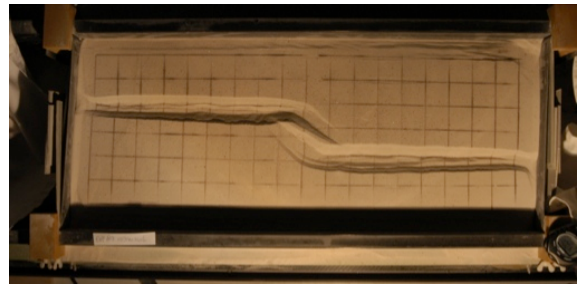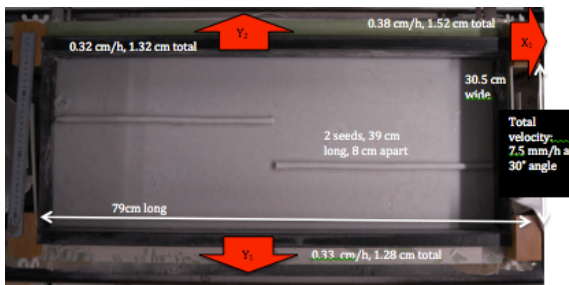
without sedimentation. 30˚ extension obliquity (dextral) Nice localization, little boundary effects, rifts grow towards each other.

EXP609 (Model H)
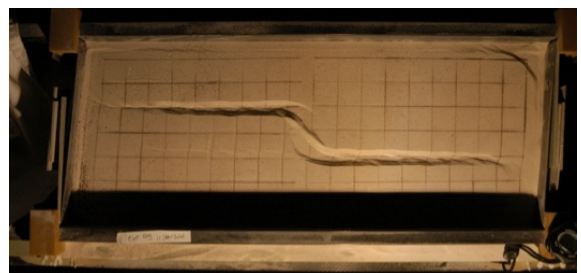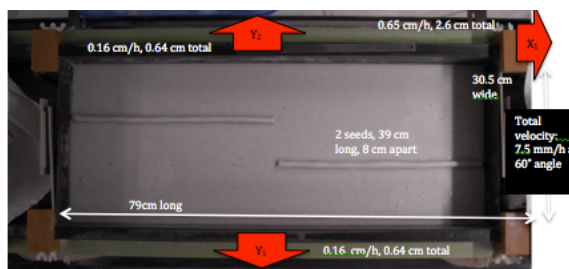
60˚ extension obliquity (dextral) No sedimentation as only little accomodation space formed

Nice localization, little boundary effects, rifts grow towards each other.

EXP610 (Model L - Sedimentation)
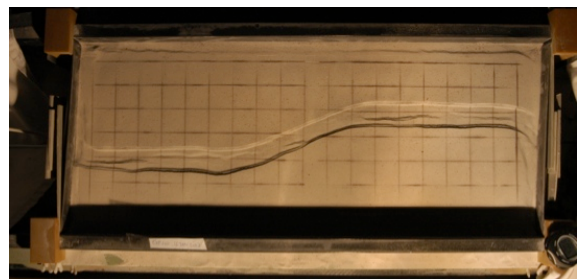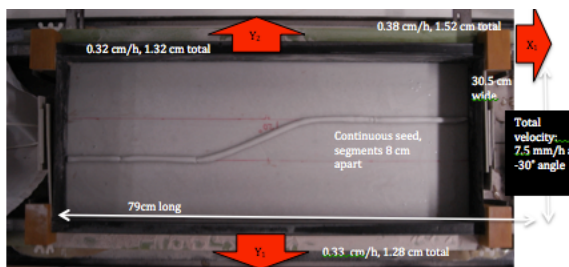
Underlap model (phi = 25˚), with secondary seed and sedimentation every hour -30˚ extension obliquity (sinistral) Nice localization, little boundary effects, oblique structures along the seed.

EXP611 (Model G - Sedimentation)
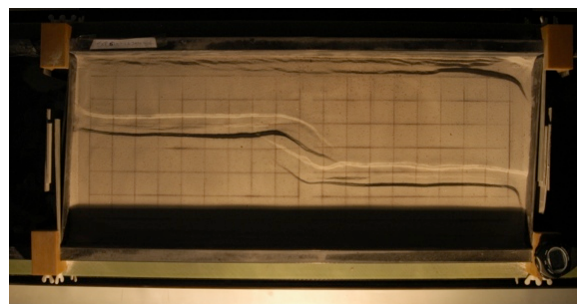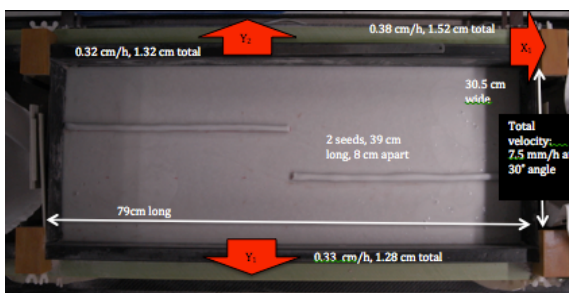
With sedimentation. (Filling in rift segment qz and cor sand every hour: at 60 min, 120 min and 180 min 30˚ extension obliquity (dextral). Nice localization, limited boundary effects, rifts grow towards each other.

EXP612 (Model F - Sedimentation - CT-scanned)
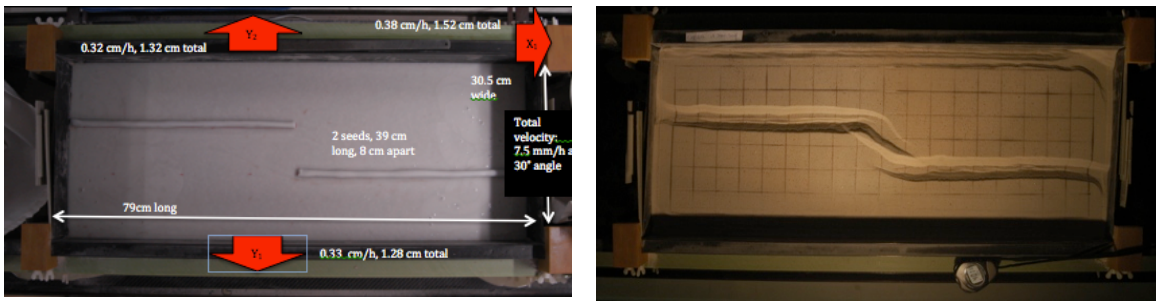
Rerun of EXP611, without sedimentation, 30° extension obliquity (dextral)

Nice localization, limited boundary effects, rifts grow towards each other.

EXP613 (Model B - Sedimentation - CT-scanned)
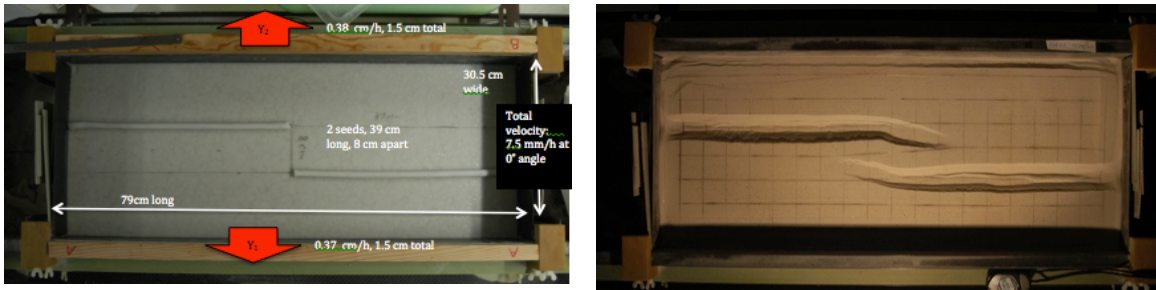
Rerun EXP605 in CT scanner. Nice localization, little boundary effects, rifts grow a bit towards each other.

Similar results as Le Calvez (same set-up basically)

EXP614 (Model C - Sedimentation, CT-scanned)

Rerun EXP605 in CT scanner, with sediments

EXP615 (Model K)
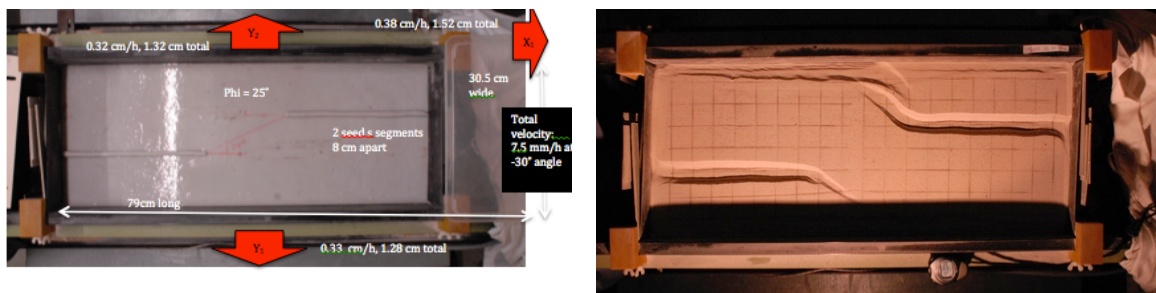
Underlap model (PHI = 25°), with secondary seed, no sedimentation, -30° extension obliquity (sinistral). This went wrong, there should be connection, as phi < 30°, but no. Maybe due to high extension velocity?

EXP516 (Model M - CT-scanned)
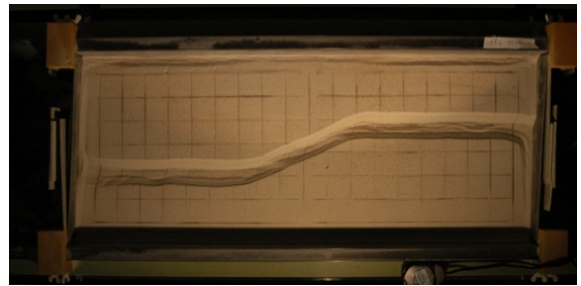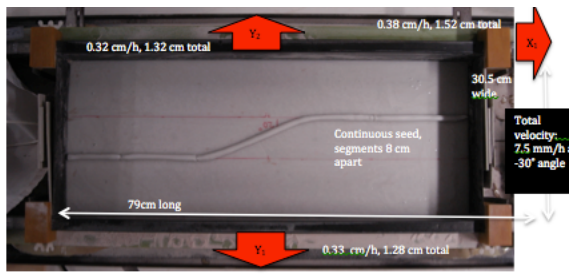
Rerun of EXP510 in the CT-scanner, no sedimentation. Underlap model (phi = 25°), with secondary seed -30° extension obliquity (sinistral) NB: the model needs to be mirrored!

EXP617 (Model N - Sedimentation, CT-scanned)
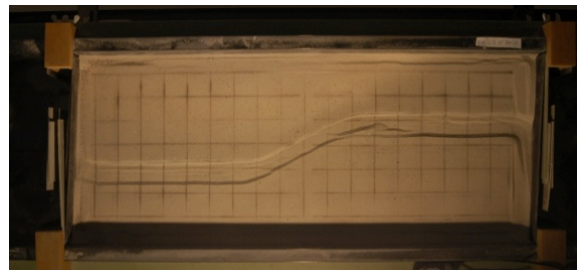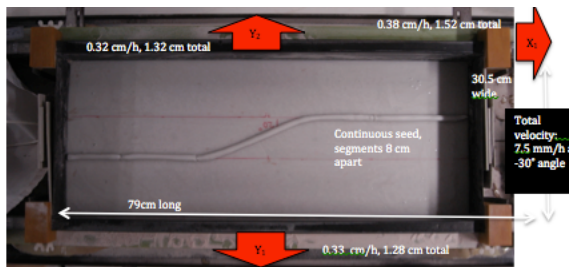
Rerun of EXP516 in the CT-scanner, sedimentation every hour. Underlap model (phi = 25°), with secondary seed. -30° extension obliquity (sinistral). NB: the model needs to be mirrored!

EXP618 (Model J - Sedimentation, CT-scanned)
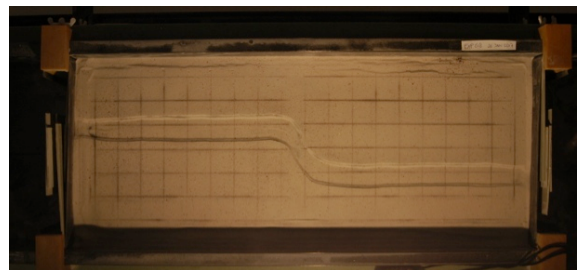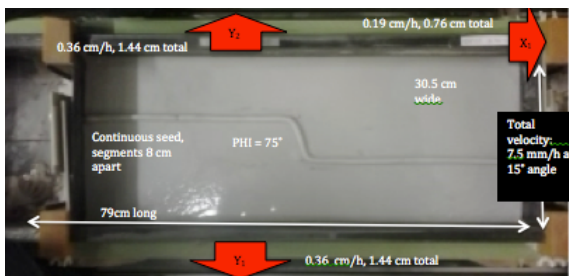
Almost rerun of EXP516 (Interpretation paper, with sedimentation. Underlap model (phi = 75°), with secondary seed, 15° extension obliquity (dextral).

EXP619 (Model I - CT-scanned)
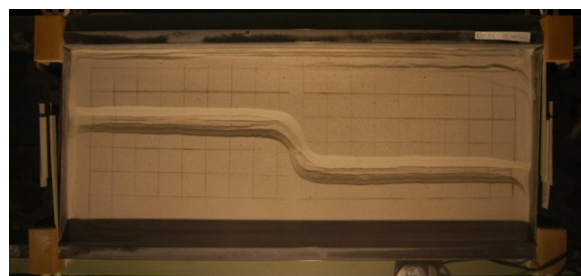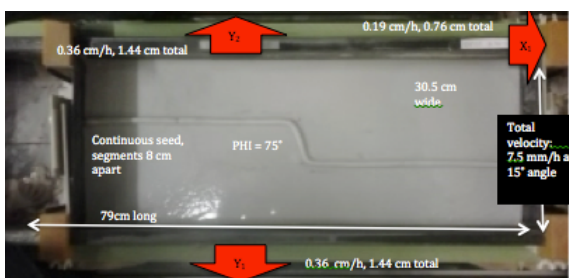
Rerun of EXP516 (Interpretation paper) no sedimentation. Underlap model (phi = 75°), with secondary seed. 15° extension obliquity (dextral). Nice localization, little boundary effects, oblique structures along the seed. Little internal structuration though?

289

Series 7. Xissor model tests A
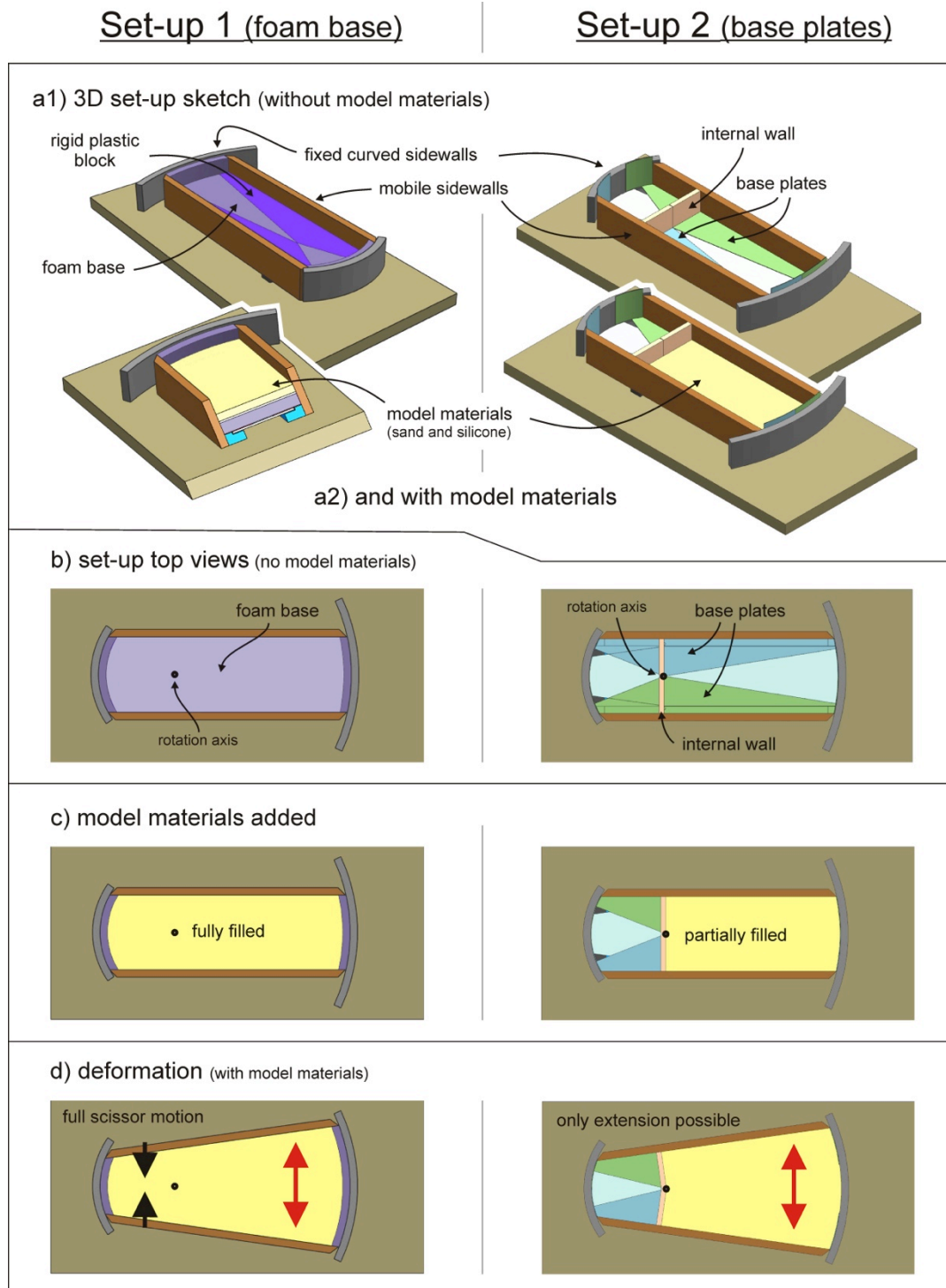
Overview of originally planned set-ups allowed by the Xissor experimental apparatus with left the foam base option and right the base plate option. (a) 3D sketch of the machine without (a1) and with model materials (a2). (b-c) Top views of the machine (b) with model materials and (c) without model materials (c). (d) Top view indication the rotational motion about the rotation axis and the resulting scissor deformation of the model materials. Note that the rigid plastic blacks are present in the models shown in this seciton, but removed from the foam base set-ups used for the models presented in Chapters 6 and 7. The base plate set-up has not been tested to date.

EXP534B

Model with the new Xissor machine to test how it functions without a seed. Only deformation along the sidewalls, strange type of deformation, the ductile part raised, but not along the sidewall, but a bit away from it.
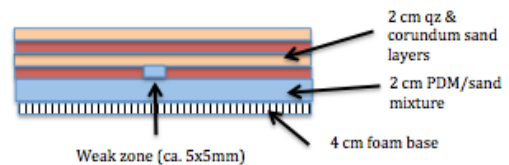
EXP535
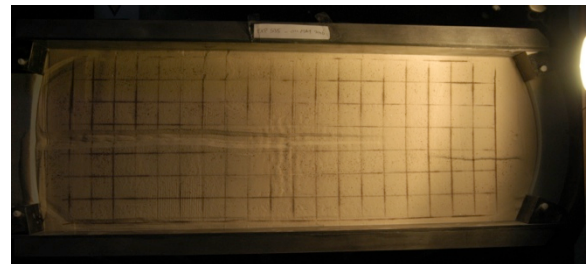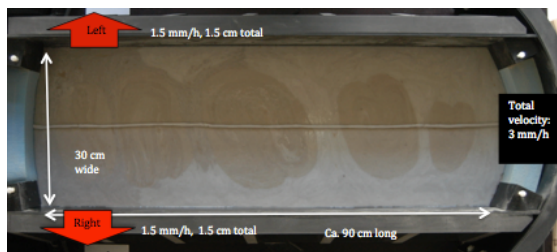
Model with the new Xissor machine to test how it functions with a seed. We get deformation. Extension where we want it and compression produces a thrust above the seed. Seed itself is only deformed in the extensional part of the model. Much less boundary effects than in the previous model. Silicone rose up to the surface after the model was standing for a day, 30 mm would be the maximum extension with a 20 mm thick sand layer. We need to go thicker for better detail.
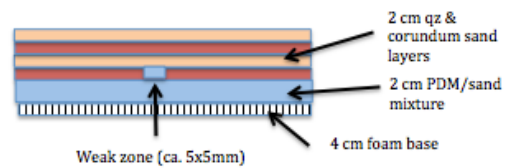
EXP536
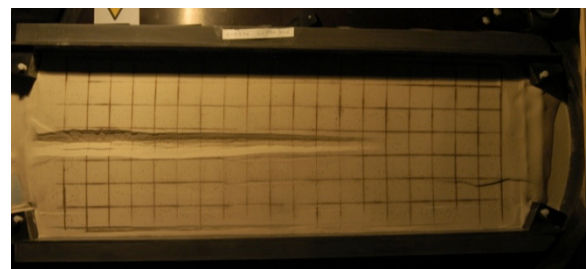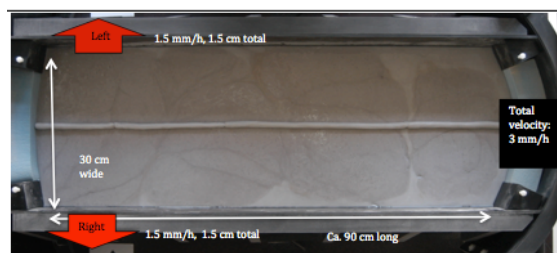
Rerun of model EXP535, with double layer and seed thickness. Nice structures, larger scale than the previous model.
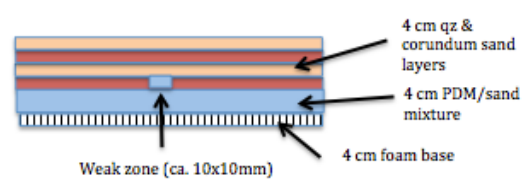
EXP537
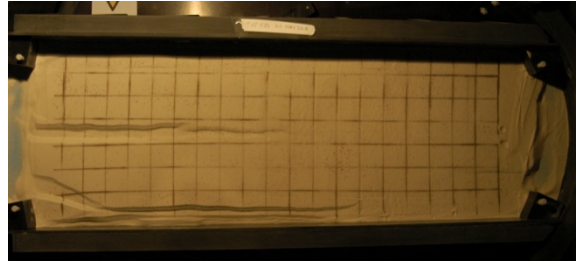
Rerun of model EXP536, with double speed to reduce run duration. Too much boundary effects, we should reduce speed again…
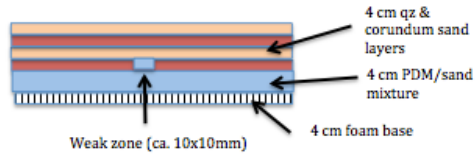
EXP538
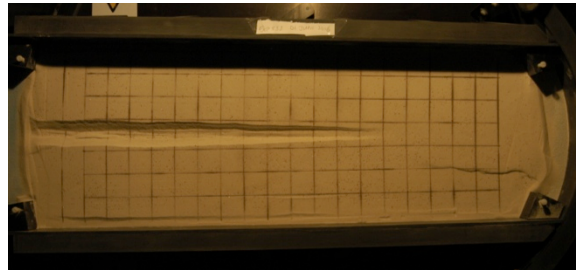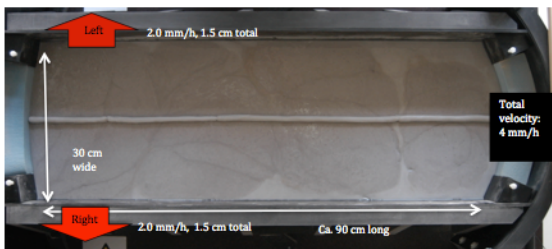
Rerun of model EXP537, but with a higher speed (but not too high) to avoid long model runs.
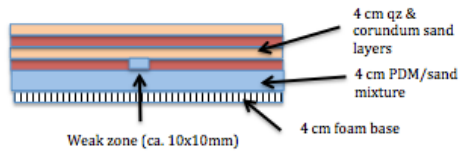
EXP539
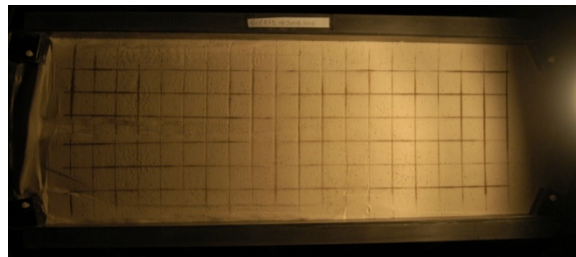
Rerun of models with thick layering, but with a lower speed to avoid boundary effects. Total velocity: 1.6 mm/h. The results are a bit strange.
Somehow less deformation in the center, where we would expect more localization. There is an additional graben structure like in the v = 3 mm/h model. This is quite counter-intuitive. Maybe the silicone is getting too viscous or so after reusing it?
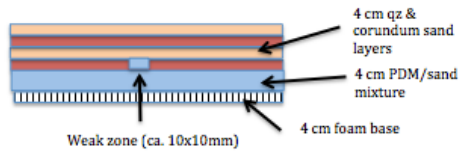
EXP540 (CT-scanned)
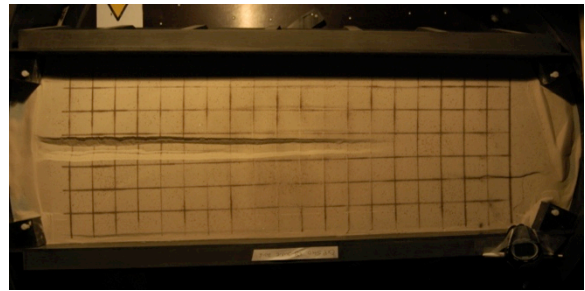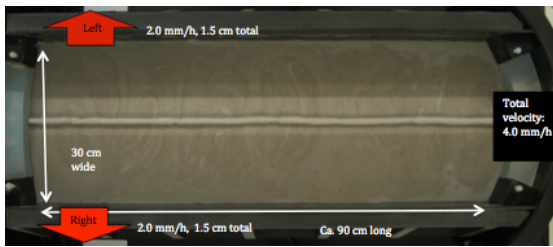
Rerun of model EXP538 in the CT-scanner. At t = 120 min, the machine was halted for 30 min due to unknown reasons. The stopwatch timing is therefore 30min ahead from that point on. We also have a double scan of t = 120 min due to this
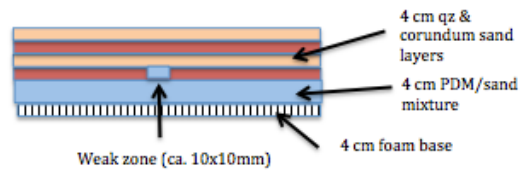
EXP573
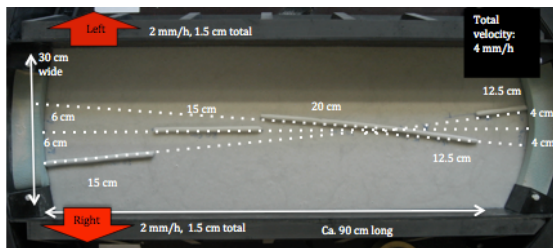
Model with multiple offsets. Mostly boundary effects, we should probably have an all-foam base
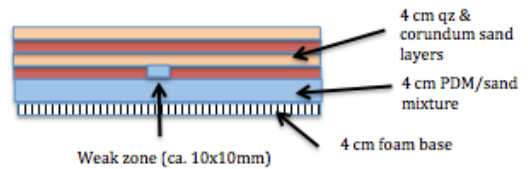
EXP576
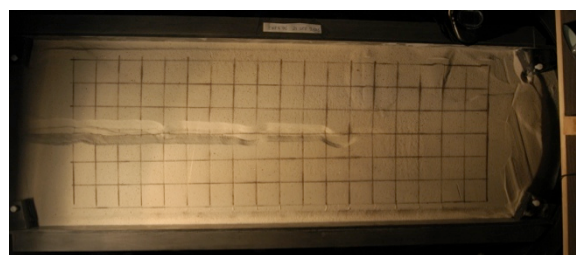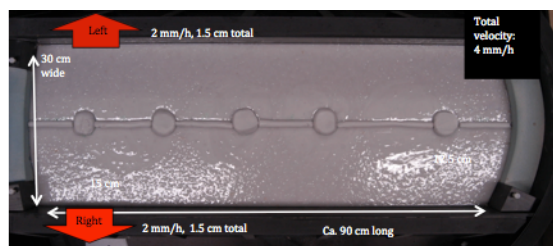
One central seed, additional blobs that could represent magma bodies along the rift

293
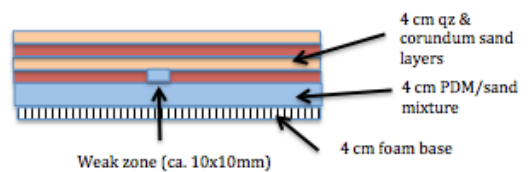
Series 8. Xissor model tests B
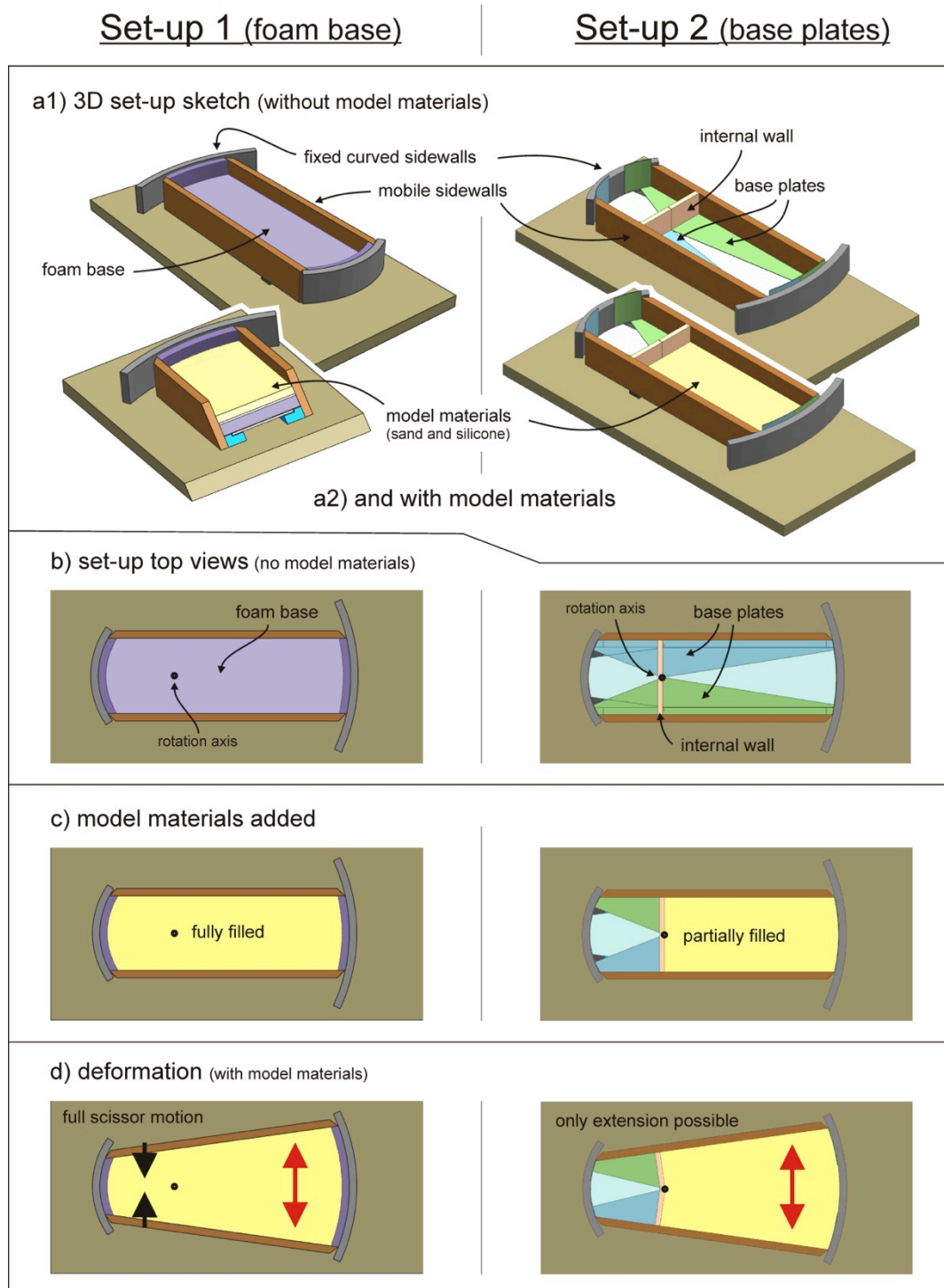
Overview of set-ups allowed by the Xissor experimental apparatus with left the foam base option and right the base plate option. (a) 3D sketch of the machine without (a1) and with model materials (a2). (b-c) Top views of the machine (b) with model materials and (c) without model materials (c). (d) Top view indication the rotational motion about the rotation axis and the resulting scissor deformation of the model materials. Note that the rigid plastic blacks are removed in these foam base set-ups used for the models presented in this section and Chapters 6 and 7. The base plate set-up has not been tested to date.

EXP578
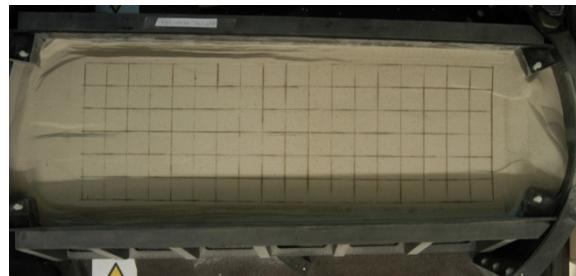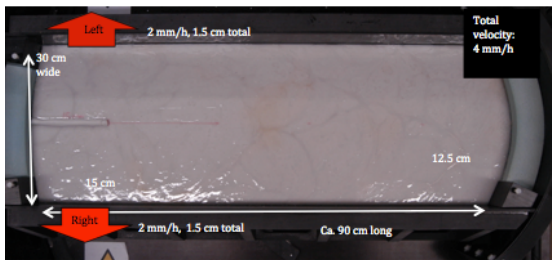
Rift propagation model. One small seed to initiate rifting and let it propagate. **New full foam base (4 cm thick) to avoid boundary effects,** 4 cm total extension possible. Slight localization, mostly boundary effects along the sides…
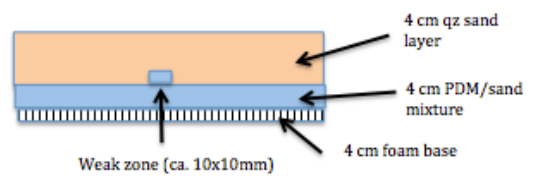
EXP582
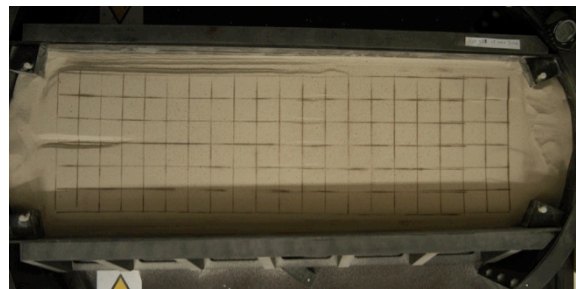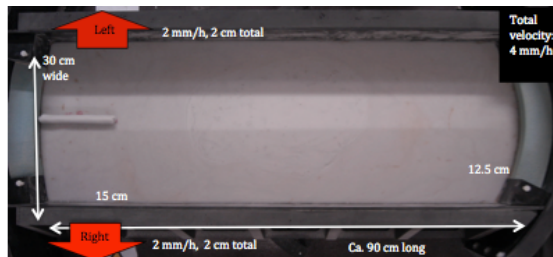
Rift propagation model. One small seed to initiate rifting and let it propagate. We tried a thicker seed (1.5 cm diameter). Slight localization, mostly boundary effects along the sides…. Bit of propagation. Proper lighting remains problematic.
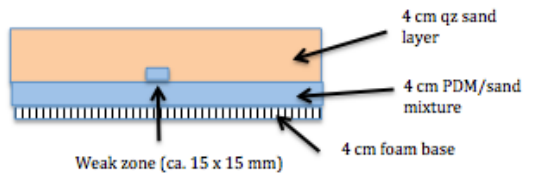
EXP584
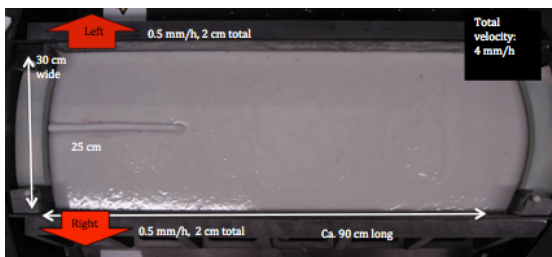
Rift propagation model. One small seed to initiate rifting and let it propagate. We tried a thicker seed: 1.5 cm diameter, 25 cm long.
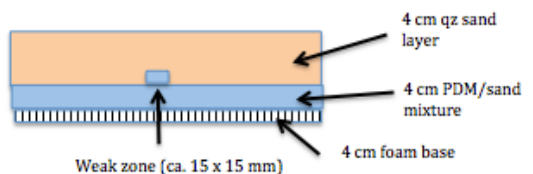
EXP589
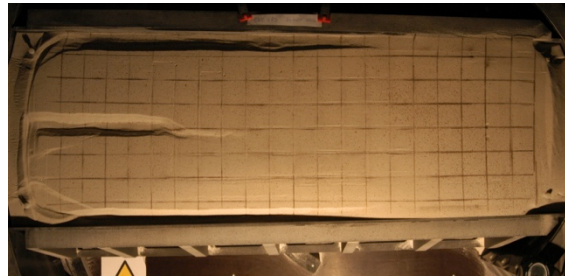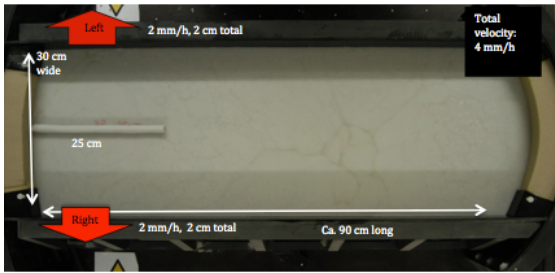
Model with new foam base (GOBAG hard foam) 8 cm thick (used for all subsequent models), no coating on top of the foam. Seed 25 cm long, ø 1.5 cm. 5 cm PDMS/sand, 5.5 cm sand. Localization along the seed, but lots of boundary effects. A bit of rift propagation occurs.
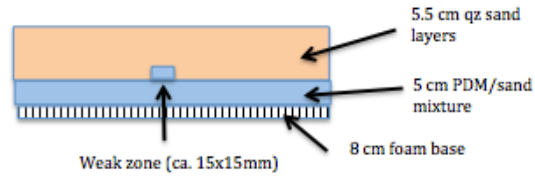
EXP591
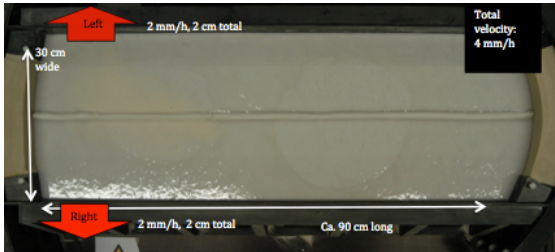
Model with new foam base (GOBAG hard foam) 8 cm thick, no coating. Continuous seed, ø 1.5 cm. 5 cm PDMS/sand, 5.5 cm sand. Localization along the seed. Little boundary effects. Wide rift structure, maybe due to scraping?
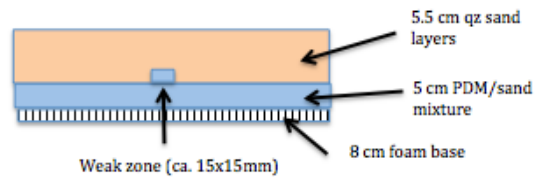
EXP595
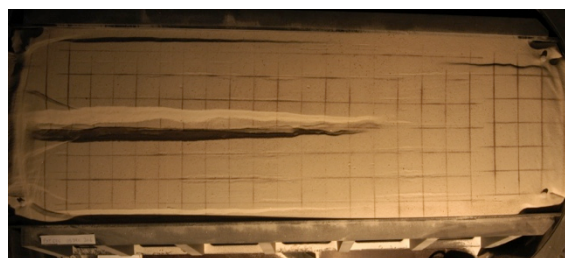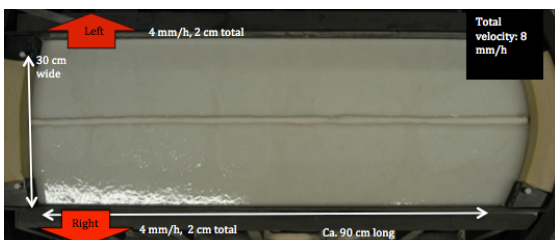
Model with new foam base (GOBAG hard foam) 8 cm thick, no coating. Continuous seed, ø 1.5 cm. 5 cm PDMS/sand, 5.5 cm sand. new speed, duration: 5h. Localization along the seed. Little boundary effects. Nice rift structure, higher speeds seem to work OK
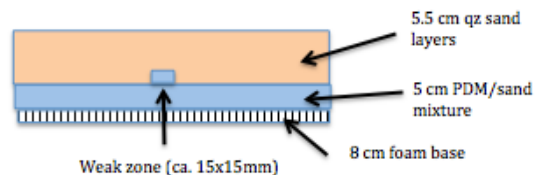
EXP598
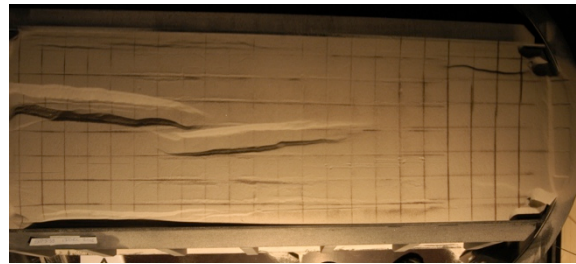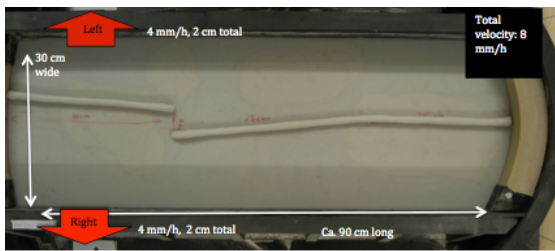
5 cm PDMS/sand, 5.5 cm sand. rift offset model, staircase offset seed, ø 1.5 cm. 4 cm offset at 35 cm from rotation axis. Localization along the seed. Little boundary effects. Nice rift structure, no linkage! But the rifts grow towards each other. Maybe more extension will cause connection?
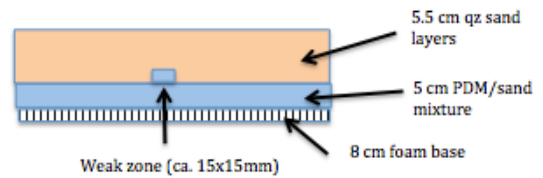
EXP600
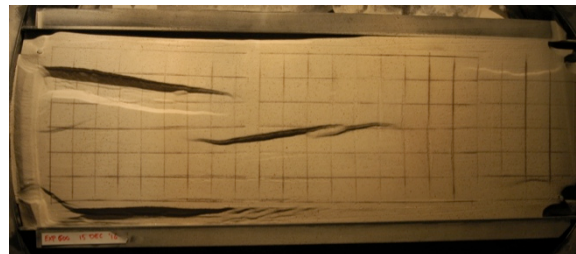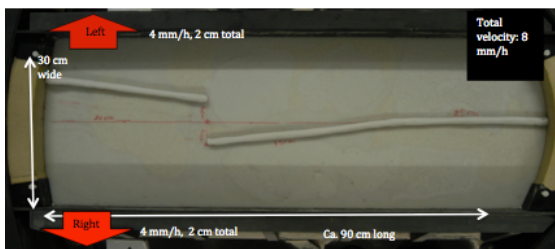
5 cm PDMS/sand, 5.5 cm sand. Rift offset model, staircase offset seed, ø 1.5 cm, 8 cm offset at 35 cm from rotation axis.
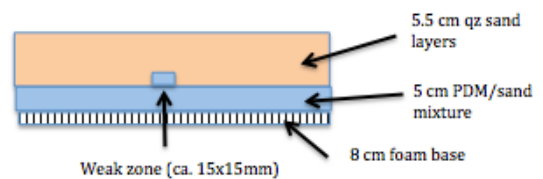
EXP626
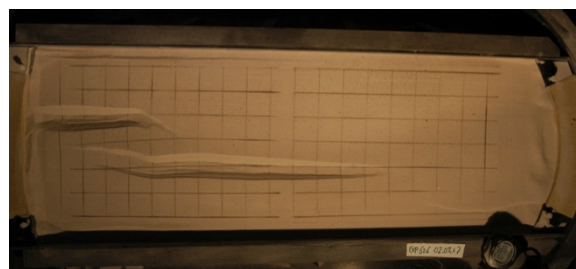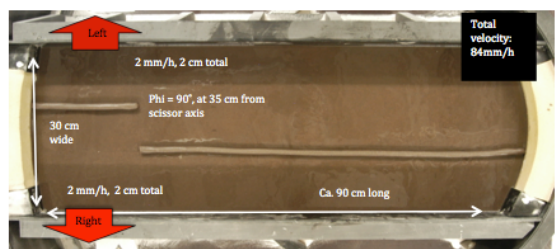
rift offset model, staircase offset seed, ø 1 cm
8 cm offset at 45 cm from rotation axis. Localization along the seed, Little boundary effects Nice rift structure, no linkage.
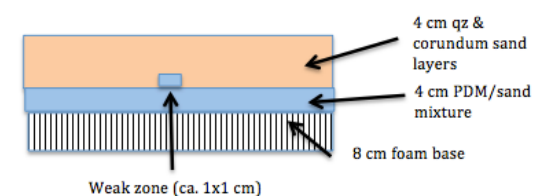
EXP627
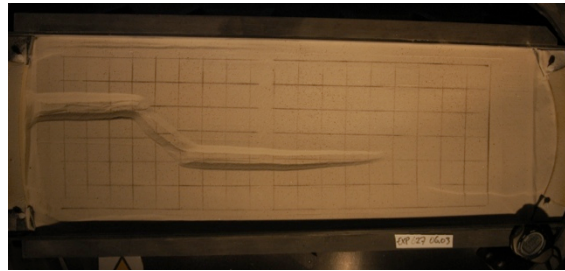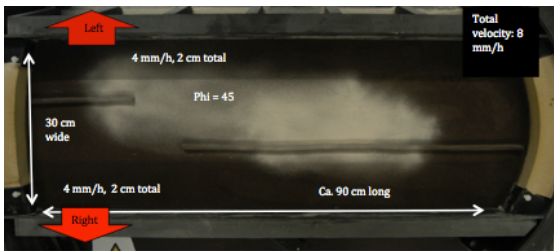
rift offset model, staircase offset seed, ø 4 cm. phi = 45˚ offset, 8 cm offset, 20 cm from model end. Localization along the seed. Little boundary effects. Nice rift structure, linkage.
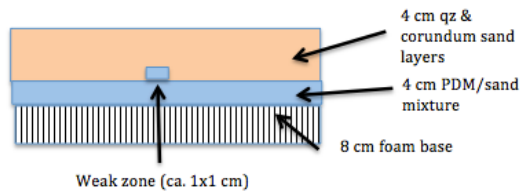
EXP643
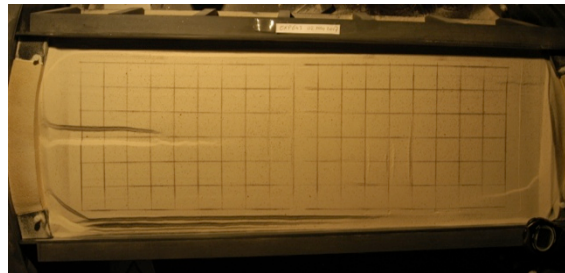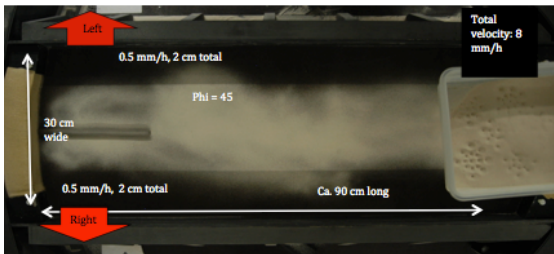
4 cm PDMS/sand, 4 cm sand. Rerun of rifprop models with small seed, 25 cm from model end very slow extension
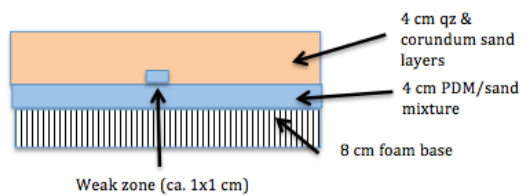
Series 9. Rift propagation models (Chapter 5)
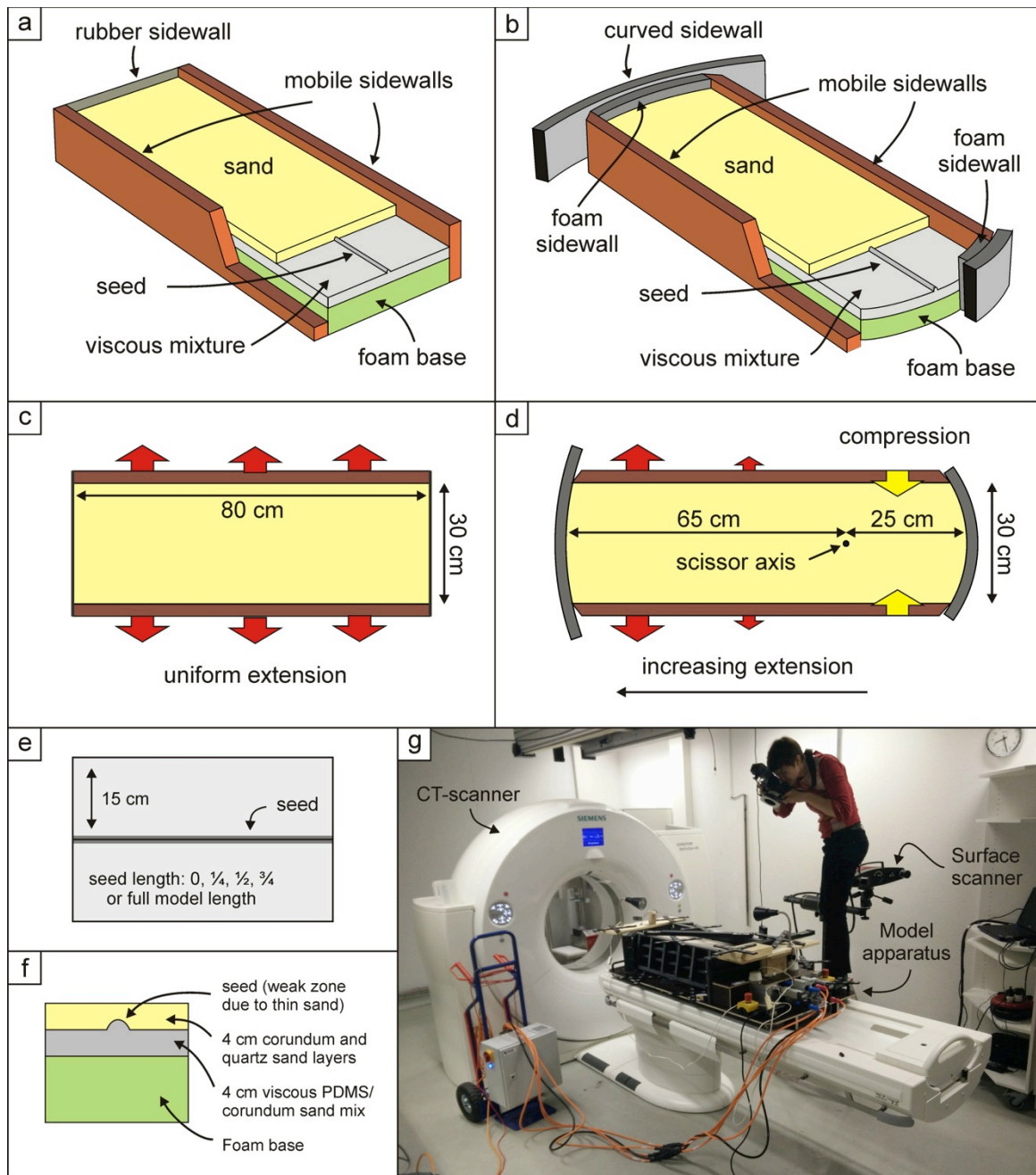
General model set-up of models from series 7 (Chapter 5). (a) 3D set-up for the orthogonal extensional models. (b) 3D set-up for the scissor extensional models. (c) Top view depicting orthogonal extension deformation. (d) Top view illustrating scissor extension deformation. (e) Seed geometries. (f) Model layering. (g) example of a model (M13) scanned with XRCT and surface scanning techniques (photo by Jakub Fedorik).

EXP540 – Model M1 (Scissor extension, CT-scanned)
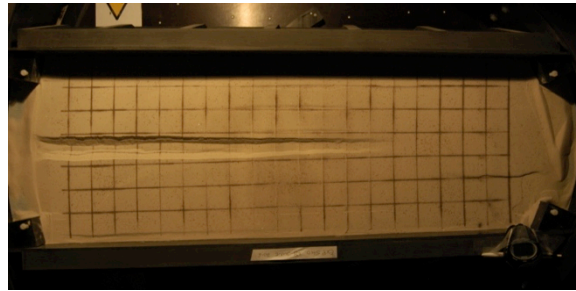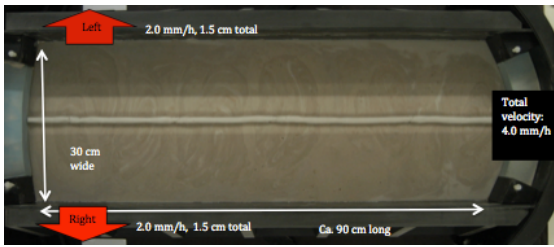
Rerun of model EXP538 in the CT-scanner (old set-up, see Series 7). At t = 120 min, the machine was halted for 30 min due to unknown reasons. The stopwatch timing is therefore 30min ahead from that point on. We also have a double scan of t = 120 min due to this
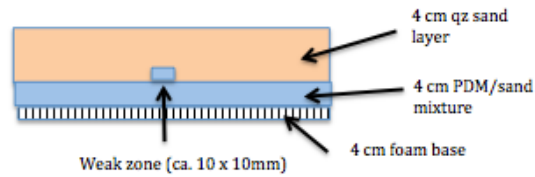
EXP654 (Scissor extension, not included in Chapter 5)
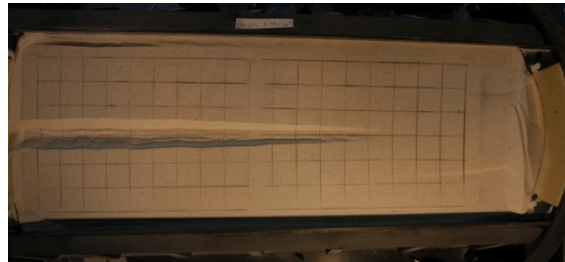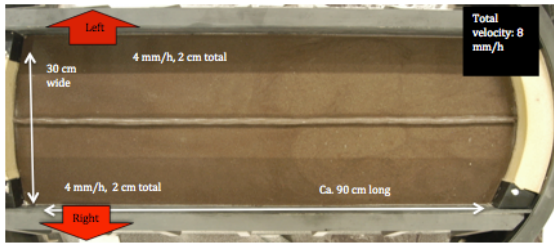
New set-up (see EXP657) continuous seed, ø 1cm. Computer halted, no photos between ca. 1h -5h. Rerun! Don't use previous models (different seed diameter and sand thickness!). Rift propagation!

EXP657 – Model M5 (Orthogonal extension)
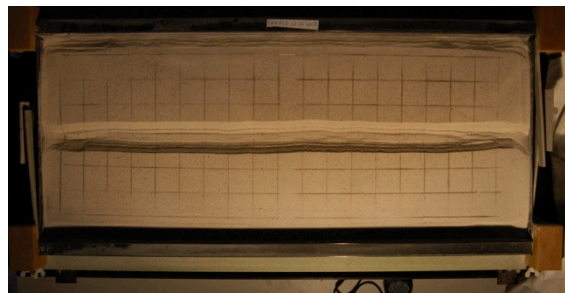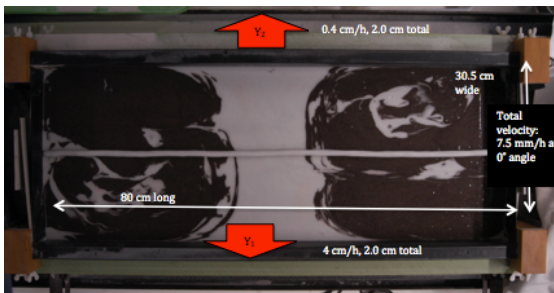
Rerun of previous models with new GOBAG foam base. Otherwise, same conditions (underlap/ overlap, 8 cm offset., 8mm/h extension). Continuous seed. Something went wrong: first 1.5 hour, one of the sidewalls was moving towards the center, causing a translation without visible deformation at the odel surface. In a second phase, the model was extended properly. Nice, continuous rift with Lower Crustal extrusion.
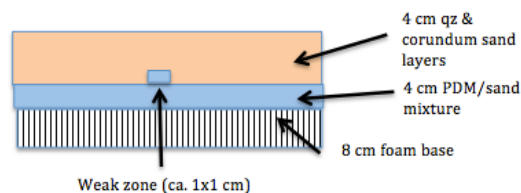
Layering used in all subsequent models in this series.

EXP658 – Model M11 (Scissor extension)
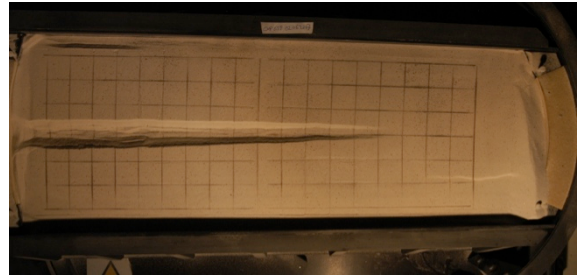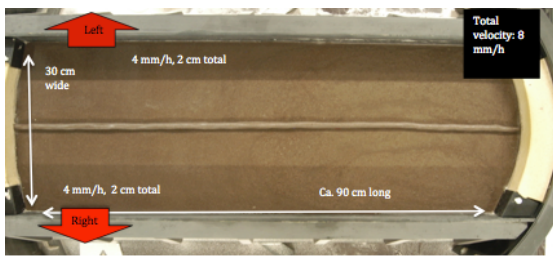
4 cm PDMS/sand, 4 cm sand. Continuous seed, ø 1 cm. Rerun of EXP645 because the camera stopped during that model run. Rift propagation occurs.

EXP661 – Model M6 (Orthogonal extension, CT-scanned)
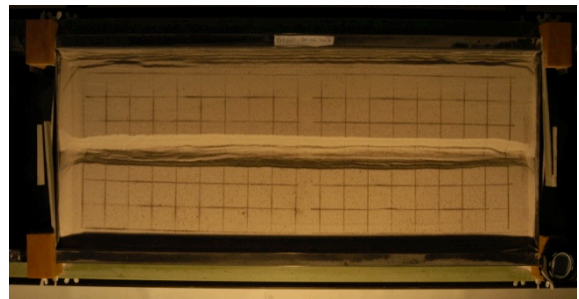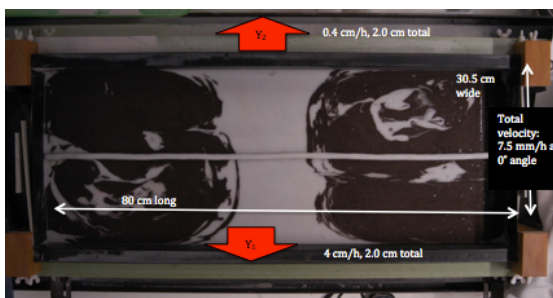
Rerun of EXP657 (continuous seed) in CT scanner. Nice, continuous rift with Lower Crustal extrusion.

EXP666 – Model M12 (Scissor extension, CT-scanned)
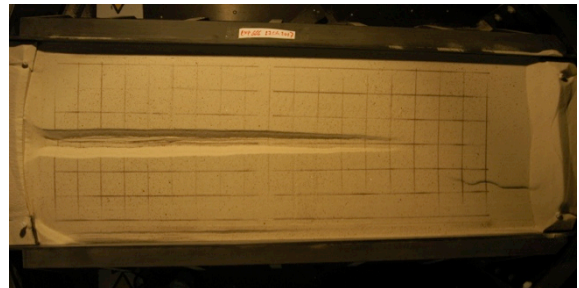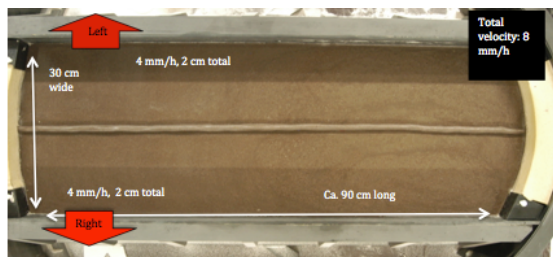
Rerun of EXP 658 in the CT scanner. Rift propagation occurs.

EXP678 – Model M1 (Orthogonal extension)
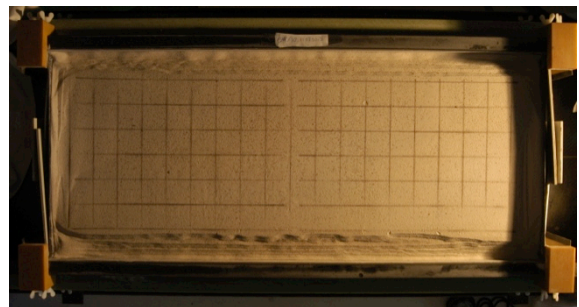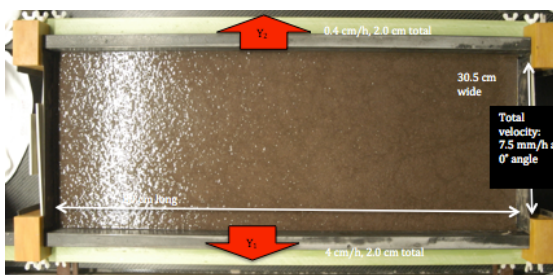
No seed (benchmark).

EXP679 – Model M7 (Scissor extension)
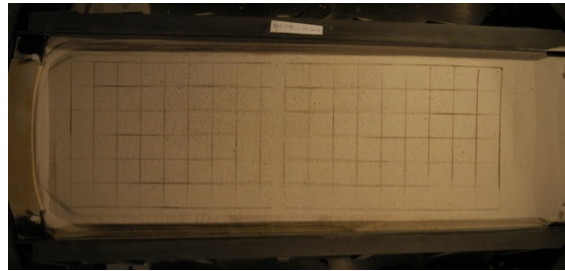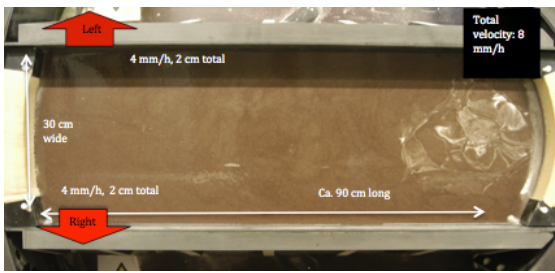
No seed as benchmark model. Mostly boundary effects, as expected. Camera halted at 180 min, so last 2 hours are missing (no big problem)

EXP680 – Model M3 (Orthogonal extension)
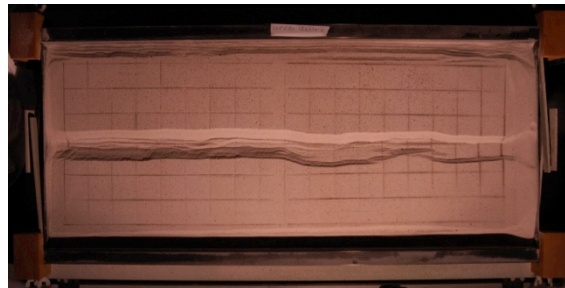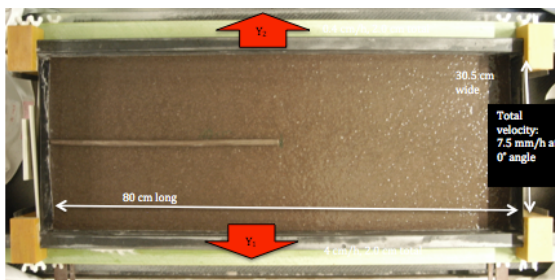
½ seed (40 cm long), Rift propagation!

EXP681 – Model M2 (Orthogonal extension)
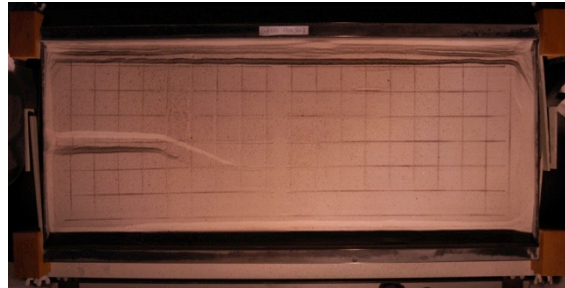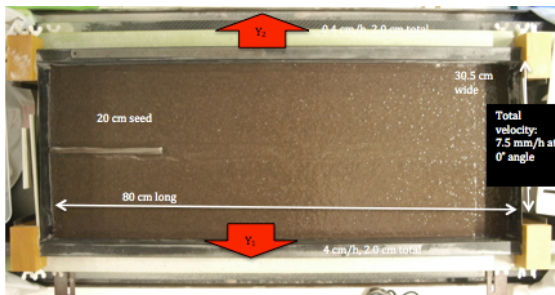
¼ seed (20 cm long), Bit of rift propagation.

EXP682 – Model M8 (Scissor extension)
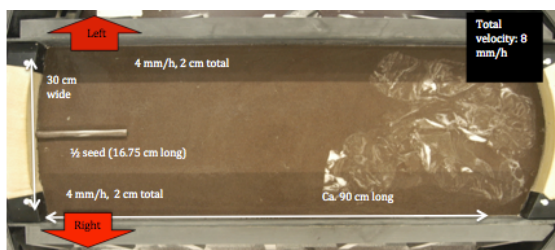
¼ seed (16.75 cm long).

EXP683 – Model M4 (Orthogonal extension)
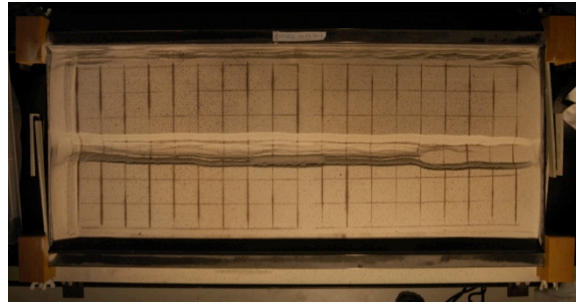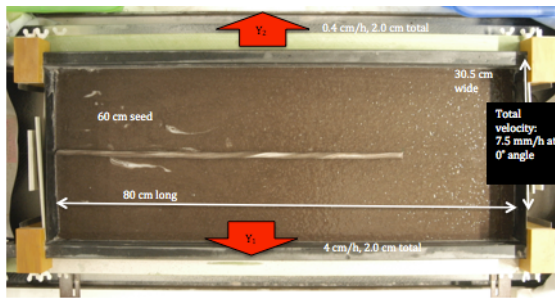
3/4 seed (60 cm long), Bit of rift propagation.

EXP684 – Model M9 (Scissor extension)
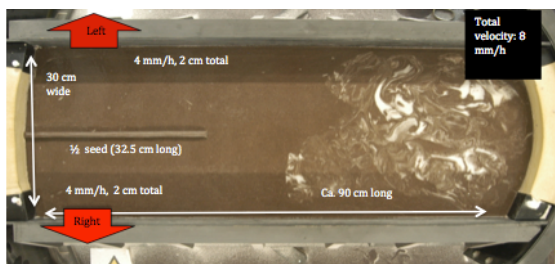
½ seed (32.5 cm long)

EXP685 – Model M10 (Scissor extension)
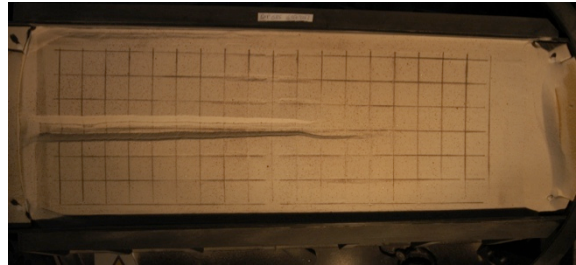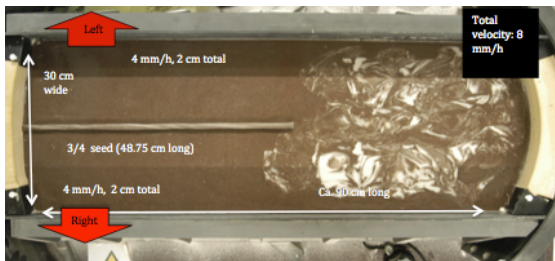
3/4 seed (48.75 cm long)

Series 10. Scissor extension rift linkage models (Chapter 6)
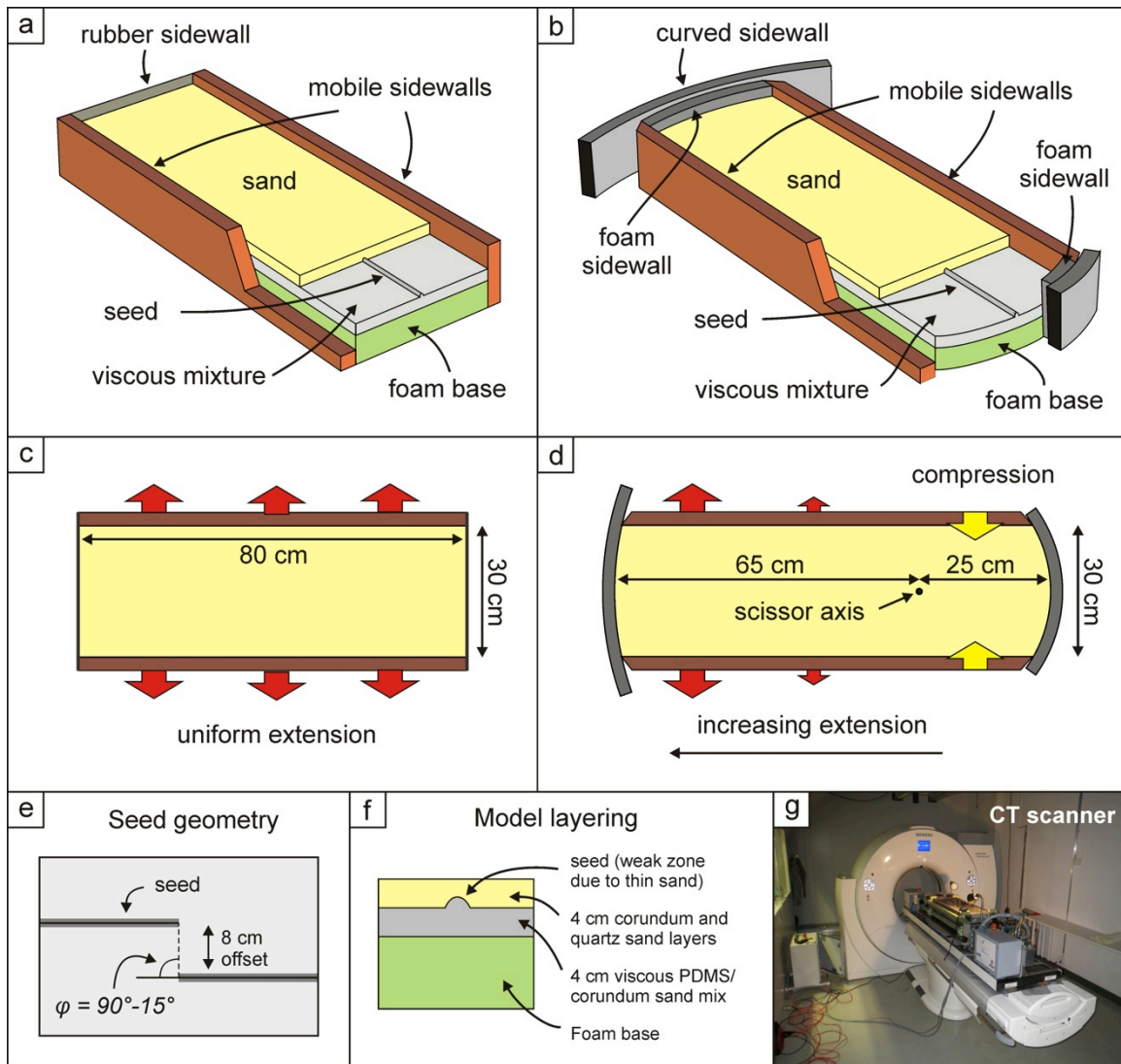
Fig. 6.2. *Model set-up. (a-b) Cut-out views of the normal extension apparatus (a) and scissor extension apparatus (b), depicting their various components. (c-d) Top views of the deformation applied in the normal extension set-up (c) and the scissor extension set-up (d). (e) Seed geometry definition. Angle φ is the angle between the seed strike and the horizontal line connecting the two seed tips, ranging between 90° and 15° in this paper. (f) Model layering, showing the brittle-ductile parts of the models, on top of the foam base, as well as the seed. (g) Example of a model run in the CT scanner.*

EXP631 – Model S17 (S: Scissor extension set-up)
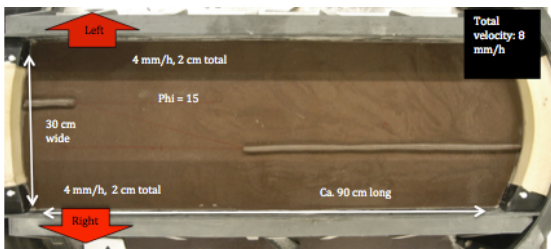
Rift offset model, staircase offset seed, ø 4 cm, phi = 15° offset, 8 cm offset, **centre of offset: 25 cm** from model end. Localization along left sees, mostly boundary effects though…

EXP634 – Model S3
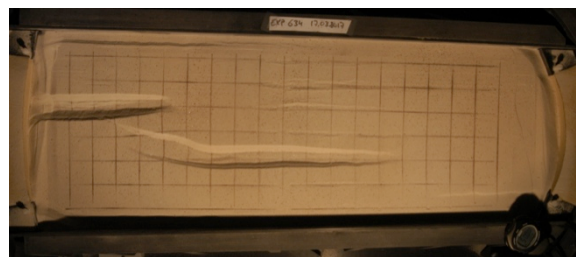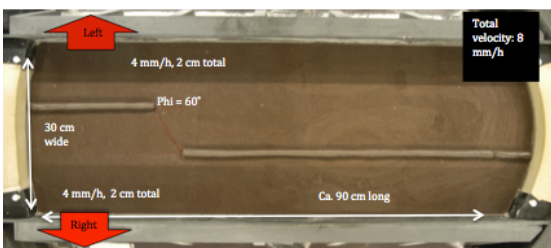
Rift offset model, staircase offset seed, ø 4 cm, phi = 60° offset, 8 cm offset, **centre of offset: 25 cm** from model end. Good localization, rifts grow towards each other.

EXP635 – Model S8
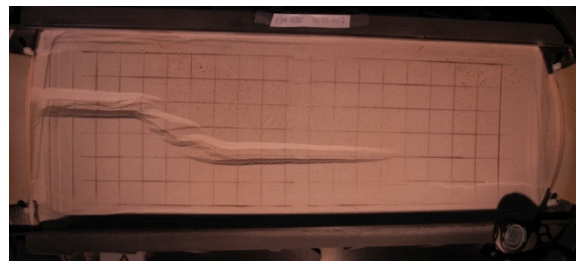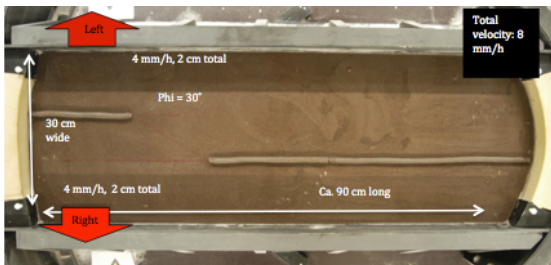
Rift offset model, staircase offset seed, ø 4 cm, phi = 30° offset, 8 cm offset, **centre of offset: 25 cm** from model end. Interesting rift interaction, with en echelon structures.

EXP636 (not included in Chapter 6)
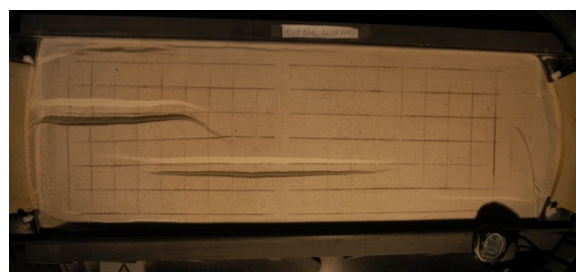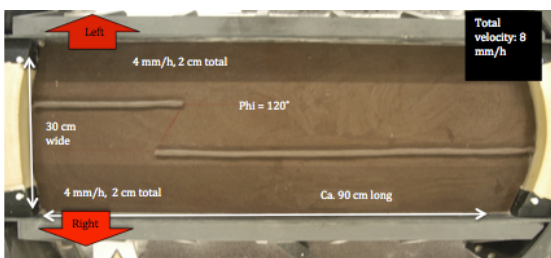
Rift offset model, staircase offset seed, ø 4 cm, phi = 120° offset, 8 cm offset, **centre of offset: 25 cm** from model end. No connection.

EXP637 (not included in Chapter 6)
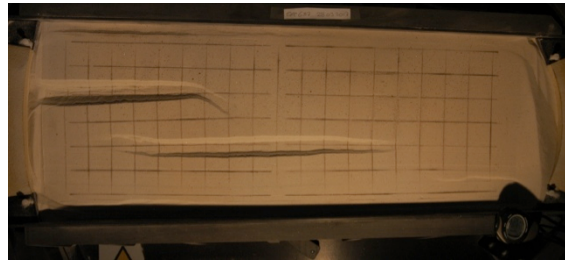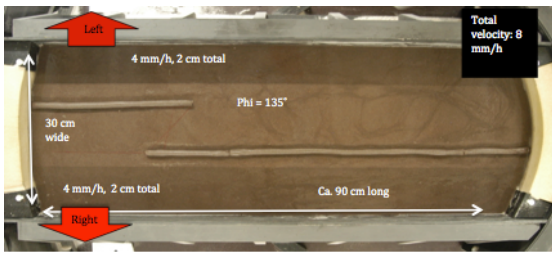
Rift offset model, staircase offset seed, ø 4 cm, phi = 135˚ offset, 8 cm offset, **centre of offset: 25 cm** from model end. No connection.

EXP638 – Model S17
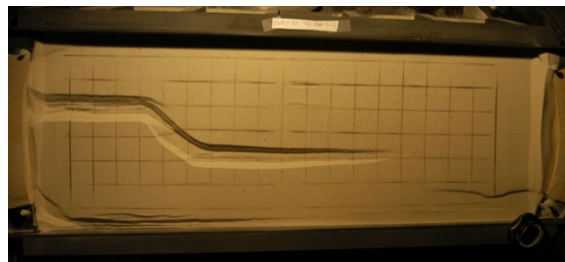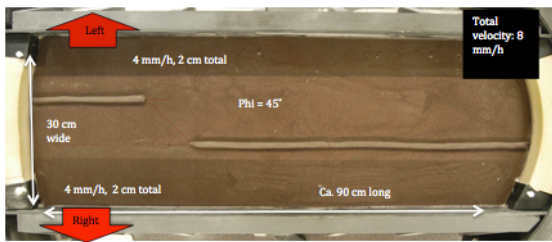
Rift offset model, staircase offset seed, ø 4 cm, phi = 45˚ offset, 8 cm offset, **centre of offset: 25 cm** from model end.

EXP639 – Model S6
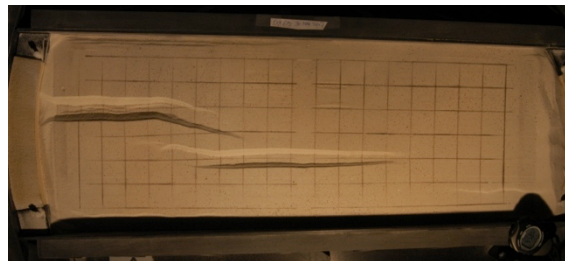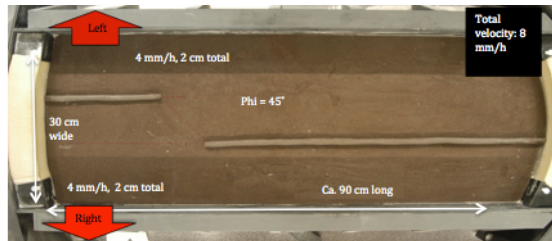
Rerun of EXP638! Rift offset model, staircase offset seed, ø 4 cm, phi = 45˚ offset, 8 cm offset, **centre of offset: 25 cm** from model end. No connection, probably phi is a bit to high (seeds not properly placed) ➔ run phi = 40˚ and 50˚ models to test

EXP640 – Model S1
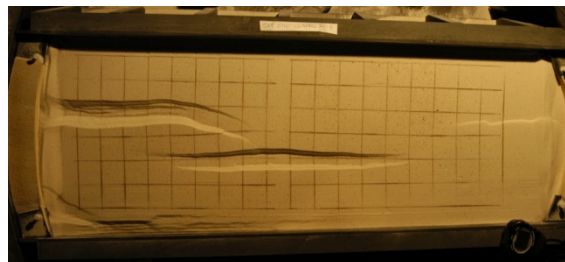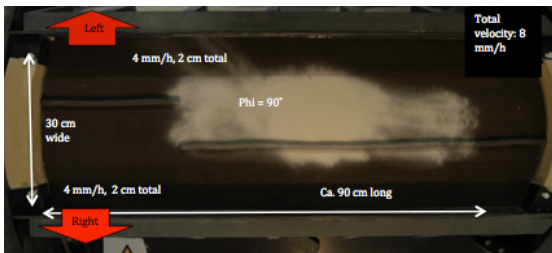
Rift offset model, staircase offset seed, ø 4 cm, phi = 90˚ offset, 8 cm offset, **centre of offset: 25 cm** from model end.

EXP641 – Model S4
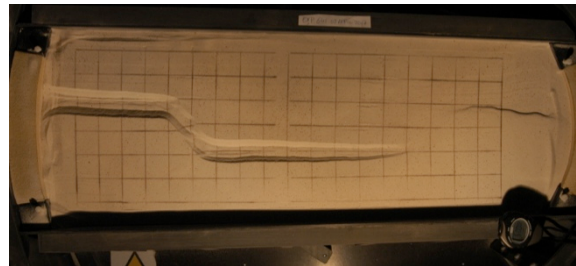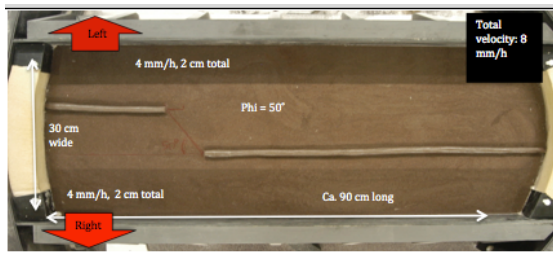
Rift offset model, staircase offset seed, ø 4 cm, phi = 50° offset, 8 cm offset, **centre of offset: 25 cm** from model end. Idea that there should be no connection, but it still occurred… (see EXP639)

EXP642 – Model S7
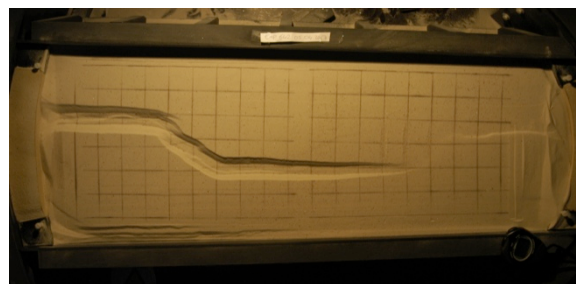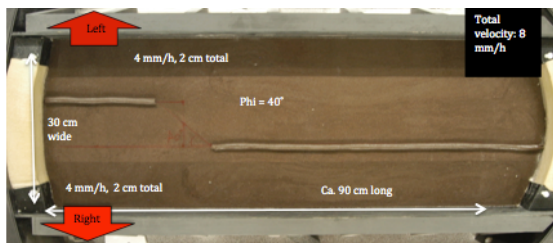
Rift offset model, staircase offset seed, ø 4 cm, phi = 40° offset, 8 cm offset, **centre of offset: 25 cm** from model end.

EXP644 – Model O5 (O: Orthogonal extension set-up)
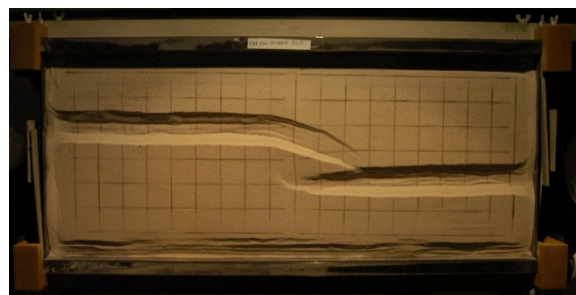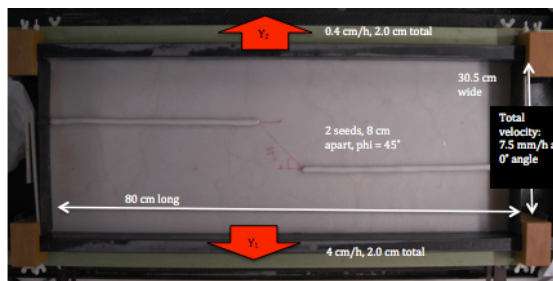
Rift offset model, staircase offset seed, ø 4 cm, phi = 45° offset, 8 cm offset, **centre of offset: 25 cm** from model end. Nice localization, little boundary effects, rifts grow a bit towards each other. Similar results as Le Calvez (same set-up basically). Quite some boundary effects though… might be problematic…

EXP645 – Model O10
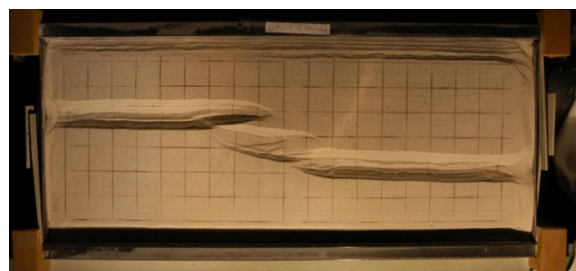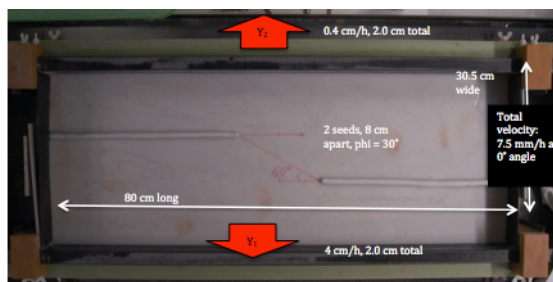
Rift offset model, staircase offset seed, ø 4 cm, phi = 30° offset, 8 cm offset, **centre of offset: 25 cm** from model end. Nice localization, little boundary effects, rifts grow a bit towards each other. We got a en echelon rift structure!

EXP646 – Model O12
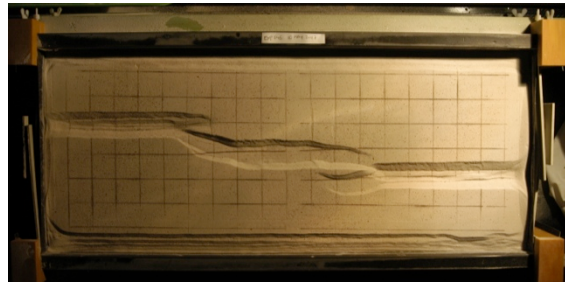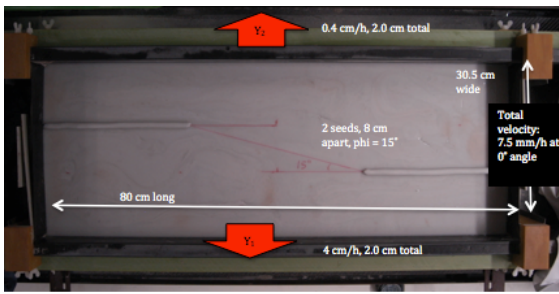
Rift offset model, staircase offset seed, ø 4 cm, phi = 15˚ offset, 8 cm offset, **centre of offset: 25 cm** from model end. Nice localization, little boundary effects, rifts grow a bit towards each other. We got a en echelon rift structure!

EXP647 – Model O3
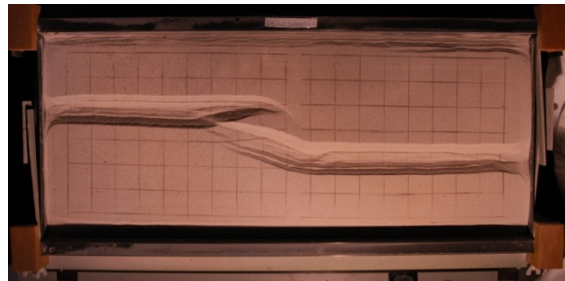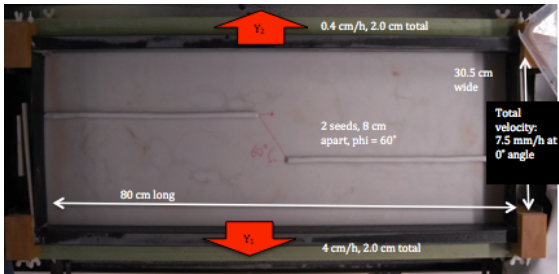
Rift offset model, staircase offset seed, ø 4 cm, phi = 60˚ offset, 8 cm offset, **centre of offset: 25 cm** from model end. Nice localization, little boundary effects, rifts grow a bit towards each other. No Transfer zone After the model end, the silicone below the rift continued rising and almost extruded

EXP648 – Model S16
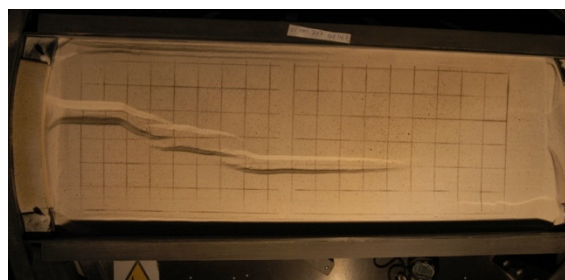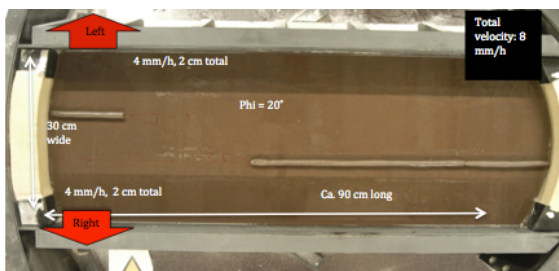
Staircase offset seed, ø 4 cm, phi = 20˚ offset, 8 cm offset, **centre of offset: 25 cm** from model end.

EXP649 – Model O6
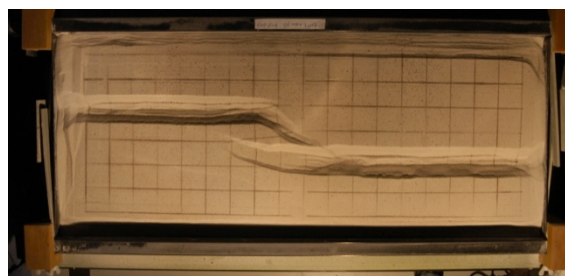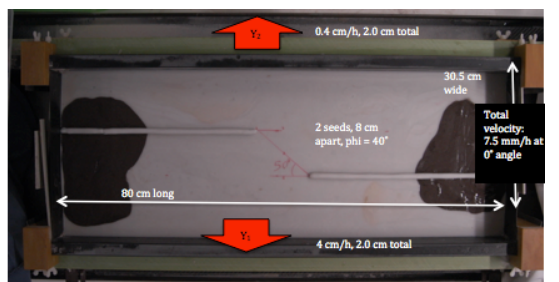
rift offset model, staircase offset seed, ø 4 cm, phi = 40˚ offset, 8 cm offset, **centre of offset: 25 cm** from model end. Nice localization, little boundary effects, rifts grow a bit towards each other.
No Transfer zone? There is a continuous connection! (see removed sand picture!)

EXP650 – Model O11
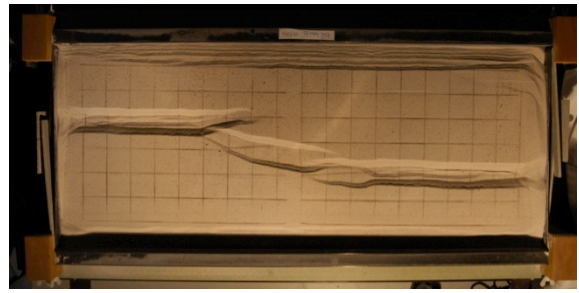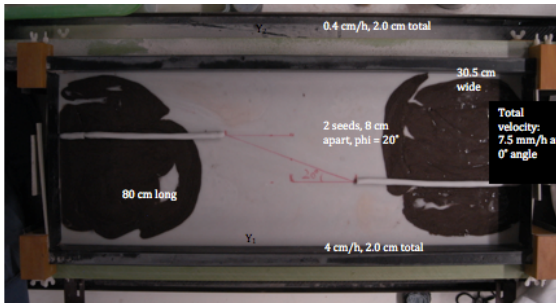
Rift offset model, staircase offset seed, ø 4 cm, phi = 20° offset, 8 cm offset, **centre of offset: 25 cm** from model end.

EXP651 – Model O1
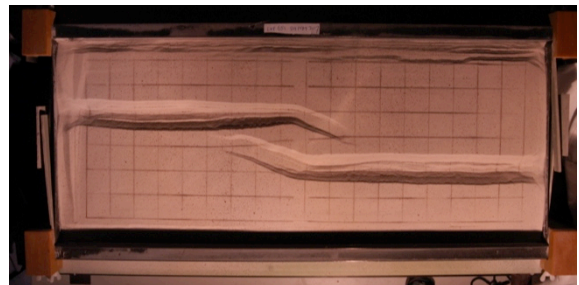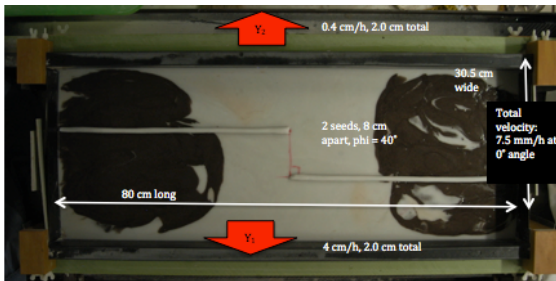
Rift offset model, staircase offset seed, ø 4 cm, phi = 90° offset, 8 cm offset, **centre of offset: 25 cm** from model end. Nice localization, little boundary effects, rifts grow a bit towards each other.

EXP652 – Model S2
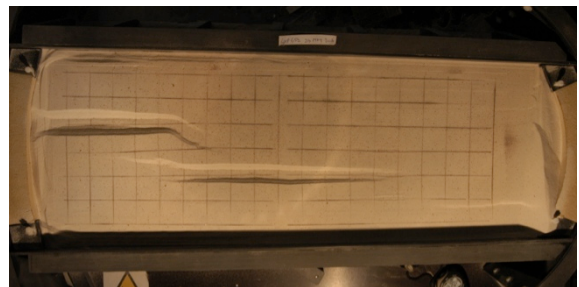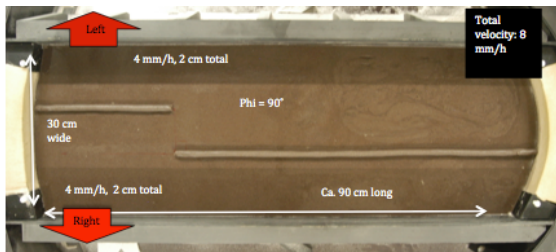
Rift offset model, staircase offset seed, ø 4 cm, phi = 90° offset, 8 cm offset, **centre of offset: 25 cm** from model end. No transfer zone.

EXP653 – Model O2
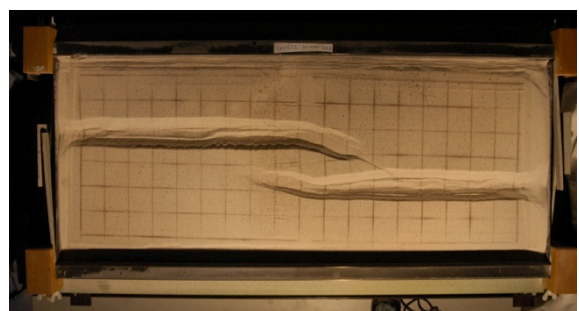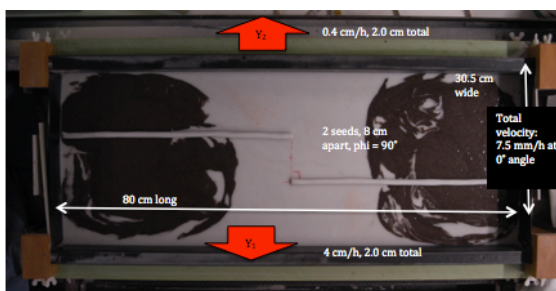
Rift offset model, staircase offset seed, ø 4 cm, phi = 90° offset, 8 cm offset, **centre of offset: 25 cm** from model end. Nice localization, little boundary effects, rifts grow a bit towards each other.

EXP655 – Model O4
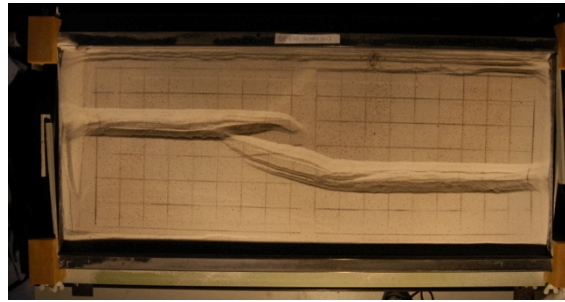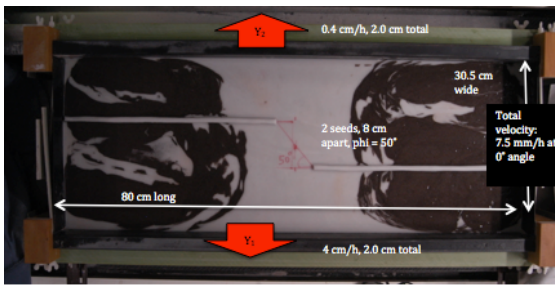
Rift offset model, staircase offset seed, ø 4 cm, phi = 50˚ offset, 8 cm offset, **centre of offset: 25 cm** from model end. Nice localization, little boundary effects, rifts grow a bit towards each other. Note the different angle the connecting structure has in the transfer zone.

EXP656 – Model O7
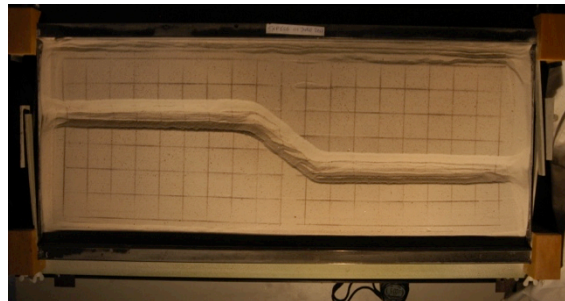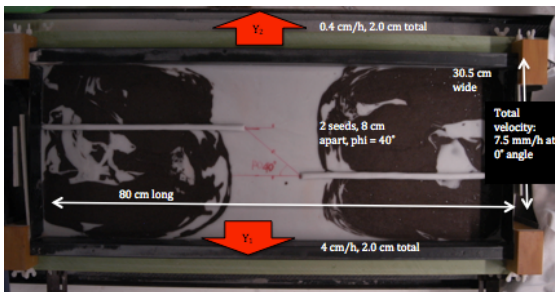
Rift offset model, staircase offset seed, ø 4 cm, phi = 40˚ offset, 8 cm offset, **centre of offset: 25 cm** from model end. Nice localization, little boundary effects, rifts grow together in a continuous transfer zone.

EXP659 – Model O9 (CT-scanned)
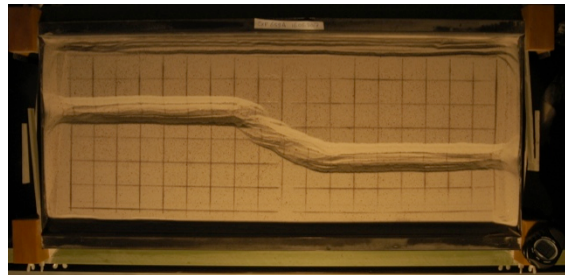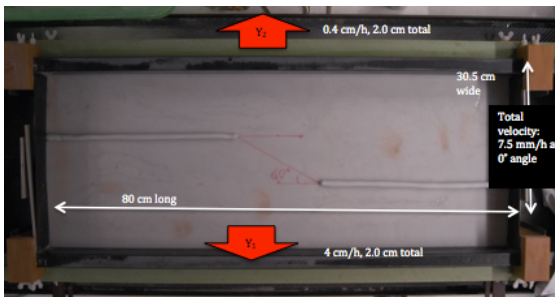
Rift offset model, staircase offset seed, ø 4 cm, phi = 30˚ offset, 8 cm offset, **centre of offset: 25 cm** from model end.

EXP662 – Model S10 (CT-scanned)
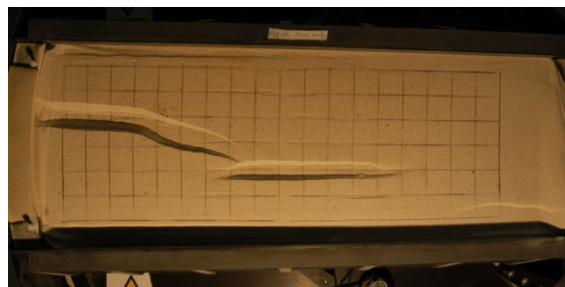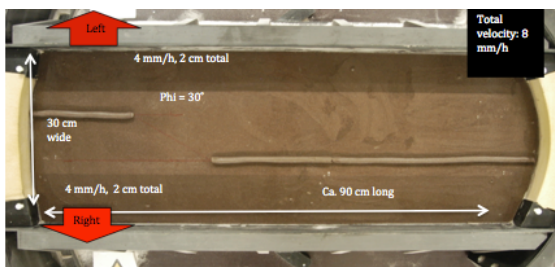
Rift offset model, staircase offset seed, ø 4 cm, phi = 30˚ offset, 8 cm offset, **centre of offset: 25 cm** from model end.

EXP663 – Model O8
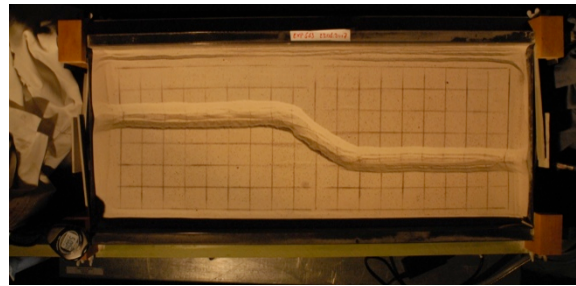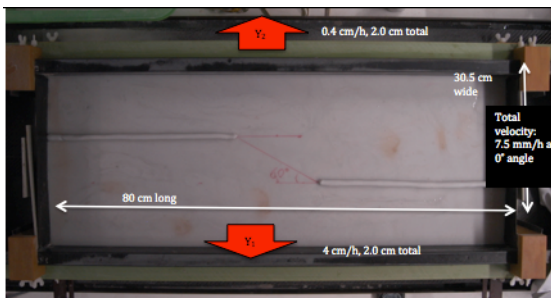
Rift offset model, staircase offset seed, ø 4 cm, phi = 30° offset, 8 cm offset, **centre of offset: 25 cm** from model end. Rerun of EXP635.

EXP664 – Model S9
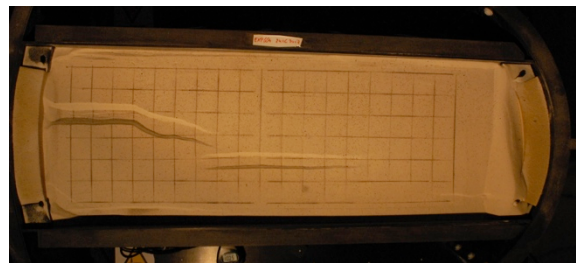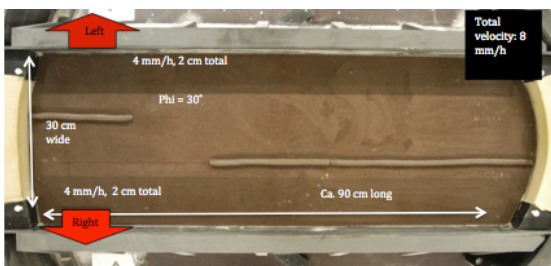
Rift offset model, staircase offset seed, ø 4 cm, phi = 30° offset, 8 cm offset, **centre of offset: 25 cm** from model end. Rerun of EXP635 and EXP662.

EXP669 – Model S11
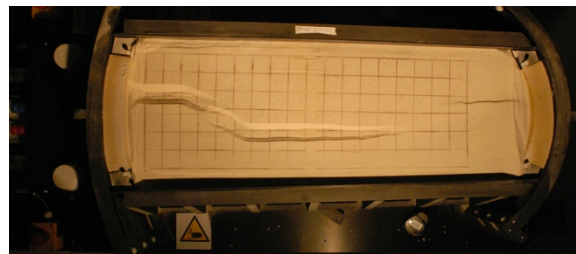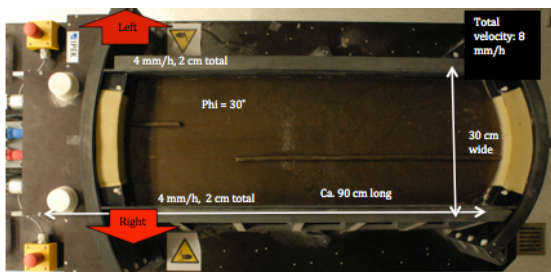
Rift offset model, staircase offset seed, ø 4 cm, phi = 30° offset, 8 cm offset, **centre of offset: 20 cm** from model end. Rerun of EXP635, EXP662 and EXP664 with a slightly different centre of offset (20 cm instead of 25) to test the problem we encountered before. Better result!

EXP671 – Model S12
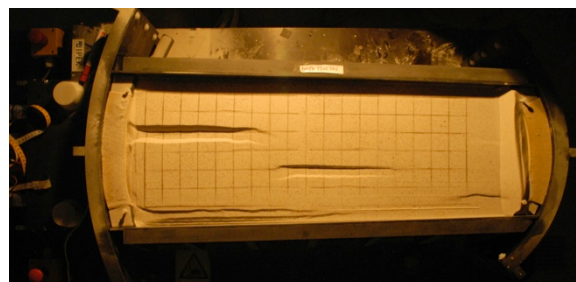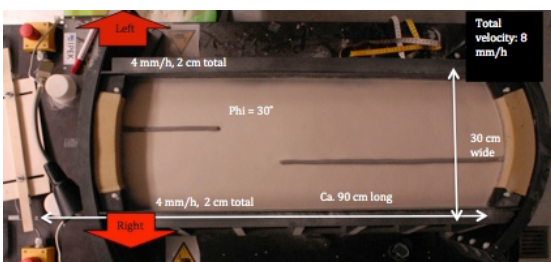
Rift offset model, staircase offset seed, ø 4 cm, phi = 30° offset, 8 cm offset, **centre of offset: 30 cm** from model end. Rerun of EXP635, EXP662, EXP664 and EXP669 with a slightly different centre of offset (30 cm instread of 25) to test the problem we encountered before. Seems like moving the centre of offset towards the scissor axis hinders rift linkage

EXP672 – Model S13
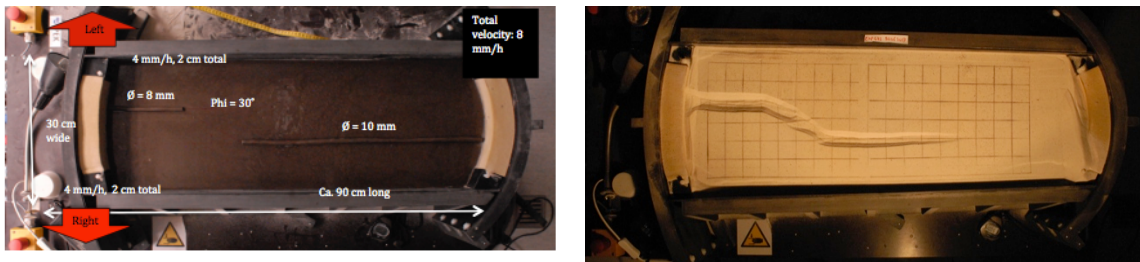
Rift offset model, staircase offset seed, ø 4 cm, phi = 30˚ offset, 8 cm offset, **centre of offset: 25 cm** from model end. Schort seed ø 8 mm, long seed 10 mm (for localization). Works well!

EXP673 – Model S14
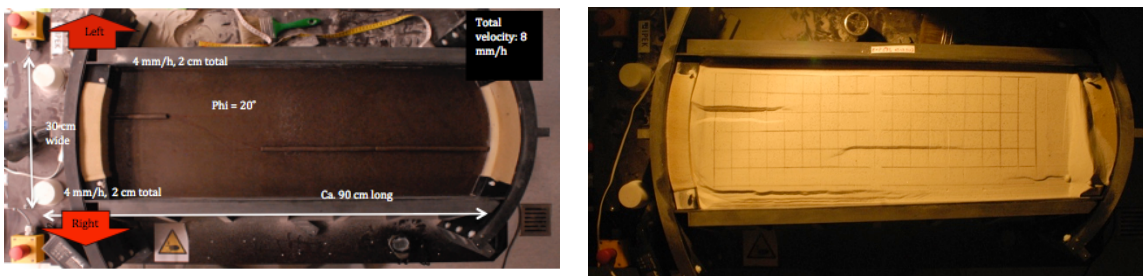
Rift offset model, staircase offset seed, ø 4 cm, phi = 20˚ offset, 8 cm offset, **centre of offset: 25 cm** from model end. Rerun of EXP648. No connection… poor localization along seed close to axis

EXP676 – Model S15 (CT-scanned)
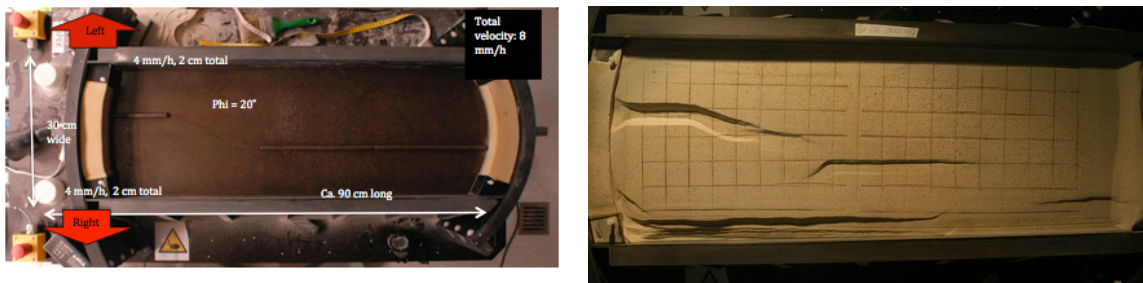
Rift offset model, staircase offset seed, ø 4 cm, phi = 20˚ offset, 8 cm offset, **centre of offset: 25 cm** from model end. No connection… poor localization along seed close to axis. Seed closer to the axis is thicker (10 mm) than the other (8 mm). Late activation of the thick seed… still and interesting structure in the end.

Series 11. Extension set-up comparison models (Chapter 7)
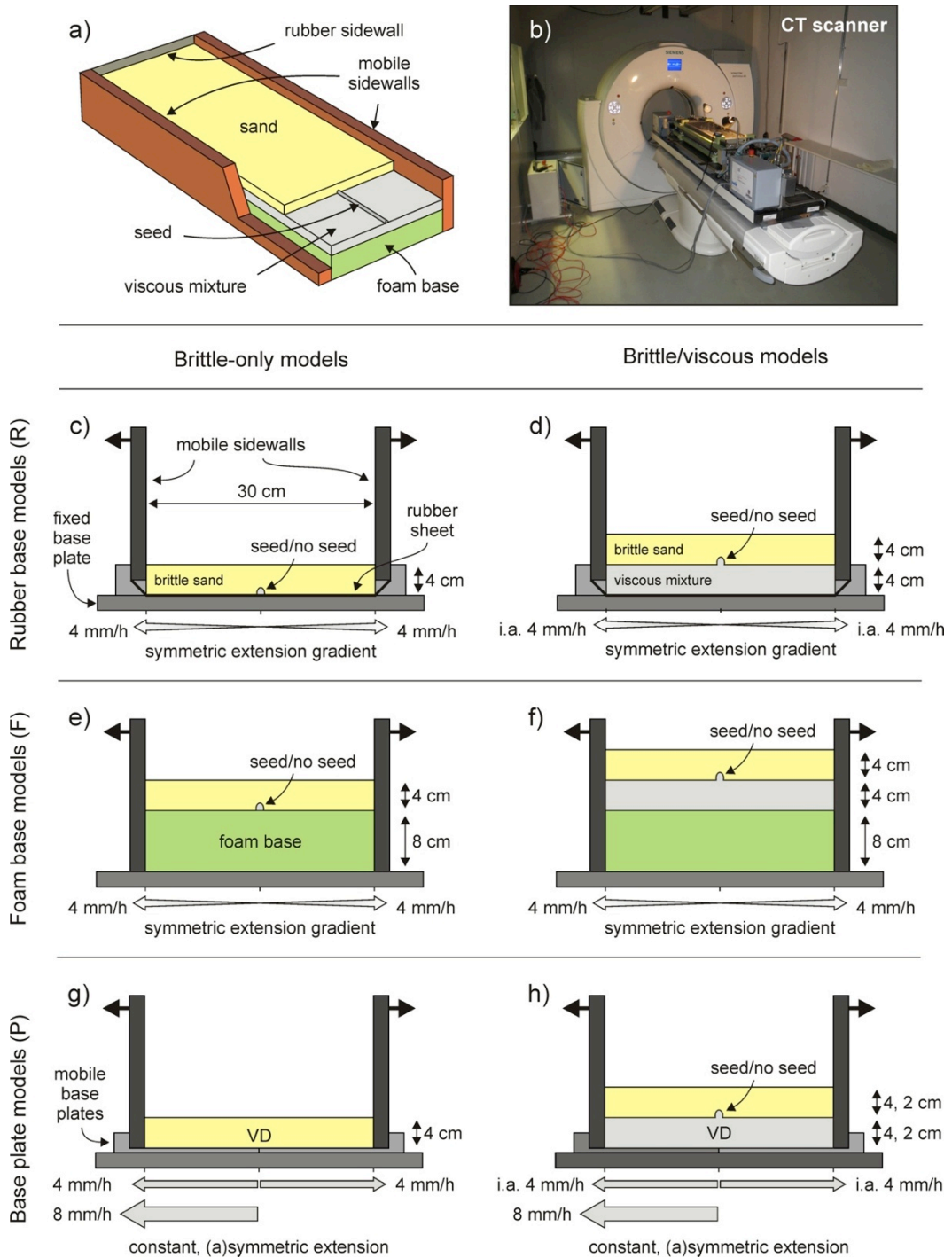
Model set-ups used for Series 11 (Chapter 7). (a) 3D cut-out sketch of a foam base model with brittle-viscous layering and a seed. (b) The experimental apparatus in the CT scanner of the University of Bern Institute of Forensic Medicine. (c-d) Rubber base set-ups for symmetric distributed extension: (c) brittle-only with or without seed, (d) brittle-viscous with or without seed. (e-f) Foam base set-ups for symmetric distributed extension: (e) brittle-only with or without seed, (f) brittle-viscous with or without seed. (g-h) Base plate set-ups controlled by a basal velocity discontinuity (VD) for symmetric and asymmetric extension. (g) brittle-only with or without seed, (f) brittle-viscous with or without seed. VD: velocity discontinuity.

EXP522 (Rubber base model test, not included in Chapter 7)
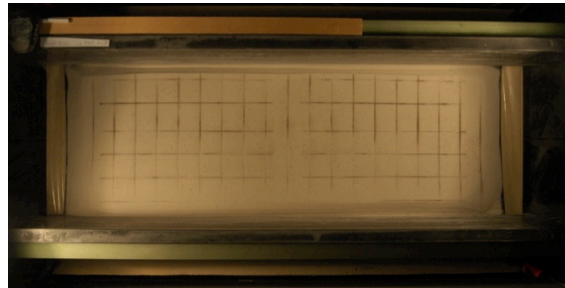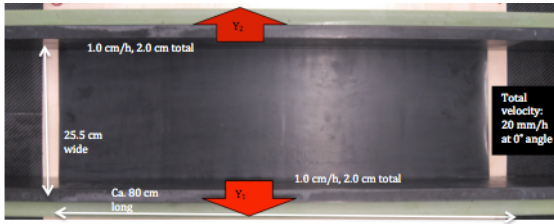
Test to see how a rubber base works. Without seed, only a layer of Qz sand. Rubber works to create deformation. Only defortmation along the sidewalls, seeds needed?
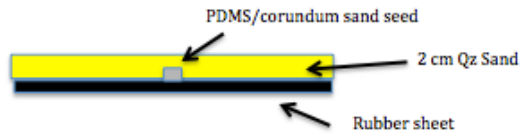
EXP523 (Rubber base model test, not included in Chapter 7)
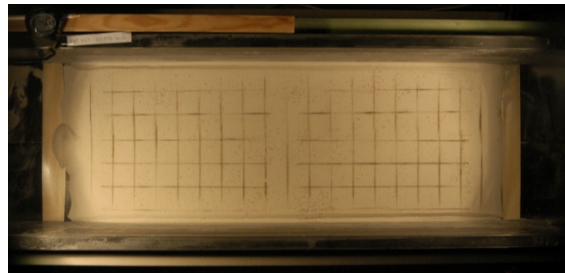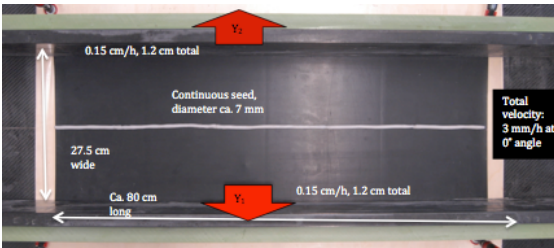
Test to see how a rubber base works. Silicone (with corundum mix) seed (diameter ca 7 mm). Rubber works to create deformation. No localization along the seed. Only defortmation along the sidewalls…
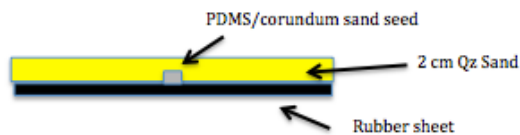
EXP524 (Rubber base model test, not included in Chapter 7)
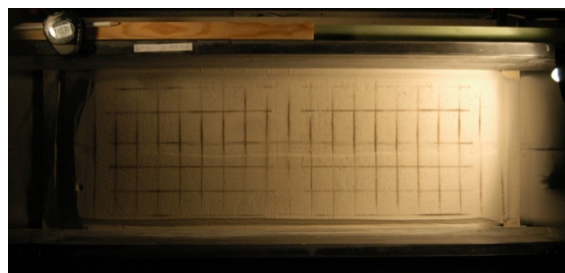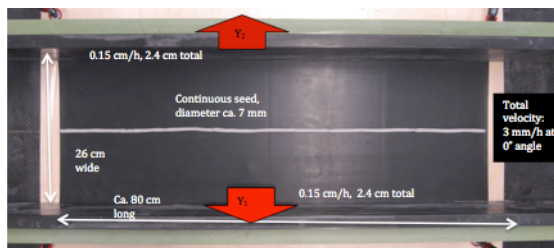
Test to see how a rubber base works. Silicone (with corundum mix) seed (diameter ca 7 mm). Vaseline between the rubber and wooden base plate to reduce friction. Rubber works to create deformation. Most deformation along the sidewalls, but we open a small rift in the middle. Note the conjugate faults on the short sides
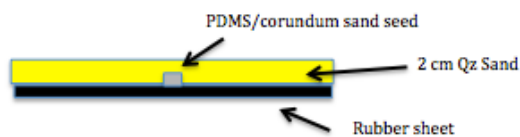
EXP532 (Rubber base model test, not included in Chapter 7)
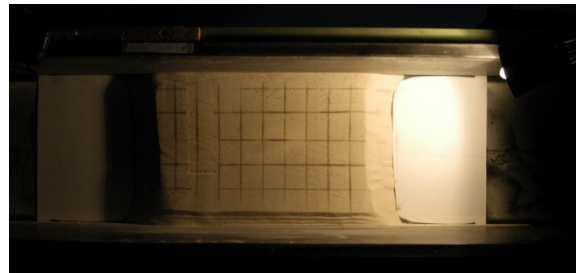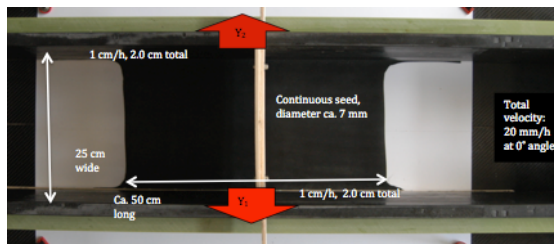
Silicone (with corundum mix) seed (diameter ca 7 mm). Deformation along sidewalls, conjugate strike-slip faults due to extension-orthogonal shortening of the rubber. Sidewall were not well attached → 1 cm of extension went lost. Too fast motion? Rubber works to create deformation. Most deformation along the sidewalls, some boundary effects → conjugate faul sets.
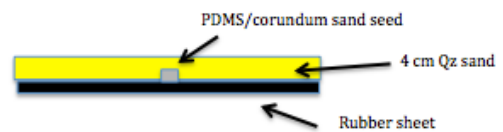
EXP533 (Rubber base model test, not included in Chapter 7)
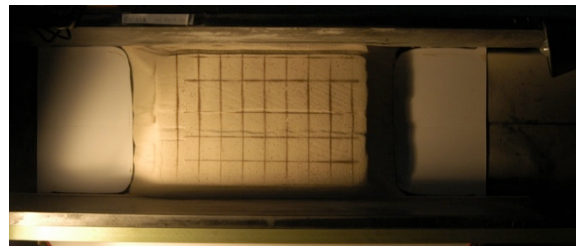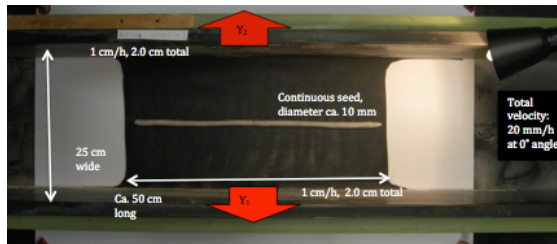
Silicone (with corundum mix) seed (diameter ca 10 mm). Deformation along sidewalls, conjugate strike-slip faults due to extension-orthogonal shortening of the rubber. Rift is created!
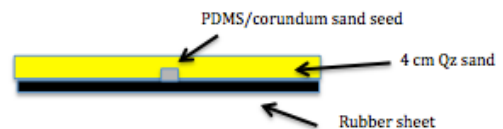
EXP534A – Model R4 (R: Rubber base model, CT-scanned)
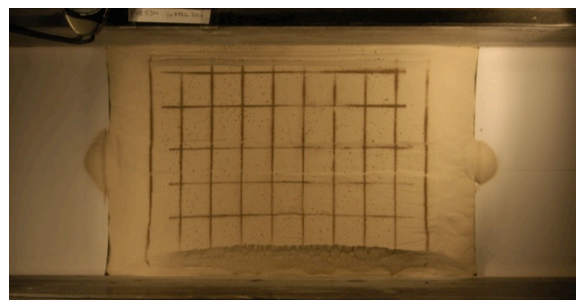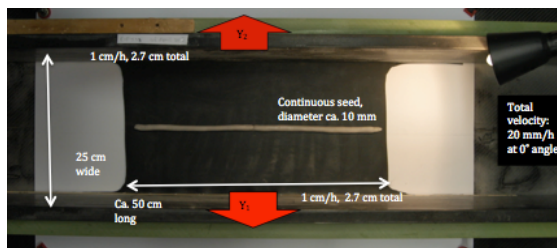
CT-scanned model for analogue-numerical comparison. We created a rift, but it looks like the rubber is shearing off at one sidewall. Most deformation along the sidewalls, some boundary effects → conjugate faul sets.
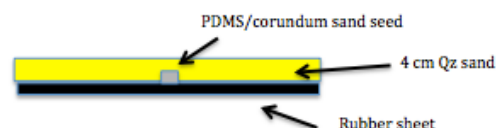
EXP628 (Rubber base model test, not included in Chapter 7)
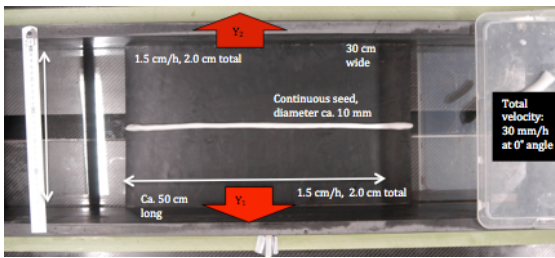
Model with rubber base for analog-numerical comparison. Seed ø ca. 1 cm. We got a rift, but it might be good to have more extension. (4 cm?).
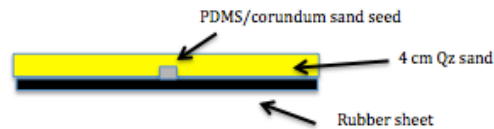
EXP629 – Model R2 (CT-scanned)
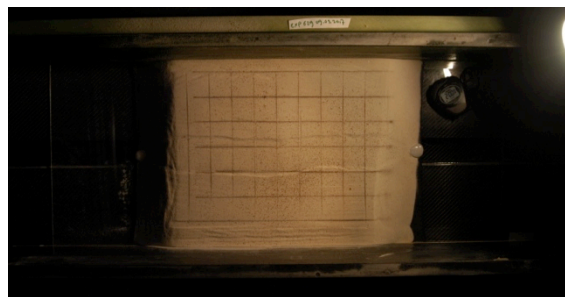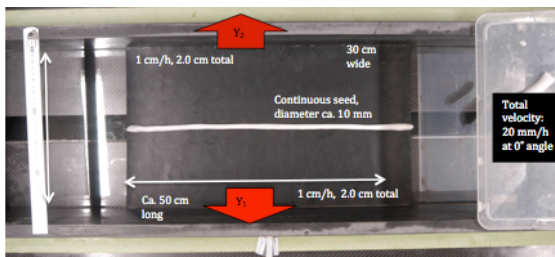
Model with rubber base for analog-numerical comparison. Seed ø ca. 1 cm. A bit more extension than EP628 and a bit slower. More extension and a rift, but also boundary effects,... we should maybe try a little slower.
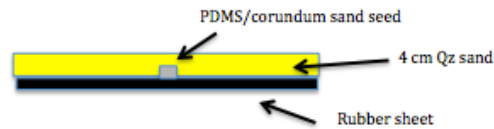
EXP630 – Model R3 (CT-scanned)
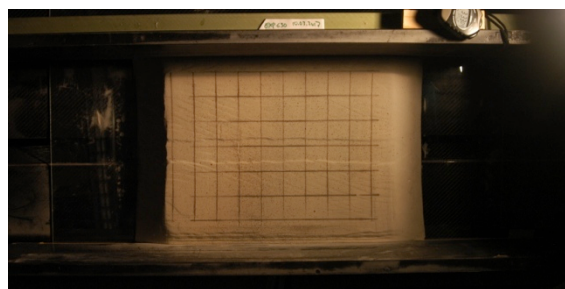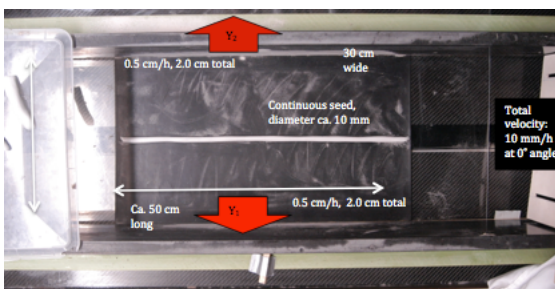
Model with rubber base for analog-numerical comparison. Seed ø ca. 1 cm. 4 cm extension, but 1 cm/h extenstion. Nice rift, with conjugate fault sets. Like in the previous CT-scanned model.
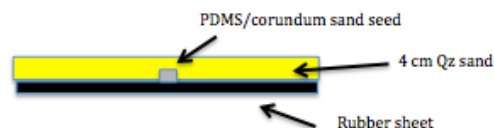
EXP657 – Model F6 (F: Foam base)
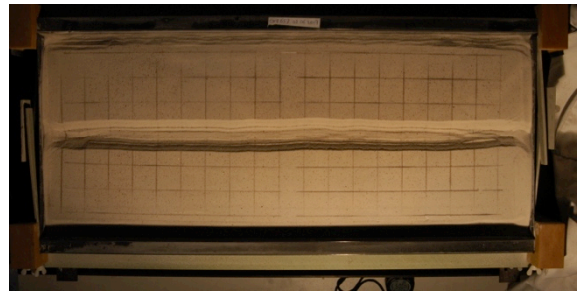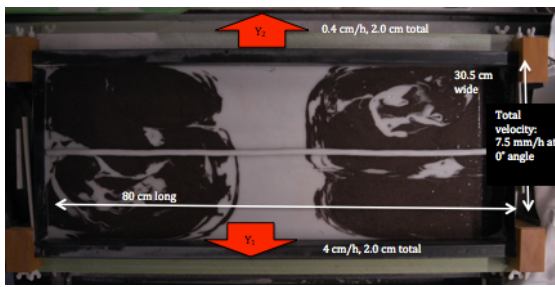
Brittle-ductile, foam base, continuous seed. Nice, continuous rift.
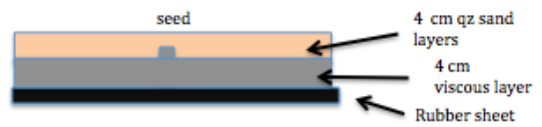
EXP661 – Model F7 (CT-scanned)
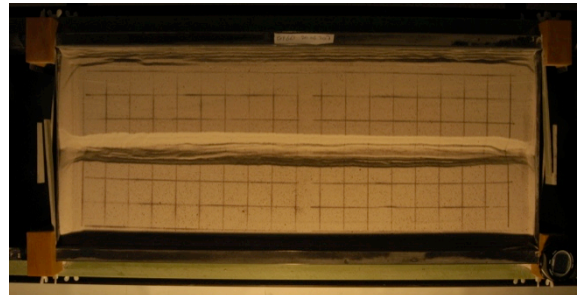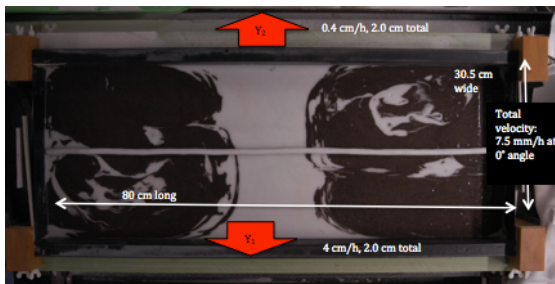
Brittle-ductile, foam base, continuous seed. Nice, continuous rift. Rerun on EXP657 in the CT scanner.
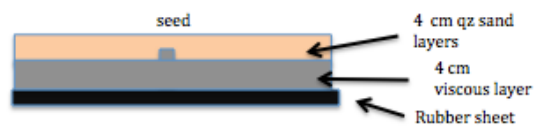
EXP665 – Model F2
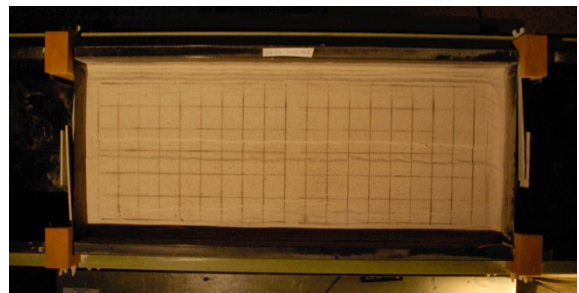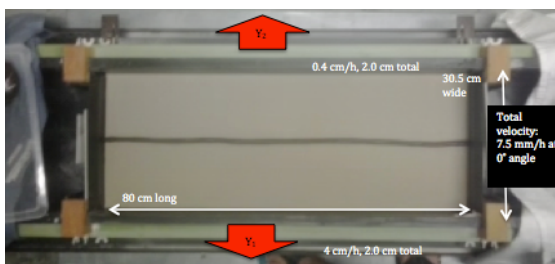
Foam base model with continuous seed for analogue-numerical comparison, tested for CT-scanning. Only sand.
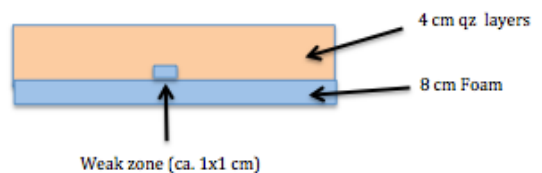
EXP667 – Model F3 (CT-scanned)
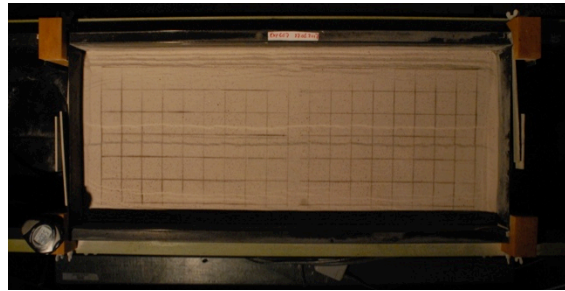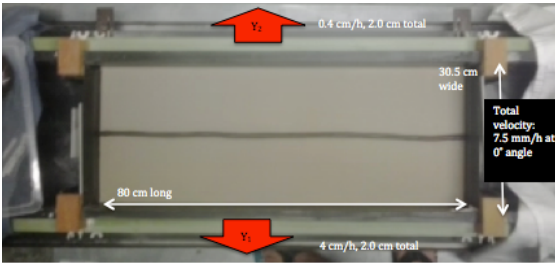
Rerun of EXP665. Only sand.
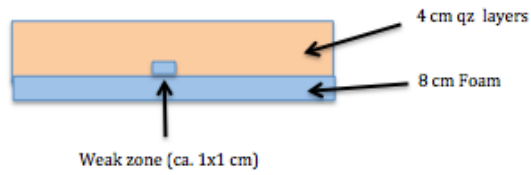
EXP668 – Model F1
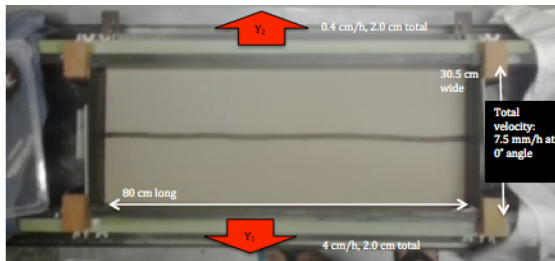
No seed, only sand.

EXP670 – Model F4 (CT-scanned)
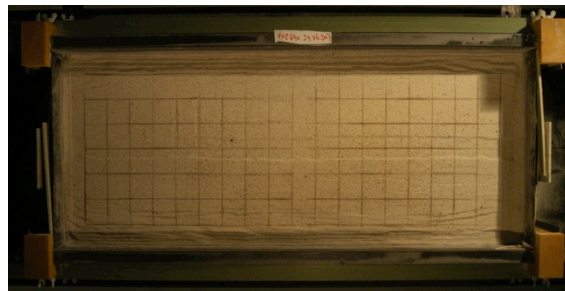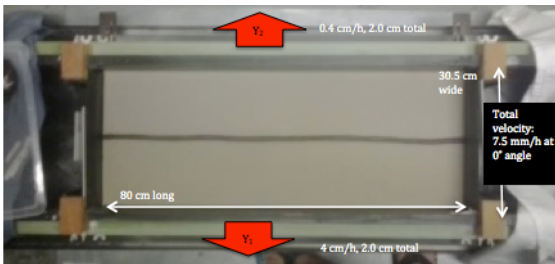
Rerun of EXP665 and EXP667 in the CT-scanner.
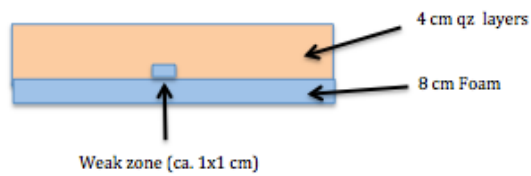
EXP674 – Model R1
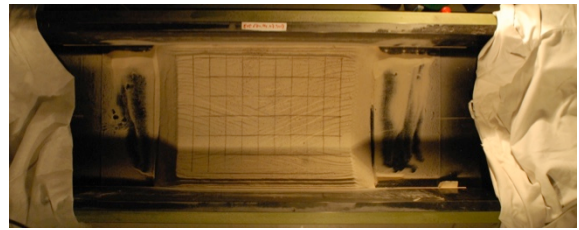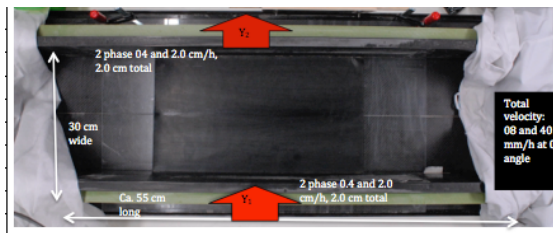
2 phase rubber base model, sand only. Conjugate fault sets, that develop rifts (oblique normal slip) after the second phase (extra).
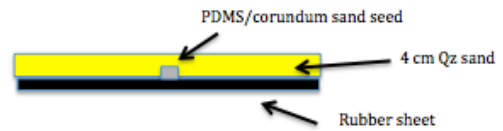
EXP686 – Model P1 (P: Base plate model)
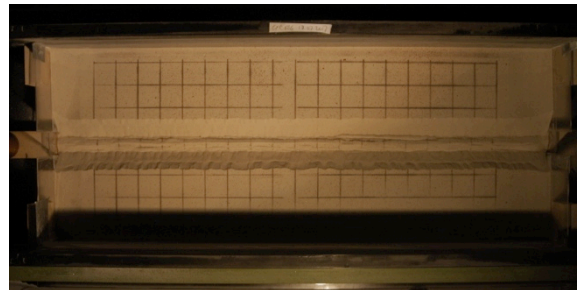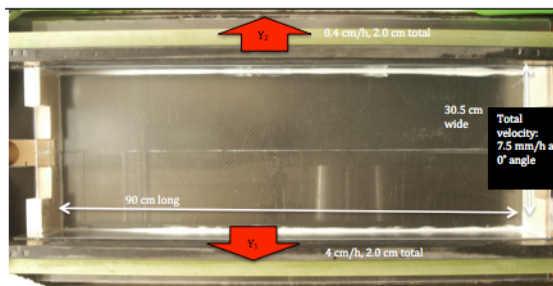
Symmetric extension, sand only. We get a big symmetric graben with a "horst" in the middle.

EXP687 – Model P2
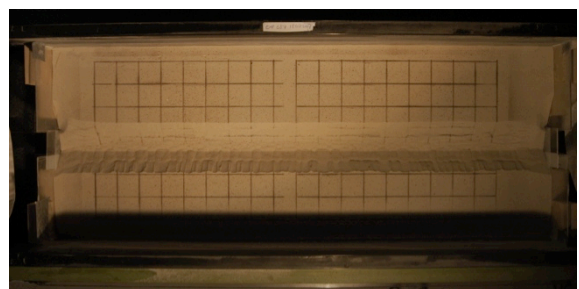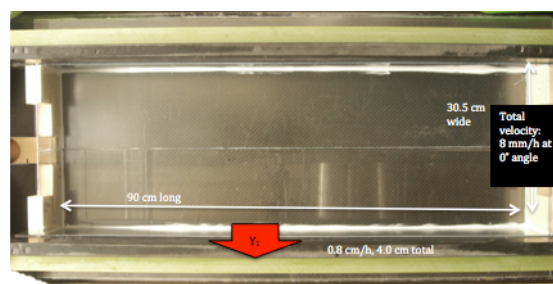
Asymmetric extension, sand only.
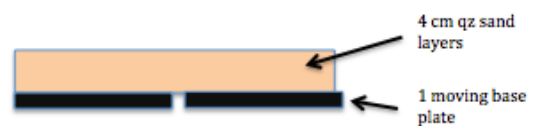
EXP688 – Model P6
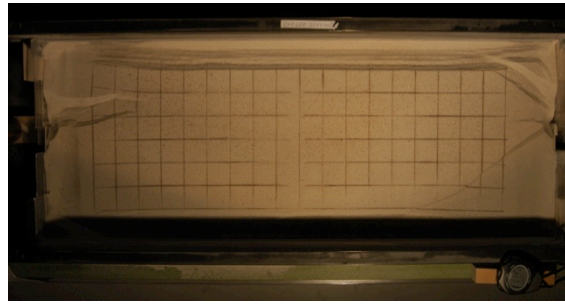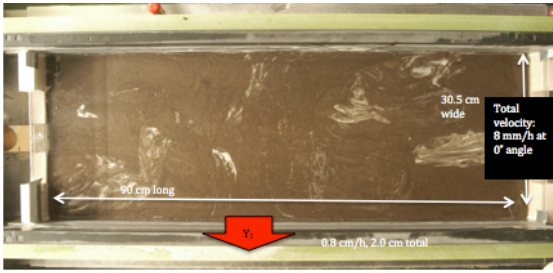
Brittle-viscous base plate model, asymmetric extension, no seed.
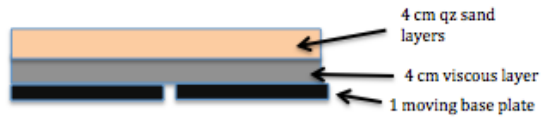
EXP689 – Model P7
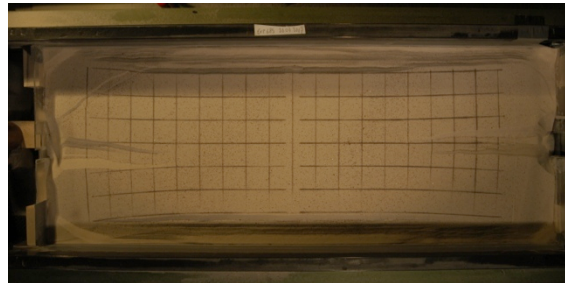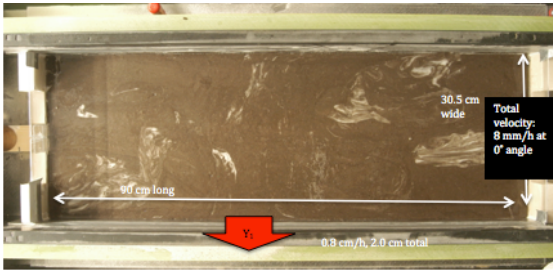
Rerun of EXP688 with different sidewall to reduce boundary effects along the model short ends
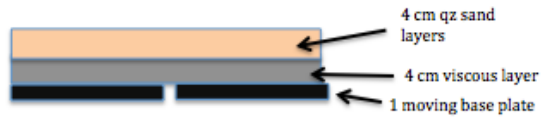
EXP690 – Model P3
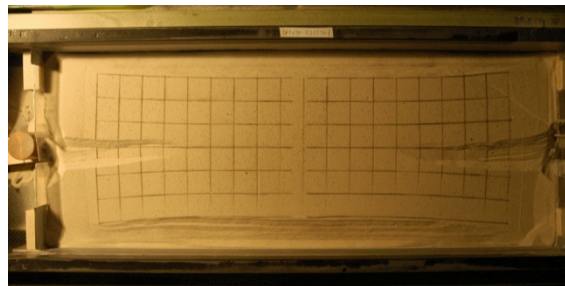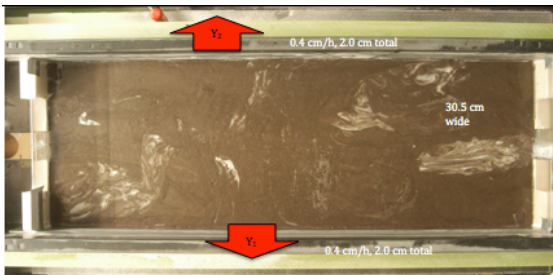
Rerun of EXP689 with symmetric opening (4 mm/h both sidewalls). Still lots of boundary effects: slower motion or seed necessary to create a rift?
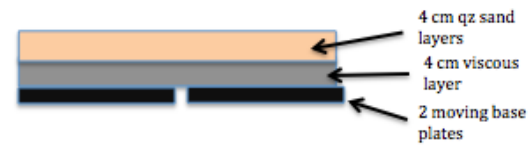
EXP691 – Model P4
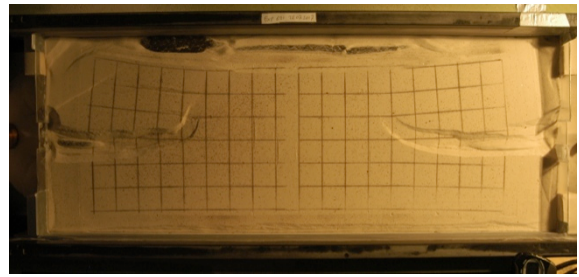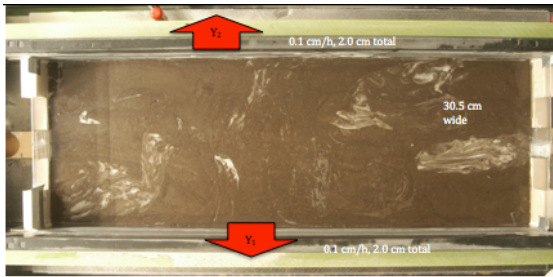
Rerun of EXP690 with slow symmetric opening (1 mm/h both sidewalls). Still lots of boundary effects (even more?)
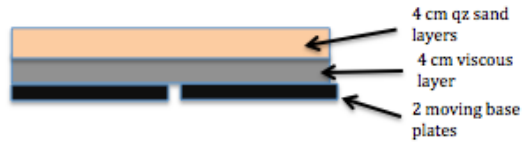
EXP692 – Model P5
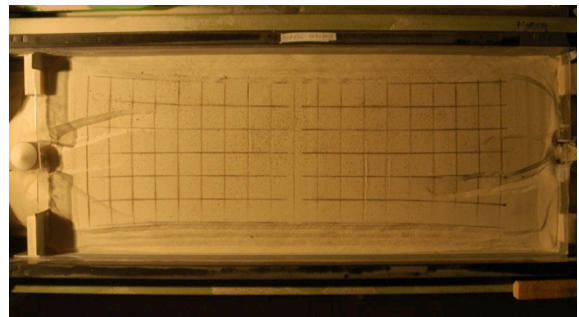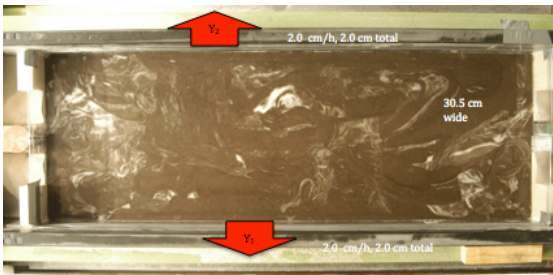
Rerun of EXP691 with fast symmetric opening (20 mm/h both sidewalls). Again till lots of boundary effects…
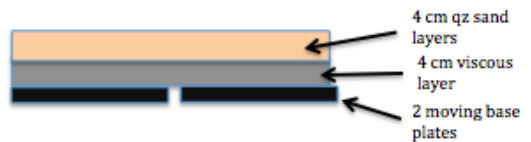
EXP693 – Model P10
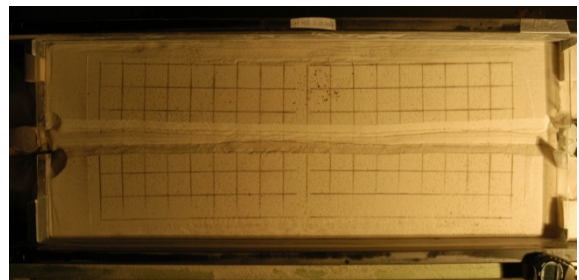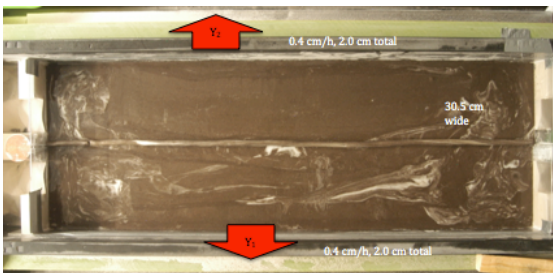
Rerun of EXP690 with symmetric opening (4 mm/h both sidewalls). With seed
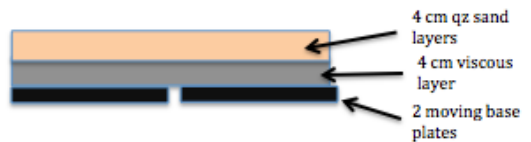
EXP694 – Model P8
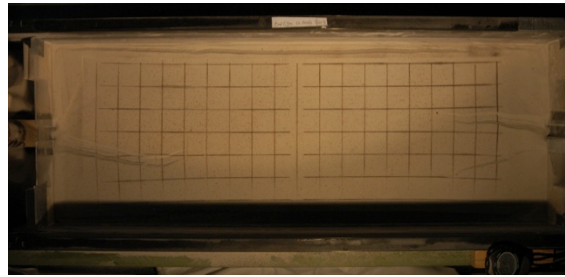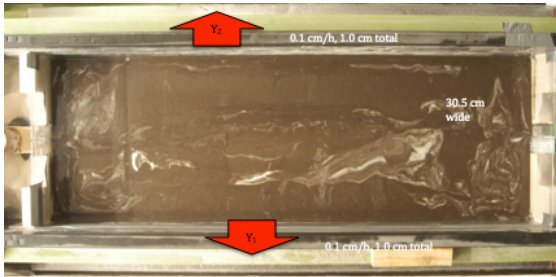
Rerun of EXP690 with symmetric opening but half the layering and a 4th of the ext velocity (1 mm/h both sidewalls). No seed.
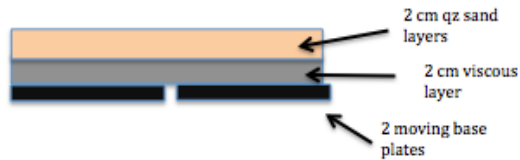
EXP695 – Model P9
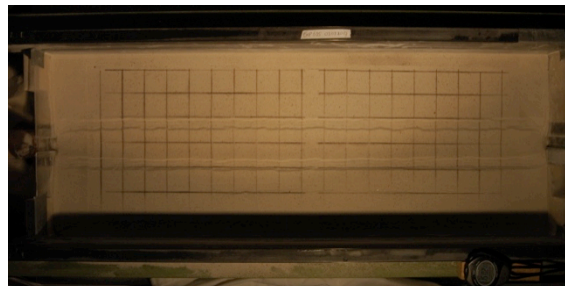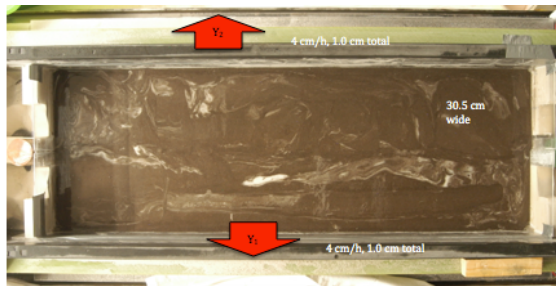
Rerun of EXP694 with symmetric opening but half the layering and a very high ext velocity (40 mm/h both sidewalls). No seed. We get flexural grabens along a flexural depression!
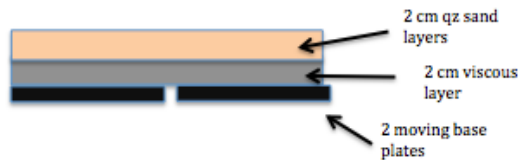
EXP696 (not included in Chapter 7)
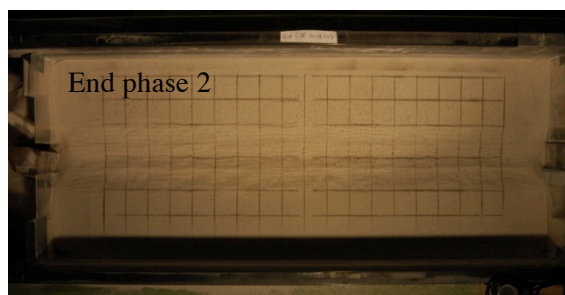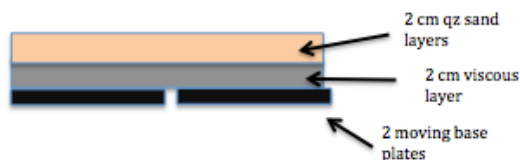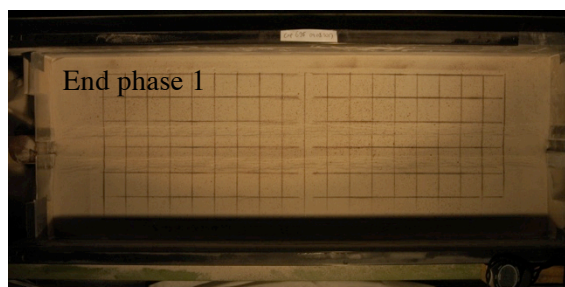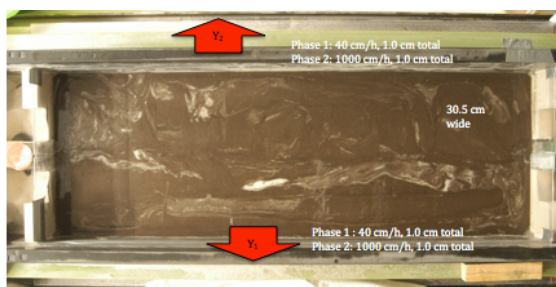
Rerun of EXP690 with symmetric opening but half the layering and a very high ext velocity (400 mm/h both sidewalls, phase 2: 10000 mm/h. No seed. We get flexural grabens along a flexural depression! In phase 2, deformation migrates towards the model center.

EXP697 (not included in Chapter 7)
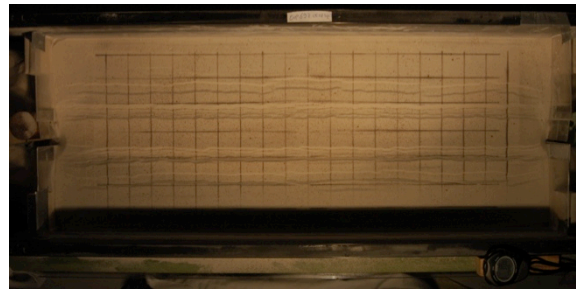
Rerun of EXP695 with double extension (40 mm total, 40 mm/h both sidewalls). No seed. We get flexural grabens along a flexural depression!
Some more grabens
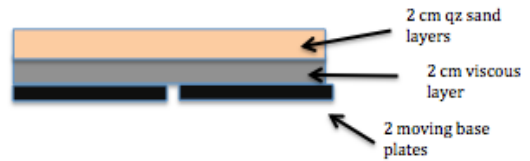
EXP698 – Model R7
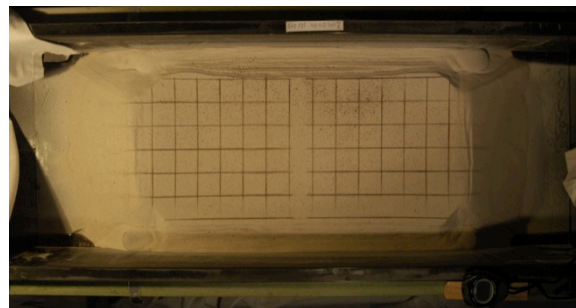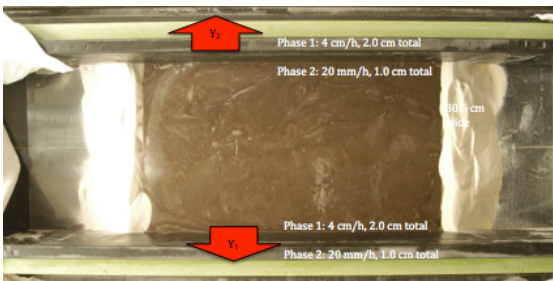
Rubber base model (brittle/ductile). 8 mm/h extendsion, second phase 20 mm/h. No seed. Mostly boundary effects. The silicone is thinned towards the end, flowed towards the end over the edge of the rubber. The ends of the model, where no silicone was, remained higher.
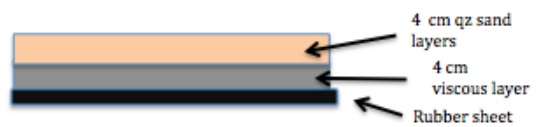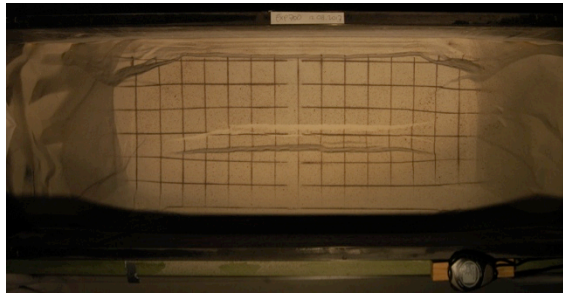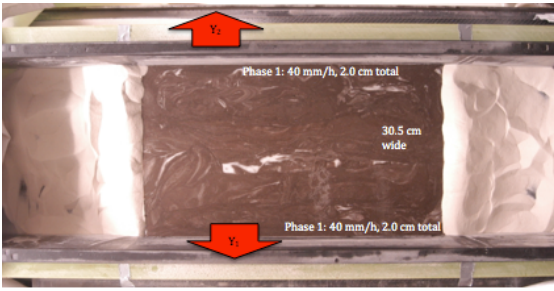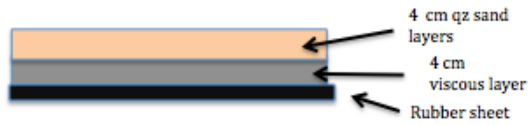

EXP699 – Model R8
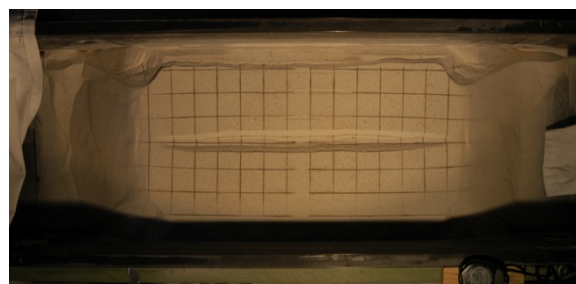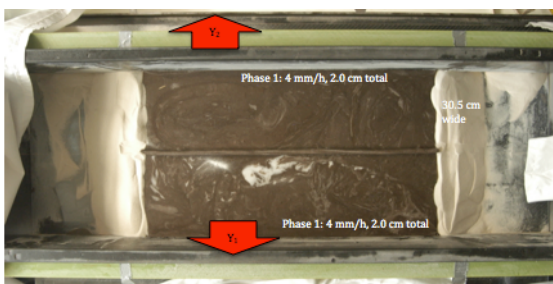
Rerun of EXP698 with seed and 1 extension phase.
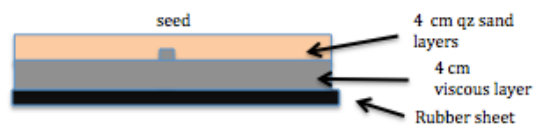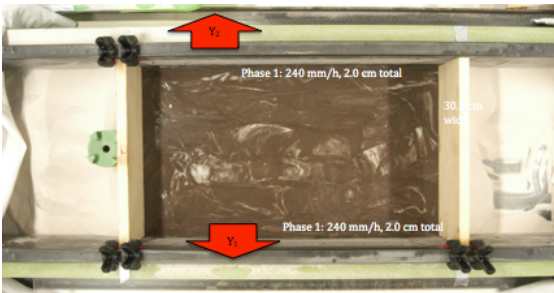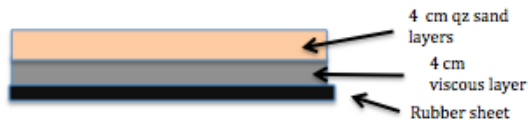
EXP700 – Model R9

Rerun of EXP699 with high speed (80 mm/h) extension. No seed. Central rift!
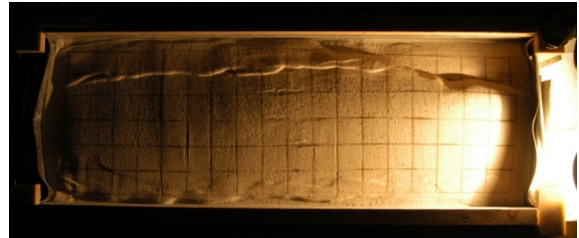

EXP701 (not included in Chapter 7)
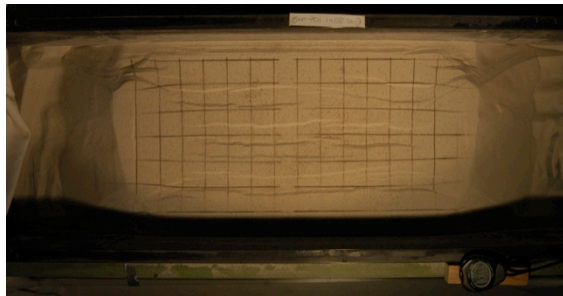
Rerun of EXP699 with very high speed (480 mm/h) extension. No seed. Central rift! Wooden sidewalls are to keep viscous layer in place, removed and replaced with sand for model run.
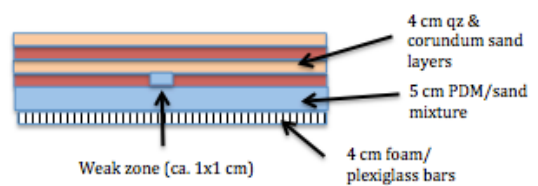
Series 12. Rift propagation tests

Early models to test rift propagation (compare with Series 9/Chapter 5)

EXP581

Rerun of EXP579 (rift propagation) but with orthogonal extension instead of scissor extension. Applying extension was the goal, but due to a programming error, it became compression… New model width (30cm) to fit with the Xissor machine Seed: 15 cm long
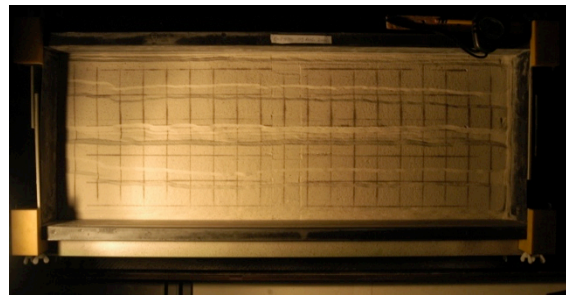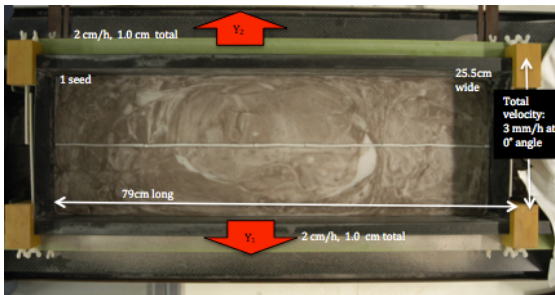
EXP583

Rerun of EXP581 (rift propagation) that was by accident a compression model. Mostly boundary effects, little localization….
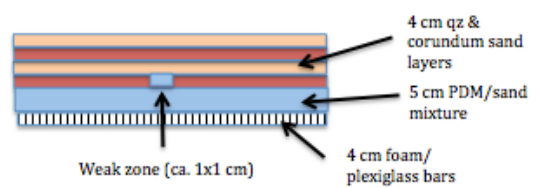
Series 13. Madagascar model tests

Models to test the assumed multiphase separation of Madagascar from the African continent. A current BSc project aims to expand on this topic.
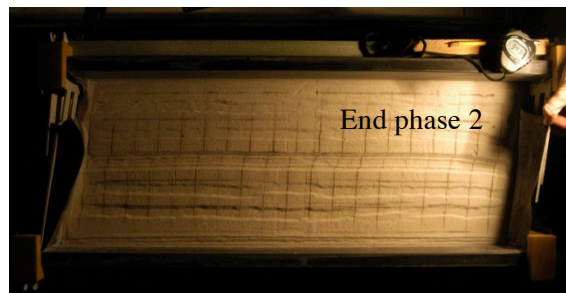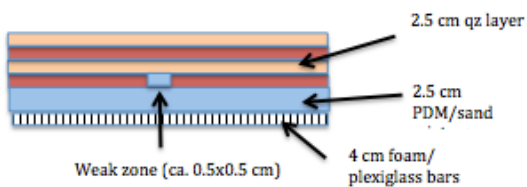
EXP570

Model to test a 2 stage extension. First stage: fast orthogonal extension/wide rifting. Second stage: slow orthogonal extension/localized rifting.

NB: Second stage was not run because the first phase did not produce the wide rifting we expected.
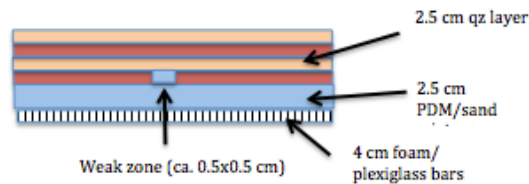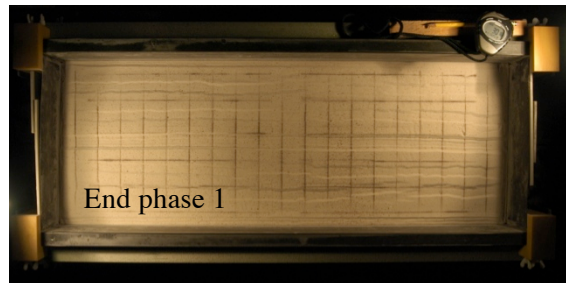

EXP571

Models to test a 2 stage extension. First stage: fast orthogonal extension/wide rifting. Second stage: slow orthogonal extension/localized rifting.

NB: Second stage was not run because the first phase velocity was set too high (4 cm/h Instead of 2 cm/h). As the maximum extension was thus already used, a pure dextral strike-slip motion was applied.

Series 14. NAGRA models

Model series in collaboration with Herfried Madritsch from Nagra (theme: Carboniferous trough reactivation in Northern Switzerland). Guido Schreurs was in charge of the project, I carried out two of the models, presented below.

EXP561
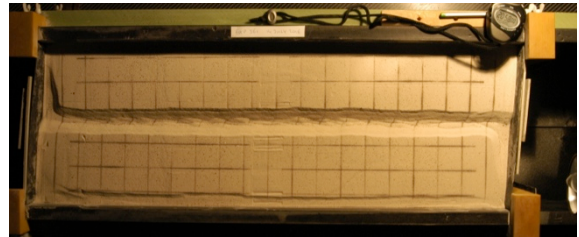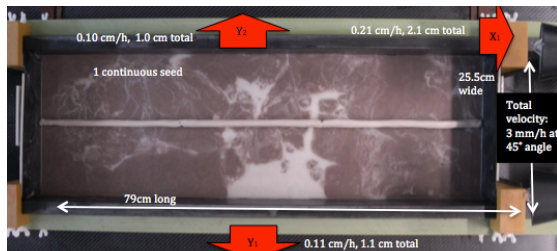
Model test run for the NAGRA collaboration on carboniferous troughs in Switzerland. One seed, 45° oblique extension model
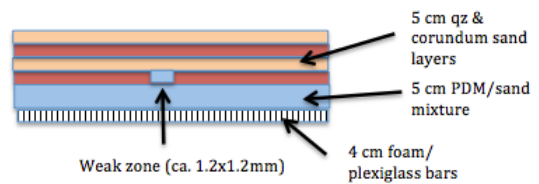
EXP562
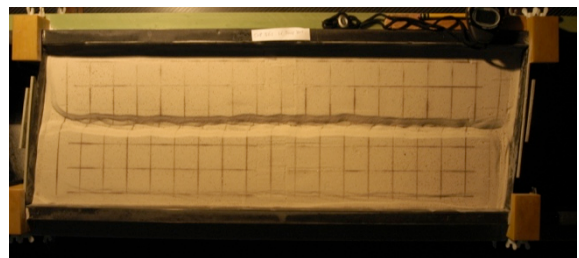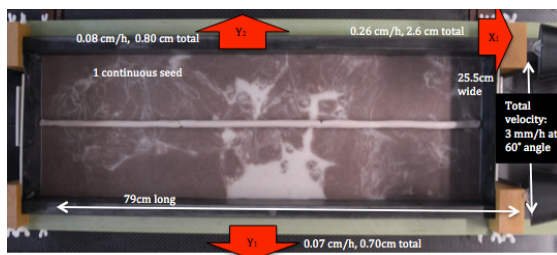
Model test run for the NAGRA collaboration on carboniferous troughs in Switzerland. One seed, 60° oblique extension model
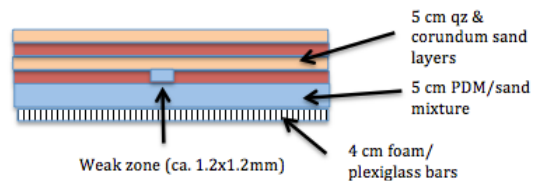
Series 15. Aar Massif tests

Model series of compression, involving a rubber base, in order to reproduce the conjugate fault sets observed in rubber base extensional models (Series 11/Chapter 7). Such structures may be present in the Aar Massif, Switzerland.

EXP675
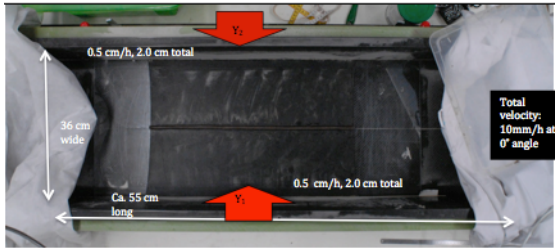
Compression test with rubber base and seed (ø 1 cm). 4 cm of sand. Idea: Aar Massif. A pop-up develops above the seed. Also other thrusts/pop ups develop away from the central pop-up. Some boundary effects (conjugae faults) at the edges.
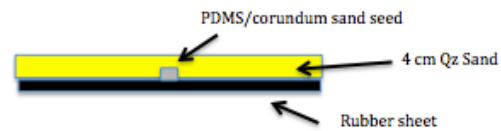
EXP677
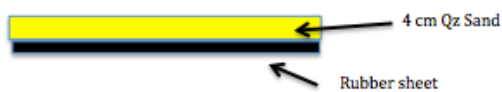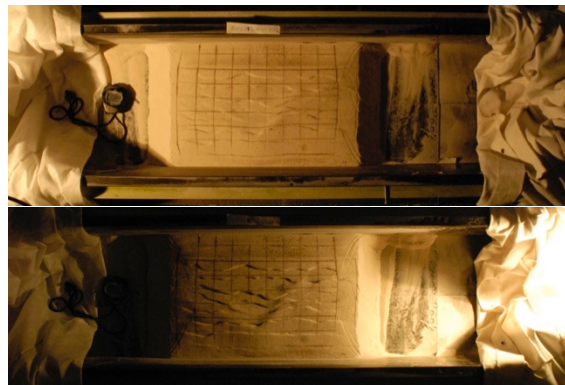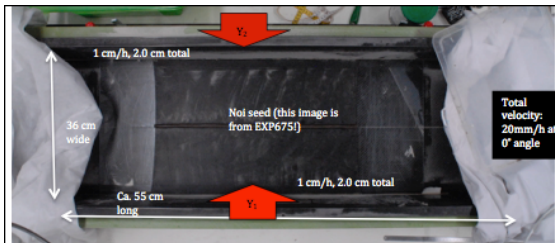
Compression test with rubber base but no seed (ø 1 cm). 4 cm of sand. Idea: Aar Massif. Lots of thrusts developing and even cutting each other. Some boundary effects (conjugae faults) at the edges.

Series 16. Scissor extension, wide weak zones and rift propagation models

These models are inspired by previous models of Molnar et al. (2017), who apply broad weak zones in their models as opposed to the narrow weak zones in the models presented in this Thesis.

EXP703
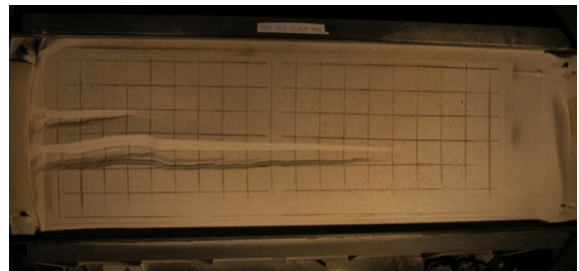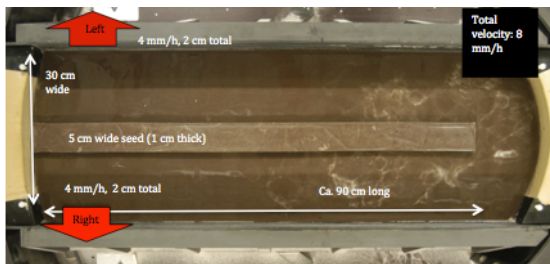
Same set-up as used in Chapters 5 and 7: 4 cm PDMS/sand, 4 cm sand on a foam base. Wider patch of viscous material (5 cm instead of 1 cm), similar to Molnar et al. 2017. The model develops rifts along the edges of the weak zone, but one becomes dominant.
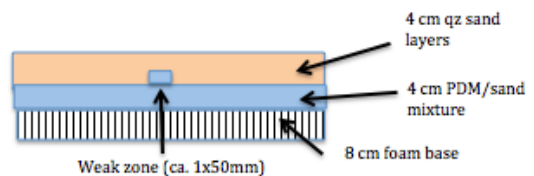
EXP704
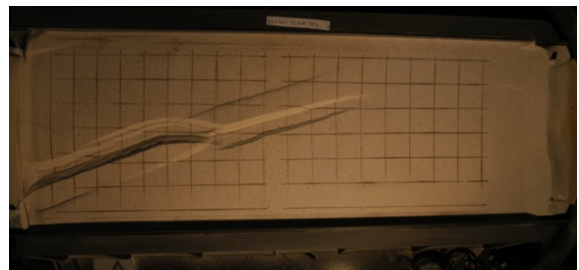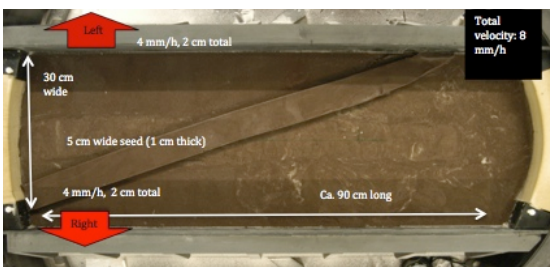
Same set-up as EXP703, but with the weak zone oriented 15° oblique to the rift axis. The weak zone edgs are activated, but the rift jumps from the one side of the weak zone to the other.

EXP705
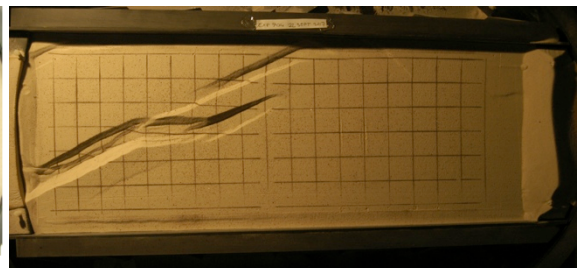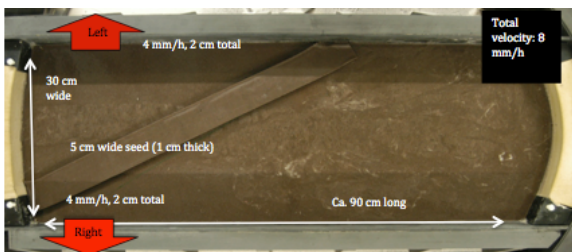
Same set-up as EXP703, but with the weak zone oriented 30° oblique to the rift axis. Very similar structure to EXP704

Declaration of consent

on the basis of Article 28 para. 2 of the RSL05 phil.-nat.

Name/First Name: Zwaan, Frank

Matriculation Number: 13-127-808

Study program: PhD PHIL NAT (Earth Sciences)

Bachelor ◯   Master ◯   Dissertation ◉

Title of the thesis: 4D laboratory experiments of oblique extension and scissor tectonics, structural inheritance and sedimentation: implications for rift evolution, rift propagation and rift segment interaction

Supervisor: Prof. Dr. Guido Schreurs

I declare herewith that this thesis is my own work and that I have not used any sources other than those stated. I have indicated the adoption of quotations as well as thoughts taken from other authors as such in the thesis. I am aware that the Senate pursuant to Article 36 para. 1 lit. r of the University Act of 5 September, 1996 is authorised to revoke the title awarded on the basis of this thesis. I allow herewith inspection in this thesis.

Place/Date   Bern, 5 October 2017

Signature

Curriculum Vitae - Frank Zwaan (Structural Geologist)

1/10. Personal Details

Date/Place of birth: 23 April 1988, Egmond aan Zee, The Netherlands
Nationality: Dutch
Researcher ID (ORCID):   0000-0001-8226-2132
Languages: Dutch (native), English (fluent), French (fluent), German (fluent), Italian (basics)

2/10. Education and previous research projects

Since 2013 - PhD Earth Sciences

University of Bern (Switzerland) with SNF grant 200021_147046/1

2017   **PhD Thesis**: 4D laboratory experiments of oblique extension and scissor tectonics, structural inheritance and sedimentation: implications for rift evolution, rift propagation and rift segment interaction. Supervisor: Prof. G. Schreurs

2010-2013 - MSc (joint degree) Geosciences of Basins and Lithosphere

VU University Amsterdam (NL) and University Rennes1 (France) Average grade: 8.1/10 (cum laude)

2013   **MSc Thesis/internship** *(Royal Dutch Shell)*
             Structural interpretation of the Norwegian Central Graben, North Sea: implications for Late Jurassic-Early Cretaceous reservoir quality sands.
             Supervisors: C. Nicolai and Prof. Dr. J. de Jager

2012   **MSc Research project 2/Stage M1** *(University Rennes1)*
             Analogue modelling to explore the influence of initial passive margin basin geometry on the development of salt tectonic structures
             Supervisors: Prof. Dr. J.-P. Brun and Dr. X. Fort

2011   **MSc Research project 1** *(VU University Amsterdam)*
             Lateral extrusion in the Eastern Alps: analogue modelling and structural fieldwork (Austria) to reconstruct the regional tectonic history.
             Supervisors: Prof. Dr. D. Sokoutis and Dr. E. Willingshofer

2006-2011 - BSc Earth Sciences/Geology

VU University Amsterdam (The Netherlands) Average grade: 7.4/10 (with merit)

2009   **BSc Thesis:** Structural and sedimentological correlation between fractures and facies in the Cariatiz Reef, SE Spain. Supervisor: Prof. Dr. J.J.G. Reijmer

2000-2006 - Pre-university education: Gymnasium (A-level (VWO) with classical education)

Murmellius Gymnasium Alkmaar, The Netherlands

3/10. Employment history

- **Since 11/2013 - PhD candidate in structural geology**
  University of Bern (Switzerland) Supervisor: Prof. G. Schreurs

- **02/2013 - 08/2013 - Apprentice in exploration geology**
  Royal Dutch Shell (Netherlands) Supervisor: C. Nicolai, J. de Jager

- **12/2008 - 12/2009** - **President of study association for geoscientists GeoVUsie**
  VU University Amsterdam (The Netherlands), 700+ members, full-time commitment

4/10. Profile

Research interests:	Structural geology, (salt) tectonics, analogue and numerical tectonic modelling, petroleum geology, geomorphology, sedimentology, natural resources and (renewable) energy
Geological skills:	(Well) logging, geological and structural mapping, GIS, sequence stratigraphy, 3D seismic interpretation, reservoir evaluation, paleostress analysis, analogue and numerical modelling, PIV and DVC
Software experience:	Matlab, Scilab, ArcGIS, Idrisi, Ansys, Gocad, Carbonate 3D, Petrel, nDI, Osirix, Coreldraw, Adobe Illustrator, Adobe Photoshop
Memberships:	Swiss Geological Society, Swiss Association of Energy Geoscientists (SASEG), Science Society Bern, Royal Geol. and Mining Society of the Netherlands (KNGMG), Swiss Association of Geologists (CH-GEOL)

5/10. List of publications

Peer-reviewed (4)

Zwaan, F., Schreurs, G., Adam, J. (accepted with minor revisions). Effects of sedimentation on rift segment and transfer zone evolution in orthogonal and oblique extension settings: insights from analogue models analysed with 4D X-ray computed tomography and digital volume correlation techniques. Global and Planetary Change.

Zwaan, F. (in press) Lower Cretaceous reservoir development in the Norwegian Central Graben and implications for the Southern Permian Basin. Geological Society, London, Special Publication.

Zwaan, F., and Schreurs, G. (2017). How oblique extension and structural inheritance influence rift interaction: Insights from 4D analogue models. Interpretation 5 (1), SD119-SD138.

Zwaan, F., Schreurs, G., Naliboff, J., Buiter S.J.H. (2016). Insights in the effects of oblique extension on continental rift interaction from 3D analogue and numerical models. Tectonophysics 693, 239-260.

Not peer-reviewed (3)

Zwaan, F. and Schreurs, G. (2015). Effects of transtension on continental rift interaction: a 4D analogue modeling study. Geotectonic Research, vol. 97, Schweizerbart Science Publishers, Germany

Zwaan, F. (2015). Plattentektonik im Sandkasten / La tectonique des plaques dans un bac à sable. GeoPanorama, 2/2015, Geosciences, Swiss Academy of Sciences, German/French, English title: Plate tectonics in the sandbox.

Zwaan, F. (2015). Plaattektoniek in de zandbak van de Universiteit Bern. Geobrief, 1/2015, KNGMG & NOW-ALW, The Netherlands. (in Dutch, English title: Plate tectonics in the sandbox at the University of Bern)

In preparation (5)

Zwaan, F., Schreurs, G. (in preparation). Rift propagation under orthogonal and scissor extension conditions: insights from analogue models analysed with 4D X-ray computed tomography.

Zwaan, F., Schreurs, G. (in preparation). Evolution of rift linkage zones in orthogonal and scissor extension settings: insights from analogue models analysed with 4D X-ray computed tomography

Zwaan, F., Schreurs, G. Naliboff, J., Buiter, S.J.H, Adam, J. (in preparation). Comparing different crustal-scale analogue extension model set-ups using X-ray computed tomography (XRCT) techniques

Martini, I., Ambrosetti, E., Brogi, A., Zwaan, F., Sandrelli, F. (in prep.). Tectonostratigraphic evolution in a "Basin and Range-type" structural setting: insights from the Pliocene Siena-Radicofani Basin (Northern Appenines, Italy).

Fedorik., J., Zwaan, f., Schreurs, G., Toscani, G., Bonini, L., Lodolo, E., Civile, D., Seno, S. (*in preparation*). 4D analogue modelling of transcurrent fault structures interacting with a thrust belt

6/10. Reviewing activities, institute and conference responsibilities

- **2 Reviews completed:** AAPG Bulletin (2017) and Materials (2017)

- **Convener:** Tectonic modelling session, EGU General Assembly Vienna 2017 (Vienna). 2 sessions are planned for the 2018 Assembly (on tectonic modelling and on rift development/propagation)

- **Responsible researcher for the University of Bern Tectonic Laboratory** (Since 11/2013)
  University of Bern (Switzerland)

7/10. Supervision of students/junior researchers

- **Since 07/2017 - BSc thesis**: Analogue modelling of multiphase rifting in the Mozambique Channel
  Student: Mario Bühler - University of Bern

- **10/2015 - 12/2015 - BSc thesis**: Designing a new experimental apparatus for lithospheric-scale models
  Student: Yves Pöltinger - IPEK/HSR Hochschule für Technik Rapperswil

- **02/2014 - 05/2014 - BSc thesis**: Designing a new experimental apparatus for scissor tectonics
  Student: Claude Grau - IPEK/HSR Hochschule für Technik Rapperswil

8/10. Teaching activities

Invited talk during SUBITOP analogue modelling workshop, Utrecht University, Netherlands (07/2017)

Tectonic laboratory demonstration for Swiss high school students (02/2017)

Teaching assistant for BSc practical "Structural Geology" (02-04/2014 and 2015), incl. fieldwork

Teaching assistant for BSc practical "Mapping and Profiles" (02/2015)

Basics of Geology course for BSc students (05/2014)

Assistant field trips: Ivrea mapping course (03/2016), From basins to mountain belts excursion (07/2015), Kandersteg excursion (06/2015), Jura excursion (05/2015), Dynamic Alps excursion (09/2014 and 09/2015), Structural geology mapping (09/2014 and 2015), Morcles Nappe excursion (05/2014).

9/10. List of conferences and events attended during the PhD project

Conference/Event	Presentation title	Type
SGM 2017 *Davos, Switzerland*	*4D Analogue modelling of rift propagation in orthogonal and scissor tectonic settings*	*To be decided*
	Effects of sedimentation on rift basin and transfer zone evolution: insights from 4D analogue models	*To be decided*
SUBITOP workshop 2017 Utrecht, Netherlands	Studying oblique extension and transfer zones: 4D analogue models and X-Ray CT analysis	Talk
EGU 2017 Vienna, Austria	An attempt to model rift propagation	Poster
	How sedimentation affects rift segment interaction during oblique extension: a 4D analogue modelling study	Poster
	Studying scissor tectonics with 4D analogue models	PICO
SwissSed Meeting 2017 Fribourg, Switzerland	Influence of sedimentation on rift and transfer zone development: Insights from 4D analogue tectonic models	Poster
SGM 2016 Geneva, Switzerland	4D analogue modelling of scissor tectonics	Poster
	Effects of oblique extension and structural inheritance on rift interaction: results from 4D analogue models	Talk
Structural Geology 2017 Research Seminar Bern, CH	Studying scissor tectonics: a 4D analog modeling approach	Talk
GeoMod 2016 Montpellier, France	A new analogue modelling machine to study scissor tectonics	Poster
	Influences of oblique extension and structural inheritance on rift interaction: a 4D analog modeling study	Poster
	Studying Scissor tectonics: a 4D analog modeling approach	Talk
ILP TopoEurope 2016 Clermont-Ferrand, France	4D Analogue modeling revealing the effects of oblique extension and structural inheritance on rift interaction	Talk
EGU 2016 Vienna, Austria	How oblique extension and structural inheritance control rift segment linkage: insights from 4D analogue models	Poster
Swiss Geology Day 2016 Lausanne, Switzerland	-	-
AGU Fall Meeting 2015 San Francisco, USA	A 4D analogue modelling study assessing the effects of transtension and inherited structures on rift interaction	Poster
Struct. Geology 2017 Research Seminar Bern, CH	A 4D analogue modelling study assessing the effects of transtension and inherited structures on rift interaction	Poster
SGM 2015 Basel, Switzerland	Transtension and structural inheritance in 4D analogue models of continental rift interaction	Talk
GeoVUsie Flex-lecture Amsterdam, Netherlands	Analogue Modelling of continental transtension tectonics: a 4D approach	Talk
DRT 2015 Aachen, Germany	Effects of Transtension on Rift Interaction (a 4D Analogue Modelling Study)	Talk
EGU 2015 Vienna, Austria	Effects of Oblique Extension on Transfer Zones in Continental Rifts (4D Analogue Modelling)	Talk
VU Geosciences Career Day 2015 Amsterdam, NL	4D Modeling of Transfer Zones in Continental Rifts	Poster
SGM 2014 Fribourg, Switzerland	4D Modeling of Transfer Zones in Continental Rifts	Talk
PETEX/PGCRS 2014 London, UK	4D Modeling of Transfer Zones in Continental Rifts	Poster
GeoMod 2014 Potsdam, Germany	4D Modeling of Transfer Zones in Continental Rifts	Talk

10/10. List of courses attended during the PhD project

Year	Course	Organizer (conference)
2017	SCCER School - Shaping the Energy Transition	SCCER*
2017	IMAGinING RIFTING workshop	
2017	Alpine Corsica Fieldtrip	CUSO-DPMS (Conférence Universitaire de Suisse Occidentale)**
2017	SUBITOP analogue modelling workshop	Utrecht University/SUBITOP
2016	Getting the writing done	CUSO
2016	Digital field data acquisition and data management	Swisstopo (Swiss Federal Office of Topography), Bern
2016	ESPP Karst, Hydrology, Carbon Cycle and Landscape Evolution workshop	CUSO
2016	Managing Relationships during the doctoral process and preparing for a successful career	CUSO
2016	Scientific Drawing	CUSO
2016	Student & Early Career Scientist Conference: Career Guidance and Professional Development	AGU (AGU Fall Meeting 2015)
2015	Conference & Seminar Skills	CUSO
2015	Physical Modeling of Geological Processes	RWTH Aachen University (DRT 2015)
2015	ESPP Workshop in Carbonate Sedimentology: Alpine carbonate platforms in the Geneva area	CUSO
2014	Constitutive Laws: from Observation to Implementation in Models	GFZ German Research Centre for Geosciences (GeoMod2014)
2014	German as a foreign language C1.2	Institute of Linguistics and Literacy Studies, University of Bern
2014	German as a foreign language C1.1	Institute of Linguistics and Literacy Studies, University of Bern
2013	Workshop on Advances in Quantitative Analogue Modeling (AiQAM)	GFZ German Research Centre for Geosciences, Potsdam

*   Swiss Competence Center for Energy Research
**   West Swiss Doctoral School

An appropriate quote to end with

"Ni el libro ni la arena tienen ni principio ni fin"*

Photo: José María "Pepe" Fernández (1969)

Jorge Luis Borges

From: "*El libro de la arena*" (1975)

* "Neither the book nor the sand
have either beginning or end"